
STRUCTURAL APPLICATIONS OF INTERMETALLIC COMPOUNDS

Edited by

J. H. Westbrook

Brookline Technologies, Ballston Spa, New York, USA

and

R. L. Fleischer

Union College, Schenectady, New York, USA

JOHN WILEY & SONS, LTD

Chichester · New York · Weinheim · Brisbane · Singapore · Toronto

Copyright © 2000 by John Wiley & Sons Ltd,
Baffins Lane, Chichester,
West Sussex PO19 1UD, England

National 01243 779777
International (+44) 1243 779777
e-mail (for orders and customer service enquiries): cs-books@wiley.co.uk
Visit our Home Page on <http://www.wiley.co.uk>
or <http://www.wiley.com>

All Rights Reserved. No part of this publication may be reproduced, stored in a retrieval system, or transmitted, in any form or by any means, electronic, mechanical, photocopying, recording, scanning or otherwise, except under the terms of the Copyright, Designs and Patents Act 1988 or under the terms of a licence issued by the Copyright Licensing Agency, 90 Tottenham Court Road, London W1P 9HE, without the permission in writing of the Publisher

Other Wiley Editorial Offices

John Wiley & Sons, Inc., 605 Third Avenue,
New York, NY 10158-0012, USA

WILEY-VCH Verlag GmbH, Pappelallee 3,
D-69469 Weinheim, Germany

Jacaranda Wiley Ltd, 33 Park Road, Milton,
Queensland 4064, Australia

John Wiley & Sons (Asia) Pte Ltd, 2 Clementi Loop #02-01,
Jin Xing Distripark, Singapore 129809

John Wiley & Sons (Canada) Ltd, 22 Worcester Road,
Rexdale, Ontario M9W 1L1, Canada

Library of Congress Cataloging-in-Publication Data

Structural applications of intermetallic compounds / edited by
J. H. Westbrook and R. L. Fleischer.
p. cm.

'This volume is one of four now being published, each of which consists of reprints of chapters from the 1995 comprehensive two-volume set—Intermetallic compounds, principles and practice . . . selected sets of chapters are collected, each set being on a single theme . . . reprint volume 3'—Pref.

Includes bibliographical references and index.

ISBN 0-471-61242-1 (pbk. : alk. paper)—ISBN 0-471-60814-9 (set)

I. Intermetallic compounds. 2. Alloys. I. Westbrook, J. H. (Jack Hall), 1924–
II. Fleischer, R. L. (Robert Louis), 1930– III. Title: Intermetallic compounds.

TA483.S77 2000
620.1'6—dc21

99-052444

British Library Cataloguing in Publication Data

A catalogue record for this book is available from the British Library

ISBN 0 471 61242 1
ISBN 0 471 60814 9 (set)

Typeset by Dobbie Typesetting Ltd, Tavistock, Devon

Printed and bound in Great Britain by Antony Rowe, Chippenham, Wiltshire

This book is printed on acid-free paper responsibly manufactured from sustainable forestry, in which at least two trees are planted for each one used for paper production.

Dedication

To the memory of
John Herbert Hollomon
1919–1985

Wise, vigorous, effective advocate of the relevance and value of scientific research in industry.

His strong belief in the synergetic interaction of Principles and Practice in the field of metallurgy impelled him to assemble an innovative, diverse staff at General Electric, and to inspire independent exploration that benefited both science and engineering.

Contributors

Donald L. Anton
United Technologies Research
Center,
East Hartford,
CT06108, USA



Santosh K. Das
Allied-Signal Co.,
P. O. Box 1021R,
Morristown, NJ 07960,
USA



Alan J. Ardell
Department of Materials Science
and Engineering, University of
California, Los Angeles,
CA 90024-1595, USA



Robert L. Fleischer
Department of Geology
Union College
Schenectady,
NY 12308 USA



Dipankar Banerjee
Defence Metallurgical Research
Laboratory,
Kanchanbagh P.O.
Hyderabad 500258, India



Shyh-Chin Huang,
General Electric Corporate
Research and Development,
P. O. Box 8, K1-MB275,
Schenectady, NY 12302, USA



James C. Chesnutt
GE Aircraft Engines,
1 Neumann Way,
Cincinnati, OH 45215,
USA



Harujuki Inui
Department of Metal Science
and Technology, Kyoto University,
Sakyo-ku,
Kyoto 606, Japan



Ram Darolia
GE Aircraft Engines,
1 Neuman Way,
Cincinnati, 45215, USA



K. Sharvan Kumar
Department of Engineering,
Box D, Brown University,
182 Hope St,
Providence, RI 02912, USA



C. T. Liu

Metals and Ceramics Division,
Oak Ridge National Laboratory,
Oak Ridge, TN 37831-6115,
USA

**Erland M. Schulson**

Thayer School of Engineering,
Dartmouth College,
Hanover,
NH 03755, USA

**Madan G. Mendiratta**

Universal Energy Systems, Inc.,
4401 Dayton-Zenia Road,
Dayton, OH 45432, USA

**Krishna Vedula**

Department of Materials Science
and Engineering,
110 Engineering Annex,
Iowa State University,
AMes, IA 50011, USA

**Daniel B. Miracle**

Air Force Wright Laboratory,
WL/MLLM Building 655,
2230 Tenth St., STE 1,
Wright-Patterson Air Force Base,
Dayton, OH 45433-7817, USA

**Masaharu Yamaguchi**

Department of Metal Science
and Technology,
Kyoto University,
Sakyo-ku, Kyoto 606, Japan

**David P. Pope**

Department of Materials and Science
and Engineering, University of
Pennsylvania, 3231 Walnut Street,
Philadelphia, PA
19104-6272, USA



Preface to the 1995 Edition

Intermetallic compounds were last comprehensively reviewed in 1967 in a volume that was edited by one of us (JHW). At that time the field was described as of special interest because it was undergoing 'exponential proliferation'. That trend continues to the present. The number of intermetallic entries in the Permuterm Subject Index shows a doubling period of less than nine years, having reached roughly 1800 entries per year in 1993. Apart from scholarly interest, intermetallics have now become of substantial commercial significance; for some, such as Ni_3Al , world-wide use is in the 1000s of tons; for others, for example III-V semiconducting compounds, although the quantities employed are not in tonnage numbers, their value as vital components of electronic circuits is in the billions of dollars.

From the 1967 book we remind the reader that 'The first published paper dealing with intermetallic compounds appeared in 1839, and more than sixty years elapsed before . . . the first review paper by Neville in 1900. However, new results were then appearing so rapidly that fifteen years later two books were printed, devoted exclusively to this subject, one by Desch in England and one by Giua and Giua in Italy'. More recently, conference volumes that deal exclusively with intermetallics but typically only within specific, limited sub-topical subject areas have become common. The scope of the present work is as broad as that of its 1967 predecessor. However, the increased volume of activity in intermetallics and the increased significance of their applications have necessitated an expansion from the 27 chapters of the earlier work to the 75 chapters of the present treatise.

First, what are intermetallic compounds? Generally, such a compound is a structure in which the two or more metal constituents are in relatively fixed abundance ratios and are usually ordered on two or more sublattices, each with its own distinct population of atoms. Often substantial or complete disorder may obtain, as a result of low ordering energy or the intervention of some external agency, for example extreme cooling rates, radiation, etc. Deviations from precise stoichiometry are frequently permitted on one or both sides of the nominal ideal atomic ratios, necessitating a partial disorder. Here we include as intermetallic compounds all metal-metal compounds, both ordered and disordered, binary and multicomponent. Even the metal-metal aspect of the definition is often relaxed by including some metal-metalloid compounds, such as silicides, tellurides, and semiconductors. We believe this inclusion is appropriate since the phenomenology of many such compounds is nearly identical to metal-metal ones, and they provide useful examples of principles, properties, and practices.

The burgeoning literature on intermetallics and the lack of a comprehensive single source of up-to-date descriptions of where we are, what we need to know, and what we can do with intermetallics created the incentive for the present pair of volumes. This work was planned to provide state-of-the-art assessments of theory, experiment, and practice that will form a solid base for workers who wish to know more than their own particular area. Each author was asked to set forth the principles of his or her subject in terms that are meaningful to scientists and engineers who are not specialists in the author's field, and then to progress to include knowledge that workers in their own areas would wish to have. Concluding sections of most chapters give the authors' critical assessment of the state of their subject and of where they believe further effort is merited.

This work is divided into two volumes in order that each be of manageable size. The first, on the theme Principles, is directed at the science of intermetallics—how do we understand their formation, structure and properties? The Practice volume considers commercial production and engineering applications of intermetallic compounds. The reader who browses carefully will recognize that the immediacy of the practice described ranges from hoped-for use, to beginnings of use, to actual commercial application—depending on the specific subject. Some of the hoped-for uses are fated never to be realized, but the authors have aimed to reveal what the obstacles are so that the reader may make his or her own assessment (and possibly provide a solution!).

We conferred carefully with many people in order to identify authorities for each subject; having recruited contributors for the project, we then strove to assist them in achieving clarity and thoroughness from outline to draft to final manuscript. The contributors cooperated superbly, and we thank them for their hard work and high achievement. We sought experts wherever they were to be found, and our international set of nearly 100 authors turned out to be almost equally divided between the United States and 14 other countries. Manuscripts have in fact come from all inhabited continents.

We planned this work as an aid to both scientists and engineers. It can serve as a base for those who wish to know about intermetallics as an area in which to begin research. Equally it is a resource to workers who are already active in the field and need, or wish, to expand their knowledge of related science or practical technology. We expect that many chapters are appropriate source matter for special topic or seminar courses at the advanced undergraduate and various graduate school levels. It is hoped that passage of the next 25 years will reveal some influence of this treatise on the further development of this field.

As an assist to readers we have provided in the following pages a consolidated acronym list and some crystallographic tables. Nomenclature for crystal structure types is often complex, and some of the authors have introduced their own. Generally we have asked authors to include both of two commonly used types of symbols as they introduce structures. The two-part table following this preface lists many of the common types—by Strukturbericht symbol, prototype name (termed a *structure type*), and Pearson symbol. Strukturbericht symbols are only partly significant and systematic: A's are not compound structures but consist of a single lattice of atoms (except for A15!); B's are equiatomic ordered structures; C's have 2-to-1 atomic abundance ratios, D0's 3-to-1. Structure type compounds are the specific ones used to designate a particular structure. Thus B2 compounds are also referred to as CsCl compounds. Many structures are better known to metallurgists and mineralogists by names other than the formula of the structure type chosen by crystallographers, e.g. Laves, fluorite, Heusler, etc. Such names have been added in selected cases. The Pearson symbols tell the crystal symmetry and the number of atoms per unit cell. Thus, B2, CsCl has a primitive (P) cubic (c) structure with 2 atoms per cell and hence the Pearson symbol (cP2). The Pearson designation is informative, but it is not necessarily unique. Although there is only one cP2 structure, Villars and Calvert list two cP4s, three cF12s and twenty-two hP9s. Thus to be definitive, both the structure type and the Pearson symbol need to be given, or the Pearson and the Strukturbericht symbol.

The index in each volume includes the subjects in *both* volumes of this work, in order that the reader may be able to locate any subject that is addressed. Although the purpose of such combined indices is not to induce the owner of a single volume to purchase the other, it possibly may help to reduce the barrier to such action.

We have benefited from outstanding secretarial help during the three years of this project, first by Phillis Liu, then Constance Remscheid at General Electric, finally Mary Carey at Rensselaer Polytechnic Institute. We appreciate the hospitality of the General Electric Research and Development Center during the inception and middle period of preparing these volumes. Assembling the final product has been eased for us by the continuing efforts and cheerful good counsel at John Wiley of Jonathan Agbenyega, Irene Cooper, Philip Hastings, Vanessa Lutman and Cliff Morgan.

J. H. WESTBROOK, *Ballston Spa, New York*

R. L. FLEISCHER, *Schenectady, New York*

Upon these considerations, we have been induced to undertake the present extensive work, the purpose of which is to instruct rather than to amuse; in which nothing will be omitted that is elegant or great; but the principal regard will be shown to what is necessary and useful.

—Isaac Ware, 1756

Preface to the Reprint Volumes from Intermetallic Compounds: Principles and Practice

This volume is one of four now being published, each of which consists of reprints of chapters from the 1995 comprehensive two-volume set *Intermetallic Compounds: Principles and Practice*. In the present volumes selected sets of chapters are collected, each set being on a single theme. In this format readers who are interested in a particular aspect of intermetallic compounds can have a less weighty volume specific to their subject; a volume that can be produced more economically than the full, original 1900-page set; and that includes a modest updating of the subject matter.

The subjects in most cases are taken from one or more chapter groupings of the original Volume 1 or 2: Hence reprint volume 1, *Crystal Structures of Intermetallic Compounds*, contains the ten chapters from the original work under the heading Crystal Structures; reprint volume 2, *Basic Mechanical Properties and Lattice Defects of Intermetallic Compounds*, contains three from Property Fundamentals, four chapters from Defect Structures, and two from Kinetics and Phase Transformations; reprint volume 3, *Structural Applications of Intermetallic Compounds* contains the thirteen chapters that were under that same topic; and finally reprint volume 4, *Magnetic, Electrical, and Optical Properties and Applications of Intermetallic Compounds*, contains two chapters from the section on Property Fundamentals, seven from Electromagnetic Applications and one from Miscellaneous. Although each chapter is reprinted nearly intact (only typographic and factual errors corrected), the author or authors were given the option of adding a brief addendum in order to add whatever new perspective has arisen over the intervening few years. Some have chosen to do so; some have not, either in the preferred case because they felt none was needed or because the four-month window of opportunity they were given to satisfy our and the publisher's desire for promptness did not fit their work schedule. Corrections to the original chapters that were so lengthy that they would upset the original pagination are to be found in the addenda at the end of each relevant chapter.

Where an addendum is particularly relevant to a portion of the original chapter being reproduced, a margin mark (*) alerts the reader to refer to the added pages at the end of the chapter. Cross-references to other chapters relate to the original 1995 two-volume work, the tables of contents of which appear at the end of this volume.

JHW
RLF

Acronyms

2D	two-dimensional	BH	buried heterostructure
3D	three-dimensional	BIS	bremsstrahlung isochromat spektroskopie
6D	six-dimensional	BM	Bowles-Mackenzie (theory of martensitic transformation)
ACAR	angular correlation of annihilation radiation	BSCCO	bismuth-strontium-calcium-copper oxide
ACPAR	angular correlation of positron annihilation radiation	BSE	back-scattered electrons
AE	atomic environment	BT	Bhatia-Thornton (partial structure factor for liquid alloys)
AES	Auger electron spectroscopy	BW	Bragg-Williams (theory of ordering)
AET	atomic environment type	BZ	Brillouin zone
AIM	argon induction melting		
ALCHEMI	atom location by channeling enhanced microanalysis	CAM	c-axis modulated
ALE	atomic layer epitaxy	CANDU	Canadian deuterium-uranium (power reactor)
AM	air mass	CAP	consolidated under atmospheric pressure
AMT	Advanced Materials Technology, Inc.	CAT	computer-assisted tomography
AN	atomic number	CBLM	cluster Bethe lattice method
AP	atom probe	CC	cluster center
AP	atomic property	CCD	charge-coupled device
APB	antiphase boundary	CCGSE	concentric-circle grating surface- emitting (laser)
APD	antiphase domain	CCIC	cabled conductor in conduit
APD	avalanche photodetector	CCMAI	crystal chemical model of atomic interactions
APE	atomic property expression	c.c.p.	cubic close-packed
APW	augmented plane wave	CCT	continuous cooling transformation
AR	antireflection	CD	compact disc
ARIPES	angle-resolved inverse photoemission spectroscopy	CD	climb dislocation
ARPES	angle-resolved photoemission spectroscopy	CEBAF	continuous electron-beam accelerator facility
ASA	atomic-sphere approximation	CEF	crystalline electric field
ASW	augmented spherical wave	CERN	Centre Européenne Recherche Nucléaire
BC	bond charge	CFT	concentration-functional theory
b.c.c.	body-centered cubic	CMC	ceramic-matrix composite
BCS	Bardeen-Cooper-Schrieffer (theory of superconductivity)	CN	coördination number
b.c.t.	body-centered tetragonal		

CO	cubo-octahedron	ESR	electroslag refined
CP	coördination polyhedron	ETP	electrolytic tough pitch (copper)
CPA	coherent-potential approximation	EXAFS	extended X-ray absorption fine structure
CRSS	critical resolved shear stress		
CS	chemisorption	f.c.c.	face-centered cubic
CSF	complex stacking fault	f.c.t.	face-centered tetragonal
CSL	coincidence-site lattice	FENIX	Fusion Engineering International Experimental Magnet Facility
CSRO	chemical short-range order		
CT	chisel toughness	FET	field effect transistor
CTE	coefficient of thermal expansion	FIM	field ion microscopy
CVD	chemical vapor deposition	FLAPW	full-potential linearized augmented plane wave
CVM	cluster variation method		
CW	cold worked	FLASTO	full-potential linearized augmented Slater-type orbital
CW	concentration wave		
CW	continuous wave	FLMTO	full-potential linearized muffin-tin orbital
CWM	Connolly-Williams method (theory of phase transformations)	FOM	figure of merit
		FP	Fabry-Perot (laser)
D-A	donor-acceptor	FT	phase transformation
DB	diffusion bonding	FZ	floating zone
DBTT	ductile-brittle transition temperature		
DC	direct chill (casting)	GB	gain \times bandwidth (product)
DC	direct current	GB	grain boundary
DCA	direct configurational averaging	GFT	glass-forming tendency
DF	density functional	GGA	generalized gradient approximation
DFB	distributed feedback	GITT	galvanostatic intermittent titration technique
DFT	density-functional theory		
DH	double heterojunction	GPM	generalized perturbation method
d.h.c.p.	double hexagonal close-packed	GRPA	generalized random-phase approximation
dHvA	de Haas-van Alphen (effect)		
DLZR	directional levitation zone melting	GS	ground state
DOS	density of states	GT	Goody-Thomas (electronegativity)
DPA	displacement per atom		
DPC	demonstration poloidal coil	HB	horizontal Bridgman
DRP	dense random packing	HBT	heterojunction bipolar transistor
DS	directional solidification	HCF	high-cycle fatigue
DSC	displacement shift complete	h.c.p.	hexagonal close-packed
		HEMT	high-electron-mobility transistor
e/a	electron/atom (ratio)	HIP	hot isostatic pressing
EAM	embedded-atom method	HPT	heterojunction phototransmitter
EBPVD	electron beam physical vapor deposition	HR	high resolution
ECI	effective cluster interaction	HREM	high-resolution electron microscopy
ECM	embedded-cluster method	HRTEM	high-resolution transmission electron microscopy
EDC	electro-optic directional coupler	HSCT	high-speed civil transport
EDM	electrodischarge machining	HTS	high-temperature superconductor
EDX	energy-dispersive X-ray (spectroscopy)	HVEM	high-voltage electron microscopy
		HVTEM	high-voltage transmission electron microscopy
EELS	electron energy-loss spectroscopy		
EMF	electromotive force		
EPI	effective pair interaction	IAE	irregular atomic environment
ESF	extrinsic stacking fault	IAET	irregular atomic environment type

IC	integrated circuit	LO	longitudinal optical (wave)
IC	investment cast	LPCVD	low-pressure chemical vapor deposition
IDOS	integrated density of states	LPE	liquid-phase epitaxy
IEM	interstitial-electron model	LPPS	low-pressure plasma spraying
IGC	Intermagnetics General	LPS	long-period superstructure
IHPTET	integrated high-performance turbine engine technology	LRO	long-range order
ILS	invariant line strain	LSDA	local spin-density approximation
IMC	intermetallic compound	LSI	large-scale integration
IMC	intermetallic matrix composite	μ SR	muon spin relaxation
IMC	inverse Monte Carlo (method)	MA	mechanical alloying
IPM	independent-particle method (approximation)	MAPW	modified augmented plane wave
IPS	invariant plan strain	MB	Martinov-Basanov (electronegativity)
IQC	icosahedral quasicrystal	MBE	molecular beam epitaxy
IR	infrared	MBT	metal-base transistor
ISF	intrinsic stacking fault	MC	Monte Carlo
IT	(positive) inner tetrahedron	MCS	Monte Carlo simulation
ITER	International Thermonuclear Experimental Reactor	MD	molecular dynamics
IV	intermediate valence	MEE	migration-enhanced epitaxy
JFET	junction field-effect transistor	MESFET	metal Schottky field-effect transistor
KKR	Korringa-Kohn-Rostoker (bond-calculation method)	MFTF	Mirror Fusion Test Facility
KSV	Khantha-Cserti-Vitek (deformation model)	MISFET	metal-insulator-semiconductor field effect transistor
KTP	potassium titanyl phosphate	MJR	McDonald jelly roll (superconducting cable construction)
KW	Kear-Wilsdorf (dislocation locking mechanism)	MLR	multi-layer reflector
LA	longitudinal acoustic (wave)	MMC	metal-matrix composite
LAPW	linearized augmented plane wave	MN	Mendeleev number
LASTO	linearized augmented Slater-type orbital	MO	magneto-optical
LCAO	linear combination of atomic orbitals	MOCVD	metal-organic chemical vapor deposition
LCF	low-cycle fatigue	MOS	metal-oxide-semiconductor
LCT	large coil task	MOSFET	metal-oxide-semiconductor field effect transistor
LCW	Lock-Crisp-West (radiation analysis)	MOVPE	metal-organic vapor phase epitaxy
LD	laser diode	MQW	multiple quantum well
LDA	local-density approximation	MRI	magnetic resonance imaging
LEC	liquid-encapsulated Czochralski	MRSS	maximum resolved shear stress
LED	light-emitting diode	MRT	orthodontic NiTi alloy
LEED	Low-energy electron diffraction	MT	muffin tin
LEISS	low-energy ion scattering spectroscopy	MTD	martensitic transformation diagram
LHC	Large Hadron Collider	MVA	million volt-amperes
LKKR	Layered KKR (structure calculation)	NASP	National AeroSpace Plane
LME	liquid metal embrittlement	NET	Next European Torus (fusion device)
LMTO	linearized muffin-tin orbital	NHE	normal hydrogen electrode
LNT	liquid nitrogen temperature	NMI	National Maglev Initiative
		NMR	nuclear magnetic resonance
		NN	nearest neighbor
		NNH	nearest-neighbor histogram

NNN	next nearest neighbor	RDS	rate-determining step
NOR	negative OR (logic operator)	RE	rare earth (metal)
NSR	notch/strength ratio	RF	radiofrequency
OAZ	oxidation-affected zone	RHE	reversible hydrogen electrode
ODR	oxygen dissolution reaction	RIM	rigid-ion model
ODS	oxide dispersion-strengthened	RKKY	Ruderman–Kittel–Kasuya–Yoshida (electron interactions)
OEIC	optoelectronic integrated circuit	r.m.s.	root mean square
OH	octahedron	RRR	residual resistivity ratio
ORNL	Oak Ridge National Laboratory	RS	rapidly solidified
OT	(negative) outer tetrahedron	RSP	rapid solidification processing
OTMC	orthorhombic Ti-matrix composites	RSS	resolved shear stress
PAS	positron annihilation spectroscopy	RT	room temperature
PBC	periodic bond chain	RUS	resonance ultrasound spectroscopy
PBT	permeable-base transistor		
PCM	phase-change material	SAD	selected-area diffraction
PCT	pressure–composition–temperature	SAED	selected-area electron diffraction
PD	phase diagram	SAGBO	stress-assisted grain-boundary oxidation
PDF	pair distribution function	SAM-APD	separate absorption and multiplication avalanche photodetector
PDOS	phonon density of states	s.c.	simple cubic
PFC	planar flow casting	SC	semiconductor
PH	<i>Pearson's Handbook</i>	SCE	standard colomel electrode
PHACOMP	phase computation	SCH	separate confinement heterostructures
PKA	primary knock-on atom	SDC	specific damping capacity
PL	photoluminescence	SDW	spin-density wave
PM	powder metallurgy	SEM	scanning electron microscopy
PMTC	phenomenological martensite transformation concept	SESF	superlattice extrinsic stacking fault
PN	periodic number	SF	stacking fault
pnpn	type of photothyristor	SG	spin glass
PPDF	partial pair distribution function	SHS	self-propagating high-temperature synthesis
PPM	path-probability method		
PPV	Paidar–Pope–Vitek (L_{12} hardening model)	SI/VLSI	semi-insulating very large-scale integration
PS	Pearson symbol	SIA	self-interstitial atom
PT	phase transformation	SIC	self-interaction correlation
PTMC	phenomenological theory of martensite crystallography	SIM	stress-induced martensite
PVD	physical vapor deposition	SIMS	secondary-ion mass spectrometry
PZT	lead zirconate titanate (ceramic)	SIS	superconductor–insulator– superconductor
QC	quasicrystal(line)	SISF	superlattice intrinsic stacking fault
QCSE	quantum confined Stark effect	SIT	static inductance transistor
QFD	quantum formation diagram	SM	semimetal
QN	quantum number	SMA	second-moment approximation
QSD	quantum structural diagram	SMA	shape-memory alloy
QW	quantum well	SME	shape-memory effect
		SPF	superplastic forming
		SQUID	superconducting quantum interference device
RBS	Rutherford back scattering	SRO	short-range order
RC	ribbon comminution	SSAR	solid-state amorphizing reaction
RCS	replacement-collision sequence	SSD	structural stability diagram
RDF	radial distribution function		

SSF	superlattice stacking fault	ULSI	ultra large-scale integration
STA	<i>Atlas of Crystal Structure Types</i>	USW	ultrasonic wave
STEM	scanning transmission electron microscopy	UTS	ultimate tensile strength
STM	scanning tunneling microscopy	UV	ultraviolet
SV	Sodani-Vitole change of Paidar <i>et al.</i> model	VAR	vacuum arc refined
		VCSEL	vertical-cavity surface-emitting laser
TA	transverse acoustic (wave)	VEC	valence-electron concentration
TB	tight binding	VGf	vertical gradient freezing
TCP	topologically close-packed	VHF	very high frequency
TD	thoria dispersion	VIM	vacuum induction melting
TDFS	temperature dependence of flow stress	VLS	vapor-liquid-solid
TE	thermoelectric	VLSI	very large-scale integration
TE	transverse electric (field)	VPE	vapor phase epitaxy
TEC	thermoelectric cooler	VPS	vacuum plasma spraying
TEG	thermoelectric generator	VUV	vacuum ultraviolet
TEM	transmission electron microscopy	WB	weak beam
TEP	triethylphosphene	WGPD	waveguide photodetector
TGW	Teatum-Gschneidner-Waber (atomic radius)	WLR	Wechsler-Lieberman-Read (theory of martensitic transformation)
TIP	thermally induced porosity	WS	Wigner-Seitz (cell)
TK	Takeuchi-Kuramoto (dislocation locking mechanism)	WSS	Winterbon-Sigmund-Sanders (model of irradiation damage)
TM	transition metal	wt.ppm	weight parts per million
TM	transverse magnetic (field)		
TMA	titanium-molybdenum-aluminum (alloy)	XC	exchange-correlation
TO	transverse optical (wave)	XD TM	exothermic dispersion (synthesis process)
TPA	two-photon absorption	XIM	X-ray inspection module
TSRO	topological short-range ordering	XPS	X-ray photoelectron spectroscopy
TT	truncated tetrahedron	XRD	X-ray diffraction
TTS	tubular tin source	XUV	extreme ultraviolet
TTT	time-temperature-transformation		
UHF	ultra-high frequency	YAG	yttrium aluminum garnet
UHV	ultra-high vacuum	ZIF	zero insertion force

Crystal Structure Nomenclature*

Arranged Alphabetically by Pearson-Symbol Designation

Pearson symbol	Prototype	Strukturbericht designation	Space group	Pearson symbol	Prototype	Strukturbericht designation	Space group
cF4	Cu	A1	$Fm\bar{3}m$	cP6	Ag ₂ O	C3	$Pn\bar{3}m$
cF8	C (diamond)	A4	$Fd\bar{3}m$	cP7	CaB ₆	D2 ₁	$Pm\bar{3}m$
	NaCl (rock salt)	B1	$Fm\bar{3}m$	cP8	Cr ₃ Si (β W)	A15	$Pm\bar{3}n$
	ZnS (sphalerite)	B3	$F43m$		FeSi	B20	$P2_13$
cF12	CaF ₂ (fluorite)	C1	$Fm\bar{3}m$		Cu ₂ VS ₄ (sylvanite)	H2 ₄	$P43m$
	MgAgAs	C1 _b	$F43m$	cP12	FeS ₂ (pyrite)	C2	$Pa3$
cF16	AlCu ₂ Mn (Heusler)	L2 ₁	$Fm\bar{3}m$		NiSbS (ullmanite)	F0 ₁	$P2_13$
	BiF ₃ (AlFe ₃)	D0 ₃	$Fm\bar{3}m$	cP20	β Mn	A13	$P4_232$
	NaTi	B32	$Fd\bar{3}m$	cP36	BaHg ₁₁	D2 ₂	$Pm\bar{3}m$
cF24	AuBe ₃	C15 _b	$F43m$	cP39	Mg ₂ Zn ₁₁	D8 ₃	$Pm\bar{3}$
	SiO ₂ (β cristobalite)	C9	$Fd\bar{3}m$	cP52	Cu ₉ Al ₄ (γ brass)	D8 ₃	$P43m$
	Cu ₂ Mg (Laves)	C15	$Fd\bar{3}m$	hP1	HgSn ₆₋₁₀	A ₁	$P6/mmm$
cF32	CuPt ₃	L1 _a	$Fm\bar{3}c$	hP2	Mg	A ₃	$P6_3/mmc$
cF52	UB ₁₂	D2 ₇	$Fm\bar{3}m$		WC	B ₄	$P6m2$
cF56	Al ₂ MgO ₄ (spinel)	H1 ₁	$Fd\bar{3}m$	hP3	AlB ₂	C32	$P6/mmm$
	Co ₂ S ₄	D7 ₂	$Fd\bar{3}m$		CdI ₂	C6	$P3m1$
cF68	Co ₂ S ₈	D8 ₈	$Fm\bar{3}m$		Fe ₂ N	L'3	$P6_3/mmc$
cF80	Sb ₂ O ₃ (senarmontite)	D5 ₄	$Fd\bar{3}m$		LiZn ₂	C ₄	$P6_3/mmc$
cF112	Fe ₃ W ₃ C (η carbide)	E9 ₃	$Fd\bar{3}m$		γ Se	A8	$P3_121$
	NaZn ₁₃	D2 ₃	$Fm\bar{3}c$	hP4	α La	A3'	$P6_3/mmc$
cF116	Cr ₂₃ C ₆	D8 ₄	$Fm\bar{3}m$		BN	B ₄	$P6_3/mmc$
	Mn ₂₃ Th ₆ , Cu ₁₆ Mg ₆ Si ₇ (G-phase)	D8 ₄	$Fm\bar{3}m$		C (graphite)	A9	$P6_3/mmc$
cI2	W	A2	$Im\bar{3}m$		NiAs	B8 ₁	$P6_3/mmc$
cI16	CoU	B ₂	$I2_13$		ZnS (wurtzite)	B4	$P6_3mc$
cI28	Th ₃ P ₄	D7 ₃	$I43d$	hP5	La ₂ O ₃	D5 ₂	$P3m1$
cI32	CoAs ₃ (skutterudite)	D0 ₃	$Im\bar{3}$		Ni ₂ Al ₃	D5 ₁₃	$P3m1$
cI40	Ge ₂ Ir ₃	D8 ₇	$Im\bar{3}m$	hP6	CaCu ₃	D2 ₄	$P6/mmm$
	Pu ₂ C ₃	D5 ₅	$I43d$		CoSn	B35	$P6/mmm$
cI52	Cu ₂ Zn ₈ (γ brass)	D8 ₂	$I43m$		Cu ₂ Te	C ₄	$P6/mmm$
	Fe ₃ Zn ₁₀ (γ brass)	D8 ₁	$Im\bar{3}m$		HgS	B9	$P3_121$
cI54	Sb ₂ Tl ₇	L2 ₂	$Im\bar{3}m$		MoS ₂	C7	$P6_3/mmc$
cI58	α Mn (χ -phase)	A12	$I43m$		Ni ₂ In	B8 ₂	$P6_3/mmc$
cI76	Cu ₁₅ Si ₄	D8 ₆	$I43d$	hP8	Na ₃ As	D0 ₁₈	$P6_3/mmc$
cI80	Mn ₂ O ₃	D5 ₃	$Ia\bar{3}$		Ni ₃ Sn	D0 ₁₉	$P6_3/mmc$
cI96	AlLi ₃ N ₂	E9 ₄	$Ia\bar{3}$		TiAs	B ₁	$P6_3/mmc$
cI162	Mg ₃₂ (Al,Zn) ₂₉	D8 ₆	$Im\bar{3}$	hP9	CrSi ₂	C40	$P6_222$
cP1	α Po	A ₁	$Pm\bar{3}m$		Fe ₂ P	C22	$P62m$
cP2	CsCl	B2	$Pm\bar{3}m$		ζ AgZn	B ₃	$P3$
cP4	AuCu ₃	L1 ₂	$Pm\bar{3}m$		SiO ₂ (high quartz)	C8	$P6_222$
	ReO ₃	D0 ₃	$Pm\bar{3}m$	hP10	Pt ₂ Sn ₃	D5 ₃	$P6_3/mmc$
cP5	AlFe ₃ C (perovskite)	L1' ₂	$Pm\bar{3}m$	hP12	CuS	B18	$P6_3/mmc$
	CaTiO ₃ (perovskite)	E2 ₁	$Pm\bar{3}m$		MgZn ₂ (Laves)	C14	$P6_3/mmc$
	Fe ₄ N	L1'	$P43m$		SiO ₂ (β tridymite)	C10	$P6_3/mmc$

continued

*Adapted (with additions and corrections) from *ASM Handbook*, Vol. 3, 10th ed, ASM International, Materials Park, OH.

Arranged Alphabetically by Pearson-Symbol Designation (*continued*)

Pearson symbol	Prototype	Strukturbericht designation	Space group	Pearson symbol	Prototype	Strukturbericht designation	Space group
<i>hP</i> 14	W ₂ B ₃	<i>D</i> 8 _h	<i>P</i> 6 ₃ / <i>mmc</i>	<i>oP</i> 8	βCu ₂ Ti	<i>D</i> 0 ₁	<i>Pmmn</i>
<i>hP</i> 16	Mn ₂ Si ₃	<i>D</i> 8 _h	<i>P</i> 6 ₃ / <i>mcm</i>		FeB	<i>B</i> 27	<i>Pnma</i>
	Ni ₃ Ti	<i>D</i> 0 ₂₄	<i>P</i> 6 ₃ / <i>mmc</i>		GeS	<i>B</i> 16	<i>Pnma</i>
<i>hP</i> 18	Al ₃ C ₂ Si	<i>E</i> 9 _h	<i>P</i> 6 ₃ / <i>mc</i>		SnS	<i>B</i> 29	<i>Pmcn</i>
	Al ₃ FeMg ₃ Si ₆	<i>E</i> 9 _h	<i>P</i> 6 ₂ / <i>m</i>		MnP	<i>B</i> 31	<i>Pnma</i>
	Mg ₂ Ni	<i>C</i> ₂	<i>P</i> 6 ₂ / <i>22</i>		TiB	<i>B</i> ₂	<i>Pnma</i>
<i>hP</i> 20	Fe ₃ Th ₇	<i>D</i> 10 ₂	<i>P</i> 6 ₃ / <i>mc</i>	<i>oP</i> 12	Co ₂ Si, NiSiTi (E-phase)	<i>C</i> 23	<i>Pnma</i>
	Th ₃ S ₁₂	<i>D</i> 8 _h	<i>P</i> 6 ₃ / <i>m</i>		Co ₂ Si	<i>C</i> 37	<i>Pbnm</i>
<i>hP</i> 24	Cu ₃ P	<i>D</i> 0 ₂₁	<i>P</i> 6 ₃ / <i>cm</i>		HgCl ₂	<i>C</i> 28	<i>Pmnb</i>
	MgNi ₃ (Laves)	<i>C</i> 36	<i>P</i> 6 ₃ / <i>mmc</i>	<i>oP</i> 16	Al ₃ Ni	<i>D</i> 0 ₂₀	<i>Pnma</i>
<i>hP</i> 28	Co ₂ Al ₃	<i>D</i> 8 ₁₁	<i>P</i> 6 ₃ / <i>mmc</i>		AsMn ₃	<i>D</i> 0 ₄	<i>Pmmn</i>
<i>hR</i> 1	αHg	<i>A</i> 10	<i>R</i> 3̄ <i>m</i>		BaS ₃	<i>D</i> 0 ₁₇	<i>P</i> 42/ <i>m</i>
	βPo	<i>A</i> ₁	<i>R</i> 3̄ <i>m</i>		CdSb	<i>B</i> ₂	<i>Pbca</i>
<i>hR</i> 2	αAs	<i>A</i> ₇	<i>R</i> 3̄ <i>m</i>		CuS ₂ Sb (wolfsbergite)	<i>F</i> ₅	<i>Pnma</i>
<i>hR</i> 3	αSm	<i>C</i> 19	<i>R</i> 3̄ <i>m</i>		Fe ₃ C (cementite)	<i>D</i> 0 ₁₁	<i>Pnma</i>
<i>hR</i> 4	NaCrS ₂	<i>F</i> 5 ₁	<i>R</i> 3̄ <i>m</i>	<i>oP</i> 20	Cr ₃ C ₂	<i>D</i> 5 ₁₀	<i>Pnma</i>
<i>hR</i> 5	Bi ₃ Te ₃	<i>C</i> 33	<i>R</i> 3̄ <i>m</i>		Sb ₂ S ₃	<i>D</i> 5 ₃	<i>Pnma</i>
	Ni ₃ S ₂	<i>D</i> 5 ₁	<i>R</i> 3̄ <i>2</i>		Sb ₂ O ₃ (valentinite)	<i>D</i> 5 ₁₁	<i>Pccn</i>
<i>hR</i> 6	CaSi ₂	<i>C</i> 12	<i>R</i> 3̄ <i>m</i>	<i>oP</i> 24	AuTe ₂ (krennerite)	<i>C</i> 46	<i>Pma</i> 2
	NiS (millerite)	<i>B</i> 13	<i>R</i> 3̄ <i>m</i>		CuFe ₂ S ₃ (cubanite)	<i>E</i> 9 ₂	<i>Pnma</i>
<i>hR</i> 7	Al ₄ C ₃	<i>D</i> 7 ₁	<i>R</i> 3̄ <i>m</i>		TiO ₂ (brookite)	<i>C</i> 21	<i>Pbca</i>
	Mo ₂ B ₃	<i>D</i> 8 ₁	<i>R</i> 3̄ <i>m</i>	<i>oP</i> 40	Cr ₃ C ₃	<i>D</i> 10 ₁	<i>Pnma</i>
<i>hR</i> 10	αAl ₂ O ₃ (corundum)	<i>D</i> 5 ₁	<i>R</i> 3̄ <i>c</i>	<i>II</i> 2	αPa	<i>A</i> ₂	<i>I</i> 4/ <i>mmm</i>
<i>hR</i> 12	BaPb ₃		<i>R</i> 3̄ <i>m</i>		In	<i>A</i> 6	<i>I</i> 4/ <i>mmm</i>
<i>hR</i> 13	Fe ₇ W ₆ (μ-phase)	<i>D</i> 8 ₃	<i>R</i> 3̄ <i>m</i>	<i>II</i> 4	βSn	<i>A</i> 5	<i>I</i> 4/ <i>amd</i>
<i>hR</i> 15	B ₄ C	<i>D</i> 1 ₂	<i>R</i> 3̄ <i>m</i>	<i>II</i> 6	CaC ₂	<i>C</i> 11 ₁	<i>I</i> 4/ <i>mmm</i>
<i>hR</i> 20	HoAl ₃		<i>R</i> 3̄ <i>m</i>		MoSi ₂	<i>C</i> 11 ₂	<i>I</i> 4/ <i>mmm</i>
<i>hR</i> 26	Cr ₂ Al ₃	<i>D</i> 8 ₁₀	<i>R</i> 3̄ <i>m</i>	<i>II</i> 8	ThH ₂	<i>L</i> ₂ ²	<i>I</i> 4/ <i>mmm</i>
<i>hR</i> 32	CuPt	<i>L</i> 1 ₁	<i>R</i> 3̄ <i>m</i>	<i>II</i> 10	Al ₃ Ti	<i>D</i> 0 ₂₂	<i>I</i> 4/ <i>mmm</i>
<i>mC</i> 6	AuTe ₂ (calaverite)	<i>C</i> 34	<i>C</i> 2/ <i>m</i>		Al ₃ Ba	<i>D</i> 1 ₃	<i>I</i> 4/ <i>mmm</i>
<i>mC</i> 8	CuO (tenorite)	<i>B</i> 26	<i>C</i> 2/ <i>c</i>	<i>II</i> 12	MoNi ₄	<i>D</i> 1 ₁	<i>I</i> 4/ <i>m</i>
<i>mC</i> 12	ThC ₂	<i>C</i> ₂	<i>C</i> 2/ <i>c</i>		Al ₃ Cu	<i>C</i> 16	<i>I</i> 4/ <i>mcm</i>
<i>mC</i> 14	δNi ₃ Sn ₄	<i>D</i> 7 ₂	<i>C</i> 2/ <i>m</i>	<i>II</i> 14	ThSi ₂	<i>C</i> ₃	<i>I</i> 4/ <i>amd</i>
<i>mC</i> 16	FeKS ₂	<i>F</i> 5 ₂	<i>C</i> 2/ <i>c</i>	<i>II</i> 16	Al ₃ CdS ₄	<i>E</i> ₃	<i>I</i> 4
<i>mP</i> 12	AgAuTe ₂ (sylvanite)	<i>E</i> 1 ₁	<i>P</i> 2/ <i>c</i>		Al ₃ Zr	<i>D</i> 0 ₂₃	<i>I</i> 4/ <i>mmm</i>
	ZrO ₂	<i>C</i> 43	<i>P</i> 2 ₁ / <i>c</i>		CuFeS ₂ (chalcopyrite)	<i>E</i> 1 ₁	<i>I</i> 42 <i>d</i>
	As ₂ S ₃	<i>D</i> 5 ₁	<i>P</i> 2 ₁ / <i>c</i>		Cu ₂ FeSnS ₄ (stannite)	<i>H</i> 2 ₂	<i>I</i> 42 <i>m</i>
<i>mP</i> 20	Co ₂ Al ₃	<i>D</i> 8 ₄	<i>P</i> 2 ₁ / <i>c</i>		Ir ₂ Si	<i>D</i> 0 ₁	<i>I</i> 4/ <i>mcm</i>
<i>mP</i> 22	FeAsS	<i>E</i> 0 ₁	<i>P</i> 2 ₁ / <i>c</i>		MoB	<i>B</i> ₂	<i>I</i> 4/ <i>amd</i>
<i>mP</i> 24	AsS (realgar)	<i>B</i> ₁	<i>P</i> 2 ₁ / <i>c</i>	<i>II</i> 18	SiU ₃	<i>D</i> 0 ₁	<i>I</i> 4/ <i>mcm</i>
	βSe	<i>A</i> ₁	<i>P</i> 2 ₁ / <i>c</i>		TiSe	<i>B</i> 37	<i>I</i> 4/ <i>mcm</i>
<i>mP</i> 64	αSe	<i>A</i> ₂	<i>P</i> 2 ₁ / <i>c</i>	<i>II</i> 26	Fe ₃ N	<i>D</i> 2 ₂	<i>I</i> 4/ <i>mmm</i>
<i>oC</i> 4	αU	<i>A</i> 20	<i>Cmcm</i>	<i>II</i> 28	Mn ₁₂ Th	<i>D</i> 2 ₂	<i>I</i> 4/ <i>mmm</i>
<i>oC</i> 8	CaSi	<i>B</i> ₂	<i>Cmcm</i>	<i>II</i> 32	MnU ₆	<i>D</i> 2 ₂	<i>I</i> 4/ <i>mcm</i>
	αGa	<i>A</i> 11	<i>Cmca</i>		Cr ₃ B ₃	<i>D</i> 8 ₁	<i>I</i> 4/ <i>mcm</i>
	CrB	<i>B</i> 33	<i>Cmcm</i>		Ni ₃ P	<i>D</i> 0 ₁	<i>I</i> 4
	I ₂	<i>A</i> 14	<i>Cmca</i>	<i>tP</i> 2	W ₂ Si ₃	<i>D</i> 8 ₂	<i>I</i> 4/ <i>mcm</i>
	P (black)	<i>A</i> 17	<i>Cmca</i>	<i>tP</i> 4	δCuTi	<i>L</i> 2 ₂	<i>P</i> 4/ <i>mmm</i>
<i>oC</i> 12	ZrSi ₂	<i>C</i> 49	<i>Cmcm</i>		βNp	<i>A</i> ₂	<i>P</i> 42 ₂
<i>oC</i> 16	BRe ₃	<i>E</i> 1 ₂	<i>Cmcm</i>		AuCu	<i>L</i> 1 ₀	<i>P</i> 4/ <i>mmm</i>
<i>oC</i> 20	PdSn ₄	<i>D</i> 1 ₁	<i>Aba</i> 2		CuTi ₃	<i>L</i> 6 ₀	<i>P</i> 4/ <i>mmm</i>
<i>oC</i> 24	PdSn ₂	<i>C</i> ₂	<i>Aba</i> 2		γCuTi	<i>B</i> 11	<i>P</i> 4/ <i>nm</i>
<i>oC</i> 28	Al ₂ Mn	<i>D</i> 2 ₁	<i>Cmcm</i>		PbO	<i>B</i> 10	<i>P</i> 4/ <i>nm</i>
<i>oF</i> 24	TiSi ₂	<i>C</i> 54	<i>Fddd</i>		Pb ₂ Sr		<i>P</i> 4/ <i>nm</i>
<i>oF</i> 40	Mn ₂ B	<i>D</i> 1 ₁	<i>Fddd</i>	<i>tP</i> 6	PtS	<i>B</i> 17	<i>P</i> 4 ₂ / <i>mmc</i>
<i>oF</i> 48	CuMg ₂	<i>C</i> ₂	<i>Fddd</i>		Cu ₂ Sb	<i>C</i> 38	<i>P</i> 4/ <i>nm</i>
<i>oF</i> 72	GeS ₂	<i>C</i> 44	<i>Fdd</i> 2		PbFCl	<i>E</i> 0 ₁	<i>P</i> 4/ <i>nm</i>
<i>oF</i> 128	αS	<i>A</i> 16	<i>Fddd</i>	<i>tP</i> 10	TiO ₂ (rutile)	<i>C</i> 4	<i>P</i> 4 ₂ / <i>nm</i>
<i>oI</i> 12	SiS ₂	<i>C</i> 42	<i>Ibam</i>		Pb ₂ Pt	<i>D</i> 1 ₁	<i>P</i> 4/ <i>nbm</i>
<i>oI</i> 14	Ta ₃ B ₃	<i>D</i> 7 ₁	<i>Immm</i>	<i>tP</i> 16	Si ₂ U ₃	<i>D</i> 5 ₁	<i>P</i> 4/ <i>mbm</i>
<i>oI</i> 20	Al ₃ U	<i>D</i> 1 ₁	<i>Imma</i>	<i>tP</i> 20	PdS	<i>B</i> 34	<i>P</i> 4 ₂ / <i>m</i>
<i>oI</i> 28	Ga ₂ Mg ₅	<i>D</i> 8 ₂	<i>Ibam</i>	<i>tP</i> 30	B ₂ Th	<i>D</i> 1 ₁	<i>P</i> 4/ <i>mbm</i>
<i>oP</i> 4	AuCd	<i>B</i> 19	<i>Pnma</i>		βU	<i>A</i> ₂	<i>P</i> 4 ₂ / <i>nm</i>
<i>oP</i> 6	FeS ₂ (marcasite)	<i>C</i> 18	<i>Pnnm</i>	<i>tP</i> 40	αCrFe	<i>D</i> 8 ₂	<i>P</i> 4 ₂ / <i>nm</i>
	CaCl ₂	<i>C</i> 35	<i>Pnnm</i>		Al ₃ Cu ₂ Fe	<i>E</i> 9 ₂	<i>P</i> 4/ <i>mnc</i>
<i>oP</i> 8	αNp	<i>A</i> ₂	<i>Pnma</i>	<i>tP</i> 50	Zn ₃ P ₂	<i>D</i> 5 ₂	<i>P</i> 4 ₂ / <i>nm</i>
	ηNiSi	<i>B</i> ₂	<i>Pbnm</i>		γB	<i>A</i> ₂	<i>P</i> 4 ₂ / <i>nm</i>

Arranged Alphabetically by Strukturbericht Designation

Struktur- bericht designation	Prototype	Pearson symbol	Space group	Struktur- bericht designation	Prototype	Pearson symbol	Space group
<i>A_a</i>	αPa	<i>tI</i> 2	<i>I</i> 4/ <i>mmm</i>	<i>B</i> 20	FeSi	<i>cP</i> 8	<i>P</i> 2 ₁ 3
<i>A_b</i>	βU	<i>tP</i> 30	<i>P</i> 4 ₂ / <i>mnm</i>	<i>B</i> 26	CuO (tenorite)	<i>mC</i> 8	<i>C</i> 2/ <i>c</i>
<i>A_c</i>	αNp	<i>oP</i> 8	<i>Pnma</i>	<i>B</i> 27	FeB	<i>oP</i> 8	<i>Pnma</i>
<i>A_d</i>	βNp	<i>tP</i> 4	<i>P</i> 42 ₂	<i>B</i> 29	SnS	<i>oP</i> 8	<i>Pmcn</i>
<i>A_f</i>	HgSn ₆₋₁₀	<i>hP</i> 1	<i>P</i> 6/ <i>mmm</i>	<i>B</i> 31	MnP	<i>oP</i> 8	<i>Pnma</i>
<i>A_g</i>	γB	<i>tP</i> 50	<i>P</i> 4 ₂ / <i>nnm</i>	<i>B</i> 32	NaTl	<i>cF</i> 16	<i>Fd</i> 3̄ <i>m</i>
<i>A_h</i>	αPo	<i>cP</i> 1	<i>Pm</i> 3̄ <i>m</i>	<i>B</i> 33(= <i>B_f</i>)	CrB	<i>oC</i> 8	<i>Cmcm</i>
<i>A_i</i>	βPo	<i>hR</i> 1	<i>R</i> 3̄ <i>m</i>	<i>B</i> 34	PdS	<i>tP</i> 16	<i>P</i> 4 ₂ / <i>m</i>
<i>A_k</i>	αSe	<i>mP</i> 64	<i>P</i> 2 ₁ / <i>c</i>	<i>B</i> 35	CoSn	<i>hP</i> 6	<i>P</i> 6/ <i>mmm</i>
<i>A_l</i>	βSe	<i>mP</i> 32	<i>P</i> 2 ₁ / <i>c</i>	<i>B</i> 37	TlSe	<i>tI</i> 16	<i>I</i> 4/ <i>mcm</i>
<i>A</i> 1	Cu	<i>cF</i> 4	<i>Fm</i> 3̄ <i>m</i>	<i>C_a</i>	Mg ₂ Ni	<i>hP</i> 18	<i>P</i> 6 ₂ 22
<i>A</i> 2	W	<i>cI</i> 2	<i>Im</i> 3̄ <i>m</i>	<i>C_b</i>	CuMg ₂	<i>oF</i> 48	<i>Fddd</i>
<i>A</i> 3	Mg	<i>hP</i> 2	<i>P</i> 6 ₃ / <i>mmc</i>	<i>C_c</i>	ThSi ₂	<i>tI</i> 12	<i>I</i> 4 ₁ / <i>amd</i>
<i>A</i> 3'	αLa	<i>hP</i> 4	<i>P</i> 6 ₃ / <i>mmc</i>	<i>C_e</i>	PdSn ₂	<i>oC</i> 24	<i>Aba</i> 2
<i>A</i> 4	C (diamond)	<i>cF</i> 8	<i>Fd</i> 3̄ <i>m</i>	<i>C_f</i>	ThC ₂	<i>mC</i> 12	<i>C</i> 2/ <i>c</i>
<i>A</i> 5	βSn	<i>tI</i> 4	<i>I</i> 4 ₁ / <i>amd</i>	<i>C_g</i>	Cu ₂ Te	<i>hP</i> 6	<i>P</i> 6/ <i>mmm</i>
<i>A</i> 6	In	<i>tI</i> 2	<i>I</i> 4/ <i>mmm</i>	<i>C_h</i>	LiZn ₂	<i>hP</i> 3	<i>P</i> 6 ₃ / <i>mmc</i>
<i>A</i> 7	αAs	<i>hR</i> 2	<i>R</i> 3̄ <i>m</i>	<i>C</i> 1	CaF ₂ (fluorite)	<i>cF</i> 12	<i>Fm</i> 3̄ <i>m</i>
<i>A</i> 8	γSe	<i>hP</i> 3	<i>P</i> 3 ₂ 1	<i>C</i> 1 _b	MgAgAs	<i>cF</i> 12	<i>F</i> 43 <i>m</i>
<i>A</i> 9	C (graphite)	<i>hP</i> 4	<i>P</i> 6 ₃ / <i>mmc</i>	<i>C</i> 2	FeS ₂ (pyrite)	<i>cP</i> 12	<i>Pa</i> 3
<i>A</i> 10	αHg	<i>hR</i> 1	<i>R</i> 3̄ <i>m</i>	<i>C</i> 3	Ag ₂ O	<i>cP</i> 6	<i>Pn</i> 3̄ <i>m</i>
<i>A</i> 11	αGa	<i>oC</i> 8	<i>Cmca</i>	<i>C</i> 4	TiO ₂ (rutile)	<i>tP</i> 6	<i>P</i> 4 ₂ / <i>mnm</i>
<i>A</i> 12	αMn (χ-phase)	<i>cI</i> 58	<i>I</i> 43 <i>m</i>	<i>C</i> 6	CdI ₂	<i>hP</i> 3	<i>P</i> 3̄ <i>m</i> 1
<i>A</i> 13	βMn	<i>cP</i> 20	<i>P</i> 4 ₃ 2	<i>C</i> 7	MoS ₂	<i>hP</i> 6	<i>P</i> 6 ₃ / <i>mmc</i>
<i>A</i> 14	I ₂	<i>oC</i> 8	<i>Cmca</i>	<i>C</i> 8	SiO ₂ (high quartz)	<i>hP</i> 9	<i>P</i> 6 ₂ 22
<i>A</i> 15	Cr ₃ Si (β-W)	<i>cP</i> 8	<i>Pm</i> 3̄ <i>n</i>	<i>C</i> 9	SiO ₂ (β cristobalite)	<i>cF</i> 24	<i>Fd</i> 3̄ <i>m</i>
<i>A</i> 16	αS	<i>oF</i> 128	<i>Fddd</i>	<i>C</i> 10	SiO ₂ (β tridymite)	<i>hP</i> 12	<i>P</i> 6 ₃ / <i>mmc</i>
<i>A</i> 17	P (black)	<i>oC</i> 8	<i>Cmca</i>	<i>C</i> 11 _a	CaC ₂	<i>tI</i> 6	<i>I</i> 4/ <i>mmm</i>
<i>A</i> 20	αU	<i>oC</i> 4	<i>Cmcm</i>	<i>C</i> 11 _b	MoSi ₂	<i>tI</i> 6	<i>I</i> 4/ <i>mmm</i>
<i>B_a</i>	CoU	<i>cI</i> 16	<i>I</i> 2 ₁ 3	<i>C</i> 12	CaSi ₂	<i>hR</i> 6	<i>R</i> 3̄ <i>m</i>
<i>B_b</i>	†AgZn	<i>hP</i> 9	<i>P</i> 3	<i>C</i> 14	MgZn ₂	<i>hP</i> 12	<i>P</i> 6 ₃ / <i>mmc</i>
<i>B_c</i>	CaSi	<i>oC</i> 8	<i>Cmcm</i>	<i>C</i> 15	Cu ₂ Mg } Laves	<i>cF</i> 24	<i>Fd</i> 3̄ <i>m</i>
<i>B_d</i>	ηNiSi	<i>oP</i> 8	<i>Pbnm</i>	<i>C</i> 15 _b	AuBe ₃	<i>cF</i> 24	<i>F</i> 43 <i>m</i>
<i>B_e</i>	CdSb	<i>oP</i> 16	<i>Pbca</i>	<i>C</i> 16	Al ₂ Cu	<i>tI</i> 12	<i>I</i> 4/ <i>mcm</i>
<i>B_f</i> (= <i>B</i> 33)	CrB	<i>oC</i> 8	<i>Cmcm</i>	<i>C</i> 18	FeS ₂ (marcasite)	<i>oP</i> 6	<i>Pnnm</i>
<i>B_g</i>	MoB	<i>tI</i> 16	<i>I</i> 4 ₁ / <i>amd</i>	<i>C</i> 19	αSm	<i>hR</i> 3	<i>R</i> 3̄ <i>m</i>
<i>B_h</i>	WC	<i>hP</i> 2	<i>P</i> 6̄ <i>m</i> 2	<i>C</i> 21	TiO ₂ (brookite)	<i>oP</i> 24	<i>Pbca</i>
<i>B_i</i>	TiAs	<i>hP</i> 8	<i>P</i> 6 ₃ / <i>mmc</i>	<i>C</i> 22	Fe ₂ P	<i>hP</i> 9	<i>P</i> 6̄2 <i>m</i>
<i>B_k</i>	BN	<i>hP</i> 4	<i>P</i> 6 ₃ / <i>mmc</i>	<i>C</i> 23	Co ₂ Si, NiSiTi (E-phase)	<i>oP</i> 12	<i>Pnma</i>
<i>B_l</i>	AsS (realgar)	<i>mP</i> 32	<i>P</i> 2 ₁ / <i>c</i>	<i>C</i> 28	HgCl ₂	<i>oP</i> 12	<i>Pmnb</i>
<i>B_m</i>	TiB	<i>oP</i> 8	<i>Pnma</i>	<i>C</i> 32	AlB ₂	<i>hP</i> 3	<i>P</i> 6/ <i>mmm</i>
<i>B</i> 1	NaCl (rock salt)	<i>cF</i> 8	<i>Fm</i> 3̄ <i>m</i>	<i>C</i> 33	Bi ₂ Te ₃	<i>hR</i> 5	<i>R</i> 3̄ <i>m</i>
<i>B</i> 2	CsCl	<i>cP</i> 2	<i>Pm</i> 3̄ <i>m</i>	<i>C</i> 34	AuTe ₂ (calaverite)	<i>mC</i> 6	<i>C</i> 2/ <i>m</i>
<i>B</i> 3	ZnS (sphalerite)	<i>cF</i> 8	<i>F</i> 43 <i>m</i>	<i>C</i> 35	CaCl ₂	<i>oP</i> 6	<i>Pnnm</i>
<i>B</i> 4	ZnS (wurtzite)	<i>hP</i> 4	<i>P</i> 6 ₃ / <i>mc</i>	<i>C</i> 36	MgNi ₂ (Laves)	<i>hP</i> 24	<i>P</i> 6 ₃ / <i>mmc</i>
<i>B</i> 8 ₁	NiAs	<i>hP</i> 4	<i>P</i> 6 ₃ / <i>mmc</i>	<i>C</i> 37	Co ₂ Si	<i>oP</i> 12	<i>Pbnm</i>
<i>B</i> 8 ₂	Ni ₂ In	<i>hP</i> 6	<i>P</i> 6 ₃ / <i>mmc</i>	<i>C</i> 38	Cu ₂ Sb	<i>tP</i> 6	<i>P</i> 4/ <i>nmm</i>
<i>B</i> 9	HgS (cinnabar)	<i>hP</i> 6	<i>P</i> 3 ₂ 1	<i>C</i> 40	CrSi ₂	<i>hP</i> 9	<i>P</i> 6 ₂ 22
<i>B</i> 10	PbO	<i>tP</i> 4	<i>P</i> 4/ <i>nmm</i>	<i>C</i> 42	SiS ₂	<i>oI</i> 12	<i>Ibam</i>
<i>B</i> 11	γCuTi	<i>tP</i> 4	<i>P</i> 4/ <i>nmm</i>	<i>C</i> 43	ZrO ₂	<i>mP</i> 12	<i>P</i> 2 ₁ / <i>c</i>
<i>B</i> 13	NiS (millerite)	<i>hR</i> 6	<i>R</i> 3̄ <i>m</i>	<i>C</i> 44	GeS ₂	<i>oF</i> 72	<i>Fdd</i> 2
<i>B</i> 16	GeS	<i>oP</i> 8	<i>Pnma</i>	<i>C</i> 46	AuTe ₂ (krennerite)	<i>oP</i> 24	<i>Pma</i> 2
<i>B</i> 17	PtS (cooperite)	<i>tP</i> 4	<i>P</i> 4 ₂ / <i>mmc</i>	<i>C</i> 49	ZrSi ₂	<i>oC</i> 12	<i>Cmcm</i>
<i>B</i> 18	CuS (rovelite)	<i>hP</i> 12	<i>P</i> 6 ₃ / <i>mmc</i>	<i>C</i> 54	TiSi ₂	<i>oF</i> 24	<i>Fddd</i>
<i>B</i> 19	AuCd	<i>oP</i> 4	<i>Pmma</i>	<i>D</i> 0 _a	βCu ₂ Ti	<i>oP</i> 8	<i>Pmmn</i>
				<i>D</i> 0 _c	SiU ₃	<i>tI</i> 16	<i>I</i> 4/ <i>mcm</i>

continued

Arranged Alphabetically by Strukturbericht Designation (*continued*)

Struktur- bericht designation	Prototype	Pearson symbol	Space group	Struktur- bericht designation	Prototype	Pearson symbol	Space group
D0 ₁	Ir ₂ Si	<i>tI</i> 16	<i>I4/mcm</i>	D8 _d	Co ₂ Al ₉	<i>mP</i> 22	<i>P2₁/c</i>
D0 ₂	AsMn ₃	<i>oP</i> 16	<i>Pmmn</i>	D8 _e	Mg ₃₂ (Al,Zn) ₄₈	<i>cI</i> 162	<i>Im</i> $\bar{3}$
D0 ₃	Ni ₃ P	<i>tI</i> 32	<i>I</i> $\bar{4}$	D8 _f	Ge ₂ Ir ₃	<i>cI</i> 40	<i>Im</i> $\bar{3}m$
D0 ₄	CoAs ₃ (skutterudite)	<i>cI</i> 32	<i>Im</i> $\bar{3}$	D8 _g	Ga ₂ Mg ₅	<i>oI</i> 28	<i>Ibam</i>
D0 ₅	BiF ₃ , AlFe ₃	<i>cF</i> 16	<i>Fm</i> $\bar{3}m$	D8 _h	W ₂ B ₅	<i>hP</i> 14	<i>P6₃/mmc</i>
D0 ₆	ReO ₃	<i>cP</i> 4	<i>Pm</i> $\bar{3}m$	D8 _i	Mo ₂ B ₅	<i>hR</i> 7	<i>R</i> $\bar{3}m$
D0 ₁₁	Fe ₃ C (cementite)	<i>oP</i> 16	<i>Pnma</i>	D8 _k	Th ₂ Si ₁₂	<i>hP</i> 20	<i>P6₃/m</i>
D0 ₁₇	BaS ₃	<i>oP</i> 16	<i>P4₂/m</i>	D8 _l	Cr ₂ B ₃	<i>tI</i> 32	<i>I4/mcm</i>
D0 ₁₈	Na ₃ As	<i>hP</i> 8	<i>P6₃/mmc</i>	D8 _m	W ₂ Si ₃	<i>tI</i> 32	<i>I4/mcm</i>
D0 ₁₉	Ni ₃ Sn	<i>hP</i> 8	<i>P6₃/mmc</i>	D8 _n	Fe ₃ Zn ₁₀	<i>cI</i> 52	<i>Im</i> $\bar{3}m$
D0 ₂₀	Al ₃ Ni	<i>oP</i> 16	<i>Pnma</i>	D8 ₂	Cu ₃ Zn ₈	<i>cI</i> 52	<i>I</i> $\bar{4}3m$
D0 ₂₁	Cu ₃ P	<i>hP</i> 24	<i>P6₃/cm</i>	D8 ₃	Cu ₃ Al ₄	<i>cP</i> 52	<i>P</i> $\bar{4}3m$
D0 ₂₂	Al ₃ Ti	<i>tI</i> 8	<i>I4/mmm</i>	D8 ₄	Cr ₂ C ₆	<i>cF</i> 116	<i>Fm</i> $\bar{3}m$
D0 ₂₃	Al ₃ Zr	<i>tI</i> 16	<i>I4/mmm</i>	D8 ₅	Fe ₂ W ₆ (μ -phase)	<i>hR</i> 13	<i>R</i> $\bar{3}m$
D0 ₂₄	Ni ₃ Ti	<i>hP</i> 16	<i>P6₃/mmc</i>	D8 ₆	Cu ₁₃ Si ₄	<i>cI</i> 76	<i>I</i> $\bar{4}3d$
D1 _a	MoNi ₄	<i>tI</i> 10	<i>I4/m</i>	D8 ₈	Mn ₂ Si ₃	<i>hP</i> 16	<i>P6₃/mcm</i>
D1 _b	Al ₃ U	<i>oI</i> 20	<i>Imma</i>	D8 ₉	Co ₃ Si ₃	<i>cF</i> 68	<i>Fm</i> $\bar{3}m$
D1 _c	PdSn ₄	<i>oC</i> 20	<i>Aba</i> 2	D8 ₁₀	Cr ₃ Al ₄	<i>hR</i> 26	<i>R</i> $\bar{3}m$
D1 _d	Pb ₃ Pt	<i>tP</i> 10	<i>P4/nbm</i>	D8 ₁₁	Co ₂ Al ₃	<i>hP</i> 28	<i>P6₃/mmc</i>
D1 _e	B ₄ Th	<i>tP</i> 20	<i>P4/mbm</i>	D10 ₁	Cr ₂ C ₃	<i>oP</i> 40	<i>Pnma</i>
D1 _f	Mn ₄ B	<i>oF</i> 40	<i>Fddd</i>	D10 ₂	Fe ₂ Th	<i>hP</i> 20	<i>P6₃/mc</i>
D1 _g	B ₄ C	<i>hR</i> 15	<i>R</i> $\bar{3}m$	E0 ₁	PbFCl	<i>tP</i> 6	<i>P4/nmm</i>
D1 _h	Al ₃ Ba	<i>tI</i> 10	<i>I4/mmm</i>	E0 ₂	FeAsS	<i>mP</i> 24	<i>P2₁/c</i>
D2 _a	Mn ₁₂ Th	<i>tI</i> 26	<i>I4/mmm</i>	E1 _a	MgCuAl ₂	<i>oC</i> 16	<i>Cmcm</i>
D2 _b	MnU ₆	<i>tI</i> 28	<i>I4/mcm</i>	E1 _b	AgAuTe ₄ (sylvanite)	<i>mP</i> 12	<i>P2₁/c</i>
D2 _c	CaCu ₂	<i>hP</i> 6	<i>P6/mmm</i>	E1 _c	CuFeS ₂ (chalcopyrite)	<i>tI</i> 16	<i>I</i> $\bar{4}2d$
D2 _d	BaHg ₁₁	<i>cP</i> 36	<i>Pm</i> $\bar{3}m$	E2 ₁	CaTiO ₃ (perovskite)	<i>cP</i> 5	<i>Pm</i> $\bar{3}m$
D2 _e	UB ₂	<i>cF</i> 52	<i>Fm</i> $\bar{3}m$	E3	Al ₂ CdS ₄	<i>tI</i> 14	<i>I</i> $\bar{4}$
D2 _f	Fe ₂ N	<i>tI</i> 18	<i>I4/mmm</i>	E9 _a	Al ₃ Cu ₂ Fe	<i>tP</i> 40	<i>P4/mnc</i>
D2 _g	Al ₆ Mn	<i>oC</i> 28	<i>Cmcm</i>	E9 _b	Al ₃ FeMg ₃ Si ₆	<i>hP</i> 18	<i>P</i> $\bar{6}2m$
D2 _h	CaB ₆	<i>cP</i> 7	<i>Pm</i> $\bar{3}m$	E9 _c	Mn ₃ Al ₃ Si	<i>hP</i> 26	<i>P6₃/mmc</i>
D2 _i	NaZn ₁₃	<i>cF</i> 112	<i>Fm</i> $\bar{3}c$	E9 _d	AlLi ₃ N ₂	<i>cI</i> 96	<i>Ia</i> $\bar{3}$
D5 _a	Si ₃ U ₃	<i>tP</i> 10	<i>P4/mbm</i>	E9 _e	CuFe ₂ S ₃ (cubanite)	<i>oP</i> 24	<i>Pnma</i>
D5 _b	Pt ₂ Sn ₃	<i>hP</i> 10	<i>P6₃/mmc</i>	E9 _f	Fe ₂ W ₃ C (η carbide)	<i>cF</i> 112	<i>Fd</i> $\bar{3}m$
D5 _c	Pu ₂ C ₃	<i>cI</i> 40	<i>I</i> $\bar{4}3d$	E9 _g	Al ₄ C ₃ Si	<i>hP</i> 18	<i>P6₃/mc</i>
D5 _d	Ni ₃ S ₂	<i>hR</i> 5	<i>R</i> $\bar{3}2$	F0 ₁	NiSbS (ullmanite)	<i>cP</i> 12	<i>P2₁/3</i>
D5 _e	As ₂ S ₃	<i>mP</i> 20	<i>P2₁/c</i>	F5 _a	FeKS ₂	<i>mC</i> 16	<i>C2/c</i>
D5 _f	α -Al ₂ O ₃ (corundum)	<i>hR</i> 10	<i>R</i> $\bar{3}c$	F5 _b	NaCrS ₂	<i>hR</i> 4	<i>R</i> $\bar{3}m$
D5 _g	La ₂ O ₃	<i>hP</i> 5	<i>P</i> $\bar{3}m$ 1	F5 _c	CuS ₂ Sb (wolfsbergite)	<i>oP</i> 16	<i>Pnma</i>
D5 _h	Mn ₂ O ₃	<i>cI</i> 80	<i>Ia</i> $\bar{3}$	H1 ₁	Al ₂ MgO ₄ (spinel)	<i>cF</i> 56	<i>Fd</i> $\bar{3}m$
D5 _i	Sb ₂ O ₃ (senarmontite)	<i>cF</i> 80	<i>Fd</i> $\bar{3}m$	H2 ₁	Cu ₃ VS ₄ (sylvanite)	<i>cP</i> 8	<i>P</i> $\bar{4}3m$
D5 _j	Sb ₃ S ₃	<i>oP</i> 20	<i>Pnma</i>	H2 ₂	Cu ₂ FeSnS ₄	<i>tI</i> 16	<i>I</i> $\bar{4}2m$
D5 _k	Zn ₃ P ₂	<i>tP</i> 40	<i>P4₂/nmc</i>	L1 ₁	Fe ₂ N	<i>cP</i> 5	<i>Pm</i> $\bar{3}m$
D5 _l	Cr ₃ C ₂	<i>oP</i> 20	<i>Pnma</i>	L1 ₂	CuPt ₃	<i>cF</i> 32	<i>Fm</i> $\bar{3}c$
D5 _m	Sb ₂ O ₃ (valentinite)	<i>oP</i> 20	<i>Pccn</i>	L1 ₃	AuCu	<i>tP</i> 4	<i>P4/mmm</i>
D5 _n	Ni ₂ Al ₃	<i>hP</i> 5	<i>P</i> $\bar{3}m$ 1	L1 ₄ (M)	AuCuII	<i>oI</i> 40	<i>Imma</i>
D7 _a	δ -Ni ₃ Sn ₄	<i>mC</i> 14	<i>C2/m</i>	L1 ₅	CuPt	<i>hR</i> 32	<i>R</i> $\bar{3}m$
D7 _b	Ta ₂ B ₄	<i>oI</i> 14	<i>Immm</i>	L1 ₆	AuCu ₂	<i>cP</i> 4	<i>Pm</i> $\bar{3}m$
D7 _c	Al ₄ C ₃	<i>hR</i> 7	<i>R</i> $\bar{3}m$	L1 ₇	AlFe ₃ C (perovskite)	<i>cP</i> 5	<i>Pm</i> $\bar{3}m$
D7 _d	Co ₃ S ₂	<i>cF</i> 56	<i>Fd</i> $\bar{3}m$	L2 ₁	δ -CuH ₂	<i>tP</i> 2	<i>P4/mmm</i>
D7 _e	Th ₃ P ₄	<i>cI</i> 28	<i>I</i> $\bar{4}3d$	L2 ₂	ThH ₂	<i>tI</i> 6	<i>I4/mmm</i>
D8 _a	Mn ₂₃ Th ₆ , Cu ₁₆ Mg ₆ Si ₇ (G-phase)	<i>cF</i> 116	<i>Fm</i> $\bar{3}m$	L2 ₃	AlCu ₂ Mn (Heusler)	<i>cF</i> 16	<i>Fm</i> $\bar{3}m$
D8 _b	σ -CrFe	<i>tP</i> 30	<i>P4₂/nmm</i>	L2 ₄	Sb ₂ Tl ₂	<i>cI</i> 54	<i>Im</i> $\bar{3}m$
D8 _c	Mg ₂ Zn ₁₁	<i>cP</i> 39	<i>Pm</i> $\bar{3}$	L3 ₁	Fe ₂ N	<i>hP</i> 3	<i>P6₃/mmc</i>
				L6 ₀	CuTi ₃	<i>tP</i> 4	<i>P4/mmm</i>

Chapter 10

Silicides: Science, Technology and Applications

K. Sharvan Kumar

Martin Marietta Laboratories, Baltimore, MD 21227, USA
Present address: Department of Engineering, Box D, Brown University,
182 Hope St, Providence, RI 02912, USA

1. Introduction

It is perhaps fair to start this chapter by saying that no other single family of intermetallics has enjoyed as diverse a popularity as the silicides. Interests in silicides include using them as high-temperature structural materials for advanced aerospace applications, heating elements (in high-temperature furnaces) and as protective high-temperature coatings particularly for refractory metals. In microelectric devices, thin silicide layers are used as contacts and interconnections because they have lower electrical resistivity than polycrystalline silicon and are compatible with the silicon substrate. When metal thin films are brought in contact with silicon substrates, the interaction results in the formation of silicides at the interface at fairly low temperatures and the thermodynamics and kinetics of the formation of such silicides have been examined. The high melting points and the good oxidation resistance of semiconducting disilicides (disilicides of Cr, Mn and Fe) are desirable properties for thermoelectric generators converting solar into electrical energy (Vedernikov, Chapter 20 in this volume). Likewise, disilicides may be useful as thermocouples in strongly corrosive environments where their chemical inertness is a critical asset. In terms of magnetic properties, silicides of the first long period transition metals are all paramagnetic with susceptibilities similar to those of the elementary transition metals, whereas silicides of the heavier transition elements are diamagnetic, with zirconium disilicide possessing a particularly large diamagnetism. Fe_3Si (see Stadelmaier and Reinsch, Chapter 14, for a discussion of $\text{Fe}_3(\text{Al}, \text{Si})$ magnets) and Fe_5Si_3 have been confirmed to be ferromagnetic (Fe_3Si has a Curie point of ~ 805 K). Several silicides exhibit superconductivity (e.g.

V_3Si , CoSi_2 , Mo_3Si , PtSi , PdSi and Th_2Si_3), and of these V_3Si exhibits a particularly high transition temperature of 17.1 K (Stekly and Gregory, Chapter 16 in this volume).

When a metallurgist begins to think about silicides, the first technological application that comes to mind is the use of MoSi_2 as furnace elements under the trade name 'Super Kanthal'. These furnace elements are available in various hairpin shapes and roughly constitute 80% MoSi_2 and the remaining 20% by volume mainly a glass phase. MoSi_2 has two important characteristics as an electric heating element. First, its resistivity increases with temperature, which means that if a new batch of charge is introduced in the furnace leading to a temperature drop, the power output of the elements rises rapidly and automatically, increasing the heat-up rate. Unlike SiC elements, resistivity does not alter as time proceeds. In addition, the elements will accept high watt loads at high temperatures so that high amounts of power can be concentrated in small areas. The second feature is the ability of MoSi_2 to form a highly protective, adhesive layer of silica glass on its surface during operation that is nonspalling and self-healing. Thus, the life spans of 'Super Kanthal' elements are typically measurable in years.

Recently, refractory metal silicides have drawn considerable attention for structural applications, although research is primarily geared towards multiphase materials where the second phase is either another silicide or a metallic species that is either in thermodynamic equilibrium with the silicide under consideration (e.g. $\text{Nb-Nb}_5\text{Si}_3$ or $\text{Cr-Cr}_3\text{Si}$) or artificially introduced with the hope of capitalizing on possible nonreactivity or sluggish kinetics. The metallic species introduced artificially can be either discontinuous (e.g. particulates)

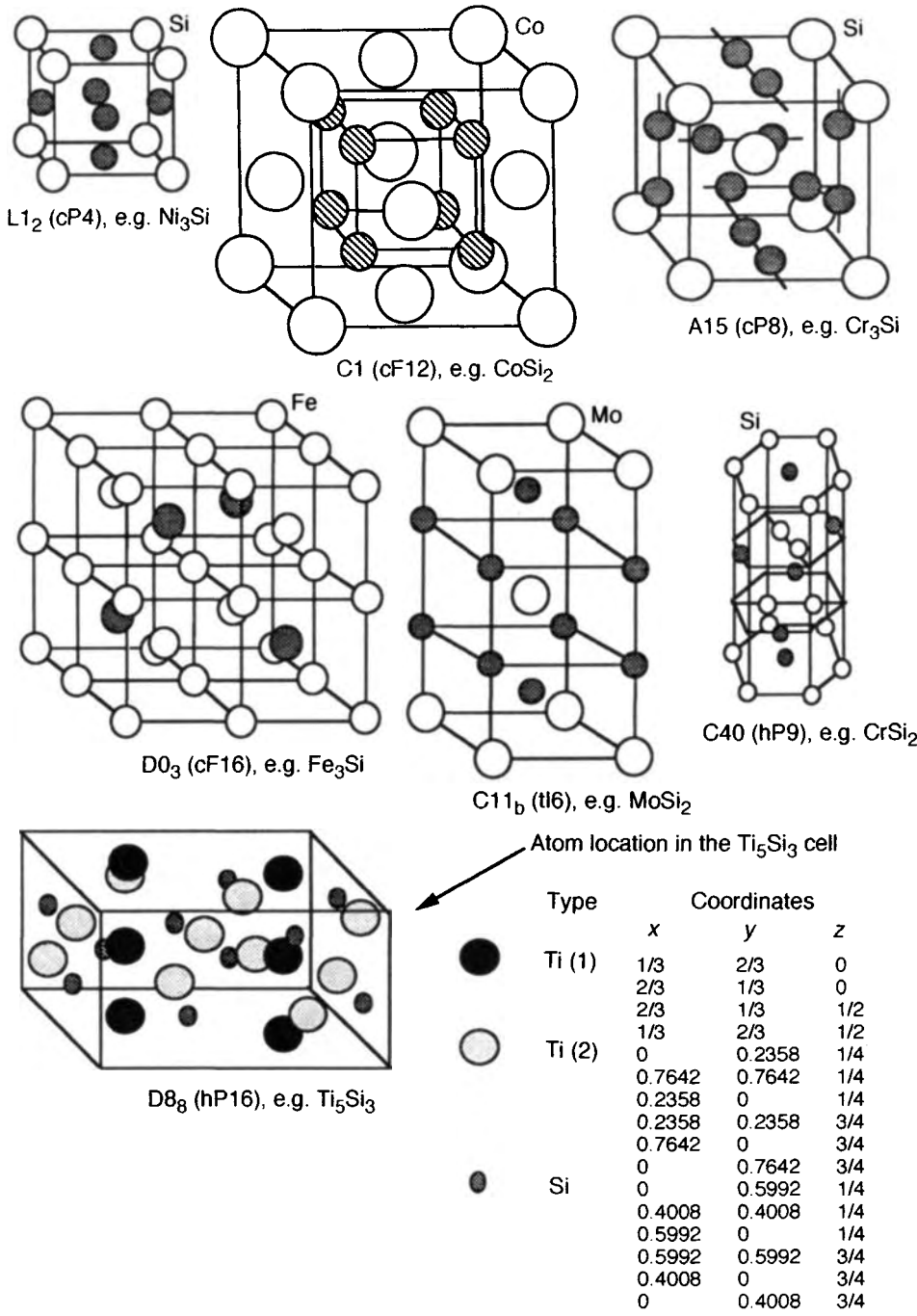


Figure 1. Hard-sphere models of crystal structures commonly encountered with silicides

or continuous (e.g. W wires). Alternatively, research has also been directed towards incorporating brittle ceramic second phases (e.g. SiC whiskers in MoSi₂) with the intention of taking advantage of toughening mechanisms such as crack deflection and whisker pull-out. These approaches are necessary to provide the desired damage tolerance to these refractory silicides that are otherwise brittle, frequently up to *ca* 1073–1273 K (Miracle and Mendiratta, Chapter 13 in this volume).

The oxidation resistance of silicides is key to using them as successful high-temperature coatings. Understanding the operating oxidation mechanisms and relating the oxidation kinetics to the structures and compositions of oxide films formed under various exposure conditions constitute the central research theme.

The formation of silicides by the interaction between thin metal films and silicon has been extensively studied because of its vital role in integrated circuit technology. Examples of the use of silicides include Schottky barrier diodes, ohmic contacts and metallization of gates and interconnects. Epitaxially grown CoSi₂ and NiSi₂ are used in novel devices like the metal-base transistors (MBT) and the permeable-base transistors (PBT). The silicides of Pt, Pd and Ir are suitable candidates for infrared (i.r.) detectors, and PtSi i.r. detectors have reached a commercial stage and are used in cameras today.

In this chapter, the physical metallurgy and mechanical properties of these silicides are reviewed with particular emphasis on their deformation modes, the effect of alloying and hence microstructure on the measured properties, their response to environment and their application potential. The next section focuses on the structural silicides and includes: (i) Group VIII transition metal silicides (Ni₃Si, Fe₃Si, CoSi₂ and NiSi₂); and (ii) refractory metal silicides of Mo, Cr, Ti, Nb and Zr. The third section is geared towards silicides as

high-temperature coating materials. The role of silicides in microelectronic devices and in the electronics industry constitutes the fourth section. With respect to the organization of this chapter, it is relevant to point out that some of these silicides (e.g. CoSi₂ and NiSi₂) have been characterized for both structural and microelectronics applications and the requirements in these cases are very different. Physical metallurgy and mechanical behavior of these compounds are covered in the structural silicide section, whereas thermal, magnetic and electrical properties are reviewed in the microelectronic devices section. Hard-sphere models of the crystal structures of several silicides are provided in Figure 1, and physical properties of some silicides, including density, melting point, Poisson's ratio, Young's modulus, shear modulus and bulk modulus are included in Table 1.

2. Structural Silicides

2.1 Group VIII Transition Metal Silicides

The binary compound Ni₃Si with an L1₂ (cP4) crystal structure exhibits an increasing yield stress with increasing temperature (Thornton and Davies, 1970), low room-temperature ductility and good oxidation resistance. Its excellent corrosion resistance in acidic aqueous solutions has made it the basis for several commercial alloys (e.g. Hastelloy D®) designed for such corrosion resistance (Kumar, 1985).

The major drawback with these alloys is that they exhibit low room-temperature ductility and poor fabricability, restricting usage to the cast condition. Nieh and Oliver (1989) have demonstrated superplasticity in these alloys in the temperature range 1273–1373 K over a wide strain-rate range, achieving as much as 650%

Table 1. Physical properties of silicides

Silicide	Structure	Density (g cm ⁻³)	T _m (K)	Elastic modulus E (GPa)	Shear modulus G (GPa)	Poisson's ratio ν
Cr ₃ Si	A15 (cP8)	6.54	2043	351	137	0.286
V ₃ Si	A15 (cP8)	5.62	2198	213	81.9	0.298
MoSi ₂	C11 _b (tI6)	6.2	2353	440	191	0.15
WSi ₂	C11 _b (tI6)	9.86	2438	468	204	0.14
CrSi ₂	C40 (hP9)	5.00	1823	347	147	0.18
VSi ₂	C40 (hP9)	4.63	2023	331	142	0.167
V ₃ Si ₃	D8 _m (tI32)	5.27	2283	257	101	0.271
TiSi ₂	C54 (oF24)	4.39	1773	265	115	—
CoSi ₂	C1 (cF12)	4.95	1600	116	—	—
Ti ₅ Si ₃	D8 ₈ (hP16)	4.32	2403	~150	—	—

elongation, the dominant mechanism being grain boundary sliding.

Weak-beam electron microscopy studies (Tounsi *et al.*, 1989) of polycrystalline, binary Ni_3Si revealed that the activated slip systems changed progressively from octahedral to cubic with increasing temperature in the temperature range where the positive strength dependence was observed. Specifically, progressive exhaustion of octahedral slip by thermally activated expansion of superdislocations on the cube cross-slip plane controls the flow stress. Binary Ni_3Si exhibits intergranular failure at room temperature and Auger electron spectroscopic examination revealed no obvious grain boundary segregation, leading to the conclusion that these boundaries are intrinsically brittle (Takasugi *et al.*, 1985). Small additions of B to Ni_3Si improve the ductility, but not as dramatically as in Ni_3Al (Taub and Briant, 1987).

Parallel efforts to improve the ductility of Ni_3Si by ternary alloying revealed that Ti substitution for Si not only significantly enhanced ductility but also suppressed the polymorphic transformations that occur in binary Ni_3Si between its melting point and its order-disorder transformation at ~ 1310 K (Williams, 1971; Oya and Suzuki, 1983; Ochia, Oya, and Suzuki, 1984). This latter feature helped overcome the difficulties involved in growing single crystals of binary Ni_3Si using the Bridgman technique. Up to 11% Ti dissolves in Ni_3Si with Ti substituting for Si (Takasugi *et al.*, 1990). The solid solubilities of various other alloying elements in Ni_3Si at 1173 K were determined (Zhang *et al.*, 1991) and their substitution modes were deduced from the way the single-phase field lobes extended in the ternary isotherm.

The microstructure and deformation behavior of $\text{Ni}_3(\text{Si}, \text{Ti})$, both in the single crystal and polycrystalline form, with and without further alloying, have been systematically characterized; the effect of the test environment on these properties has also been examined for alloys with and without boron doping. Some of the results of these investigations are shown in Figures 2 to 5. The variations in the compressive yield strength versus temperature profiles for ternary single-phase alloys containing 9.0 at% Ti and various Ni levels (Figure 2a) revealed that lowering the Ni content from 80 at% to 78 at% significantly influenced the strength over the entire temperature range examined (Takasugi, Nagashima, and Izumi, 1990). This effect, however, was shown not to be as drastic for a Ti level of 11.3 at%. When the Ni content was fixed at 78 at% and the Ti content was varied from 0 to 11.3 at%, it was found that not only was strength affected but also the temperature

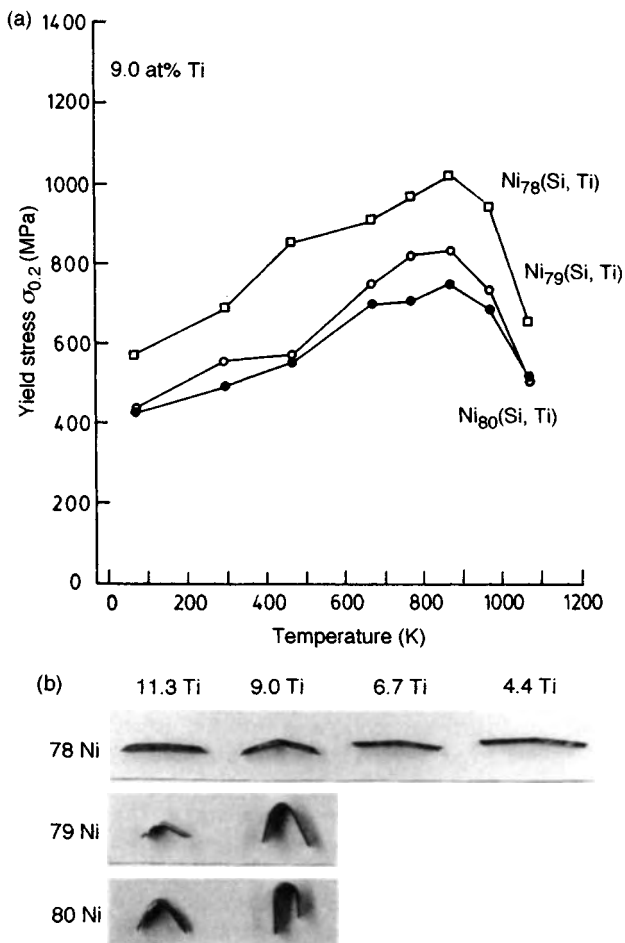


Figure 2. The effect of stoichiometry on the mechanical properties of $\text{Ni}_3(\text{Si}, \text{Ti})$: (a) compressive yield strength versus temperature; (b) bend ductility at room temperature. Reprinted with permission from Takasugi *et al.*, *Acta Metall. Mater.*, **38**, 747. Copyright (1990) Pergamon Press Ltd

of the peak strength shifted. The influence of ternary alloying on the ductility of the L_{12} compound is illustrated in Figure 2(b) which shows bend tests conducted on ternary alloys containing various levels of Ti and Ni. The relevance of alloy stoichiometry and Ti content on ductility is evident. Single-crystal compression studies (Takasugi *et al.*, 1989; Yoshida and Takasugi, 1991, 1992) revealed octahedral slip at all temperatures for single crystals oriented close to $[001]$, whereas octahedral slip below the peak temperature and cube slip above the peak temperature were reported in specimens oriented close to $[011]$ and $[111]$. At temperatures below the yield stress peak of 673 K, screw dislocations of $\mathbf{b} = [101]$ were dissociated into

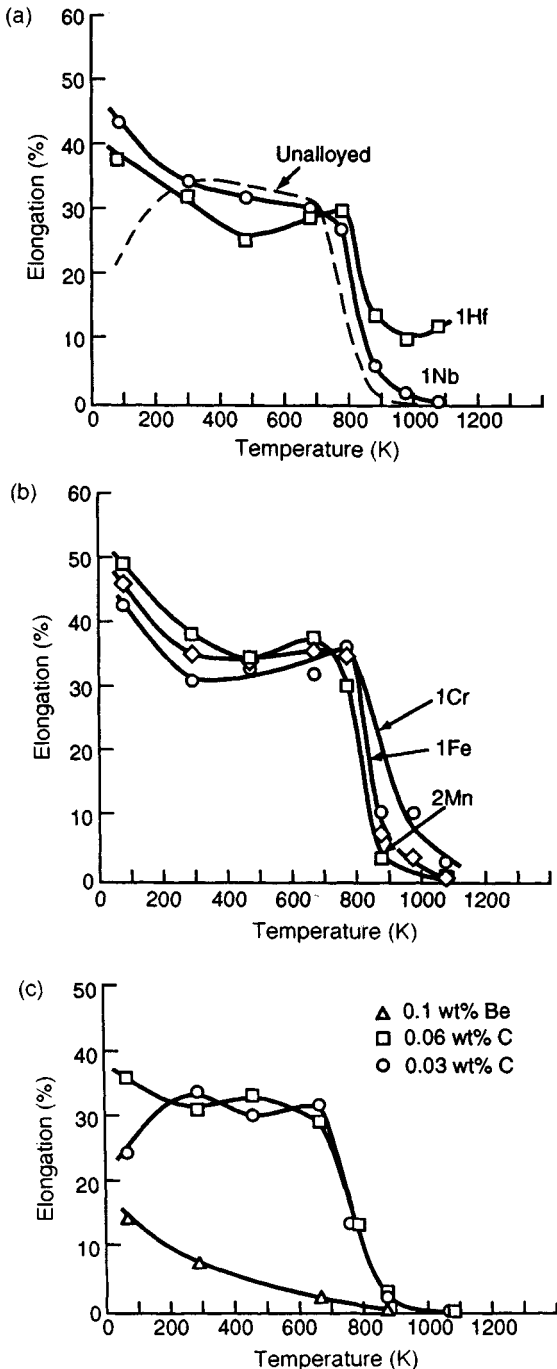


Figure 3. The effect of minor quaternary alloying on the tensile elongation-temperature profile of $\text{Ni}_3(\text{Si}, \text{Ti})$ in vacuum: (a) Hf and Nb additions; (b) Cr, Mn and Fe additions; and (c) C and Be additions (reproduced by permission of Chapman and Hall from Takasugi and Yoshida, 1991a)

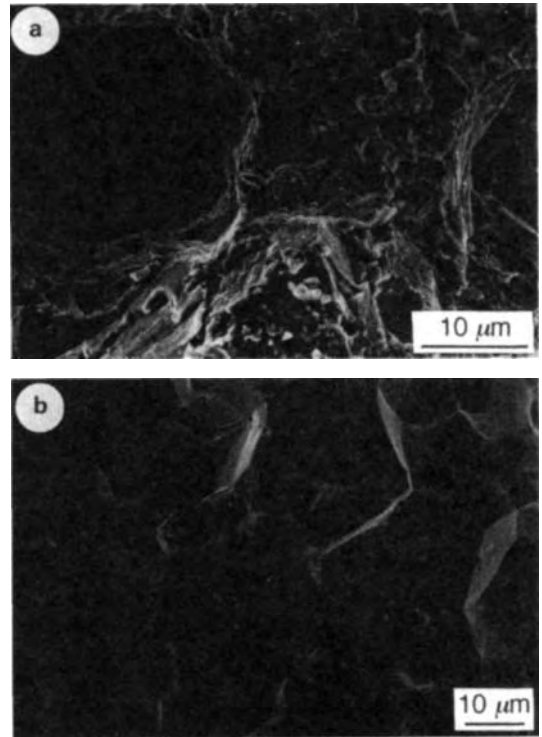


Figure 4. The 1073 K tensile fracture surfaces of $\text{Ni}_3(\text{Si}, \text{Ti})$ containing minor amounts of (a) Hf and (b) Nb (reproduced by permission of Chapman and Hall from Takasugi and Yoshida, 1991a)

$\frac{1}{2}$ [101] superpartials bounding an antiphase boundary (APB). At temperatures of 293 K and 77 K the features were very similar, although at 77 K a fourfold dissociation was noted with Shockley partials bounding an APB and complex stacking faults (CSF). Above the peak temperature where cube slip dominated, edge dislocations along [110] were observed to transform into Lomer-Cottrell locks and a tendency for loop formation was noted.

The effect of minor quaternary alloying (Hf, Nb, Cr, Mn, Fe, C, Be) on the tensile properties of $\text{Ni}_3(\text{Si}, \text{Ti})$ has been studied (Takasugi and Yoshida, 1991a, b), and while a significant improvement in strength was not observed for Hf, Nb, C or Be additions, the Cr, Mn and Fe additions caused a decrease in strength in the positive temperature dependence range and also a 'Co₃Ti-like' profile (i.e a gradual increase in strength at low temperatures) rather than a profile like that observed for ternary $\text{Ni}_3(\text{Si}, \text{Ti})$. These alloying additions, however, significantly influenced tensile ductility, as can be seen in Figure 3 where the reported data are for tests

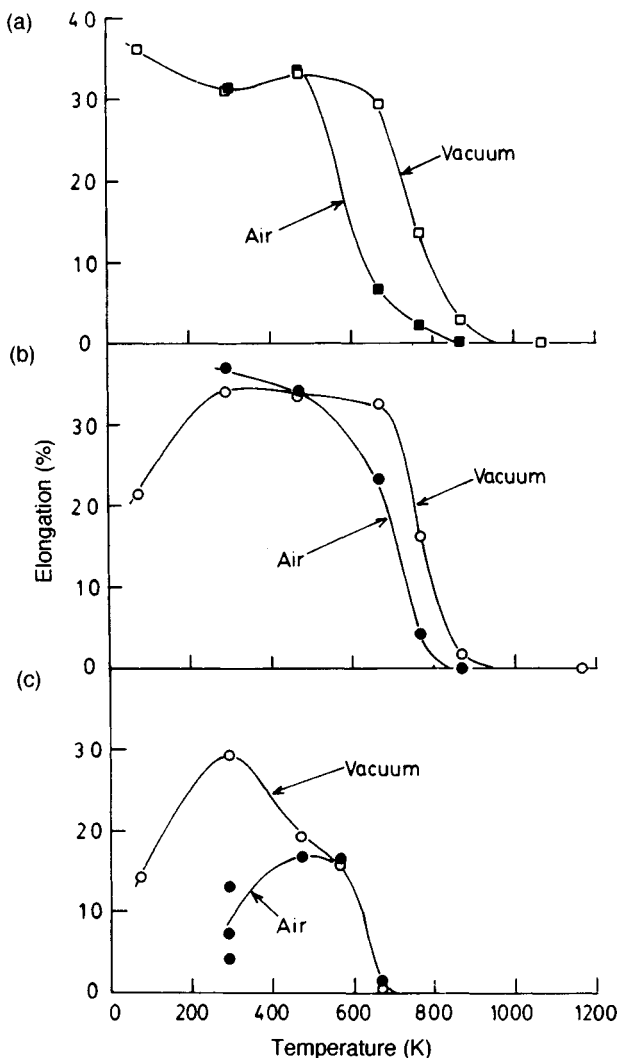


Figure 5. The effect of test environment on the tensile elongation-temperature profiles for (a) carbon-doped $\text{Ni}_3(\text{Si}, \text{Ti})$, (b) $\text{Ni}_3(\text{Si}, \text{Ti})$ containing B, and (c) unalloyed $\text{Ni}_3(\text{Si}, \text{Ti})$ (reproduced by permission of Chapman and Hall from Takasugi and Yoshida, 1991b)

conducted in vacuum. The addition of Hf and Nb produced a remarkable enhancement in ductility at 77 K over the ternary counterpart, although from room temperature to ~800 K a loss in ductility is noted for the Hf-containing alloy. At 1073 K, where the ternary alloy loses all its ductility, the Hf addition is beneficial, permitting the retention of significant ductility (Figure 3a). A similar trend is observed for the Cr, Mn and Fe additions, with the exception that at 1073 K only Cr is

effective in restoring ductility to the ternary alloy, but not to the same extent as Hf (Figure 3b). Carbon addition (0.06 wt%) produces some ductility enhancement at 77 K over the unalloyed material (compare Figure 3c with 3a), although ductility is lost completely in the C-containing alloys at temperatures exceeding 1073 K (Figure 3c). Beryllium addition has, by far, the worst effect on ductility, causing ductility loss over the whole range of temperature (Figure 3c). The 1073 K fracture surfaces for the Hf-containing and Nb-containing alloys are compared in Figure 4. While intergranular faceting is observed in both cases, the facets are smooth and clean in the Nb-containing alloy, whereas in the Hf-containing alloy ductile features are observed on the facets which are reminiscent of dynamic recrystallization.

The effect of environment on the ductility at various temperatures of C-doped and B-doped $\text{Ni}_3(\text{Si}, \text{Ti})$ and unalloyed $\text{Ni}_3(\text{Si}, \text{Ti})$ is shown in Figure 5. At ambient temperature in both the C-doped and B-doped alloys, ductility is not affected by the environment, whereas in the undoped material a significant ductility loss is noted when tested in air. This is attributed to hydrogen embrittlement. The loss in ductility at high temperature for the undoped material appears to be independent of environment, whereas the C-doped and B-doped alloys indicated a ductility loss at lower temperatures in air than in vacuum. Various speculative arguments have been provided to explain these observations at high temperatures (Takasugi and Yoshida, 1991b; Takasugi, Suenaga, and Izumi, 1991). The effect of B addition was also concluded to be harmful (Takasugi, Rijukawa, and Hanada, 1991) to the superplastic formability of $\text{Ni}_3(\text{Si}, \text{Ti})$. The effects of Hf, Zr and Ta additions on the creep resistance of $\text{Ni}_3(\text{Si}, \text{Ti})$ have been investigated, and it was shown that Hf and Zr enhanced creep ductility and creep rupture time, whereas Ta reduced the creep rate (Hasegawa *et al.*, 1991).

Although the binary compound NiSi_2 with the cubic C1 (cF12) structure (calcium fluorite) has been extensively examined in the microelectronics industry, it has not been characterized in terms of its mechanical properties. Its companion CoSi_2 and the ternary $(\text{Co}, \text{Ni})\text{Si}_2$ solid solution, however, have received some recent research attention. In an early study, Sauer and Freise (1968) examined the deformation modes of single-crystal and coarse-grained polycrystalline cobalt silicides CoSi_2 , CoSi and Co_2Si using hardness indentations. They concluded that the cubic compounds CoSi_2 and CoSi deformed primarily by slip on {100} planes, whereas the orthorhombic compound Co_2Si deformed by both slip and twinning. The observed cube slip in CoSi_2 was

rationalized on the basis of the existence of strong Co–Si covalent bonds. More recently, a report of high-temperature (>700 K) deformation in columnar-grained CoSi_2 occurring by $\{110\}\langle\bar{1}10\rangle$ slip was published (Takeuchi, Hashimoto, and Shibuya, 1992), and it was suggested that the deformation was controlled by the Peierls mechanism. The yield strength in compression was shown to increase steeply with decreasing temperature and, below 700 K, the specimens failed prior to yielding. Extensive compressive plasticity was noted above 900 K. In another study (Ito *et al.*, 1992), the room-temperature compression response of single-crystal CoSi_2 was examined and it was observed that while $\{001\}$ -oriented crystals fractured prior to yielding, those oriented in the $\{011\}$, $[\bar{1}11]$, $[\bar{1}23]$ and $[\bar{1}35]$ directions exhibited appreciable fracture strains following a yield drop. Electron microscopy revealed the slip systems in the plastically deformed crystals to be $\{001\}\langle100\rangle$ with most dislocations with edge orientation. The observation of yield drop and dislocations with edge character led to the suggestion that plastic deformation in CoSi_2 at room temperature is controlled by the Peierls mechanism. It thus appears that octahedral slip is activated in CoSi_2 only at high temperatures and is likely associated with the onset of polycrystalline ductility. In this context, the primary slip system for other compounds that exhibit a structure similar to CoSi_2 is reported to be of either the $\{001\}\langle110\rangle$ type (e.g. CaF_2 , Evans and Pratt, 1970; BaFe , Liu and Li, 1964) or alternatively the $\{111\}\langle\bar{1}10\rangle$ type (e.g. TiH_2 , Irving and Beevers, 1972; ZrH_2 , Barraclough and Beevers, 1969). The difference in the primary slip system in these compounds has been attributed to differences in the dislocation core structure as a consequence of ionic bonding character in the former group and metallic bonding character in the latter group (Ito *et al.*, 1992). CoSi_2 exhibits covalency and metallicity and would be expected to lie in between.

Takeuchi, Hashimoto and Shibuya (1991) have also compared the compressive yield strength variation with temperature of ternary solid-solution compounds of the type $(\text{Co}_{1-x}\text{Ni}_x)\text{Si}_2$ with binary CoSi_2 (Figure 6) and found that the behaviors are similar and that only weak solid-solution hardening effects occur as a consequence of the small misfit between Co and Ni atoms. They observed, however, that the increase in yield strength with decreasing temperature was more gradual for the solid-solution compounds than for binary CoSi_2 .

The compound Fe_3Si exists over a wide composition range (ca 8–27 at% Si) with a D0_3 (cF16) at room temperature. Upon heating the structure transforms first into a B2 (cP2) arrangement which on further heating

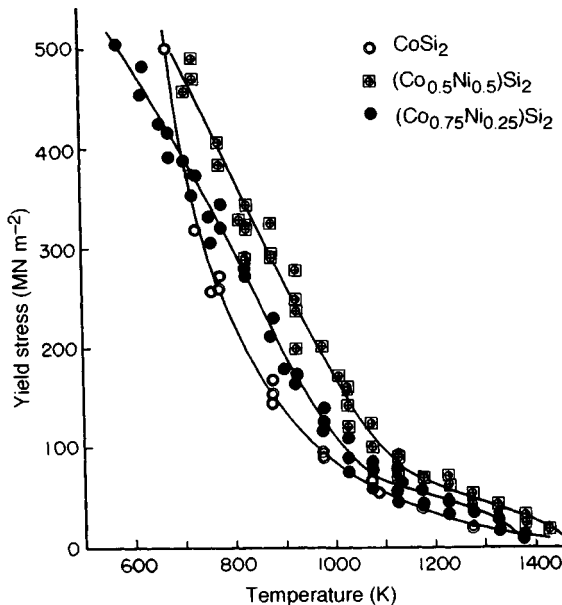


Figure 6. Compressive yield strength versus temperature for CoSi_2 and $(\text{Co}_{1-x}\text{Ni}_x)\text{Si}_2$ (reproduced by permission of the Japan Institute of Metals from Takeuchi, Hashimoto, and Shibuya, 1991)

becomes disordered prior to melting. The exact transformation temperatures and the actual sequence of phase changes on heating or cooling depend on the composition under consideration. This binary compound exhibits at high temperature an unlimited solid solubility in Fe_3Al (Figure 7), and this has been exploited commercially to give several ternary Fe–Al–Si alloys. The addition of Al to Fe_3Si , however, lowers the order–disorder transformation temperature (Sato and Yamamoto, 1950). The phase equilibria of the ternary Al–Fe–Si system have been critically reviewed (Rivlin and Raynor, 1981). A major drawback of Fe_3Si is that it is extremely brittle and hard and is usually processed by grinding, rather than machining the casting to the final size and shape. Fe_3Si exhibits excellent corrosion resistance and this has led to commercial alloys such as the Duriron alloy containing 25.2 at% Si (Uhlig and Revie, 1985) which is resistant even to boiling sulfuric acid. Likewise, ternary alloys of Fe–Al–Si that exhibit high magnetic permeability have been exploited for cores in magnetic heads ('Sendust' alloys, standard composition Fe–16.6 at% Si–9.7 at% Al). In addition to their superior magnetic properties they also exhibit good wear resistance and corrosion resistance, features that are essential in a magnetic head. Since these alloys are extremely brittle, these cores are usually made by

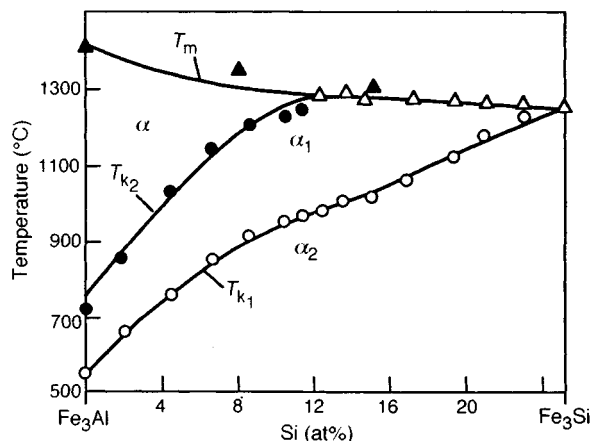


Figure 7. The Fe_3Si - Fe_3Al pseudobinary phase diagram (reproduced by permission of the publisher from Katsnel'son and Polishchuk, 1973). Here $\alpha = \text{A1}$; $\alpha_1 = \text{B2}$; $\alpha_2 = \text{D0}_3$.

slicing and grinding as previously mentioned, and therefore there has been substantial research to understand the deformation behavior of these materials and to identify a possible 'processing window' in single crystals and polycrystals (Lakso and Marcinkowski, 1969; Hanada *et al.*, 1981b; Watanabe *et al.*, 1984). Other studies have tried to identify alloying additions to enhance the processibility of these alloys (Oh and McNallan, 1987; Lou, Zhang, and Zhu, 1991).

Saburi and Nenno (1967) followed the evolution of defects upon cooling $\text{Fe}_3(\text{Si}, \text{Al})$ (13 at% Si) from the disordered state via the B2 range to the D0_3 structure and found that $\frac{1}{4}\mathbf{a}_0\langle 111 \rangle$ antiphase boundaries (APBs) were generated during the disordered structure to B2 transformation. Further cooling resulted in the formation of $\frac{1}{2}\mathbf{a}_0\langle 100 \rangle$ APBs in the B2 domains during transformation from B2 to D0_3 at ≤ 1073 K. Finally, in the D0_3 superlattice, dislocations were observed to move as pairs of ordinary dislocations bound together by $\frac{1}{4}\mathbf{a}_0\langle 111 \rangle$ APBs on $\{110\}$, $\{112\}$ and $\{123\}$ planes. Lakso and Marcinkowski (1969) examined the deformation behavior of single-crystal and polycrystalline Fe_3Si and showed that the stress-strain curve obtained from a single crystal of Fe_3Si exhibited three stages and that the work hardening is remarkable for a crystal oriented for multiple slip compared to that oriented for single slip. Based on electron microscopy observations, stage I of the three stages was related to generation of D0_3 superlattice dislocations, stage II to locking of these dislocations and stage III to dynamic recovery processes. A similar three-stage deformation was noted by Hanada *et al.* (1981a) in 'Sendust' single

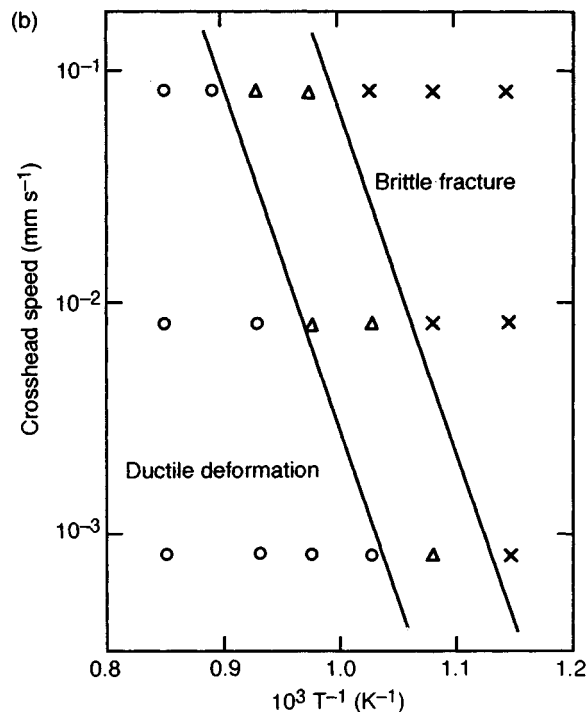
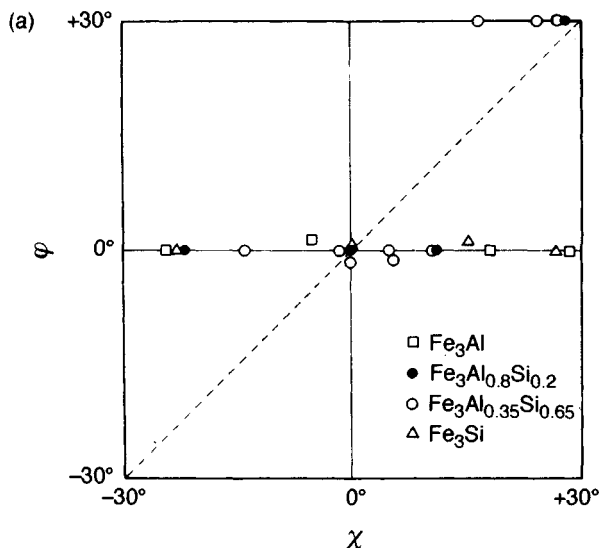


Figure 8. (a) The ϕ - χ plots for binary Fe_3Si , Fe_3Al and ternary $\text{Fe}_3(\text{Al}, \text{Si})$ deformed at room temperature in compression revealing the orientation dependence of slip planes (ϕ and χ are defined in the text); (b) strain-rate and temperature effects on ductile and brittle failure of 'Sendust' polycrystals in bending (reproduced by permission of the Japan Institute of Metals from Hanada *et al.*, 1981b, c).

crystals (nominally Fe–9.6 wt% Al). The operative slip systems were identified as $\{110\}\langle 111 \rangle$ and $\{112\}\langle 111 \rangle$ depending on the compression axis. The orientation dependence of the slip plane for Fe_3Si , $\text{Fe}_3(\text{Al}, \text{Si})$ and Fe_3Al at room temperature (Hanada *et al.*, 1981c) is shown in Figure 8(a). (In this figure, ϕ is the angle between the observed slip plane and the $(\bar{1}01)$ plane and χ is the angle between the maximum resolved shear stress plane in the $\langle 111 \rangle$ zone and the reference $(\bar{1}01)$ plane.) Although the two binary compounds glide on $\{110\}$ irrespective of orientation, the ternary alloys glide on either $\{110\}$ or $\{112\}$ depending on orientation. This difference in behavior cannot be attributed to separation of coupled $a_0\langle 110 \rangle$ dislocations because the width of the separation is thought to be inversely proportional to the B2–D0₃ transformation temperature, and this has been shown to increase almost linearly from Fe_3Al to Fe_3Si as Si substitutes progressively for Al. The reason(s) for the ternary compounds behaving differently from the binary counterparts remains elusive at present. The workability of these ‘Sendust’ alloys has been examined (Hanada *et al.*, 1981b; Watanabe *et al.*, 1984) and it was shown that these alloys could be successfully hot rolled if the processing parameters and alloy composition were optimized. Regions of ductile and brittle deformation were determined in bending as a function of strain rate and temperature, as shown in Figure 8(b); it was argued that extrapolating the boundary linearly to higher strain rates would permit determination of the optimum hot rolling and/or forging conditions.

2.2 Refractory Metal Silicides

The recent quest for materials for applications at very high temperatures (≥ 1773 K) has focused research attention on the refractory silicides, particularly the disilicides of Mo, W, Ti and Cr that also exhibit excellent oxidation resistance. The lack of ductility and toughness in these compounds up to ~ 1273 K has, however, been a major concern, and approaches to enhance the damage tolerance of these silicides include the incorporation of a continuous and/or discontinuous second phase that may be either ductile (e.g. metallic) or brittle (ceramic). The role of a second phase in enhancing the damage tolerance of these silicides is covered in detail elsewhere in this volume (Miracle and Mendiratta, Chapter 13) and therefore is not reviewed.

However, single-crystal and polycrystalline monolithic refractory silicides have been characterized in compression as a function of orientation and temperature, and the operating slip systems have been identified. The physical and mechanical properties of

some of these compounds have also been measured, and alloying approaches to improve these properties have been explored.

2.2.1 The Disilicides

The transition metal disilicides crystallize typically in one of four related crystal structures: (i) the tetragonal C11_b (tI6) structure (e.g. MoSi_2) that can be thought of as being obtained by stacking three b.c.c. lattices and then compressing them in the c direction ($c/a = 2.452$); (ii) the hexagonal C40 (hP9) structure (CrSi_2 , VSi_2 , NbSi_2 , TaSi_2); (iii) the orthorhombic C54 (oF24) structure (TiSi_2); and (iv) the orthorhombic C49 (oC12) structure (ZrSi_2 , HfSi_2). The relative energies of the C11_b, C40 and C54 structures have been calculated using the augmented spherical wave (ASW) method (Carlsson and Meschter, 1991, and Chapter 3 of Volume 1). A strong correlation was noted between the structural energy differences among these three structures and the d-band filling. The C40 was stabilized relative to C54 and the C11_b relative to C40 as the transition metal d-electron count increased. Crystallographically, the instability of the C11_b structure relative to the C40 structure is related to the formation of pure stacking faults by the motion of $\frac{1}{4} [111]$ partial dislocations on (110) planes (Umakoshi *et al.*, 1990a). Frankwicz and Perepezko (1991) have examined the phase equilibria along the TiSi_2 – MoSi_2 pseudobinary (Figure 9) and noted that the C54 binary TiSi_2 structure underwent transition through an intermediate C40 ternary silicide of the form $(\text{Ti}_{1-x}\text{Mo}_x)\text{Si}_2$ before reaching the C11_b (tI6) structure of MoSi_2 , in agreement with the relative energy calculations of Carlsson and Meschter (1991).

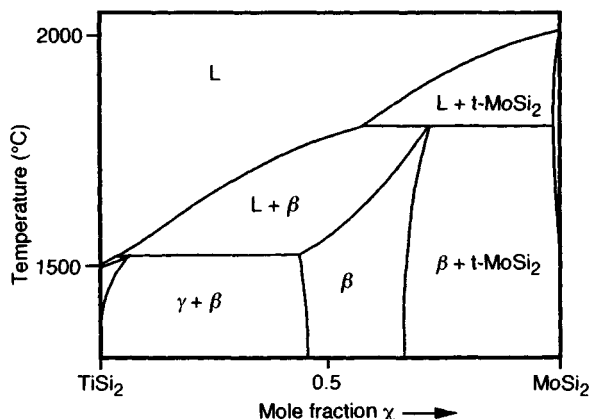


Figure 9. The MoSi_2 – TiSi_2 pseudobinary phase diagram (reproduced by permission of the Materials Research Society from Frankwicz and Perepezko, 1991). L = liquid; t = tetragonal

Of the various transition metal disilicides, MoSi_2 has perhaps received the most attention. This is a direct consequence of its high melting point, excellent oxidation resistance and reasonable density. Until recently, it was believed that MoSi_2 exhibits the C11_b

(tI6) structure below ~ 2173 K and the C40 (hP9) structure between 2173 K and its melting temperature of ~ 2300 K. Two recent investigations, however, indicate that this is not possible based on ternary phase equilibria studies, that the C11_b structure is maintained

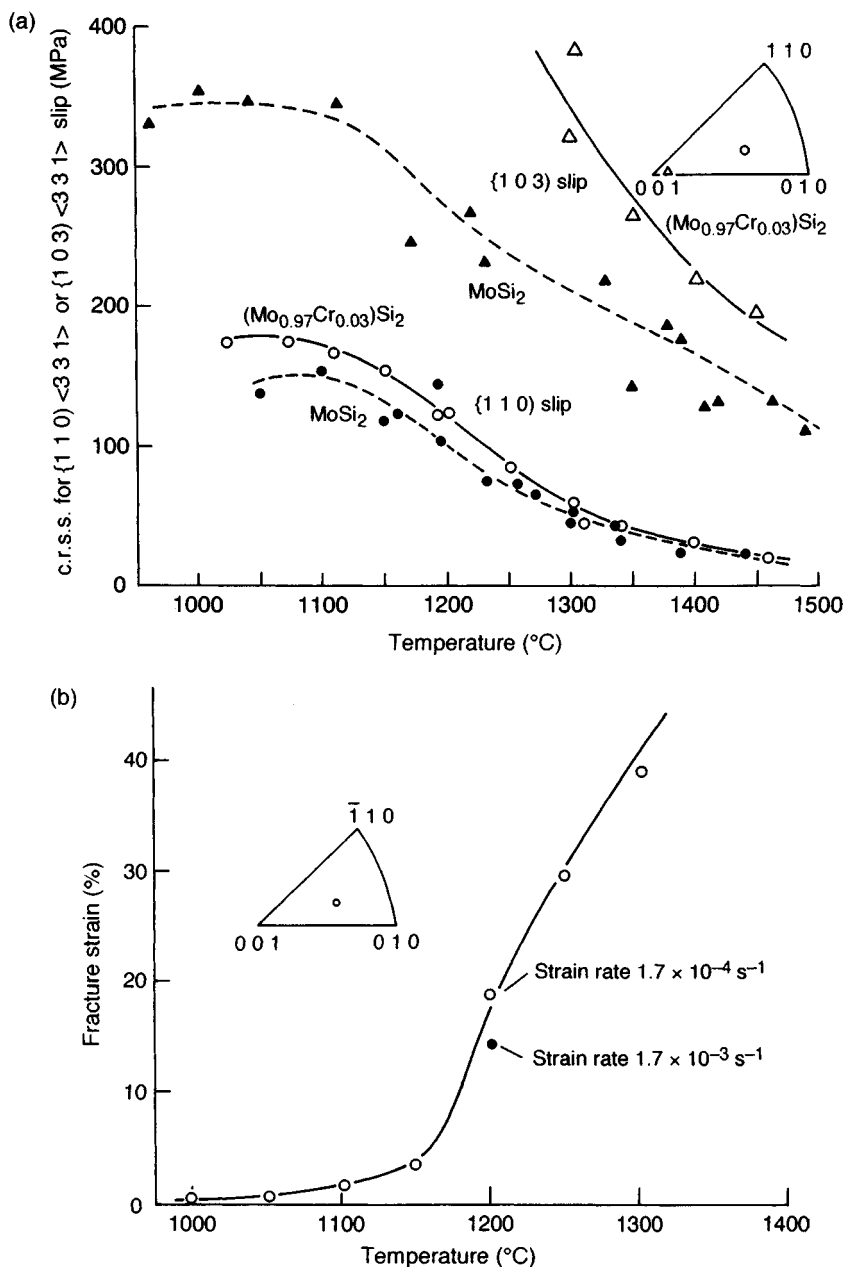


Figure 10. Temperature dependence of (a) critical resolved shear stress (c.r.s.s.) of MoSi_2 and $(\text{Mo}_{0.97}\text{Cr}_{0.03})\text{Si}_2$ single crystals and (b) fracture strain in compression of MoSi_2 single crystal (reproduced by permission of the Japan Institute of Metals from Umakoshi *et al.*, 1991)

up to the melting point, and that the previous observation of the C40 structure at high temperatures must therefore be attributed to the presence of impurities (Frankwicz and Perepezko, 1991; Boettinger *et al.*, 1992). The variation with temperature of the elastic and shear moduli, heat capacity, thermal conductivity and coefficient of thermal expansion of MoSi_2 were recently reported (Bose and Hecht, 1992; Lugscheider *et al.*, 1991; Nakamura, 1991).

Single crystals of MoSi_2 have been successfully grown with low nitrogen, oxygen and carbon levels using the floating zone method (Umakoshi *et al.*, 1989). The compression behavior of these single crystals has been characterized in the temperature range 1173–1773 K as a function of orientation, and the operational slip systems were analyzed by examining slip traces on the specimen surfaces as well as by transmission electron microscopy (Umakoshi *et al.*, 1990b). For most orientations, slip occurred on the $\{110\}$ planes, although $\{013\}$ slip was noted when the specimen was oriented close to $[001]$. Dislocation analysis revealed the Burgers vector to be of the $[\bar{3}31]$ type and the observed mild anomalous strength peak around 1300 K was attributed to cross slip from the $\{110\}$ to $\{013\}$ planes of some parts of the superlattice dislocations. At higher temperatures (~ 1573 K), ordinary $\langle 100 \rangle$ and $\langle 110 \rangle$ dislocations are activated, tending to form nodes, and an improvement in ductility is noted. Pure stacking faults, created by the motion of $\frac{1}{4}[111]$ partials on (110) planes, have also been observed; and, as previously indicated, the formation of these faults is believed to be closely related to the stability of the C11_b structure relative to the C40 structure. The replacement of Mo by Cr, for example, causes a substantial increase in the faulting activity. This was sought as a method to improve the ductility of MoSi_2 (Umakoshi *et al.*, 1990a), although the improvement realized was reported as not being remarkable, possibly countered by the solid-solution hardening effect of Cr. The temperature dependences of the critical resolved shear stress of MoSi_2 and $(\text{Mo}_{0.97}\text{Cr}_{0.03})\text{Si}_2$ and the variation of fracture strain with temperature for MoSi_2 are shown in Figure 10. While the substitution of Cr for Mo does not significantly influence $\{110\}$ slip, it appears to affect the $\{103\}$ slip strongly. This latter effect has been claimed to be a consequence of solution hardening, although it is not clear from the investigation whether the binary and ternary compositions had precisely the same near- $[001]$ orientation. Fracture strain versus temperature data for the ternary alloy are not reported.

Polycrystalline MoSi_2 has also been characterized as a function of temperature in compression and at high temperatures as a function of strain rate. The major drawback appears to be the poor high-temperature strength of MoSi_2 , and this has been attributed to the presence of a grain boundary Si-rich phase that may be viscous at these temperatures. In a recent investigation, Maloy *et al.* (1991) successfully overcame this problem by adding 2 wt% C to MoSi_2 . The carbon acted as a deoxidant and reduced the SiO_2 phase to SiC; some C reacted with MoSi_2 to form a ternary carbide. Elimination of the grain boundary SiO_2 resulted in a continuously increasing fracture toughness with increasing temperature as opposed to the decrease observed in binary MoSi_2 (Figure 11a). The compressive creep response of polycrystalline MoSi_2 in the

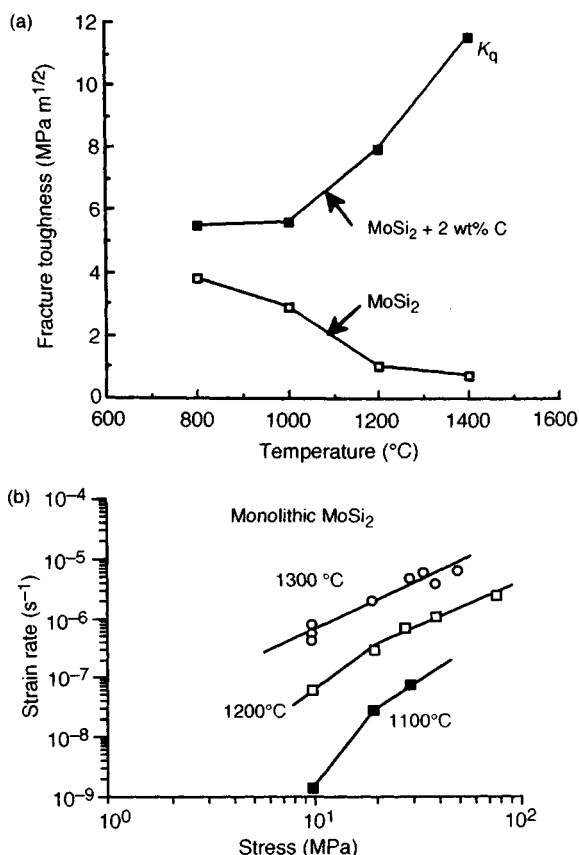


Figure 11. Mechanical properties of polycrystalline MoSi_2 : (a) fracture toughness–temperature profile with and without carbon addition (reprinted by permission of the American Ceramics Society from Maloy *et al.*, 1991); and (b) compressive creep response at various temperatures (reprinted by permission of the American Ceramics Society from Sadananda *et al.*, 1991)

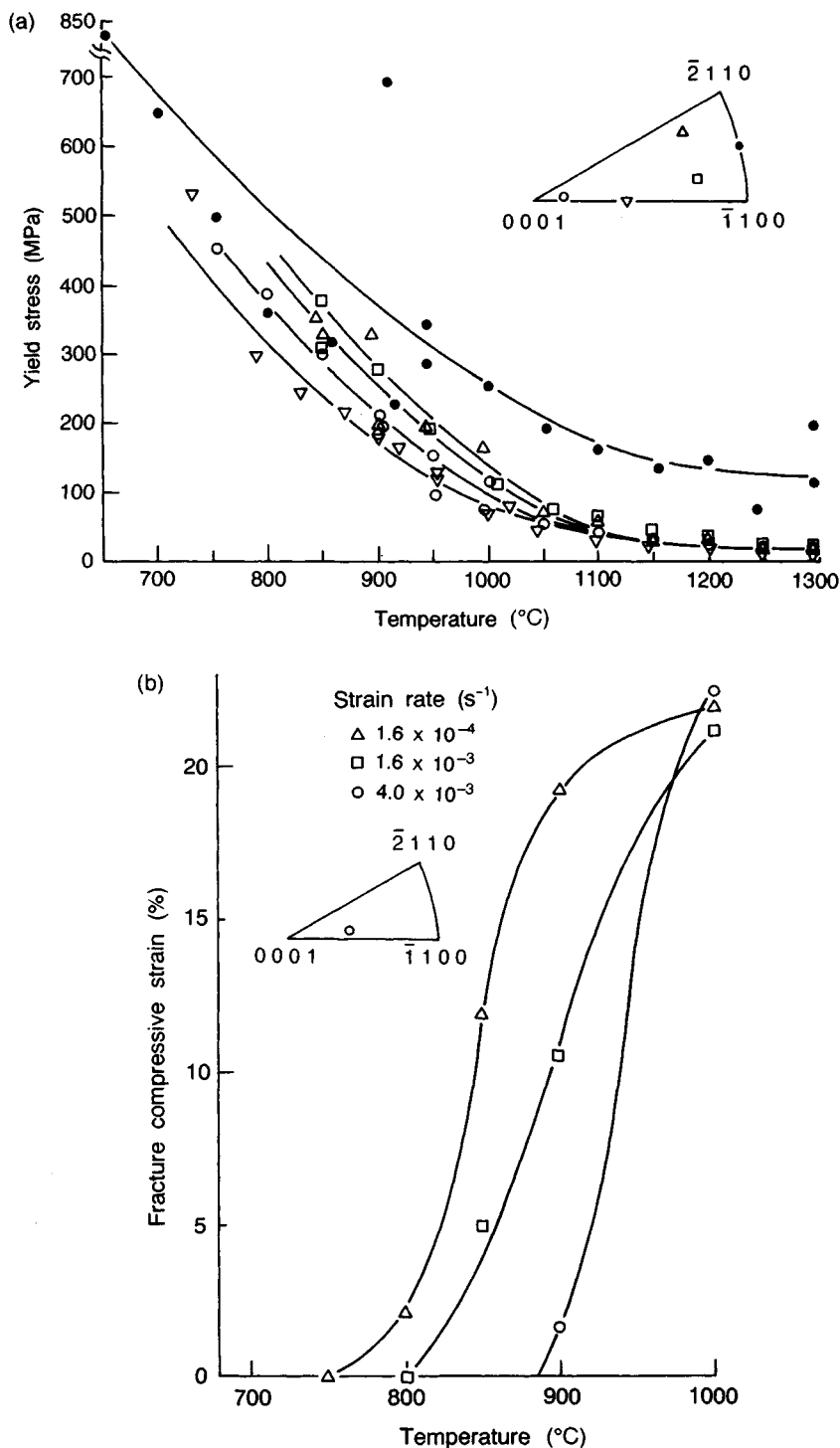


Figure 12. Mechanical properties of single-crystal CrSi_2 : (a) compressive yield stress versus temperature; and (b) fracture strain versus temperature at various strain rates (reproduced by permission of the Japan Institute of Metals from Umakoshi *et al.*, 1991)

temperature range 1373–1673 K has been examined (Sadananda *et al.*, 1991), and the variation in the steady-state creep rate as a function of stress and temperature is shown in Figure 11(b). The stress exponent n at 1373 K varies from ~ 10 at low stress to ~ 3 at high stresses. At the higher temperature of 1673 K, $n=3$ and dislocation climb involving bulk diffusion controls the creep behavior, whereas at the lower temperatures and stresses where n is high the contribution from grain boundary sliding is considered significant. An activation energy for creep of 430 kJ mol^{-1} was reported.

It should be evident by now that monolithic MoSi_2 in single crystal and polycrystalline forms is simply not adequate for structural applications because of its poor low-temperature damage tolerance as well as insufficient high-temperature creep resistance. Thus, several investigations are in progress to examine the potential of this material as a matrix for discontinuous and long fiber reinforced composites. Progress in this area was recently summarized in an extensive review by Vasudevan and Petrovic (1992). In this review, the beneficial roles of particulates and whiskers in the fracture toughness, strength and creep resistance of MoSi_2 are elucidated, and directions for future research to overcome some of the current limitations are outlined.

The companion compound to MoSi_2 is WSi_2 , which exhibits a slightly higher melting point and a higher density than MoSi_2 . These two compounds with identical crystal structures (tI6) exhibit a continuous solid solution, and some investigations have attempted to improve the high-temperature strength of MoSi_2 by alloying with WSi_2 . Single crystals of WSi_2 have also been produced by the floating zone technique (Hirano *et al.*, 1991). Compression tests have been conducted on them in the 1173–1773 K temperature range to determine the orientation and temperature dependence of strength. It was noted that WSi_2 exhibits better high-temperature strength as compared to MoSi_2 , although, interestingly, the orientation dependence of strength for WSi_2 is opposite that of MoSi_2 , in that for WSi_2 the 0.2% offset stress for specimens oriented near $[100]$ is larger than that for samples oriented near $[001]$. In both materials, slip occurs on $\{110\}$ and $\{013\}$ planes with a $\langle 311 \rangle$ Burgers vector. The reverse orientation dependence of the strength in WSi_2 relative to MoSi_2 was correlated with the difference in critical resolved shear stress on $\{110\}$ and $\{013\}$ planes and was speculated to originate from the large number of stacking faults on $\{110\}$ planes in WSi_2 relative to MoSi_2 (Kimura *et al.*, 1990).

A third disilicide that has received some recent research attention is CrSi_2 with the hexagonal C40

(hP9) structure (Umakoshi *et al.*, 1991). Single crystals of CrSi_2 have been characterized in compression as a function of orientation and temperature in the range 973–1573 K. The variation in yield stress with test temperature and orientation is shown in Figure 12(a), and the influence of strain rate on the compressive fracture strain at various temperatures is shown in Figure 12(b). It is seen in Figure 12(a) that the yield stress depends strongly on specimen orientation, particularly at the lower temperatures. In the temperature range 973–1373 K, strength decreases sharply, as does the orientation dependence of strength. Basal slip was noted and three types of $\frac{1}{8}\langle 11\bar{2}0 \rangle$ dislocations were confirmed by transmission electron microscopy. Stacking faults caused by the motion of $\frac{1}{8}\langle 112 \rangle$ dislocations were also observed. The temperature dependence of fracture strain (Figure 12b) confirms the increase in the ductile to brittle transition temperature with increasing strain rate.

The mechanical properties of TiSi_2 were recently reported (Lugscheider *et al.*, 1991), and it was shown that both the elastic and shear moduli of TiSi_2 were significantly lower than those for MoSi_2 at room and elevated temperatures. The thermal conductivity of TiSi_2 is higher than that of MoSi_2 , and at temperatures above $\sim 1300 \text{ K}$ TiSi_2 exhibits a higher bend strength than MoSi_2 .

2.2.2 The A15 Silicides

Several intermetallic compounds with the A15 (cP8) crystal structure exhibit superconductivity with a high critical temperature (T_c) and are therefore attractive for use in thermonuclear reactors, generators, power transmission and in high-energy physics. Of these various compounds, V_3Si has been studied extensively because it shows a relatively high T_c ($\sim 17 \text{ K}$).

These compounds are brittle not only at ambient temperatures but also up to fairly high temperatures and are therefore not amenable to conventional deformation processing. The mechanical properties of these compounds at various temperatures are therefore important to successful processing. Novel but often tedious fabrication techniques not involving deformation processing have been developed to produce suitably shaped composite superconductors for comparatively small solenoids. Wright (1977) has drawn together some of the literature that has a direct bearing on the prospects for deformation processing of the A15 structure and proposes the use of high-temperature hydrostatic extrusion to process A15 compounds successfully. He cautions, however, that plastic deformation during fabrication may influence the critical current density and

T_c , and should therefore be given due consideration. Chin *et al.* (1978) proposed the existence of strong covalent bonds in these A15 compounds along the V–V chains in V_3Si .

The desire to process V_3Si by deformation has led to several studies that have investigated the high-temperature deformation characteristics of the compound, and it was shown (Levinstein *et al.*, 1966) that $\{100\} \langle 001 \rangle$ slip was active at 1793 K. Subsequently, Mahajan *et al.* (1978), from their compression study of single-crystal V_3Si in the temperature range 1473–2073 K, showed yield strength to be extremely temperature sensitive in the range 1473–1773 K and that the introduction of a substructure did not adversely affect T_c or the transition widths (ΔT_c). In a detailed study on the effect of elevated-temperature plastic deformation on the superconducting properties of V_3Si single crystals, Quyen *et al.* (1979) showed that the critical temperature T_c can be increased or decreased by hot working, but that the change is small enough not to discourage high-temperature deformation processing. Further, the nature of the change in T_c (i.e. increase or decrease) was found to depend on the type of point defect available on either side of stoichiometry. The dislocation structures that result from deformation in the temperature range from ~ 1550 K to 1773 K were examined in an electron microscope, and plastic deformation was attributed to glide and climb of these dislocations (Kramer, 1983). The rationale for the $\{001\}$ planes being operational slip planes was based on the smaller number of covalent bonds broken by gliding dislocations relative to those on the $\{110\}$ planes. Creep behavior of V_3Si has been investigated (Nghiep *et al.*, 1980), and it was shown that the compound could be plastically deformed at a constant load above ~ 1550 K with creep rates of the order of $\sim 10^{-6} s^{-1}$ being obtainable at normal stresses of ~ 10 MPa. Deviations from the V_3Si stoichiometry were shown to improve creep resistance, and the dominant role of point defects has been cited as an explanation for the observed improvement.

More recently, the A15 compound Cr_3Si has been examined for its potential as an oxidation-resistant, high-temperature structural material, not as a single-phase material but as a two-phase alloy with Cr dispersed in it. However, during the course of these studies, it was deemed necessary to understand the deformation behavior of single-phase Cr_3Si and to evaluate its physical and mechanical characteristics as these would undoubtedly influence the behavior of the two-phase alloy. The temperature dependence of the elastic constants for some A15 compounds is abnormal in that the compounds soften with decreasing

temperature, and this can be explained as an electronic effect. Bujard and Walker (1981) have, however, shown this abnormality not to be present in Cr_3Si and attribute the behavior to the high Debye temperature that Cr_3Si exhibits relative to other A15 compounds. Cr_3Si is also different from the typical A15 compound (e.g. V_3Si) in that the bonding is not covalent as in V_3Si , and further it does not exhibit superconductivity. Chang and Pope (1991) examined the compression response of single-crystal Cr_3Si in the temperature range 1473–1673 K and showed by two-surface slip trace analysis that the predominant slip system was of the $\{100\} \langle 001 \rangle$ type; further, a sharp ductile to brittle transition was observed at ~ 1500 K. Duplex slip was noted in all specimens, a direct consequence of which is the reduced mobility of edge dislocations due to their interaction, leading to dipoles and networks. Such interactions rapidly deplete mobile dislocations and restrict further deformation, making these A15 materials inherently brittle up to very high temperatures. It thus appears, at least at present, that for Cr_3Si to be considered for a load-bearing, high-temperature application requiring some simultaneous damage tolerance it must incorporate a ductile second phase.

2.2.3 The 5:3 Silicides

As a group, the M_5Si_3 ($M = Nb, Ta, Mo, Ti, Zr$) compounds exhibit some of the highest melting temperatures among intermetallic compounds. Of these compounds, to date, Nb_5Si_3 , Ti_5Si_3 and Zr_5Si_3 have received some attention (note that in recent phase diagrams, Hf_5Si_3 stoichiometry does not exist and Zr_5Si_3 is stable only at high temperatures). These compounds typically crystallize in either a hexagonal $D8_8$ (hP16) or a tetragonal $D8_m$ (tI32) structure. Some of them occur as line compounds, whereas most exhibit a small range of existence. Some of them exhibit a large solubility for a ternary element like Al (e.g. Zr_5Si_3 , and to a much lesser extent Ti_5Si_3).

The $D8_8$ compound Ti_5Si_3 has been produced in the polycrystalline form as a substantially single-phase material and its physical and mechanical properties have been measured (Frommeyer, Rosenkranz, and Luedecke, 1990; Liu, Lee, and Henson, 1988; Meschter and Schwartz, 1989; Reuss and Vehoff, 1990). Ternary alloying with elements such as Cr, Zr, V and Nb improves oxidation resistance but does not significantly influence mechanical properties (Murata *et al.*, 1991). The thermal expansion coefficient for polycrystalline Ti_5Si_3 in the temperature range 373–1273 K is $\sim 7.0 \times 10^{-6} K^{-1}$, although due to its hexagonal symmetry

it exhibits coefficient of thermal expansion 'CTE' anisotropy. In this temperature interval, a minimal change in elastic modulus occurs, the Young's modulus remaining around 150 GPa for the single-phase material. The yield strength in compression at 1273 K is ≥ 1000 MPa but decreases dramatically to ~ 250 MPa at 1573 K. Compressive creep studies in the temperature range 1273–1473 K revealed a power law creep behavior with a stress exponent $n = 3$ and an associated activation energy of 350 ± 20 kJ mol⁻¹. Plasticity in compression is noted only above 1473 K, and then slip occurs on planes such as ($\bar{1}101$) and ($2\bar{3}11$). The fracture toughness of Ti₅Si₃ in four-point bending was measured in the temperature range 293–1373 K and was reported to increase from ~ 5 MPa m^{1/2} to ~ 7 MPa m^{1/2} for grain sizes in the range 10–30 μ m. Several efforts that include Ti₅Si₃ as a major component in multiphase alloys are underway in an attempt to incorporate some damage tolerance into this otherwise attractive material.

With respect to other 5:3 single-phase silicides, there has been one study on Zr₅Si₃ (Celis and Ishizaki, 1991), one on a ternary Zr₃Ti₂Si₃ compound (Celis *et al.*, 1991) and some studies on binary Mo₅Si₃ and the effect of ternary alloying on its creep behavior (Anton and Shah, 1991). There has been a lot of recent research interest in the two-phase Nb–Nb₅Si₃ alloy, but this effort is not within the scope of this chapter (see Miracle and Mendiratta, Chapter 13 in this volume).

2.2.4 Multicomponent Refractory Silicides

As is evident by now, there has been very little systematic characterization of the microstructures and mechanical properties of ternary and higher-order, single-phase silicides or multiphase materials that incorporate these refractory silicides. There have, however, been some significant phase equilibria studies, and a few ternary isotherms are included in this section (Figure 13) to illustrate advances in this area and the advantages that can potentially be realized from such phase equilibria data. Knowledge of phase relationships in such ternary systems enhances the ability to examine further the potential to design multiphase silicides where the second phase is either another silicide, a refractory carbide, perhaps a ductile solid solution or even an aluminate. Alternatively, such isotherms will enable us to recognize the solid solubility limits of different alloying elements in a specific silicide. Recently, these isotherms have been used to demonstrate an understanding of interfacial reactions in MoSi₂ reinforced with metallic Nb (Boettinger *et al.*, 1992). Additionally, uniquely ternary silicides (i.e. those that do not occur in the binary

systems) may exhibit interesting properties of their own and may be in equilibrium with a metallic solid solution that may provide a balance of properties in two-phase materials that include such ternary silicides and the solid solution. In the next few paragraphs, such features are highlighted in the specific ternary systems shown in Figure 13.

The Fe–Cr–Si system (Figure 13a) is extremely interesting in that it consists of several binary silicides already discussed, including Cr₃Si, Fe₃Si and CrSi₂. In addition, the 5:3 silicides of the type Cr₅Si₃ and Fe₅Si₃ are also present, as is FeSi₂. The two disilicides CrSi₂ and FeSi₂ are nearly insoluble in each other and form a pseudobinary eutectic system, with a eutectic reaction at ~ 1423 K and 6.1 at% Cr (Raghavan, 1987). In contrast, the Cr₅Si₃ phase exhibits about 5 at% solubility for Fe at 1173 K and Fe₅Si₃ dissolves up to 18 at% Cr. The Cr₃Si phase is in equilibrium with elemental Cr as a ductile second phase to enhance the low-temperature damage tolerance of Cr₃Si have been futile because Cr itself is brittle at room temperature, largely a consequence of its intolerance to interstitials, particularly nitrogen. In the ternary Fe–Cr–Si system, Cr exhibits a large solubility (unlimited at 1173 K) for Fe, thereby extending the α solid-solution phase field to compositions containing large amounts of Fe. This in turn may improve the ductility of the solid-solution phase, by perhaps making it less sensitive to interstitials. Also intriguing is the fact that the Cr₃Si phase is in equilibrium with another region of the α solid solution that is Fe rich, the situation being created by the presence of the 'circular' σ -phase field. (In the binary Fe–Cr phase diagram, the σ phase precipitates congruently from the solid-solution α phase at ~ 1100 K, and then at ~ 710 K the σ phase decomposes via a eutectoid reaction into α' (Fe-rich) and α'' (Cr-rich) solid-solution phases.) These situations provide opportunities for creative alloy designs that could perhaps take advantage of the positive high-temperature characteristics of the Cr₃Si phase.

The presence of ternary silicides (e.g. A, B and E in Figure 13b) in the Zr–Mo–Si system that are in equilibrium with a binary silicide (A–MoSi₂ and B–MoSi₂) provides opportunities for examining multiphase silicides. Perhaps more interesting is the two-phase region of ZrMoSi (E phase)–Mo solid solution which provides a thermodynamically compatible system, where the Mo can provide the much-needed damage tolerance. Important considerations here include the melting temperature of the E phase, its creep resistance and the absence of other ternary compounds at lower temperatures that may disrupt this two-phase equilibrium.

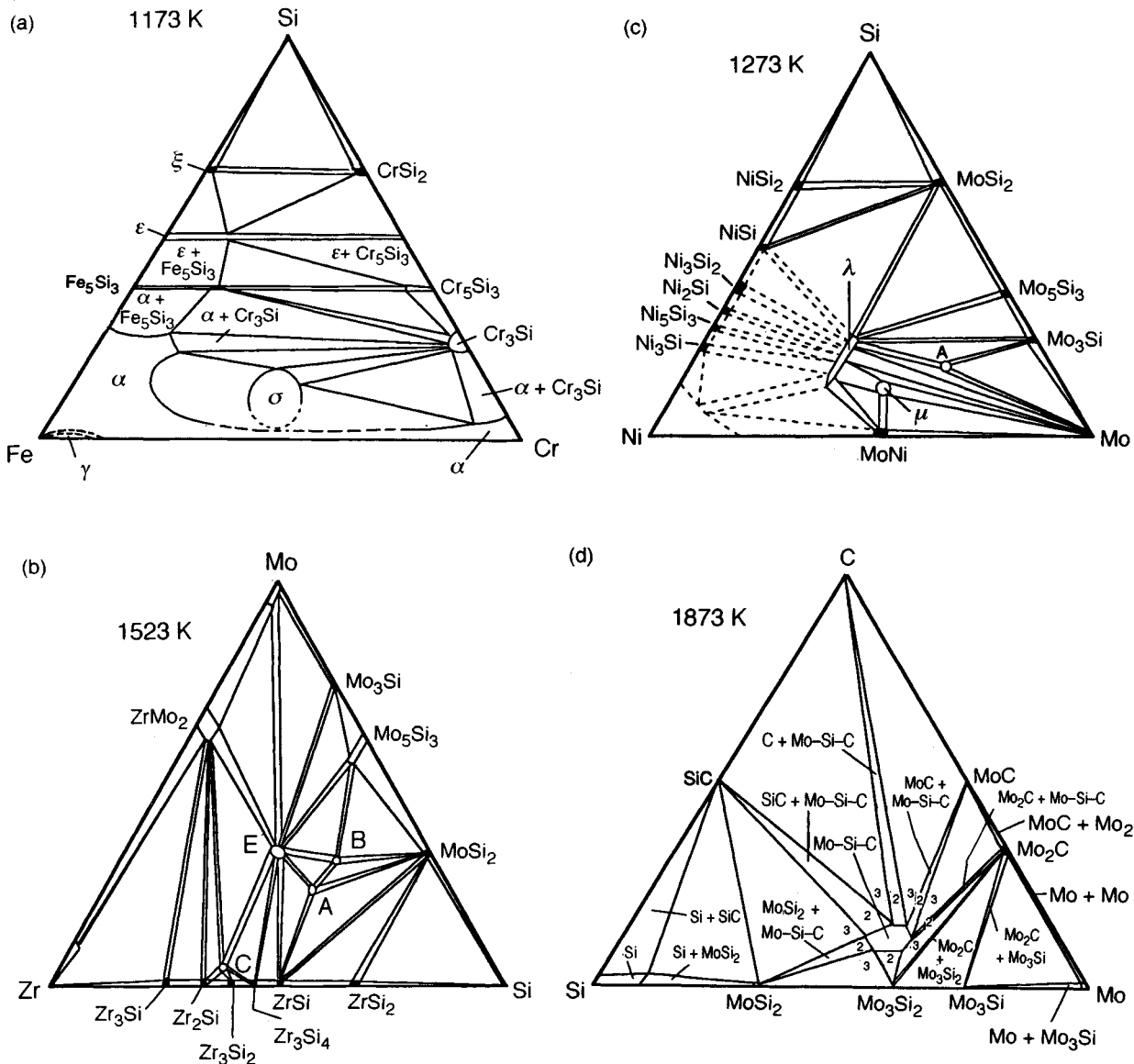


Figure 13. Ternary isotherms in (a) the Cr-Si-Fe system at 1173 K (Raghavan, 1987, after Gladyshevskii and Borusevich, 1966), (b) the Zr-Mo-Si system at 1523 K (Kocherzhinskii and Kulik, 1976), (c) the Mo-Ni-Si system at 1273 K (reproduced from Skolozdra and Gladyshevskii, 1967), and (d) the Mo-Si-C system at 1873 K (reproduced from Nowotny *et al.*, 1965)

A similar situation is seen in the Mo-Ni-Si system (Figure 13c) where the ternary λ phase is in equilibrium with Mo and Ni solid solutions. In addition, the A and the μ phases are in equilibrium with Mo solid solutions. At 1273 K, a two-phase equilibrium is also noted between MoSi_2 and NiSi_2 , which have very little solubility in each other.

The ternary Mo-Si-C system is of particular interest

because of the numerous research efforts on composites of MoSi_2 reinforced with SiC whiskers. As is evident from the ternary isotherm (Figure 13d), a pseudobinary equilibrium exists between MoSi_2 and SiC. A eutectic reaction occurs between the two at ~ 2173 K, indicating that SiC is thermodynamically stable in MoSi_2 to very high temperatures. A ternary silicide-carbide (Mo-Si-C) is also present in this system and is in equilibrium

with both MoSi_2 and SiC with a four-phase invariant eutectic reaction occurring at ~ 2123 K within this three-phase region.

3. Silicides as High-Temperature Coatings

3.1 An Introduction to Silicide Coatings

Silicide coatings have proven to be invaluable in providing high-temperature oxidation resistance in Ni-based alloys, steels, and, most importantly, in refractory metals and alloys. The excellent hot corrosion resistance of silicides has been well established (for example, from degradation from sulfidation; Meier, 1987). More recently, silicides have been examined for their potential to provide some carburization resistance in helium in high-temperature, gas-cooled reactors and in coal-conversion plants (Singheiser *et al.*, 1982; Southwell *et al.*, 1987).

Historically, the excellent oxidation resistance of MoSi_2 coatings on Mo has led to extensive investigations of various other binary and higher-order complex silicides as coatings for virtually all of the refractory metals and alloys. The oxidation resistance of MoSi_2 coatings is derived from a surface layer of pure or nearly pure silica through which diffusion transport of the reacting elements is slow. A similar argument would be valid for WSi_2 , ReSi_2 and the platinum group silicides, where either the metallic element is more noble than Si or the oxide of the metallic element is volatile so that only SiO_2 remains in the condensed phase.

In contrast, when a binary silicide exhibits relatively poor high-temperature oxidation resistance (as in the case of NbSi_2 , TaSi_2 , TiSi_2 , ZrSi_2 and CrSi_2), improvement is obtained by the addition of other elements. For these systems, the mechanisms of oxidation, both before and after addition of the alloying elements, are almost certainly quite different from that of MoSi_2 and likely more complex. Alternatively, overlay coatings of MoSi_2 on Nb and Ta have been used, and in this case success relies on the appropriate processing technique being used. If an M_2Si_3 diffusion barrier is not established during processing, the coating fails. For example, in this case vapor deposition of the disilicide at low temperatures would not be the choice technique as the interlayer will not form.

Clearly, requirements for optimum protective coatings are not simply restricted to chemical surface stability. The mechanical and chemical properties of the coating have to be 'fitted' to the respective properties of the

substrate material to prevent degradation by cracking, spalling and interdiffusion. Silicide brittleness and thermal expansion mismatch can give rise to cracking and spalling during thermal cycling. The brittleness problem has been addressed by influencing the thermal expansion of silicides by alloying additions (e.g. Ge and B) and/or by using tough matrices with silicide reservoir phases as in the case of the Ni-Cr-Si system (Grünling and Bauer, 1982). Interdiffusion of coating and substrate elements during service can also change the inherent properties by alloying effects and can lead to degradation. However, this problem can be rectified by using diffusion barriers of alloying elements that control diffusion.

Various oxidation modes are possible for these silicides depending on the particular silicide as well as on the environment to which it is exposed. A scheme of these various modes is reproduced in Figure 14 from the paper by Grünling and Bauer (1982). Total oxidation occurs, producing a mixture of metal oxides and SiO_2 , when the inward diffusion rate of oxygen through the passive oxide layer exceeds the outward silicon diffusion rate through the silicide sublayer containing less silicon. Conversely, selective oxidation of silicon will occur when the transport of silicon through the silicide is higher than the transport of oxygen through the SiO_2 . At low oxygen partial pressures, active oxidation due to the formation of gaseous SiO will occur because the oxygen transport to the substrate surface is too slow. In some cases, as in Cr-rich silicides or mixed Cr-Ni silicides, passive oxidation with the formation of SiO_2 scale is expected based on thermodynamic and kinetic data.

3.2 Coating Techniques

Several techniques are available to incorporate a protective intermetallic coating on high-temperature structural components and these were recently reviewed by Patnaik (1989). Common coating techniques, including those pertinent to silicides, are as follows:

- (i) pack coating;
- (ii) slurry processes;
- (iii) chemical vapor deposition (CVD);
- (iv) electrolytic deposition;
- (v) fluidized bed processing;
- (vi) hot dipping;
- (vii) cladding;
- (viii) plasma and flame spray processes;
- (ix) vacuum vapor deposition; and
- (x) detonation gun processes.

For a more comprehensive discussion on coatings, see Nicholls and Stephenson, Chapter 22 in this volume.

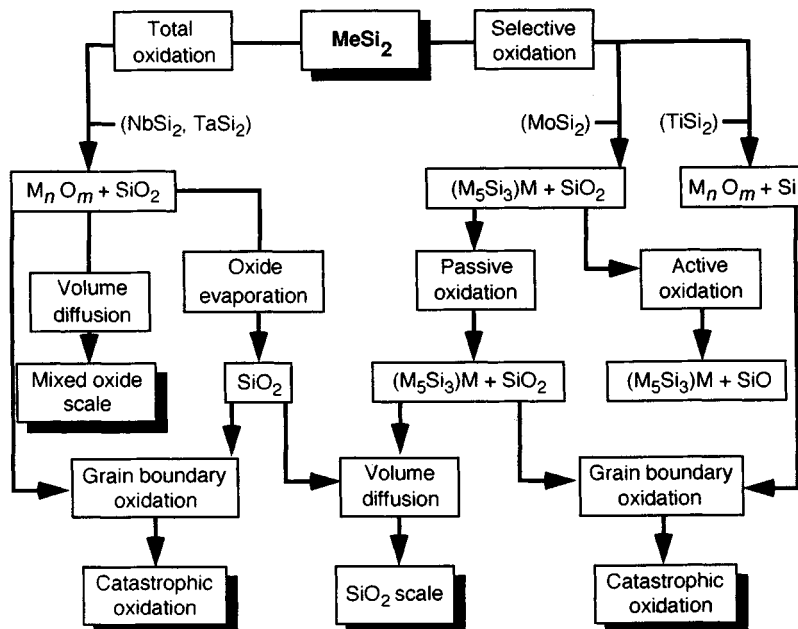


Figure 14. A schematic diagram showing the various possible oxidation modes in silicides (reproduced by permission of Elsevier Sequoia from Grünling and Bauer, 1982)

3.3 Silicide Coatings on Specific Alloy Systems

In this subsection, various metallic systems that incorporate silicide coatings are reviewed with the important distinction that coating systems that incorporate Si only as a solid-solution alloying element are excluded.

In Ni-based superalloys such as Nimonic 80A and IN 100, silicide coatings have been obtained by either pack cementation or by CVD. The type of silicide formed is usually a complex multiphase Ni–Cr–silicide. Using a slurry fusion technique, Fitzer *et al.* (1979) showed that a CrSi₂–NiSi₂ coating could be successfully applied to Ni-based superalloys and that such coatings provide enhanced oxidation and hot corrosion resistance and limited carburization resistance. Attempts to use silicide coatings to inhibit carburization in cast heat-resistant steels have, however, not been successful (Southwell *et al.*, 1987). Silicide coatings for improved oxidation resistance of titanium alloys are being examined. Such coated Ti alloys consist of a sequence of layers going from TiSi₂ at the surface to TiSi, Ti₅Si₃, and an unknown compound at the alloy interface (Patnaik, 1989; Guille *et al.*, 1985). The mechanical behavior of such coatings is under investigation.

Although currently there are no commercial Cr-based alloys that see widespread use in the turbine engine

industry, there are several experimental alloys that have been developed with properties of interest to that community. While Cr-based alloys have higher melting points and significantly lower densities than their Ni-based counterparts, they are embrittled by nitrogen contamination, and silicide coatings have been examined as a possible means to remedy this problem (Brentnall *et al.*, 1966; Stephens and Klopp, 1969; see also the National Materials Advisory Board report, *High-Temperature Oxidation-Resistant Coatings*, 1970). A variety of techniques and complex silicides have been examined, although the best results were obtained from an iron-modified silicide coating incorporated via a slurry technique.

Niobium-based alloys are prime candidates as structural materials for advanced aerospace vehicles and flight propulsion systems. However, they suffer severe degradation in elevated-temperature oxidizing environments and thus require protective coatings. Silicides have proved to be the most thermally stable diffusion alloy coatings available for the protection of Nb alloys (Restall, 1968; see also the National Materials Advisory Board report, *High-Temperature Oxidation-Resistant Coatings*, 1970). A variety of complex silicides have been examined, using various techniques to produce them, including silicides of Cr + Ti, Cr + Ti + V, Cr + Fe,

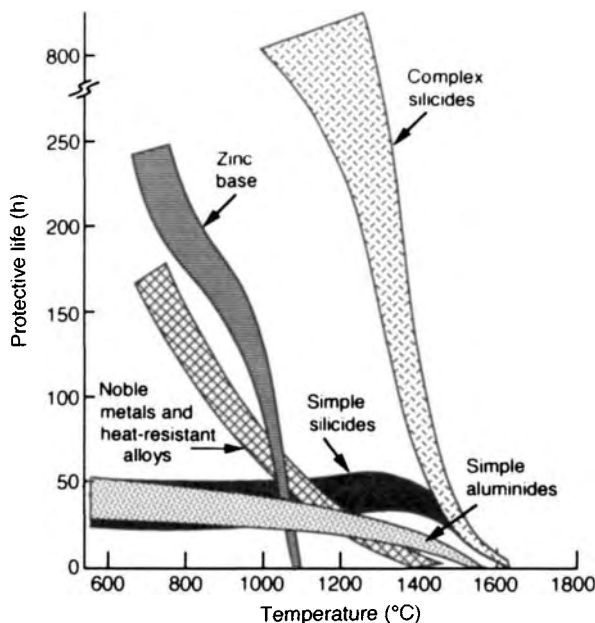


Figure 15. Cyclic oxidation—protective characteristics of various types of coatings on Nb-based alloys (reproduced by permission of the National Materials Advisory Board from *High-Temperature Oxidation-Resistant Coatings*, 1970)

Cr + Al + B, Mo + Cr + Al + B, Mo + Cr + Ti and Mo + Ti. Of these various systems, the most successfully and widely utilized system is the Cr–Ti–Si coating developed by TRW, Inc. It is typically applied by a two-cycle vacuum pack process utilizing all-metal granular packs. Other processes have been examined to apply this coating to Nb alloys, including CVD, electrophoresis, electroless fused salt, fluidized bed and vacuum pack cementation. The cyclic oxidation resistances of various coating types on Nb-based alloys are compared in Figure 15 schematically, and the four coating systems that are most popular are listed in Table 2.

Although these silicides have been by far the most effective protective coatings for Nb alloys, the reliability of such coatings has been a major concern to potential users. The low ductility of silicides combined with the

high incidence of structural defects have discouraged their use. Coated Nb alloys have been considered for structural use in manned reentry glide vehicles, for the Apollo and Transtage exit cones, for heat-shield materials in hypersonic vehicles, and in gas turbine engines as blade and vane alloys.

The development of oxidation-resistant coatings for Mo and its alloys has been actively pursued since the time that designers sought materials for use beyond the capabilities of Ni-based and Co-based superalloys in gas turbine engines and in high-performance ram jets. Since the first useful class of coatings based on MoSi_2 evolved in the early 1950s, several coatings centered on MoSi_2 have been developed and include $(\text{MoSi}_2 + \text{Cr})$, $(\text{MoSi}_2 + \text{Cr}, \text{B})$, $(\text{MoSi}_2 + \text{Cr}, \text{Al}, \text{B})$ and $(\text{MoSi}_2 + \text{Sn-Al})$. Most of these coatings are deposited by pack cementation diffusion processes and this processing route limits the coating to a simple, unalloyed or lightly modified silicide coating. The performance of these coatings is largely defect controlled. The major drawback with silicide-based coatings is their deficient performance in low-pressure environments where Si is lost to the environment in the form of Si, SiO and SiO_2 vapors. This loss can be a serious problem for space-based applications.

4. Silicides in the Electronics Industry

4.1 Superconducting Silicides

In this section, the role of silicides in the microelectronics industry is examined (see also Chapter 15 in this volume by Masumoto *et al.*). The potential for use of A15 silicides as superconductors was discussed in the section on structural silicides and will not be given any further consideration here.

More recently, ternary silicides that contain Ce or U as one of the components and fall under the heading of heavy fermion compounds have been extensively investigated for their magnetic and superconducting properties (Aronson and Coles, Chapter 10 in Volume 1). Examples of such compounds include CeCu_2Si_2 ($T_c = 0.7 \text{ K}$), URu_2Si_2 ($T_c = 1.5 \text{ K}$) and CeRh_2Si_2 . (URu_2Si_2 was the first compound in which superconductivity and magnetic order were found to coexist.) In comparing the low-temperature properties (resistivity, specific heat, d.c. magnetization and low-field a.c. susceptibility) of LaCu_2Si_2 and CeCu_2Si_2 , Steglich *et al.* (1979) showed that whereas LaCu_2Si_2 behaved like a normal metal, CeCu_2Si_2 exhibited low-temperature anomalies and superconductivity. These low-temperature anomalies

Table 2. Popular coating systems and processing routes for Nb-based alloys (source: National Materials Advisory Board report, *High-Temperature Oxidation-Resistant Coatings*, 1970)

System	Process	Developer
Cr–Ti–Si	Vacuum pack	TRW
V–Cr–Ti–Si	Pack	Solar
20Cr–5Ti–Si	Fused silicide	Sylvania
10Cr–2Si–Al	LB-2 slurry	McDonnell–Douglas

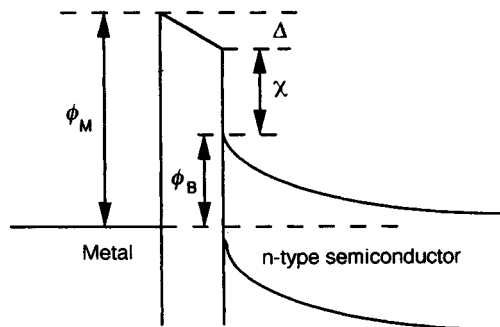
were attributed to the instability of the 4f shell and it was argued that conventional superconductivity theories do not explain the superconducting behavior observed in CeCu_2Si_2 . The superconductivity in CeCu_2Si_2 is easily suppressed by off-stoichiometric Cu, which influences the magnetic characteristics of the compound, thus implying that magnetism plays a critical role in the superconductivity (Nakamura *et al.*, 1988). The co-existence of antiferromagnetism with superconductivity may be realized by a pairing mechanism (superconducting Cooper pairs) as a consequence of anti-ferromagnetic spin fluctuation.

4.2 Microelectronic Devices

4.2.1 The Schottky Barrier and Ohmic Contacts

In microelectronic devices, metal silicides are widely used for ohmic contacts and Schottky barriers in integrated circuit applications (see also De Reus, Chapter 29 in this volume). In general, after the deposition of a metal film on a silicon substrate, a heat treatment is used to form the silicide at the metal-silicon interface.

The interface between a semiconductor (Si) and a conducting silicide is of great technological interest because of its rectifying properties. When a metal and a semiconductor are brought into contact, their individual Fermi levels will adjust to be identical on either side of the interface. Such an adjustment occurs on a local atomic scale (1–10 Å range) near the interface where electronic charge can flow from the metal to the semiconductor or vice versa and build up a small interfacial dipole Δ . This local charge rearrangement can be the consequence of tunneling of metal electrons into the semiconductor or due to the formation of new chemical bonds, etc. The bulk semiconductor, which is doped either n or p type, has a well-defined Fermi level inside the bulk and it adjusts to the interface behavior by long-range band bending (1000–10 000 Å). Such a situation is shown schematically for an n-type semiconductor in Figure 16. The rectifying barrier height ϕ_B (Schottky barrier) is the energy necessary to transport a metal electron into the semiconductor conduction band. (Note that the barrier height of any material to an n-type semiconductor plus that to a p-type semiconductor equals the semiconductor band gap.) A list of Schottky barrier heights of various silicides on n-type silicon (Murarka, 1980; Tu, Thompson, and Tsaur, 1981) is given in Table 3. Clearly, disilicides of the rare-earth metals exhibit low Schottky barrier heights on n-type silicon.



ϕ_B = barrier height

ϕ_M = metal work function

Δ = interface dipole

χ = semiconductor electron affinity

Figure 16. A schematic diagram showing band bending at a metal-semiconductor (n-type) interface and the presence of a Schottky barrier

Formation of silicides by metallurgical interaction between a pure metal film and silicon leads to the most reliable and reproducible Schottky barriers due to the fact that the silicide/silicon interface tends to be automatically clean and free of surface imperfections and contaminations, thereby avoiding variability in contact properties that may otherwise occur.

Schottky diodes are solid-state devices formed by placing a metal in intimate contact with a lightly doped semiconductor. These devices find many applications in the semiconductor industry as 'clamps' to prevent transistors from going into saturation and as discrete devices in logic and memory arrays. In circuit applications, the Schottky diode parameter of most interest

Table 3. Schottky barrier heights (ϕ_B) of various silicides on n-type silicon (Murarka, 1980; Tu *et al.*, 1981)

Disilicides	ϕ_B (eV)	Other silicides	ϕ_B (eV)
TiSi ₂ (oF24)	0.6	HfSi (oP8)	0.53
CrSi ₂ (hP9)	0.57	MnSi (cP8)	0.76
ZrSi ₂ (oC12)	0.55	CoSi (cP8)	0.68
MoSi ₂ (tI6)	0.55	NiSi (oP8; cP8)	0.7–0.75
TaSi ₂ (hP9)	0.59	Ni ₃ Si (oP12; hP6)	0.7–0.75
WSi ₂ (tI6)	0.65	RhSi (oP8; cP8)	0.74
CoSi ₂ (cF12)	0.64	Pd ₂ Si (hP9)	0.74
NiSi ₂ (cF12)	0.7	Pt ₂ Si (tI6)	0.78
DySi ₂ (oI12)	0.37	PtSi (oP8)	0.87
ErSi ₂ (hP3)	0.39	IrSi (oP8)	0.93
GdSi ₂ (oI12)	0.37	Ir ₂ Si ₃ (?)	0.85
HoSi ₂ (oI12)	0.37	IrSi ₃ (hP8)	0.94
YSi ₂ (oI12; hP3)	0.39		

is the forward voltage drop at some specified current level. In large-scale integration the chip affords little room to vary the diode area, and therefore the desired voltage drop is achieved by adjusting the barrier height of the diode by using different metals in contact with the Si substrate.

Ohmic contacts (Sinha, 1973; Chang *et al.*, 1971; Yu, 1970; Ting and Chen, 1971) are usually made by metals on heavily doped semiconductors (note that the barrier height is substantially independent of semiconductor doping concentration) and are an essential part of most semiconductor devices. For a good ohmic contact, the specific contact resistance evaluated at zero bias (R_c) should be sufficiently small that the observed linear current-voltage characteristic is mainly due to the series resistance of the semiconductor material near the contact. The specific contact resistance is defined as the reciprocal of the derivative of current density with respect to voltage. For a given semiconductor, R_c depends on temperature, the barrier height and the impurity concentration. In Si integrated circuits, low-resistance ohmic contacts are extensively utilized in bipolar transistors and in MOS (metal oxide semiconductor) field effect transistors (FETs), and such contacts are usually accomplished using PtSi and/or Pd₂Si.

4.2.2 Silicides for Metallization in Integrated Circuits

More recently, these silicides have attracted attention because of their low resistivity and high-temperature stability as metallization for gates and interconnects. In addition to the low resistivity desired for these applications, the usefulness of the silicide metallization scheme depends on the ease with which the silicides can be formed and patterned and on the stability of the silicides throughout the device-processing stages and ultimate use. A list of the resistivities of various silicides formed by reacting their metal film with single-crystal or polycrystalline silicon or by cosputtering and sintering a mixture of metal and silicon is given in Table 4 (Murarka, 1980). Of these silicides, TiSi₂ has the lowest resistivity (< 15 $\mu\Omega$ cm). Silicides of Fe, Ir and Cr have very high resistivities, whereas Mo and W disilicides have thin-film resistivities in the range 60–100 $\mu\Omega$ cm.

Other important considerations in selecting a silicide for integrated circuits include the stability of the silicide on SiO₂ and in oxidizing environments, the volume change associated with the metal-silicon reaction leading to the silicide formation, and the stresses arising from thermal expansion mismatch between the silicide and silicon. Additional constraints placed on deter-

Table 4. Resistivities of various silicides (Murarka, 1980)

Silicide	Resultant resistivity ($\mu\Omega$ cm)
TiSi ₂ (oF24)	13–16
ZrSi ₂ (oC12)	35–40
HfSi ₂ (oC12)	45–50
VSi ₂ (hP9)	50–55
NbSi ₂ (hP9)	50
TaSi ₂ (hP9)	35–45
CrSi ₂ (hP9)	~ 600
MoSi ₂ (tI6)	~ 100
WSi ₂ (tI6)	~ 70
FeSi ₂ (oC48; tP3)	> 1000
CoSi ₂ (cF12)	18–20
NiSi ₂ (cF12)	~ 50
PtSi (oP8)	28–35
Pd ₂ Si (hP9)	30–35

mining the usefulness of a silicide in integrated circuit technology include the ability to etch the silicide and generate the required patterns.

4.2.3 Epitaxial Silicides

The discovery of epitaxial growth of some silicides on silicon substrates (Tung *et al.*, 1982; Derrien and Arnaud d'Avitaya, 1987; von Kanel, 1992) has made it possible to generate metal-semiconductor interfaces that enable first-principles calculations of the electronic structure of the interface and allows fundamental understanding of the electronic properties of metal-semiconductor contacts. The use of ultrahigh vacuum techniques and the advancement of molecular beam epitaxy (MBE) processes have permitted the growth of perfect single-crystal epitaxial CoSi₂ on silicon. Other compounds that have been epitaxially grown on Si substrates include Pd₂Si, NiSi₂ and PtSi. Such single-crystal films have a lower resistivity and better stability and reliability than polycrystalline silicides and can therefore lead to improved performance of contacts and interconnects where such improvement is demanded by reduced device dimensions. Such improvements in performance also permit the application of such epitaxially grown silicides to high-speed devices such as the metal-base transistor (MBT) and the permeable-base transistor (PBT). In the former, two Schottky diodes are arranged face to face and the common metal which constitutes the base of the transistor is thin enough to be 'transparent' to ballistically injected electrons. The MBT is a replacement for the conventional bipolar transistor as a high-speed device. In the PBT, the metal base is not continuous but consists of a grid fabricated by techniques such as lithography and etching. The Si

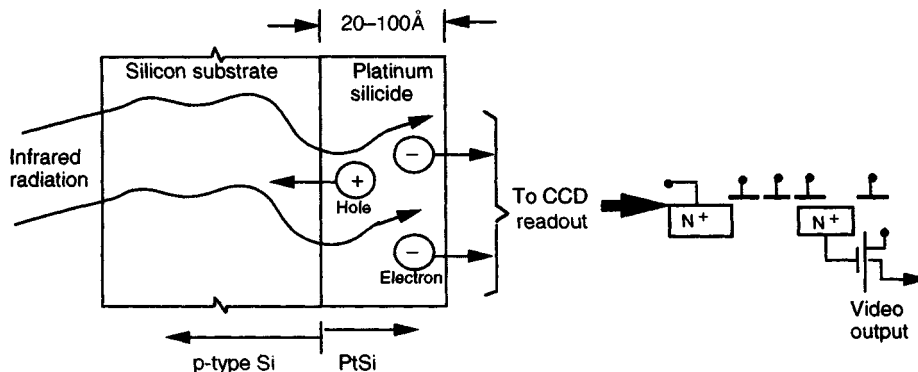


Figure 17. A schematic diagram showing the operation of a PtSi Schottky barrier infrared detector (reproduced by permission of SPIE from Kosonocky and Elabd, 1984)

PBT has generated considerable interest as a device for use in discrete and integrated microwave circuits with the potential for delivering useful gains at frequencies above those achieved by any other three-terminal Si device. Finally, epitaxial growth of a silicide on silicon opens up the possibility of growing multiple layers of Si and silicides on top of one another, thereby paving the way for three-dimensional integration of micro-electronic components on Si.

4.2.4 Infrared Detectors

Infrared detectors and sensors are being extensively developed for a variety of military and civilian applications. These detectors fall into two broad categories: (i) thermal detection and (ii) photon detection. Both have been utilized for infrared imaging, but the current requirements of high sensitivity and high resolution are only satisfied by detectors based on photon detection.

All infrared sensors are exposed to intense infrared background radiation levels and hence the ability to detect a small signal is ultimately determined by the photon noise associated with the background radiation. An additional problem in measuring weak infrared signals is knowing where to look. The charge-coupled device (CCD) developed for small-signal detection facilitates the acquisition problem by providing the large field of view characteristic of an array (focal plane array consisting of a two-dimensional array of detectors) while retaining the small field of view of each detector element which is necessary for low background photon noise. All the photon-induced charge, integrated for a frame time on each element, can be sequentially read out by a single, low-noise preamplifier formed directly on the substrate.

Infrared cameras based on silicide Schottky diodes have received wide interest and are currently commercial (Shepherd, 1984; Kosonocky and Elabd, 1984; Kosonocky *et al.*, 1980). These devices are similar to television cameras except that photo response is extended above one micron in wavelength by the use of internal photoemission. Sensing takes place in a focal plane array composed of silicide Schottky electrodes which emit hot carriers when illuminated by infrared radiation. The resulting signal is collected for video readout. Such cameras are used for infrared astronomy and in medical applications such as mapping of near-surface veins.

The basic construction and operation of a back-illuminated PtSi Schottky barrier infrared detector integrated with a silicon CCD readout are illustrated in Figure 17. The infrared radiation with photon energies less than the band gap of silicon ($E_g = 1.1$ eV) is transmitted through the substrate. The absorption of this radiation in the silicide layer results in the excitation of a photocurrent across the Schottky barrier by internal photoemission. The 'hot' holes (those that have sufficient energy to go over the Schottky barrier between the silicide and p-type silicon) are injected into the Si substrate, and hence a negative charge accumulates on the silicide electrode. This negative charge is transferred into a CCD readout structure to complete the signal detection.

The first Schottky barrier infrared CCD image sensors were made with thick Pd_2Si and PtSi detectors using about 600 Å of deposited palladium or platinum. These devices showed relatively small photo response. Subsequently, thin PtSi detectors showed a large improvement in the photo response when a CCD array size of 25×50 elements was used. Since then, array sizes have been expanded to 64×128 in the United States and

a 256×256 detector array was developed in Japan. The use of Pd_2Si electrodes on p-type silicon leads to an operational range of $1\text{--}3.5\ \mu\text{m}$ wavelength and is thus unsuitable for applications involving ambient thermal imaging. The use of PtSi electrodes extended this range to $4.6\ \mu\text{m}$. Subsequent development in device-processing techniques further extended this range from $4.6\ \mu\text{m}$ to beyond $6\ \mu\text{m}$.

5. Summary

A variety of applications, current and potential, have been highlighted in this chapter. These range from structural applications (including furnace elements), to coatings for environmental resistance, to microelectronic devices. While most of the emphasis for structural applications has been targeted towards the high-temperature capabilities, examples have been shown that take advantage of the excellent corrosion resistance of some of these silicides (e.g. Ni_3Si and Fe_3Si). The deformation behavior and mechanical properties of these compounds have been reviewed. The evaluation of refractory silicides for very high temperature applications is being aggressively pursued, but progress has been painfully slow and it is not evident that any of the relevant silicides will ever be used in the monolithic form for such applications, as they simply do not have the required damage tolerance. While composites of these silicides (where the reinforcing phase imparts some of the much-needed damage tolerance) are being examined for high-temperature applications, particularly nonrotating components, problems in chemical and mechanical compatibility between the reinforcing phase and the matrix silicide have hampered progress. Significant advances in fabrication, joining and machining technologies for such materials are required before they can be used commercially. The use of silicides as high-temperature, oxidation-resistant coatings on refractory metals and alloys has, however, enjoyed better success, and it appears that these compounds will continue to be popular for such applications. In the microelectronics industry, the silicides have enjoyed increasing popularity, primarily because of their desirable physical characteristics, the need for only thin films of material as opposed to large volume, and the well-developed silicon semiconductor technology. The silicide/silicon interface has been extensively examined down to the atomic level and the implications of impurity level and interface strain on device performance have been understood. Unfortunately, however, there is no significant interdisciplinary research

ongoing at present, and therefore volumes of useful information remain compartmentalized. Perhaps in the future, strong interactions between these various scientific disciplines will lead to development of materials with multifunctional capabilities.

6. References

- Anton, D. L., and Shah, D. M. (1991). Final report for the period January 1987–April 1990. Submitted by United Technologies Corporation to the Air Force Materials Laboratory (WRDC-TR-90-4122), Wright Patterson Air Force Base, OH.
- Barracough, K. G., and Beevers, C. J. (1969). *J. Mater. Sci.*, **4**, 518.
- Boettinger, W. J., Perepezko, J. H., and Frankwicz, P. S. (1992). *Mater. Sci. Eng. A*, **155**, 33.
- Bose, S., and Hecht, R. J. (1992). *J. Mater. Sci.*, **27**, 2749.
- Brentnall, W. D., Shoemaker, H. E., and Stetson, A. R. (1966). Summary report submitted by the Solar Division of International Harvester to NASA Lewis Research Center (NASA CR-54535; also Solar RDR 1398-2), Cleveland, OH.
- Bujard, P. and Walker, E. (1981). *Solid-State Commun.*, **39**, 667.
- Carlsson, A. E., and Meschter, P. J. (1991). *J. Mater. Res.*, **6**, 1512.
- Celis, P. B., and Ishizaki, K. (1991). *J. Mater. Sci.*, **26**, 3497.
- Celis, P. B., Kagawa, E., and Ishizaki, K. (1991). *J. Mater. Res.*, **6**, 2077.
- Chang, C. S., and Pope, D. P. (1991). In *High Temperature Ordered Intermetallic Alloys IV* (eds L. A. Johnson, D. P. Pope, and J. O. Stiegler). *MRS Proc.*, **213**, 745.
- Chin, G. Y., Wernick, J. H., Geballe, T. H., Mahajan, S., and Nakahara, S. (1978). *Appl. Phys. Lett.*, **33**, 103.
- Derrien, J., and Arnaud d'Avitaya, F. (1987). *J. Vac. Sci. Technol.*, **A5**, 2111.
- Evans, A. G., and Pratt, P. L. (1970). *Philos. Mag.*, **21**, 951.
- Fitzner, E., Maurer, H. J., Nowak, W., and Schlichting, J. (1979). *Thin Sol. Films*, **64**, 305.
- Frankwicz, P. S., and Perepezko, J. H. (1991). In *High Temperature Ordered Intermetallic Alloys IV* (eds L. A. Johnson, D. P. Pope, and J. O. Stiegler). *MRS Proc.*, **213**, 169.
- Frommeyer, G., Rosenkranz, R., and Luedecke, C. (1990). *J. Metall.*, **81**, 307.
- Gladyshevskii, E. I., and Borusevich, L. K. (1966). *Izv. Akad. Nauk SSSR, Metall.*, **7**, 159 (in Russian); *Russ. Metall.*, **1**, 87 (in English).
- Grünling, H. W., and Bauer, R. (1982). *Thin Sol. Films*, **95**, 3.
- Guille, J., Matini, L., and Clauss, A. (1985). In *Titanium Science and Technology*, Vol. 2 (eds G. Lutjering, U. Zwicker, and W. Bunk). DGM, Oberursel, p. 973.
- Hanada, S., Watanabe, S., Sato, T., and Izumi, O. (1981a). *J. Jpn Inst. Met.*, **45**, 1279.

- Hanada, S., Watanabe, S., Sato, T., and Izumi, O. (1981b). *J. Jpn Inst. Met.*, **45**, 1293.
- Hanada, S., Watanabe, S., Sato, T., and Izumi, O. (1981c). *Trans. JIM*, **22**, 873.
- Hasegawa, S., Wada, S., Takasugi, T., and Izumi, O. (1991). In *Intermetallic Compounds—Structure and Mechanical Properties* (ed. O. Izumi). The Japan Institute of Metals, Sendai, p. 427.
- Hirano, T., Nakamura, M., Kimura, K., and Umakoshi, Y. (1991). *Ceram. Eng. Sci. Proc.*, **12**, 1619.
- Irving, P. E., and Beevers, C. J. (1972). *J. Mater. Sci.*, **7**, 23.
- Ito, K., Inui, H., Hirano, T., and Yamaguchi, M. (1992). In *Proceedings of the International Conference on High Temperature Aluminides and Intermetallics* (eds S. H. Whang, D. P. Pope, and C. T. Liu), Elsevier Sequoia, Barking, pp. 153–159. San Diego.
- Ito, K., Inui, H., Hirano, T., and Yamaguchi, M. (1992). *Mater. Sci. Eng., A*, **152**, 153.
- Katsnel'son, A. A., and Polishchuk, V. Ye. (1973). *Phys. Met. Metallogr.*, **36**, 86.
- Kimura, K., Nakamura, M., and Hirano, T. (1990). *J. Mater. Sci.*, **25**, 2487.
- Kocherzhinskii, Yu. A., and Kulik, O. G. (1976). *Metallofizika*, **64**, 44.
- Kosonocky, W. F., and Elabd, H. (1984). In *Infrared Detectors* (ed. W. L. Wolfe). *Proc. SPIE*, **443**, 167.
- Kosonocky, W. F., Erhardt, H. G., Meray, G., Shallcross, F. V., Elabd, H., Cantella, M. J., Klein, J., Skolnik, L. H., Capone, B. R., Taylor, R. W., Ewing, W., Shepherd, F. D., and Roosild, S. A. (1980). In *Infrared Image Sensor Technology* (ed. B. Krikorian). *Proc. SPIE*, **225**, 69.
- Kramer, U. (1983). *Philos. Mag. A*, **47**, 721.
- Kumar, P. (1985). In *High Temperature Ordered Intermetallic Alloys* (eds C. C. Koch, C. T. Liu, and N. S. Stoloff). *MRS Proc.*, **39**, 537.
- Lakso, G. E., and Marcinkowski, M. J. (1969). *Trans. Metall. Soc. AIME*, **245**, 1111.
- Levinstein, H. J., Greiner, E. S., and Mason, H., Jr (1966). *J. Appl. Phys.*, **37**, 164.
- Liu, C. T., Lee, E. H., and Henson, T. J. (1988). Oak Ridge National Laboratory Report, ORNL-6435.
- Liu, T. S., and Li, C. H. (1964). *J. Appl. Phys.*, **35**, 3325.
- Lou, L., Zhang, T. X., and Zhu, Y. (1991). In *High Temperature Ordered Intermetallic Alloys IV* (eds L. A. Johnson, D. P. Pope, and J. O. Stiegler), *MRS Proc.*, **213**, 833.
- Lugscheider, E., Westermann, U., Wonka, J., Meinhardt, H., Neisius, H., and Arnold, R. (1991). In *Intermetallic Compounds—Structure and Mechanical Properties* (ed. O. Izumi). The Japan Institute of Metals, Sendai, p. 621.
- Mahajan, S., Wernick, J. H., Chin, G. Y., Nakahara, S., and Geballe, T. H. (1978). *Appl. Phys. Lett.*, **33**, 972.
- Maloy, S., Heuer, A. H., Lewandowski, J., and Petrovic, J. (1991). *J. Am. Ceram. Soc.*, **74**, 2704.
- Meier, G. H. (1987). In *High Temperature Ordered Intermetallic Alloys II* (eds N. S. Stoloff, C. C. Koch, C. T. Liu, and O. Izumi). *MRS Proc.*, **81**, 443.
- Meschter, P. J., and Schwartz, D. S. (1989). *JOM*, **41**, 52.
- Murarka, S. P. (1980). *J. Vac. Sci. Technol.*, (1980). **17**, 775.
- Murata, Y., Higuchi, T., Takeda, Y., Morinaga, M., and Yukawa, N. (1991). In *Intermetallic Compounds—Structure and Mechanical Properties* (ed. O. Izumi). The Japan Institute of Metals, Sendai, p. 627.
- Nakamura, H., Kitaoka, Y., Yamada, H., and Asayama, K. (1988). *J. Magn. Magn. Mater.*, **76/77**, 517.
- Nakamura, M. (1991). In *Intermetallic Compounds—Structure and Mechanical Properties* (ed. O. Izumi). The Japan Institute of Metals, Sendai, p. 655.
- National Materials Advisory Board (1970). *High-Temperature Oxidation-Resistant Coatings*. National Research Council, Washington, DC.
- Nghiep, D. M., Paufler, P., Kramer, U., Kleinstück, K., and Quyen, N. H. (1980). *J. Mater. Sci.*, **15**, 1140.
- Nieh, T. G., and Oliver, W. C. (1989). *Scripta Metall.*, **23**, 851.
- Nowotny, H., Parthé, E., Kieffer, R., and Benesovsky, F. (1954). *Monatsh. Chem.*, **85**, 255.
- Ochia, S. Oya, Y., and Suzuki, T. (1984). *Acta Metall.*, **32**, 289.
- Oh, J. M., and McNallan, M. J. (1987). *Corrosion*, **43**, 561.
- Oya, Y., and Suzuki, T. (1983). *Z. Metallk.*, **74**, 21.
- Patnaik, P. C. (1989). *Mater. Manuf. Proc.*, **4**, 133.
- Quyen, N. H., Paufler, P., Berthel, K. H., Bertram, M., Kramer, U., Nghiep, D. M., San Martin, A., Gladun, A., and Kleinstück, K. (1979). *Phys. Stat. Sol. (A)*, **56**, 231.
- Raghavan, V. (1987). In *Phase Diagrams of Ternary Iron Alloys*, Part 1 (ed. H. Baker). The Indian Institute of Metals and ASM International, p. 31.
- Restall, J. E. (1968). *J. Less-Common Met.*, **16**, 11.
- Reuss, S., and Vehoff, H. (1990). *Scripta Metall. Mater.*, **24**, 1021.
- Rivlin, V. G., and Raynor, G. V. (1981). *Int. Met. Rev.*, **26**, 133.
- Saburi, T., and Nenno, S. *Philos. Mag.*, **15**, 813.
- Sadananda, K., Jones, H., Feng, J., Petrovic, J. J., and Vasudevan, A. K. (1991). *Ceram. Eng. Sci. Proc.*, **12**, 1671.
- Sato, H., and Yamamoto, H. (1950). *J. Phys. Soc. Jpn*, **6**, 65.
- Sauer, R. W., and Freise, E. J. (1968). In *Anisotropy in Single Crystal Refractory Compounds*, Vol. 2 (eds F. W. Vahldiek and S. A. Mersol). Plenum Press, New York, p. 459.
- Shepherd, F. D., Jr (1984). In *Infrared Detectors* (ed. W. L. Wolfe). *Proc. SPIE*, **443**, 42.
- Singheiser, L., Wahl, G., and Thiele, W. (1982). *Thin Sol. Films*, **95**, 35.
- Sinha, A. K. (1973). *J. Electrochem. Soc.: Solid-State Sci. Technol.*, **120**, 1767.
- Skolozdra, R. V., and Gladyshevskii, E. I. (1967). *Vysn. L'viv. Derzh. Univ., Ser. Khim.*, **9**, 21.
- Southwell, G., MacAlpine, S., and Young, D. J. (1987). *Mater. Sci. Eng.*, **88**, 81.
- Steglich, F., Aarts, J., Bredl, C. D., Lieke, W., Meschede, D., Franz, W., and Schafer, H. (1979). *Phys. Rev. Lett.*, **43**, 1892.
- Stephens, J. R., and Klopp, W. D. (1969). NASA Technical Note, NASA TN D-5157. NASA Lewis Research Center, Cleveland, OH.

- Takasugi, T., George, E. P., Pope, D. P., and Izumi, O. (1985). *Scripta Metall.*, **19**, 551.
- Takasugi, T., Nagashima, M., and Izumi, O. (1990). *Acta Metall.*, **38**, 747.
- Takasugi, T., Rikukawa, S., and Hanada, S. (1991). *Scripta Metall. Mater.*, **25**, 889.
- Takasugi, T., Shindo, D., Izumi, O., and Hirabayashi, M. (1990). *Acta Metall.*, **38**, 739.
- Takasugi, T., Suenaga, H., and Izumi, O. (1991) *J. Mater. Sci.*, **26**, 1179.
- Takasugi, T., Watanabe, S., Isumi, O., and Fat-Halla, N. K. (1989). *Acta Metall.*, **37**, 3425.
- Takasugi, T., and Yoshida, M. (1991a). *J. Mater. Sci.*, **26**, 3517.
- Takasugi, T., and Yoshida, M. (1991b). *J. Mater. Sci.*, **26**, 3032.
- Takeuchi, S., Hashimoto, T., and Shibuya, T. (1991). In *Intermetallic Compounds—Structure and Mechanical Properties* (ed. O. Izumi). The Japan Institute of Metals, Sendai, p. 645.
- Takeuchi, S., Hashimoto, T., and Shibuya, t. (1992). *J. Mater. Sci.*, **27**, 1380.
- Taub, A. I., and Briant, C. L. (1987). *Acta Metall.*, **35**, 159.
- Thornton, P. H., and Davies, R. G. (1970). *Metall. Trans.*, **1**, 549.
- Ting, C.-Yu., and Chen, C. Y. (1971). *Solid-State Electron.*, **14**, 433.
- Touns, B., Beauchamp, P., Mishima, Y., Suzuki, T., and Veyssi re, P. (1989). In *High Temperature Ordered Intermetallic Alloys III* (eds C. T. Liu, A. I. Taub, N. S. Stoloff, and C. C. Koch). *MRS Proc.*, **133**, 731.
- Tu, K. N., Thompson, R. D., and Tsaur, B. Y. (1981). *Appl. Phys. Lett.*, **38**, 626.
- Tung, R. T., Poate, J. M., Bean, J. C., Gibson, J. M., and Jacobson, D. C. (1982). *Thin Sol. Films*, **93**, 77.
- Uhlig, H. H., and Revie, R. W. (1985). *Corrosion and Corrosion Control*, 3rd edn. John Wiley & Sons Ltd, Chichester, p. 389.
- Umakoshi, Y., Hirano, T., Sakagami, T., and Yamane, T. (1989). *Scripta Metall.*, **23**, 87.
- Umakoshi, Y., Hirano, T., Sakagami, T., and Yamane, T. (1990a). In *High Temperature Aluminides and Intermetallics* (eds S. H. Whang, C. T. Liu, D. P. Pope, and J. O. Stiegler). The Minerals, Metals and Materials Society, Warrendale, PA, p. 111.
- Umakoshi, Y., Hirano, T., Sakagami, T., and Yamane, T. (1990b). *Acta Metall. Mater.*, **38**, 909.
- Umakoshi, Y., Nakashima, T., Yamane, T., and Senba, H. (1991). In *Intermetallic Compounds—Structure and Mechanical Properties* (ed. O. Izumi). The Japan Institute of Metals, Sendai, p. 639.
- Vasudevan, A. K., and Petrovic, J. J. (1992). *Mater. Sci. Eng.*, **155**, 1.
- Von Kanel, H. (1992). *Mater. Sci. Rep.*, **8**, 193.
- Watanabe, S., Nakamura, Z., Hanada, S., Sato, T., and Izumi, O. (1984). *Trans. JIM*, **25**, 477.
- Williams, K. J. (1971). *J. Inst. Met.*, **99**, 310.
- Wolfe, P. (1988). *J. Magn. Magn. Mater.*, **76/77**, 492.
- Wright, R. N. (1977). *Metall. Trans.*, **8A**, 2024.
- Yoshida, M., and Takasugi, T. (1991). In *Intermetallic Compounds—Structure and Mechanical Properties* (ed. O. Izumi). The Japan Institute of Metals, Sendai, p. 403.
- Yoshida, M., and Takasugi, T. (1992). *Philos. Mag. A*, **65**, 41.
- Yu, Y. V. (1970). *Solid-State Electron.*, **13**, 239.
- Zhang, T., Li, Y., Zheng, Z., and Zhu, Y. (1991). In *High Temperature Ordered Intermetallic Alloys IV* (eds L. A. Johnson, D. P. Pope, and J. O. Stiegler). *MRS Proc.*, **213**, 137.

This chapter was originally published in 1995 as Chapter 10 in *Intermetallic Compounds*, Vol. 2: *Practice*, edited by J. H. Westbrook and R. L. Fleischer.

Chapter 3

NiAl and its Alloys

Daniel B. Miracle

Air Force Wright Laboratory, Wright-Patterson AFB, Dayton, OH 45433, USA

Ramgopal Darolia

General Electric Aircraft Engines, 1 Neumann Way, Cincinnati, OH 45215, USA

1. Introduction

NiAl has been studied extensively as a potential structural material in the aerospace industry for over three decades. The attractive attributes of NiAl leading to this interest include a high melting temperature, low density, good environmental resistance, high thermal conductivity, attractive modulus, metal-like properties above a modest ductile-to-brittle transition temperature (DBTT), and low raw materials cost. NiAl can be processed relatively easily by conventional melting, powder, and metal-forming techniques. The two principal limitations of unalloyed NiAl are poor toughness and damage tolerance at room temperature (RT), and inadequate strength and creep resistance at elevated temperature. In spite of these limitations, the payoffs associated with the successful development of NiAl are substantial. The reduced density alone may produce a 30% reduction in the weight of a typical turbine rotor stage (turbine blades and disk), and the high thermal conductivity provides improved cooling efficiency and a significant reduction in airfoil temperatures and thermal gradients.

Investigations of the mechanical properties of NiAl have been conducted on polycrystalline alloys, single-crystal alloys, and NiAl-based composites. Although basic mechanical properties, such as flow strength and ductility, and the mechanisms of deformation have been studied extensively in polycrystalline NiAl, a comprehensive characterization of the full spectrum of physical and mechanical properties required for advanced

aerospace structural applications has not been undertaken for NiAl polycrystals. In contrast, a comprehensive, intensive, and focused activity with the specific goal of developing NiAl single crystals for structural applications in turbine engines has been undertaken. While both polycrystalline NiAl and NiAl single crystals will be discussed in this chapter, the emphasis in the present work reflects the level of understanding and the potential for near-term success with respect to structural applications of NiAl single crystals in gas-turbine engines. NiAl composite materials will be covered in Chapter 13 of this volume by Miracle and Mendiratta.

The goal of this chapter is to provide a focused, critical discussion and assessment of the development activity aimed at establishing NiAl as a high-temperature structural material in turbine engines. Science-based issues and engineering concerns which limit the application of NiAl will be discussed, along with creative approaches to overcoming the identified deficiencies. Insight gained from studies of deformation and failure mechanisms will be provided. In the following section, the physical and mechanical properties of NiAl (stoichiometric and nonstoichiometric) and NiAl alloys will be discussed, and will be compared with the requirements for advanced aerospace structural components (primarily blades and vanes in the high- and low-pressure turbine sections). Specific design considerations dictated by the properties of NiAl will be described in Section 3, and the issues of processing, machining, and component fabrication will be discussed in Section 4. Unless

otherwise stated, compositions will be given in atom % (at %).

2. Physical and Mechanical Properties of NiAl

While it is clear that a 'balance of properties' is required for structural applications in gas-turbine engines, this phrase is often interpreted to emphasize ductility (as a measure of damage tolerance) and strength. However, a stringent balance of a broad range of physical and mechanical properties is required for a successful turbine engine airfoil material, including high melting temperature, low density, moderate stiffness, high thermal conductivity, excellent damage tolerance (even at very high impact rates), good strength, good high- and low-cycle fatigue resistance, and environmental resistance. In addition to satisfying the above physical and mechanical requirements, a new material must address the practical considerations of processibility, machinability, fabrication, and cost effectiveness to compete successfully with existing materials. In this section, the principal physical and mechanical properties of binary and alloyed NiAl will be presented, and will be discussed with respect to the requirements for turbine blades and vanes. Many of the properties of NiAl are linked closely to the crystal structure and the high degree of long-range order, and so a brief review of the bonding, crystal structure, and phase stability is provided.

2.1 Physical Properties

2.1.1 Bonding, Crystal Structure, and Phase Stability

The electronic band structure of stoichiometric NiAl has been calculated using a variety of computational techniques (Lui *et al.*, 1990 and references therein), and the results of these calculations present evidence of strong Ni *d*-Al *p* hybridization along $\langle 111 \rangle$ directions between nearest neighbor Ni-Al atom pairs. Experimental measurements of the electron distribution show a number of features (Fox and Tabernor, 1991). A depletion of electrons occurs at both the Ni and Al sites, as well as from regions midway between next-nearest neighbors along $\langle 100 \rangle$ directions. Associated with these regions of electron depletion is a concomitant increase in electron density between nearest neighbor Ni-Al atom pairs along $\langle 111 \rangle$ directions. The strong Ni *d*-Al *p* hybridization and the buildup of electrons suggest a strong covalent bond along $\langle 111 \rangle$ directions between nearest neighbor Ni-Al atom pairs, and a weak ionic

repulsion between second-nearest neighbor atoms along $\langle 100 \rangle$ is suggested by the experimental observations. These directional bonds are superimposed over a metallic bond. The strong atomic bond along $\langle 111 \rangle$ and the weak bond along $\langle 100 \rangle$ are suggested to produce the observed elastic anisotropy of NiAl and the small shear constant C' . Further, the strength of the Ni-Al bond is qualitatively consistent with the large heat of formation (-72 kJ mol^{-1}) (Dannohl and Lukas, 1974; Henig and Lukas, 1975), the high congruent melting temperature of 1911 K (1638 °C) at the stoichiometric composition (Figure 1) (Nash *et al.*, 1991), the low degree of intrinsic disorder in NiAl (Neumann *et al.*, 1976; Ettenberg *et al.*, 1970), and the presence of short-range order in molten NiAl (Ayushina, 1969; Petrushevskii *et al.*, 1971).

NiAl possesses the ordered cubic B2 (cP2) CsCl crystal structure, which consists of two interpenetrating primitive cubic cells, where Al atoms occupy the cube corners of one sublattice and Ni atoms occupy the cube corners of the second sublattice (Figure 2). NiAl is strongly ordered, even above $0.65T_m$, with an intrinsic disorder parameter of less than 5×10^{-3} (Neumann *et al.*, 1976; Ettenberg *et al.*, 1970). The B2 structure is stable for large deviations from stoichiometry (Figure 1), and significant long-range order is reported for both Ni-rich and Al-rich compositions (Hughes *et al.*, 1971; West, 1964). Deviations from stoichiometry are accommodated by a variable defect structure, where excess Ni atoms occupy Al sites in Ni-rich compositions, and Al-rich compositions result by the formation of vacant Ni sites (Bradley and Taylor, 1937; Taylor and Doyle, 1972). Thermal defects are proposed to involve two lattice sites, and an asymmetric triple defect involving three lattice sites has also been proposed (Wasilewski, 1968). However, it has not been shown that the triple defect occurs in a strongly ordered compound such as NiAl (Miracle, 1993). Additional information on point defects in ordered alloys is provided in Chapter 23 of Volume 1 by de Novion. A martensitic transformation occurs after quenching Ni-rich NiAl (Guard and Turkalo, 1960). NiAl martensite has been reported to possess either a crystal structure related to the face-centred tetragonal $L1_0$ (tP4) structure (Rosen and Goebel, 1968; Enami *et al.*, 1973) or a unique rhombohedral unit cell with 7R stacking in the Ramsdell notation (Tanner *et al.*, 1990). The M_s temperature rises sharply with increasing Ni content, and varies from about 0 K for Ni-40% Al to 1000 K for Ni-32% Al (Smialek and Hehemann, 1973; Chakravorty and Wayman, 1976a; Au and Wayman, 1972). The three requirements for a material to possess the reversible

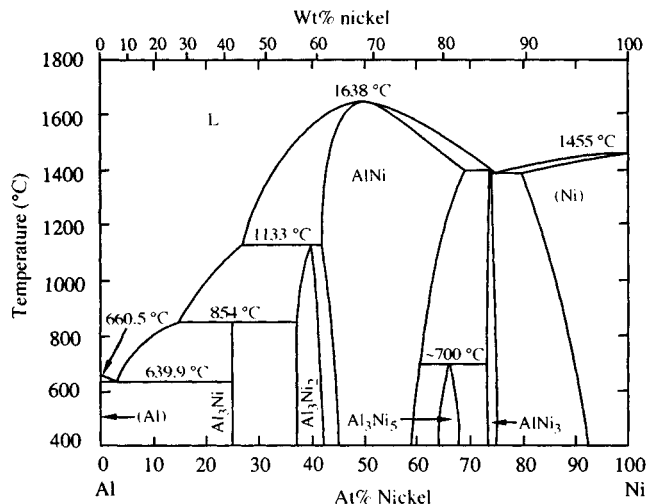


Figure 1. The binary Ni–Al phase diagram from Nash, Singleton, and Murray (1991)

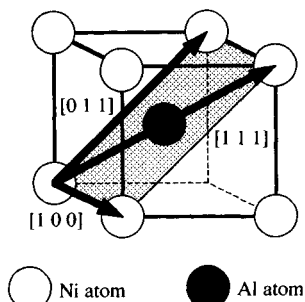


Figure 2. The B2 (cP2) crystal structure (space group $Pm\bar{3}m$, CsCl prototype) of NiAl, with the observed $a[100]$, $a[110]$ and $a[111]$ slip vectors shown on the (011) slip plane

shape memory effect have been shown to occur in NiAl: (i) the martensitic transformation is thermoelastic (Smialek and Hehemann, 1973; Chakravorty and Wayman, 1976a); (ii) the parent and product phases are ordered (Rosen and Goebel, 1968; Enami *et al.*, 1973); and (iii) the martensite is internally twinned (Enami *et al.*, 1973; Chandrasekaran and Mukherjee, 1974; Chakravorty and Wayman, 1976b). These findings are consistent with the observed reversible shape memory effect in NiAl (Enami and Nenno, 1971; Nagasawa *et al.*, 1974). Additional information on the shape memory effect is provided in Chapter 25 of this volume by Schetky.

2.1.2 Density

The density of nonstoichiometric NiAl ranges from 5.35 g cm^{-3} at the Al-rich boundary of the NiAl phase

field to 6.50 g cm^{-3} at the Ni-rich boundary (Bradley and Taylor, 1937; Taylor and Doyle, 1972; Rusovic and Warlimont, 1977; Harmouche and Wolfenden, 1987). The density of binary NiAl at the stoichiometric composition (5.85 g cm^{-3}) is roughly two thirds that of typical Ni-based superalloys, and this provides one of the major benefits of NiAl as an aerospace structural material. The decreased density results in lower self-induced stresses in rotating turbine airfoils, and the turbine disks may be downsized to reflect the lower operating stresses imposed by the reduced mass of the blades. The total reduction in weight for the turbine rotor stage (blades plus disk) is projected to range from 30 to 40% (Darolia, 1991; Darolia *et al.*, 1992a), which represents a decrease of up to 50 kg per rotor stage in a typical turbine engine. This decrease in weight has a cascading effect, whereby the mass of other support structures, such as shafts and bearings, may similarly be reduced. As an added performance benefit, lower weight blades and disks result in lower inertial mass for rotating parts, providing better engine acceleration. The decreased density of NiAl also offers an increased level of flexibility to airfoil designers, whereby increased wall thickness leading to reduced stresses and increased life may be considered, while still providing a weight reduction over existing turbine airfoil materials. In addition, a lower density provides a higher natural frequency of vibration for a given airfoil geometry, so that vibrational modes may be avoided which otherwise would be excited for a particular operational regime.

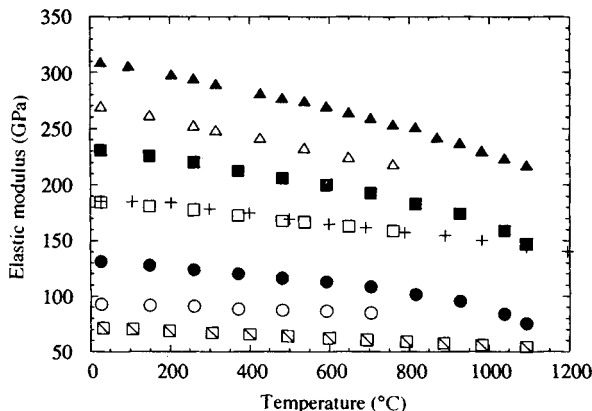


Figure 3. Young's modulus as a function of temperature for single-crystal NiAl along the $\langle 100 \rangle$ (\circ), $\langle 110 \rangle$ (\square), and $\langle 111 \rangle$ (\triangle) directions (Wasilewski, 1966), and for a single-crystal, Ni-based superalloy along the $\langle 100 \rangle$ (\bullet), $\langle 110 \rangle$ (\blacksquare), and $\langle 111 \rangle$ (\blacktriangle) directions (Lahrman and Darolia, 1992). The Young's modulus (+) and shear modulus (\boxtimes) of polycrystalline NiAl are also provided (Moose, 1991)

2.1.3 Melting Temperature

Significant improvements in engine cycle efficiency are made possible by increasing the operating temperature of materials in the gas path. Stoichiometric NiAl has a congruent melting temperature of 1638 °C, which is nearly 300 °C higher than the melting temperature of conventional Ni-based superalloys. Nonstoichiometric compositions possess a reduced melting temperature (Figure 1), but still maintain an advantage over current airfoil materials. Melting temperature not only specifies the physical upper limit on use temperature, but also defines the homologous temperature scale, which dictates the temperature at which diffusion-controlled deformation mechanisms begin to dominate. Bulk diffusion in body-centered cubic (b.c.c.) and ordered b.c.c. derivative structures, such as NiAl, typically becomes important above $0.5T_m$ (680 °C), leading to poor high-temperature creep and stress-rupture behavior of binary NiAl. Therefore, while the higher melting temperature of NiAl may provide an opportunity for higher operating temperatures, additional strengthening mechanisms must be developed to utilize this advantage. This will be discussed in more detail in Section 2.2.3 on the creep and stress-rupture behavior of NiAl.

2.1.4 Modulus

A high elastic modulus is often considered to be beneficial in aerospace applications, since service loads

produce smaller elastic deflections. In addition, a higher modulus of elasticity influences the frequency of harmonic vibrations, and a higher modulus increases the natural frequency of vibrations, thereby possibly avoiding vibrational modes at the highest rotational speeds. However, smaller elastic deflections and higher natural frequencies may also be achieved by increasing the section modulus of the airfoil shape. Thermally induced stresses are directly proportional to the elastic modulus, and so larger thermal stresses are produced in a material with a higher modulus for a given thermal gradient. Since thermal fatigue is one of the primary modes of failure in a turbine airfoil, a lower modulus is desirable to improve the thermal fatigue resistance.

Young's modulus of polycrystalline, stoichiometric NiAl at room temperature (188 GPa) (Moose, 1991; Rusovic and Warlimont, 1979) is slightly lower than the Young's moduli of transition metals such as Fe, Co, and Ni (200–210 GPa) and Ni-based superalloys. However, the modulus of NiAl exhibits a reduced sensitivity to temperature, dropping about 2% at 100 °C (Figure 3) (Wasilewski, 1966), compared to 2.4 to 3.2% for the same transition metals. In addition, the lower density of NiAl offsets this lower modulus of NiAl in rotating (self-loading) parts. The modulus of polycrystalline binary NiAl is reported to be relatively insensitive to composition within 6% of the stoichiometric composition (Harmouche and Wolfenden, 1987; Rusovic and Warlimont, 1979), but the single-crystal elastic constants show a significant temperature dependence (Rusovic and Warlimont, 1977). The Young's modulus of NiAl single crystals is highly anisotropic (Figure 3), and the ratio of $E_{\langle 111 \rangle}/E_{\langle 100 \rangle}$ is nearly 2.9 for NiAl at RT, compared to a value of 2.4 for a typical Ni-based superalloy (Lahrman and Darolia, 1992). However, this ratio attains a value of about 2.6 for both NiAl and the Ni-based superalloy at 980 °C. The shear modulus G for polycrystalline NiAl is also given in Figure 3 (Moose, 1991). The temperature dependence of Poisson's ratio for NiAl has been calculated from the Young's modulus and the shear modulus, and is given as

$$\nu = 0.307 + 2.15 \times 10^{-5} T$$

where T is the temperature in Kelvin (Moose, 1991).

2.1.5 Thermal Conductivity

Thermal conductivity influences the design and application of airfoil materials in two ways. First, more efficient

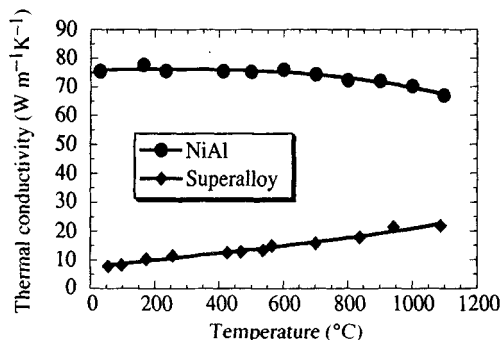


Figure 4. The thermal conductivity of NiAl single crystals as a function of temperature. Data for a typical Ni-based superalloy are provided for comparison (Darolia, 1991)

airfoil cooling is achieved with the rapid heat transfer afforded by high thermal conductivity, providing either a lower metal temperature or a reduction in the amount of cooling air required. The peak temperature for a typical NiAl turbine airfoil may be reduced by as much as 50 °C compared to an Ni-based airfoil using an equivalent amount of cooling air (Lahrman and Darolia, 1992; Darolia *et al.*, 1992). Higher thermal conductivity also produces lower thermal gradients. This reduces the magnitude of thermally induced stresses, since thermal stresses are directly proportional to the thermal gradients.

The thermal conductivity of NiAl is 70–80 W m⁻¹K⁻¹ over the temperature range 20–1100 °C (Darolia, 1991). This is three to eight times larger than the thermal conductivity of Ni-based superalloys (Figure 4), and about one third that of Al. While the overall bulk airfoil temperature may be expected to increase slightly, the thermal gradients are reduced significantly (Lahrman and Darolia, 1992), resulting in lower thermal stresses and improved thermal fatigue. However, the higher thermal conductivity of NiAl may result in higher heat loads to the disk. Alloying tends to reduce the thermal conductivity of NiAl, but significant advantages over Ni-based superalloys are retained (Walston, 1992a; Walston and Darolia, 1993).

2.1.6 Environmental Resistance

High-temperature structural components of advanced aerospace systems typically require service in an oxidizing environment, and this is especially true for turbine airfoils. Resistance to hot salt corrosion and sulfidation is also required. Environmental attack leads to degradation of mechanical properties, and compromises the structural integrity of turbine airfoils, especially in areas with thin cross-sections. NiAl forms the basis of a family

of high-temperature, oxidation-resistant and corrosion-resistant alloys which have been used as coatings on Ni-based and Co-based superalloys in gas-turbine engines over the past 30 years (Goward, 1970; Boone and Goward, 1970). Binary NiAl forms a continuous, protective layer of alumina over a range of temperatures and compositions in the single-phase field (Hutchings and Loretto, 1978). The parabolic rate constant is very low, even in compositions with up to 60 at% Ni, and is typically two orders of magnitude lower than for typical Ni-based superalloys (Barrett, 1988; Smialek and Meier, 1987; Doychak *et al.*, 1989). The oxidation rate in binary compositions is relatively independent of the crystallographic orientation of the oxidized surface on single crystals (Jedlinski and Mrowec, 1987). A variety of alloying additions have been applied to improve performance in static and cyclic oxidation. A significant improvement in oxidation resistance by addition of 0.1% Zr is noteworthy (Barrett, 1988). NiAl has not been shown to exhibit a pest phenomenon. While NiAl is significantly better in environmental resistance than Ni-based superalloys, it has not yet been determined that NiAl alloyed for improved mechanical properties will possess adequate environmental resistance to operate uncoated. It should be mentioned that the coatings used on virtually all turbine blades and vanes are essentially NiAl which has been modified by diffusion of alloying elements from the underlying superalloy, such as Cr, Ti, Mo, W, and Ta.

The rate of sulfidation attack is also parabolic for binary NiAl, and is several orders of magnitude faster than the oxidation of NiAl (Mrowec *et al.*, 1989). The hot-corrosion resistance of unalloyed NiAl is inferior to that of many conventionally cast Ni-based superalloys and is comparable to the newer single-crystal alloys. The corrosion resistance of NiAl can be increased substantially by small additions of Cr and Y (McCarron *et al.*, 1976). The reader is referred to the chapters on oxidation (Doychak, Chapter 43) and corrosion (Duquette, Chapter 42) in Volume 1 for more detailed information.

2.1.7 Coefficient of Thermal Expansion

The coefficient of thermal expansion (CTE) is important for structural applications since thermal stresses depend directly on the magnitude of the CTE. The CTE of NiAl is comparable to that typical for Ni-based superalloys, and is 15.1×10^{-6} K⁻¹ from 820 °C to 1560 °C for stoichiometric NiAl (Wachtell, 1952). Deviations from stoichiometry and minor alloying additions have little influence on the CTE (Rusovic and Warlimont, 1977; Clark and

Whittenberger, 1984; Walston, 1992b; Walston and Darolia, 1993).

2.2 Mechanical Properties

The defect structures and mechanisms of deformation have a strong influence on the mechanical properties of NiAl and their anisotropy in single crystals. These are briefly outlined below to provide a basis for discussion of the mechanical properties of NiAl.

NiAl has a low formation energy for thermal vacancies, and up to 2% of the lattice sites are vacant near the melting temperature (Epperson *et al.*, 1978; Parthasarathi and Fraser, 1984). In addition to these thermal point defects, a large concentration of constitutional point defects (of the order of several % of the lattice sites) is possible in NiAl. As stated earlier, deviations from stoichiometry are accommodated by a variable defect structure, where excess Ni atoms occupy Al lattice sites in Ni-rich NiAl and Ni vacancies form in Al-rich compositions. These constitutional defects have been suggested to form clusters with short-range order, which may act as nuclei for phases adjacent to NiAl (Fox and Tabernor, 1991; Taylor and Doyle, 1972), and may strengthen nonstoichiometric NiAl (Lasalmonie *et al.*, 1979).

$a\langle 100 \rangle$ is the primary Burgers vector in NiAl, and this slip vector operates on the $\{100\}$ and $\{110\}$ planes (see Figure 2) (Ball and Smallman, 1966a; Kim, 1991; Field *et al.*, 1991a). Although $a\langle 100 \rangle$ screw dislocations are elastically unstable, these dislocations may be stabilized under stress, allowing profuse cross slip to occur (Loretto and Wasilewski, 1971). The critical resolved shear stress (c.r.s.s.) for $a\langle 100 \rangle$ dislocations on $\{110\}$ planes is about 70 MPa in nominally stoichiometric, binary NiAl at RT (Wasilewski *et al.*, 1967; Ball and Smallman, 1966b; Pascoe and Newey, 1968), but there is zero resolved shear stress on these preferred dislocations for single crystals deformed along a $\langle 100 \rangle$ axis. These cube-oriented single crystals are called 'hard' crystals, since they have anomalously high flow stress. The compressive plastic deformation of 'hard' crystals occurs by the motion of $a\langle 111 \rangle$ dislocations on $\{110\}$ or $\{112\}$ planes below 300 °C (Loretto and Wasilewski, 1971; Veyssi re and Noebe, 1992; Campy *et al.*, 1973; Kim, 1991), and is accompanied by the activation of $a\langle 110 \rangle$ dislocations on $\{110\}$ planes above this temperature (Miracle, 1991; Field *et al.*, 1991b; Kim, 1991). $a\langle 111 \rangle$ dislocations are not typically observed in 'hard' crystals tested in tension below 300 °C (Darolia *et al.*, 1992). The c.r.s.s. for $a\langle 111 \rangle$ dislocations is about 600 MPa at RT (nearly 1% of the

shear modulus), and drops only slightly at 300 °C to about 575 MPa (Pascoe and Newey, 1968). $a\langle 110 \rangle$ dislocations begin to operate above 300 °C (Miracle, 1991; Kim, 1991; Field *et al.*, 1991b), and the c.r.s.s. for these dislocations drops rapidly with increasing temperature from about 575 MPa at 300 °C to less than 100 MPa above 700 °C (Miracle, 1993 and references therein). Above 700 °C, an analysis of the available evidence suggests that NiAl deforms by diffusional processes (Miracle, 1993).

It has been suggested that a reduction of the $a/2\langle 111 \rangle$ antiphase boundary (APB) energy will favor the activation of $a\langle 111 \rangle$ dislocations, providing the five independent slip systems necessary for polycrystalline ductility (Rachinger and Cottrell, 1956). A number of computational algorithms have been applied to calculate this quantity in NiAl, and to assess the influence of ternary additions on the APB energy. Calculations using the embedded atom method (for a discussion of this technique, see Voter, Chapter 4 in Volume 1) provide APB energies ranging from 240 to 460 mJ m⁻² (Clapp *et al.*, 1989; Rao *et al.*, 1991), while first-principles calculations predict values near 900 mJ m⁻² (Fu and Yoo, 1991; Hong and Freeman, 1991a). *Ab initio* calculations suggest that large additions of ternary elements, such as Cr and Mn, as well as large deviations from stoichiometry, significantly reduce the APB energy of NiAl (Hong and Freeman, 1991a,b). Shear-induced planar defects, such as APBs, have not been observed in NiAl, and an experimentally determined lower bound on the APB energy ranges from 500 to 750 mJ m⁻² (Veyssi re and Noebe, 1992). Thus, the high APB energy in NiAl has been suggested to contribute to the difficulty in moving non- $a\langle 100 \rangle$ dislocations. Further discussion of planar defects in NiAl is provided elsewhere (Miracle, 1993), and the reader is also referred to Chapter 21 by Sun in Volume 1.

2.2.1 Ductility

The RT tensile ductility of polycrystalline binary NiAl can range from 0 to 2%, depending upon stoichiometry (Hahn and Vedula, 1989), texture (Hahn and Vedula, 1989; Vedula *et al.*, 1989), grain size (Schulson and Barker, 1983), and possibly impurity content and substructure. The $\langle 100 \rangle$ slip direction provides only three independent slip systems, and this limitation has been used to explain the lack of significant RT tensile plasticity in polycrystalline NiAl. Above the DBTT of about 400 °C, polycrystalline NiAl becomes very ductile, and plastic elongations of over 40% are observed at 600 °C (Hahn and Vedula, 1989). Additional slip systems

have not been verified to operate in NiAl polycrystals, and it has been proposed that both climb and glide are responsible for the ductility of polycrystalline NiAl up to about 800 °C (Hahn and Vedula, 1989; Miracle, 1993). Above 800 °C, diffusion-assisted processes are likely to control the deformation of polycrystalline NiAl (Miracle, 1993).

The RT tensile ductility of binary NiAl single crystals is anisotropic. 'Hard' single crystals fail after only elastic strains, while other orientations (termed 'soft' crystals), such as $\langle 110 \rangle$ and $\langle 111 \rangle$, possess up to 2% plastic deformation (Lahrman *et al.*, 1991). In compression, 'hard' single crystals typically deform by 'kinking', an extremely localized shear instability which occurs by the glide of $\frac{1}{2}\langle 100 \rangle$ dislocations (Fraser *et al.*, 1973a; Fraser *et al.*, 1973b). Again, the plastic behavior is highly sensitive to stoichiometry and interstitial content. Potential factors limiting ductility in single crystals include inadequate dislocation sources, low dislocation mobility, inhomogeneous slip, and low fracture stress. Each of these have been postulated to explain the brittle failure of 'hard' single crystals, and it is uncertain as to what extent these may apply to the deformation of 'soft' single crystals and polycrystals. The DBTT for 'soft' crystals is 200 °C, while 'hard' crystals become ductile just below 400 °C (Lahrman *et al.*, 1991). NiAl single crystals become very ductile above the DBTT, and both 'hard' and 'soft' crystals exhibit more than 20% elongation at 400 °C (Lahrman *et al.*, 1991; Wasilewski, *et al.*, 1967). The dependence of ductility and the DBTT on strain rate is small in both 'hard' and 'soft' single crystals between strain rates of 8.3×10^{-5} and $8.3 \times 10^{-3} \text{ s}^{-1}$ (Lahrman *et al.*, 1991). However, the ductility of NiAl at impact strain rates has not been determined.

While fundamental concepts exist which address potential sources of limited ductility in NiAl, such as poor grain boundary cohesion, an insufficient number of independent slip systems, and slip localization, these concepts do not provide clear guidance on the selection of alloying additions which can modify these effects. Therefore, efforts to improve the intrinsic RT ductility of NiAl have typically been based on empirical reasoning. Boron additions to strengthen NiAl grain boundaries have not succeeded in improving ductility significantly, since B is a potent solid-solution strengthener, and the yield strength of NiAl + B typically exceeds the fracture strength (George and Liu, 1990). Alloying additions to increase the number of independent slip systems by lowering the APB energy have been rationalized in various ways (Field *et al.*, 1991; Law and Blackburn, 1987), and it has been

reported that Cr additions favor the activation of $\frac{1}{2}\langle 111 \rangle$ dislocations (Law and Blackburn, 1987; Miracle *et al.*, 1989; Field *et al.*, 1991c). However, these approaches address a condition that has been found to be necessary but insufficient for ductility. Theoretical and practical approaches which are able to address the basic issues of the nucleation and mobility of a sufficient number of glide dislocations and the homogeneity of slip have not yet been established.

Impurities (especially interstitial elements) are generally considered to have a strong influence on the ductility of intermetallic alloys. While both B and C have been shown to increase the DBTT at levels $\geq 300 \text{ p.p.m.}$ by weight (w.p.p.m.) (George and Liu, 1990; Law and Blackburn, 1987; George *et al.*, 1990), no definite effect has been established for most potential interstitial contaminants in NiAl. Typical impurity levels are 40–80 w.p.p.m. for O and C, and 1–5 w.p.p.m. for S, P, and N. However, much higher levels may result from powder processing or careless handling. Although the Si content is expected to be low in polycrystalline material, Si can be as high as 1000 w.p.p.m. in NiAl single crystals due to contamination from the mold material during single-crystal processing.

Microalloying with Fe, Ga, and Mo has recently been shown to improve significantly the RT tensile ductility of NiAl single crystals tested along a $\langle 110 \rangle$ direction, increasing the failure strain from a typical value of 1% for stoichiometric NiAl to as high as 6% for NiAl + 0.25% Fe (Darolia *et al.*, 1992a; Darolia *et al.*, 1992b). The plastic elongation to failure at RT as a function of Fe, Ga, and Mo concentration for the $\langle 110 \rangle$ -oriented specimens is shown in Figure 5(a), and the 0.2% yield strengths are plotted as a function of alloying concentration in Figure 5(b). Solid-solution softening may be occurring in NiAl with Fe and Ga, while solid-solution strengthening is suggested for Mo additions (Figure 5). While the alloys containing Fe and Ga are single phase, the NiAl + Mo alloys contain very small (5–20 nm) α -Mo precipitates, which could explain the increased yield strength in these alloys. Single crystals with 0.25% Fe showed similar increases in plastic strains to failure for other orientations, except for crystals tested along $\langle 100 \rangle$. However, the DBTT of $\langle 100 \rangle$ -oriented single crystals decreased with additions of 0.1% Fe and 0.25% Fe (Darolia *et al.*, 1992b). The slip system is unchanged with these microalloying additions. Even though substantial plastic elongation is observed, the fracture surface still consists of cleavage facets.

The mechanism(s) by which these elements enhance the RT ductility of $\langle 110 \rangle$ NiAl single crystals have not been established, and are only speculative at this point.

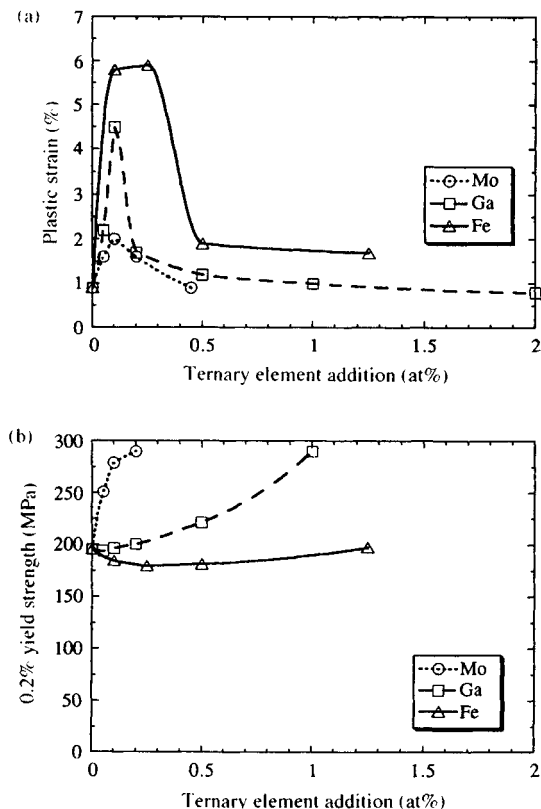


Figure 5. The compositional dependence of (a) ductility, and (b) 0.2% yield strength of NiAl single crystals tested in tension along a $\langle 110 \rangle$ direction at RT (Darolia *et al.*, 1992b)

The c.r.s.s. for a $\langle 111 \rangle$ dislocations is not significantly reduced, and transmission electron microscopy (TEM) observations do not suggest the activation of additional slip systems. One speculation is that alloying additions affect the electronic structure and bonding characteristics of NiAl, which may then alter the dislocation core structure, and hence modify dislocation mobility, the Peierls stress, and thermally activated slip processes. Indirect effects, arising from interactions with point defects or impurities in NiAl (particularly interstitial elements such as O, N, C, or S) could also be responsible for the ductility enhancement, as could closer effective approach to precise stoichiometry made possible by substitutional atoms. The large increases in tensile ductility by microalloying are exciting and provide an approach for producing ductile NiAl alloys. It is important to note that many earlier studies investigated alloy additions $\geq 1\%$, where little or no improvement in ductility was measured by Darolia (1991), and additional activity in the area of microalloying may be fruitful.

Alloy additions to polycrystalline NiAl have been largely unsuccessful in producing RT tensile ductility, with the possible exception of small Mo additions (Grala, 1960; Law and Blackburn, 1987; Russell *et al.*, 1991). Although a critical grain size has been postulated below which apparent ductility may be induced by stable microcracking (Schulson and Barker, 1983; Schulson, 1985), an analysis of the available experimental data does not fully support this proposition (Miracle, 1993). It has been shown that extruded NiAl near the stoichiometric composition can exhibit as much as 2% RT tensile elongation (Hahn and Vedula, 1989). This material is strongly textured, but the reasons why a textured material should possess enhanced ductility have not been addressed.

2.2.2 Strength

A turbine airfoil is subjected to stresses from centrifugal loading, thermal stresses from temperature gradients, stresses from the high-velocity gas, and vibrational excitation. Depending on the airfoil design, temperature, and location on the turbine blade, a typical Ni-based superalloy requires a tensile yield strength of approximately 700–1000 MPa at RT, and up to 500 MPa at temperatures as high as 800 °C. The creep and stress-rupture performance, and the high- and low-cycle fatigue resistance, are also strongly dependent on the tensile properties of the airfoil material. Overall, the strength properties of NiAl alloys must at least equal those of older Ni-based superalloys such as René 80, B1900 or MarM 200, which have been used for over 20 years as blade materials. The density and the thermal conductivity advantages would then make NiAl alloys attractive replacements for the newer single-crystal superalloys.

The temperature dependence of the tensile yield strength of single-crystal and polycrystalline stoichiometric NiAl is shown in Figure 6 (Darolia, 1991; Darolia *et al.*, 1992a; Field *et al.*, 1991). The strength is compared with René 80, a conventionally cast, Ni-based superalloy commonly used as a turbine blade material. The yield strength of NiAl polycrystals and ‘soft’ single crystals is too low to be of interest in the stoichiometric, unalloyed state. Although ‘hard’ single crystals are somewhat more attractive, the strength drops rapidly with increasing temperature. It is obvious that the strength of binary NiAl needs significant improvement to be competitive with Ni-based superalloys. Deviations from stoichiometry can have a potent strengthening effect, and a Ni–40% Al alloy provides a significant strengthening increment in compression up to 700 °C

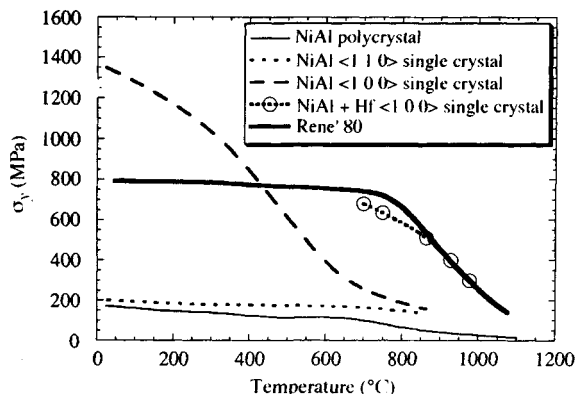


Figure 6. The temperature dependence of the tensile yield strength of binary, polycrystalline NiAl (Rozner and Wasilewski, 1966) and binary NiAl single crystals tested along $\langle 110 \rangle$ (Darolia *et al.*, 1992a) and $\langle 100 \rangle$ (Field *et al.*, 1991b). Data for polycrystalline René 80 (Darolia, 1991) are included for comparison. The strength improvement for NiAl alloyed with Hf tested along a $\langle 100 \rangle$ axis is also shown (Darolia *et al.*, 1992c)

(Bowman *et al.*, 1989). This effect diminishes with increasing temperature, and at 1200 °C stoichiometric NiAl is as strong as nonstoichiometric NiAl (Vandervoort *et al.*, 1966). Stoichiometric and Ni-rich NiAl follow the Hall–Petch relationship

$$\sigma_y = \sigma_0 + k d^{-1/2}$$

and both σ_0 and k increase with increasing deviation from stoichiometry (Schulson and Barker, 1983; Baker *et al.*, 1991). The strain-hardening rate is high below the DBTT, but decreases significantly above this temperature (Hahn and Vedula, 1989; Raj *et al.*, 1989; Ball and Smallman, 1966b; Rozner and Wasilewski, 1966; Lautenschlager *et al.*, 1965). Disagreement exists between different studies concerning the effect of strain rate on the yield strength of NiAl at different temperatures, but drastic changes in strength are not observed under strain rates from roughly 10^{-2} to 10^{-4} s^{-1} (Lahrman *et al.*, 1991; Wasilewski *et al.*, 1967; Pascoe and Newey, 1968).

The high-temperature strength of NiAl may be improved by solid-solution strengthening, precipitate strengthening (with metallic, intermetallic, or ceramic particles), elimination of grain boundaries by the single-crystal route, and composite strengthening. NiAl composites will be addressed in Chapter 13 of this volume by Miracle and Mendiratta.

Solid-solution strengthening can be significant even at low levels of the ternary element, especially with

addition of Group IVB and VB elements such as Ti, Hf, Zr, V, and Ta. For example, additions of 0.2% Hf to NiAl can increase the RT tensile strength of a $\langle 110 \rangle$ -oriented specimen from a typical value of 210 MPa for stoichiometric NiAl to 600 MPa (Darolia *et al.*, 1992). Limited low-temperature solubility ($< 1\%$) exists for elements such as Cr, Mo, and Re. When added beyond their solubility limit, these elements precipitate a disordered b.c.c. phase, which strengthens NiAl. Proper solution and aging treatments can result in control of the size and distribution of these precipitates. NiAl ternary alloys with b.c.c. refractory metals often possess a eutectic reaction, and directionally solidified microstructures result in a dramatic increase in high-temperature strength (Stover, 1966), as shown in Figure 7.

Additions of Group IVB or VB elements beyond their solubility limits in NiAl produce several ternary intermetallic compounds, including the $L2_1$ (cF16) Heusler (or β') phase Ni_2AlX , and the primitive hexagonal Laves phase (hP12) NiAlX . These phases can contribute significantly to the strengthening of the NiAl alloys (Rudy and Sauthoff, 1986; Sauthoff, 1989; Polvani *et al.*, 1976). The close relationship between the B2 and $L2_1$ crystal structures (Figure 8) results in coherent or semicoherent precipitates, which can strengthen NiAl alloys to levels equivalent to those of the Ni-based superalloy MarM 200 (Polvani *et al.*, 1976). NiAl alloys strengthened by the Laves phase are more brittle than alloys strengthened by the β' phase, and are more difficult to machine into test specimens. Si contamination (600–1000 w.p.p.m) from mold materials during single-crystal processing results in 10–40 nm cuboidal precipitates of the ordered G phase ($\text{Ni}_6\text{X}_6\text{Si}$; (cF116), where X is Zr or Hf) (Locci *et al.*, 1991). These precipitates are coherent with NiAl and are fairly resistant to coarsening. The G phase is known to have attractive high-temperature properties (Westbrook, 1956), and it is possible that the G phase contributes to strengthening in NiAl. However, its exact role needs further exploration. Significant potential exists for further improvement in strength (and perhaps ductility and toughness) by careful development of the volume fraction and morphology of the β' precipitates in NiAl, similar to the development of $\gamma-\gamma'$ Ni-based superalloys. A fundamental, systematic study of the precipitate volume fraction, morphology, lattice mismatch and coherency strains, size effects, precipitate stability, and solid-solution contributions is warranted. NiAl alloys strengthened with incoherent dispersoids such as Al_2O_3 , TiB_2 and HfC are being developed by various research groups (Whittenberger and Viswanadham 1989; Jha *et al.*,

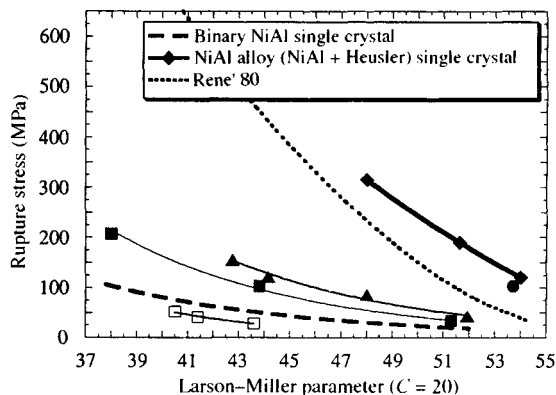


Figure 7. The stress-rupture properties of NiAl and NiAl alloys. The Larson-Miller parameter is calculated as $P = (T_R/1000)(\log t + 20)$, where T_R is the absolute temperature in Rankine, and t is the time in hours. The data are for binary polycrystalline NiAl (\square) (Grala, 1960), and alloys of NiAl + 9% Mo aligned eutectic (\bullet) (Stover, 1966), NiAl + 6 vol% ThO_2 (\blacksquare) (Seybolt, 1966), and NiAl + 20 vol% TiB_2 (\blacktriangle) (Kumar, 1991). The dashed lines are from Figure 12 of Darolia (1991). The line for the NiAl single-crystal alloy with Heusler precipitates represents the upper bound of a range of data (Darolia *et al.*, 1992a; Darolia *et al.*, 1992b), and this alloy is equivalent to the single-crystal, Ni-based superalloy René N4

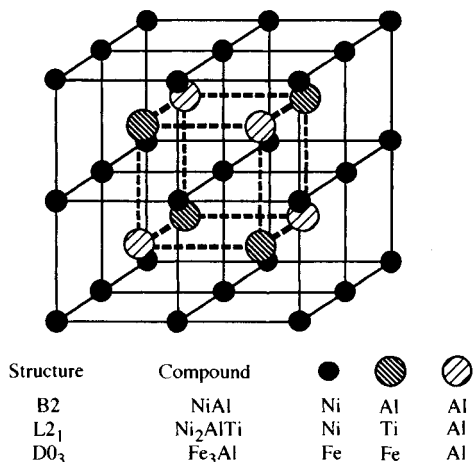


Figure 8. Crystal structure of the B2 derivative lattices, illustrating the close relationship between the B2 (cP2) and L2₁ Heusler (cF16, or β') structures

1989; Whittenberger *et al.*, 1990), but these alloys do not yet compete with the β' -strengthened NiAl, as shown in Figure 7 (Kumar *et al.* 1992b).

NiAl single-crystal alloys show dramatic improvements in high-temperature strength over NiAl polycrystals, and their strengths can equal Ni-based, single-crystal

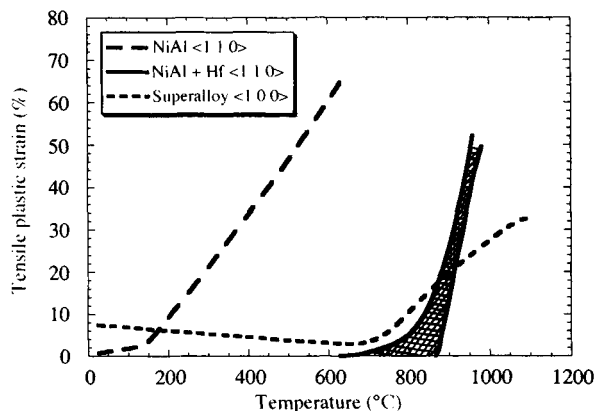


Figure 9. Tensile ductility as a function of temperature typical of strengthened NiAl single-crystal alloys in the cross-hatched area (Darolia *et al.*, 1992a). The ductilities of binary NiAl and a typical Ni-based superalloy are shown for comparison

strength levels (Figures 6 and 7). Accounting for the higher thermal conductivity and lower density of NiAl (the stresses in Figure 6 and 7 are not corrected for density), these NiAl alloys are attractive replacements for current single-crystal, Ni-based superalloys.

NiAl single-crystal alloys which possess the best high-temperature strengths are generally less ductile than binary NiAl, have DBTTs which increase substantially as the strength is increased, and possess low fracture toughness values. Figure 9 shows ductility as a function of temperature typical of strengthened NiAl alloys (Darolia *et al.*, 1992c). The high DBTT of strengthened NiAl single-crystal alloys remains an issue which must be resolved through further alloy development or design methodology. Development of intermetallic alloys possessing both RT ductility and sufficient high-temperature strength is a very difficult challenge and may prove to be an elusive goal.

2.2.3 Creep and Stress-rupture

Highly creep-resistant materials are desirable to maintain the aerodynamic shape of the airfoil and a tight clearance between the blade tip and the gas path seal, which controls the cycle efficiency of the turbine engine. Typical creep requirements for a Ni-based superalloy include stresses up to 200 MPa at temperatures as high as 1000 °C for over 300 h. A creep strain of 1% is often considered to constitute a creep failure. Therefore, both the steady-state creep rate and the amount of primary creep strain must be very low for acceptable creep performance. Ni-based superalloys rely on precipitation

Table 1. Summary of creep parameters for NiAl

Al (at%)	Grain size (μm)	Temperature (°C)	<i>n</i>	<i>Q</i> (kJ mol ⁻¹)	Reference
48.25	5–9	723–1123	6–7.5	313	Whittenberger (1988)
49.2	15–20	823–1123	5.75	314	Whittenberger (1987)
50	12	923–1023	6	350	Whittenberger, Arzt, and Luton (1990)
50	450	800–1045	10.2–4.6	283	Yang and Dodd (1973)
50	500	900	4.7		Rudy and Sauthoff (1985)
50.4	1000	802–1477	7–3.3	230–290	Vandervoort, Mukherjee, and Dorn (1966)
50	SX [123]	750–950	7.7–5.4		Hocking, Strutt, and Dodd (1971)
50	SX	750–1055	4–4.5	293	Bevk, Dodd, and Strutt (1973)
50	SX [001]	723–1023	6	440	Noebe and Whittenberger (1991)

SX = single crystal.

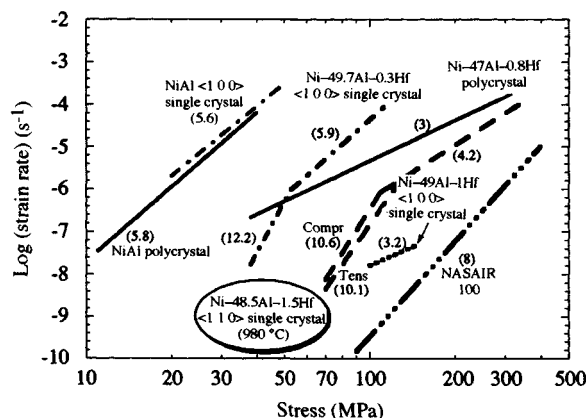


Figure 10. Log (strain rate) versus stress (logarithmic scale) for single-crystal and polycrystalline NiAl at 1023 °C (Whittenberger, 1987; Nathal and Ebert, 1985; Whittenberger *et al.*, 1991; Field, 1991; Nathal, 1992; Locci *et al.*, 1992). The stress exponent *n* is shown in parentheses. Data for several NiAl + Hf alloys and for the Ni-based superalloy NASAIR 100 are included for comparison (Compr = compression testing; Tens = tensile testing) (Darolia *et al.*, 1992)

strengthening to allow operation at 85% of their homologous melting temperature (~1150 °C), while binary NiAl, being a b.c.c.-derivative structure, does not have useful creep strength above about 50% of its absolute melting temperature (~680 °C).

The creep deformation of NiAl can be divided into primary, secondary and tertiary stages, as commonly observed for metals and alloys. The secondary creep rate has been expressed in the form of Dorn's equation

$$\dot{\epsilon} = A \sigma_n \exp(-Q/RT)$$

where σ is the applied stress, *n* is the stress exponent, *Q* is the activation energy for creep, *R* is the gas constant, *T* is the absolute temperature, and *A* is a constant related to the structure of the material. A summary of reported

creep parameters for binary NiAl is presented in Table 1 (from Nathal, 1992), and a comparison of the creep behavior of NiAl single crystals and polycrystals is presented in Figure 10 (Whittenberger, 1987; Nathal and Ebert, 1985; Whittenberger *et al.*, 1991; Field, 1991; Nathal, 1992; Locci *et al.*, 1992). An analysis of data in the literature for the stress exponent *n*, substructural observations, and activation energies clearly establish the role of diffusional processes in the creep of binary NiAl above about 900 °C (Miracle, 1993). The exponent *n* appears to depend on orientation in single crystals (Forbes *et al.*, 1992). Although the scatter in *n* makes it difficult to specify with confidence a particular deformation mechanism (for example, dislocation climb versus viscous glide), a recently developed strain rate change test has shown that Ni-rich NiAl exhibits 'pure metal' behavior between 800–1000 °C, indicating that dislocation substructure (climb, with *n* = 5), rather than lattice friction (viscous glide, or solute drag, with *n* = 3) controls deformation in this temperature range (Yaney and Nix, 1988). Deformation appears to be controlled by viscous glide of dislocations above 1200 °C (Miracle, 1993 and references therein). Although considerable scatter exists, the activation energy has been assessed to be between 250 and 300 kJ mol⁻¹ (Miracle, 1993), which agrees reasonably well with the activation energy for the diffusion of ⁶³Ni in stoichiometric NiAl (Hancock and McDonnell, 1971).

The high-temperature deformation properties of binary, stoichiometric NiAl single crystals have recently been studied systematically as a function of orientation in tensile creep and in constant-strain-rate compression tests at temperatures between 850 and 1200 °C (Forbes *et al.*, 1992). The samples exhibited a strong orientation dependence in the strength as well as in other deformational characteristics. 'Soft' single crystals reach a steady state rapidly and develop little dislocation substructure. Deformation in these crystals is also characterized by

Table 2. Dependence of n on temperature and orientation

Temperature (°C)	Polycrystals ^a	[223]	[111]	[110]	[001]
850	6.9–10.1	7.0	5.5	7.2	11.4
1000	4.9–6.5	4.6	4.7	6.0	4.7
1200	3.8–4.0	4.6	4.5	4.5	3.8

^aPolycrystal data from Yang and Dodd (1973), Vandervoort, Mukherjee, and Dorn (1966), and Whittenberger (1987).

an activation energy which is significantly below that for volume diffusion in NiAl. These characteristics suggest that deformation in 'soft' crystals is controlled by glide of $a\langle 100 \rangle$ dislocations. However, diffusive aspects of deformation were evident at temperatures above 1000 °C. 'Hard' single crystals show strain hardening even at 1200 °C, and develop an extensive dislocation substructure. The dislocation substructure is composed of $a\langle 100 \rangle$ dislocations which are unstressed for glide in this orientation and can move only by diffusive processes. The creep curves are sigmoidal, also suggesting sluggish dislocation motion. In addition, the activation energy for steady-state creep in the 'hard' orientation is near that for diffusion. In contrast to deformation in 'soft' crystals, deformation in 'hard' crystals was strongly controlled by climb. The stress exponents for the various temperatures and orientations are presented in Table 2. The orientation dependence of the stress exponent is clearly evident at 850 °C from the data in Table 2. Overall, the stress exponents show a temperature dependence similar to polycrystalline NiAl.

The creep resistances of NiAl alloys have followed the improvements in the high-temperature tensile and stress-rupture strengths (Figure 10). Several conclusions can be drawn from Figure 10. As expected, single-crystal NiAl has better creep resistance than polycrystalline NiAl of the same composition. Significant improvement in creep resistance is obtained with the addition of Hf to NiAl, and the creep resistance of a single-crystal NiAl alloy containing 1% Hf approaches that of a Ni-based single-crystal superalloy. The stress exponents of the single-crystal alloys appear to depend upon the alloy composition and stress, though it is not clear why the 1.5% Hf alloy, which has a higher volume fraction of the Heusler phase, has a lower n than the 1.0% Hf alloy. At lower stresses, the stress exponents for single-crystal NiAl alloys ($n \approx 10$) are often much higher than those of polycrystalline alloys, and can match those for single-crystal, Ni-based superalloys. This implies that creep is not controlled by simple diffusional processes, and the dislocation/particle interactions responsible for the excellent creep resistance of superalloys may be

controlling the creep resistance. There appears to be no difference in creep behavior whether the creep test is conducted under constant load or constant velocity (Whittenberger, 1987; Nathal, 1992; Nathal and Ebert, 1985; Whittenberger *et al.*, 1991; Locci *et al.*, 1992; Field, 1992a). However, it is surprising to note that the tensile creep rates appear to be nearly half an order of magnitude lower than the compressive creep rates.

Limited work indicates that the creep behavior and stress-rupture strengths are highly anisotropic in NiAl single crystals (Field, 1992b). The steady-state creep rate in 'hard' crystals can be as much as half an order of magnitude lower than along $\langle 110 \rangle$ and $\langle 111 \rangle$ 'soft' orientations, and this may result from the competition between the viscous glide of $a\langle 100 \rangle$ dislocations in 'soft' crystals ($n = 3$), and the climb of $a\langle 100 \rangle$ dislocations in 'hard' crystals ($n = 5$). With the limited data available, it is difficult to comment on the operative creep mechanisms, and further work with various alloy compositions and test conditions is needed.

2.2.4 Fracture Properties

The fracture mode of binary, polycrystalline NiAl is primarily intergranular at RT (Hahn and Vedula, 1989; Locci *et al.*, 1992; George and Liu, 1990; Law and Blackburn, 1987; Lewandowski *et al.*, 1990), changes to transgranular cleavage around 400–500 °C (Hahn and Vedula, 1989; Law and Blackburn, 1987), and occurs by ductile rupture above 600 °C (Hahn and Vedula, 1989). Transgranular cleavage is favored at RT in notched samples (Rigney *et al.*, 1989; Kumar *et al.*, 1992a), in nonstoichiometric NiAl (Nagpal *et al.*, 1991; Vehoff, 1992), and in coarse-grained NiAl fractured at a high strain rate (Guard and Turkalo, 1960). Additions of ≥ 30 w.p.p.m. B suppress intergranular fracture in stoichiometric NiAl at RT (George and Liu, 1990; Law and Blackburn, 1987; George *et al.*, 1990), but 300 w.p.p.m. C does not (George and Liu, 1990). Fracture in NiAl single crystals does not occur on a single cleavage plane, and several crystallographic facets are often seen. For example, fracture initiates on $\{115\}$ or $\{117\}$ planes prior to final fracture on $\{110\}$ planes in notched, single-crystal bend specimens stressed along a $\langle 110 \rangle$ direction (Chang *et al.*, 1991). Low-index fracture planes, such as $\{115\}$, $\{117\}$, $\{123\}$, and $\{221\}$, are often quoted (Schneibel *et al.*, 1992). No evidence of ductile rupture is evident on single-crystal fracture surfaces.

While current design methodology does not specify a minimum requirement for fracture toughness, 50 MPa m^{1/2} is typical for Ni-based superalloys. The

fracture toughness (K_{IC}) of polycrystalline, binary NiAl is 4–6 MPa m^{1/2} at RT for a wide range of grain sizes (Kumar *et al.*, 1992a; Russell *et al.*, 1991; Reuss and Vehoff, 1990). For zone-refined NiAl, K_{IC} increases from about 5 MPa m^{1/2} at RT to 50 MPa m^{1/2} at 400 °C, whereas K_{IC} increases only to 10 MPa m^{1/2} at 400 °C for as-cast material (Reuss and Vehoff, 1990). The fracture toughness in single crystals depends upon specimen configuration, crystallographic direction with respect to loading direction, and the geometry of the notch. K_{IC} for binary, single-crystal bend specimens with a straight notch tested along $\langle 110 \rangle$ is 4–5 MPa m^{1/2} (Vehoff, 1992; Reuss and Vehoff, 1990), and 8 MPa m^{1/2} is obtained for samples tested along $\langle 100 \rangle$ (Chang *et al.*, 1991). RT values of K_{IC} for $\langle 100 \rangle$ samples determined in tension with a chevron-notched sample can be a factor of two higher than the value obtained with a single notch in a bending test (Bain, 1992b). The fracture toughness increases with increasing temperature to about 15 MPa m^{1/2} near 300 °C for $\langle 110 \rangle$ specimens, and increases to about 30 MPa m^{1/2} for $\langle 100 \rangle$ samples. The largest increase in toughness occurs near the DBTT, but the toughness drops, then increases, just above the DBTT for both $\langle 100 \rangle$ and $\langle 110 \rangle$ specimens (Reuss and Vehoff, 1990). The fracture toughness increases with temperature due to increased plasticity at the tip of the growing crack (Chang *et al.*, 1991).

The ductility-improving additions of Fe and Ga, which increase the RT ductility of $\langle 110 \rangle$ single crystals, improve the RT fracture toughness by 50% (Darolia and Chang, 1991), while 50% reduction in the RT fracture toughness is measured in high-strength NiAl alloys (Bain, 1992b). The low toughness of NiAl alloys below the DBTT is a critical issue that must be addressed. The alternative toughening approach of ductile reinforcements in an NiAl matrix is discussed in Chapter 13 of this volume by Miracle and Mendiratta.

Few impact data are available for NiAl, and a value of 6.9 ± 0.4 J cm⁻² is given as the fracture energy of stoichiometric polycrystalline NiAl (Russell *et al.*, 1991), and 0.8 J cm⁻² is given as the impact energy of unnotched polycrystalline NiAl (Nardone *et al.*, 1990).

2.2.5 Fatigue Behavior

The low-cycle and high-cycle fatigue lives and behavior of NiAl alloys in the $\langle 100 \rangle$ orientation have recently been found to be similar to Ni-based superalloys (Wright *et al.*, 1992; Bain, 1992a). In low-cycle fatigue, an NiAl alloy containing Mo (which showed some RT ductility in $\langle 110 \rangle$ single crystals) was tested at 760 °C in a $\langle 100 \rangle$ orientation (Bain, 1992a). This alloy followed Manson–

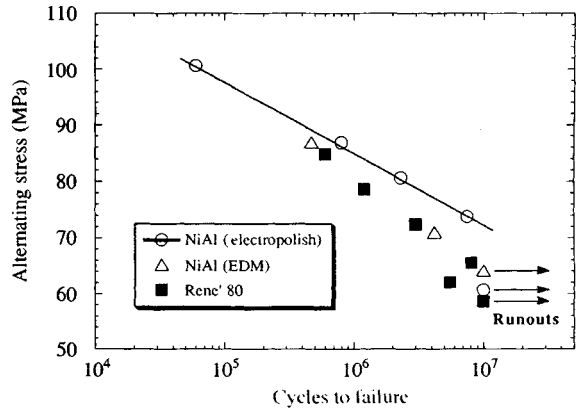


Figure 11. The high-cycle fatigue behavior of a Hf-containing NiAl single-crystal alloy compared to that of René 80 (Wright *et al.*, 1992)

Coffin strain-life behavior, typical of Ni-based superalloys. The low-cycle fatigue lives of an Hf-containing NiAl alloy (with stress-rupture properties equivalent to René 80) are similar to the lives of single-crystal, Ni-based superalloy René N4 at temperatures above as well as below the DBTT of the NiAl + Hf alloy. The high-cycle fatigue behavior of this alloy tested in the $\langle 100 \rangle$ orientation at 980 °C with an R ratio of 0.025 at 30 Hz was found to be equal to René 80 (Figure 11). Electrodischarge machining (EDM), which typically produces a recrystallized layer and surface cracks up to 25 μm deep, did not significantly degrade the high-cycle properties compared to electropolished specimens where cracks and the recrystallized layer were removed. This suggests that the alloy is sufficiently ductile at the test temperature to ameliorate surface-related degradation. With the limited data available, it appears that the fatigue lives of NiAl alloys follow improvements in their strengths.

3. Design of NiAl Airfoils

Each of the physical and mechanical properties discussed in the previous section influence the design of structural components. Of particular importance in the design of turbine airfoils are the issues of limited ductility and damage tolerance, strain-rate sensitivity, and anisotropic properties.

3.1 Ductility and Toughness

Although minimum levels of neither ductility nor toughness are specified in the design of turbine blades,

some amount is desirable for processability, handling and assembly, component reliability, and attachment to the turbine disk. Plastic accommodation is required to relieve high contact stresses between the airfoil and the turbine disk in the attachment region, especially at radii in the dovetail. Appropriate handling and assembly techniques must therefore be established and verified to enable the use of materials with limited RT ductility, such as NiAl. In the absence of ductility at RT (where engine assembly is accomplished), a compliant material between the NiAl airfoil and the turbine disk may be used to accommodate point stresses. Redesign of the dovetail geometry, such as reducing the number of attachment lobes and increasing their radii, may be employed to reduce the magnitude of stress concentrations. In addition, the anisotropic elastic and plastic properties of NiAl offer unique challenges for the design of turbine airfoils, and the crystallographic orientations of both the primary (axial) and secondary (normal to blade axis) airfoil axes should be carefully controlled to best accommodate strains along the airfoil and in the root section. Although the toughness of NiAl is higher at the airfoil-operating temperature, the fracture behavior under impact-loading conditions may still be a concern.

Of more general concern, a low defect tolerance is likely to exist in NiAl; and the size, type, and location of defects become important in components made from NiAl. Internal defects, such as inclusions and porosity, may originate from processing, while machining may introduce surface defects such as scratches, grinding marks, and cracks. Although postprocessing treatments such as hot isostatic pressing (HIP) and electropolishing have been employed to reduce the number and size of defects in NiAl, the limited data available preclude unambiguous conclusions regarding whether these procedures are beneficial. In addition to quantifying and reducing the defect population in NiAl components, design methodologies which can account for the size, type, and location of defects likely to be encountered in the part must be established. The design database must include not only properties determined on laboratory specimens and subcomponents, but also properties from component testing in a variety of simulated conditions on parts with actual configurations. These parts must be made utilizing the same processes which will be used in production in order to reproduce reliably the defect distributions of manufactured hardware. For example, dovetail testing on NiAl blades with actual dovetail geometries has been successfully carried out to alleviate the concerns of low ductility in the attachment area (Darolia *et al.*, 1992c).

The design of the blade should utilize the minimum among the fluctuations in properties, and not the average properties. Design safety margins will depend on the criticality of the part in the total system, and allowed safety factors will be greater than for ductile metals until an experience base for alloys such as NiAl with limited ductility and damage tolerance is established.

3.2 Impact Resistance and Strain-Rate Sensitivity

The DBTT, strain-to-failure, and yield stress of NiAl are relatively constant over the strain rates typically encountered in a turbine engine during normal operation (Lahrman *et al.*, 1991), as presented in Section 2. However, much higher strain rates can be encountered in an impact situation, or when the rotating turbine blades rub against the stationary turbine seals. Although very little information is available concerning the impact resistance of NiAl (Russell *et al.*, 1991; Nardone *et al.*, 1990), many intermetallic compounds fail in a brittle manner even at temperatures above the DBTT. A critical need exists to quantify the impact properties of NiAl over a wide range of temperatures, strain rates, impact angles, and microstructural conditions. Since alloying is unlikely to improve significantly the impact resistance of NiAl, design methodologies which can accommodate the low impact resistance of NiAl need to be established.

3.3 Anisotropic Behavior

The modulus of NiAl is the only relevant basic physical property which shows significant anisotropy; the coefficients of expansion and thermal conductivity are not anisotropic, as expected from the cubic symmetry of NiAl. The modulus has a strong effect on the low- and high-cycle fatigue response of the airfoil, although the magnitude of this effect diminishes slightly near 1000 °C. As described in Section 2, the mechanical properties of NiAl single crystals, specifically the strength and ductility, are much more anisotropic than those of typical Ni-based superalloys. This is true since a single-crystal orientation exists for which the preferred slip systems have zero resolved shear stress, a situation that cannot be produced in typical practical materials such as Ni-based superalloys. However, the magnitude of the anisotropy in ductility becomes small above about 600 °C, and the strength anisotropy diminishes above about 800 °C. While orientations (both primary and secondary) can be specified for independently improving the creep and stress-rupture response, fatigue behavior, strength, and ductility of NiAl single-crystal airfoils,

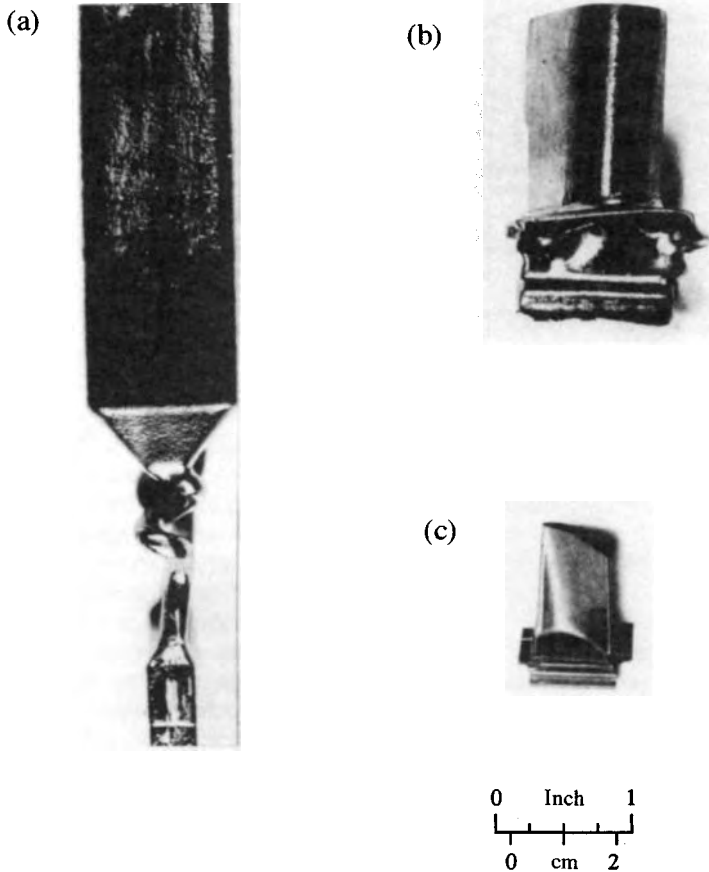


Figure 12. (a) A typical $2.5 \text{ cm} \times 4 \text{ cm} \times 12 \text{ cm}$ NiAl single crystal. (b) A solid, near-net-shape NiAl single-crystal airfoil produced by a modified Bridgman process. (c) A small, single-crystal, high-pressure turbine blade machined from a single-crystal bar (Darolia *et al.*, 1992a)

compromises will have to be made to provide an optimum balance of these competing requirements.

4. Processing, Fabrication, and Machining

Due to the high ductility and low flow stress of binary NiAl above 600°C , conventional thermomechanical processes, such as hot isostatic pressing (HIP) and hot pressing of powder compacts, extrusion, hot rolling, forging, and swaging have been successfully applied to NiAl. However, directional solidification and single-crystal growth are currently the preferred processing routes for turbine blades and vanes, since the elimination of grain boundaries is necessary to obtain adequate high-temperature creep strength. Single-crystal bars of NiAl alloys up to $4 \text{ cm} \times 4 \text{ cm}$ in cross-section have been produced by a modified Bridgman technique

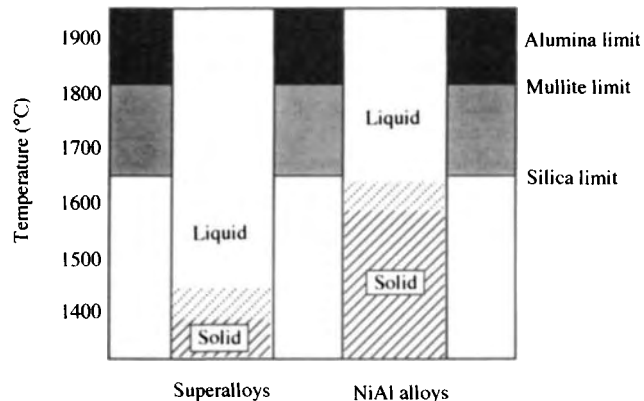


Figure 13. Temperature limits for investment casting mold and core materials with respect to the melting ranges for Ni-based superalloys and NiAl alloys (Darolia *et al.*, 1992a)

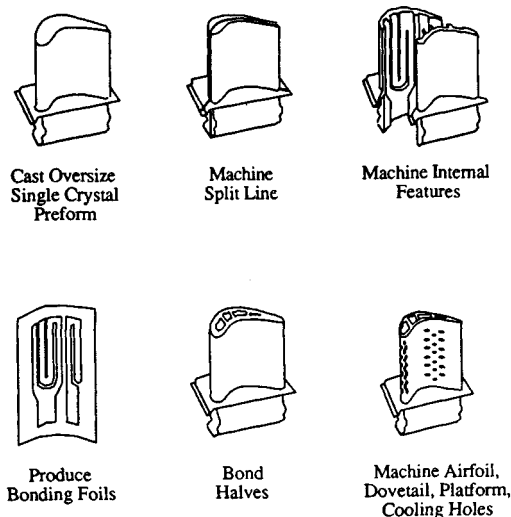


Figure 14. Fabricated blade processing sequence (Darolia *et al.*, 1992a)

(Darolia, 1991; Darolia *et al.*, 1992a). A typical 2.5 cm × 4 cm × 12 cm single crystal is shown in Figure 12(a), and a near-net-shape solid NiAl single-crystal blade is shown in Figure 12(b). A small, single-crystal, high-pressure turbine blade machined from a single-crystal bar is shown in Figure 12(c). Float-zone processes, Czochralski crystal growth, and modified, edge-defined, film-fed growth (where a shaped crystal is grown by drawing liquid metal through a shaped die) have also successfully produced NiAl single crystals, although size limitations with these three processes have not yet been overcome.

The major challenge in producing single crystals of NiAl alloys is the high melting temperature, which is roughly 300 °C higher than the most advanced Ni-based superalloys. In addition to making furnace-related issues more complex (temperature capability, furnace durability, and temperature measurement and control), the higher processing temperatures approach the limits of existing ceramic mold and core materials in terms of structural capability and reactivity with molten NiAl (Figure 13). While large NiAl single-crystal bars and airfoil shapes can be made using the modified Bridgman process, casting of hollow, thin-walled structures has not been demonstrated. The limited low-temperature plasticity of most NiAl alloys, combined with the strains generated when the metal shrinks around the ceramic core during cooling from the casting temperature, results in severe cracking of the metal. Also, core-related problems such as shift, sag, breakage and reactivity are

a major source of low yields in casting superalloy turbine blades in advanced designs, and are anticipated to be a major technical challenge for advanced single-crystal NiAl airfoils.

As an alternative to cast and cored single-crystal blades, a fabricated airfoil approach (Figure 14) is being evaluated to produce complex, thin-walled NiAl alloy turbine airfoils (Darolia *et al.*, 1992a; Goldman, 1992). In this process, a single-crystal preform is split by wire EDM to produce two single-crystal 'matching halves'. Internal cooling passages are machined into each half by electrode EDM or other methods, and the two halves are bonded back together by a process which produces a single crystal across the joint. Single-crystal bond joints, with properties equivalent to the base metal, have been produced in NiAl single crystals using an activated diffusion-bonding process similar to those used for Ni-based superalloys (Goldman, 1992). Finish machining of the airfoil contours and other external blade features is performed, and film-cooling holes are drilled by a combination of mechanical and electrochemical processes. This fabricated blade approach can result in improved dimensional tolerances and improved inspectability, while allowing the freedom to incorporate advanced cooling designs.

Many conventional and nonconventional material removal techniques (grinding, EDM, electrochemical machining, chemical milling, electrostream drilling, ultrasonic machining, abrasive waterjet) have been used on NiAl alloys (Goldman, 1992). Low-stress processes such as EDM, electrochemical milling, chemical milling, and ultrasonic machining are preferred to accommodate the low RT plasticity of NiAl. The recrystallized layer generated by the EDM process has been removed by subsequent chemical milling. Processes such as laser drilling which generate high thermal gradients should be avoided (Goldman, 1992).

A number of manufacturing-related challenges must be addressed to enable the successful application of the fabricated airfoil approach. Methods to control the propagation of positioning errors must be established, including tight control of machining tolerances between the two matching halves of the blades, control of the alignment between the two halves during the bonding cycle (up to 1400 °C), and careful design of a reference datum to allow for precise positioning of the single-crystal halves between the fabrication steps. In-process control and inspection of the crystallographic orientation between the two halves need to be established within a few degrees to obtain parent-metal properties in a bonded blade (Jang *et al.*, 1986). In-process controls and detection methods for both internal and surface

defects need to be established. Computerized tomography, termed XIM (X-ray inspection module), has been used successfully to detect bond-line defects in NiAl (Goldman, 1992).

5. Concluding Remarks

Alloys based on NiAl offer significant potential payoffs as structural materials in gas-turbine applications due to a unique range of physical and mechanical properties. These properties include high melting temperature, low density, high thermal conductivity, excellent environmental resistance, and anisotropic elastic and plastic properties. Excellent progress has been made in understanding these properties in binary NiAl, and significant improvements in the strength and ductility of NiAl single crystals have been achieved through alloying. Tensile strength and stress-rupture properties which compete with current Ni-based superalloys have been achieved through precipitation of an ordered L2₁ Heusler phase in NiAl single crystals. An RT tensile ductility as high as 6% has been produced in NiAl single crystals containing less than 0.5% (atomic) of Fe, Ga, or Mo. However, a single alloy with both RT ductility and sufficient high-temperature strength has not yet been developed, and may prove to be an elusive goal. While activity to develop an alloy with both high-temperature strength and RT ductility continues, the current approach also emphasizes design and test methodologies which can accept a material with limited ductility and damage tolerance. More work is required on measuring and understanding strain-rate sensitivity and impact behavior. While several significant challenges still remain, excellent progress has been made in many areas, and the prognosis for using NiAl alloys as high-temperature structural materials is promising.

6. Acknowledgements

We would like to acknowledge several of our colleagues who have contributed to the progress made on NiAl. They are R. D. Field, D. F. Lahrman, J. R. Dobbs, E. H. Goldman, W. S. Walston, K. Bain, P. K. Wright, J. C. Nickley, and D. G. Konitzer of General Electric Aircraft Engines; K.-M Chang of General Electric Corporate Research and Development Center; M. V. Nathal of NASA Lewis Research Center; K. Vedula of the Iowa State University; and R. Gibala of the University of Michigan. Portions of the work reported in this chapter were supported under the Independent

Research and Development projects at GE Aircraft Engines, and by the Air Force Office of Scientific Research (A. H. Rosenstein, Air Force Wright Laboratory (W. A. Troha, M. J. Kinsella, and R. H. Lilley), and the Naval Air Propulsion Center (A. S. Culbertson).

7. References

- Au, Y. K., and Wayman, C. M. (1972). *Scripta Metall.*, **6**, 1209.
- Ayushina, G. D., Levin, E. S., and Gel'd, P. V. (1969). *Russ. J. Phys. Chem.*, **43**, 1548.
- Bain, K. (1992a). Unpublished research under Air Force Contract F33615-90-C-9008, General Electric Aircraft Engines, Cincinnati, OH.
- Bain, K. (1992b). In *Intermetallic HP Turbine Technology Development*, Phase I Interim Report. Air Force Contract F33615-90-C-2006, WL-TR-92-2016, AF Wright Laboratory.
- Baker, I., Nagpal, P., Liu, F., and Munroe, P. R. (1991). *Acta Metall. Mater.*, **39**, 1637.
- Ball, A., and Smallman, R. E. (1966a). *Acta Metall.*, **14**, 1517.
- Ball, A., and Smallman, R. E. (1966b). *Acta Metall.*, **14**, 1349.
- Barrett, C. L. (1988). *Oxid. Met.*, **30**(5/6), 361–390.
- Bevk, J., Dodd, R. A., and Strutt, P. R. (1973). *Metall. Trans.*, **4**, 159.
- Boone, D. H., and Goward, G. W. (1970). In *Ordered Alloys—Structural Applications and Physical Metallurgy*, Proceedings 3rd Bolton Landing Conference (eds B. Kear, C. T. Sims, N. S. Stoloff, and J. H. Westbrook). Claitor's Pub. Div., Baton Rouge, p. 545.
- Bowman, R., Noebe, R., and Darolia, R. (1989). In *HITEMP Review*, NASA Conference Publication 10039, 47-1.
- Bradley, A. J., and Taylor, A. (1937). *Proc. R. Soc. London, Ser. A*, **159**, 56.
- Campany, R. G., Loretto, M. H., and Smallman, R. E. (1973). *J. Microsc.*, **98**, 174.
- Chakravorty, S., and Wayman, C. M. (1976a). *Metall. Trans.*, **7A**, 555.
- Chakravorty, S., and Wayman, C. M. (1976b). *Metall. Trans.*, **7A**, 569.
- Chandrasekaran, M., and Mukherjee, K. (1974). *Mater. Sci. Eng.*, **14**, 97.
- Chang, K.-M., Darolia, R., and Lipsitt, H. A. (1991). In *High Temperature Ordered Intermetallic Alloys IV* (eds L. A. Johnson, J. O. Stiegler, and D. P. Pope). *MRS Proc.*, **213**, 597.
- Clapp, P. C., Rubins, M. J., Charpenay, S., Rifkin, J. A., and Yu, Z. Z. (1989). In *High Temperature Ordered Intermetallic Alloys III* (eds C. T. Liu, A. I. Taub, N. S. Stoloff, and C. C. Koch). *MRS Proc.*, **133**, 29.
- Clark, R. W., and Whittenberger, J. D. (1984). In *Proceedings of the 8th International Thermal Expansion Symposium* (ed. T. A. Hahan). Plenum Press, New York, p. 189.
- Dannohl, H.-D., and Lukas, H. L. (1974). *Z. Metallk.*, **65**, 642.
- Darolia, R. (1991). *J. Met.*, **43**(3), 44.

- Darolia, R., and Chang, K.-M. (1991). Independent research and development program, General Electric Aircraft Engines.
- Darolia, R., Lahrman, D. F., Field, R. D., Dobbs, J. R., Chang, K.-M., Goldman, E. H., and Konitzer, D. G. (1992a). In *Ordered Intermetallics—Physical Metallurgy and Mechanical Behavior*, Vol. 213 (eds C. T. Liu, R. W. Cahn, and G. Sauthoff). NATO ASI Series E: Applied Sciences. Kluwer Academic, Dordrecht, p. 679.
- Darolia, R., Lahrman, D. F., and Field, R. (1992b). *Scripta Metall. Mater.*, **26**, 1007.
- Darolia, R., Walston, W. S., and Lahrman, D. (1992c). Unpublished research, General Electric Aircraft Engines, Cincinnati, OH.
- Doychak, J., Smialek, J. L., and Barrett, C. A. (1989). In *Oxidation of High Temperature Intermetallics* (eds T. Grobstein and J. Doychak). TMS, Warrendale, PA, pp. 41–55.
- Enami, K., and Nenno, S. (1971). *Metall. Trans.*, **2**, 1487.
- Enami, K., Nenno, S., and Shimizu, K. (1973). *Trans. Jpn Inst. Met.*, **14**(2), 161.
- Epperson, J. E., Gerstenberg, K. W., and Berner, D. (1978). *Philos. Mag. A*, **38**, 529.
- Ettenberg, M., Komarek, K. L., and Miller, E. (1970). In *Ordered Alloys—Structural Applications and Physical Metallurgy*, Proceedings 3rd Bolton Landing Conference (eds B. Kear, C. T. Sims, N. S. Stoloff, and J. H. Westbrook). Claitor's Pub. Div., Baton Rouge, p. 49.
- Field, R. D. (1991). Unpublished research, General Electric Aircraft Engines, Cincinnati, OH.
- Field, R. D. (1992a). In *Intermetallic HP Turbine Technology Development*, R&D Status Report 8. Air Force Contract F33615-90-C-2006, AF Wright Laboratory.
- Field, R. D. (1992b). In *Intermetallic HP Turbine Technology Development*, Phase I Interim Report. Air Force Contract F33615-90-C-2006, WL-TR-92-2016, AF Wright Laboratory.
- Field, R. D., Darolia, R., Lahrman, D. F., and Freeman, A. J. (1991). In *Alloy Modeling and Experimental Correlation for Ductility Enhancement in Near Stoichiometric Single Crystal Nickel Aluminide*, Final Report. AFOSR Contract F49620-88-C-0052, Bolling AFB, Washington, DC.
- Field, R. D., Lahrman, D. F., and Darolia, R. (1991a). In *High Temperature Ordered Intermetallic Alloys IV* (eds L. A. Johnson, J. O. Stiegler, and D. P. Pope). *MRS Proc.*, **213**, 255.
- Field, R. D., Lahrman, D. F., and Darolia, R. (1991b). *Acta Metall. Mater.*, **39**, 2951.
- Field, R. D., Lahrman, D. F., and Darolia, R. (1991c). *Acta Metall. Mater.*, **39**, 2961.
- Forbes, K. R., Glatzel, U., Darolia, R., and Nix, W. D. (1993). Presented at the MRS Symposium on Ordered Intermetallic Alloys V, Boston, p. 45.
- Fox, A. G., and Tabernor, M. A. (1991). *Acta Metall. Mater.*, **39**, 669.
- Fraser, H. L., Loretto, M. H., and Smallman, R. E. (1973a). *Philos. Mag.*, **28**, 667.
- Fraser, H. L., Smallman, R. E., and Loretto, M. H. (1973b). *Philos. Mag.*, **28**, 651.
- Fu, C. L., and Yoo, M. H. (1991). In *High Temperature Ordered Intermetallic Alloys IV* (eds L. A. Johnson, J. O. Stiegler, and D. P. Pope). *MRS Proc.*, **213**, 667.
- George, E. P., and Liu, C. T. (1990). *J. Mater. Res.*, **5**, 754.
- George, E. P., Liu, C. T., and Liao, J. J. (1990). In *Alloy Phase Stability and Design* (eds G. M. Stocks, A. F. Giamei, and D. P. Pope). *MRS Proc.*, **186**, 375.
- Goldman, E. H. (1992). In *Advanced NiAl Turbine Blade*, Phase I Interim Report. Air Force Contract F33615-90-C-5938, AF Wright Laboratory.
- Goward, G. W. (1970). *J. Metal.*, **22**(10), 31.
- Grala, E. M. (1960). In *Mechanical Properties of Intermetallic Compounds* (ed. J. H. Westbrook). John Wiley & Sons Ltd, New York, p. 358.
- Guard, R. W., and Turkalo, A. M. (1960). In *Mechanical Properties of Intermetallic Compounds* (ed. J. H. Westbrook). John Wiley & Sons Ltd, New York, p. 141.
- Hahn, K. H., and Vedula, K. (1989). *Scripta Metall.*, **23**, 7.
- Hancock, G. F., and McDonnell, B. R. (1971). *Phys. Stat. Sol. (A)*, **4**, 143.
- Harmouche, M. R., and Wolfenden, A. (1987). *J. Test. Eval.*, **15**(2), 101.
- Henig, E.-T., and Lukas, H. L. (1975). *Z. Metallk.*, **66**, 98.
- Hocking, L. A., Strutt, P. R., and Dodd, R. A. (1971). *J. Inst. Met.*, **99**, 98.
- Hong, T., and Freeman, A. J. (1991a). *Phys. Rev. B*, **43**, 6446.
- Hong, T., and Freeman, A. J. (1991b). Unpublished research, Northwestern University, Chicago, IL.
- Hughes, T., Lautenschlager, E. P., Cohen, J. B., and Brittain, J. O. (1971). *J. Appl. Phys.*, **42**, 3705.
- Hutchings, R., and Loretto, M. H. (1978). *Met. Sci.*, **12**, 503.
- Jang, H., Eichelberger, P. M., and Wright, P. K. (1986). In *Fatigue and Fracture of Fabricated Turbine Blades*, Final Report. Air Force Contract F33615-83-5041, AFWAL-TR-86-4073, AF Wright Laboratory.
- Jedlinski, J., and Mrowec, S. (1987). *Mater. Sci. Eng.*, **87**, 281.
- Jha, S. C., Ray, R., and Gaydos, D. J. (1989). *Scripta Metall.*, **23**, 805.
- Kim, J. T. (1991). PhD dissertation, University of Michigan.
- Kumar, K. S. (1991). *ISIJ Int.*, **31**, 1249.
- Kumar, K. S., Darolia, R., Lahrman, D., and Mannan, S. K. (1992b). *Scripta Metall. Mater.*, **26**, 1001.
- Kumar, K. S., Mannan, S. K., and Viswanadham, R. K. (1992a). *Acta Metall. Mater.*, **40**, 1201.
- Lahrman, D. F. and Darolia, R. (1992). In *Intermetallic HP Turbine Technology Development*, Phase I Interim Report. Air Force Contract F33615-90-C-2006, WL-TR-92-2016, AF Wright Laboratory.
- Lahrman, D. F., Field, R. D., and Darolia, R. (1991). In *High Temperature Ordered Intermetallic Alloys IV* (eds L. A. Johnson, J. O. Stiegler, and D. P. Pope). *MRS Proc.*, **213**, 603.
- Lasalmonie, A., Lequeux, M. J., and Costa, P. (1979). In *Strength of Metals and Alloys: Proceedings of the 5th International Conference*, Vol. 2 (eds P. Haasen, V. Gerold, and G. Kostorz). Pergamon Press, New York, p. 1317.

- Lautenschlager, E. P., Kiewit, D. A., and Brittain, J. O. (1965). *Trans. Metall. Soc. AIME*, **233**, 1297.
- Law, C. C. and Blackburn, M. J. (1987). In *Rapidly Solidified Lightweight Durable Disk Materials*. AFWAL TR-87-4102, AF Wright Laboratory.
- Lewandowski, J. J., Michal, G. M., Locci, I., and Rigney, J. D. (1990). In *Alloy Phase Stability and Design* (eds G. M. Stocks, A. F. Giamei, and D. P. Pope). *MRS Proc.*, **186**, 341.
- Locci, I. E., Dickerson, R., Bowman, R. R., Whittenberger, J. D., Nathal, M. V., and Darolia, R. (1992). Presented at the MRS Symposium on Ordered Intermetallic Alloys V, Boston, p. 635.
- Locci, I. E., Noebe, R. D., Bowman, R. R., Minor, R. V., Nathal, M. V., and Darolia, R. (1991). In *High Temperature Ordered Intermetallic Alloys IV* (eds L. A. Johnson, J. O. Stiegler, and D. P. Pope). *MRS Proc.*, **213**, 1013.
- Loretto, M. H. and Wasilewski, R. J. (1971). *Philos. Mag.*, **23**, 1311.
- Lui, S.-C., Davenport, J. W., Plummer, E. W., Zehner, D. M., and Fernando, B. W. (1990). *Phys. Rev. B*, **42**, 1582.
- McCarron, R. L., Lindblad, N. R., and Chatterji, K. (1976). *Corrosion*, **32**, 476.
- Miracle, D. B. (1991). *Acta Metall. Mater.*, **39**, 1457.
- Miracle, D. B. (1993). *Acta Metall. Mater.*, **41**, 649.
- Miracle, D. B., Russell, S., and Law, C. C. (1989). In *High Temperature Ordered Intermetallic Alloys III* (eds C. T. Liu, A. I. Taub, N. S. Stoloff, and C. C. Koch). *MRS Proc.*, **133**, 225.
- Moose, C. A. (1991). MS thesis, Pennsylvania State University.
- Mrowec, S., Danielewski, M., Godlewska, E., and Godlewski, K. (1989). In *Oxidation of High Temperature Intermetallics* (eds T. Grobstein and J. Doychak). TMS, Warrendale, PA p. 147.
- Nagasawa, A., Enami, K., Ishino, Y., Abe, Y., and Nenno, S. (1974). *Scripta Metall.*, **8**, 1055.
- Nagpal, P., Baker, I., Liu, F., and Munroe, P. R. (1991). In *High Temperature Ordered Intermetallic Alloys IV* (eds L. A. Johnson, J. O. Stiegler, and D. P. Pope). *MRS Proc.*, **213**, 533.
- Nardone, V. C., Strife, J. R., and Prewo, K. M. (1990). In *Intermetallic Matrix Composites* (eds D. L. Anton, P. L. Martin, D. B. Miracle, and R. McMeeking). *MRS Proc.*, **194**, 205.
- Nash, P., Singleton, M. F., and Murray, J. L. (1991). In *Phase Diagrams of Binary Nickel Alloys*, Vol. 1 (ed. P. Nash). ASM International, Metals Park, OH, p. 3.
- Nathal, M. V. (1992). In *Ordered Intermetallics—Physical Metallurgy and Mechanical Behavior*, Vol. 213 (eds C. T. Liu, R. W. Cahn, and G. Sauthoff). NATO ASI Series E: Applied Sciences. Kluwer Academic, Dordrecht, p. 541.
- Nathal, M. V. and Ebert, L. J. (1985). *Metall. Trans.*, **16A**, 427.
- Neumann, J. P., Chang, Y. A., and Lee, C. M. (1976). *Acta Metall.*, **24**, 593.
- Noebe R. and Whittenberger, J. D. (1991). Unpublished research, NASA–Lewis Research Center, Cleveland, OH.
- Parthasarathi, A. and Fraser, H. L. (1984). *Philos. Mag. A*, **50**, 89.
- Pascoe, R. T. and Newey, C. W. A. (1968). *Met. Sci. J.*, **2**, 138.
- Petrushevskii, M. S., Levin, E. S., and Gel'd, P. V. (1971). *Russ. J. Phys. Chem.*, **45**, 1719.
- Polvani, R. S., Tzeng, W. S., and Strutt, P. R. (1976). *Metall. Trans.*, **7A**, 33.
- Rachinger, W. A. and Cottrell, A. H. (1956). *Acta Metall.*, **4**, 109.
- Raj, S. V., Noebe, R. D., and Bowman, R. R. (1989). *Scripta Metall.*, **23**, 2049.
- Rao, S. I., Woodward, C., and Parthasarathy, T. A. (1991). In *High Temperature Ordered Intermetallic Alloys IV* (eds L. A. Johnson, J. O. Stiegler, and D. P. Pope). *MRS Proc.*, **213**, 125.
- Reuss, S. and Vehoff, H. (1990). *Scripta Metall. Mater.*, **24**, 1021.
- Rigney, J. D., Khadkikar, P. S., Lewandowski, J. J., and Vedula, K. (1989). In *High Temperature Ordered Intermetallic Alloys III* (eds C. T. Liu, A. I. Taub, N. S. Stoloff, and C. C. Koch). *MRS Proc.*, **133**, 603.
- Rosen, S. and Goebel, J. A. (1968). *Trans. Metall. Soc. AIME*, **242**, 722.
- Rozner, A. G. and Wasilewski, R. J. (1966). *J. Inst. Metl.*, **94**, 169.
- Rudy, M. and Sauthoff, G. (1985). In *High Temperature Ordered Intermetallic Alloys* (eds C. C. Koch, C. T. Liu, and N. S. Stoloff). *MRS Proc.*, **39**, 327.
- Rudy, M. and Sauthoff, G. (1986). *Mater. Sci. Eng.*, **81**, 525.
- Rusovic, N. and Warlimont, H. (1977). *Phys. Stat. Sol. (A)*, **44**, 609.
- Rusovic, N. and Warlimont, H. (1979). *Phys. Stat. Sol. (A)*, **53**, 283.
- Russell, S. M., Law, C. C., Blackburn, M. J., Clapp, P. C., and Pease, D. M. (1991). In *Lightweight Disk Alloy Development*. WRDC TR-90-4125, AF Wright Research and Development Center.
- Sauthoff, G. (1989). *Z. Metallk.*, **80**, 337.
- Schneibel, J. H., Darolia, R., Lahrman, D. F., and Schmauder, S. (1992). *Metall. Trans.*, submitted.
- Schulson, E. M. (1985). In *High Temperature Ordered Intermetallic Alloys* (eds C. C. Koch, C. T. Liu, and N. S. Stoloff). *MRS Proc.*, **39**, 193.
- Schulson, E. M. and Barker, D. R. (1983). *Scripta Metall.*, **17**, 519.
- Seybolt, A. U. (1966). *Trans. ASM*, **59**, 860.
- Smialek, J. L. and Hehemann, R. F. (1973). *Metall. Trans.*, **4**, 1571.
- Smialek, J. L. and Meier, G. H. (1987). In *Superalloys II* (eds C. T. Sims, N. S. Stoloff, and W. C. Hagel). John Wiley & Sons Ltd, Chichester, pp. 293–326.
- Stover, E. T. (1966). In *Effects of Alloying and Deformation Processing on Mechanical Behavior of NiAl*, WADC-TDR-60-184, Part VII, Vol. II. USAF Contract AF-33(615)-1497, Wright Air Development Center.

- Tanner, L. E., Pelton, A. R., VanTendeloo, G., Schryvers, D., and Wall, M. E. (1990). *Scripta Metall. Mater.*, **24**, 1731.
- Taylor, A. and Doyle, N. J. (1972). *J. Appl. Cryst.*, **5**, 201.
- Vandervoort, R. R., Mukherjee, A. K., and Dorn, J. E. (1966). *Trans. ASM*, **59**, 930.
- Vedula, K., Hahn, K. H. and Boulogne, B. (1989). In *High Temperature Ordered Intermetallic Alloys III* (eds C. T. Liu, A. I. Taub, N. S. Stoloff, and C. C. Koch). *MRS Proc.*, **133**, 299.
- Vehoff, H. (1992). In *Ordered Intermetallics—Physical Metallurgy and Mechanical Behavior*, Vol. 213 (eds C. T. Liu, R. W. Cahn, and G. Sauthoff). NATO ASI Series E: Applied Sciences. Kluwer Academic, Dordrecht, p. 299.
- Veyssi re, P. and Noebe, R. (1992). *Philos. Mag. A*, **65**, 1.
- Wachtell, R. L. (1952). In *Investigation of Various Properties of NiAl*, Technical Report 52-291, Wright Air Development Center.
- Walston, W. S. (1992a). In *Intermetallic HP Turbine Technology Development*, Phase I Interim Report. Air Force Contract F33615-90-C-2006, WL-TR-92-2016, AF Wright Laboratory.
- Walston, W. S. (1992b). In *Intermetallic HP Turbine Technology Development*, R&D Status Report 8. Air Force Contract F33615-90-C-2006, AF Wright Laboratory.
- Walston, W. S. and Darolia, R. (1993). In *High Temperature Ordered Intermetallic Alloys V* (eds I. Baker, R. Darolia, J. D. Whittenberger, and M. H. Yoo). *MRS Proc.*, **288**, 237.
- Wasilewski, R. J. (1966). *Trans. Metall. Soc. AIME*, **236**, 455.
- Wasilewski, R. J. (1968). *J. Phys. Chem. Solids*, **29**, 39.
- Wasilewski, R. J., Butler, S. R., and Hanlon, J. E. (1967). *Trans. Metall. Soc. AIME*, **239**, 1357.
- West, G. W. (1964). *Philos. Mag.*, **9**, 979.
- Westbrook, J. H. (1956). Unpublished research, General Electric CR&D Center, Schenectady, N.Y.
- Whittenberger, J. D. (1987). *J. Mater. Sci.*, **22**, 394.
- Whittenberger, J. D. (1988). *J. Mater. Sci.*, **23**, 235.
- Whittenberger, J. D., Arzt, E., and Luton, M. J. (1990). *J. Mater. Res.*, **5**, 271.
- Whittenberger, J. D., Nathal, M. V., Raj, S. V., and Pathare, V. M. (1991). *Mater. Lett.*, **11**, 267.
- Whittenberger, J. D. and Viswanadham, R. K. (1989). In *High Temperature Ordered Intermetallic Alloys III* (eds C. T. Liu, A. I. Taub, N. S. Stoloff, and C. C. Koch). *MRS Proc.*, **133**, 621.
- Wright, P. K., Maurer, N., and Bain, K. (1992). Unpublished research, General Electric Aircraft Engines, Cincinnati, OH.
- Yaney, D. L. and Nix, W. D. (1988). *J. Mater. Sci.*, **23**, 3088.
- Yang, W. J. and Dodd, R. A. (1973). *Met. Sci. J.*, **7**, 41.

This chapter was originally published in 1995 as Chapter 3 in *Intermetallic Compounds*, Vol. 2: *Practice*, edited by J. H. Westbrook and R. L. Fleischer.

Chapter 13

Intermetallic Composites

Daniel B. Miracle

Air Force Wright Laboratory, Wright-Patterson Air Force Base, Dayton, OH 45433, USA

Madan G. Mendiratta

UES, Inc., 4401 Dayton-Xenia Road, Dayton, OH 45432, USA

1. Introduction

Interest in intermetallic composites has grown significantly over the past several years as an extension of two separate materials development activities: the development of advanced monolithic intermetallic compounds with a balance of strength and toughness for high-temperature aerospace structural applications, and the development of metal matrix composites (MMCs) for aerospace applications at temperatures above those achievable with conventional Al-based and Ti-based MMCs. The field of intermetallic composite materials has come to include any two-phase alloy with an intermetallic compound as a principal constituent. This usage has complicated traditional definitions, and the term 'reinforcement' may refer not only to ceramic constituents, such as particles, rods, platelets, whiskers, or fibers, but is also commonly used to describe another intermetallic compound or a terminal solid solution, as in ductile-phase toughened intermetallic composites. The term 'matrix' is sometimes misleading, as many intermetallic composites, most notably intermetallic eutectic composites, possess interpenetrating, or co-continuous, phases (Figure 1). Laminated composites possess alternating laminae, each of which is continuous in two dimensions but discontinuous normal to the plane of the laminae.

Advanced aerospace systems, including a high performance turbine engine with twice the thrust-to-weight achievable using current materials and design methodology (IHPTET), the National Aerospace Plane

(NASP), and the high speed civil transport (HSCT) require a wide range of advanced structural materials. To develop materials with application temperatures higher than those possible with conventional Al-based and Ti-based MMCs, a major activity has begun on intermetallic composites utilizing continuous SiC reinforcements in Ti aluminide matrices (primarily based on the Ti_3Al , or α_2 , class of intermetallic alloys). A large database has been established, including fatigue, creep, tensile, and fracture properties, and significant experience has been gained in the areas of composite processing and component fabrication. A significant effort is also underway to develop advanced intermetallic compounds for structural applications at temperatures in excess of 1000 °C for the IHPTET, NASP, and HSCT aerospace systems. To be successful, a candidate intermetallic compound requires a stringent balance of a range of physical and mechanical properties, including a high melting temperature, low density, good stiffness, high strength, damage tolerance, environmental resistance, and fatigue resistance. However, potential single compounds typically suffer from inadequate damage tolerance and insufficient strength at elevated temperatures. Approaches to improve these properties have led to consideration of multiphase alloys and intermetallic composites. Careful control of the composite architecture and constituent properties may provide the opportunity to achieve a balance of strength and toughness.

While intermetallic composites share much with metal matrix composites, a wide range of composite

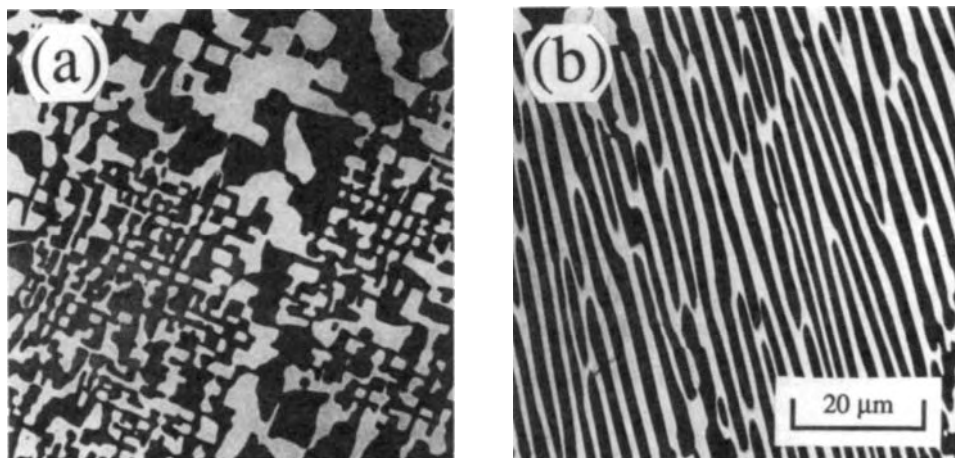


Figure 1. Co-continuous phases in an $\text{MoSi}_2 + \text{Mo}_5\text{Si}_3$ intermetallic eutectic composite as seen in (a) transverse, and (b) longitudinal sections

architectures, sparked by novel approaches to the processing and development of intermetallic composites, provides notable differences. In addition, the unique attributes of intermetallic alloys lead to several key features in intermetallic composites. Such issues are briefly discussed below.

Many intermetallic compounds possess anisotropic elastic and plastic properties, and it is likely that this anisotropy will persist (and perhaps increase) in intermetallic composites. It is unlikely that any particular intermetallic composite will provide the wide balance of properties (strength, toughness, and crack-growth resistance under triaxial loading) currently exhibited by Ni-based superalloys, and so it will be important to develop an intermetallic composite for a somewhat narrower range of applications specifically suited to that particular composite. It may be that interfaces play a more critical role in the behavior and development of intermetallic composites (as opposed to MMCs) due to the wider range of (sometimes conflicting) requirements. Interfaces in intermetallic composites provide not only load transfer from the matrix to the reinforcement, as in MMCs, but are also critical for toughening. Higher temperatures of use will require better chemical stability to avoid degradation of the reinforcement, and to avoid the formation of brittle reaction products. The mismatch in coefficients of thermal expansion (CTE), the high moduli of intermetallic compounds and high processing temperatures required for adequate consolidation often result in significant residual stresses (Cox *et al.*, 1990).

In addition, the operating temperatures for many intermetallic composite applications may range from cryogenic temperatures to over 800 °C. Techniques to assess these residual stresses experimentally and analytically, and procedures for managing or reducing residual stresses, are required. Environmental resistance is likely to be an issue in intermetallic composites, since environmental embrittlement has been shown to be a major problem in a wide range of intermetallic compounds (Liu and George, 1991; Liu and McKamey, 1990). The pest phenomenon observed in a number of intermetallic materials is also likely to be an issue in composites of these compounds.

The potential application temperatures of intermetallic composites and ceramic matrix composites (CMCs) overlap, and so the relative merits of these two materials systems will be briefly described. The principal advantages of CMCs are a higher potential operating temperature and, typically, lower density. The various approaches to improve the toughness (crack deflection, fiber pullout, transformation toughening) have met with limited success. In addition, the low thermal conductivity of most CMCs leads to the possibility of large thermal gradients, especially (although not exclusively) in cooled components. The combination of large thermal gradients and high modulus results in very large thermally induced stresses. The principal advantage of intermetallic composites is the metal-like properties of the matrix. The metallic thermal conductivity of intermetallic compounds typically results in significantly reduced thermal stresses compared to

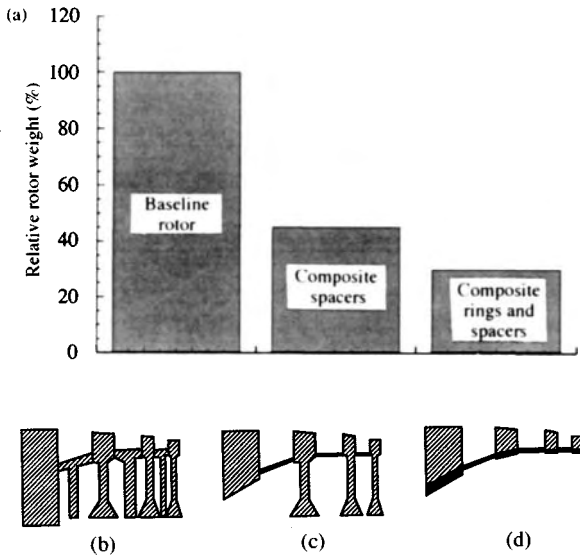


Figure 2. (a) Payoffs associated with continuously reinforced intermetallic composites in an advanced compressor ring rotor (MacKay *et al.*, 1991). A schematic of the baseline compressor rotor (b) illustrates the solid metal disks required to support each compressor stage, as well as the spacers between stages. Intermetallic composite compressor spacers (c) and intermetallic composite rings (d) dramatically reduce the weight of the compressor by eliminating the need for solid metal support disks

CMCs. If the intermetallic matrix has a moderate ductile-to-brittle transition temperature (DBTT), then improved damage tolerance at the operating temperature and metal-like processing can result. However, below the DBTT intermetallic composites fail in much the same fashion as CMCs.

The successful development and application of intermetallic composites is required in each of the advanced aerospace systems mentioned (IHPTET, NASP, and HSCT). Intermetallic composites are being developed for the skin and structural members (I-beams, hat stiffeners) of the NASP fuselage, flaps in the nozzle of the HSCT, and as ring components, structural rods, ducts, and shafts in advanced gas-turbine engines. While significant advances in aerospace technology are anticipated from advanced designs, new materials are required to allow new design methodologies to be employed. For example, an intermetallic composite drum rotor capable of replacing several solid compressor disks is shown in Figure 2, along with the attendant decrease in weight (MacKay *et al.*, 1991). This new design is possible only by the unique properties afforded by continuously reinforced intermetallic composites.

These properties include a 30–50% increase in density-corrected ultimate strength and a 30–60% increase in density-corrected modulus for Ti aluminide composites tested along the fiber axes, compared to IN-100 (Larsen *et al.*, 1992).

Much of the detailed technical information of current activity is available in conference proceedings (Anton *et al.*, 1990; HITEMP, 1990, 1991, 1992; Smith *et al.*, 1991; Smith and Revelos, 1992; Miracle *et al.*, 1992). The intent of this chapter is therefore not to provide a detailed review of the information collected to date, but is rather to provide a focused perspective and discussion of the various activities and issues associated with the development of intermetallic composites for structural applications. The combination of properties offered by intermetallic composite materials (low density, high modulus, and high operating temperature) is most attractive for aerospace applications, where high payoffs provide the incentive required to offset the development costs and risk. The work on intermetallic composites for structural applications has been almost exclusively for aerospace applications, and the perspective taken in this chapter reflects that emphasis.

2. Intermetallic Composite Classes

Intermetallic composite materials are in the very early stages of development, and it is not apparent whether composite classification based on laminate architecture will be useful for many intermetallic composites currently under consideration. Therefore, with the exception of continuously reinforced Ti aluminide intermetallic composites, classification at the present is related to different morphologies, orientations, and distributions of strengthening or toughening constituents in an intermetallic matrix. As development efforts evolve, and conventional and novel processing techniques mature, an architecture-related classification may become important for the majority of intermetallic composites, just as laminate theory has become important in continuously reinforced Ti aluminide intermetallic composites. The types of intermetallic composites presently being explored are discussed in the following sections.

2.1 Discontinuous Reinforcements

In discontinuous composites, an intermetallic matrix contains particulates, whiskers or chopped fibers. Examples of these composites are SiC whiskers in a MoSi₂ matrix and NiAl with TiB₂ particulates.

Moderate toughening and reasonable levels of strengthening can be achieved in these composites (Petrovic *et al.*, 1990; Yang and Jeng, 1990; Wang and Arsenault, 1990). In general, these types of composites are being studied to assess thermochemical and thermomechanical compatibilities, but may not lead to materials with a balance of properties that is appropriate for structural applications. The reinforcements can have various aspect ratios, and are usually distributed in random orientations. Some alignment of the compositing phases is possible through special powder-metallurgy processing techniques, such as hot extrusion and injection molding.

At high temperatures, where the plasticity of the intermetallic matrix is significant, the morphology and aspect ratio of the discontinuous reinforcements strongly influence the strength and creep resistance of intermetallic composites. At low temperatures, where the matrix is mostly elastic, the same microstructural parameters of the discontinuous reinforcements influence damage tolerance. Theoretical analyses and experimental results indicate that needle-like reinforcements with a high aspect ratio provide the greatest strengthening and toughening (Christman *et al.*, 1989; Bao *et al.*, 1990; Faber and Evans, 1983a,b). Plate-like reinforcements are less effective, and the least improvement in mechanical properties is provided by equiaxed particles.

2.2 Continuous Reinforcements

These composites contain continuous fibers or filaments, typically distributed in a uniaxial direction in an intermetallic matrix. As in metal matrix composites, fibers with high strength and stiffness—by taking up most of the load—enhance significantly the strength and creep resistance of the intermetallic constituent. Prime examples of such composites are Ti aluminide alloys reinforced by SiC fibers. By control of the interfacial bond strength it may be possible in these composites to introduce some measure of toughening. Since the mechanical properties are highly anisotropic in these unidirectional composites, their application as structural materials is limited to specific engineering components, such as turbine blades, ring components, and structural rods in turbine engines, where transverse properties are not critical (Larsen *et al.*, 1992). Composite architectures with different orientations of fibers, such as alternating laminae with fibers parallel and normal to the axis of loading ($[0/90]$) and quasi-isotropic laminates ($[0/\pm 45/90]$), are studied for applications where more isotropic

properties are required, and this approach has been pursued for sheet applications of Ti aluminide–SiC composites (Larsen *et al.*, 1992).

2.3 Hybrid Composites

In addition to composites with only a single type of reinforcement, it is possible to incorporate multiple types of reinforcements in an intermetallic matrix. Each type of reinforcement may be designed to enhance specific (but competing) mechanical properties, although possible synergism cannot be ruled out. For example, continuous uniaxial fibers may primarily enhance high-temperature strength and creep resistance while, in the same composite, a dispersion of whiskers in the matrix may enhance toughness and transverse mechanical properties. This general approach has been pursued in ‘microstructurally toughened’ intermetallic composites of NiAl with TiB₂ and stainless steel tubes (Nardone *et al.*, 1990), and by Maloney and Hecht (1992), who added SiC particulates and platelets to the MoSi₂ matrix to match better the CTE of the continuous fiber reinforcement. In addition, NiAl has been reinforced with W and sapphire fibers to provide a balance of creep resistance and toughness (Bowman, 1992; Bowman and Noebe, 1990).

Another fruitful emerging area of research is fabrication of 2D continuous laminate composites by physical vapor deposition processes, and evaluation of their mechanical behavior. The toughening of a brittle matrix by ductile sheets has been demonstrated both theoretically and experimentally (Cao and Evans, 1991; Rowe and Skelly, 1992). *In situ* fabrication by high-rate magnetron sputtering in ultrahigh vacuum provides a means of producing laminates with good control of compositions of both ductile and intermetallic phases, volume fraction, interstitial content, and layer thickness. Recent work has shown that magnetron sputtering has been successful in producing Nb₃Al–Nb (Rowe and Skelly, 1992) and Cr₂Nb–Cr (Rowe, 1992) laminated composites possessing controlled microstructure (Figure 3).

3. Composite Systems

There are a large number of intermetallic systems currently being explored as potential aerospace structural materials (Anton *et al.*, 1990; Miracle *et al.*, 1992). Matrices that have been studied include alloys based on the Ti aluminides (Ti₃Al, TiAl, orthorhombic Ti₂AlNb, and Al₃Ti), Ni aluminides (Ni₃Al and NiAl),

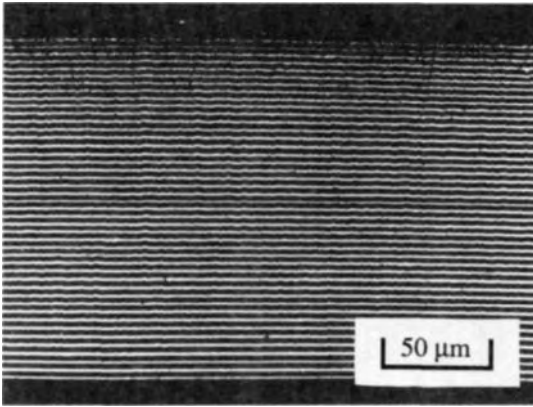


Figure 3. An Nb_3Al -Nb laminated composite produced by physical vapor deposition (PVD) and possessing a highly controlled microstructure (Rowe and Skelly, 1992)

Nb aluminides (Nb_3Al and Al_3Nb), MoSi_2 , and a number of advanced intermetallic compounds. A wide range of intermetallic eutectic composites has also been studied. With the exception of composites based on continuously reinforced Ti_3Al alloys, most of these trial matrices are far from usable. Here we present a review of the status and prospects of those intermetallic composite systems which either have the greatest potential for development as structural materials or upon which extensive work has been done.

3.1 Ti Aluminide Composites

Continuously reinforced Ti aluminide matrix composites represent the largest single activity in the area of intermetallic matrix composites. While initial considerations included composites based on TiAl , the vast majority of the work has been conducted on Ti_3Al -based alloys reinforced with continuous SiC fibers. The principal applications include sheet and structural members (I-beams and hat stiffeners) for the NASP and other high-mach vehicles, flat plates for nozzle flaps, and a range of shafts, tubes, rods, and rings in turbine engines. Rods and plates are likely to see earliest qualification due to simplicity of fabrication and low risk in the event of component failure. In contrast, rings for compressor rotors provide the largest payoff (Figure 2) due to a large free hoop radius, but such applications are likely to be further in the future because of the higher risk associated with component failure, and since a significant redesign of the engine core and engine cycle is required. Projected operating temperatures range from below 650°C for low-risk

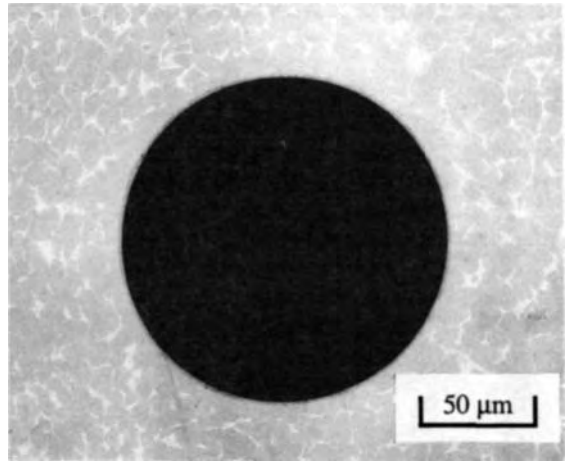


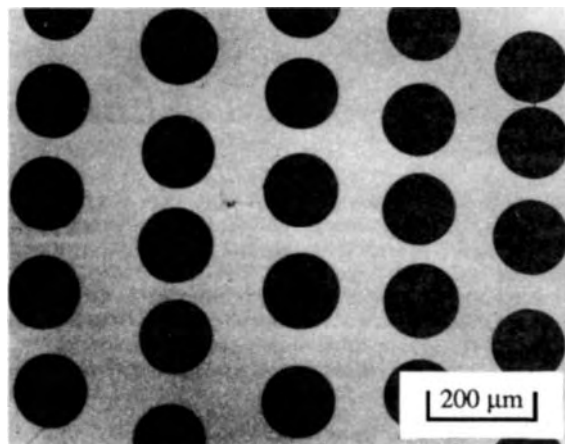
Figure 4. Cross section of an SCS-6 SiC fiber in a Ti-24Al-11Nb matrix, illustrating the (black) C monofilament core, the (gray) SiC deposited by chemical vapor deposition, and the (black) C-rich fiber coating. A thin ($1.6\ \mu\text{m}$) reaction zone is seen between the fiber coating and the matrix, and a wider region ($\sim 6\ \mu\text{m}$) depleted in the ductile β phase is also present. Cracks in the brittle β -depleted zone have formed after cooling from the processing temperature as a result of residual stresses due to the mismatch in coefficient of thermal expansion between the fiber and the matrix

applications to as high as 800°C for limited times and low stresses.

Until recently, the SCS-6 monofilament (a $142\ \mu\text{m}$ diameter fiber produced by chemical vapor deposition (CVD) of SiC on a C core, with two C-rich outer layers, each about $1\ \mu\text{m}$ thick, Figure 4) has been the only commercially available SiC fiber. SiC monofilaments produced by CVD on a W core are now also available, and have properties that compete with a SCS-6 fiber, as shown in Table 1 (Schoenberg and Kumnick, 1989; Krutenat, 1992; Sigma product literature, 1991; Fry, 1992). Matrices based on disordered Ti alloys have been studied, such as Ti-6Al-4V (wt%) and $\beta 21\text{S}$, a β -Ti alloy, but are not considered viable for applications above about 650°C . The largest activity for applications above 650°C has focused on composites of Ti-24Al-11Nb (at%; all compositions are in at% unless noted otherwise) reinforced with the SCS-6 fiber (Figure 5). The Ti-24Al-11Nb/SCS-6 composite was established as the baseline system as a matter of practicality in response to the aggressive schedule for NASP and IHPTET, the two principal technology drivers. Ti-24Al-11Nb had (at the time of selection) the best balance of mechanical properties of available α_2 (Ti_3Al) alloys (see Banerjee, Chapter 5 in this volume) and the SCS-6 fiber

Table 1. Properties of SiC fibers

Fiber	Diameter (μm)	Core/coating	Density (g cm^{-3})	Ultimate tensile strength (MPa)	Standard deviation (%)	Weibull modulus	Modulus (GPa)
Amercom	127	W/none	3.3	3540	5.8	18	427
Sigma	100	W/none	3.4	3750	6		400
Textron	142	C/C + Si	3.0	4130	13.9 ^a	9	395

^aCoefficient of variance.**Figure 5.** Cross section of a Ti-24Al-11Nb/SCS-6 intermetallic composite with 35 vol% of SiC reinforcements

was the only commercially available continuous reinforcement with adequate mechanical properties. Activity focused on characterization of reaction zones, mechanical property determination, and mechanics, modeling, and life prediction under time-dependent loading (Gambone, 1990; Smith *et al.* 1991).

Many critical deficiencies have been identified for the Ti-24Al-11Nb/SCS-6 composite. The Ti-based matrix is chemically incompatible with both the C-rich outer layers of the SCS-6 fiber and the SiC fiber itself. A layer of brittle reaction products consisting of Ti carbides and Ti silicides forms during processing (Rhodes, 1992), and the growth of this layer follows a parabolic law (Figure 6, from Smith *et al.*, 1992). In addition, the diffusion of C into the $\alpha_2 + \beta$ matrix stabilizes the α_2 phase, thereby forming a brittle β -depleted zone, where cracks are often seen to nucleate (Figure 4). Although the axial properties of Ti aluminide intermetallic composites are clearly superior to existing materials (Larsen *et al.*, 1992), most applications will require resistance to off-axis loading. A weak bond exists in SCS-6 monofilaments between the outer C layers and the SiC fiber (Gambone

and Bain, 1988), and this weakness leads to poor transverse tensile and creep properties (Figure 7, from Larsen *et al.*, 1992). The Ti aluminide matrices have a CTE that is larger than that of the SiC fiber, and this leads to significant residual stresses after cool-down from the processing temperature (Cox *et al.*, 1990). It is likely that these residual stresses produce an enhanced interface bond due to a 'clamping' effect. However, these clamping stresses can be high enough to result in plastic flow of the matrix near the fiber, and matrix cracking in the brittle zone around the fiber (Figure 4). Finally, the Ti-24Al-11Nb matrix is embrittled when exposed to air at elevated temperature, leading to a significant reduction in tensile elongation (Balsone, 1989). As shown in Figure 8 (from Smith *et al.*, 1992), Ti-24Al-11Nb/SCS-6 composites lose as much as 85% of their room-temperature (RT) tensile strength after 500 cycles in air between 150 and 815 °C, due to a combination of environmental embrittlement of the matrix and residual stresses resulting from the CTE mismatch between the matrix and the fiber (Revelos and Smith, 1992; Russ, 1990). Similar thermal cycling in an inert environment does not result in significant loss of tensile properties (Revelos and Smith, 1992), although a drop in properties is observed after 10 000 cycles in vacuum (Brindley *et al.*, 1991).

It is important to emphasize that very little development activity has been conducted in the past for this class of composites, and so the potential of continuously reinforced Ti aluminide composites is still difficult to assess. However, development activity is currently underway to address the deficiencies noted above. Increasing the Nb content of α_2 alloys has been found to introduce an orthorhombic Ti_2AlNb phase. Alloys containing the orthorhombic, or 'O', phase have been shown to possess improved strength over α_2 alloys, while maintaining adequate ductility (Graves *et al.*, 1992). Composites produced with matrices possessing the orthorhombic phase (other phases present may include the ordered α_2 phase, an 'ordered β' ' B2 (cP2) phase, and a disordered b.c.c. β phase) have

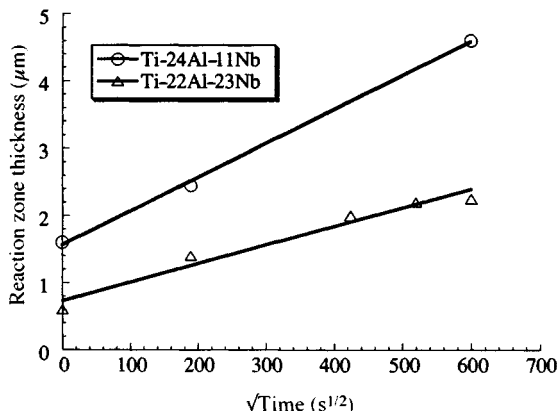


Figure 6. Reaction zone thickness versus the square root of annealing time for an SCS-6 fiber and matrices of Ti-24Al-11Nb and the 'orthorhombic' alloy Ti-22Al-23Nb (from Smith *et al.*, 1992). Slower kinetics are measured for reaction of the SCS-6 SiC fiber with a Ti-22Al-23Nb matrix compared to a Ti-24Al-11Nb matrix

improved chemical compatibility with the SCS-6 fiber (Figure 6), and also have markedly improved strength retention after thermal cycling in air (Figure 8). The orthorhombic matrix alloys show reduced sensitivity to interstitial contamination and are easily rolled to foil, even with as much as 1790 parts per million by weight (w.p.p.m.) of oxygen (Graves *et al.*, 1992). Efforts are now underway to alloy existing ternary orthorhombic compositions for improved composite properties (Graves, 1992). Several new interface coatings for SiC monofilaments are being investigated for improved transverse properties and chemical compatibility (Graves, 1992). From a composite material development perspective, additional work is required in the areas of long-term microstructural and phase stability, environmental resistance, and microstructural flexibility of the matrix through thermal treatment. In addition, continued activity on new matrices, new fibers, and new interface coatings for chemical compatibility and transverse properties is required.

3.2 Ni Aluminide Composites

The physical properties which make NiAl attractive as a matrix material for advanced aerospace composites include a low density (5.9 g cm^{-3}), high melting temperature (1640°C), and good thermal conductivity ($75 \text{ W m}^{-1} \text{ C}^{-1}$). In addition, NiAl has an attractive modulus (190 GPa at RT), a relatively low ductile-to-brittle transition temperature ($\sim 400^\circ\text{C}$), and good

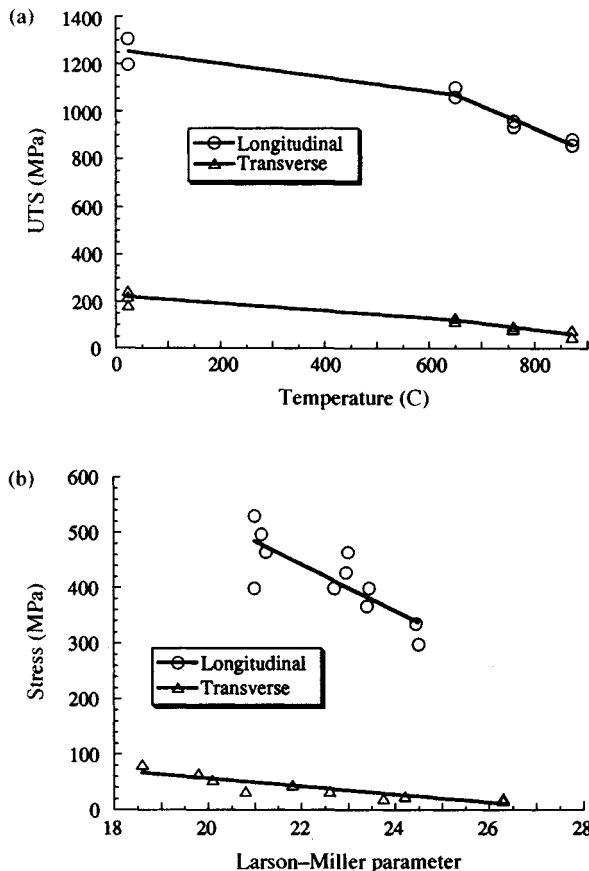


Figure 7. The (a) ultimate tensile strength (UTS) and (b) creep strength of Ti-24Al-11Nb/SCS-6 intermetallic composites in both longitudinal and transverse orientations. The Larson-Miller parameter is given as $T(20 + \log t)/1000$, where T is the absolute temperature in Kelvin and t is the time in hours. The data were taken from Larsen *et al.* (1992) using a density of 4.07 g cm^{-3} for the Ti-24Al-11Nb composite

environmental resistance. However, most of the current work on NiAl is as a monolithic alloy (see Miracle and Darolia, Chapter 3 in this volume), while activity on NiAl composites is in the feasibility stage, and is aimed primarily at determining basic mechanical properties and chemical compatibility.

Discontinuous reinforcements in NiAl include dispersoids, metallic precipitates (including eutectic alloys), ordered intermetallic precipitates, ceramic particulates, and ceramic whiskers. Many dispersoids have been added to NiAl, including TiB_2 , TiC , and W . HfB_2 (Whittenberger *et al.*, 1991), HfC (Whittenberger *et al.*, 1990b), and AlN (Whittenberger *et al.*, 1990a) are the most effective dispersoids, although it should be

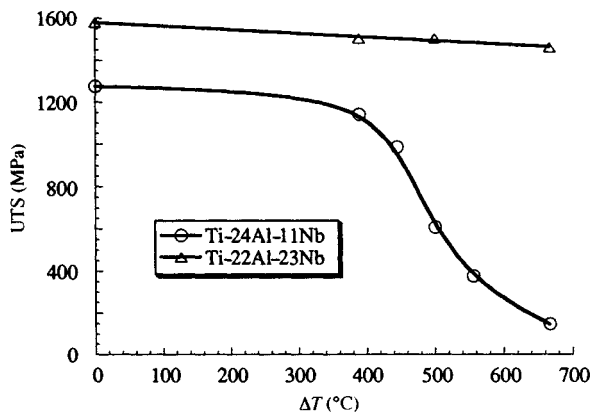


Figure 8. The room-temperature ultimate tensile strength after 500 thermal cycles in air for Ti-24Al-11Nb and the 'orthorhombic' alloy Ti-22Al-23Nb, each reinforced with 35 vol% SCS-6 SiC fibers. The maximum temperature for each thermal cycle was 815 °C, and the temperature differential is plotted on the horizontal axis. The data for Ti-24Al-11Nb composites were taken from Russ (1990), and the data for Ti-22Al-23Nb composites were taken from Smith *et al.* (1992), using a density of 4.21 g cm⁻³ for the 'orthorhombic' composite

noted that Hf is a potent solid-solution strengthener of NiAl (Darolia *et al.*, 1992; Law and Blackburn, 1987), and the contributions from solid-solution strengthening and dislocation pinning have not been isolated. Although modest strengthening is achieved with metallic precipitates (Darolia, 1991; Darolia *et al.*, 1992), once again, the contribution of solid-solution strengthening may account for a significant amount of the observed increase. Discontinuous ceramic particles and whiskers (Whittenberger *et al.*, 1989) also show only modest improvements in strength, and such composites do not yet compete with conventional Ni-based superalloys (Kumar *et al.*, 1992). However, ordered precipitate phases such as Ni₃AlTi and NiAlNb provide significant strengthening both in creep and tension (see Miracle and Darolia, Chapter 3 in this volume, and references therein).

Continuously reinforced NiAl has been produced *in situ* as directionally solidified eutectic composites (see Section 3.4) and artificially by the introduction of continuous fibers into NiAl powder (Noebe *et al.*, 1990; Bowman and Noebe, 1990; Bowman, 1992; Anton and Shah, 1992; Shah and Anton, 1992a). A composite of NiAl + B₄C and '304' stainless steel tubes has also been produced for improved impact resistance (Nardone *et al.*, 1990). Reinforcements of alumina and TiC are stable in NiAl, while SiC, Si₃N₄, and yttria show some reaction (Shah and Anton, 1992a). Although not

reported, it is likely that both W and Mo are stable in NiAl, since NiAl forms a eutectic reaction with each, and has only limited solubility for these elements. As expected, the magnitude of the interface bond strength plays a significant role in the properties of NiAl composites (Bowman, 1992; Bowman and Noebe, 1990; Nardone *et al.*, 1990). Mechanical data are scarce, and are likely to depend sensitively on microstructural integrity.

The principal motivation for studying NiAl composites is to improve the damage tolerance of (brittle) NiAl at RT, and to improve the strength and creep resistance at high temperatures. The greatest improvement in damage tolerance has been achieved with stainless steel reinforcements (Nardone *et al.*, 1990), which are expected to provide poor high-temperature properties. A similar approach with a ductile, chemically compatible refractory metal would be worthwhile. Other NiAl composites have thus far provided toughness values that are insufficient for most fracture-critical applications. The most promising improvements in high-temperature strength have been achieved in precipitation-strengthened NiAl (see Miracle and Darolia, Chapter 3 in this volume, and references therein). High-temperature properties for other NiAl composites are less promising. It is important to point out that an NiAl composite with both improved damage tolerance at RT and high-temperature strength has not been produced. Much work is required to develop NiAl composites with a balance of useful physical and mechanical properties for structural applications.

3.3 MoSi₂-Based Composites

The compound MoSi₂ has a high melting temperature (2010 °C), a density (6.05 g cm⁻³) about 25–30% lower than that of Ni-based superalloys, and a high Young's modulus at RT (379 GPa). This compound also has a high thermal conductivity (~145 W m⁻¹ °C⁻¹ in the temperature range 1000–2000 °C) and is machinable by an electrical discharge technique. In addition, MoSi₂ exhibits excellent oxidation and hot corrosion resistance (Schlichting, 1978; Wehrmann, 1967) in the temperature range 1000–1700 °C, which stems from the formation of a viscous and highly protective external silica scale. The attributes listed above are favorable for potential turbine-engine applications. However, like most intermetallics, the major problem which has impeded the utilization of MoSi₂ as a structural material is brittleness. MoSi₂ is brittle below 1000 °C with an extremely low resistance to fracture ($K_{Ic} < 4$ MPa m^{1/2}). Above approximately 1000 °C, the compound exhibits a

brittle to ductile transition; however, the tensile strength and creep resistance decrease rapidly with increasing temperature.

In order to alleviate these deficiencies in mechanical behavior, a number of recent investigations have been carried out on various MoSi_2 matrix composites. These studies can be divided into two broad categories: (i) composites containing brittle phases as the toughening/strengthening reinforcements; and (ii) composites containing a ductile refractory metal phase, primarily for improved toughness. The types of reinforcements and possible strengthening/toughening mechanisms, which include particle strengthening, load transfer to ceramic whiskers or fibers, crack deflection, crack bridging and whisker or fiber pullout, have been summarized in a recent publication by Meschter and Schwartz (1989). The same report also lists the potential ceramic reinforcements that are thermochemically stable in MoSi_2 ; these are SiC , Al_2O_3 , TiB_2 , TiC , ZrO_2 , and ZrB_2 . Of these, SiC whisker reinforced MoSi_2 has received the most attention (Gac and Petrovic, 1985; Gibbs *et al.*, 1987; Carter and Hurley, 1987; Carter *et al.*, 1989). These studies have shown that the strength of MoSi_2 at 1400°C can be tripled by the incorporation of SiC whiskers made by a vapor-solid technique. However, only a modest (absolute) increase in the RT fracture toughness from less than $5 \text{ MPa m}^{1/2}$ to about $8 \text{ MPa m}^{1/2}$ was achieved.

Fitzer and coworkers (Schlichting, 1978; Fitzer and Remmele, 1985; Fitzer and Schmidt, 1971) have investigated MoSi_2 -based composite materials that consist of solid-solution alloying the matrix with Ge to replace Si, and incorporation of refractory metal particles or wires into the MoSi_2 matrix. None of the refractory metals studied are in thermochemical equilibrium with MoSi_2 at high temperatures and, therefore, this approach is limited by the most rapid kinetics of interdiffusion of these metals in contact with MoSi_2 . The data indicate that Nb is the least reactive refractory metal in MoSi_2 below 1400°C ; however, a recent study (Carter and Martin, 1990) has shown that Ta is kinetically more stable than Nb when in contact with MoSi_2 . Investigations are ongoing which seek to combine a brittle ceramic reinforcement and a ductile phase into the MoSi_2 matrix (Maloney and Hecht, 1992). For these and all other composite engineering approaches, further information is required on the thermochemical and thermomechanical control of the interface region between reinforcements and the MoSi_2 matrix.

Research is also needed to investigate the role of coatings as diffusion barriers to retard thermochemical

degradation of reinforcements and as a means to accommodate thermal expansion mismatch (see de Reus, Chapter 29 in this volume). In addition, novel processing techniques are needed, possibly including plasma spraying, chemical and physical vapor deposition, and *in situ* two-phase synthesis where a high degree of compositional and microstructural control can be exercised.

3.4 Intermetallic Eutectic Composites

The large number of intermetallic eutectic systems offers the opportunity to explore those two-phase composites possessing a high degree of thermochemical stability. Eutectics also allow for the simultaneous, or *in situ*, fabrication of an intermetallic matrix and a reinforcement phase in one step, and the opportunity to control the microstructure through the control of solidification conditions. The reinforcement phase can be another strong intermetallic (providing high-temperature strength and creep resistance, but limited damage tolerance) or a metallic solid-solution phase (providing ductile-phase toughening). Extensive work is in progress on the latter type of reinforcements (Shah and Anton, 1992b, and references therein). Screening studies (Mazdiyasn and Miracle, 1990) on $\text{Cr-Cr}_2\text{Zr}$, $\text{Cr-Cr}_2\text{Hf}$, $\text{Cr-Cr}_2\text{Ta}$, $\text{Cr-Cr}_3\text{Si}$, $\text{Ta-Cr}_2\text{Ta}$, and $\text{Ta-Ta}_3\text{Si}$ eutectics have shown that, with the exception of the $\text{Ta-Cr}_2\text{Ta}$ and $\text{Cr-Cr}_2\text{Ta}$ systems, each of the eutectic alloys exhibits potential RT metallic-phase toughening of the brittle matrix. In addition, the systems $\text{Cr-Cr}_3\text{Si}$ and $\text{Cr-Cr}_2\text{Hf}$ also exhibit reasonable oxidation resistance at both 800°C and 1200°C . Extensive quantitative data are needed on the processing, mechanical behavior and environmental resistance of the selected systems for them to be candidates for further engineering development.

Mendiratta and coworkers (Mendiratta and Dimiduk, 1989; Mendiratta *et al.*, 1991; Rigney *et al.*, 1991; Mendiratta and Dimiduk, 1991; Mendiratta and Dimiduk, 1993) have studied the relationships between the microstructure and the mechanical properties and fracture behavior of $\text{Nb-Nb}_5\text{Si}_3$ composites formed in the Nb-Si system. A significant variability in microstructure is possible through control of composition (hypoeutectic, hypereutectic, and eutectic compositions, Figure 9) and processing, and their studies have shown good potential for low-temperature toughness and high-temperature strength to 1400°C . However, the high-temperature environmental resistance of these composites is extremely poor, and primary reliance on an environmentally resistant coating system would therefore be required. Recent research has

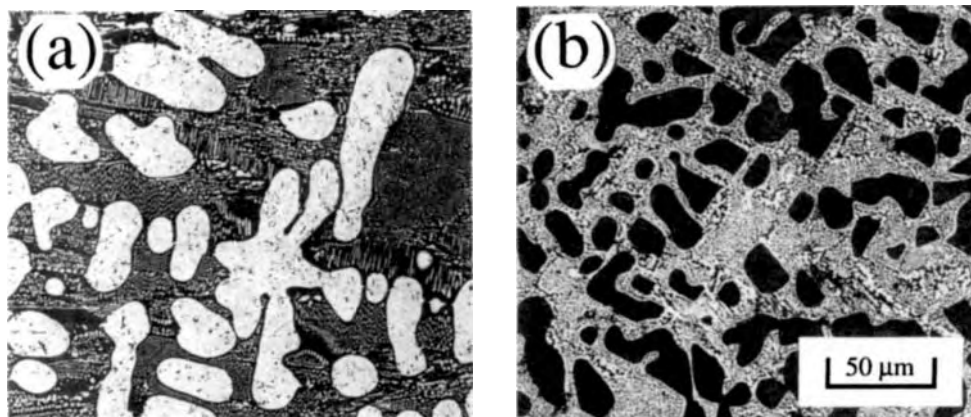


Figure 9. Microstructures of intermetallic eutectic composites in the Nb-Si system: (a) an Nb-10Si hypoeutectic alloy, containing the eutectic microconstituent and primary dendrites of Nb; and (b) an Nb-25Si hypereutectic alloy containing the eutectic microconstituent and particles of primary Nb_5Si_3 . A fine homogeneous eutectic microstructure (not shown) is obtained for alloys at the eutectic composition

shown encouraging results on the development of a high-temperature coating system for Nb alloys (Mueller *et al.*, 1992).

The large activity on directionally solidified Ni-based eutectic alloys (based on the intermetallic compound Ni_3Al) conducted during the 1970s for turbine-engine applications provides an historical antecedent to the current activity on Ni aluminide eutectic composites. Many studies have been conducted on the intermetallic eutectic system of Ni_3Al -Mo (Sriramamurthy and Tewari, 1984; Sprenger *et al.*, 1976, and references therein), while more recent studies have focused on eutectic reactions with the intermetallic compound NiAl. NiAl undergoes eutectic reactions with the ordered compounds NiAlNb (hP12) (Whittenberger *et al.*, 1992) and $(\text{Ni}, \text{Al})_2\text{Hf}_2$ (Baldan, 1984) and a wide range of refractory metals, including Cr, Mo, V, Re, and W (Stover, 1966; Subramanian *et al.*, 1990; Cotton *et al.*, 1991; Darolia *et al.*, 1992; Chang, 1992). Aligned NiAl eutectic composites show very attractive tensile strength (Walter and Cline, 1970) and stress-rupture properties (Stover, 1966) which compete with Ni-based superalloys (see Figure 8 in Miracle and Darolia, Chapter 3 in this volume). Studies on NiAl eutectic systems have shown a significant improvement in RT fracture toughness (Chang, 1992; Heredia *et al.*, 1992; Darolia *et al.*, 1992). However, extensive development is required in order to establish what compositions have sufficient environmental resistance along with favorable mechanical properties.

4. Composite Development

The field of intermetallic composites is very new; and it is important to point out that, while many potential applications are being pursued, there are currently no intermetallic composite components in use. A significant portion of the research on intermetallic composites is in the stage of attempting to demonstrate feasibility, where basic physical, chemical, and mechanical features are determined and the potential for development is identified. Activity on model composites to investigate and verify specific mechanisms, such as crack bridging and ductile-phase toughening, is included in this category. The development of intermetallic composites for structural applications, where both intuition and materials-based knowledge are used to formulate solutions to specific deficiencies in composite properties, has not yet been conducted in a focused, systematic fashion. However, some activity in this direction has recently been initiated in the area of continuously reinforced Ti aluminide composites (Graves, 1992). Nonetheless, the current state of the art provides neither the foundation of fundamental understanding nor the experimental and analytical techniques required for the effective development of intermetallic composites. Several fundamental issues required to guide the development activity of intermetallic composites (and also metal matrix composites) are now described.

Before a systematic approach to developing intermetallic composites may be undertaken, a firm foundation of the basic relationships between constituent (matrix, reinforcement, interface) properties and composite properties is required. Aside from basic intuition, which might suggest, for example, that increasing the creep resistance of the matrix will increase the creep resistance of the composite, or that increasing the normal strength of the interface will improve the off-axis properties of continuously reinforced composites, there is little fundamental understanding to guide composite development. This fundamental understanding is required to define an acceptable range of values of important composite constituent properties, such as the amount of matrix ductility required to utilize fully the load-carrying capability of the reinforcement. Basic understanding is also necessary to address trade-offs between competing properties, such as the requirement of a strong interface bond for off-axis properties versus the desirability of a weak interface bond for crack deflection, crack bridging, and toughening. Currently, finite element models are typically used to evaluate the influence of composite constituent properties on the properties of the composite. However, these techniques are cumbersome and inappropriate for the development of new materials since the basic information required for these models, such as time-dependent and temperature-dependent constitutive properties and the magnitude of interface properties, is typically not available.

While the importance of interface properties is commonly acknowledged, it is not always clear which interface property (such as work of adhesion, chemical bond, energy release rate, shear and normal strength) is dominant with respect to a particular composite property. For example, the normal strength of an interface is likely to dominate the ability of a composite to support off-axis tensile loads, but it is not entirely clear which interface property (or properties) it is important to focus on when developing a composite for improved crack-growth resistance or ductile-phase toughening. It is important to address both intrinsic and extrinsic contributions to the interface properties. In particular, properties such as interface strength may be dominated by extrinsic effects, including residual stresses which can cause the matrix to 'squeeze' the reinforcement, and reinforcement roughness. With respect to the intrinsic aspects of interface bonding, there is a need to establish a fundamental understanding of the basic parameters which influence interface bonding in order to guide development of better interfaces. For example, if a stronger interface between

an alumina reinforcement and a TiAl matrix were desired, there is little fundamental understanding to guide the selection and effectiveness of potential interface modifications. In the absence of this understanding, a clear need exists to establish simple, reproducible experimental techniques and analyses capable of measuring the appropriate interfacial parameters.

Several other issues are important in intermetallic composites. One of the principal objectives in the development of intermetallic composites is to improve the damage tolerance of monolithic intermetallic compounds. Various mechanisms of toughening (such as ductile-phase toughening, crack deflection and bifurcation, and crack bridging by the reinforcement) have been addressed for composite materials in general, and some understanding of the operative mechanisms has been obtained. However, there is only limited evidence that intermetallic composites with brittle reinforcements offer acceptable damage tolerance below the DBTT of the intermetallic matrix. Intermetallic compounds often deform in an inhomogeneous fashion, and the effect of inhomogeneous deformation on damage accumulation and failure initiation in intermetallic composites has not been studied in detail. The effect of elastic and plastic constraint of the intermetallic compound by the reinforcement may further reduce the amount of plastic deformation, and the degree of constraint is likely to depend upon the magnitude of the interface strength. In intermetallic composites where the 'matrix' and 'reinforcement' are mechanically combined, the resulting composite may not be in thermochemical equilibrium. Therefore, interface barrier coatings or slow kinetics of interfacial reaction are required for long-term stability. In addition, considerable care must be exercised in fabricating these composites to ensure that the required control over the microstructure (morphology, volume fraction, and distribution) and composition (bulk composition, as well as the type and amount of impurities) of the constituent phases is maintained. The processing environment must also be controlled to ensure reproducibility of the product. An additional difficulty concerns the limited commercial availability of reinforcing phases with reproducible properties. As mentioned earlier, intermetallic composites are also susceptible to damage caused during thermal cycling by a large thermal coefficient of expansion mismatch between the matrix and the reinforcement phases.

5. Processing

Processing is critical to the effective control of composition and microstructure in intermetallic

composites. In addition, techniques which offer the potential of low cost and transition beyond the laboratory scale are vital to the success of intermetallic composites for structural applications. However, a detailed discussion of the many processing approaches for producing intermetallic composites is outside the scope of this chapter. A brief discussion of candidate processing techniques is given below, and references are provided for additional detailed information. Many of the processing techniques of intermetallic compounds discussed elsewhere in this book are applicable, with some modification, to intermetallic composites (see Martin and Hardwick, Chapter 27 in Volume 1).

Many novel techniques have been proposed to process intermetallic composites, including powder processing, melt processing, and vapor-phase processing (Smith *et al.*, 1991; Stoloff and Alman, 1990; Everett and Arsenault, 1991). In general, powder approaches offer the benefit of low cost, but provide poor control of microstructure and are susceptible to contamination by interstitial atoms. On the other hand, vapor techniques, such as are used to make matrix-coated fibers (Ward-Close and Partridge, 1990) and laminated composites (Rowe and Skelly, 1992), can provide excellent control of composition and microstructure (Figure 3). While typical deposition rates are often quite low for physical vapor deposition (PVD), recent advances may allow cost-effective processing by this technique. Chemical vapor deposition (CVD) provides higher deposition rates and lower start-up costs than PVD, but the process chemistry is often complex, difficult to control, and often has the added difficulty of producing hazardous by-products. The high melting temperature and reactivity of many intermetallic alloys make incorporation of the matrix into a reinforcement preform by melt processing difficult. However, melt processing of *in situ* composites, such as intermetallic eutectic composites, offers many attractive benefits (Shah and Anton, 1992b).

While much of the processing information for continuously reinforced intermetallic composites is restricted or proprietary (Smith *et al.*, 1991), a recent review of the open literature has been provided (Semiati *et al.*, 1992). Methods discussed include the powder cloth, matrix-coated fiber, and liquid metal infiltration techniques, with an emphasis on deformation processing by the foil-fiber-foil technique. The foil-fiber-foil technique is costly, and is limited to intermetallic matrix alloys which can be rolled to foil. In addition, interstitial contamination often occurs during the foil-rolling process, and control of fiber spacing is still an issue. Modifications to the

foil-fiber-foil technique have been based on powder approaches, such as plasma deposition and powder cloth. While more cost effective, these processes offer no improvement in control of fiber spacing, and typically result in higher interstitial contents.

It is difficult to overstate the criticality of processing in the successful development and implementation of intermetallic composites. Novel techniques are necessary to provide the required control of microstructure and composition, and to pursue new avenues of composite architecture. Reproducible techniques are required to provide intermetallic composites for both fundamental and practical studies. Cost-effective techniques are required to foster the transition of intermetallic composites to structural applications.

6. Concluding Remarks

The study of intermetallic composites for structural applications is still in the exploratory and feasibility stage. Very little has been done to establish the fundamental relationships between the properties of the composite constituents (matrix, interface, and reinforcement) and the composite properties, which is important to efficient and economical development activity. Simple, reproducible techniques to quantify interface properties have not yet been established. Focused and systematic development for structural applications is just beginning to be conducted, and much is still required to establish the basic science of intermetallic composites. Novel, reproducible, and cost-effective processing techniques are required to allow the application of intermetallic composites to structural purposes. The wide range of intermetallic materials available for consideration and the various innovative processing techniques and composite architectures make the field of intermetallic composites one of great challenge and potential.

7. Acknowledgements

We would like to acknowledge the contributions of several of our colleagues: Bill Revelos, Paul Smith, Jim Larsen, and Mary Lee Gambone for help with locating data and references and for critical comments on Ti aluminide composites; Grant Rowe for permission to use Figure 3; and Andy Kraus, Judy Paine, Andy Johnson, and Chris Palser for assistance with the figures.

8. References

- Anton, D. L., and Shah, D. M. (1992). In *Intermetallic Matrix Composites II* (eds D. B. Miracle, D. L. Anton, and J. A. Graves). *MRS Proc.*, **273**, 157.
- Anton, D. L., Martin, P. L., Miracle, D. B., and McMeeking, R. (eds) (1990). *Intermetallic Matrix Composites*. *MRS Proc.*, **194**.
- Baldan, A. (1984). *Phys. Stat. Sol. (A)*, **83**, 47.
- Balsone, S. J. (1989). In *Oxidation of High Temperature Intermetallics* (eds T. Grobstein and J. Doychak). TMS, Warrendale, PA, p. 219.
- Bao, G., Genna, F., Hutchinson, J. W., and McMeeking, R. (1990). In *Intermetallic Matrix Composites* (eds D. L. Anton, P. L. Martin, D. B. Miracle, and R. McMeeking). *MRS Proc.*, **194**, 3.
- Bowman, R. R. (1992). In *Intermetallic Matrix Composites II* (eds D. B. Miracle, D. L. Anton, and J. A. Graves). *MRS Proc.*, **273**, 145.
- Bowman, R. R., and Noebe, R. D. (1990). In *Advanced High Temperature Engine Materials Technology Program*. NASA Conference Publication 10 051, 40-1.
- Brindley, P. K., MacKay, R. A., and Bartolotta, P. A. (1991). In *Titanium Aluminide Composites*, Air Force Wright Laboratory, WL-TR-91-4020. Wright-Patterson AFB, OH, p. 484.
- Cao, H. C., and Evans, A. G. (1991). *Acta Metall. Mater.*, **39**, 2997.
- Carter, D. H., and Hurley, G. F. (1987). *J. Am. Ceram. Soc.*, **70**(4), C-79.
- Carter, D. H., and Martin, P. L. (1990). In *Intermetallic Matrix Composites* (eds D. L. Anton, P. L. Martin, D. B. Miracle, and R. McMeeking). *MRS Proc.*, **194**, 131.
- Carter, D. H., Petrovic, J. J., Honnell, R. E., and Gibbs, W. S. (1989). *Ceram. Eng. Sci. Proc.*, **10**(9/10), 1121.
- Chang, K.-M. (1992). In *Intermetallic Matrix Composites II* (eds D. B. Miracle, D. L. Anton, and J. A. Graves). *MRS Proc.*, **273**, 191.
- Christman, T., Needleman, A., and Suresh, S. (1989). *Acta Metall.*, **37**, 3029.
- Cotton, J. D., Kaufman, M. J., and Noebe, R. D. (1991). *Scripta Metall. Mater.*, **25**, 1827.
- Cox, B. N., James, M. R., Marshall, D. B., and Addison, R. C., Jr. (1990). *Metall. Trans.*, **21A**, 2701.
- Darolia, R. (1991). *J. Met.*, **43**(3), 44.
- Darolia, R., Lahrman, D. F., and Field, R. (1992a). *Scripta Metall. Mater.*, **26**, 1007.
- Darolia, R., Lahrman, D. F., Field, R. D., Dobbs, J. R., Chang, K.-M., Goldman, E. H., and Konitzer, D. G. (1992b). In *Ordered Intermetallics—Physical Metallurgy and Mechanical Behavior*, Vol. 213 (eds C. T. Liu, R. W. Cashn, and G. Sauthoff). NATO ASI Series E: Applied Sciences. Kluwer Academic, Boston, p. 679.
- Everett, R. K., and Arseneault, R. J. (eds) (1991) *Metal Matrix Composites: Processing and Interfaces*. Academic Press, New York.
- Faber, K. T., and Evans, A. G. (1983a). *Acta Metall.*, **31**, 565.
- Faber, K. T., and Evans, A. G. (1983b). *Acta Metall.*, **31**, 577.
- Fitzer, E., and Remmele, W. (1985). In *5th International Conference on Composite Materials* (eds W. C. Harrigan, Jr., J. Strife, and A. K. Dhingra). *Met. Soc.*, **515**.
- Fitzer, E., and Schmidt, F. K. (1971). *High Temp. High Press.*, **3**, 445.
- Fry, V. (1992). Unpublished Research, Amercom.
- Gac, F. D., and Petrovic, J. J. (1985). *J. Am. Ceram. Soc.*, **68**(8), C-200.
- Gambone, M. L. (1990). In *Fatigue and Fracture of Titanium Aluminides*, Air Force Wright Laboratory Final Technical Report, WRDC-TR-89-4145, Vol. II. Wright Patterson Air Force Base, Ohio.
- Gambone, M. L., and Bain, K. R. (1988). In *Proceedings of the 2nd International SAMPE Metals Conference*, Vol. 2 (eds F. H. Froes and R. A. Cull). SAMPE, Covina, CA, p. 487.
- Gibbs, W. S., Petrovic, J. J., and Honnell, R. E. (1987). *Ceram. Eng. Sci. Proc.*, **8**(7/8), 645.
- Graves, J. A. (1992). In *Advanced Ti-Based MMC Development*, Interim Technical Reports. Contract F33615-91-C-5647, Air Force Wright Laboratory, Wright-Patterson AFB, OH.
- Graves, J. A., Smith, P. R., and Rhodes, C. G. (1992). In *Intermetallic Matrix Composites II* (eds D. B. Miracle, D. L. Anton, and J. A. Graves). *MRS Proc.*, **273**, 31.
- Heredia, F. E., Valencia, J. J., Levi, C. G., and Evans, A. G. (1992). In *Intermetallic Matrix Composites II* (eds D. B. Miracle, D. L. Anton, and J. A. Graves). *MRS Proc.*, **273**, 197.
- HITEMP Review (1990). *Advanced High Temperature Engine Materials Technology Program*. NASA Conference Publication 10 051.
- HITEMP Review (1991). *Advanced High Temperature Engine Materials Technology Program*. NASA Conference Publication 10 082.
- HITEMP Review (1992). *Advanced High Temperature Engine Materials Technology Program*. NASA Conference Publication 10 104.
- Krutenat, R. C. (1992). Private communication.
- Kumar, K. S., Darolia, R., Lahrman, D., and Mannan, S. K. (1992). *Scripta Metall. Mater.*, **26**, 1001.
- Larsen, J. M., Revelos, W. C., and Gambone, M. L. (1992). In *Intermetallic Matrix Composites II* (eds D. B. Miracle, D. L. Anton, and J. A. Graves). *MRS Proc.*, **273**, 3.
- Law, C. C., and Blackburn, M. J. (1987). In *Rapidly Solidified Lightweight Durable Disk Materials*. AFWAL TR-87-4102, Air Force Wright Aeronautical Laboratory, Wright-Patterson Air Force Base, Ohio.
- Liu, C. T., and McKamey, C. G. (1990). In *High Temperature Aluminides and Intermetallics* (eds S. H. Whang, C. T. Liu, D. P. Pope, and J. O. Stiegler). TMS, Warrendale, PA, p. 133.
- Liu, C. T., and George, E. P. (1991). In *High Temperature Ordered Intermetallic Alloys IV* (eds L. A. Johnson, D. P. Pope, and J. O. Stiegler). *MRS Proc.*, **213**, 527.

- MacKay, R. A., Brindley, P. K., and Froes, F. H. (1991). *J. Met.*, **43**(5), 23.
- Maloney, M. J., and Hecht, R. J. (1992). *Mater. Sci. Eng. A*, **155**, 19.
- Mazdiyassni, S., and Miracle, D. B. (1990). In *Intermetallic Matrix Composites* (eds D. L. Anton, P. L. Martin, D. B. Miracle, and R. McMeeking). *MRS Proc.*, **194**, 155.
- Mendiratta, M. G., and Dimiduk, D. M. (1989). In *High Temperature Ordered Intermetallic Alloys III* (eds C. T. Liu, A. L. Taub, N. S. Stoloff, and C. C. Koch). *MRS Proc.*, **133**, 441.
- Mendiratta, M. G., and Dimiduk, D. M. (1991). *Scripta Metall.*, **25**, 237.
- Mendiratta, M. G., and Dimiduk, D. M. (1993). *Metall. Trans.*, **24A**, 501.
- Mendiratta, M. G., Lewandowski, J. J., and Dimiduk, D. M. (1991). *Metall. Trans.*, **22A**, 1573.
- Meschter, P. J., and Schwartz, D. S. (1989). *J. Met.*, **41** (11), 52.
- Miracle, D. B., Anton, D. L., and Graves, J. A. (eds) (1992) *Intermetallic Matrix Composites II*. *MRS Proc.*, **273**.
- Mueller, A., Wang, G., Rapp, R. A., and Courtright, E. L. (1992). *J. Electrochem. Soc.*, **139**, 1266.
- Nardone, V. C., Strife, J. R., and Prewo, K. M. (1990). In *Intermetallic Matrix Composites* (eds D. L. Anton, P. L. Martin, D. B. Miracle, and R. McMeeking). *MRS Proc.*, **194**, 205.
- Noebe, R. D., Bowman, R. R., and Eldridge, J. (1990). In *Intermetallic Matrix Composites* (eds D. L. Anton, P. L. Martin, D. B. Miracle, and R. McMeeking). *MRS Proc.*, **194**, 323.
- Petrovic, J. J., Honnell, R. E., and Vasudevan, A. K. (1990). In *Intermetallic Matrix Composites* (eds D. L. Anton, P. L. Martin, D. B. Miracle, and R. McMeeking). *MRS Proc.*, **194**, 123.
- Revelos, W. C., and Smith, P. R. (1992). *Metall. Trans.*, **23A**, 587.
- Rhodes, C. G. (1992). In *Intermetallic Matrix Composites II* (eds D. B. Miracle, D. L. Anton, and J. A. Graves). *MRS Proc.*, **273**, 17.
- Rigney, J. D., Lewandowski, J. J., Matson, L., Mendiratta, M. G., and Dimiduk, D. M. (1991). In *High Temperature Ordered Intermetallic Alloys IV* (eds J. O. Stiegler, L. A. Johnson, and D. P. Pope). *MRS Proc.*, **213**, 1001.
- Rowe, R. G. (1992). Unpublished research, GE Corporate Research and Development Center.
- Rowe, R. G., and Skelly, D. W. (1992). In *Intermetallic Matrix Composites II* (eds D. B. Miracle, D. L. Anton, and J. A. Graves). *MRS Proc.*, **273**, 411.
- Russ, S. M. (1990). *Metall. Trans.*, **21A**, 1595.
- Schlichting, J. (1978). *High Temp., High Press.*, **10**(3), 241.
- Schoenberg, T., and Kumnick, A. (1989). In *8th Metal Matrix Composites Technology Conference Proceedings*, Vol. I, 1-1. MMCIAC, California.
- Semiatin, S. L., Goetz, R. L., and Kerr, W. R. (1992). In *Intermetallic Matrix Composites* (eds D. B. Miracle, D. L. Anton, and J. A. Graves). *MRS Proc.*, **273**, 351.
- Shah, D. M., and Anton, D. L. (1992a). In *Intermetallic Composite Feasibility*, Final Technical Report. Contract F33615-88-C-5405, Air Force Wright Laboratory, Wright-Patterson AFB, OH.
- Shah, D. M., and Anton, D. L. (1992b). In *Intermetallic Matrix Composites II* (eds D. B. Miracle, D. L. Anton, and J. A. Graves). *MRS Proc.*, **273**, 385.
- Sigma (1991). Sigma Fiber Ltd, BP Research Centre, Chertsey Road, Sudbury on Thames, Middlesex, TW16 7LN, UK.
- Smith, P. R., and Revelos, W. C. (eds) (1992). *Titanium Matrix Composites*. Air Force Wright Laboratory, WL-TR-92-4035, Wright-Patterson AFB, OH.
- Smith, P. R., Balson, S. J., and Nicholas, T. (eds) (1991). *Titanium Aluminide Composites*. Air Force Wright Laboratory, WL-TR-91-4020, Wright-Patterson AFB, OH.
- Smith, P. R., Graves, J. A., and Rhodes, C. G. (1992). In *Intermetallic Matrix Composites II* (eds D. B. Miracle, D. L. Anton, and J. A. Graves). *MRS Proc.*, **273**, 43.
- Sprenger, H., Richter, H., and Nickl, J. J. (1976). *J. Mater. Sci.*, **11**, 2075.
- Sriramamurthy, A. M., and Tewari, S. N. (1984). *Metall. Trans.*, **15A**, 1905.
- Stoloff, N. S., and Alman, D. E. (1990). In *Intermetallic Matrix Composites* (eds D. L. Anton, P. L. Martin, D. B. Miracle, and R. McMeeking). *MRS Proc.*, **194**, 31.
- Stover, E. T. (1966). In *Effects of Alloying and Deformation Processing on Mechanical Behavior of NiAl*, WADC-TDR-60-184, Part VII, Vol. II. USAF Contract AF-33(615)-1497, Wright Air Development Center.
- Subramanian, P. R., Mendiratta, M. G., Miracle, D. B., and Dimiduk, D. M. (1990). In *Intermetallic Matrix Composites* (eds D. L. Anton, P. L. Martin, D. B. Miracle, and R. McMeeking). *MRS Proc.*, **194**, 147.
- Walter, J. L., and Cline, H. E. (1970). *Metall. Trans.*, **1**, 1221.
- Wang, L., and Arsenault, R. J. (1990). In *Intermetallic Matrix Composites* (eds D. L. Anton, P. L. Martin, D. B. Miracle, and R. McMeeking). *MRS Proc.*, **194**, 199.
- Ward-Close, C. M., and Partridge, P. G. (1990). *J. Mater. Sci.*, **25**, 4315.
- Wehrmann, R. (1967). In *High Temperature Materials and Technology* (eds I. E. Campbell, and E. M. Sherwood). John Wiley & Sons Ltd, New York, p. 399.
- Whittenberger, J. D., Mannan, S. K., and Kumar, K. S. (1989). *Scripta Metall.*, **23**, 2055.
- Whittenberger, J. D., Arzt, E., and Luton, M. J. (1990a). In *Intermetallic Matrix Composites* (eds D. L. Anton, P. L. Martin, D. B. Miracle, and R. McMeeking). *MRS Proc.*, **194**, 211.
- Whittenberger, J. D., Gaydos, D. J., and Kumar, K. S. (1990b). *J. Mater. Sci.*, **25**, 2771.
- Whittenberger, J. D., Ray, R., Jha, S. C., and Draper, S. (1991). *Mater. Sci. Eng. A*, **138**, 83.
- Whittenberger, J. D., Riviere, R., Noebe, R. D., and Oliver, B. (1992). *Scripta Metall. Mater.*, **26**, 987.
- Yang, J.-M., and Jeng, S. M. (1990). In *Intermetallic Matrix Composites* (eds D. L. Anton, P. L. Martin, D. B. Miracle, and R. McMeeking). *MRS Proc.*, **194**, 139.

Addendum

Intermetallic matrix composites (IMCs) continue to be studied as an approach to achieve high temperature strength for aerospace structural applications. As a structural material, fracture properties of engineering significance must also be provided over the entire range of application temperatures. Thus, the principal technological challenge in the development of IMCs continues to be the conception and development of IMCs that can simultaneously provide both of these characteristics. The need for chemical compatibility and environmental resistance, the ability to predict and control residual stresses, and the ability to effect consolidation of the IMC while avoiding damage to the matrix or reinforcement, while also providing control over composite microstructure, all add significant complexity to the successful development of IMCs.

Significant progress has been made in the technology of continuously-reinforced Ti-aluminide intermetallic matrix composites (IMCs) since *Intermetallic Compounds: Principles and Practice* was originally published. Multi-phase matrix alloys based on the ordered orthorhombic Ti_2AlNb (O) phase have been developed with significant improvements on ductility and environmental resistance over earlier IMCs based on the $\text{Ti}_3\text{Al}(\alpha_2)$ phase. Composites based on these O alloys (orthorhombic Ti-matrix composites, or OTMCs), reinforced with continuous SiC reinforcements, have been developed with an enabling balance of first- and second-tier properties up to 760 °C. Both strength and toughness have been achieved in OTMCs. Environmental resistance and improved transverse properties remain as the primary technology issues that require additional improvement.

Important improvements in the properties of Nb/Nb-silicide IMCs have also been made over the past six years. Concepts for achieving good high temperature strength and adequate fracture properties have each been validated. In addition, alloys with dramatic

improvements in environmental resistance have also been produced. While the approaches for obtaining strength and toughness as well as environmental resistance in the same IMC are not intrinsically incompatible, significant risk remains in the effort to combine these advancements in a single IMC system.

The development of IMCs for structural use continues to be either in the feasibility stage, where concepts for obtaining both high temperature strength and adequate engineering fracture properties have been identified but have not yet been validated, or is in the exploratory phase, where concepts for obtaining both of these properties in a single system have yet to be defined. Much of the work over the past thirty years has focused on obtaining improved strength in intermetallic alloys by adding various forms of reinforcements. This work has been only marginally successful. While improvements in strength are sometimes achieved, many of the IMCs produced have strengths lower than the unreinforced matrix. Extrinsic concepts for improving the toughness of intermetallic alloys have been even less successful. When improvements are achieved, the magnitude of the improvement is too small to be of engineering significance. In many cases, the concepts for improving the fracture properties are incompatible with simultaneously achieving improved high temperature strength.

An extensive review of intermetallic composites technology has recently been written (Miracle, in press). The interested reader is referred to this publication for more detailed information and a complete discussion and list of references.

Reference

- Miracle, D. B. (in press). *Intermetallic Matrix Composites*, in *Comprehensive Composites Materials; Volume 3 (Metal Matrix Composites)* (ed. T.W. Clyne), Elsevier Science Ltd, Oxford, UK.

Chapter 6

Zr₃Al: A Potential Nuclear Reactor Structural Material

Erland M. Schulson

Thayer School of Engineering, Dartmouth College, Hanover, NH 03755, USA

1. Introduction

This chapter considers the L1₂ (cP4) intermetallic Zr₃Al and its potential utility as a structural material. Nuclear engineering is highlighted, because it was in response to some special needs of the nuclear industry that the alloy was first proposed (Schulson, 1972, 1974). Studies have been performed on various aspects of the metallurgy of Zr₃Al, including recrystallization and grain growth (Gagné and Schulson, 1976), oxidation and corrosion (Murphy, 1975; Schulson and Trottier, 1980a, b), radiation damage (Howe and Rainville, 1977, 1979; Carpenter and Schulson, 1978; Howe and Rainville, 1991), dislocation structure (Howe *et al.*, 1974; Douin, 1991), and the crystalline to amorphous transformation induced by hydrogen (Meng *et al.*, 1988; Lee *et al.*, 1991), by irradiation (Rehn *et al.*, 1987; Okamoto *et al.*, 1988) and by mechanical attrition (Gialanella *et al.*, 1992). This chapter focuses on the mechanical behavior. Other chapters in Volume 1 of this work (Howe, Chapter 34; Veyssi re and Douin, Chapter 22) note some of the other aspects of the material as do two earlier reviews (Schulson, 1980a, 1984).

2. Background

2.1 Requirements of Nuclear Structural Alloys

Zr₃Al was conceived to satisfy the needs of nuclear engineering and, more specifically, the special requirements of the CANDU (*Canadian Deuterium*

Uranium) power reactor. This system uses natural uranium as fuel and heavy water as both moderator and coolant, and it distributes the coolant amongst a large number of thin-walled, small-diameter pressure tubes (about 500 of them in a 500 MW power device). The CANDU reactor thus requires structural elements (fuel sheaths and pressure tubes) which not only resist oxidation, corrosion, and creep deformation, but which are also relatively transparent to thermal neutrons. The last requirement is particularly important, and accounts largely for the current use of the zirconium-based alloys* Zircaloy-2, Zircaloy-4, and Zr-2.5% Nb.

The efficiency of the CANDU and other nuclear systems is around 30%. This is set mainly by the difference between the temperature of the (pressurized) water as it leaves the reactor core, which is currently around 300  C, and by its temperature as it leaves a heat exchanger. The latter temperature is difficult to alter. Improvements in efficiency, therefore, are sought essentially through a higher core temperature. And herein lies the challenge to materials engineering: the commercial zirconium-based alloys currently used begin to lose their strength at temperatures above 300  C and, for this reason, are unsuitable for long-term service at higher temperatures. Higher efficiencies, therefore, require better materials.

*Zircaloy-2: 1.2-1.7 wt% Sn, 0.07-0.2 wt% Fe, 0.05-0.15 wt% Cr, 0.03-0.08 wt% Ni, balance Zr. Zircaloy-4: 1.2-1.7 wt% Sn, 0.18-0.24 wt% Fe, 0.07-0.13 wt% Cr, balance Zr. Zr-2.5% Nb: 2.4-2.8 wt% Nb, balance Zr.

Table 1. Physical properties of Zr_3Al

Property	Value	Reference
Crystal structure	$L1_2$ (cP4)	Keeler and Mallery (1955)
Lattice parameter (nm)	0.437	
Density ($kg\ m^{-3}$)	5970	
Young's modulus (GPa)	$E(T) = 149.8 - 0.047T$ for T in Kelvin	Turner <i>et al.</i> (1978)
Thermal expansion coefficient (K^{-1})	8.3×10^{-6}	Turner <i>et al.</i> (1978)
Electrical resistivity ($\mu\Omega m$)	0.493	Schulson and Turner (1978)
Thermal coefficient of electrical resistivity (K^{-1})	2.33×10^{-3}	Schulson and Turner (1978)
Decomposition temperature ($^{\circ}C$)	960	
Melting temperature ($^{\circ}C$)	1350	
Specific thermal neutron absorption capture cross section ($m^2\ m^{-3}$)	0.96	

2.2 Why an Intermetallic and Why Zr_3Al ?

The reason an intermetallic and, particularly, the reason the zirconium aluminide Zr_3Al may have potential may be seen as follows.

Within the context of the long-term (30 year) operation of CANDU power reactors, strength is taken to be the resistance of pressure tubes to irradiation creep; that is, to time-dependent plastic flow under a flux of particles (unmoderated neutrons) sufficiently energetic ($E \approx 1$ MeV) to displace atoms from their lattice sites. At the intermediate temperatures and stresses under which the component operates, creep is governed by dislocation climb. In turn, this is limited by the rate of migration of irradiation-produced self-interstitials to edge dislocations. From the point of view of climb, interstitials are more serious than vacancies (which are produced in equal numbers) because they are more strongly attracted to the dislocations and are more mobile. Thus, to reduce creep it is essential to reduce the flow of interstitials. In principle this reduction can be achieved by increasing the rate at which interstitials recombine with vacancies, and this is where long-range atomic order (LRO) enters the picture (Schulson, 1977).

Owing to a higher degree of correlated atom-vacancy exchange, LRO effectively 'cages' vacancies within 'leaky cells' of atomic dimensions. In so doing, LRO impedes their migration (e.g. see Huntington's (1958) six-jump cycle for B2 (cP2) alloys) to vacancy sinks, resulting in a higher steady-state concentration. Consequently, interstitials flowing towards dislocations have greater chance of recombining with vacancies. Even the intermediate degree of order which is likely to characterize the microstructure at steady state (Schulson, 1979) may be effective, as suggested through calculations (Schulson *et al.*, 1978) on interstitial-vacancy recombination and on steady-state irradiation

creep within a hypothetical $L1_2$ (cP4) alloy exposed to a typical fast-neutron flux.

The idea is not easily tested, however. The competition between disordering and ordering under irradiation makes it impossible to study the steady-state behavior of the same alloy in both the fully ordered and the completely disordered states. Only transient behavior can be examined, and that behavior offers little insight into long-term response. The alternative is to adopt the idea as a working hypothesis and to proceed with alloy development from this new perspective. And that is what was done.

Zr_3Al was selected (Schulson, 1972) for a variety of reasons. It has a relatively low absorption cross section for thermal neutrons (Table 1), a relatively high melting point (Table 1), a moderate density ($5970\ kg\ m^{-3}$), and a simple crystal structure (cP4). Also, from the original investigators of the Zr-Al phase diagram (McPherson and Hansen, 1954) it was known to be ductile, albeit as a precipitate within a solid solution under a compressive stress state. Ductility was considered to be rather important and accounts for the rejection of a number of brittle compounds, including some neutron-transparent silicides and beryllides of high melting points and some other zirconium aluminides.

3. Processing and microstructure of Zr_3Al

3.1 Peritectoid Transformation

Zr_3Al contains 8.97 wt% Al and exists as a peritectoidally formed 'line' compound on the Zr-Al phase diagram (Figure 1). Arc-melted ingots (Schulson, 1975) of this composition, whether large (230 mm diameter, 225 kg) or small (12 mm diameter, 150 g), consist of a metastable 50/50 mixture of transformed

β -Zr, plus precipitates of hexagonal Zr₂Al. The average size of the particles depends upon the rate of cooling through the two-phase field, and varies from 8 to 10 μm in diameter in the larger ingots to about 1 μm in the smaller ones. When annealed at temperatures below about 975 °C, the two-phase structure transforms to Zr₃Al via the peritectoid transformation $\text{Zr} + \text{Zr}_2\text{Al} \rightarrow \text{Zr}_3\text{Al}$ (Figure 2). The transformation velocity (Schulson and Graham, 1976) for Zr₂Al particles of about 3 μm diameter, for instance, reaches a maximum around 888 °C (i.e. at about 70 °C below the equilibrium), at which temperature the transformation is complete within 8 h. Figure 3 shows the corresponding T-T-T curves. Nucleation occurs heterogeneously at the Zr/Zr₂Al interfaces, and growth occurs through the long-range, diffusion-controlled migration in opposite directions of the Zr₂Al/Zr₃Al and Zr₃Al/Zr interphase boundaries. Correspondingly, the transformation velocity decreases with increasing size of the parent Zr₂Al particles (Schulson, 1980b).

To the author's knowledge, Zr₃Al has never been produced as a truly single-phase alloy. There are two reasons for this: its very narrow compositional range generally leads to the synthesis of off-stoichiometric compositions; and impurities such as Fe segregate (Schulson and Davidson, 1977) to one of the parent phases, Zr₂Al, during the transformation, thereby stabilizing a three-phase field. Thus, 'fully transformed'

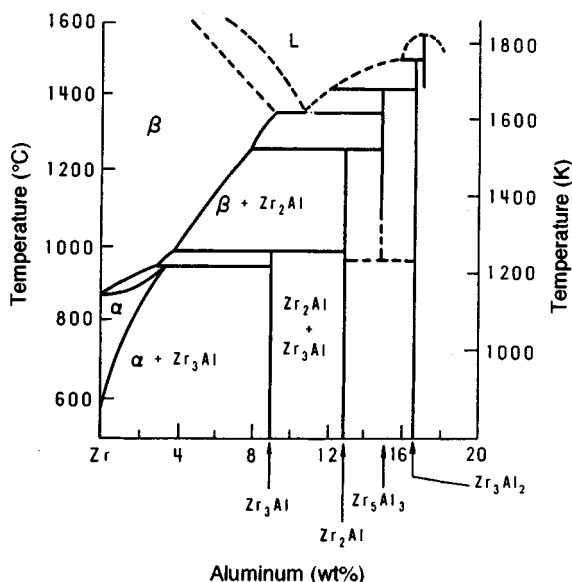


Figure 1. Zr-Al phase diagram illustrating the formation of Zr₃Al

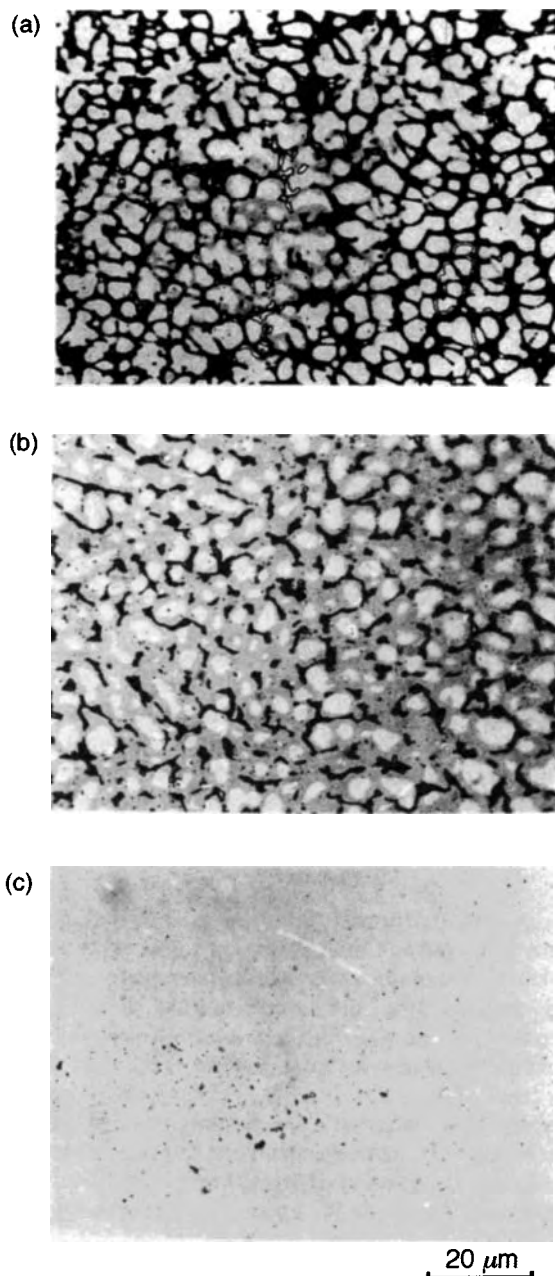


Figure 2. Optical micrographs illustrating the formation of Zr₃Al via the peritectoid transformation Zr (dark) + Zr₂Al (light) \rightarrow Zr₃Al (gray) during isothermal annealing at 850 °C. After 0.5 h (a), only a small amount of Zr₃Al has formed, localized at specific Zr₂Al/Zr interfaces. After 2 h (b), nucleation is complete and rims of Zr₃Al grow on every Zr₂Al particle. The transformation is complete within 8 h (c). Note in (c) the residual α -Zr and Zr₂Al. This alloy contained 8.9 wt% Al

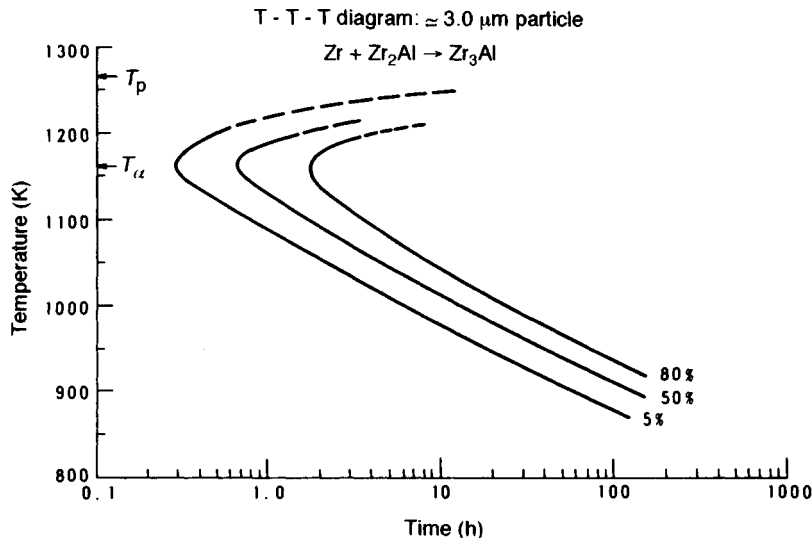


Figure 3. The T-T-T diagram for the peritectoid formation of Zr_3Al within the alloy shown in Figure 2. The curves shift to the right for alloys containing coarser parent particles (i.e. $\approx 3 \mu\text{m}$) of Zr_2Al

ingots generally contain micrometer-sized residual particles of Zr_2Al and $\alpha\text{-Zr}$. For instance, the best experimental alloys prepared to date via ingot metallurgy from high-purity elements contain around 0.1 vol% of each of these phases. Perhaps a single-phase material could be prepared via powder metallurgy.

3.2 Forming to Shape

Zr_3Al can be formed (Schulson and Stewart, 1976) into strip, rod and tubing, first by hot working above 1000°C within the $\beta + \text{Zr}_2\text{Al}$ two-phase field and then by transforming the microstructure at a lower temperature as described above. Processing in this manner produces material characterized by a fully ordered, L_{12} (cP4) type of polycrystalline matrix consisting of equiaxed and randomly oriented grains, each of which is a single domain (i.e. free from antiphase boundaries) and relatively free from dislocations. The residual $\alpha\text{-Zr}$ and Zr_2Al are sited at grain boundaries and intragranularly, respectively.

4. Physical Properties

Table 1 summarizes some physical properties. Where temperature is a factor, the parameters are given for room temperature, unless otherwise specified. Note that the electrical resistivity is relatively high and is similar to that for Zr ($0.45 \mu\Omega\text{m}$) and Ti ($0.55 \mu\Omega\text{m}$). This

suggests that Zr_3Al is not a particularly good conductor, in keeping with the character of other intermetallic compounds (Hume-Rothery, 1931). It also suggests from the Wiedemann-Franz relationship that Zr_3Al might be expected to be a relatively poor thermal conductor.

5. Mechanical Properties

The mechanical behavior of Zr_3Al has been investigated mainly through the short-term tensile testing of cylindrical and flat specimens of binary alloys. Recent work (Chen *et al.*, 1991; Li *et al.*, 1991) has been performed by bend testing miniature disks. Hardness (Schulson and Roy, 1977a) and thermal creep (Cameron *et al.*, 1976) have also been examined. Microalloying and macroalloying have not been examined systematically. The following discussion emphasizes the tensile properties, particularly yield strength, work-hardening rate, ductility and fracture. Only polycrystals have been studied. Information from single crystals would be desirable, but, owing to the peritectoid origin, material in this form is difficult to produce.

5.1 Yielding

Zr_3Al yields discontinuously at low temperatures (Schulson and Roy, 1978a). This is evident from a yield plateau on the stress-strain curve, which corresponds

to a lower yield point. This feature is characteristic of many strongly ordered L1₂ (cP4) intermetallics (e.g. Ni₃Al, Ni₃Ga, Ni₃Si, and Ni₃Ge) and results from the steady but jerky propagation of Lüders bands along the gauge section. The Lüders strain ϵ_L increases with decreasing grain size d and is described by the relationship

$$\epsilon_L = \lambda d^{-q} \quad (1)$$

where (for d in meters) $\lambda = 5 \times 10^{-5} \text{ m}^{0.5}$ at room temperature and $6 \times 10^{-5} \text{ m}^{0.5}$ at 400 °C and $q = 0.5$. In physical terms ϵ_L is the plastic strain the material undergoes to recover, through strain hardening, the strength it loses when it first yields. The discontinuous yielding is attributed to the generation of dislocations which, as noted above, are in low abundance within the as-transformed material.

The plateau yield strength σ_y at low temperatures increases sharply with decreasing grain size (Figure 4). This behavior is also characteristic of the strongly ordered L1₂ intermetallics noted above and is described by the conventional Hall–Petch relationship (Schulson and Roy, 1978a)

$$\sigma_y = \sigma_0 + k_y d^{-0.5} \quad (2)$$

where $\sigma_0 = 90 \text{ MPa}$ and $k_y = 0.76 \text{ MPa m}^{0.5}$ at room temperature. The yield strength is described (Takeyama and Liu, 1988) as well by another expression, namely

$$\sigma_y = \sigma'_0 + k'_y d^{-0.8} \quad (3)$$

where $\sigma'_0 = 165 \text{ MPa}$ and $k'_y = 0.02 \text{ MPa m}^{0.8}$. This relationship was first proposed by Schulson *et al.* (1985) for Ni₃Al, but has now been shown to describe several other strongly ordered L1₂ intermetallics, namely Ni₃Si (Schulson *et al.*, 1990), Ni₃Ge (Fang and Schulson, 1992), and Ni₃Ga (Xu and Schulson, 1994). For all these Ni-based compounds the conventional Hall–Petch description leads to negative values of σ_0 which are physically meaningless. The $d^{-0.8}$ dependence can be straightforwardly derived (Schulson *et al.*, 1985; Schulson, 1989) by incorporating both the discontinuous nature of yielding and the attendant work hardening within the Lüders bands. Owing to its generality, equation (3) is the better one to use. In both descriptions the first term is a measure of the resistance of the lattice (with its defects) to the glide of dislocations, and the constant in the second term is a measure of the effectiveness with which grain boundaries impede slip.

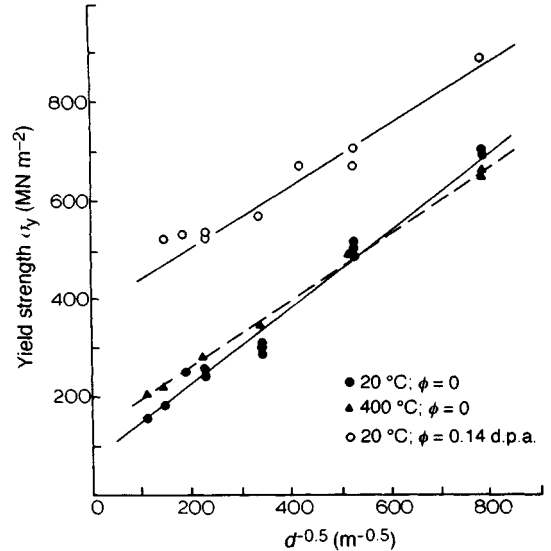


Figure 4. Hall–Petch plots of the yield strength of Zr₃Al at room temperature and at 400 °C and at room temperature after irradiation at 300 °C with fast ($E > 1 \text{ MeV}$) neutrons to the dose noted ($1.4 \times 10^{24} \text{ n m}^{-2} = 0.14 \text{ d.p.a.}$). The intercept increases and the slope decreases both with increasing temperature and upon irradiation. The alloy contained 8.9 wt% Al

Over the intermediate range of temperature from around room temperature to 400–500 °C, the yield strength of the more coarsely grained polycrystals increases with increasing temperature (Schulson and Roy, 1978a), as shown in Figure 5. The strength of the more finely grained material, on the other hand, decreases. The difference reflects both the differing contributions to the yield strength from the lattice and from the grain boundaries plus the opposing effects of temperature on the lattice resistance and on the grain boundary impediment to slip. For instance, upon raising the temperature from 20 to 400 °C, the lattice resistance rises by about 80%, while the grain boundary impediment falls by about 14%. The thermal strengthening of the lattice is probably related to a Kear–Wilsdorf kind of dislocation mechanism (Kear and Wilsdorf, 1962), as in other L1₂ alloys (Paidar *et al.*, 1984; Hirsch, 1992; Sun and Hazzledine, 1992), while the reduction of the boundary impediment may be related to thermal modifications of the dislocation structure.

At elevated temperatures Zr₃Al yields smoothly and the yield strength decreases with decreasing grain size (Figure 5). These changes begin at temperatures around 400–500 °C within relatively finely grained material ($d = 3.5 \mu\text{m}$) strained at rates around 10^{-4} s^{-1} , but are displaced to higher temperatures upon increasing both

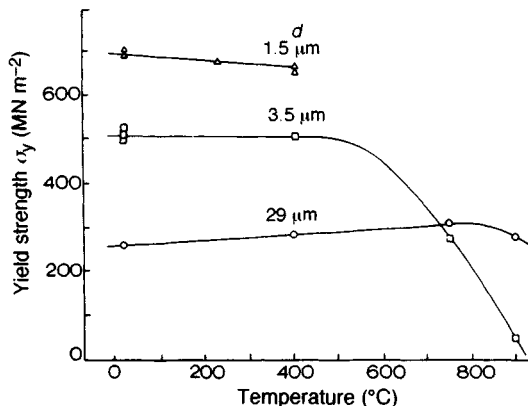


Figure 5. Plots of the yield strength versus temperature for Zr_3Al of three different grain sizes strained at $3 \times 10^{-4} s^{-1}$. The slope at the lower temperatures changes from negative to zero to positive upon increasing the grain size. Grain refinement strengthens the material at the lower temperatures (as in Figure 4), but weakens it above $700^\circ C$. The alloy contained 8.9 wt% Al

the grain size and the strain rate. They reflect the onset of grain boundary sliding.

Irradiation by fast neutrons ($E > 1$ MeV) increases the yield strength (Schulson, 1978a; Rosinger, 1980; Rosinger and Wilkins, 1980). For instance, irradiation to 0.14 d.p.a. (displacement per atom) at $300^\circ C$ in a pressurized water reactor raises the strength at room temperature by over 200 MPa (depending upon grain size) (Figure 4). The effect saturates at a dose of around 1 d.p.a. The strengthening is caused by closely spaced (around 50 nm) small clusters (a few nanometers in diameter) of point defects that increase the lattice resistance to slip. Interestingly, irradiation reduces the grain boundary impediment to slip by about 36%. The origin of this effect is not known. One possible explanation, albeit speculative, is irradiation-induced grain boundary disordering.

5.2 Work Hardening

Once yielding has occurred throughout the material, plastic flow continues uniformly (Schulson and Roy, 1978b), at least initially. At low temperatures the flow stress increases throughout the deformation process, whereas at high temperatures it reaches a maximum and then falls, reaching zero at the highest temperatures. Figure 6 illustrates this behavior. Strain rate has no measurable effect until the temperature reaches around $100^\circ C$, beyond which the flow stress rises upon increasing the rate. Grain refinement increases the flow

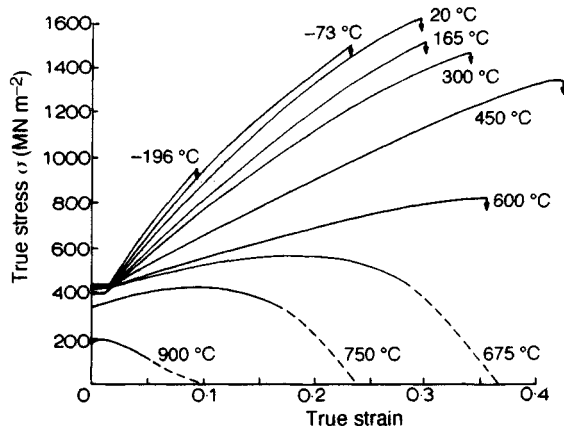


Figure 6. True stress-true strain curves versus temperature for Zr_3Al of $5 \mu m$ grain size strained in tension at $3 \times 10^{-4} s^{-1}$. Note the extensive strain to failure (≤ 0.3) at temperatures from 20 to $600^\circ C$. The alloy contained 8.6 wt% Al (with a residual α -Zr content of $8 \pm 2\%$ by volume)

stress at the lower (500 – $600^\circ C$) temperatures, but does not affect the rate of hardening. At the higher temperatures, grain refinement reduces the flow stress, analogous to its influence on the yield strength at these temperatures. Fast-neutron irradiation increases the flow stress but lowers the hardening rate such that the fracture stresses of material irradiated to 0.14 d.p.a. and unirradiated material are about equal, at least at room temperature.

The room-temperature flow stress of well-annealed material can be expressed in terms of a Hall-Petch-type expression. (Once uniform deformation occurs there is no need to invoke $d^{-0.8}$ functionality.) Accordingly (Schulson and Roy, 1978b)

$$\sigma_f = \sigma_e + k_f d^{-0.5} \quad (4)$$

where σ_e (MPa) = $90 + 500\epsilon$ and $k_f = k_y = 0.76 \text{ MPa m}^{0.5}$. The room-temperature flow stress of the lightly neutron-irradiated material (to 0.14 d.p.a.) obeys a similar relationship (Schulson, 1978a)

$$\sigma_f^\phi = \sigma_e^\phi + k_f^\phi d^{-0.5} \quad (5)$$

where σ_e^ϕ (MPa) = $380 + 2900\epsilon$ and $k_f^\phi = k_y^\phi = 0.49 \text{ MPa m}^{0.5}$. That neither k_f nor k_f^ϕ varies with strain ϵ indicates that the effectiveness with which the grain boundaries impede slip within both the unirradiated and the irradiated material does not change during plastic flow. Therefore, work hardening occurs predominantly through dislocation interactions within the grains.

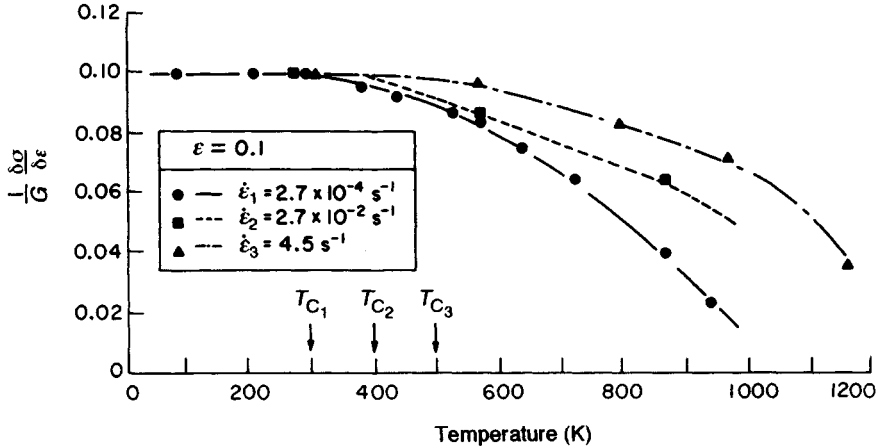


Figure 7. Plots of the work-hardening rate $\partial\sigma/\partial\epsilon$, normalized with respect to the shear modulus G , versus temperature for Zr_3Al strained in tension at three different strain rates. Note the high hardening rate ($G/10$) and the strain rate independent behavior at low temperatures. Note, too, the decrease in hardening rate with increasing temperature at intermediate temperatures, beginning at a temperature T_c which increases with increasing strain rate. The alloy is the same as the one described in Figure 6

The rate of hardening $\partial\sigma/\partial\epsilon$ when normalized with respect to the shear modulus G is essentially independent of temperature below a critical temperature T_c ; at higher temperatures, $(1/G)(\partial\sigma/\partial\epsilon)$ versus T shows negative curvature (Figure 7). T_c increases with increasing strain rate $\dot{\epsilon}$ and obeys the expression (Schulson and Roy, 1978b)

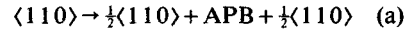
$$T_c = (Q/k)\ln(\dot{\epsilon}_0/\dot{\epsilon}) \quad (6)$$

where Q is an apparent activation energy of 0.6 ± 0.1 eV, k is Boltzmann's constant, and $\dot{\epsilon}_0$ is an experimental constant which is approximately equal to $1.2 \times 10^8 \text{ s}^{-1}$. This behavior indicates that plastic flow becomes thermally activated above T_c , and is attributed to the thermally activated dragging of jogs on dislocations.

The normalized hardening rate is unusually high, i.e. $G/10$. It exceeds by about a factor of two to four that for other f.c.c. polycrystals, including the weakly ordered L_{12} alloys Cu_3Au , Ni_3Mn and Ni_3Fe (see Schulson and Roy, 1978b), but is similar to that for other strongly ordered L_{12} alloys such as Ni_3Al (Weihs *et al.*, 1987), Al_3Sc (Schneibel and George, 1990) and $\text{Al}_3\text{Ti}_2\text{Fe}$ (Zhang *et al.*, 1990). This feature has been attributed to a low multiplicity of slip, which is evident from the observation (Schulson and Roy, 1978b) that many grains within material quite highly strained ($\epsilon = 0.3$) exhibit only a single, planar slip trace (Figure 8), even within the vicinity of grain boundaries.

Why slip is planar, incidentally, can be understood in terms of the dislocation structure. As in other L_{12}

alloys, dislocations in Zr_3Al dissociate into pairs of partial dislocations. Two modes have been observed (Howe *et al.*, 1974; Douin, 1991)



and



where APB and SISF denote a ribbon of antiphase boundary and superlattice intrinsic stacking fault, respectively. Both modes have been seen also on a single dislocation (Douin, 1991), where the mode (a) transformation characterizes the dissociated near-screw segment. Mode (b) is more easily detected, however, because the microstructure of the deformed material contains many SISFs lying on the (111) slip planes. From the viewpoint of slip character the ribbons, and particularly the wider SISFs, confine slip to a plane.

Concerning the work softening at the higher temperatures, dynamic recrystallization followed by grain boundary sliding within the recrystallized zone is important. This is evident from four observations: (i) the higher the temperature, the lower is the strain at which softening begins; (ii) recrystallized grains are seen on the high-temperature fracture surfaces (Schulson, 1978b; discussed below); (iii) recrystallization, at least of cold-rolled strip (Gagné and Schulson, 1976), occurs within the timescale of the deformation tests; and (iv) recrystallization during deformation is nucleated at grain boundaries.

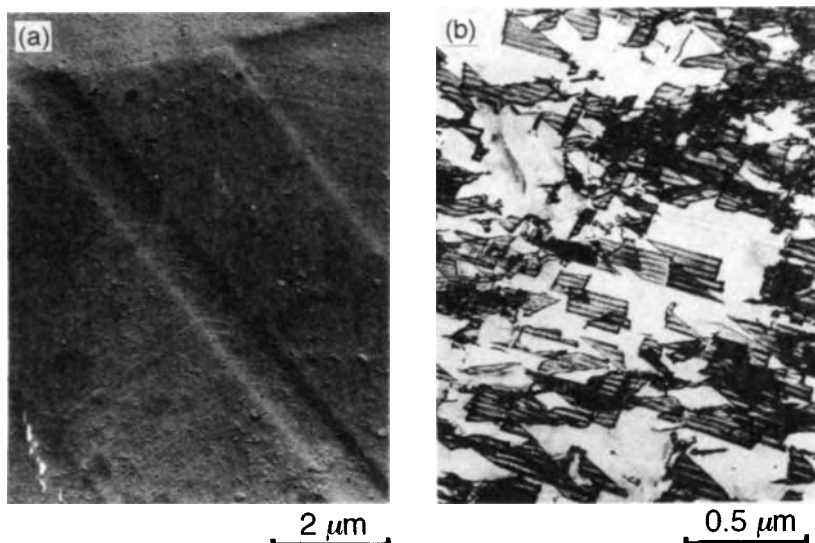


Figure 8. Transmission electron micrographs showing planar slip in Zr_3Al strained in tension at room temperature at $3 \times 10^{-4} \text{ s}^{-1}$: (a) replica; and (b) thin foil showing superlattice intrinsic stacking faults. Note that annealing twins in (a) appear not to impede slip

5.3 Ductility and Fracture

The most striking mechanical characteristic of Zr_3Al is its intrinsic ductility, as shown in Figure 6. Even alloys of commercial purity elongate by 30% or more at room

temperature before breaking. This characteristic depends neither upon grain refinement, microalloying nor macroalloying, and contrasts markedly with the essential brittleness at ambient temperatures of most other polycrystalline aluminides. Instead, it depends

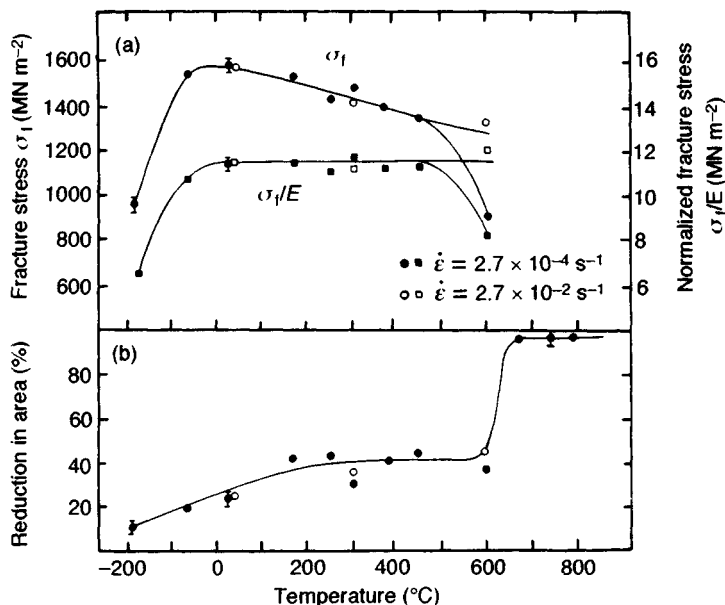


Figure 9. Plots of the fracture stress σ_f , the fracture stress normalized with respect to Young's modulus σ_f/E , and the reduction in area at fracture all versus temperature for Zr_3Al strained in tension at the strain rates noted. The sudden rise in the area reduction at 600–700 °C corresponds to the onset of localized plastic flow. The alloy is the same as the one described in Figure 6

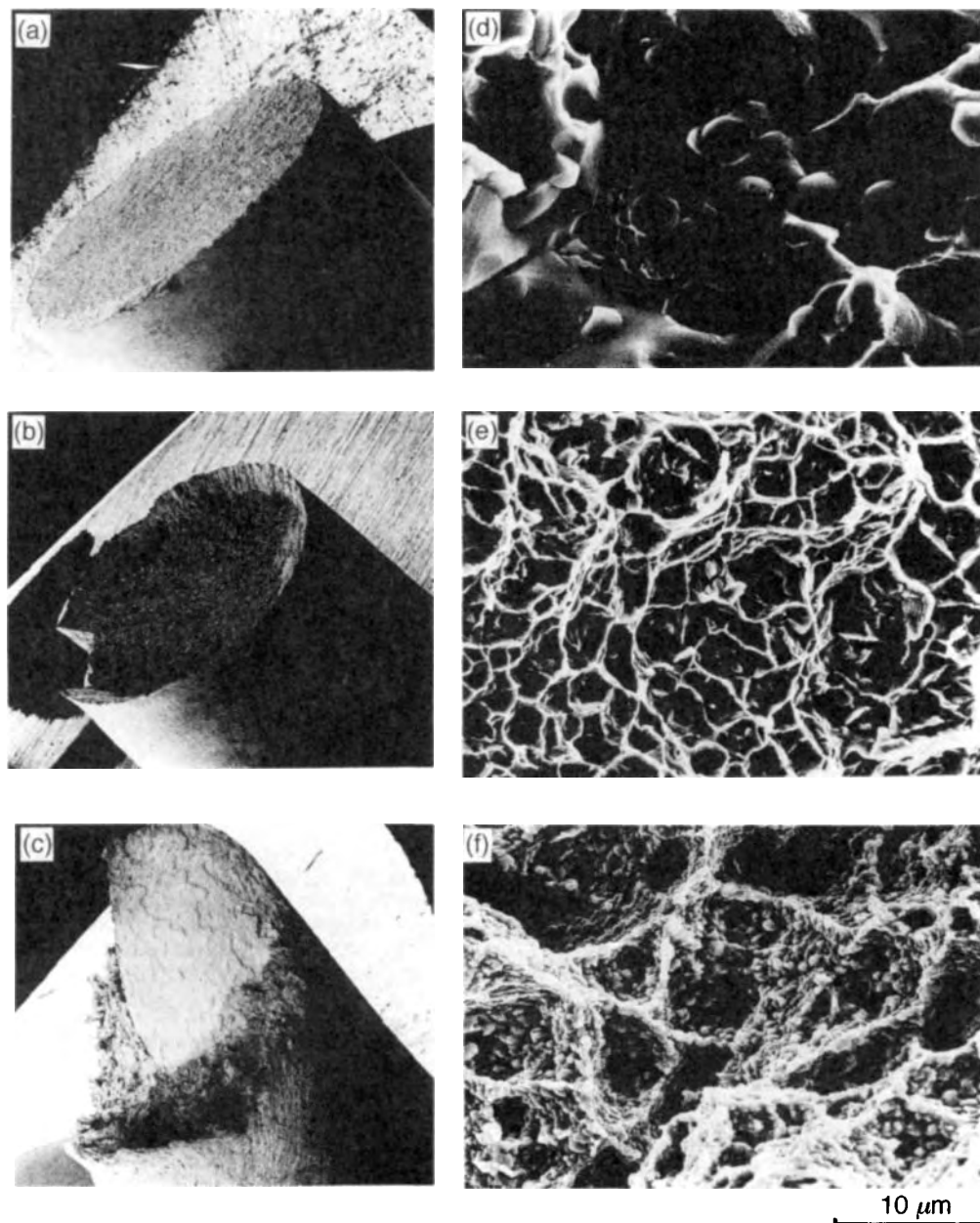


Figure 10. Scanning electron fractographs illustrating the macroscopic (a–c) and the microscopic (d–f) features on the fracture surface of Zr₃Al fractured in tension at $-196\text{ }^{\circ}\text{C}$ (a, d), at room temperature (b, e) and at $750\text{ }^{\circ}\text{C}$ (c, f). Note the intergranular fracture mode and the α -Zr particles on the grain boundary at $-196\text{ }^{\circ}\text{C}$ (d), the ductile transgranular mode at room temperature (e), and the granular mode at $750\text{ }^{\circ}\text{C}$ (f), where the nodules correspond to recrystallized grains. The alloy is the same as the one described in Figure 6

upon the composition of the alloy. Hypostoichiometric (Zr-rich) alloys exhibit the ductility noted, but hyperstoichiometric (Al-rich) alloys are brittle (Schulson, 1974).

Figure 9 shows the fracture stress and the reduction in area versus temperature for a hypostoichiometric alloy containing 8.6% Al (Schulson, 1978b). At temperatures below *ca* 600 °C (for material of 5 μm grain size strained slowly, $2.7 \times 10^{-4} \text{ s}^{-1}$) two thermal regimes exist. From -196°C (and possibly below) to room temperature, the reduction in area increases with increasing temperature; correspondingly, the fracture stress rises to the relatively high level of $11.4 \times 10^{-3} E$, where E is Young's modulus (Table 1). From room temperature to around 600 °C, on the other hand, thermal effects are rather small. The reduction in area rises slowly to about 40% at around 200 °C and then remains constant, while the fracture stress is unchanged up to 450 °C and then decreases. Grain size has no significant effect either on the ductility or on the fracture stress over the range (1 to 60 μm) investigated.

Necking is not observed below *ca* 300 °C, and even up to 600 °C is slight. At higher temperatures, on the other hand, necking becomes pronounced and reductions in area exceed 90%. The tensile elongations, however, decrease sharply, from 45% at 600 °C to around 10% at 900 °C.

Clearly, a change occurs in the nature of fracture between -196°C and room temperature, and another change occurs between 600 and 670 °C, at least for relatively finely grained material strained slowly. The first transition corresponds to a change in fracture mode from intergranular at -196°C to ductile transgranular at room temperature; the second, to a change from ductile transgranular fracture to sliding along the freshly created boundaries of grains dynamically recrystallized within the vicinity of prior grain boundaries. Figure 10 illustrates these points. While unusual, fracture following dynamic recrystallization at high temperatures has also been observed in two other polycrystalline L1_2 alloys, namely $(\text{Fe}_{0.22}\text{Co}_{0.78})_3\text{V}$ (Liu and Schulson, 1984) and Ni_3Al (Baker *et al.*, 1984).

The origin of the grain boundary separation remains to be elucidated. The picture is more complete for the transgranular failure. In this case microcracks nucleate at second-phase Zr_2Al particles, through both particle cleavage and particle/matrix decohesion (Figure 11). The number density of the cracks increases with strain, implying that they form more or less continuously during plastic flow. The rate of crack formation decreases with increasing temperature, not because the particles become more plastic but probably

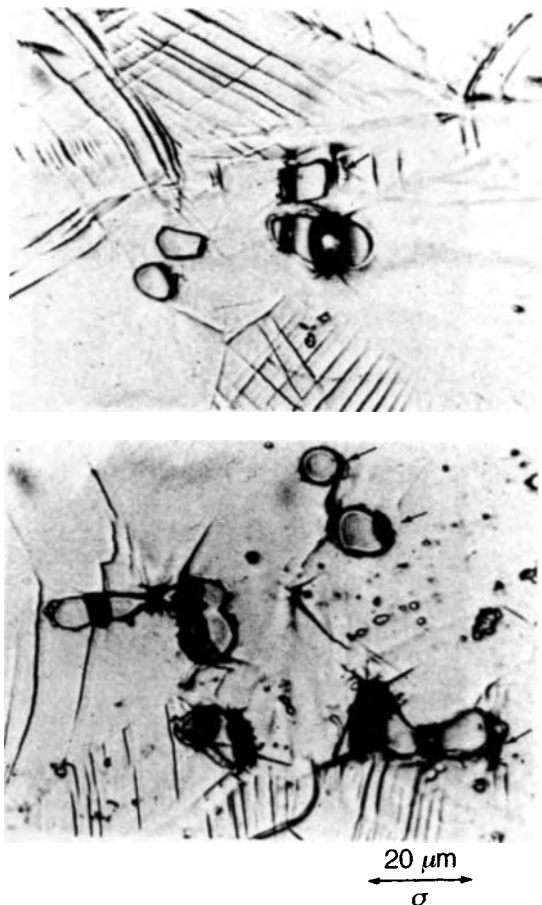


Figure 11. Optical micrographs showing cracked particles of residual Zr_2Al and cracks (arrowed) at the particle/matrix interface. The matrix is Zr_3Al and the short lines (dark) in the matrix are slip lines. The direction of tensile loading is noted. The alloy is the same as the one described in Figure 6

because the work-hardening rate of the matrix decreases, as already noted. Once formed, the cracks widen but do not lengthen. They are thus stable defects and are blunted by plastic flow. Eventually, the bridges of metal between the cracks become overstressed and failure occurs through plastic shearing. In other words, fracture occurs through a plastic instability which develops when the work-hardening rate can no longer compensate for the reduction in load-bearing area, i.e. when $\partial\sigma/\partial\epsilon = \sigma$, as observed by Schulson and Roy (1978b). Strain rate hardening becomes important above *ca* 300 °C and stabilizes a small neck, as already noted.

In considering why Zr_3Al is so ductile at low temperatures, note several points. The operation of five

independent {111}K110 slip systems certainly helps, but this factor alone is not sufficient. Five systems are available in many other L1₂ intermetallics as well (Ni₃Al, Ni₃Ga, Ni₃Si, and Ni₃Ge), yet polycrystals of these alloys are brittle. Similarly, the relatively fine grain size of the materials tested is probably not by itself the answer, for equally finely grained aggregates of the above Ni-based intermetallics are brittle (Weihs *et al.*, 1987; Xu and Schulson, 1994; Schulson *et al.*, 1990; Fang and Schulson, 1992). Nor can the ductility be attributed to the absence of impurities, for as already noted many of the test specimens were made from commercial purity elements, which were almost certainly contaminated. One possible explanation relates to the structure of the grain boundaries, particularly to the ease with which dislocations are generated and/or accommodated within the boundary region. Perhaps the grain boundaries of the ductile alloys are disordered, thereby allowing dislocations to be nucleated and slip to be accommodated/transmitted more easily than otherwise. While no evidence exists to support this hypothesis, the fact that ductility characterizes alloys only on the Zr-rich side of stoichiometry (i.e. alloys which are in equilibrium with a disordered Zr(Al) solid solution) is at least consistent with the idea. The notion is also consistent with the hypothesis (Baker and Schulson, 1989) that at least partial grain boundary disorder may be a requirement for extensive tensile ductility in intermetallic compounds.

5.4 Notch Sensitivity

All of the mechanical properties considered above were obtained from material having 'good' electrochemically polished surfaces. When the surface is not good, i.e. freshly machined or abraded, pronounced differences are observed. For instance, damage caused by turning in a lathe reduces both the room-temperature fracture stress to just above the yield strength and the elongation to 1.5%; correspondingly, the fracture mode changes from ductile transgranular to brittle intergranular (Schulson and Roy, 1977b). Even circumferential abrasion with 180 grade SiC paper reduces the elongation to 15%. Zr₃Al, in other words, is notch sensitive.

Another indication of this sensitivity is the notch strength ratio (NSR). This is defined as the net tensile strength for notched specimens divided by the ultimate tensile strength of unnotched specimens. At room temperature NSR \approx 0.7 and is independent of grain size, at least over 3.5–41 μ m. It is also independent of the concentration (at the p.p.m. level) of the ternary

element, boron (Schulson and Roy, 1977b). At temperatures above 300 °C, however, the notch sensitivity is reduced and the NSR reaches 0.9.

Curiously, irradiation to low doses suppresses the phenomenon (Schulson and Roy, 1977b). For instance, upon fast-neutron ($E > 1$ MeV) irradiation at 300 °C to 0.14 d.p.a., the NSR at room temperature increases to 1.07; correspondingly, the fracture mode changes from brittle intergranular to ductile transgranular. The dimple depth, however, is less than that for the well-annealed state, in keeping with the attendant reduction of the work-hardening rate already noted. Zr₃Al, incidentally, appears not to be the only intermetallic for which a little radiation is a good thing: Ni₃Al also appears to experience a change in fracture mode (at least near its surface) from brittle intergranular to ductile transgranular upon irradiation with energetic protons (Cheng *et al.*, 1989).

The cause of notch sensitivity is not known, nor is the cause of the unusual, but beneficial, effect of irradiation. One possibility relates to the high work-hardening rate (Schulson, 1991) and to its reduction upon raising the temperature and upon irradiation, as already noted. It may be fortuitous, but both the NSR and $\partial\sigma/\partial\epsilon$ become thermally sensitive around the same temperature and change in proportion to each other. Similarly, the change in the NSR upon irradiation is similar to the change in $\partial\sigma/\partial\epsilon$. The physical explanation may be that materials of high work-hardening rate are intolerant of notches because near the notch tip the plastic strain locally hardens the material to above the fracture stress before the material deforms far from the notch. The other factor, and possibly a dominant one, is the environment (Liu, 1991). The tensile ductility of many strongly ordered intermetallics, for instance, is adversely affected by water vapor (Liu, 1992), and this effect could be important in Zr₃Al as well. Whatever the origin, notch sensitivity is a phenomenon to be kept clearly in mind when considering Zr₃Al for any application.

5.5 Fracture Toughness

Owing to its notch sensitivity one might expect Zr₃Al to possess little toughness. In fact, the opposite appears to be true. At room temperature the fracture toughness K_{Ic} for alloys containing 8.6 wt% Al is reported (Rosinger and Wilkins, 1980) to be around 50 MPa m^{0.5}. At higher temperatures K_{Ic} is higher (Rosinger and Wilkins, 1980), rising roughly linearly with temperature to around 85 MPa m^{0.5} at 400 °C. The toughness G_c therefore appears to be significant, rising from about

$2 \times 10^4 \text{ J m}^{-2}$ at room temperature to over $6 \times 10^4 \text{ J m}^{-2}$ at 400°C (as estimated from $G_c = K_{Ic}^2/E$). Why, then, the alloy is notch sensitive is a mystery. Perhaps, as already noted, the environment plays a role. While this possibility remains to be tested, it is nevertheless consistent with the relatively high toughness, for the deformation at the tips of cracks in fracture toughness specimens may have occurred too quickly for the environment to influence the behavior. That high-rate loading can suppress environmental embrittlement, at least of an iron aluminide (FeAl), has been observed (Nagpal, 1992).

6. Comparison with Zircaloy-2 and Zr-2.5% Nb

Table 2 compares Zr_3Al with two commercial Zr-based alloys. The intermetallic appears to be superior on several fronts. Its resistance to in-flux stress relaxation and, by implication, to irradiation creep appears to be greater; its short-term tensile strength and uniform elongation to failure, both before and after moderate irradiation, are greater; and it exhibits greater resistance to the formation of brittle zirconium hydride. Its oxidation resistance in pressurized water is similar to that of Zircaloy-2, provided that the volume fraction of second phase $\alpha\text{-Zr(Al)}$ solid solution is $<1\%$. Zr_3Al

is inferior, however, with respect to the reduction in area at fracture and to notch sensitivity. More importantly, it appears to become embrittled under fast-neutron irradiation to $>1 \text{ d.p.a.}$ at 325°C .

This last point is a particularly serious one: if true, it would mean that Zr_3Al has no potential at all for service in thermal nuclear power reactors operating at temperatures around 325°C . The point is questioned, however, because the test specimens (Rosinger and Wilkins, 1980) upon which the observation is based were immersed in an organic coolant and were corroded during the exposure. The question is whether the corrosion affected the mechanical behavior. While this would not be an issue for Zr_3Al *per se*, it is in this case because the specimens were of hypostoichiometric composition and contained only $80 \pm 7\%$ (by volume) Zr_3Al ; the remainder consisted of $6 \pm 6\%$ Zr_2Al and $13 \pm 6\%$ $\alpha\text{-Zr}$. The last constituent is important, because $\alpha\text{-Zr}$ contains in solution $1\text{--}2 \text{ wt}\%$ Al which has an extremely detrimental effect on the corrosion resistance of this phase. It is possible, therefore, that within localized regions of the microstructure where the vol% of $\alpha\text{-Zr}$ was the highest (i.e. $13\% + 6\% = 19\%$), this easily corrodible phase was nearly interconnected. If so, preferential corrosion may have occurred and contributed to the embrittlement. Until this possibility is ruled out, it is premature to conclude that the

Table 2. Some engineering properties of zirconium alloys^a

Engineering property	Zr_3Al	Zr-2.5% Nb (CW 20%)	Zircaloy-2 (CW 20%)
In-reactor strain rate ^b ($\times 10^7 \text{ h}^{-1}$)	1.4	2.8	3.5
Unirradiated tensile strength at 300°C (MPa)	1050	559	364
Irradiated tensile strength at 300°C ^c (MPa)	850–950	772	446
Unirradiated tensile elongation at 300°C (%)	30–40	6	26
Irradiated tensile elongation at 300°C ^c (%)	≥ 13	4.5	4
Unirradiated reduction in area at 300°C (%)	23–28	50	60
Irradiated reduction in area at 300°C ^c (%)	≥ 12	22	30–40
Unirradiated notch strength ratio at 20°C	0.6–0.7	1.5	~ 1.7
Irradiated notch strength ratio at 20°C ^c	1.0–1.1	—	—
Fracture toughness K_{Ic} at 300°C (MPa $\text{m}^{0.5}$)	80 ^d	—	—
Oxidation rate in pressurized water (300°C ; 8.3 MPa) ($\text{mg dm}^{-2} \text{ d}^{-1}$)	≈ 0.02 ^e	—	0.05
Specific thermal neutron absorption capture cross section ($\text{m}^2 \text{ m}^{-3}$)	0.96	0.91	0.87

^aThe mechanical properties for Zircaloy-2 and Zr-2.5% Nb are for the longitudinal direction in cold-worked (CW) pressure tubing. Those for Zr_3Al are for hot-rolled plate (Zr-8.6 wt% Al) which was transformed to Zr_3Al after rolling by annealing at 888°C for 8 h.

^bDeduced from bent-beam stress-relaxation and irradiation-growth experiments at 300°C in a fast-neutron flux of $2 \times 10^{17} \text{ n m}^{-2} \text{ s}^{-1}$ (Causey *et al.*, 1977); given for an applied tensile stress of 100 MPa.

^cAt a fast-neutron fluence of $ca 3 \times 10^{24} \text{ n m}^{-2}$ (Causey *et al.*, 1977; Rosinger, 1977).

^dFor material containing by volume $13 \pm 6\%$ $\alpha\text{-Zr}$ and $6 \pm 6\%$ Zr_2Al (Rosinger and Wilkins, 1980).

^eFor material containing $<1\%$ of second-phase $\alpha\text{-Zr}$. For an $\alpha\text{-Zr}$ content between 6 and 10% the oxidation rate increases by about an order of magnitude (Schulson and Trotter, 1980a).

embrittlement noted (Rosinger and Wilkins, 1980) is the result of radiation damage *per se*.

Finally, returning to long-term deformation, the thermal (i.e. nonirradiation) creep rate of Zr₃Al at 300 °C is lower by a factor of two or three than that of Zircaloy-2 and Zr-2.5% Nb; at higher temperatures (400–500 °C) it is lower by a factor of 10 or more (Schulson and Cameron, 1978). And, as inferred from the in-reactor stress-relaxation experiments, the irradiation creep rate of Zr₃Al is also lower. Direct tests in flux, however, remain to be done.

7. Status

In conclusion, Zr₃Al is a novel intermetallic awaiting further irradiations and testing before a considered judgment can be made on its potential utility as a nuclear alloy. The material is currently not an active topic of research, however, owing in part to the present status of the nuclear industry. As an engineering material for other purposes, Zr₃Al may have potential for use in tools and dies and other things, but these possibilities remain to be explored.

8. Acknowledgements

The author would like to acknowledge L. M. Howe and A. R. Causey, both of Atomic Energy of Canada Ltd, Chalk River, Ontario, for helpful discussions. This chapter was written with support from the US Department of Energy, grant number DE-FG02-86ER45260.

9. References

- Baker, I., and Schulson, E. M. (1989). *Scripta Metall.*, **23**, 345–348.
- Baker, I., Viens, D. V., and Schulson, E. M. (1984). *Scripta Metall.*, **18**, 237–240.
- Cameron, D. J., Murphy, E. V., Rosinger, H. E., and Wilkins, B. J. S. (1976). Unpublished report, Atomic Energy of Canada Ltd, WNRE-297-1.
- Carpenter, G. J. C., and Schulson, E. J. (1978). *J. Nucl. Mater.*, **23**, 180–189.
- Causey, A. R., Fidleris, V., Rosinger, H. E., Schulson, E. M., and Urbanic, V. F. (1977). ASTM-STP 633, 437–454.
- Chen, F. C., Ardell, A. J., and Pedraza, D. F. (1991). *Mater. Res. Soc. Symp. Proc.*, **213**, 763–768.
- Cheng, J., Lee, C.-S., Wagner, N. J., and Ardell, A. J. (1989). *Mater. Res. Soc. Symp. Proc.*, **133**, 499–504.
- Douin, J. (1991). *Philos. Mag. Lett.*, **63**, 109–116.
- Fang, J., and Schulson, E. M. (1992). *Mater. Sci. Eng. A*, **152**, 138–145.
- Gagné, M., and Schulson, E. M. (1976). *Metall. Trans.*, **7A**, 1175–1178.
- Gialanella, S., Yavari, A. R., and Cahn, R. W. (1992). *Scripta Metall.*, **26**, 1233–1238.
- Hirsch, P. B. (1992). *Philos. Mag. A*, **65**, 569–612.
- Howe, L. M., and Rainville, M. (1977). *J. Nucl. Mater.*, **68**, 215–234.
- Howe, L. M., and Rainville, M. (1979). *Philos. Mag.*, **39**, 195–212.
- Howe, L. M., and Rainville, M. (1991). *Mater. Res. Soc. Symp. Proc.*, **201**, 215–220.
- Howe, L. M., Rainville, M., and Schulson, E. M. (1974). *J. Nucl. Mater.*, **50**, 139–154.
- Hume-Rothery, W. (1931). *The Metallic State*, Oxford University Press, Oxford, p. 57.
- Huntington, H. B. (1958). Personal communication to L. Slifkin. Reported by Elcock, E. W., and McCombie, C. W. (1958). *Phys. Rev.*, **109**, 605–606.
- Kear, B. H., and Wilsdorf, H. G. (1962). *Trans. Metall. Soc. AIME*, **224**, 382–386.
- Keeler, J. H., and Mallery, J. H. (1955). *Trans. Metall. Soc. AIME*, **203**, 394.
- Lee, J.-Y., Choi, W.-C., Kim, Y.-G., and Lee, J.-Y. (1991). *Acta Metall. Mater.*, **39**, 1693–1701.
- Li, H., Chen, F. C., and Ardell, A. J. (1991). *Metall. Trans.*, **22A**, 2061–2068.
- Liu, C. T. (1991). Personal communication.
- Liu, C. T. (1992). In *Ordered Intermetallics—Physical Metallurgy and Mechanical Behavior*, Vol. 213 (eds C. T. Liu, R. W. Cahn, and G. Sauthoff). NATO ASI Series E: Applied Sciences. Kluwer Academic, Boston, pp. 321–334.
- Liu, C. T., and Schulson, E. M. (1984). *Metall. Trans.*, **15A**, 701–706.
- McPherson, D. J., and Hansen, M. (1954). *Trans. ASM*, **46**, 354–374.
- Meng, W. J., Okamoto, P. R., Thompson, L. J., Kestel, B. J., and Rehn, L. E. (1988). *Appl. Phys. Lett.*, **53**, 1820–1822.
- Murphy, E. V. (1975). *J. Nucl. Mater.*, **55**, 117–118.
- Nagpal, P. (1992). PhD thesis, Dartmouth College.
- Okamoto, P. R., Rehn, L. E., Pearson, J., Bhadra, R., and Grimsditch, M. (1988). *J. Less-Common Met.*, **140**, 231–244.
- Paidar, V., Pope, D. P., and Vitek, V. (1984). *Acta Metall.*, **32**, 435–448.
- Rehn, L. E., Okamoto, P. R., Pearson, J., Bhadra, R., and Grimsditch, M. (1987). *Phys. Rev. Lett.*, **59**, 2987–2990.
- Rosinger, H. E. (1977). *J. Nucl. Mater.*, **66**, 192–196.
- Rosinger, H. E. (1980). *J. Nucl. Mater.*, **95**, 171–180.

- Rosinger, H. E., and Wilkins, B. J. S. (1980). *J. Nucl. Mater.*, **89**, 347–353.
- Schneibel, J. H., and George, E. P. (1990). *Scripta Metall.*, **24**, 1069–1074.
- Schulson, E. M. (1972). Unpublished report, Atomic Energy of Canada Ltd, CRNL-786.
- Schulson, E. M. (1974). *J. Nucl. Mater.*, **50**, 127–138.
- Schulson, E. M. (1975). *J. Nucl. Mater.*, **56**, 38–46.
- Schulson, E. M. (1977). *J. Nucl. Mater.*, **66**, 322–324.
- Schulson, E. M. (1978a). *Acta Metall.*, **26**, 1189–1198.
- Schulson, E. M. (1978b). *Metall. Trans.*, **9A**, 527–538.
- Schulson, E. M. (1979). *J. Nucl. Mater.*, **83**, 239–364.
- Schulson, E. M. (1980a). *Rev. High-Temp. Mater.*, **IV**(3), 195–257.
- Schulson, E. M. (1980b). *Metall. Trans.*, **11A**, 1918–1920.
- Schulson, E. M. (1984). *Int. Met. Rev.*, **29**, 195–209.
- Schulson, E. M. (1989). *J. Mater. Res.*, **4**, 470–472.
- Schulson, E. M. (1991). Unpublished proposal to US Department of Energy.
- Schulson, E. M., and Cameron, D. J. (1978). *US Pat.*, 4 094 706.
- Schulson, E. M., and Davidson, R. D. (1977). *Metall. Trans.*, **8A**, 2019–2021.
- Schulson, E. M., and Graham, D. B. (1976). *Acta Metall.*, **24**, 615–625.
- Schulson, E. M., and Roy, J. A. (1977a). *Metall. Trans.*, **8A**, 377–378.
- Schulson, E. M., and Roy, J. A. (1977b). *J. Nucl. Mater.*, **71**, 124–133.
- Schulson, E. M., and Roy, J. A. (1978a). *Acta Metall.*, **26**, 29–38.
- Schulson, E. M., and Roy, J. A. (1978b). *Acta Metall.*, **26**, 15–28.
- Schulson, E. M., and Stewart, M. J. (1976). *Metall. Trans.*, **7B**, 363–368.
- Schulson, E. M., and Trottier, T. P. (1980a). *Metall. Trans.*, **11A**, 727–738.
- Schulson, E. M., and Trottier, T. P. (1980b). *Metall. Trans.*, **11A**, 1459–1464.
- Schulson, E. M., and Turner, R. B. (1978). *Phys. Stat. Sol.*, **50**, 83–86.
- Schulson, E. M., Swanson, M. L., and MacEwen, S. R. (1978). *Philos. Mag. A*, **37**, 575–589.
- Schulson, E. M., Weihs, T. P., Viens, D. V., and Baker, I. (1985). *Acta Metall.*, **33**, 1587–1591.
- Schulson, E. M., Briggs, L. J., and Baker, I. (1990). *Acta Metall. Mater.*, **38**, 207–213.
- Sun, Y. Q., and Hazzledine, P. M. (1992). In *Ordered Intermetallics—Physical Metallurgy and Mechanical Behavior*, Vol. 213 (eds C. T. Liu, R. W. Cahn, and G. Sauthoff). NATO ASI Series E: Applied Sciences. Kluwer Academic, Boston, pp. 177–196.
- Takeyama, M., and Liu, C. T. (1988). *J. Mater. Res.*, **3**, 665–674.
- Turner, R. B., Wolgemuth, G. A., and Schulson, E. M. (1978). *J. Nucl. Mater.*, **74**, 363–364.
- Weihs, T. P., Zinoviev, V., Viens, D. V., and Schulson, E. M. (1987). *Acta Metall.*, **35**, 1109–1118.
- Xu, Y., and Schulson, E. M. (1994). Unpublished
- Zhang, S. J., Nic, P., Milligan, W. W., and Mikkola, D. E. (1990). *Scripta Metall.*, **24**, 1099–1104.

This chapter was originally published in 1995 as Chapter 6 in *Intermetallic Compounds*, Vol. 2: *Practice*, edited by J. H. Westbrook and R. L. Fleischer.

Chapter 7

Al₃Ti and its L1₂ Variations

Masaharu Yamaguchi and Haruyuki Inui

Department of Metal Science and Technology, Kyoto University, Sakyo-ku, Kyoto 606-8501, Japan

1. Introduction

Al₃X-type compounds of aluminum with transition metals of Groups IV and V are of interest in the development of new, high-temperature, lightweight structural materials. The reasons are as follows:

- (i) They crystallize into a tetragonal structure of the D₀₂₂ (tI8) type or the D₀₂₃ (tI16) type (Villars and Calvert, 1985; Massalski *et al.*, 1986), which is not too complicated for the occurrence of some plasticity.
- (ii) Aluminum atoms constitute as much as 75% of the compounds. Thus, they have, in general, low densities and good oxidation resistance. The density of Al₃Ti is 3.4 Mg m⁻³, which is the lowest of this class of trialuminides. Nevertheless, they have high elastic moduli and, consistent with this, high melting points.

The first report of the deformation behavior of this class of trialuminides appeared in 1974. It was on Al₃Nb by Shechtman and Jacobson (1975). Later, Yamaguchi *et al.*, (1987) reported on the stress-strain behavior and deformation modes in Al₃Ti. These two early studies revealed that Al₃Nb and Al₃Ti were brittle at ambient temperature. However, at the same time, the two studies showed that a specific twinning, which does not disturb the D₀₂₂ order, played an important role in the deformation of the two compounds and, in particular, that Al₃Ti was deformable, at least to such an extent that much additional work has been stimulated in the area of improving the low-temperature ductility of the compound since then.

The following two approaches have been attempted to improve the ductility of Al₃Ti by alloying: (i) alloying

to enhance the deformation modes of Al₃Ti with the D₀₂₂ structure (microalloying approach), and (ii) alloying to change the crystal structure to the higher symmetry L1₂ (cP4) structure in the hope that the increased number of independent slip systems in the cubic structure will encourage plastic deformation (macroalloying approach). The microalloying of Al₃Ti (D₀₂₂) with some ternary elements has been found to enable the D₀₂₂ Al₃Ti to be somewhat more deformable. However, no substantial improvement in the ductility of D₀₂₂ Al₃Ti has yet been made. In contrast, the macroalloying approach has been producing more promising results. A series of ternary cubic L1₂ trialuminides based on Al₃Ti has been shown to be formed by alloying with fourth-period elements ranging from Cr to Zn, and some fifth- and sixth-period elements. Among these cubic forms, Zhang *et al.* (1990a) have shown that the cubic compounds with Cr and Mn additions have a slight ductility when tested in bending. However, the cubic Al₃Ti compounds are, in general, still quite brittle from an engineering point of view. Their brittleness at ambient temperature must be overcome first for structural applications to be possible. Yield stresses of the cubic Al₃Ti compounds are, however, not as high as would be expected from their brittleness. They are relatively soft materials in this sense. This unusual phenomenon, brittleness in relatively soft materials, is another problem to be solved.

In this chapter, the physical metallurgy and mechanical properties of Al₃Ti in the D₀₂₂ form and the L1₂ variations of Al₃Ti are reviewed with particular emphasis on their deformation modes and dislocation structures, the effect of alloying on their mechanical properties, their oxidation properties and their

application potential. In addition to this, relevant studies on Al_3Zr , Al_3V and Al_3Nb , which are akin to Al_3Ti , are briefly reviewed. The reader is also referred to the review by Yamaguchi *et al.* (1988) for the deformation of Al_3Ti , the review by Yamaguchi and Umakoshi (1990) for the deformation of intermetallic superlattice compounds, the review by George *et al.* (1991) for the deformation and fracture of L_{12} trialuminides, the review by Mikkola *et al.* (1991) for alloying of Al_3Ti to form cubic phases and the review by Morris (1992d) for antiphase boundary (APB) faults in some L_{12} variations of Al_3Ti .

2. Al_3Ti with the D0_{22} Structure

2.1 Crystal Structure

The D0_{22} (tI8) structure is derived from the L_{12} (cP4) structure (Figure 1a) by introducing an antiphase boundary (APB) with a displacement vector of $\frac{1}{2}\langle 110 \rangle$ on every (001) plane (Figure 1b). Al_3Ti crystallizes into this L_{12} -derivative, long-period superlattice structure. The D0_{23} (tI16) structure is formed by introducing the APB on every second (001) plane (Figure 1c). Al_3Zr and Al_3Hf (at low temperatures), which are akin to Al_3Ti , possess this structure. The lattice parameters of Al_3Ti are $a = 0.3848 \text{ nm}$ and $c = 0.8596 \text{ nm}$ ($c/a = 2.23$) (Villars and Calvert, 1985). The density of

Al_3Ti calculated from these lattice parameters is 3.36 Mg m^{-3} .

2.2 Elastic Constants

The elastic constants of Al_3Ti are given in Table 1. The elastic stiffness constants C_{ij} were obtained through measurements of ultrasonic sound wave velocity in single crystals of the compound (Nakamura and Kimura, 1991). Values of Young's modulus (E), shear modulus (G), bulk modulus (K) and Poisson's ratio (ν) for the polycrystalline form of the compound were calculated from the stiffness constants. For comparison with these values, the corresponding elastic constants of Al_3Ti calculated using a first-principles approach, the full-potential linearized augmented plane-wave method (Fu, 1990; Yoo and Fu, 1991), and those of the constituent elements, Al and Ti (Nadgornyi, 1988; Smithells, 1976), are also listed in the table. The calculated values of elastic constants are in reasonably good agreement with experimental values.

Both experimental and theoretical values of E and G for Al_3Ti are approximately three and a half times those for pure aluminum and about two and a half times those of pure titanium, even though its primary constituent is aluminum and hence the density of Al_3Ti is only 24% higher than that of pure aluminum. Thus, the specific Young's and shear moduli of Al_3Ti are much larger than those of the constituent elements. Al_3Ti is consequently a material with an excellent strength to weight ratio. The elastic stiffness constants of Al_3Zr , which is another example of a compound with an L_{12} -derivative, long-period structure, have also been measured (Nakamura and Kimura, 1991), and the values of E and G of the compound have also been found to be much higher than the corresponding values of aluminum. Thus, this seems to be characteristic of this class of trialuminides. The first-principles calculation indicates that this stiffening is caused by the strong hybridization between the aluminum p electrons and the transition metal d electrons (Fu, 1990). In contrast, the bulk modulus of Al_3Ti is only 44% higher than that of pure aluminum. This is also the case for Al_3Nb (Nakamura and Kimura, 1991). Thus, these trialuminides, in general, have smaller K/G ratios, which correlates with the tendency toward brittleness for the trialuminides (Pugh, 1954) since a high value of G implies a high critical stress for dislocation generation at the crack tip, and a low value of K is associated with easy crack opening.

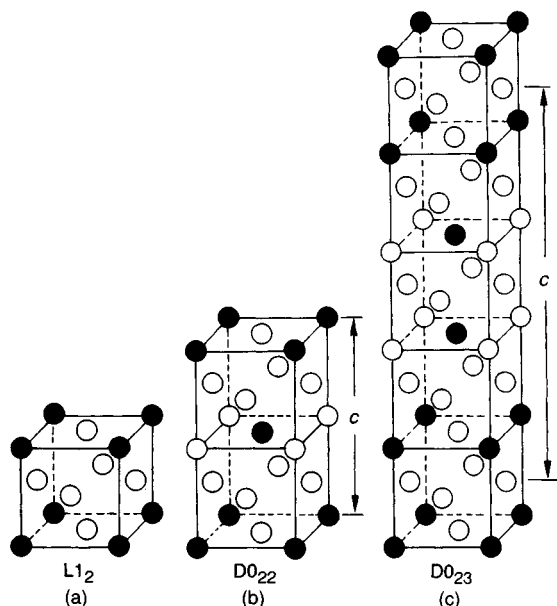


Figure 1. The L_{12} , D0_{22} and D0_{23} structures

Table 1. The elastic stiffness and elastic constants of Al₃Ti and its constituent elements in units of 10² GPa

	C_{11}	C_{33}	C_{44}	C_{66}	C_{12}	C_{13}	Bulk modulus K	Young's modulus E	Shear modulus G	Poisson's ratio ν	E/ρ^e	G/ρ^e
Al ₃ Ti ^a	2.177	2.175	0.920	1.165	0.577	0.455	1.056	2.157	0.930	0.160	0.63	0.27
Al ₃ Ti ^b	2.02	2.43	1.45	1.00	0.88	0.60	1.22	2.30	0.97	0.19	0.68	0.29
Al ^{c,d}	1.082	C_{11}	0.285	C_{44}	0.613	C_{12}	0.752	0.706	0.262	0.345	0.26	0.10
Ti ^{c,d}	1.624	1.807	0.467	C_{44}	0.920	0.690	1.084	1.202	0.456	0.361	0.27	0.10

^aExperimentally measured by Nakamura and Kimura (1991).^bTheoretically calculated by Fu (1990).^cFrom Table IV in Nakamura and Kimura (1991).^dSmithells (1976).^e ρ is the density at room temperature. E/ρ and G/ρ are given in units of 10² GPa Mg⁻¹ m³.

2.3 Possible Planar Faults and Dislocation Burgers Vectors

The atomic arrangement on (111)* in an A₃B compound with the D0₂₂ structure is shown in Figure 2. The periodic introduction of APB into the L1₂ structure transforms the triangular arrangement of B atoms on (111) in the L1₂ structure into a rectangular arrangement. On the basis of a hard-sphere model and geometrical considerations, five possible planar faults may be considered on {111}. These are APB-I, APB-II, CSF-I, CSF-II and SISF, where CSF and SISF are the complex stacking fault and superlattice intrinsic stacking fault, respectively. In the case of the (111) plane, the displacement vectors characterizing these faults are, for example, \mathbf{b}_{A1} for APB-I, \mathbf{b}_{A2} for APB-II, \mathbf{b}_{C1} for CSF-I, \mathbf{b}_{C2} for CSF-II and \mathbf{b}_S for SISF. Assuming $c/a = 2$ and considering first- and second-nearest neighbor interactions only, the energies of these faults are given as follows (Yamaguchi and Umakoshi, 1990)

$$E_{\text{APB-I}} = \frac{2V^{(1)} - 2V^{(2)}}{a^2\sqrt{3}} \quad (1)$$

$$E_{\text{APB-II}} = \frac{2V^{(1)} - 4V^{(2)}}{a^2\sqrt{3}} \quad (2)$$

$$E_{\text{CSF-I}} = E_{\text{APB-I}} + \frac{4[\Phi_{AA}(r') + \Phi_{AB}(r')]}{a^2\sqrt{3}} \quad (3)$$

$$E_{\text{CSF-II}} = E_{\text{APB-II}} + \frac{4[\Phi_{AA}(r') + \Phi_{AB}(r')]}{a^2\sqrt{3}} \quad (4)$$

$$E_{\text{SISF}} = \frac{2[3\Phi_{AA}(r') + \Phi_{BB}(r')]}{a^2\sqrt{3}} \quad (5)$$

where the $V^{(k)}$ are the k th-neighbor ordering energies given as $V^{(k)} = (\phi_{AA}^{(k)} + \phi_{BB}^{(k)} - 2\phi_{AB}^{(k)})/2$ and the $\phi_{ij}^{(k)}$ are the pairwise interaction energies between the k th-neighbor atoms i and j . $\phi_{ij}(r')$ is the interaction energy at the separation $r' = (2/\sqrt{3})a$. The SISF, which involves no first- and second-nearest neighbor wrong bonds, is expected to have generally a much lower energy than the other possible faults on {111} such as APB and CSF. The displacement vector \mathbf{b}_{A1} forms an APB also on (001) without creating first-nearest neighbor wrong bonds. Its energy is

$$E_{\text{APB-I}}^{(001)} = \frac{2V^{(2)}}{a^2} \quad (6)$$

For the D0₂₂ structure to be stable with respect to both the D0₂₃ and L1₂ structures, $E_{\text{APB-I}}^{(001)} > 0$ and hence $V^{(2)} > 0$. The energies of the five possible faults on {111} are thus generally expected to be in the following decreasing order

$$E_{\text{CSF-I}} > E_{\text{CSF-II}} > E_{\text{APB-I}} > E_{\text{APB-II}} > E_{\text{SISF}} \quad (7)$$

APB-I on (001) has a smaller energy than CSF-I, CSF-II, APB-I and APB-II on {111}. However, which of the two faults APB-I on (001) and SISF on {111} has the lower energy may not be judged on the basis of a hard-sphere model and geometrical considerations of wrong bonds. The APB-I on (001) is always stable for obvious symmetry reasons, while the stability of the faults on

*Miller indices for planes and directions in the tetragonal D0₂₂ structure are given using f.c.c. notations for simplicity. The mixed notations $\{hkl\}$ and $\langle hkl \rangle$ are used to differentiate the first two indices from the third index which does not play the same role as the first two because of the tetragonality of the D0₂₂ structure.

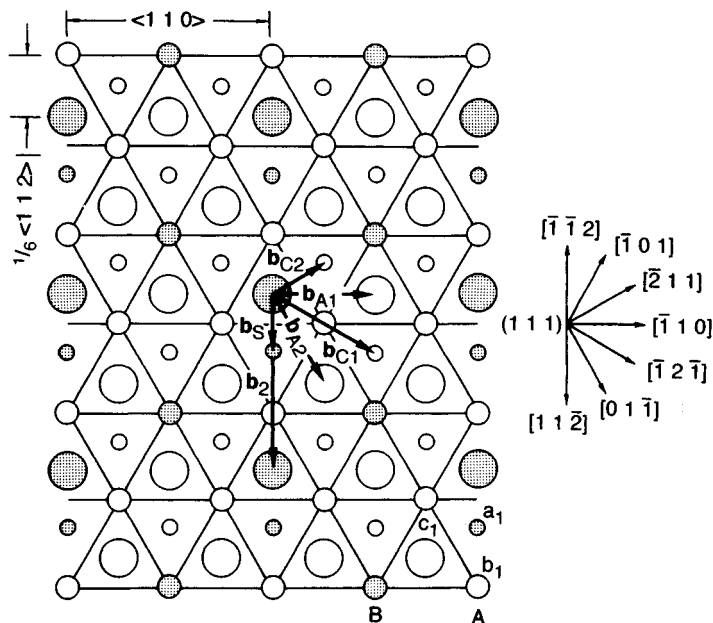


Figure 2. The atomic arrangement on the (111) plane in an A_3B compound with the $D0_{22}$ structure. The a_1 , b_1 and c_1 layers show a part of the stacking sequence $a_1b_1c_1a_2b_2c_2 \dots$ along the $[111]$ direction representing a $D0_{22}$ structure. The shading shows the B atoms relative to the A atoms (unshaded)

$\{111\}$ is not guaranteed on symmetry grounds (Yamaguchi *et al.*, 1981a,b). They can be unstable.

In the $D0_{22}$ structure, relatively short lattice translation vectors occur along $\langle 110 \rangle$ and $\langle 112 \rangle$ on $\{111\}$, and along $\langle 110 \rangle$ and $\langle 100 \rangle$ on $\{001\}$. These vectors are $\langle 110 \rangle$ (e.g. $2b_{A1}$ in Figure 2), $\frac{1}{3}\langle 112 \rangle$ (e.g. b_2 in Figure 2) and $\langle 100 \rangle$, respectively. Dislocations with Burgers vectors corresponding to such relatively short lattice translation vectors are perfect ones which are expected to be observed in compounds with the $D0_{22}$ structure. Such perfect dislocations may be dissociated into partial dislocations, and the character of dislocation dissociation will depend on the relative stabilities and energies of the faults involved.

Cubic superlattices based on f.c.c. or b.c.c. structures cannot be twinned by the twinning mode of the corresponding disordered structure (Cahn and Coll, 1961; Bolling and Richman, 1965), while noncubic superlattices derived from a f.c.c. lattice may form true twins in some variants of the usual disordered mode (Christian and Laughlin, 1988; Yoo, 1989). The twinning systems of the $\{111\}\langle 112 \rangle$ type are the variants in which the $D0_{22}$ superlattice is mechanically twinned without disturbing the $D0_{22}$ symmetry of the lattice. We call such true twinning 'ordered twinning' since the ordered arrangement of atoms in the lattice is not disturbed by

such twinning. On the (111) plane in the $D0_{22}$ structure, SISF corresponds to the stacking fault in the underlying f.c.c. structure. The ordered twinning on the $(111)[11\bar{2}]$ system may thus result from the propagation of Shockley partials with $b = b_s$ on the adjacent (111) planes trailing the SISF.

2.4 Deformation of Al_3Ti with the $D0_{22}$ Structure

2.4.1 Deformation Mode

Transmission electron microscope observations of deformation structures in Al_3Ti have been reported by Yamaguchi *et al.* (1987, 1988), Vasudevan *et al.* (1989), and Morris and Lerf (1991). There is a general agreement that the major deformation mode of Al_3Ti is ordered twinning of the $\{111\}\langle 112 \rangle$ type, as described earlier for the deformation of Ni_3V which also has the $D0_{22}$ structure (Vanderschaeve and Sarrazin, 1977; Vanderschaeve *et al.*, 1979; Vanderschaeve and Escaig, 1983). Figure 3(a) shows deformation twins in a $(1\bar{1}0)$ foil from an Al_3Ti single crystal deformed at 800 °C. The (111) twin boundaries are seen end-on. The corresponding selected area diffraction (SAED) pattern is shown in Figure 3(b), in which both fundamental and

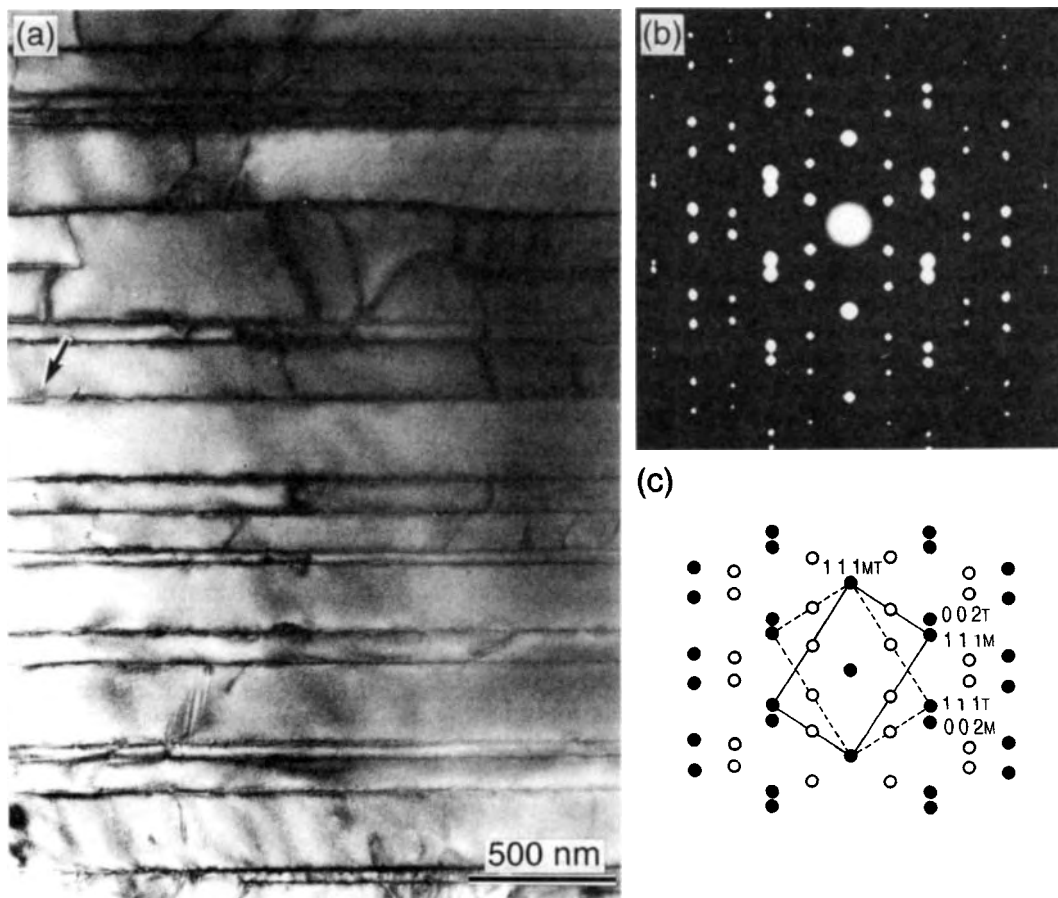


Figure 3. Deformation twins observed in a single crystal of Al₃Ti deformed in compression at 800 °C: (a) bright-field image, (b) the corresponding SAED pattern and (c) its indexed pattern. Closed and open circles represent fundamental and superlattice reflections, respectively

D0₂₂ superlattice reflections occur, not only from the matrices but also from the twins. Figure 4 shows a high-resolution electron microscope (HREM) image of the area indicated by an arrow in Figure 3(a). The twin boundary, which is located horizontally at the center of the image, is seen to be atomistically flat and parallel to (111). The atomic arrangement characteristic of Al₃Ti projected onto (1 $\bar{1}$ 0) is evident in both the matrix and the twin. Image calculations indicate that the strongly bright spots correspond to the atomic rows composed of alternately arranged Al and Ti atoms while the weakly bright spots correspond to those composed of Al atoms only. All the bright spots are arranged in mirror symmetry with respect to the twin boundary, indicating that the twinning does not disturb the D0₂₂ order, consistent with the SAED pattern shown in Figure 3(b).

At high temperatures, the four $\langle 112 \rangle$ -type ordered twinning systems are augmented by slip of the types $\langle 110 \rangle$, $\langle 100 \rangle$ (Yamaguchi *et al.*, 1987, 1988; Vasudevan *et al.*, 1989; Morris and Lerf, 1991) and $\langle 112 \rangle$ (Vasudevan, *et al.*, 1989; Morris and Lerf, 1991). In particular, significant deformation occurs by slip on (001) $\langle 110 \rangle$ at temperatures higher than 600 °C. Dislocations with $\mathbf{b} = \langle 110 \rangle$ (e.g. $2\mathbf{b}_{A1}$ in Figure 2) on (001) are widely dissociated into two superlattice partial dislocations with $\mathbf{b} = \frac{1}{2}\langle 110 \rangle$ (e.g. \mathbf{b}_{A1} in Figure 2) separated by a ribbon of APB-I on (001) as shown in Figure 5(a), a bright-field image of superlattice dislocations with $\mathbf{b} = [110]$ in an Al₃Ti single crystal deformed at 800 °C. The figure is viewed nearly along $[001]$ with $\mathbf{g} = 0\bar{2}0$. The corresponding dark-field image with the $10\frac{1}{2}$ superlattice reflection shows that the ribbons of APB-I with the displacement vector

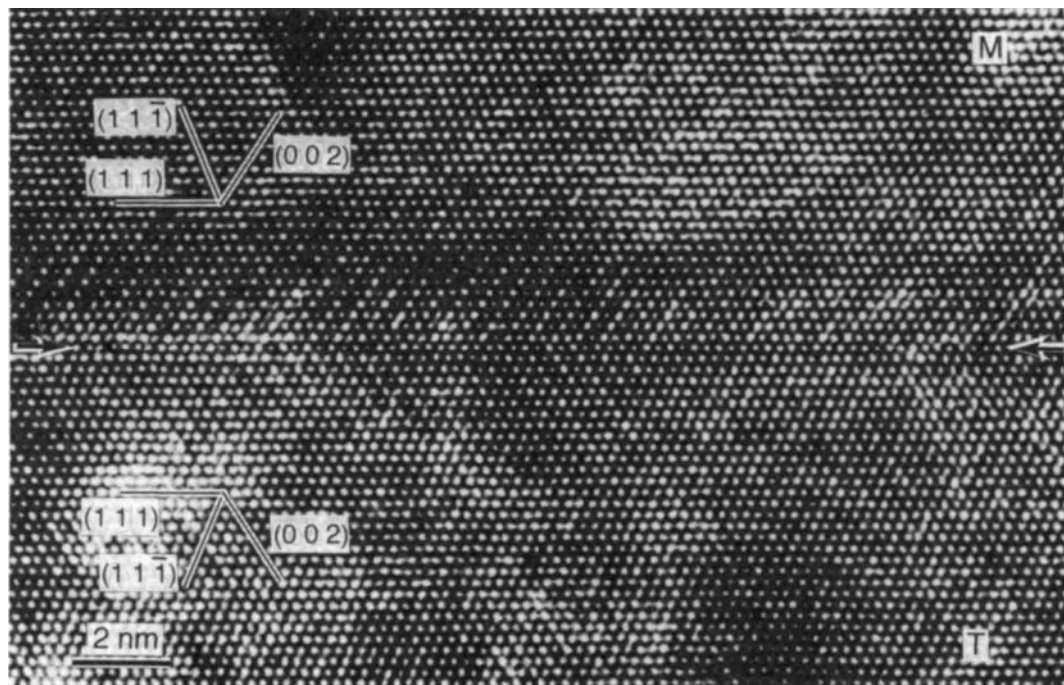


Figure 4. HREM image of a deformation twin in a single crystal of Al_3Ti deformed in compression at 800 °C

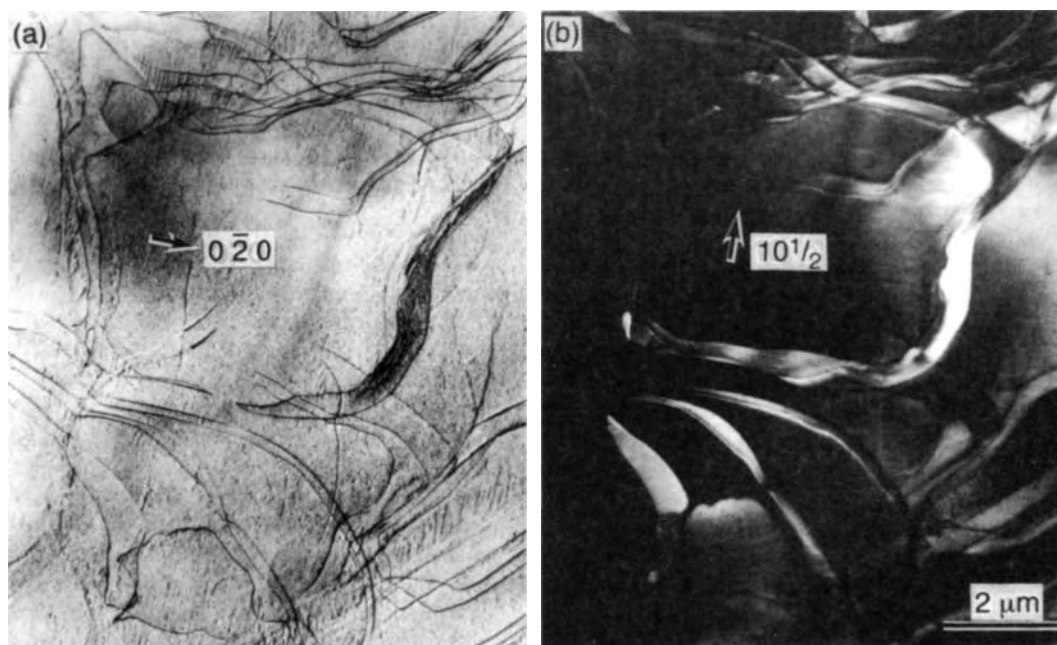


Figure 5. Dislocations observed in a single crystal of Al_3Ti deformed in compression at 800 °C: (a) bright-field image and (b) $10\frac{1}{2}$ dark-field image

$\frac{1}{2}\{110\}$ are in contrast between superlattice partial dislocations.

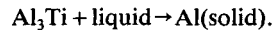
Such $\{110\}$ dislocations are also occasionally split on $\{111\}$ planes; however, the separation of the partial dislocations is much smaller, indicating a highly anisotropic APB energy. The spacing between the partials on $\{001\}$ and $\{111\}$ has been measured, giving the values of APB-I energies of 25–32 mJ m⁻² on $\{001\}$ (Vasudevan *et al.*, 1989; Hug *et al.*, 1989; Morris and Lerf, 1991) and 190–200 mJ m⁻² on $\{111\}$ (Hug *et al.*, 1989; Morris and Lerf, 1991). The energy of the $\frac{1}{2}\langle 110 \rangle$ -type APB in the L1₂ structure is also lowest on $\{001\}$, and the motion of pairs of superlattice partial dislocations with $\mathbf{b} = \frac{1}{2}\langle 110 \rangle$ joined by the APB on $\{001\}$ is the major high-temperature deformation mode in many L1₂ compounds. Slip of the type $\{001\}\langle 110 \rangle$ may be a common high-temperature deformation mode in L1₂ and L1₂-derivative, long-period ordered structures.

While perfect dislocations with $\mathbf{b} = \frac{1}{2}\langle 112 \rangle$ (e.g. \mathbf{b}_2 in Figure 2) were not detected in the earlier studies (Yamaguchi *et al.*, 1987, 1988), $\frac{1}{2}\langle 112 \rangle$ dislocations have recently been found to exist in Al₃Ti (Vasudevan *et al.*, 1989; Morris and Lerf, 1991). Vasudevan *et al.*, (1989) suggested that they are dissociated as $\frac{1}{2}\langle 112 \rangle \rightarrow \frac{1}{6}\langle 112 \rangle + \frac{1}{3}\langle 112 \rangle$, and the separation has been measured by Morris and Lerf (1991) as giving an SISF energy of 91–107 mJ m⁻². This SISF energy is not as low as would be expected from the abundance of ordered twins in deformed specimens of Al₃Ti. The observation of extensive twinning in this compound is believed to be a reflection of the difficulty of dislocation propagation rather than a reflection of easy twinning (Morris and Lerf, 1991). This is in agreement with the results of recent atomistic studies (Khantha *et al.*, 1991, 1992) of screw dislocation cores in a model D0₂₂ crystal using a set of empirical many-body potentials of the Finnis–Sinclair type (Finnis and Sinclair, 1984). The only glissile screw dislocation with a planar core has been found to be the Shockley partial $\frac{1}{6}\langle 112 \rangle$ (e.g. \mathbf{b}_3 in Figure 2) bounding an SISF. Other screw dislocations such as the partial dislocation $\frac{1}{2}\langle 112 \rangle$, which is one of the products of the dissociation reaction of $\frac{1}{2}\langle 112 \rangle$, and the superlattice partial dislocation $\frac{1}{2}\langle 110 \rangle$, bounding an APB-I on $\{001\}$, are all sessile, and hence thermal activation is needed for their movement.

Bands of $\frac{1}{2}\langle 110 \rangle$ dislocations trailing the APB-I on $\{001\}$ and loosely coupled in pairs have been often found to form at points where twins intersect or at some distance away along one of the intersecting twins. The formation of such dislocations may be a mechanism for relaxing stress concentrations at twin intersections (Yamaguchi *et al.*, 1988; Vasudevan *et al.*, 1989; Morris and Lerf, 1991). The $\{001\}\langle 110 \rangle$ slip corresponds to the conjugate deformation mode to the complementary ordered twinning system (Yoo, 1989). The full implication of the conjugate relation between the $\{001\}\langle 110 \rangle$ slip mode and ordered twinning is not yet understood. However, the formation of $\frac{1}{2}\langle 110 \rangle$ dislocations at the twin intersections might be related to this conjugate relationship.

2.4.2 Strength and its Temperature Dependence

Al₃Ti has very little off-stoichiometry and is formed via a peritectic reaction; any remaining liquid, equilibrium or not, ultimately solidifies via another peritectic reaction, slightly above the melting point of aluminum



Thus, polycrystalline specimens prepared by usual ingot metallurgy methods normally contain a small volume fraction of dispersed secondary phase, mostly aluminum. The dispersion of aluminum enhances the plastic deformation of Al₃Ti. In fact, the two-phase Al/Al₃Ti mixture containing 50–80 vol% Al₃Ti can be extruded at 600 °C with an extrusion ratio of 10:1. The overall deformation must be much greater than the deformation of the hard Al₃Ti component of the composite, which nevertheless suffers significant plastic deformation (Morris and Lerf, 1991). In particular, fine-grained, two-phase composites have been reported to exhibit good compressive ductility even at room temperature (Srinivasan *et al.*, 1992). The following interpretation for this has been proposed: the presence of aluminum surrounding the Al₃Ti grains provides a sink for the relief of stress concentrations during the deformation of Al₃Ti, leading to a pseudo-augmentation of the low-temperature deformation of Al₃Ti (Srinivasan *et al.*, 1992).

Single crystals of Al₃Ti can be grown using the floating zone method of melting (Shimokawa *et al.*, 1991). In order for such single crystals to be deformed plastically, the deformation temperature should be raised to at least 400 °C, usually to 600 °C. Figure 6 shows typical stress–strain curves of single crystals of

*Using equations (1) to (6) and the values of energies of APB-I on $\{001\}$ and $\{111\}$ and SISF on $\{111\}$, energies of other faults can be estimated as follows: $E_{\text{APB-I}} = 165\text{--}190 \text{ mJ m}^{-2}$, $E_{\text{CSF-I}} = 280\text{--}310 \text{ mJ m}^{-2}$ and $E_{\text{CSF-II}} = 260\text{--}300 \text{ mJ m}^{-2}$. Energies of CSF-I and CSF-II are estimated by assuming that $\phi_{\text{AA}}(r') = 2\phi_{\text{AB}}(r')$.

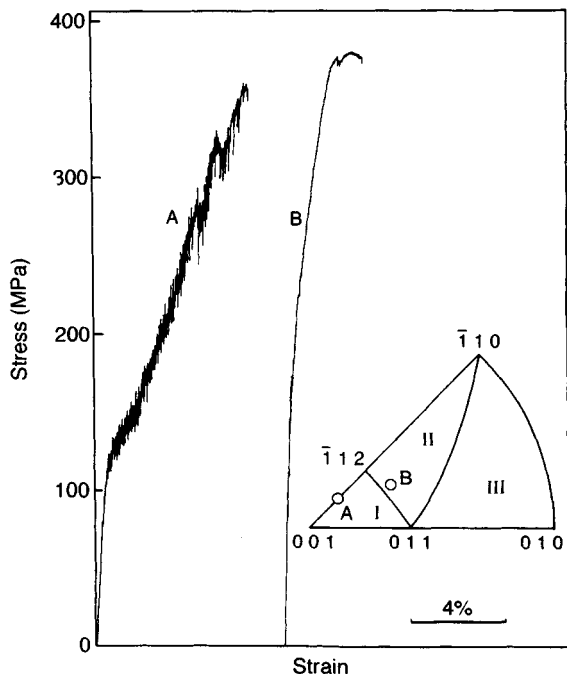


Figure 6. Compression stress-strain curves of Al_3Ti single crystals with orientations given in the figure at 800°C

Al_3Ti at 800°C in two different compression axis orientations. The stress-strain behavior of single crystals of Al_3Ti depends strongly on crystal orientation. In region I in the $[001]-[010]-[\bar{1}10]$ stereographic triangle shown in Figure 6, all four ordered twinning systems can be activated in compression since twins on the four ordered twinning systems produce compression strain, and hence deformation by ordered twinning can occur rather easily when compared with other orientation regions. As seen from the stress-strain curve for orientation A in Figure 6, serrations are commonly observed on the stress-strain curves for orientations in this region. We believe that they are due to the discontinuous generations of twins.

In region II, only two of the four ordered twinning systems can be operative and none of them in region III. For orientations in region II with large values of the Schmid factor for slip on $(001)[\bar{1}10]$, a smooth stress-strain curve which is like that for orientation B in Figure 6 is often obtained. When such a smooth stress-strain curve is obtained, slip traces corresponding to slip on $(001)[\bar{1}10]$ are observed on the specimen surface. However, partially serrated and partially smooth stress-strain curves are also often obtained, depending on crystal orientation. More annoyingly,

stress-strain behavior often varies from specimen to specimen even when they have the same crystal orientation. It can happen that one of two specimens with the same orientation shows a serrated stress-strain curve and the other shows a smooth one. Such observations suggest that the nucleation of ordered twins in Al_3Ti is sensitive to the local stress environment. It is thus difficult to determine the twinning stress accurately. The twinning stress was taken as the stress corresponding to the first serration and was resolved on the corresponding twinning system. Such resolved twinning stress is plotted in Figure 7 as a function of temperature. Although the scatter in the results is large, the resolved twinning stress is seen to be almost independent of temperature. Since the onset of twinning probably occurs in the presence of local stress concentrations at microstructural irregularities, the upper limit of the spread is thought to be close to the true twinning stress in Al_3Ti . On the other hand, the yield stress exhibited by specimens which are deformed by slip of the $(001)[\bar{1}10]$ type shows a strong temperature dependence. The critical resolved shear stress (c.r.s.s.) for slip, calculated by resolving the yield stress on the corresponding slip system, is also plotted as a function of temperature in Figure 7 (dashed line). Such a strong temperature dependence of the c.r.s.s. for slip of the $(001)[\bar{1}10]$ type in the D_{022} structure has been interpreted in terms of the low mobility of superlattice partial dislocations of the type $\mathbf{b} = \frac{1}{2}[\bar{1}10]$ due to their sessile core structure (Khantha, Vitek, and Pope, 1991, 1992).

2.5 Attempts to Improve Ductility

On the basis of crystal structure data of various intermetallic compounds of the types Al_3X and X_3Ti , a microalloying strategy has been proposed to enhance ordered twinning on $[111][12]$ or slip on $(001)[\bar{1}10]$ and thereby improve the ductility of Al_3Ti with the D_{022} structure (Yamaguchi *et al.*, 1988; Yamaguchi and Umakoshi, 1990; Wheeler *et al.*, 1990).

Figure 8(a) shows the atomic arrangement on a (111) plane in a D_{022} Al_3B compound. The stacking of such (111) planes in the sequence 1, 2, 3, 4, 5, 6, . . . represents a D_{022} lattice. When layer 3 and the layers above it are displaced by a vector $\frac{1}{6}[\bar{1}12]$ (\mathbf{b}_s in Figure 2) with respect to the layers below, producing an SISF (Figure 8(b)), an atomic configuration resembling the D_{0a} (oP8) structure (Figure 8(c)) is formed in the two (111) layers above and below the plane of the SISF (Yamaguchi *et al.*, 1988; Yamaguchi and Umakoshi, 1990). This suggests that the addition

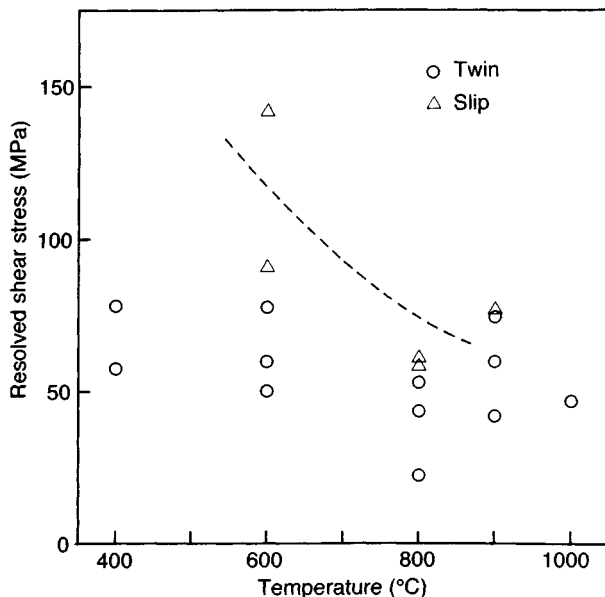


Figure 7. Temperature dependence of resolved shear stress for slip and twinning in Al₃Ti single crystals

of alloying elements which form a D0_a phase of the type Al₃X or X₃Ti would decrease the SISF energy and thereby enhance ordered twinning.

The same strategy can be used to make a search for elements which decrease the APB energy on (001). As seen from Figure 9, introducing a $\frac{1}{2}\langle 110 \rangle$ APB on (001) in the D0₂₂ structure is equivalent to creating a local stacking of (001) layers of the D0₂₃ type or the L1₂ type in the D0₂₂ structure. This suggests that the addition of alloying elements which form a stable D0₂₃ or L1₂ phase of the type Al₃X or X₃Ti would decrease the energy of the $\frac{1}{2}\langle 110 \rangle$ APB on (001) in the D0₂₂ phase and thereby lower the magnitude of the Burgers vector of the dislocations carrying slip on (001) $\langle 110 \rangle$. The addition of lithium, which forms a metastable Al₃Li phase with aluminum, has been found to improve the ductility of Al₃Ti to some extent (Yamaguchi *et al.*, 1988). However, no substantial practical improvement in the ductility of Al₃Ti has yet been achieved through this alloying strategy.

To improve the ductility of Al₃Ti, not only should enhancement of slip or twin mechanisms be attempted, but also refinement of slip or twins. The presence of massive macrotwins often leads to brittle fracture (Yoo *et al.*, 1991). In the case of Al₃V, which is isostructural to Al₃Ti and is also brittle at low temperatures, both the enhancement and refinement of twins have been achieved by alloying Al₃V with titanium, thereby giving rise to an increase in compressive fracture strain

at low temperatures (Umakoshi *et al.*, 1988; Yamaguchi *et al.*, 1988; Yamaguchi and Umakoshi, 1990). Al₃V has been known to deform via the motion of dislocations with $\mathbf{b} = \frac{1}{2}\langle 110 \rangle$ and $\langle 100 \rangle$ only at high temperatures (Umakoshi *et al.*, 1988; Wheeler *et al.*, 1990). In this regard, Al₃V is different from Al₃Ti whose major deformation mode is twinning. Twinning activity is thus expected to be induced in Al₃V by partial substitution of titanium for vanadium. In Al₃(V_{0.95}Ti_{0.05}), which exhibits 7% compressive fracture strain at room temperature, numerous fine, thin deformation twins as well as stacking faults have been observed (Umakoshi *et al.*, 1988; Yamaguchi *et al.*, 1988). Refining the scale of deformation, if somehow possible, would be effective in increasing the low-temperature ductility of Al₃Ti.

3. L1₂ Variations of Al₃Ti

3.1 Phase Stability

Recent *ab initio* quantum mechanical calculations have shown that, for the transition metal trialuminides dominated by the hybridized bonding between the transition metal d and aluminum p electrons, the stable crystal structure will be the one which has the maximum bandfilling of the bonding states, i.e. the structure for which the Fermi level lies in a deep valley separating the bonding and nonbonding states in the electronic DOS (density of states) distribution (Nicholson *et al.*, 1989;

Chapter 11

Miscellaneous Novel Intermetallics

Robert L. Fleischer*

General Electric Research & Development Center, Schenectady, NY 12301, USA

1. Introduction

Nearly 300 binary intermetallic compounds are known to melt above 1500 °C, and an estimated 80 more melt between 1400 and 1500 °C (Fleischer, 1987a). They include many different types of ordered crystal structures, ranging from those that have the minimum of two atoms per unit cell up to those with more than 100 atoms per cell. A review of density and melting temperatures for the nearly 300 compounds (Fleischer, 1987a) included examples of 41 different structure types. Since detailed deformation mechanisms depend on crystal structure, the task of understanding this group would be formidable even if all examples of a given structure deformed identically. They do not, as Baker and Monroe's (1990) review of the simplest structure type, B2 (cP2), describes. For example, even among aluminides such as AlFe, AlRu, AlNi, and AlCo a progressive, striking increase in brittleness occurs in this particular sequence. The situation is further complicated by ternary and higher-order B2 compositions, which multiply the number of distinct materials indefinitely and allow additional, more complicated crystal structures to be formed.

One aim of this introduction is to convince the reader that our present vast gaps in understanding should have been expected. We lack detailed data such as are needed for reasonable insight into the crystallographic deformation processes—stacking fault energies, dislocation mobilities, solid-solution hardening, ductility (or its absence), and the strength as a function of various parameters. These quantities are available for only a few intensely studied compounds, and our limitation is

accentuated by the consideration here of the less-studied compounds and the conscious elimination of what are considered the most promising high-temperature intermetallics, since they are described in detail elsewhere in this volume. These include the Fe, Ni, and Ti aluminides, silicides, and certain Al–Zr compounds.

By far the major incentives for seeking materials that have both strength at high temperature and damage tolerance at room temperature are the needs of advanced aerospace and engine applications. Among the most demanding uses are those in the heart of the jet engine: blades and disks at the hottest locations. High strength per unit density and high elastic stiffness per unit density are desired.

It is interesting to note that in a 1960 review of the mechanical properties of intermetallic compounds (Westbrook, 1960), only 14 compounds with melting temperatures T_m above 1400 °C were included, and 11 with T_m above 1500 °C. Of these, seven were beryllides (Stonehouse, *et al.*, 1960). As noted previously, in recent years hundreds of high-temperature compounds have been considered.

In Section 2 we look at a few of the more basic properties that are known for the structure types to be considered. In Section 3 we take the alternative tack—searches of many materials but with much less definitive data for each.

2. Basic Studies

2.1 Basics That We Wish to Know

There is a gulf between what we would like to know and need to know for useful high-temperature intermetallics and what we do know. This mismatch exists on both theoretical and experimental levels. We need to know whether a material will plastically deform,

*Present address: Department of Geology, Union College, Schenectady, NY, USA.

weaken, or break under specified conditions of stress, temperature, and corrosive environment. Rarely for the alloys considered here do we have more than limited data.

We would like to be able to calculate for a given crystal structure made up of specified atoms what its various surface energies, dislocation structures, and elastic moduli are, and predict slip systems, dislocation interactions, stress-strain curves and fracture properties. Such theory has begun, and now some elastic moduli can be reasonably well calculated for certain stoichiometric binary compounds, for example the work of Mehl *et al.* (1990), which is updated and extended in Volume 1 of this work by Mehl *et al.*

Once the further major step of dealing with dislocations by computerized models is mastered and its abilities and limitations are recognized, the second-order modeling for how dislocations move and interact must be attempted. Although vastly more is known of dislocations now than when Thornton Read wrote his classic book on dislocations (Read, 1953), his description is still widely true. He noted in his preface that '... it became the fashion to invent a dislocation theory of almost every experimental result in plastic deformation,' but that after further time, 'it became apparent that dislocations could explain not only any actual result but virtually any conceivable result, usually in several different ways.'

This rather unsatisfactory situation has occasional exceptions, by far the most notable of which is the prediction by Johnston (1962) of the stress-strain curves of LiF from the measured number of mobile dislocations and their velocity-stress (v - τ) relationship (Johnston and Gilman, 1959). The remarkable agreement between the observed and the calculated behaviors in Figure 1 confirms the basic understanding of yielding and deformation in this system.

We must note, however, that the more basic theoretical understanding of how new mobile dislocations are generated is lacking, and the basic understanding of the velocity-stress relation is semi-quantitative at best (Fleischer, 1962). Also Johnston's results apply only to single crystals under simple stresses and to LiF, which, although it is an ordered compound, is not widely regarded as an intermetallic.

To the author's knowledge, for only one ordered intermetallic compound have v versus τ relations been measured, the Laves phase C14 (hP12) type compound MgZn₂. In this case over a limited range of stress a linear v versus τ plot is observed for both prismatic and basal slip (Paufler *et al.*, 1970, 1971). Data were taken near where plasticity begins, at 390 °C, which is 0.77 of the melting temperature, i.e. far below the temperatures of interest for high-temperature use. The

v versus τ behavior and rate of generation of dislocations imply that Johnston-type yield points are expected (Johnston, 1962), and such yield points were observed (Paufler and Schulze, 1967). They are also seen in the other major Laves-type phase C15 (cF24) Cu₂Mg (Moran, 1965; Livingston *et al.*, 1989). Like other single-phase Laves structures it is brittle in tension below $\sim 3T_m/4$. Livingston (1992), however, has noted some cases where Laves phases show some ductility at room temperature, usually associated with the presence of a second phase.

2.1.1 Solid-solution Hardening

Limited, incomplete work exists on solid-solution hardening in high-temperature intermetallics. The subject is complicated by the possibility of multiple types of atomic defects occurring in single samples, depending on both added solute and the 'constitutional defects' that are produced by off-stoichiometry. The subject is further complicated if high-temperature defects are retained during cooling from elevated temperatures. Meaningful assessment of solute effects is best done by separately assessing first off-stoichiometry and then substitution of ternary solute in a single sublattice. Even with this simplification, multiple defects can result: both vacancies and substitutions can be produced by either off-stoichiometry or by ternary solute, for example in AlCo (Fleischer, 1993a).

Among conventional high-temperature intermetallics, L1₂ (cP4) Ni₃Al has received the most attention, as described by Liu and Pope in Chapter 2 of this volume. Hardening effects from ternary solute have been observed and correlated to first order with size-misfit interactions, as measured by lattice parameter changes on alloying. However, the extent of effects from elastic modulus mismatch has yet to be evaluated, and hence the source of the observed hardening cannot be regarded as known. However, Fleischer (1993f) noted that, at least for Ni₃Al, the same elastic interactions that produce the solid solution hardening in dilute metal alloys also dominate in ordered alloys—as inferred from equal hardening by solutes in Ni₃Al (Mishima *et al.*, 1986a) as in Ni (Mishima *et al.*, 1986b).

Among the miscellaneous compounds considered here two B2 (cP2) structures, AlCo (Fleischer, 1993a, b) and AlRu (Fleischer, 1993c, d), have been studied along with two C15 (cF24) Laves phases, Cu₂Mg (Livingston *et al.*, 1989) and Cr₂Zr (Fleischer, 1992). Of these, Cu₂Mg is not commonly regarded as a high-temperature compound ($T_m = 797$ °C); nevertheless, plasticity is obtained only well above room temperature, so that it is expected to respond similarly to other C15 high-temperature compounds. A brief summary of the results is given by Fleischer (1993e).

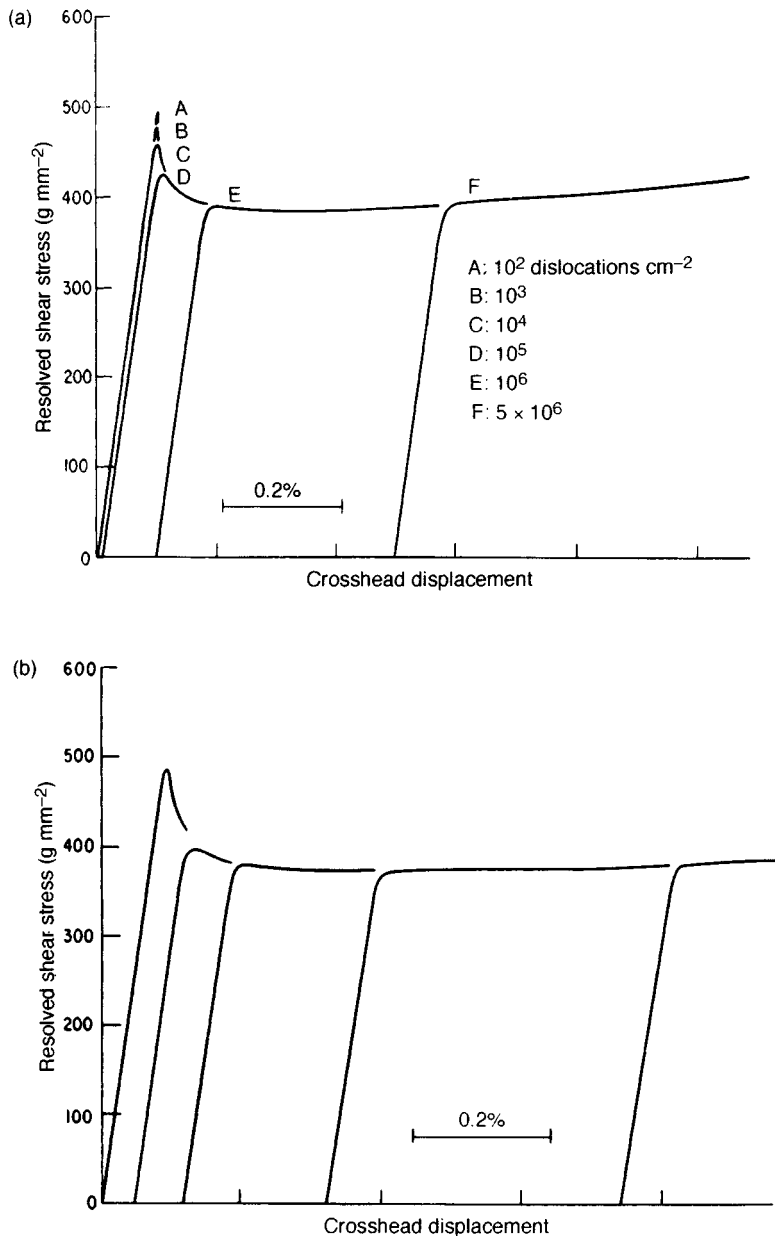


Figure 1. Calculated (a) and observed (b) stress-strain curves for LiF. Assumed initial dislocation densities are given for the calculations. The experimental curves were obtained by repeated straining, unloading, and reloading (Johnston, 1962) Reproduced by permission of the American Institute of Physics

In virtually all cases hardening was observed both from solute atoms (Livingston *et al.*, 1989; Fleischer, 1992, 1993b, d, e) and from off-stoichiometry (Fleischer, 1992, 1993b, d, e). The defect structure in ternary, off-stoichiometric compounds was complicated (Fleischer, 1993a, c), so that a proper test of existing theories

was not possible. However, the typical magnitude of the hardening was consistent with the usual sum of size plus modulus effects, and for AlCo the hardening by constitutional defects was in the expected ratio for the two sides of off-stoichiometry. More definitive work is needed to identify better the point defects and to

model how their effects on dislocations should be superimposed.

2.2 Mechanical Properties of Selected Systems

Although the basic properties described in Section 2.1 are not yet available for high-temperature intermetallics, for a number of systems some of the conventional properties of general interest have been measured for selected compounds. Many of the data to be noted can be found in the series of reviews by Sauthoff (1986, 1989, 1990a, b), and further data (mostly for somewhat lower T_m compounds) are given by Yamaguchi and Umakoshi (1990).

Figure 2 is a redrawn composite diagram of yield stresses (at 0.2% strain) given by Sauthoff as a function of temperature. They include the D0₂₂ (tI8) Al₃Ti-type structure Al₃Nb, B2 (cP2) CsCl-type AlNi, three Laves phases of C14 (hP12) MgZn₂ type—AlFeTa, AlNiTa, and AlNbNi, all from Sauthoff (1990a)—and another C14 structure, Cr₂Ti (Sauthoff, 1989). The data for D8₈ (hP16) Mn₃Si₃-type Si₃Ti₅ are from Frommeyer *et al.* (1990). For comparison MA6000, an Ni-based superalloy, is included. The diagram shows clearly the potential advantages of intermetallics at high temperature. Since the curves that do not extend to low temperatures end because of the intervention of brittle failure, the diagram also reminds one of the major

obstacle to widespread mechanical use of intermetallics. Umakoshi *et al.* (1990) give similar data for the yield stress of the C11_b (tI6) structure MoSi₂ from 950 to 1500 °C. When suitably averaged, the stresses lie in the range of the intermetallics above MA6000 in Figure 2.

Comparison for Si₃Ti₅ (which has $T_m = 2130$ °C) of the toughness and flow strength shows the difficult trade-off to be made (Figure 3). Toughness only rises where the flow stress becomes low. For the binary compound, only a narrow temperature range could be used for a specified pair of useful properties. With Si₃Ti₅ as part of a two-phase eutectic, high-temperature strength is strikingly lowered, and fracture toughness is greatly enhanced (Frommeyer *et al.*, 1990).

The same need to compromise is encountered as composition is varied in the series of Cr–Ti alloys considered in Figure 4 (Fleischer and Zabala, 1990a). Hardness, as a measure of strength, rises with the concentration of Cr and toughness declines. The samples include two-phase alloys with the single-phase C14 (hP12) structure expected at the composition Cr₂Ti and C15 (cF24) at Cr₆₄Ti₃₆. A2 (cI2) Ti (i.e. body-centered cubic) is present as a minority phase for Cr levels below 64 at%. These alloys are the toughest ones in Figure 4.

Similarly, Savitskii (1960) showed that for the B20 (cP8) FeSi-type compound CoSi ($T_m = 1460$ °C) hardness decreased from 10 GPa to 1.2 GPa between

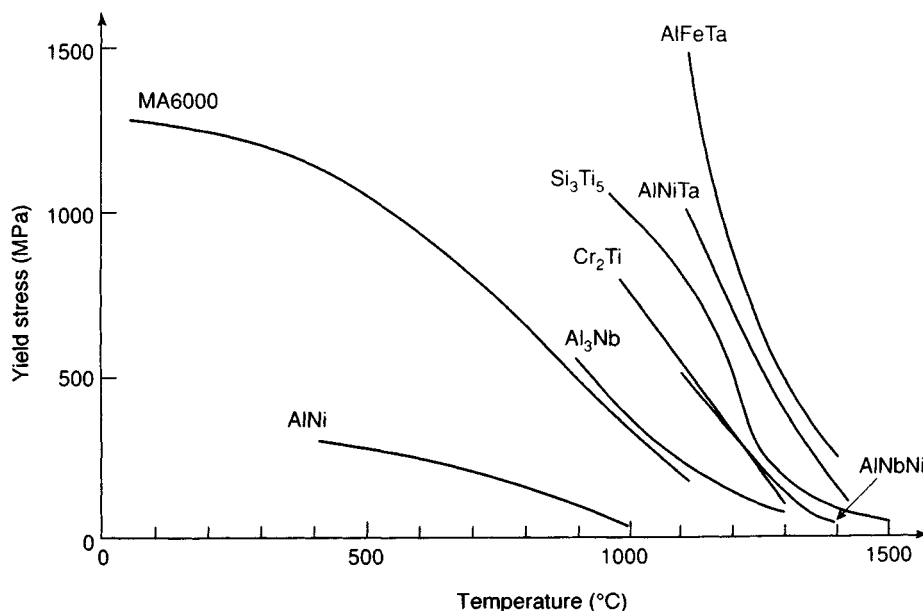


Figure 2. Yield strength at a strain of 0.2% as a function of temperature for a variety of crystal structures, compared to an Ni-based superalloy INCO MA6000. The data are from Sauthoff (1989, 1990a) and Frommeyer *et al.* (1990)

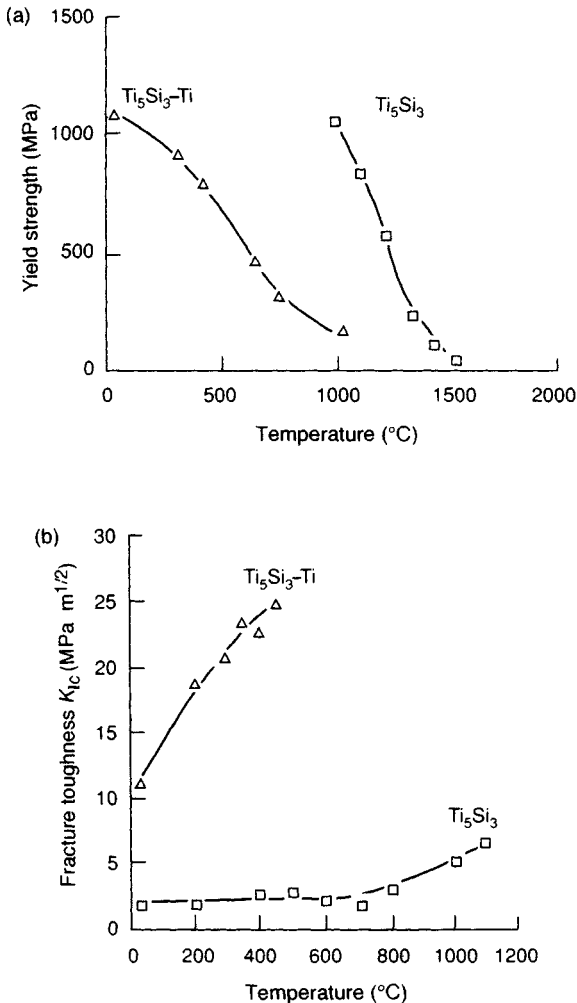


Figure 3. (a) Yield strength (compression with 10^{-4} s^{-1} strain rate) and (b) plane strain fracture toughness K_{Ic} (four point bending) as a function of temperature for two-phase, directionally solidified eutectic Ti_5Si_3 -Ti and single-phase Ti_5Si_3 (Frommeyer *et al.*, 1990) Reproduced with permission

20 and 1000 $^{\circ}\text{C}$, while the ultimate compressional strength increased from 38 MPa to 340 MPa between 20 and 750 $^{\circ}\text{C}$.

3. Screening High Melting-Temperature Compounds

Given 300 to 400 binary compounds to consider, how does one proceed? Since time and cost limit the number that can be examined, systematic criteria of potential goodness must be set and used to decide what

compounds should be tested first. This task was given by the US Air Force via Wright-Patterson Air Force Base to two separate groups, one at United Technologies Corporation (Anton and Shah, 1991b) and the other at General Electric Company (Fleischer and Field, 1990). The criteria used were similar, but with significant differences. The selections of compounds were overlapping but mostly separate, and the tests were different, but with similar aims. This section begins with the selection criteria, describes the two approaches, and summarizes the results.

3.1 Selection Criteria

3.1.1 Primary Criteria

The most general approach to screening is to make use of structure-insensitive properties, i.e. ones that are not significantly influenced by processing variables and the resultant microstructure and only slightly altered by minor variation in alloying elements. The ones of use here are melting temperature T_m , specific gravity ρ , and elastic modulus E (Young's modulus) (Fleischer, 1985). These quantities are useful indicators of several vital properties.

For several reasons, T_m is by far the most useful structure-insensitive property. First, it specifies the thermal region where materials are solid. Second, its relative magnitude is a reasonable first approximation to the stiffness of a material, since the elastic moduli have a strong correlation with melting temperature (Fine *et al.*, 1984). In addition, in all models of strengthening, values of flow stress increase with the magnitude of the elastic constants, which in turn increase with T_m . Also, expansion coefficients (which for convenience should be small) vary inversely with T_m . Finally, the limiting creep rate defines a maximum operating temperature that increases with T_m . Approximate limits set on operating temperatures for single-phase materials are estimated to lie between $T_m/2$ and $2T_m/3$, with $T_m/2$ being more common (Frost and Ashby, 1982). A simple zero-order rule of thumb is that if the melting temperature is expressed in degrees centigrade, the operating temperature is roughly the same number in degrees Fahrenheit (Johnson, 1985).

For use above the earth and in rotating parts, high specific strength (strength per unit density) and specific stiffness are important. It is therefore necessary to know the elastic moduli (as measures of stiffness and as structure-insensitive indicators of strength) and the specific gravity. Unfortunately, in 1985 for intermetallic compounds there was a dearth of data on elastic moduli.

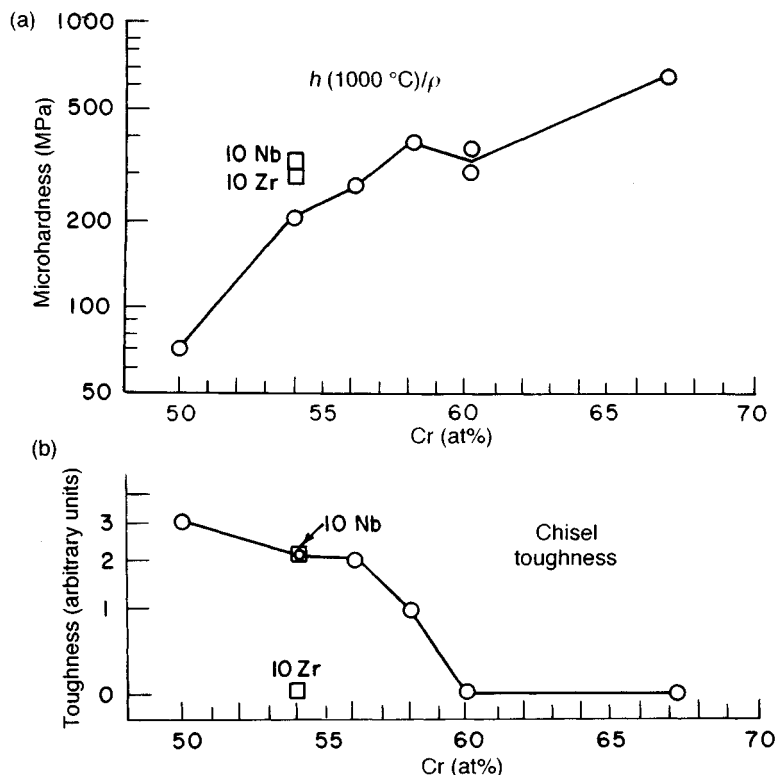


Figure 4. Mechanical properties of Ti-Cr alloys as a function of composition: (a) microhardness at 1000 °C divided by the specific gravity; (b) chisel toughness at ambient temperature (Fleischer and Zabala, 1990a) Reproduced with permission

Measurements of E existed for only 24 from around 300 intermetallics that melt at or above 1500 °C. Although E/ρ is the specific stiffness (which we want to know) and the specific strength σ/ρ is roughly proportional to E/ρ , we will in most cases be forced to reason more indirectly from T_m/ρ as roughly proportional to E/ρ , and in turn still more roughly proportional to σ/ρ . Many more elastic moduli are now available (Fleischer *et al.*, 1988, 1989, 1990, 1991b,c; Fleischer and Field, 1990; Fleischer, 1991b) and Nakamura, Chapter 37 in Volume 1). Figure 5 is a useful display of the correlation between T_m and ρ (Fleischer, 1987a). The nearness to the approximate boundary curve gives indication of the maximum T_m for a given ρ or the minimum ρ at a given T_m . This selection route optimizes the chances for high strength and low density at high temperature, but tells one nothing of the critical properties of toughness and ductility.

3.1.2 Additional Criteria

Many other factors influence the likelihood that a specific ordered compound will be mechanically useful. Table 1 lists a number of the considerations in groupings of (in some cases) overlapping or interdependent factors.

The crystal structure and bonding character determine matters connected with dislocation structure and mobility. The unit cell determines the magnitudes of Burgers vectors b , and the complexity of the cell will influence whether the full dislocation can dissociate into partial dislocations of strength b_p , bound by stacking faults or antiphase boundaries of energies γ_{SF} and γ_{APB} . Large values of b or b_p make dislocation energies higher (and hence dislocations more difficult to nucleate), and they probably imply that lattice-controlled dislocation mobilities are lower. Crystals with complicated unit cells tend to deform less and be more

brittle. Dissociation of dislocations into partials is likely to diminish cross slip and encourage planar deformation, except where partials themselves cross slip readily (Fleischer, 1959).

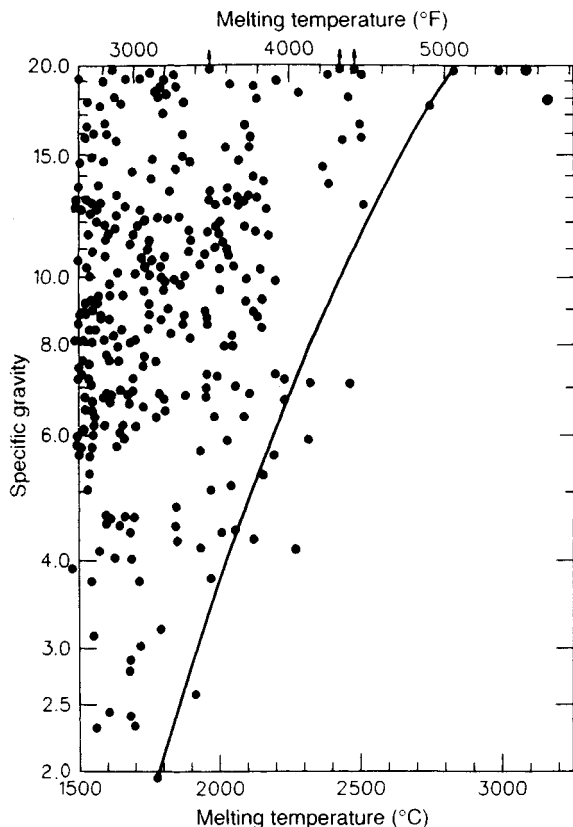


Figure 5. ρ against T_m for 293 binary intermetallic compounds. The solid line is an empirical, approximate envelope to the data (Fleischer, 1987a) Reproduced by permission of Chapman & Hall

Table 1. Factors to consider in selecting compounds

Crystal structure
Size of unit cell: $b = ?$
Complexity of cell: $b_p = ?$; γ_{SF} , $\gamma_{APB} = ?$
Number of slip systems
Compatible polycrystalline deformation?
Planar slip?
$d\tau/dT > 0$
Better symmetry?
Alloying
Composition range Δc
Potential for ternary additions
Equilibrium with ductile phase
Purity
Environmental resistance

Compatible deformation of polycrystalline samples and, presumably, ductility are aided by the existence of multiple equivalent slip vectors and slip planes, cross slip, and twinning. For uniform deformation, five independent slip systems are required (von Mises, 1928); in actual nonuniform deformation, fewer are observed to be sufficient (Fleischer, 1987b).

The positive temperature variation of the flow stress $d\tau/dT$, which enhances high-temperature strength in some intermetallics, is thought to result from an interplay of dislocation interactions, work hardening, and cross slip. Hence $d\tau/dT$ also is intimately dependent on crystal structure.

An assumption has often been made that higher-symmetry structures allow more equivalent but independent slip systems and hence more plastic deformation and ductility in polycrystalline form. Exceptions make it evident that this assumption lacks universality. One of the more plastic structures in the Al-Ti-Nb system has orthorhombic symmetry (Banerjee *et al.*, 1988; Banerjee, Chapter 5 of this volume), and the B1 (cF8) NaCl structure is normally brittle at low temperatures even though it has cubic symmetry.

Phase equilibria data are critical to various alloying considerations. For compounds that can exist away from strict stoichiometry, the permitted composition range Δc allows one type of alloying—substitutions or vacancies in at least one of the sublattices. The existence of $\Delta c > 0$ is also commonly taken as a hint that ternary additions are likely to go into solid solution. A special case where the tendency for solution is statistically known to be enhanced occurs where isostructural compounds exist with an element in common. For example, if Mo_3Si and Cr_3Si are both A15 (cP8) compounds, then Cr is expected to dissolve in Mo_3Si (for Mo) and Mo is expected to replace Cr in Cr_3Si . In half such cases full replacement is possible, and in 95% of cases at least 5% solubility obtains (Fleischer, 1988).

A further meritorious consideration for an intermetallic is being in equilibrium with an unordered metallic phase of high melting temperature. Such an equilibrium opens up possibilities of toughening an intermetallic by adding a small fraction of a ductile phase. We will see that AlRu + Ru is one such system.

Finally, the question as to what role interstitial atoms play is naggingly uncertain. In metallic systems, particularly body-centered cubic metals, they can have major effects. It is likely but unproved that they can have similar roles in intermetallics.

A third category of consideration is environmental resistance. An alloy that forms a volatile oxide at elevated temperature has a predictably short useful life.

Table 2. Binary intermetallics studied by Pratt and Whitney^a

Compound	Crystal type	T_{bd}^f (°C)	Creep parameters ^b		Ultimate strength ^c at 1200 °C	Oxidation at 1200 °C	Melting temperature (°C)	Specific gravity
			n	Q (eV)				
AlNb ₃	A15 (cP8) WO ₃	800	2.86	3.60	250	High	1960	7.29
AlNb ₂	D8 _h (tP30) CrFe	> 1200	1.2	3.55	260	—	1871	6.87
CoHf	B2 (cP2) CsCl	500	3.04	1.40	—	High	1640	12.50
Co ₂ Nb	C15 (cF24) Cu ₂ Mg	1100	2.94	3.68	320	High	1520	9.0
CoSi ₂	C1 (cF12) CaF ₂	1000	7.05	8.44	—	Low	1326	4.98
Cr ₂ Nb	C15 (cF24) Cu ₂ Mg	1200	2.0	1.34	60	High	1720	7.66 ^d
Cr ₃ Si	A15 (cP8) WO ₃	> 1200	3.4	5.15	160	Low	1770	6.46
Mo ₅ Si ₃	D8 _m (tI32) Si ₃ W ₅	500	1.9	0.43	15	—	2180	8.20 ^e
MoSi ₂	C40 (hP9) CrSi ₂	> 1200	2.9	3.68	320	Low	2032	6.24
Ti ₃ Sn	D0 ₁₉ (hP8) Ni ₃ Sn	900	3.19	1.05	—	High	1670	5.29

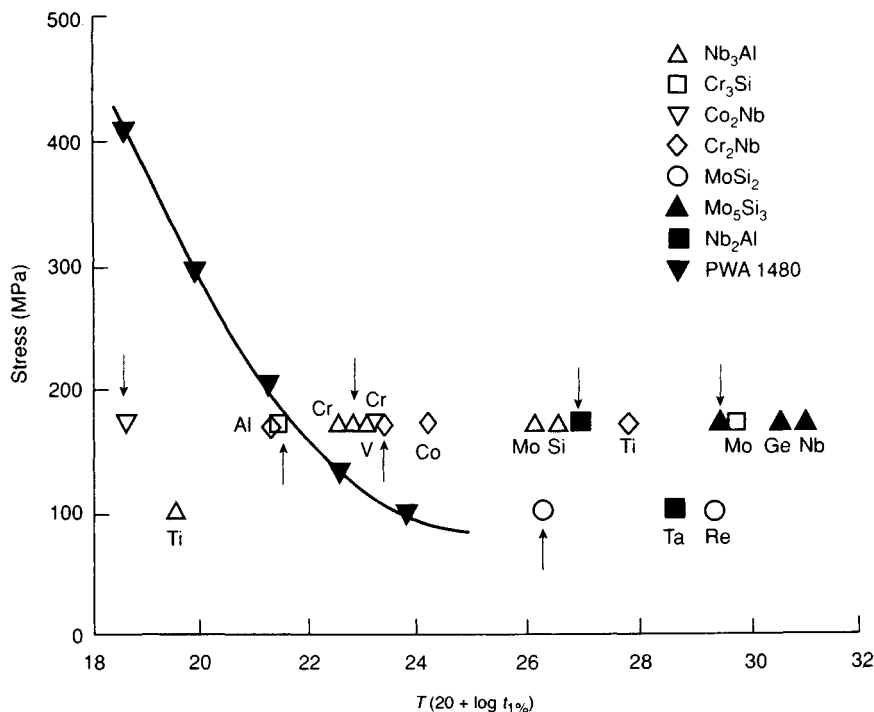
^aAnton and Shah (1989, 1991a) and Anton *et al.* (1989).^bSteady-state creep assumed to be described by a strain rate that is proportional to $\sigma^n \exp(-Q/kT)$.^cIn bending.^dFleischer and Zabala (1990b).^eCalculated.^fBrittle-ductile transition temperature.**Figure 6.** Larson-Miller (temperature-time) plot of the stress for 1% creep in steady state, comparing creep resistances of intermetallic compounds and 14 of their alloys with superalloy single-crystal PWA 1480 (Anton and Shah, 1991b). T is in 10^{-3} °C, t in hours. For each intermetallic the pure binary is marked by an arrow. Repeats of the same symbol are alloys that include as ternary elements Al, Co, Cr, Ge, Mo, Nb, Re, Ta, Ti or V

Table 3. Binary intermetallics studied by General Electric^a

Crystal structure	Nominal atomic composition	Measured atomic composition	Melting temperature (°C)	Specific gravity	Young's modulus (GPa)	Volume fraction observed (100 points counted)	Chisel toughness	Brittle to ductile transition temperature (°C)
B2 (cP2)	AlCo	51:49	1635	5.86	259	1.0	0	< 23
D0 ₂₂ (tI8)	Al ₃ Nb	75:25	1680	4.50	—	1.0	0	850
D8 ₈ (tP8)	AlNb ₂	34:66	1940	6.80	—	1.0	0	> 1170
B2 (cP2)	AlRu	52:48	2060	7.97	267	1.0	3	< 23
Cu ₂ Zn ₃ (cI52)	Al ₅ V ₅	62:38	1675	3.97	155	1.0	0	100
C15 (cF24)	Al ₂ Y	67:33	1485	3.93	158	1.0	0	> 950
D0 ₂₃ (tI16)	Al ₂ Zr	74:26	1580	4.12	205	0.99	0	750
C14 (hP16)	Al ₂ Zr	66:34	1645	4.60	222	1.0	0	870
D2 _b (tI26)	Be ₁₂ Nb ^b	—	1672	2.48	222	0.99	—	100
Be ₁₇ (Nb ₂ (hR19)	Be ₁₇ Nb ₂ ^b	—	1800	3.23	320	0.97	—	1020
D2 _b (tI26)	Be ₁₂ Ti ^b	—	1550	2.25	282	0.99	—	1050
D2 ₃ (cF112)	Be ₁₃ Zr ^b	—	1645	2.72	289	0.96	—	> 1150
C15 (cF24)	Cr ₃ Nb	66:34	1770	7.66	218	1.0	0	> 1150
A15 (cP8)	Cr ₃ Si	76:24	1770	6.54	351	0.98	0	> 1150
D8 _m (tI32)	Cr ₂ Si ₃	64:36	1680	5.96	—	0.93	0	1000
C14 (hP12)	Cr ₂ Ti ^c	67:33	1550	5.89	184	0.91	0	700
C15 (cF24)	Cr ₆₀ Ti ₄₀ ^c	60:40	1450	6.01	186	0.82	1	850
D8 ₈ (hP16)	Ge ₂ Ti ₅ ^c	—	~ 1800	5.94	121	1.0	0	> 800
L1 ₀ (tP4)	IrNb	48:52	1900	15.25	268	0.98	3	< 23
A12 (cI58)	Re ₂₄ Ti ₅ ^c	84:16	2750	17.5	300	1.0	0 ^d	> 1300
B2 (cP2)	RuSc	50:50	2200	7.40	155	0.93	3—	< 23
L1 ₀ (tP4)	Ru ₁₁ Ta ₉	55:45	2080	14.41	243	0.98	0+ ^e	< 23
B2 (cP2)	RuTi ^c	49:51	2120	8.55	282	1.0	0+	< 23
B1 (cF8)	SbY	48:52	2310	5.90	101	0.73	0	> 1100
A15 (cP8)	SiV ₃	25:75	1925	5.62	213	0.99	0	1100
L1 ₂ (cP4)	Si ₃ U	—	1510	8.1	—	0.84	0	—
CrSi ₂ (hP9)	Si ₂ V	65:35	1677	4.63	331	0.99	0	900
D8 _m (tI32)	Si ₃ V ₅	38:62	2110	5.27	257	1.0	0	> 1100
D8 ₈ (hP19)	Si ₃ Y ₅	38:62	1850	4.50	—	0.96	0	1000
D0 ₁₉ (hP8)	SnTi ₃ ^c	—	1690	6.03	207	1.0	0	> 1150

^aFleischer and Zabala (1990b).^bFleischer and Zabala (1989).^cFleischer and Zabala (1990c).^dRe₈₂Ti₁₈ has chisel toughness 2—.^eRu₄₉Ta₅₁ has chisel toughness 2.

Corrosion and oxidation are subjects of separate chapters in these volumes and will be only briefly discussed later in this chapter.

3.1.3 Two Screening Approaches

At the start of this section we noted that two different approaches were taken by General Electric and United Technologies in screening unusual high-temperature intermetallics. They were characterized by the *Journal of Metals* as the 'materials science approach' (Fleischer and Taub, 1989) and the 'engineering approach' (Anton *et al.*, 1989). The latter was more engineering primarily in excluding alloys with expensive components, such as the platinum group metals, and those with significant

safety problems, such as Be, which must be carefully controlled when it is in fine particulate form. A more tenable distinction is that the United Technologies group tended to acquire more extensive data on the alloys studied and consequently had time to examine fewer compounds. Here we describe the two approaches as 'limited-choice, data-intensive' and 'extensive, less intensive'.

3.2 Limited-choice, Data-intensive Survey

Anton and Shah (1989, 1991a, b) and Anton *et al.* (1989) reported the results of the United Technologies approach. Originally they considered 20 binary compounds with 13 crystal structure types (Anton and Shah, 1991b). Melting temperatures ranged from 1326

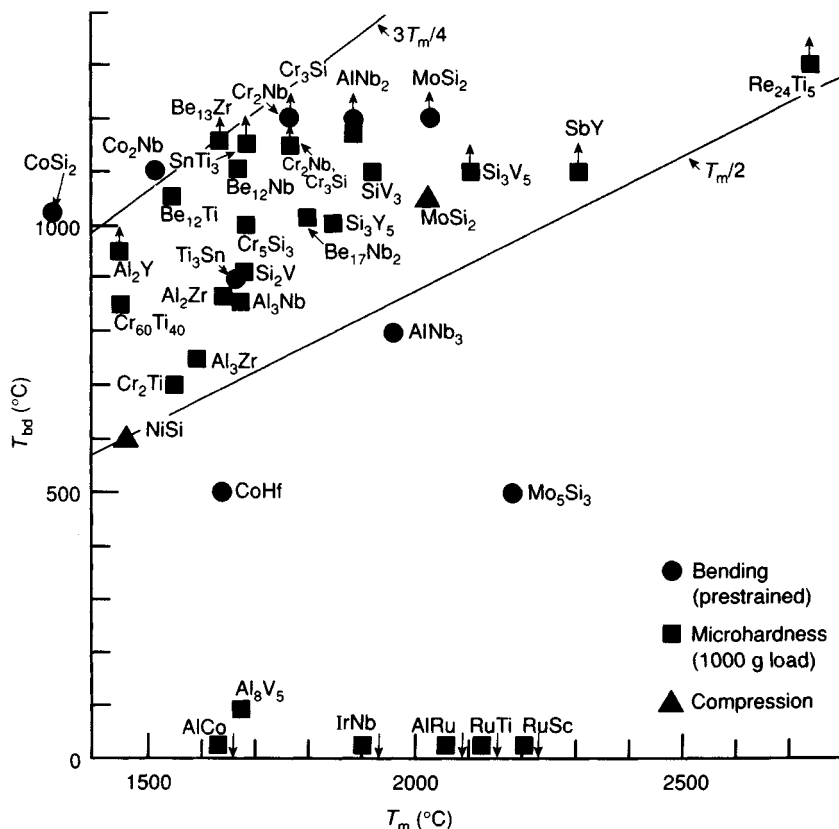


Figure 7. Brittle to ductile transition temperatures as a function of melting temperature derived from data for bending (Anton *et al.*, 1989; Anton and Shah, 1989, 1991a, b), microhardness (Fleischer and Zabala, 1989, 1990b, c), and compression of MoSi₂ (Umakoshi *et al.*, 1990) and NiSi (Savitskii, 1960). Most of the values of T_{bd} lie between $T_m/2$ and $3T_m/4$

to 2700 °C and specific gravities from 4.32 to 17.6. For moderately intensive study they chose the 10 intermetallics that are listed in Table 2. Results are also given for creep, brittle to ductile transition temperature T_{bd} , and in most cases for ultimate tensile strength and oxidation resistance. Since studies of multiple materials are most economically done by using a minimum of material, simplified methods of determining conventional quantities were devised. By bending by a sample 0.5% at high temperature, then the same sample by an additional 0.5% at a lower temperature, and so on until fracture, the transition temperature was bracketed. Creep tests were done on small compression samples and the results fitted to a relation of the form $\sigma^n \exp(-Q/kT)$, where n and Q are respectively the stress exponent and activation energy for steady-state creep. The unusually high values for CoSi₂ probably mean that this relation is not the best description of creep in that compound. Ultimate tensile strengths were

derived from outer-fiber stresses in bending tests (Anton and Shah, 1991a). For oxidation, samples were cycled between 1150 °C and room temperature. The qualitative results are included in Table 2.

Three of the silicides show low oxidation rates, but suffer from very high T_{bd} . Ultimate tensile strengths do not correlate with T_m , nor with Q .

Figure 6 from Anton and Shah (1991b) shows that many of their intermetallics and their alloys have superior creep resistance that is well above that of the state-of-the art Pratt and Whitney superalloy single-crystal blade alloy PWA 1480.

3.2.1 Summary

Two critical properties are oxidation resistance and toughness or ductility. For materials where oxidation rates are tolerable, low-temperature brittleness is particularly great. In fact all of the materials studied are

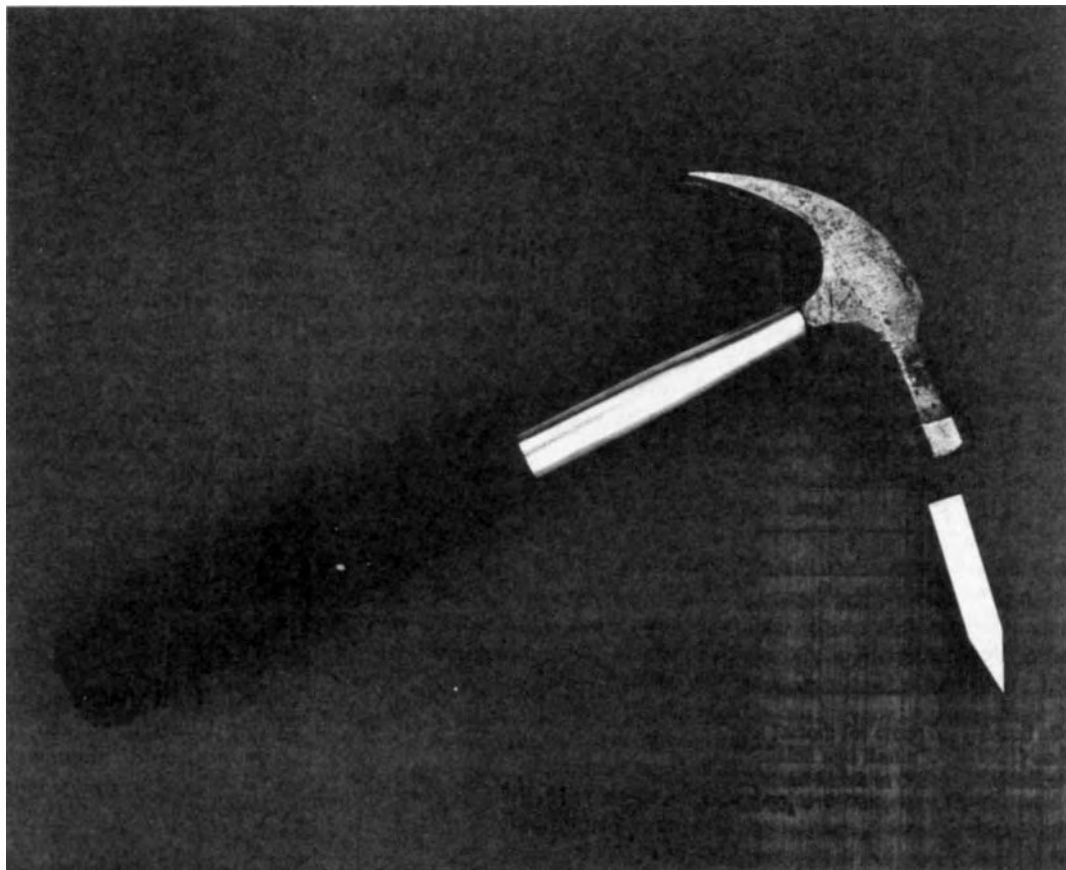


Figure 8. Tools for room-temperature measurements of toughness (Fleischer, 1991a) Reproduced by permission of the Japan Institute of Metals

brittle below 500 °C. The major positive conclusions from Table 2 and Figure 6 are that several intermetallics are strong and creep resistant at high temperature. Although brittleness makes them presently unsuitable candidates for monolithic structural use, there is hope that they can be employed as part of a composite in which a second phase imparts the desired low-temperature toughness or ductility. The reader is referred to Chapter 13 by Miracle and Mendiratta and Chapter 12 by Ardell for consideration of those prospects. Anton and Shah (1990)

and Fleischer (1990) consider possibilities for some of the systems in Tables 2 and 3.

3.3 Extensive, Less Intensive Survey

Fleischer (1991a), Fleischer *et al.* (1991), Fleischer and Field (1990), and Fleischer and Zabala (1990b) have summarized the results of the General Electric survey. More specialized aspects are given in other papers for some oxidation measurements (McKee and Fleischer,

1991), for Ti compounds (Fleischer and Zabala, 1990c), and for their elastic properties (Fleischer *et al.*, 1988); and for diverse other compounds (Fleischer and Zabala, 1990b) and their elastic properties (Fleischer *et al.*, 1989), for beryllides (Fleischer and Zabala, 1989), Cr-Nb-Ti alloys (Fleischer and Zabala, 1990a), Ir-Nb alloys (Fleischer *et al.*, 1990), Ru-Ta alloys (Fleischer *et al.*, 1991b), and Al-Ru alloys (Fleischer *et al.*, 1991c; Fleischer, 1991b).

As Table 3 indicates, the aim in these studies was to be inclusive in rapidly testing many types of crystal structures, hopefully to identify promising compounds to explore in more depth. Table 3 includes 29 binary compounds and 18 crystal structure types. T_m values range from 1450 to 2750 °C and specific gravities from 2.25 to 17.5. In these studies less conventional mechanical properties were tested as measures of strength and toughness, which allowed much information to be extracted from single samples.

3.3.1 Tests

One simplification was the choice of microhardness as a function of temperature as a surrogate for flow stress versus temperature. A brittle to ductile temperature was defined as that temperature above which cracks did not form at microhardness indentations. T_{bd} so defined does not necessarily agree with those derived from other measurements. In some cases it does; in others it is highly discrepant. Figure 7 shows that data from Tables 2 and 3 and from two compression-based T_{bd} measurements lie in the upper left, the notable exceptions being several B2 (cP2) and L1₀ (tP4) compounds. Some of these are indeed tough at room temperature (as shortly will be shown), but two of them, AlCo and RuTi, are brittle in bending even though cracks do not form at Vickers microhardness indentations using the standard 1 kg load.

Another set of observations whose test equipment both looks and is remarkably simple is the chisel test (Figure 8). By breaking samples with a set of graded blows using a light (160 g) or, if necessary, heavy (729 g) hammer (Fleischer and Zabala, 1990b, c), a four-level chisel toughness scale is defined, where 0 is highly brittle and 3 is the case where no fracture could be produced. Although this is by no means an absolute scale, it gives useful, reproducible relative values that correlate with the possibility of ductility. Figure 9 shows that high ductility in compression occurs only in samples of high chisel toughness (CT), so that the pool of high-CT samples is a proper catalog to search for tough intermetallics.

In the third set of measurements room-temperature elastic constants were obtained by conventional pulse-echo ultrasonic measurements (Fleischer *et al.*, 1988, 1989; Fleischer and Field, 1990). Extensive elastic data are given by Fleischer *et al.* (1988, 1989), Fleischer and Field (1990), Fleischer (1991b) and Nakamura, Chapter 37 in Volume 1.

3.3.2 Results

Many high- T_m intermetallics are hard and remain hard to high temperatures, i.e. above $T_m/2$. For others the hardness declines monotonically with temperature (Fleischer, 1989), as shown in Figure 10. Those that remain hard decrease in hardness so slightly that if they were normalized to the typical temperature variation of the elastic moduli the values would not decrease, implying that no thermally activated deformation occurs. Brittleness is therefore expected, and it is observed. Compounds such as Al₃Nb appear to allow thermally activated deformation, and some (but not all) similarly behaving alloys do show plasticity at room temperature.

Those that do display significant room-temperature plasticity were first recognized through the chisel toughness test—the results are given in Table 3. Fracture

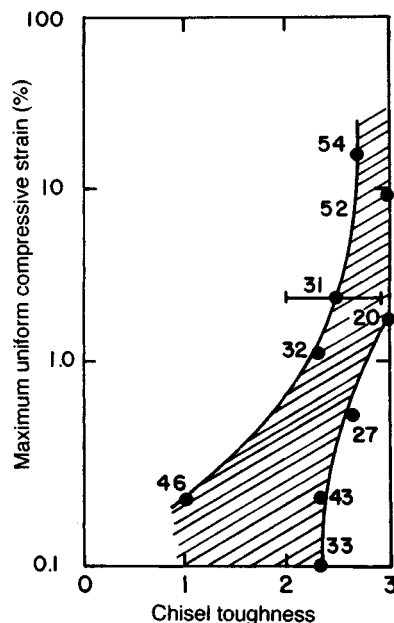


Figure 9. Chisel toughness versus plastic strain to maximum load in compression. Only tough alloys have strains of more than 1% (Fleischer, 1990). Each point has a sample identification number

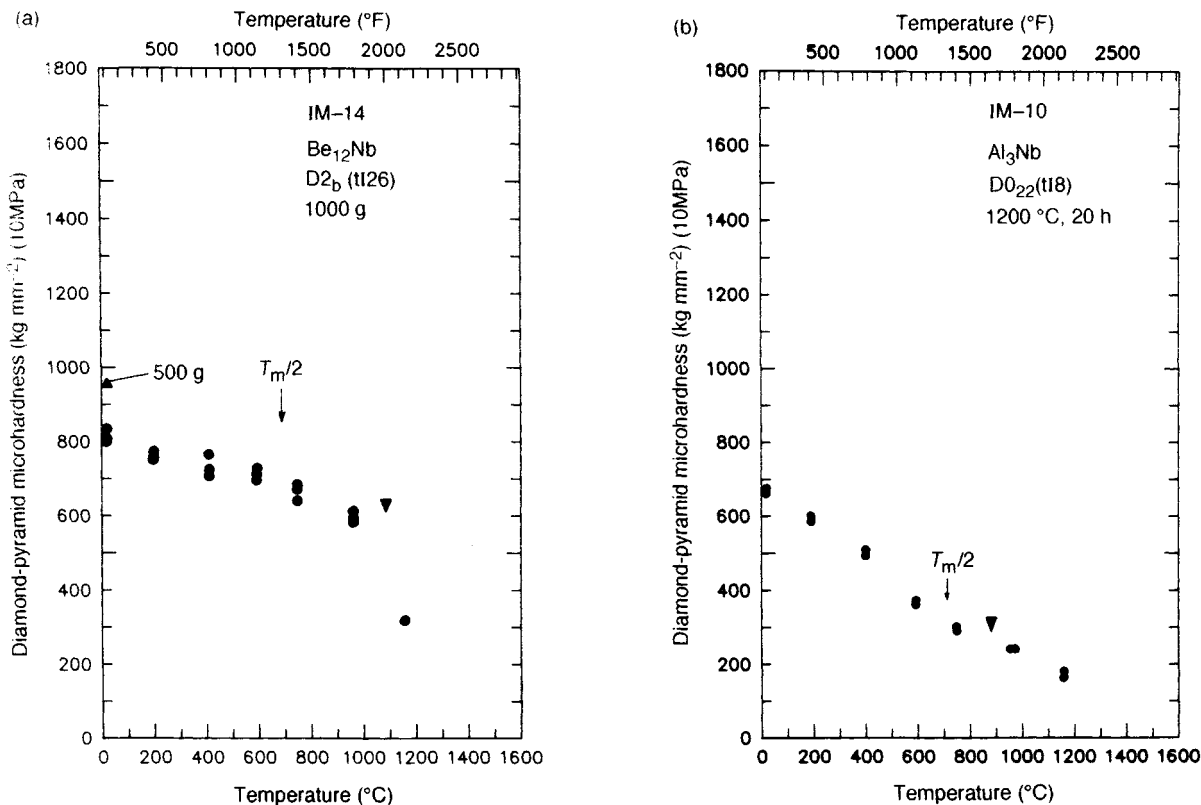


Figure 10. Diamond-pyramid microhardness h versus temperature for (a) Be_{12}Nb and (b) Al_3Nb . The black triangle gives the temperature above which cracks are not found at indentations. For the complicated D_{2b} (t126) structure Be_{12}Nb , h decreases by only 16% from 23 °C to $T_m/2$; for the simpler $\text{D}_{0_{22}}$ (t18) structure Al_3Nb , h drops by 54% over the same range (Fleischer, 1989)

Table 4. Properties of tough binary compounds

Compound	AlRu	IrNb	RuSc	RuTa ^a
Structure type	B2	L1 ₀	B2	L1 ₀
Specific gravity	7.95	15.20	7.40	14.83
Young's modulus (GPa)	267	268	155	250
Melting temperature (°C)	2060	1900	2200	2080
Microhardness (GPa)				
at 23 °C	3.1	6.9	2.9	9.1
at 1000 °C	2.0	4.0	1.5	2.2

^aAverage of $\text{Ru}_{51}\text{Ta}_{49}$ and $\text{Ru}_{49}\text{Ta}_{51}$.

in 29 of the 30 compounds in this table is transgranular. Only AlRu with more than 50% Al showed intergranular fracture, and that behavior was minimized by adding 0.5% boron. Four alloys have given CT values of 3 or 3-. Some of their properties are given in Table 4 (Fleischer, 1991a), and examples of compressional stress-strain curves appear in Figure 11. The curves in Figure 11 include variants of the L1₀ (tP4) compounds

RuTa and IrNb ($\text{Fe}_{10}\text{Ru}_{45}\text{Ta}_{45}$ and $\text{Ir}_{25}\text{Ni}_{25}\text{V}_{50}$) and the B2 (cP2) compounds AlRu ($\text{Al}_{47}\text{Ru}_{53}$ plus 0.5% B) and RuSc. The two L1₀ compounds have small but definite plastic strain prior to fracture; the two B2 compounds show much greater plasticity.

The existence of toughness at room temperature is a precious quality since even materials for use at high temperature spend most of their life at ambient temperatures, and some forgiveness for human errors in processing and subsequent handling aids reliability. Once compounds with desirable properties are found, the next step in development is to alloy in order to improve the balance of properties. For example, Figure 6 shows data in which Anton and Shah (1991b) concentrated on alloying AlNb_3 , AlNb_2 , Co_2Nb , Cr_2Nb , Cr_3Si , MoSi_2 , and Mo_5Si_3 , and measured creep at 1200 or 1400 °C for the binary compounds and for 14 alloys based on those binaries. We now turn to alloying of the tough intermetallics.

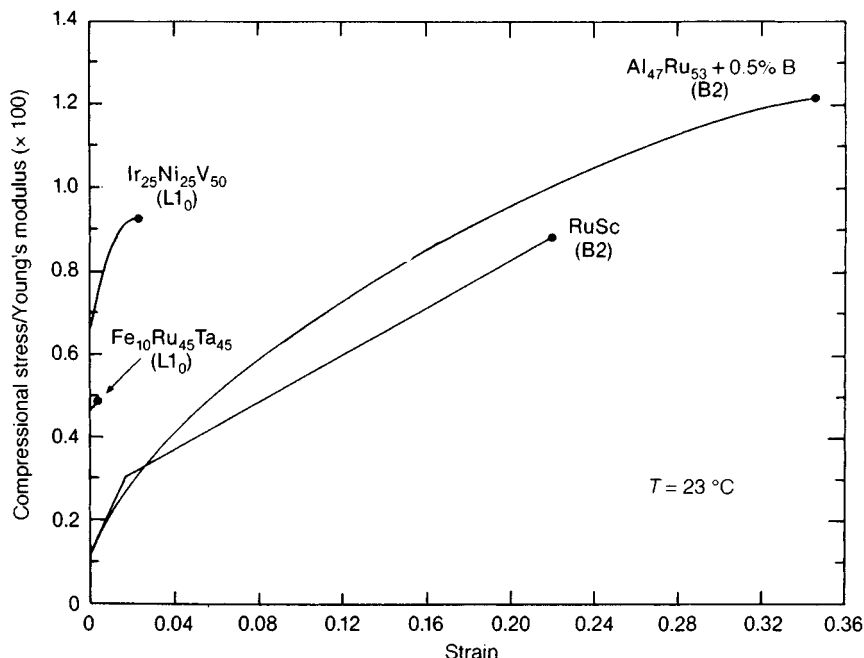


Figure 11. Compressional stress-strain behavior of four tough alloys, normalized to their Young's moduli

3.4 Special Tough Intermetallics

Tables 3 and 4 and Figure 11 indicate several good properties of two B2 and two $L1_0$ compounds. Since damage tolerance at ambient temperature is a rare and desirable property, three of the four were chosen for further alloying. On the basis of 1986 cost [US\$9300 kg^{-1} for IrNb, US\$3800 kg^{-1} for RuSc, US\$1800 kg^{-1} for AlRu, and US\$900 kg^{-1} for RuTa (Taub, 1986)], RuSc and IrNb were considered for deletion. However, see section 3.4.1.

3.4.1 IrNb

In spite of its being expensive, IrNb, because it or a variant might be a candidate to replace still more expensive Ir in radioisotope thermoelectric generators, was the subject of multiple experiments to replace Ir with Co or Fe (Fleischer *et al.*, 1990). Of these, 10% Co for Ir was the least deleterious addition. Toughness was retained, and strengthening to 750 °C was attained, but at the cost of cracks appearing at hardness indentations below 600 °C. Toughening appeared to be associated with extensive fine-scale twinning in some cases and an intimate mixture of the $L1_0$ and an

orthorhombic phase (nominally $\text{Ir}_{11}\text{Nb}_9$) in others. This phase conceptually can be derived from the $L1_0$ by passing a series of twinning dislocations along a single set of parallel planes.

3.4.2 RuTa

The best of the tough high-temperature alloys on the basis of cost per unit weight is RuTa. Like IrNb it commonly has a highly twinned lamellar structure or a lamellar microstructure composed of alternating phases, in this case the $L1_0$ and B2 structures (Fleischer *et al.*, 1991b). Here, alloying was more successful, replacements of Ru by 15 to 30 at% Co and by up to 15 at% Fe giving tough alloys. Those with 15% Fe or 10% Co also had improved strength (as inferred from hardness) up to 1150 °C. The benefits in toughness, strength, and price are to be balanced against a decrease in Young's modulus of 1.5% per at% of alloying addition.

3.4.3 AlRu

The most promising of the tough intermetallics is AlRu. On a cost per unit volume or per unit elastic stiffness

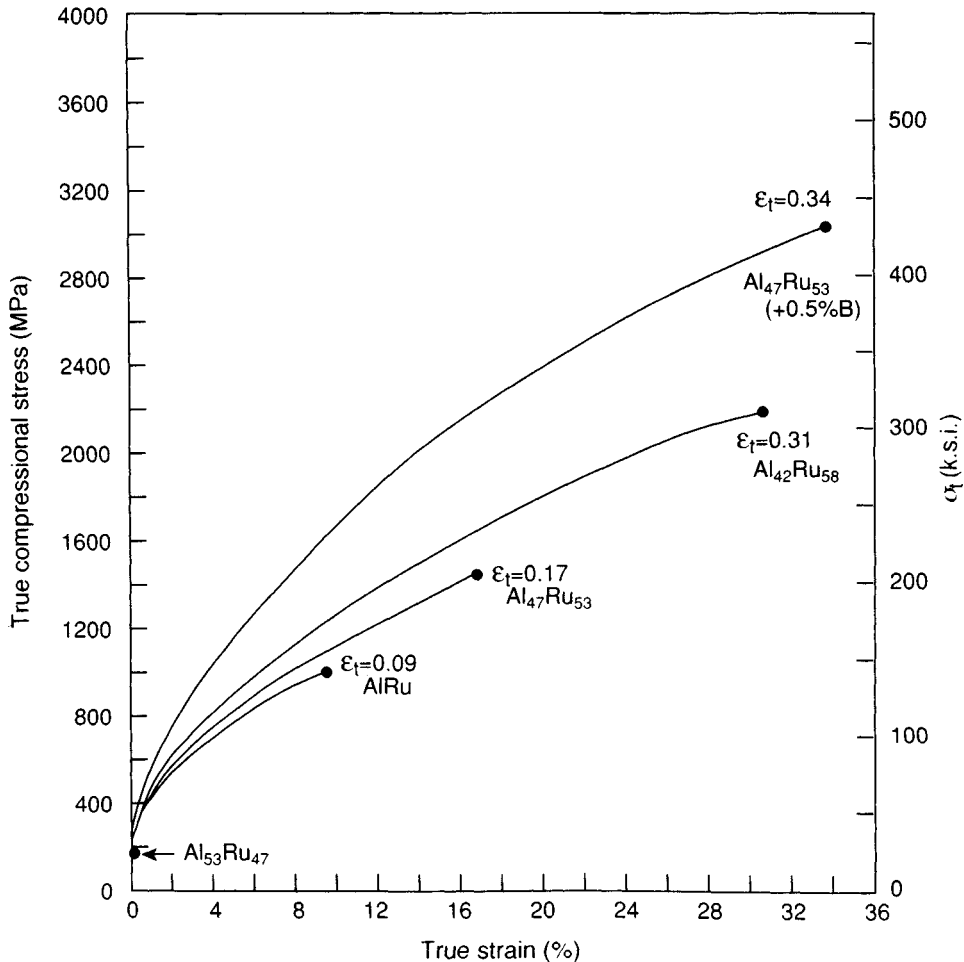


Figure 12. Compressional stress-strain curves of five Al-Ru Alloys. Al-rich alloys are intergranularly brittle. Ru-rich alloys consist of B2 AlRu grains coated by A3 (hP2) Ru (Fleischer, 1991a)

basis it is equal to RuTa, but it has far greater ductility (Fleischer *et al.*, 1991c) and oxidation resistance (McKee and Fleischer, 1991). Observed slip vectors of $\langle 111 \rangle$, as well as $\langle 100 \rangle$ and $\langle 110 \rangle$, insure that ample slip systems are available for polycrystalline deformation. Alloying with 0.5% B has been successful in enhancing ductility (and suppressing the intragranular fracture that occurs in Al-rich AlRu), and 4 or 5% Sc enhances high-temperature strength (Fleischer *et al.*, 1991c) without compromising low-temperature toughness (Fleischer, 1991b). As Figure 12 shows, an excess of Ru increases strength and ductility. The published oxidation measurements (McKee and Fleischer, 1991) imply that unprotected $\text{Al}_{47}\text{Ru}_{53}$ could be used in oxidizing

environments to $\sim 1250^\circ\text{C}$. IrNb and RuTa would require protective coatings that are yet to be devised.

3.4.4 Ternary Alloys

Recently, Waterstrat *et al.* (1993) showed that a ternary B2 (cP2) structure $\text{Zr}(\text{Pd}_{0.7}\text{Ru}_{0.3})$ has both toughness and tensile ductility. Although cracks formed at about 1% tensile strain, macroscopic fracture was at greater than 6% strain. Slip with $\langle 100 \rangle$ slip vectors was accompanied by $\{114\}$ twinning, which was suggested as the mechanism that allowed plasticity. T_m is $1760 \pm 10^\circ\text{C}$ (R. M. Waterstrat, personal communication). Earlier work (Moberly *et al.*, 1990) on another B2 (cP2) alloy

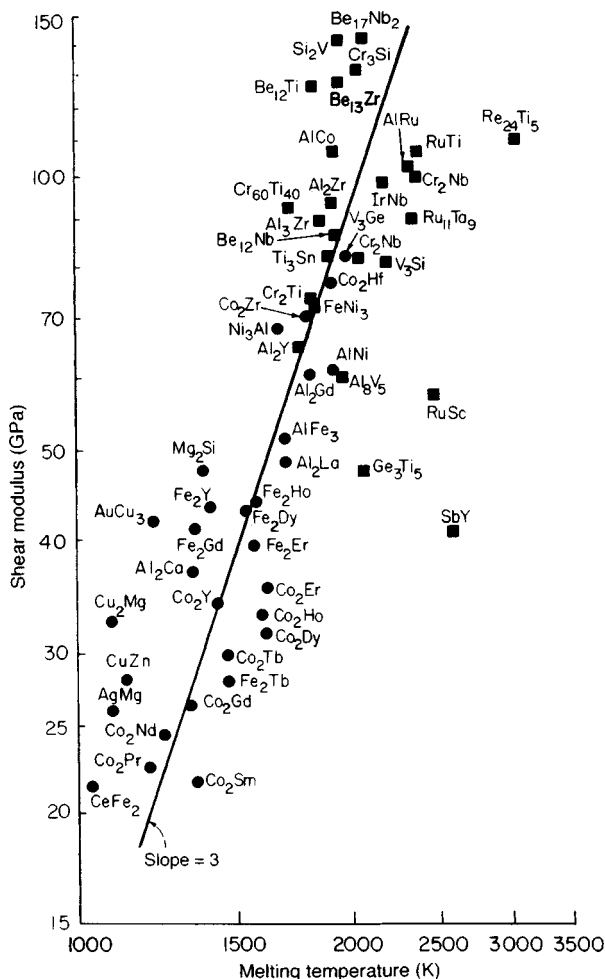


Figure 13. Shear moduli at 23 °C of intermetallic compounds as a function of their melting temperatures. Earlier data are given by filled circles, General Electric data by squares (Fleischer, 1991a) Reproduced by permission of the Japan Institute of Metals

with a lower melting temperature (~ 1300 °C) showed $\text{Ti}(\text{Ni}_{0.94}\text{Fe}_{0.06})$ to have $<25\%$ tensile ductility and the same $\langle 100 \rangle$ slip and $\{114\}$ twinning deformation modes.

4. Systematics, Trends, and Conclusions

Having described extensive searches for compounds with special high-temperature strength and stiffness and room-temperature toughness, it is worth reviewing the assumptions of the two most extensive surveys, in

particular that strength and stiffness would increase with melting temperature.

4.1 Elastic Moduli versus Melting Temperature

Do moduli increase with T_m ? Figure 13 tests the relationship (Fleischer, 1991a). The answer is that there is a trend, but with wide fluctuations. At any temperature widely varying values of the shear modulus G can be found. On the other hand, seeking high- T_m materials was clearly productive, since the highest values of G obtain only for high T_m . The assumption was useful, but the relation is not deterministic.

4.2 Microhardness versus Melting Temperature

As a measure of strength, microhardness is widely available. Figure 14 shows a collection of hardness versus T_m data, mostly those collected by Paufler (1976), with additions from the General Electric studies (Fleischer and Zabala, 1990b, c) and from Ivanko (1971). The expectation of correlation is less direct than for elastic moduli (moduli increase with T_m , and strength increases with moduli), and the correlation is even more statistically variable than that in Figure 13. Nevertheless, it is true that the highest values of microhardness occur among the materials with the highest T_m values. In short, they were indeed appropriate materials to scan for high-strength materials.

4.3 Simple versus Complicated Crystal Structures

It is noteworthy that the four high-temperature compounds that were found to have the critical property of being tough at room temperature as single-phase materials are of either B2 (cP2) or $L1_0$ (tP4) structure. With two or four atoms per unit cell, these are among the simpler ordered structures; and the best of the group, B2 (cP2), is the simplest imaginable, high-symmetry ordered structure. Complicated structures will have large unit cells and therefore large Burgers vectors for dislocations. The observations are consistent with the belief that dislocations of large Burgers vectors will require large stresses for their motion, giving strong crystals, but magnifying the possibility of opening cracks and producing brittle failure.

4.3.1 Costs

As a scientific matter, the four tough compounds were recognized because cost was not a criterion in the initial

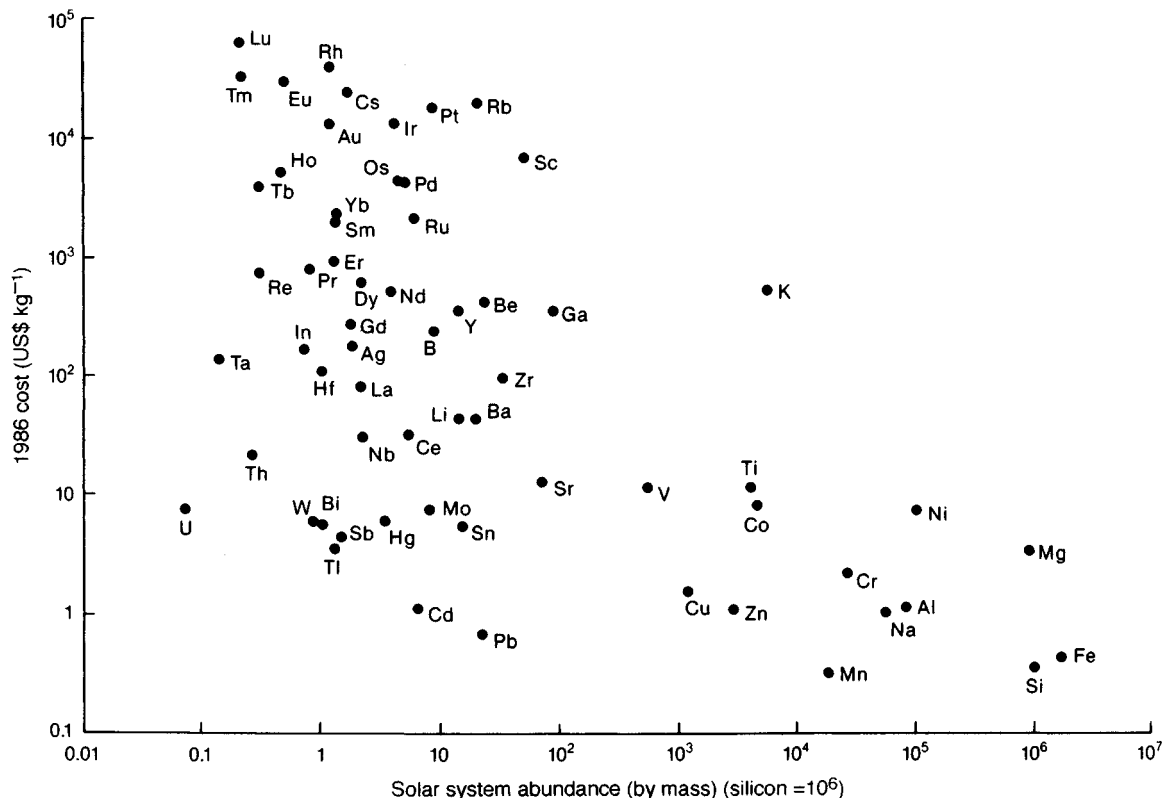


Figure 15. Cost versus abundance for metals. The cost data were assembled by Taub (1986); the solar system abundance came from analysis of meteorites and solar spectra (Fleischer, 1991a). Reproduced by permission of the Japan Institute of Metals.

selection process. When practical choices are made, however, cost must enter as a major consideration. Each of the four involves a platinum group element, Ru at US\$2250 kg⁻¹ being far less expensive than Ir. This is a 1989 price in a very limited market (~10⁵ ounces per year). What change in price would accompany a greatly increased demand is not known. As an indication of the volatility of the price of ruthenium, in August 1993 it was offered at US\$ 970 kg⁻¹, and in September 1993 at US\$ 420 to 700 kg⁻¹. Price could increase with demand. However, Figure 15 shows that cost and natural abundance are only weakly correlated. For example, uranium is both rare and inexpensive. Alternatively, economies of scale could enter and lower prices, as did occur for Re. And further successful alloying may show how to lower the fractions of the alloys that consist of expensive components.

4.4 The Future

Two routes are worth considering for producing higher-temperature materials from high-temperature intermetallics. This chapter has concentrated on monolithic,

nearly single-phase structures. For these the inherent room-temperature toughness and ductility are critical, and these lead to the choices considered in Section 3.4.

A massive gap in the intermetallics considered is the omission here of the ternary and higher-order single-phase compounds, whose number is immense but uncertain (Villars, Chapter 11 in Volume 1). Data for such compounds are sparse. Hardness versus temperature is given for a few ternary compounds by Westbrook (1957) and Vulf (1960). There is an indication that binary alloys decrease in hardness with temperature more rapidly than do related ternary alloys. It is premature to state whether there are significant prospects for enhanced toughness or ductility in ternary alloys.

The alternative—composite structures—is considered Chapter 13, by Miracle and Mendiratta, in this volume. Toughness must be attained here too, but multiple approaches are possible, not all of these strongly dependent on the room-temperature properties of the intermetallic compound that is used. Many of the other compounds that are strong at high temperature but brittle at ambient temperatures can

therefore be candidates for supplying part of the special properties that are required in a successful composite. Nevertheless, some ductility in the intermetallic component is a very useful quality to have available, and the routes described here to such properties may facilitate the finding of composites of better quality.

5. Acknowledgements

The author thanks D. L. Anton and J. H. Westbrook for supplying helpful information.

6. References

- Anton, D. L., and Shah, D. M. (1989). *Mater. Res. Soc. Symp. Proc.*, **133**, 361.
- Anton, D. L., and Shah, D. M. (1990). *Mater. Res. Soc. Symp. Proc.*, **194**, 45.
- Anton, D. L., and Shah, D. M. (1991a). *Mater. Res. Soc. Symp. Proc.*, **213**, 733.
- Anton, D. L., and Shah, D. M. (1991b). In *Development Potential of Advanced Intermetallic Materials*, Final Report WRDC-TR-90-4122. Submitted to US Air Force, Wright-Patterson Air Force Base, OH.
- Anton, D. L., Shah, D. M., Duhl, D. M., and Giamei, A. F. (1989). *J. Met.*, **41** (No. 9), 12.
- Baker, I., and Monroe, P. J. (1990). In *High Temperature Aluminides and Intermetallics* (eds S. H. Whang, C. T. Liu, D. P. Pope, and J. O. Stiegler). AIME, Warrendale, PA, p. 425.
- Banerjee, D., Gogia, A. K., Nandy, T. K., and Joshi, V. (1988). *Acta Metall.*, **36**, 87.
- Fine, M. E., Brown, L. D., and Marcus, H. L. (1984). *Scripta Metall.*, **18**, 951.
- Fleischer, R. L. (1959). *Acta Metall.*, **7**, 134.
- Fleischer, R. L. (1962). *J. Appl. Phys.*, **33**, 3504.
- Fleischer, R. L. (1985). *J. Met.*, **37**(12), 16.
- Fleischer, R. L. (1987a). *J. Mater. Sci.*, **22**, 2281.
- Fleischer, R. L. (1987b). *Acta Metall.*, **35**, 2129.
- Fleischer, R. L. (1988). *J. Mater. Sci. Lett.*, **7**, 525.
- Fleischer, R. L. (1989). *Mater. Res. Soc. Symp. Proc.*, **133**, 305.
- Fleischer, R. L. (1990). *Mater. Res. Soc. Symp. Proc.*, **194**, 249.
- Fleischer, R. L. (1991a). In *Proc. Int. Symp. Intermetallic Compounds* (ed. O. Izumi). The Japan Institute of Metals, Sendai, p. 157.
- Fleischer, R. L. (1991b). *ISIJ Int.*, **31**, 1186.
- Fleischer, R. L. (1992). *Scripta Metall. Mater.*, **27**, 799.
- Fleischer, R. L. (1993a). *J. Mater. Res.*, **7**, 49.
- Fleischer, R. L. (1993b). *J. Mater. Res.*, **7**, 59.
- Fleischer, R. L. (1993c). *Acta Metall. Mater.*, **41**, 863.
- Fleischer, R. L. (1993d). *Acta Metall. Mater.*, **41**, 1197.
- Fleischer, R. L. (1993e). *Mater. Res. Soc. Symp. Proc.*, **288**, 165.
- Fleischer, R. L. (1993f). In *Structural Intermetallics* (eds R. Darolia, J. J. Lewandowski, C. T. Liu, P. L. Martin, D. B. Miracle, and M. V. Nathal). The Minerals, Metals and Materials Society, Warrendale, PA, p. 691.
- Fleischer, R. L., Gilmore, R. S., and Zabala, R. J. (1988). *J. Appl. Phys.*, **64**, 2964.
- Fleischer, R. L., Gilmore, R. S., and Zabala, R. J. (1989). *Acta Metall.*, **37**, 2801.
- Fleischer, R. L., Field, R. D., Denike, K. K., and Zabala, R. J. (1990). *Metall. Trans.*, **21A**, 3063.
- Fleischer, R. L., Brian, C. L., and Field, R. D. (1991a). *Mater. Res. Soc. Symp. Proc.*, **213**, 463.
- Fleischer, R. L., Field, R. D., and Briant, C. L. (1991b). *Metall. Trans.*, **22A**, 129.
- Fleischer, R. L., Field, R. D., and Briant, C. L. (1991c). *Metall. Trans.*, **22A**, 403.
- Fleischer, R. L., and Field, R. D. (1990). In *Development Potential of Advanced Intermetallic Materials*, Final Report WRDC-TR-90-4046. Submitted under Contract F33615-86-C-5055 to US Air Force, Wright-Patterson Air Force Base, OH.
- Fleischer, R. L., and Taub, A. I. (1989). *J. Met.*, **41**(9), 8.
- Fleischer, R. L., and Zabala, R. J. (1989). *Metall. Trans.*, **20A**, 1279.
- Fleischer, R. L., and Zabal, R. J. (1990a). *Metall. Trans.*, **21A**, 2149.
- Fleischer, R. L., and Zabala, R. J. (1990b). *Metall. Trans.*, **21A**, 2709.
- Fleischer, R. L., and Zabala, R. J. (1990c). *Metall. Trans.*, **21A**, 1951.
- Frommeyer, G. R., Rosenkranz, R., and Lüdecke, C. (1990). *Z. Metallk.*, **81**, 307.
- Frost, H. J., and Ashby, M. F. (1982). *Deformation Mechanism Maps*. Pergamon Press, Oxford.
- Ivanko, A. A. (1971). In *Handbook of Hardness Data* (ed. G. V. Samsonov). First published by Akad. Sci. Ukrainian SSSR (Kiev, 1968). English translation by Israel Program for Scientific Translations, Jerusalem.
- Johnson, L. A. (1985). Personal communication.
- Johnston, W. G. (1962). *J. Appl. Phys.*, **33**, 2716.
- Johnston, W. G., and Gilman, J. J. (1959). *J. Appl. Phys.*, **30**, 129.
- Livingston, J. D. (1992). *Phys. Stat. Sol. (A)*, **131**, 415.
- Livingston, J. D., Hall, E. L., and Koch, E. F. (1989). *Mater. Res. Soc. Symp. Proc.*, **133**, 243.
- McKee, D. W., and Fleischer, R. L. (1991). *Mater. Res. Soc. Symp. Proc.*, **213**, 969.
- Mehl, M. J., Osburn, J. E., Papaconstantopoulos, D. A., and Klein, B. M. (1990). *Phys. Rev. B.*, **41**, 10 311.
- Mishima, Y., Ochiai, S., Hamed, N., Yodogawa, M., and Suzuki, T. (1986a). *Trans. Japan Inst. Met.*, **27**, 648.
- Mishima, Y., Ochiai, S., Hamed, N., Yodogawa M., and Suzuki, T. (1986b). *Trans. Japan Inst. Met.*, **27**, 656.
- Moberly, W. J., Proft, J. L., Duerig, T. W., and Sinclair, R. (1990). *Acta Metall.*, **38**, 2601.
- Moran, J. B. (1965). *Trans. AIME*, **233**, 1473.

- Paufler, P. (1976). In *Intermetalliche Phasen*, VEB Deutscher Verlag für Grundstoffindustrie, Leipzig, pp. 165–187.
- Paufler, P., Marschner, J., and Schulze, G. E. R. (1970). *Phys. Stat. Sol.*, **40**, 573.
- Paufler, P., Marschner, J., and Schulze, G. E. R. (1971). *Phys. Stat. Sol.*, **43**, 279.
- Paufler, P., and Schulze, G. E. R. (1967). *Phys. Stat. Sol.*, **24**, 77.
- Read, W. T. (1953). *Dislocations in Crystals*. McGraw-Hill, New York.
- Sauthoff, G. (1986). *Z. Metallk.*, **77**, 654.
- Sauthoff, G. (1989). *Z. Metallk.*, **80**, 337.
- Sauthoff, G. (1990a). *Z. Metallk.*, **81**, 855.
- Sauthoff, G. (1990b). In *High Temperature Aluminides and Intermetallics* (eds S. H. Whang, C. T. Liu, D. P. Pope, and J. O. Stiegler). AIME, Warrendale, PA, p. 329.
- Savitskii, E. M. (1960). In *Mechanical Properties of Intermetallic Compounds* (ed. J. H. Westbrook). John Wiley & Sons, Inc., New York, p. 87.
- Stonehouse, A. J., Paine, R. M., and Beaver, W. W. (1960). In *Mechanical Properties of Intermetallic Compounds* (ed. J. H. Westbrook). John Wiley & Sons, Inc., New York, p. 297.
- Taub, A. I. (1986). Unpublished research.
- Umakoshi, Y., Sakagami, T., Hirano, T., and Yamane, Y. (1990). *Acta Metall.*, **38**, 909.
- von Mises, R. (1928). *Z. Angew. Math. Mech.*, **8**, 161.
- Vulf, B. K. (1960). *Russ. Chem. Rev.*, **29**, 364.
- Waterstrat, R. M., Bendersky, L. A., and Kuentzler, R. K. (1993). *Mater. Res. Soc. Symp. Proc.*, **246**, 115.
- Westbrook, J. H. (1957). *Trans. AIME*, **209**, 899.
- Westbrook, J. H. (ed.) (1960). *Mechanical Properties of Intermetallic Compounds*. John Wiley & Sons, Inc., New York.
- Yamaguchi, M., and Umakoshi, Y. (1990). *Prog. Mater. Sci.*, **34**, 1.

This chapter was originally published in 1995 as Chapter 11 in *Intermetallic Compounds*, Vol. 2: *Practice*, edited by J. H. Westbrook and R. L. Fleischer.

Addendum

The preceding prior survey of ‘novel’ intermetallics, primarily for possible high-temperature uses, found many compounds with low-temperature brittleness and only occasional prospects for a combination of resistance to fracture and strength while hot. The most promising compound that was examined for these purposes is AlRu. It and several of its alloys showed very good toughness at room temperature, room-temperature plasticity up to compressive strains exceeding 0.3, a melting temperature of 2330 K, and hardness that persists to at least 1470 K. This brief update describes some of the subsequent advances in the understanding of the deformation, properties, processing, and uses of AlRu. It also gives references to progress on a few other ‘novel intermetallics.’

Lu and Pollock (1999) used transmission electron microscopy to identify dislocations in AlRu(+0.5 at.% boron) produced by deformation at 77 K and 295 K. Three slip vectors were present; $\langle 100 \rangle$ (frequent), $\langle 110 \rangle$ (frequent), and $\langle 111 \rangle$ (occasional). Slip traces on $\{110\}$ planes were observed. The multiplicity of slip systems means that arbitrary uniform deformation is possible, which requires five independent systems to be available; and that criterion is more than sufficient to allow ductility, since it is known that

non-brittle deformation is possible with still fewer systems (Fleischer, 1987). Thus Lu and Pollock have provided reasons for the observed unusual ductility of AlRu.

Other mechanical properties of AlRu-based intermetallics are given by Wolff and Sauthoff (1996a,b) and by Wolff *et al.* (1997). Replacing half of the Ru with Ni led to a striking reduction in the ductility (Wolff and Sauthoff, 1996a). Increasing the Ru content to 70%, which produces a AlRu–Ru eutectic, leads to major strengthening relative to AlRu—an increase in stress at 0.002 strain that persists to at least 1570 K (Wolff and Sauthoff, 1996b). However, the compressive strain to fracture is cut in half. Wolff *et al.* (1997) show effects on microhardness of substitutions for Ru of Co, Ni, and Ti—each of which gradually raises the hardness. The addition of Co reduces the toughness (Fleischer, 1993), as does the replacement of Al by Ti. Wolff *et al.* do not report on ductility for these alloys.

Wolff (1997) describes a variety of properties of AlRu. Most notable is the aqueous corrosion resistance. Mass-loss (linear corrosion) rates are given for three compositions (AlRu, Al₅₃Ru₄₇, and Al₄₇Ru₅₃ + 0.5% B) in an assortment of reagents that includes HNO₃, aqua regia, H₂SO₄, HCl, HF, NaOCl, NaCl, and Cl in

water. Temperatures up to 310 K were used. And most of the rates were in the range 0 to 0.08 mm/yr. Only for sodium hypochlorite was higher mass loss seen—up to 52 cm/yr.

Processing of AlRu presents problems—as is to be expected for a material that melts at so high a temperature. Arc melting, followed by electrical discharge machining was suitable for experimental testing (Fleischer, 1993), but it is cumbersome for wider use. Wolff (1996) describes a promising alternative, reactive hot isostatic pressing of mixed powders of Al and of Ru. The energy release due to the formation energy of AlRu supplies local heating and hot pressing allows an approach to full density. After pressing at 770 to 970 K, sintering was carried out 1470 K.

In two papers Wolff (1997,1999) has described a number of technological uses, or potential uses, of AlRu. Corrosion resistance, as noted above, is one special feature. AlRu can be used as a coating that is laid down by physical vapor deposition or by electroplating. It also has relatively good electrical and thermal conductivity and hence may be well suited for electrical contacts in electronic devices. Corrosion resistance and high-temperature strength are combined properties that are utilized in electrodes for spark plugs. Trial prototypes have reached the present target of 60 000 km in automobile engines—and at a material cost of about 3% of that of platinum electrodes.

Among other intermetallics, the drive toward better toughness has utilized several compounds—mostly as components of composite materials. Although these do not strictly fit within the present discussion of single-phase materials, they are referenced here, so that the interested reader can seek out more extensive literature. The base intermetallics are Ti_2AlNb (Nandy and Banerjee, 1997), NiTi (Murakami *et al.*, 1997), Nb_3Al (Nomura *et al.*, 1997), MoSi_2 (Hebsur and Nathal, 1997), and various Ti and Mo silicides (Mitra *et al.*, 1997). The use of the particular base compounds was in some cases motivated by the hope of improved

ductility in compounds with relatively high ratios of the bulk modulus K to the shear modulus G . Cottrell (1997) has noted a trend for ductility for $G/K < 0.4$, the idea being that if shear is relatively easy, plastic deformation by motion of dislocations is facilitated. My extensive data from General Electric (a letter to A. H. Cottrell, 1 July, 1997) shows that a better divider is $G/K = 0.5$, but that exceptions to this first-order relation abound.

References

- Cottrell, A. H. (1997) *MRS Bull.*, **22**(No. 5, May), 15.
- Fleischer, R. L. (1987). *Acta Metall.*, **35**, 2129.
- Fleischer, R. L. (1993). *Acta Metall. Mater.*, **41**, 1197.
- Hebsur, M. G., and Nathal, M. V. (1997). In *Structural Intermetallics*. (eds. M. V. Nathal, *et al.*). Minerals, Metals, and Materials Soc., p. 949.
- Lu, D. C., and Pollock, T. M. (1999). *Acta Mater.*, **47**, 1035.
- Mitra, R., Prasad, N. F., Rao, A. V., and Mahajan, Y. R. (1997). In *Structural Intermetallics*. (eds. M. V. Nathal, *et al.*). Minerals, Metals, and Materials Soc., p. 959.
- Murakami, H., Warren, P. J., Kumeta, K., Koizumi, Y., and Harada, H. (1997). In *Structural Intermetallics*. (eds. M. V. Nathal, *et al.*). Minerals, Metals, and Materials Soc., p. 877.
- Nandy, T. K., and Banerjee, D. (1997). In *Structural Intermetallics*. (eds. M. V. Nathal, *et al.*). Minerals, Metals, and Materials Soc., p. 777.
- Nomura, N., Yoshimi, K., and Hanada, S. (1997). In *Structural Intermetallics*. (eds. M. V. Nathal, *et al.*). Minerals, Metals, and Materials Soc., p. 923.
- Wolff, I. M. (1996). *Metall. Mater. Trans.*, **27A**, 3688.
- Wolff, I. M. (1997). *JOM January*, p. 34.
- Wolff, I. M. (1999). *S. African J. Science*, **95**, 539.
- Wolff, I. M. and Sauthoff, G. (1996a). *Metall. Mater. Trans.*, **27A**, 1395.
- Wolff, I. M. and Sauthoff, G. (1996b). *Metall. Mater. Trans.*, **27A**, 2642.
- Wolff, I. M., Sauthoff, G., Cornish, L. A., DeV. Steyn, H., and Coetzee, R. (1997). In *Structural Intermetallics*. (eds. M. V. Nathal, *et al.*). Minerals, Metals, and Materials

Chapter 9

FeAl and Fe₃Al

Krishna Vedula

Iowa State University, Ames, IA 50011, USA

1. Introduction

Iron aluminides based on Fe₃Al and FeAl are ordered intermetallic alloys that offer good oxidation resistance, excellent sulfidation resistance, and potentially lower cost than many high-temperature structural materials. They have low densities in the range 5.4–6.7 g cm⁻³, which is about 30% lower than that of commercial high-temperature structural materials such as stainless steels and superalloys, and they therefore offer better strength to weight ratios. In addition, they have the potential for reducing the use of strategic elements such as Cr in materials for such applications. However, limited ductility at ambient temperature and a sharp drop in strength above about 873 K have been major deterrents to their acceptance for structural applications. Recent studies (Sikka *et al.*, 1991a; McKamey, 1990) have shown that adequate engineering ductility of 15 to 20% can be achieved, at least in Fe₃Al-based alloys, through control of composition and microstructure. Because of these advances, interest is renewed in the use of iron aluminides for a wide range of applications. Iron aluminides based on FeAl are somewhat more difficult to consider than Fe₃Al for structural applications on account of the more brittle behaviour that results from the higher aluminum content. Nevertheless, the additional advantage in density has led to a large number of recent research activities on these alloys as well. However, prior to commercial applications, a full understanding of their processing and fabrication parameters is essential.

2. Phase Stability and Defect Structures

The Fe–Al phase diagram in Figure 1 (Vedula and Stephens, 1987) has been modified from the Metals Handbook (ASM, 1973) such that it is in general agreement with recent investigations (Swann *et al.*, 1969, 1970, 1972; Allen and Cahn, 1975, 1976). FeAl has the ordered cubic B2 (cP2) crystal structure in the range 35–50 at% Al, and Fe₃Al has the ordered cubic D0₃ (cF16) crystal structure in the vicinity of Fe–25Al (all compositions in at% unless stated otherwise). The crystal structures of the two phases of interest are illustrated in Figure 2. The melting temperature continuously decreases with Al concentration to about 1523 K at 52 at% Al and, hence, FeAl does not possess a high melting temperature, in contrast to Fe₃Al, which has a reasonably high melting temperature. Fe₃Al transforms from the D0₃ crystal structure to a defective ordered cubic B2 crystal structure at temperatures above the critical ordering temperature T_c of ~814 K. At the higher Al content, FeAl remains B2 up to the melting temperature. The iron-rich end of the Fe–Al system was reinvestigated more recently (Swann *et al.*, 1969, 1970, 1972; Inouye, 1985), and the investigations confirmed the existence of three b.c.c. phases (a disordered solid solution (α), ordered FeAl (B2), and ordered Fe₃Al (D0₃)) and two two-phase regions (α + D0₃ and α + B2).

The aluminides have complex point-defect structures, consisting of antistructure (substitutional) atoms, vacancies, or both (Ridley, 1966; Bradley and Taylor, 1932, 1937; Stephens, 1985). Of the iron aluminides, the defect structure has been explored largely in B2 FeAl. With deviations from stoichiometry in B2 alloys,

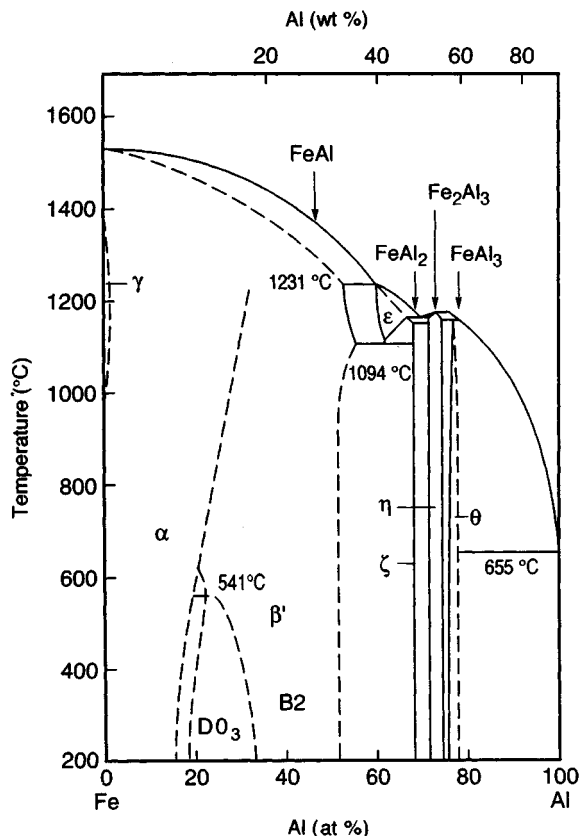


Figure 1. Fe-Al phase diagram

antistructure defects are predominant in Fe-rich alloys where excess Fe atoms fill Al sites. The defect structures in Al-rich and stoichiometric FeAl alloys are somewhat uncertain, although combinations of antistructure defects and Fe vacancies have been suggested (Bradley and Taylor, 1932; Neumann, 1980; Taylor and Jones, 1958; Neumann, Chang and Lee, 1976; Paris, Lesbats and Levy, 1975). For Al-rich B2 alloys, excess Al atoms generally do not form antistructure defects. In comparison to metals, these aluminides can contain enormous numbers of vacant atom sites—approaching 10% for Al-rich alloys (Bradley and Taylor, 1937; Stephens, 1985; Neumann, 1980). Although the composition dependence of the type and number of point defects in FeAl alloys has been explored extensively, their temperature dependence has not been examined in any great detail. The limited information shows that in FeAl, even at 1073 K (homologous temperature T/T_m of only 0.71), the concentration of vacancies is about 40 times greater than that found in normal metals at melting temperatures (Ho and Dodd, 1978). Such

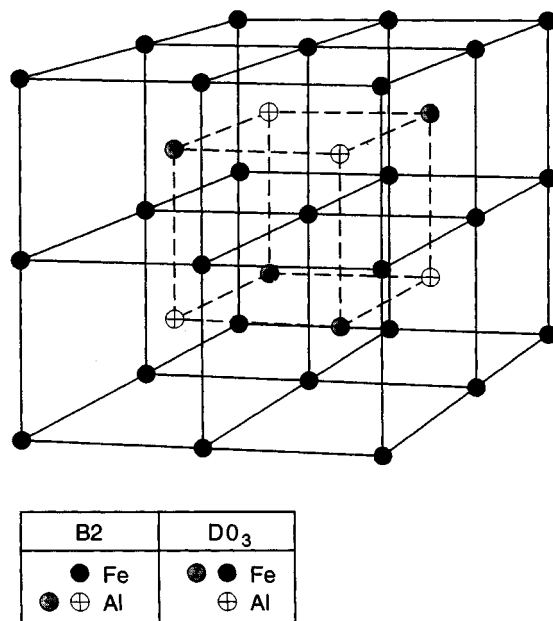


Figure 2. Crystal structures of the phases of interest in the Fe-Al system

vacancies play a major role in mechanical deformation because of the importance of defect hardening at low temperatures and of diffusion processes at high temperatures.

In view of the inadequate strengths of the binary alloys at temperatures of interest, introduction of point defects through alloying is needed to modify properties. For example, ternary elements and vacancies are known to exhibit solid-solution hardening. Since a low ordering temperature T_c has an adverse effect on high-temperature strength of Fe₃Al, it is important to know which ternary elements significantly increase T_c . However, information on phase diagrams for ternary additions to Fe₃Al or FeAl is scarce (Mantravadi, 1986; Mendiratta *et al.*, 1987; Mendiratta and Lipsitt, 1985). Additions ranging from 3 to 10 at% Ti, Cr, Mn, Ni, Mo and Si to Fe₃Al have been shown to raise T_c . In particular, Ti and Si additions to Fe-25Al increased T_c significantly. The ternary Si atoms substitute at the Al sublattice sites and result in an increase in T_c with increasing Si content. For B2 FeAl, additions of 1 to 5 at% Cr, Ti, Mn and Co show solid solubility; 0.8 to 5 at% B, Zr, Ta, Nb, Re and Hf showed limited solubility and formation of ternary intermetallic phases. W and Mo have very limited solubilities and no ternary compound formation was detected, based on hot-extruded blends of elemental powders and

prealloyed binary FeAl powders (Vedula and Stephens, 1987).

Another important feature of the ordered arrangement of atoms is the presence of antiphase boundaries (APBs) along certain planes. The presence of order leads to the possibility of formation of unit dislocations as well as superdislocations, as illustrated in Figure 3. In the D0₃ phase field, two types of APB vectors have been observed, $\frac{1}{4}a'_0\langle 111 \rangle$ and $\frac{1}{2}a'_0\langle 111 \rangle$, a'_0 being the lattice parameter of the B2 phase. In the B2 phase field only one type of domain with an APB fault vector of $\frac{1}{2}a'_0\langle 111 \rangle$ exists. Although these aluminides display high elastic anisotropy, results of computer simulations on the effect of elastic energy on APB anisotropy show that these elastic effects would not result in any substantial APB anisotropy in Fe–Al alloys (Van der Heide and Allen, 1991). This is reflected in the binary Fe–Al alloys having highly isotropic APBs, i.e. they are smoothly curving with no preference to any specific crystallographic planes, although their directions are specific within these planes. See Chapter 21 by Sun in Volume 1.

Grain boundaries in ordered alloys typically have unique structures with high energies. This plays a role in other grain boundary properties such as mobility, segregation, and fracture. Grain growth studies (Strothers, 1990; Crimp, 1987) of B2 FeAl indicate that grain boundary mobility is fairly high in these ordered microstructures and the grain growth rate was found to decrease with increasing aluminum content. In powder-processed alloys, grain growth is slow at low temperatures but takes off very rapidly at high temperatures where grain boundary mobility is high. This

change in growth rate is believed to be due to the presence of prior particulate oxides, which could also lead to abnormal grain growth at high temperatures if oxide particles are nonuniformly distributed. Another interesting observation is the evidence of very rapid grain growth in samples that are compression tested at about 1273 K, suggesting a significant stress-assisted increase in the mobility of grain boundaries. See Chapter 24 by Takasugi in Volume 1.

3. Processing

Conventional casting of iron aluminides has proven to be difficult. Segregation results in regions of very high aluminum content which are brittle and cause microcracking during cooling or subsequent processing. An added disadvantage is that the grain size of castings is very large. Secondary processing is essential in order to obtain any reasonable microstructure. Fe₃Al suffers from these problems to a slightly lesser extent than FeAl.

Processing by casting of Fe₃Al alloys (Sikka, 1991a,b) of composition Fe–28Al was optimized for maximum room-temperature ductility, maximum sulfidation resistance or maximum high-temperature strength by altering the levels of Cr and other additions such as Zr, Nb and C. These alloys can be prepared by non-consumable arc melting, argon induction melting (AIM), vacuum induction melting (VIM), vacuum arc refining (VAR) and electro slag refining (ESR) techniques. All these processes have been used successfully to melt heats varying in size from 500 g to a commercial scale up to 230 kg. The retention of alloying elements

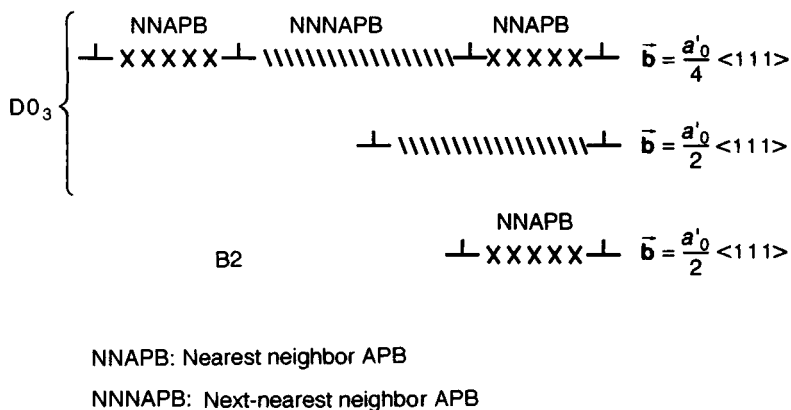


Figure 3. Possible types of perfect dislocations in Fe–Al alloys

during the melting of these heats is excellent. Careful charge preparation and melting practice can minimize gas pickup and other impurities from crucibles even in air melts. The alloys are sufficiently ductile to be hot worked in the temperature range 923–1273 K. Ingots of these alloys have been fabricated into sheet, bar, plate, and tubing. No problems were encountered during the hot-bar rolling and centerless grinding into final product.

Fe₃Al powder produced by nitrogen and argon atomization and containing 2 and 5% Cr can be readily consolidated by hot extrusion at 1273 K to a reduction ratio of >9:1. Consolidated powder is easily processible into 0.76 mm thick sheet by hot forging at 1273 K, hot rolling at 1123 K, and finish warm rolling at 923 K (Sikka *et al.*, 1991c,d).

On the other hand, FeAl is more difficult to process. Hot extrusion of small castings of B2 FeAl in containers has been shown to be effective in breaking up the cast structure and in refining the grain size through dynamic recrystallization (Gaydos and Crimp, 1985). Standard secondary operations such as hot rolling of cast blocks of B2 FeAl at elevated temperatures have, however, been unsuccessful so far.

Powder processing by hot extrusion of canned FeAl powders at 1173 K with extrusion ratios of 8:1 to 12:1 has been the most effective means for obtaining fine-grained, fully dense materials. Vacuum hot pressing and hot isostatic pressing have also been demonstrated to be effective. However, only the hot extrusion process is effective in breaking up the prior oxide particulate boundaries. The resultant microstructure consists of fine, equiaxed, recrystallized grains. Some preferred orientation of the recrystallized grains is evident.

Rapid solidification of FeAl alloys by melt spinning has been attempted. Grain sizes are not much finer than hot-extruded microstructures. No metastable microstructures and no particular property enhancements can be observed in Fe–40Al and Fe–45Al (Baker and Gaydos, 1987).

Weldability of iron aluminide alloys (David and Zacharia, 1991) has been found to be a strong function of alloy composition, welding process, and process parameters. Defect-free welds have been produced in several of these alloys by careful selection of welding processes and parameters.

4. Mechanical Properties

4.1 Single-crystal Behavior

Very little information on the behavior of single crystals of Fe₃Al is available, although quite a bit of work on

single crystals of FeAl has been reported. Single crystals of both phases are ductile at room temperature. The details of operative slip systems in B2 FeAl have been studied to some extent, and the behavior is shown to be a sensitive function of orientation and temperature. FeAl single crystals deform in the slip direction $\langle 111 \rangle$ at low temperatures, although there is some disagreement about the slip plane being either $\{211\}$ or $\{101\}$ (Yamagata and Yoshida, 1973). The $\langle 111 \rangle$ dislocations and the formation of APBs between partials of superdislocations have been confirmed by many studies in thin foils cut from a room-temperature, compression-tested B2 Fe–35Al single crystal (Ray *et al.*, 1970). The APB energies were measured and found to increase linearly with increasing Al content.

The fracture behavior of Fe–40Al single crystals has been investigated using smooth and notched specimens with orientations along three different crystalline directions. Though the direction of propagation of a macroscopic crack was decided by the applied stress field, the cleavage plane was always found to be $\{100\}$. The existence of a preferred cleavage plane results in anisotropy of fracture properties (Chang and Rosa, 1990; Chang and Darolia, 1991). First-principle calculations have shown that the high cleavage strength of FeAl occurs as a result of the directional d-bond formation at the Fe sites (Fu and Yoo, 1991).

A transition in active slip systems from $\{110\}\langle 111 \rangle$ to $\{110\}\langle 1\bar{1}0 \rangle$ and/or $\{100\}\langle 001 \rangle$ as the test temperature increases in the range 470–1000 K for B2 FeAl single crystals in vacuum has been observed (Umakoshi and Yamaguchi, 1980, 1981). This transition temperature was found to change with deviations from stoichiometry.

4.2 Polycrystalline Behavior

4.2.1 Room-temperature properties

Iron aluminides are typically brittle at room temperature. The brittle fracture behavior in polycrystalline Fe₃Al and FeAl is surprising since the observed predominant slip $\{110\}\langle 111 \rangle$ provides the necessary five independent slip systems. One of the first attempts at judging the potential of intermetallic compounds for use as high-temperature structural materials (Westbrook, 1956) showed through microhardness testing that the strength of FeAl is dependent on both composition and temperature. More recently, several studies have obtained information on strength and ductility of these alloys at room temperature. In general, yield strength and strain hardening rate were found to increase and the ductility was found to decrease with increasing

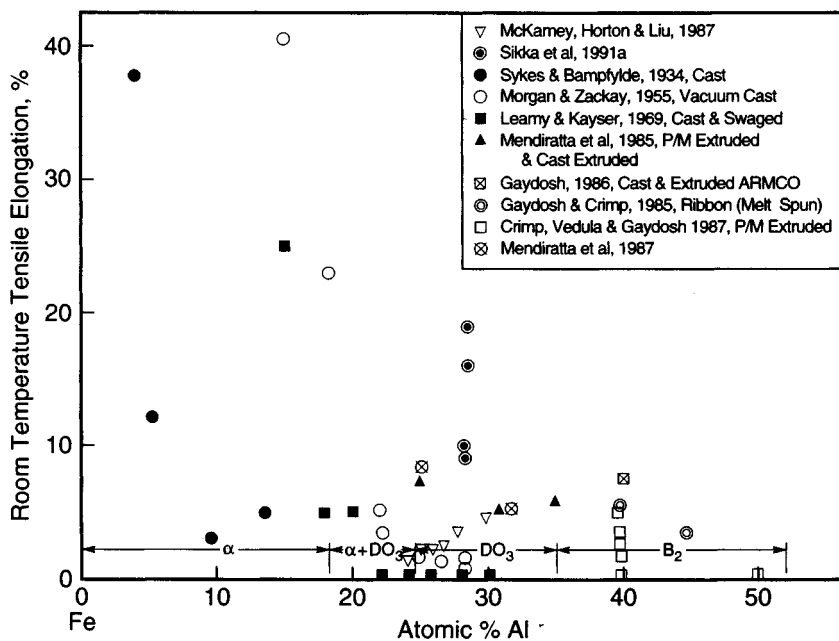
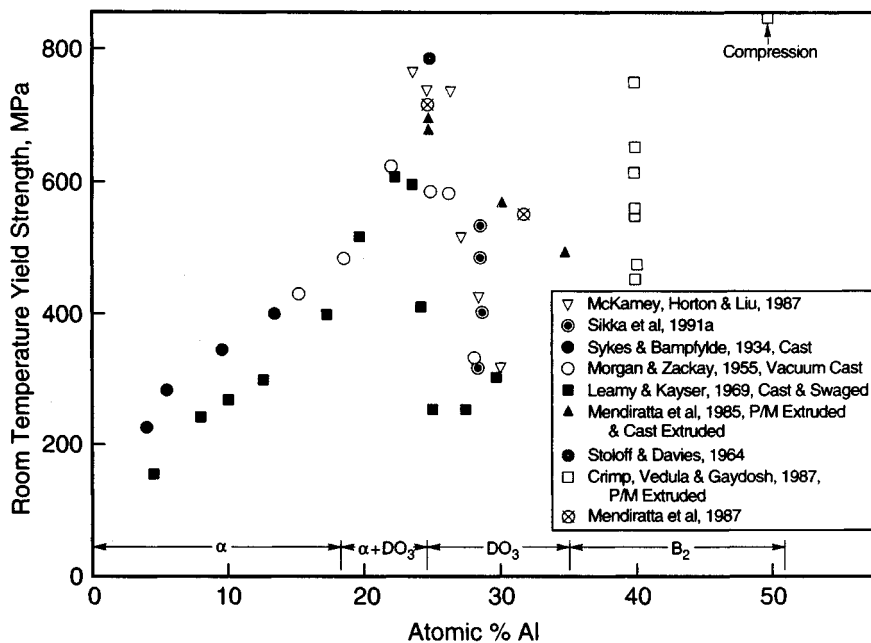


Figure 4. (a, top) Room-temperature yield strength dependence on Al content. (b, bottom) Room-temperature tensile elongation dependence on Al content (P/M = powder metallurgy)

aluminum content. Results from some of these studies are summarized in Figure 4. It is important to note that a wide range of strengths and ductilities is reported at some of the compositions and this is believed to be as a result of variations in processing conditions, thereby emphasizing the importance of optimizing processing conditions in order to obtain useful properties in these alloys.

In one group of studies (Mendiratta *et al.*, 1987; Sainfort *et al.*, 1963, 1971; Chatterjee and Mendiratta, 1981) it was clearly shown that, with Al content ranging from 25 to 50 at%, alloys were mostly ductile at room temperature, ductility decreasing to 2.5% with increasing Al content for Fe–40Al and brittle fracture with no ductility for Fe–50Al alloys. Maximum ductility and strength were exhibited by Fe–25Al (8% elongation for a grain size of 50 μm). A larger grain size (150 μm) Fe–31Al cast alloy exhibited a ductility of 5.6%, while 7% ductility was obtained for a finer-grained Fe–35Al alloy. Other studies of FeAl alloys (Crimp, Vedula and Gaydos, 1987; Crimp and Vedula, 1986) have confirmed that iron-rich deviations from stoichiometry can result in appreciable tensile ductilities at room temperature.

The variation in room-temperature strength and ductility is believed to be due to the $\langle 111 \rangle$ -type dislocations which form antiphase boundaries and the effect of deviations from stoichiometry on APB energy. Transmission electron microscopy (TEM) of alloys of Fe–25Al deformed at room temperature shows that deformation is governed by movement and cross slip of ordinary dislocations, which therefore create APB bands. In contrast, with increasing Al content plastic flow occurs by movement of superlattice dislocations. Higher ductility at low Al contents has been attributed to the lower antiphase boundary energy with lower aluminum content making it easier to move $\langle 111 \rangle$ dislocations and allowing plastic yielding to take place before intergranular failure.

These results (reasonable ductilities, extensive motion of ordinary and superlattice $\langle 111 \rangle$ dislocations) provide sufficient evidence that iron aluminides are not inherently brittle at room temperature.

Small boron additions have been found to result in some improvement in the room-temperature tensile ductility of B2 Fe–40Al, and this benefit is believed to be due to strengthening of the grain boundaries. In addition, the rate of cooling from an annealing temperature of 1273 K has been found to play a very dominant role in controlling the properties of the alloy. For example, hardness measurements made on both as-extruded and annealed samples (Schmidt, Nagpal and Baker, 1989) showed an increase in hardness with increasing aluminum content and this increase was greater in the annealed,

air-cooled samples. The cooling rate effect is believed to be due to vacancy retention.

Recent studies (Liu and George, 1991; Liu, Lee and McKamey, 1989, 1990) show that environmental embrittlement is a major cause of low tensile ductility and brittle fracture in many ordered intermetallics including FeAl and Fe₃Al. When tested in air, Fe–36Al with a coarse grain structure is relatively brittle and shows tensile ductilities in the range of 2–4%; but by careful control of test environment using a dry oxygen atmosphere, a high room-temperature ductility of 17.6% has been achieved. High room-temperature ductility values are obtained for Fe–28Al alloys when the hydrogen effect, owing to reaction of aluminum with moisture, is kept to a minimum (Sikka *et al.*, 1991c) by quenching the specimens from the annealing temperature in oil. Higher aluminum alloys with 40 and 43 at% Al, however, are found to be much less sensitive to change in test environment and surface coating.

The low ductility is owing to environmental embrittlement involving the reaction of aluminum atoms at the crack tips, promoting brittle crack propagation mainly along cleavage planes, resulting in brittle cleavage fracture. The effect of hydrogen on the bonding mechanism has been recently identified by a first-principles calculation as an Fe to H charge transfer effect (Fu and Painter, 1991).

The grain size dependence of the yield strength of FeAl with various Al concentrations follows the standard Hall–Petch equation. The lattice resistance and Hall–Petch slope according to this relationship have maxima at the stoichiometric composition and decrease off this composition. Fracture is predominantly intergranular at the stoichiometric compositions and becomes increasingly transgranular with decreasing aluminum concentration.

In order to explore the possibility that Fe₃Al might exhibit ductile behavior if prepared with a grain size below some critical value, Fe₃Al with 1.5 mol% TiB₂ was rapidly solidified (Yamagata and Yoshida, 1973; Stoloff *et al.*, 1987) by centrifugal atomization and subsequent hot isostatic pressing. After thermomechanical treatment, a fine uniform dispersion of TiB₂ (77 nm particle diameter) was observed. The TiB₂ dispersion apparently stabilized a fine grain (or subgrain) size of 1–2 μm in the Fe₃Al. Mechanical testing revealed a beneficial effect of rapid solidification on the mechanical properties.

4.2.2 Elevated-temperature properties

The yield strength of Fe–25Al has been shown to drop rapidly with increasing temperature at about T_c . The

low T_c of 814 K is believed to have an adverse effect upon the high-temperature tensile strength of Fe₃Al owing to the transition from D0₃ to the more simply ordered B2 phase formed at the higher temperature. However, B2 FeAl alloys containing higher Al show more reasonable strength at 873 K.

Below T_c , Fe₃Al shows an anomalous temperature dependence of the strength which has been observed for some other phases, too (Jung *et al.*, 1986). It has been found that the yield stress of alloys near the Fe₃Al composition increases with temperature above 673 K to a peak value just below T_c (Inouye, 1985). Within this same temperature interval, the long-range order parameter S decreases from about 0.8 to 0, and the yield peak was earlier explained in terms of the transition from superdislocation to unit dislocation interactions at a critical degree of order. However, more recent studies (Swann, Duff and Fisher, 1969, 1970, 1972) suggest that alloys could have age hardened when they order transformed on heating to $\alpha + D0_3$ and $\alpha + B2$. It has been established that alloys near Fe₃Al are age hardenable above 673 K owing to precipitation of α from ordered D0₃. Consequently, the yield strength of D0₃ increased with temperature since the kinetics of age hardening increased with temperature. The yield peaks were caused by a combination of α precipitation and B2 precipitation.

In polycrystalline binary FeAl alloys a change in slip direction similar to that in single crystals, i.e. from $\langle 111 \rangle$ to $\langle 100 \rangle$, is observed as a function of temperature and aluminum content (~ 623 K for 50 at% Al and increasing with decreasing Al content) (Mendiratta *et al.*, 1984, 1985), although there is disagreement as to whether the temperature for the transition in slip direction increases or decreases with aluminum content. Dislocations observed in hot-extruded, polycrystalline B2 Fe–50Al alloys (Crimp, 1987) are found to be essentially all $\langle 100 \rangle$ dislocations, whereas the B2 Fe–40Al alloy contains some $\langle 111 \rangle$ dislocations along with the $\langle 100 \rangle$ type, suggesting that the deformation mechanism at high temperatures changes from $\langle 111 \rangle$ to $\langle 100 \rangle$ as Al content increases. Extruded rods of iron-rich FeAl consisted of elongated grains with a $\langle 111 \rangle$ fiber texture containing a high dislocation density. Subsequent plastic deformation of the B2 Fe–40Al alloy at room temperature clearly shows an increased number of $\langle 111 \rangle$ dislocations.

Hence, although not correlated with the slip transition, the strength of FeAl decreases with increasing temperature, as for regular metals. A drastic decrease in strength accompanied by a sudden increase in the ductility is observed in FeAl at about $0.4 T_m$ (Baker and Gaydosch, 1987), as illustrated in Figure 5. The

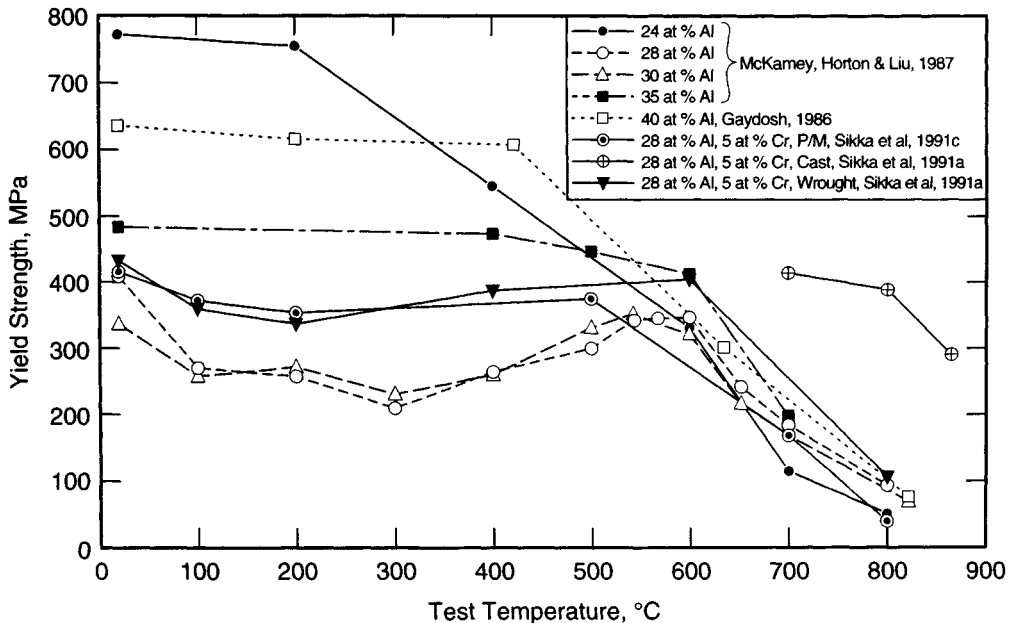


Figure 5. Yield strength dependence on temperature

reasons for this brittle-to-ductile transition are not entirely clear. The temperature dependence of slip behavior and the onset of diffusion-assisted processes must definitely play a role in this transition behavior.

The high-temperature deformation mechanisms of these aluminides have not been extensively studied. Earlier studies of creep in Fe–Al alloys have been limited to alloys containing up to 28 at% Al (Lawley, Coll and Cahn, 1960). Recent studies (Whittenberger, 1983, 1986; Vedula and Stephens, 1987; Titran *et al.*, 1985) restricted to compression creep deformation have shown that B2 FeAl deforms by two independent deformation mechanisms with the same activation energy in the temperature range 1100–1400 K. Both mechanisms are dependent on grain size; however, for the higher stress exponent regime ($n \approx 5$) strength increases with a decreasing grain size, while for the lower stress exponent regime ($n \approx 1$) the opposite is true. These results suggest that Hall–Petch-type grain boundary strengthening may be important up to higher fractions (0.75) of the melting point in iron aluminides than is typically observed in conventional metals. In addition, grain boundary strengthening owing to fine grain sizes as well as segregation of boron has been observed. No subboundaries or subgrain structures are found, suggesting that creep is controlled by viscous glide of dislocations. Mechanisms of dislocation creep in B2 phases do not differ from those in conventional disordered alloys, i.e. the special structure of the intermetallic phase does not lead to special creep effects.

It was mentioned earlier (Mendiratta *et al.*, 1987) that certain alloying additions, e.g. Ti and Si, to Fe–25Al increase T_c significantly. Tensile testing shows a significant increase in elevated-temperature strength for increases in T_c . Ti substitutes at specific Fe sites and T_c increases, but these ternary alloys were found to be totally brittle at room temperature. Ternary alloys based on B2 Fe–35Al with 1, 2 or 4 at% Ti, Cr, V or Ni and 1 or 2 at% Nb, Mo, Ta, W or Si all produced significant solid-solution strengthening at 873 and 973 K and all exhibited some room-temperature ductility. Si-containing alloys were the most brittle.

Ternary additions result in substantial improvements in the high-temperature compressive creep of FeAl alloys (Sainfort *et al.*, 1963; Titran, Vedula and Anderson, 1984; Vedula and Stephens, 1987). Several elements have been studied, including those which have large solubilities (Cr, Mn, Ti and Co) and those which have limited solubilities (Nb, Ta, Hf, Mo, W, Zr and B) in the binary alloys. Substantial solution hardening in ternary (Fe, Ni, Co) alloys is obtained, partially at high temperatures (Westbrook, 1954). Alloys containing 0.15 wt% Zr

and 160–500 p.p.m. C have been shown to have improved impact strength over a range of temperatures (Sainfort *et al.*, 1963). Boron has been found to have a significant impact on the creep behavior of FeAl in addition to its effect on room-temperature ductility. An alloy containing 0.1 at% Zr and 0.2 at% B has been found to be the best among the alloys investigated at 1100 K (Mantravadi, 1986). The results of constant-rate compression tests at elevated temperatures clearly indicate that the commonly accepted strengthening mechanisms operate in the B2 FeAl intermetallic system containing ternary additions: solid-solution strengthening for alloys containing 1–5 at% Cr, Ti, Mn and Co which exhibit a single-phase microstructure and some strengthening compared with binary B2 FeAl alloys; and second-phase strengthening for alloys containing 0.8–5 at% B, Zr, Ta, Nb, Re and Hf, in which the ternary additions do go into solution and precipitate ternary intermetallic compounds that serve to pin dislocations. In particular, alloying with up to 6 at% Cr results in an increase in room-temperature ductility from 4% to 8–10% along with a change in fracture mode from transgranular cleavage to a mixed mode. These phenomena can be discussed in terms of a series of changes in APB energies and dislocation substructures. The effect of Cr has led to the development of alloys with optimized properties and processing as discussed earlier in the processing section.

Two-phase iron aluminides Fe–25Al–2Nb containing coherent precipitates of Fe₂Nb exhibit significant precipitation strengthening at 873 K and at room temperature (Mendiratta *et al.*, 1987). However, the thermal stability of the precipitates was not encouraging for long-term elevated-temperature applications. In both Fe–25Al and B2 Fe–35Al, TiB₂ and Hf-rich and Zr-rich particles refined the grain size to 1 μ m and produced a high density of dislocations and subgrains and a fine dispersion of incoherent particles. These dispersoids provide substructure and subboundary strengthening, but not above 873 K. Studies have been conducted of the mechanical properties of Fe₃Al alloys containing 24–30 at% Al to which 0.5 wt% TiB₂ was added for grain refinement (Baker and Gaydosh, 1987). Fe–35Al containing various amounts of ZrB₂ has been prepared by melt spinning and its microstructure and stability examined. The additions lead to increases in hardness and strength. In addition, small amounts of ZrB₂ lead to significant increases in ductility. Because the microstructure is fairly stable, these improvements in properties are maintained even after high-temperature exposures (Morris and Morris, 1991).

High-temperature strengths for cast material of Fe₃Al-type alloys are significantly higher than for the wrought material. The cast material has >60% elongation at temperatures over 1073 K, which permits conventional hot processing of these alloys.

Creep rupture data on Fe₃Al alloys show minimum variation from heat to heat, and the strengths of the current alloy compositions match that of 403 stainless steel (Sikka *et al.*, 1991a). The creep resistance was low even at moderate temperature, e.g. Fe-25Al exhibited a minimum creep rate of $\sim 10^{-2} \% \text{ h}^{-1}$ at 40 kp.s.i. and 723 K, and Fe-35Al a rate of $0.5 \% \text{ h}^{-1}$ at 843 K and the same stress level. These high rates may be associated with the relatively open structures of B2 and D0₃.

Elastic modulus is a key factor in the design of high-temperature structural parts, and some effort is being devoted to quantifying moduli of FeAl as a function of temperature (Wolfenden, 1985). These measurements show high values of modulus at low temperatures with a gradual decrease as temperature increases.

4.2.3 Fatigue Properties

Limited work has been carried out on fatigue of polycrystalline Fe-25Al and Fe-35Al. In a tension-tension cyclic mode with a stress level ratio $R=0.1$, Fe-25Al was found to have a reasonable room-temperature fatigue strength of $\sim 90 \text{ kp.s.i.}$ at 10^6 cycles with a ratio of 0.6 for fatigue strength/tensile fracture stress. The high-cycle fatigue behavior of Fe₃Al is found to be dependent upon stoichiometry and temperature in a complex way that is connected with the formation of superlattice dislocations and with phase changes at high temperature. High-cycle fatigue results for Fe₃Al-type alloys reveal an unexpected reversal in properties between Fe-23.7Al and Fe-28.7Al tested at room temperature and at 773 K (Stoloff *et al.*, 1987). The hypostoichiometric (in Al) alloy is less fatigue resistant than the Al-rich alloy at room temperature, but is more resistant at 773 K. This reversal appears to arise from an aging effect, since a two-phase, coherent $\alpha + \text{D0}_3$ structure develops in Fe-23.7Al at 773 K but not in Fe-28.7Al. It has been concluded that enhanced fatigue resistance of the higher Al alloy at room temperature is owing to the presence of superlattice dislocations which cause crack initiation to be more difficult than in the hypostoichiometric alloy; the latter deforms by the motion of unpaired dislocations (Stoloff *et al.*, 1987).

The crack growth behavior of Fe₃Al-type alloys as a function of long-range order and temperature is much

more complex. There is no clear pattern of behavior demonstrated except at 873 K (Stoloff *et al.*, 1986), where crack growth rates are unusually high compared to those of other ordered alloys.

No significant reports of fatigue of polycrystalline FeAl are available. However, single-crystal Fe-40Al was cyclically deformed in fully reversed tension-compression tests run in plastic strain control at room temperature. Rapid cyclic hardening was observed (Hartfield-Wunsch and Gibala, 1991). However, intergranular failure occurred before saturation was reached at all plastic strain amplitudes. Significant ductility enhancement was achieved by the application of thin nickel films, which introduce mobile dislocations at the film-substrate interface.

5. Oxidation and Corrosion Resistance

Iron aluminides depend on the formation of an alumina scale for their oxidation and corrosion resistance. At low concentrations of Al, internal oxidation of Al occurs and Fe₂O₃ and Fe₃O₄ form on the exterior of the alloys. At intermediate Al concentrations, although a transient alumina layer is formed, it tends to be disrupted by iron nodules. Approximately 15 at% Al must be added to Fe to produce a continuous layer of Al₂O₃ during oxidation. Small Cr additions reduce the aluminum requirement, but Ni additions require increased amounts of Al to avoid the formation of nodules of Fe-rich oxides that disrupt the alumina scale.

The oxidation resistance of B2 FeAl alloys (34–51 at% Al) is superior to that of 304 stainless steel at 1473 K (Schmid, Nagpal and Baker, 1988). Little oxidation is found to occur at 1173 K, but at 1473 K the oxidation rate was found to decrease with increasing aluminum concentration. The predominant oxide was $\alpha\text{-Al}_2\text{O}_3$ (Stephens, 1985). The large thermal expansion of FeAl compared with Al₂O₃ could pose problems from spalling of the oxide during cyclic heating and cooling. However, initial oxidation testing suggests that this is not the case. FeAl alloys have also been reported to exhibit 'pest' oxidation which has been formed in other intermetallic compounds (Sawada *et al.*, 1960).

Iron aluminides are of particular interest because of their potential for performance in coal gasifiers involving gases with relatively low oxygen activities ($< 10^{-19} \text{ atm}$) but high sulfur activities ($> 10^{-8} \text{ atm}$). To evaluate corrosion resistance under the latter conditions, tests were conducted initially in H₂S-H₂-H₂O at 973–1073 K and selected compositions (Fe₃Al containing 0–10 at% Cr and 1–2 at% Nb, Mo, V, Zr

or Y) were exposed in the product gas stream of an operating coal gasifier (DeVan, 1991). Most of the alloys were highly resistant to oxidation and sulfidation in the mixed gases even when the oxygen activity was below 10^{-21} atm. However, alloys containing greater than 2 at% Cr were less resistant to sulfur attack. Tests of an alloy containing 2 at% Cr and 28 at% Al in an operating gasifier environment have confirmed the excellent corrosion resistance demonstrated in laboratory tests.

The corrosion resistances of several alloys (Fe–28Al containing Cr and Mo) were tested in a series of acidic, basic and chloride-containing solutions (Buchanan and Kim, 1992). The behavior was found to be comparable with 304L stainless steel. Increasing the Cr and Mo levels is generally effective in reducing aqueous rates over the range of electrolytes investigated. At a given Cr level, addition of Mo has a major effect in improving resistance to chloride-induced localized corrosion.

6. Composites

Reinforcements for iron aluminides in order to improve their low-temperature toughness as well as their high-temperature creep resistance are being investigated. However, suitable choice of fibers is hampered by the lack of availability of fibers that are compatible with iron aluminide matrices. The powder cloth method was used to investigate the chemical compatibility of B2 Fe–40Al with several commercially available fibers for potential composite applications (Gaydosch *et al.*, 1990; Vedula, 1991). SiC, (Mo, Hf)C and B₄C fibers were found to exhibit severe reaction with the B2 Fe–40Al matrix and were therefore incompatible, as predicted by thermodynamic calculations. Although W fibers were not expected to react any more than by some dissolution of the elements, they did exhibit significant reaction. The only fiber which was found experimentally to be chemically compatible was Al₂O₃. However, the coefficient of thermal expansion mismatch for Al₂O₃ may still be too large. Fiber pull-out tests, thermal expansion behavior of composites, fiber displacement during thermal cycling and low tensile strengths indicated a weak fiber–matrix bond. However, the interfacial bond strength may be increased by coatings, and Ti coating appears promising. Hence, although some efforts have led to positive results, a large number of developments are needed in order to make the composite approach viable.

7. Summary

Iron aluminides have been shown to have potential for elevated-temperature applications. They possess adequate low-temperature ductilities, particularly at lower Al contents, if processed carefully. Optimizing the compositions and processing conditions is the key to the successful development of these alloys. The temperature range of application will be more modest than state-of-the-art superalloys because of inadequate melting temperatures and creep resistance. Nevertheless, the formability of some of these alloys (combined with their low densities and excellent oxidation and corrosion resistance) provides a window of opportunity for economic alloys. However, a wide range of additional property evaluations, including fatigue and tensile creep testing, is essential before effective commercialization is possible.

8. References

- Allen, S. M., and Cahn, J. W. (1975). *Acta Metall.*, **23**, 1017.
- Allen, S. M., and Cahn, J. W. (1976). *Acta Metall.*, **24**, 425.
- American Society for Metals (1973). *Metals Handbook*, 8th edn, Vol. 8. (ed. ASM Handbook Committee), published by American Society for Metals, p. 260. ASM, Metals Park, OH.
- Baker, I., and Gaydosch, D. J. (1987). *Mater. Res. Soc. Symp. Proc.*, **81**, 315.
- Baker, I., and Gaydosch, D. J. (1987). *Mater. Sci. Eng.*, **96**, 147.
- Bradley, A. J., and Taylor, A. (1932). *Proc. R. Soc. London. Ser. A*, **136**, 210.
- Bradley, A. J., and Taylor, A. (1937). *Proc. R. Soc. London. Ser. A*, **159**, 56.
- Buchanan, R., and Kim, J. G. (1992). ORNL Report, Subcontract 88-07685CT92/02.
- Chang, K. M., and Darolia, R. (1991). *Mater. Res. Soc. Symp. Proc.*, **213**, 597.
- Chang, K. M., and Rosa, R. A. (1990). GE Research and Development Center, Physical Metallurgy Laboratory, Report 90CRD222.
- Chatterjee, D. K., and Mendiratta, M. G. (1981). *J. Met.*, **33**(12), 5.
- Crimp, M. A. (1987). PhD thesis, Case Western Reserve University.
- Crimp, M. A., and Vedula, K. (1986). *Mater. Sci. Eng.*, **78**, 193.
- Crimp, M. A., Vedula, K., and Gaydosch, D. J. (1987). *Mater. Res. Soc. Symp. Proc.*, **81**, 499.
- David, S. A., and Zacharia, T. (1991). In *Heat Resistant Materials* (eds K. Natesan and D. J. Tillack), p. 169.
- DeVan, J. H. (1991). In *Heat Resistant Materials* (eds K. Natesan and D. J. Tillack), p. 235.

- Fu, C. L., and Painter, G. S. (1991). *J. Mater. Res.*, **6**, 719.
- Fu, C. L., and Yoo, M. H. (1991). *Mater. Res. Soc. Symp. Proc.*, **213**, 667.
- Gaydosch, D. J. (1986). Unpublished research, NASA Lewis Research Center.
- Gaydosch, D. J., and Crimp, M. A. (1985). *Mater. Res. Soc. Symp. Proc.*, **39**, 429.
- Gaydosch, D. J., Draper, S. L., Eldridge, J. I., and Tsui, P. (1990). In *HITEMP Review 1990*. NASA Lewis Research Center Conference Publications, 10051, 39-1.
- Hartfield-Wunsch, S. E., and Gibala, R. (1991). *Mater. Res. Soc. Symp. Proc.*, **213**, 575.
- Ho, K., and Dodd, R. A. (1978). *Scripta Metall.*, **12**, 1055.
- Inouye, H. (1985). *Mater. Res. Soc. Symp. Proc.*, **39**, 255.
- Jung, I., Rudy, M., and Sauthoff, G. (1987). *Mater. Res. Soc. Symp. Proc.*, **81**, 263.
- Lawley, A., Coll, J. A., and Cahn, R. W. (1960). *Trans. Metall. Soc. AIME*, **218**, 166.
- Leamy, H. J., and Kayser, F. X. (1969). *Phys. Status Solidi*, **34**, 765.
- Liu, C. T., and George, E. P. (1991). *Mater. Res. Soc. Symp. Proc.*, **213**, 527.
- Liu, C. T., Lee, E. H., and McKamey, C. G. (1989). *Scripta Metall.*, **23**, 875.
- Liu, C. T., McKamey, C. G., and Lee, E. H. (1990). *Scripta Metall.*, **24**, 385.
- Mantravadi, N. (1986). PhD thesis, Case Western Reserve University.
- McKamey, C. G. (1990). In *Proc. 4th Annual Conference on Fossil Energy Materials*, Oak Ridge, Tennessee, p. 197; ORNL/FMP-90/1, Oak Ridge National Laboratory.
- McKamey, C. G., Horton, J. A., and Lui, C. T. (1987). High-Temperature Ordered Intermetallic Alloys II. *MRS Symposia Proceedings*, **81**, 321.
- Mendiratta, M., Kim, H. M., and Lipsitt, H. A. (1984). *Metall. Trans.*, **15A**, 395.
- Mendiratta, M. G., and Lipsitt, H. A. (1985). *Mater. Res. Soc. Symp. Proc.*, **39**, 155.
- Mendiratta, M., Ehlers, S., Dimiduk, D., Kerr, W., Mazdiyasi, S., and Lipsitt, H. A. (1987). *Mater. Res. Soc. Symp. Proc.*, **81**, 393.
- Morgan, E. R., and Zackay, V. F. (1955). *Metal Progress*, **68**, 126.
- Morris, D. G., and Morris, M. A. (1991). *Mater. Res. Soc. Symp. Proc.*, **213**, 847.
- Neumann, J. P. (1980). *Acta Metall.*, **28**, 1165.
- Neumann, J. P., Chang, Y. A., and Lee, C. M. (1976). *Acta Metall.*, **24**, 593.
- Paris, D., Lesbats, P., and Levy, J. (1975). *Scripta Metall.*, **9**, 1373.
- Ray, I. L. F., Crawford, R. C., and Cockayne, D. J. H. (1970). *Philos. Mag.*, **21**, 1027.
- Ridley, N. (1966). *J. Inst. Met.*, **94**, 255.
- Sainfort, G., Gregoire, J., Mouturat, P., and Romegio, M. (1971). In *Frailite et Effet de L'irradiation* (eds M. Salesse and M. Cauldron). Presses Universitaires de France, Paris, p. 187.
- Sainfort, G., Mouturat, P., Pepin, P., Petit, J., Cabane, G., and Salesse, M. (1963). *Mem. Sci. Rev. Met.*, **40**, 125.
- Sawada, H., Masuda, A., Atobe, Y., and Aoki, T. (1960). *Nippon Kinzoku Gakkaishi*, **11**, 723-735.
- Schmidt, B., Nagpal, P., and Baker, I. (1989). *Mater. Res. Soc. Symp. Proc.*, **133**, 754.
- Sherman, M., and Vedula, K. (1986). *J. Mater. Sci.*, **21**, 1974.
- Sikka, V. K. (1991a). In *Heat Resistant Materials* (eds K. Natesan and D. J. Tillack), p. 141.
- Sikka, V. K. (1991b). *Mater. Res. Soc. Symp. Proc.*, **213**, 907.
- Sikka, V. K., Baldwin, R. H. N., Reinshagen, J. H., Knibloe, J. R., and Wright, R. N. (1991c). *Mater. Res. Soc. Symp. Proc.*, **213**, 901.
- Sikka, V. K., Gleske, B. G., and Baldwin, R. H. (1991d). In *Heat Resistant Materials* (eds K. Natesan and D. J. Tillack), p. 363.
- Stephens, J. R. (1985). *Mater. Res. Soc. Symp. Proc.*, **39**, 381.
- Stoloff, N. S., and Davies, R. G. (1964). *Acta Metall.*, **12**, 473.
- Stoloff, N. S., Fuchs, G. E., Kuruvilla, A. K., and Choe, S. J. (1987). High Temperature Ordered Intermetallic Alloys, MRS Symposium Proceedings, Vol 51, 247.
- Strothers, S. D. (1990). PhD thesis, Case Western Reserve University.
- Swann, P. R., Duff, W. R., and Fisher, R. M. (1969). *Trans. Metall. Soc. AIME*, **245**, 851.
- Swann, P. R., Duff, W. R., and Fisher, R. M. (1970). *Phys. Stat. Sol.*, **37**, 577.
- Swann, P. R., Duff, W. R., and Fisher, R. M. (1972). *Metall. Trans.*, **3**, 409.
- Sykes, C., and Bampfylde, J. W. (1934). *J. Iron and Steel Inst.*, **130(II)**, 389.
- Taylor, A., and Jones, R. M. (1958). *J. Phys. Chem. Sol.*, **6**, 16.
- Titran, R. H., Vedula, K., and Anderson, G. (1985). *Mater. Res. Soc. Symp. Proc.*, **39**, 319.
- Umakoshi, Y., and Yamaguchi, M. (1980). *Philos. Mag. A*, **41**, 573.
- Umakoshi, Y., and Yamaguchi, M. (1981). *Philos. Mag. A*, **44**, 711.
- Van der Heide, R. G., and Allen, S. M. (1991). *Mater. Res. Soc. Symp. Proc.*, **213**, 181.
- Vedula, K. (1991). In *Heat Resistant Materials* (eds K. Natesan and D. J. Tillack), p. 159.
- Vedula, K., Pathase, V. M., Aslanidis, I., and Titran, R. H. (1985). *Mater. Res. Soc. Symp. Proc.*, **39**, 411.
- Vedula, K., Pathase, V. M., Anderson, G., and Aslanidis, I. (1984). *Mod. Devel. Powder Metall.*, **16**, 727.
- Vedula, K., and Stephens, J. R. (1987). *Mater. Res. Soc. Symp. Proc.*, **81**, 381.
- Westbrook, J. H. (1954). *Gen. Elect. Res. Lab. Report*, 1199.
- Westbrook, J. H. (1956). *J. Electrochem. Soc.*, **103**, 54.
- Whittenberger, J. D. (1983). *Mater. Sci. Eng.*, **57**, 77.
- Whittenberger, J. D. (1986). *Mater. Sci. Eng.*, **77**, 103.
- Wolfenden, A. (1985). NASA Report WAG3-314.
- Yamagata, T., and Yoshida, H. (1973). *Mater. Sci. Eng.*, **12**, 95.

Index

Note: Figures and Tables are indicated [in this index] by *italic page numbers*

<u>Index terms</u>	<u>Links</u>				
A					
A15 compounds					
crystal structure	216				
silicides	227				
as superconductors	227				
A-286 [superalloy]	1	5	40	276	278
	282	290			
<i>Ab initio</i> calculations, antiphase-boundary energies	60				
Abundance of elements, and cost/price considerations	258				
Aeroengine applications	44	89	90	241	293
	300				
Aerospace applications	57	215	233	241	293
Ag-Al-Ti system	164	168			
Al-Ce-Fe system	182				
Al-Co-Ti system	163				
Al-Cr-Nb-Si-Y system	173				
Al-Cr-Nb-Ti system	85	88			
Al-Cr-Si system	233				
Al-Cr system	190				
Al-Cr-Ti system	162	167	167	168	169
	172	173	174	177	
phase diagram	177				
Al-Cr-X intermetallics	190				
Al-Cr-Y system	191				
Al-Cr-Zr system	189	191			
Al-Cu-Li-Mg-Zr system	193	194	196		

<u>Index terms</u>	<u>Links</u>			
Al-Cu-Ti system	163	168		
Al-Fe-Mn-Si system	190			
Al-Fe-Mo-V system	189			
Al-Fe-Nb system	210			
Al-Fe-Si system	221			
dispersoids in aluminum alloys	180			
Al-Fe-Si-V system	182	184		
coarsening rates	190			
phase relationships	187	197		
physical properties of alloys	188			
structure of alloys	184			
Al-Fe-Si-X intermetallic compounds	184			
Al-Fe system				
dispersoids in aluminum alloys	180			
<i>see also</i> Fe-Al system; Iron aluminides				
Al-Fe-Ti system	163	168	169	
Al-Fe-V system	188			
Al ₃ Hf	191			
Al-Li system	192			
Al-Li-Zr system	192			
Alloy 8009 [aluminum alloy]	182	198		
Alloy design	38	82	196	288
Alloying additions				
ductility affected by	36	61	82	219
in iron aluminide alloys	210			
in nickel aluminides	32	44	61	63
oxidation behavior and				
in Al-Ni system	59			
in Al-Ti system	83			
and selection of high-temperature intermetallics	247			
in superalloys	6			
in titanium aluminides	82			

<u>Index terms</u>	<u>Links</u>		
Al-Mn compounds	189		
Al-M-Ni system, phase diagram	33		
Al-Mn-Nb-Ti system	88		
Al-Mn-Si alloys	190		
Al-Mn-Ti system	162	168	169
Al-Mn-Ti-V system	164	173	
Al-Mo-Nb-Ta-Ti system	93	95	
Al-Mo-Nb-Ti system	95	127	128
Al-Mo-Nb-V-Ti system	93	95	
Al-Mo-Ni system	41	44	
Al ₃ Nb	161	173	191
Al ₃ Nb-based compounds	173		
Al-Nb system, properties	248	249	253
Al-Nb-Ti system	93	247	
crystal structures	96		
oxidation-resistant coatings	126	172	
phase diagram	95		
SiC-fiber-reinforced composites	297	299	300
AlNi ₃ -based alloys			
alloying effects	44		
environmental embrittlement	44		
at elevated temperatures	44		
future research	44		
Al-Ni system			
antiphase-boundary energies	276		
in composites	296	299	
phase diagram	57		
Al-Ni-Ti system	163		
Al-Pd-Ti system	164		
Al-Ru alloys	254		
deformation of	255	260	
effect of alloying additions	260		

<u>Index terms</u>	<u>Links</u>				
Al-Ru alloys (<i>Continued</i>)					
processing of	261				
properties	249	253	254	255	260
AlTi ₃ <i>see</i> Ti ₃ Al					
AlTi <i>see</i> TiAl					
Al ₃ Ti					
brittleness	170				
crystal structure	152				
D0 ₂₂ -structure compounds	192				
deformation structures in	154				
ductility	170				
ways of improving	158				
elastic constants	152	153			
phase stability	159				
processing and microstructure	161				
strength, temperature dependence	157	168			
Al ₃ Ti-based compounds	151				
applications	173				
D0 ₂₂ -structure	152	171			
L1 ₂ -structure	159	172			
microstructures	165				
oxidation behavior	171				
Al-Ti-V system	126				
Aluminides					
coatings based on	59	126	172	174	
environmental embrittlement of	26				
<i>see also</i> Iron...; Nickel...; Titanium aluminides					
Aluminum alloys					
Al-Fe-based	180				
strengthening of	179	288			
Aluminum-lithium alloys, Al ₃ Zr in	192				
Aluminum-rich intermetallic dispersoids					
in aluminum alloys	179	288			

Index terms**Links**

Aluminum-rich intermetallic dispersoids (<i>Continued</i>)					
coarsening rates	189				
Al ₃ V	191				
Al-V-Zr system	189	192			
AlZr ₃ <i>see</i> Zr ₃ Al					
Al-Zr system	189				
phase diagram	139				
Al ₃ Zr	161	191			
in Al-Li alloys	192				
Anisotropy, of mechanical properties	68	294			
Anomalous yield-stress behavior	5	6	22	169	247
Antiferromagnetism, co-existence with superconductivity	234				
Antiphase boundaries (APBs)					
in Al ₃ Ti	153				
in D0 ₂₂ /D0 ₂₃ /L1 ₂ relation	160				
dissociation with	20				
in iron aluminides	205				
in L1 ₂ compounds	17	18	143		
Antiphase-boundary (APB) energies					
<i>ab initio</i> calculations	60				
for AlNi ₃ and alloys	276	289			
for D0 ₂ compounds	157				
for dispersoids/precipitates	275	276			
effect of alloying additions	61				
for L1 ₂ compounds	21				
for Ni ₃ Al and alloys	21				
for superalloys	290				
Antisite defects					
in AlNi ₃ -based alloys	16				
in trialuminides	161				
Astroloy [superalloy]	4	40			
Auger electron spectroscopy (AES)	25	26	32	218	

<u>Index terms</u>	<u>Links</u>				
Augmented plane-wave (APW) method, applications	223				
Austenitic stainless steels	1				
<i>see also</i> A-286; Tinidur					
Automobile applications	43	90	261		
B					
B2 type compounds, crystal structure	56	57	64	204	
B-1900 [superalloy]	4				
Be-Nb system, properties	249	253			
Beryllium, ductility of Ni ₃ Al alloys affected by	36	37			
Boron					
creep behavior affected by	210				
ductility affected by	15	27	29	61	208
ductility of Ni ₃ Al alloys affected by	36	37			
Boron-doped Al-Ni alloys					
ductility	15				
environmental embrittlement of	49				
Boron-doped Ni ₃ Al					
crack propagation rates	40				
ductility	27	29			
at elevated temperatures	38				
at room temperature	36				
fatigue life, temperature effects	30				
yield strength	39				
Bridgman [single-crystal growth] method	69	69			
Brittleness					
at grain boundaries	25				
criteria	170				
dynamic effect	31				
in titanium aluminides	79	151			
in trialuminide compounds	152	167	170		

Index termsLinks

Brittle-to-ductile transition temperature			
as function of melting temperature	250		
high-temperature intermetallics	248	249	250
silicides	222		
Bulk modulus, for Al_3Ti	153		
Burgess vectors	246		
C			
C1 structure	216		
C11 _b structure	216		
C40 structure	216		
CANDU nuclear power reactor	137		
Cast alloys			
iron aluminides	205		
nickel-based superalloys	5	6	
titanium aluminides	85		
Ceramic matrix composites	294		
compared with intermetallic composites	294		
Charge-coupled devices (CCDs)	236		
Chemical vapor deposition (CVD)	297	304	
Chisel toughness			
Cr-Ti alloys	246		
high-temperature intermetallics	249	252	
tools for measurement	251	252	
Chromium, ductility of Ni_3Al alloys affected by	38		
Chromium-based alloys	38		
coatings used	232		
Chromium disilicide	227		
mechanical properties	226		
C-Mo-Si system	230		
phase isotherm	230		
Coal gasifier applications	211		

<u>Index terms</u>	<u>Links</u>				
Coatings	126				
Al ₃ Ti-based	172	174			
aluminide	59	126	172	174	178
corrosion-resistant	59				
NiAl-based	59				
oxidation-resistant	174				
for reinforcement fibers	299				
silicide-based	215	231			
Ti ₃ Al-based	126				
Coating techniques	231				
Cobalt silicides	220				
properties	248				
Co-continuous phases	293	294			
Co-Cr-Ni alloys, strengthening of	278	282			
Co-Cr-Ni-Ti alloys	287				
Coefficient of thermal expansion, of NiAl	59				
Coherency strengthening	272	289			
Coherent precipitates	2	3			
Columnar grain structures, Ni ₃ Al alloys	37				
Combustion synthesis	42				
Complex stacking faults (CSFs)	18	153			
dissociation with	20				
Composites	174	227	258	293	
Al ₃ Ti-based	174				
application temperatures	294				
continuous reinforcements used	296				
developments	302	308			
diffusion barriers used	301				
discontinuous reinforcements used	295				
hybrid	296				
iron-aluminide-based	212				
MoSi ₂ -based	227	300			

<u>Index terms</u>	<u>Links</u>					
Composites (<i>Continued</i>)						
nickel-aluminide-based	299					
processing of	303					
systems used	296					
titanium-aluminide-based	297					
Compressional stress-strain curves, Al-Ru alloys	255					
Computer models						
dislocations	21	242				
strengthening	266					
Co-Ni-Si system	220					
Consolidation under atmospheric pressure (CAP) technique	42					
Continuous cooling transformations (CCTs), in Ti ₃ Al-based alloys	100	101				
Continuously reinforced composites	296					
payoffs associated	295					
Corrosion resistance						
Al-Ru alloys	260					
iron aluminides	211					
Zr ₃ Al	148					
Co-Si system, mechanical properties	244	248				
Cost considerations	254	256	258			
Crack propagation rates	40					
Creep behavior						
high-temperature intermetallics	248					
iron aluminides	210	211				
in irradiation conditions	138					
nickel aluminides	40	41	65			
silicides	229					
superalloys	12	64	76			
titanium aluminides	76	80	84	85	94	
	116	134				
Creep resistance, effect of second phase	84					
Cr-Fe-Si system	229	230				

Index termsLinks

Critical resolved shear stress (c.r.s.s.)

effect of ternary additions	35	
temperature dependence		
anomalous behavior	22	
Ni ₃ (Al,Ta)	24	
nickel aluminides	17	60
normal behavior	21	
silicides	224	
titanium aluminides	104	133
trialuminide compounds	166	
in underaged alloys	275	

Cr-Mo-Si system 224 225

Cr-Ni-Si system 232

Cross slip	23	76		
models	22	23	25	35

Cr-Si-Ti system 233

Cr-Si-Ti-V system 233

Cr-Ti alloys, mechanical properties 244 246

Cr-Ti system 246

Crystal structures

Al-Ce-Fe system 183

of Al-Fe-Si-V compounds 184 186

of aluminides	15	16	16	56	57
	76	96	203	204	

effect on deformation mechanisms 246

of high-temperature intermetallics 244 248 249 253

illustrated	57	64	76	96	152
-------------	----	----	----	----	-----

TiAl 76

of trialuminides 152

Cube slip 11

Cu-Mg system 242

Cutting tools 44

<u>Index terms</u>	<u>Links</u>				
Cyclic oxidation	126	172	173		
CZ42 [aluminum alloy]	182				
Czochralski [single-crystal growth] technique	70				
D					
D0 ₃ structure	64	204	216		
D0 ₂₂ structure	152	160			
Al ₃ Ti-based compounds	152				
relation to L1 ₂ structure	152	160	160		
D0 ₂₃ structure	152	160			
relation to L1 ₂ structure	152	160	160		
D0 _a structure	160				
D8 ₈ structure	216				
Damage tolerance, in composites	300	303			
Defect structures, in iron aluminides	203				
Defect tolerance, in aluminides	68				
Deformation					
high-temperature intermetallics	246				
iron aluminide alloys	209				
nickel aluminide alloys	44	65			
silicides	220	222			
superalloys	11				
titanium aluminide alloys	75	103			
trialuminides	154	166			
Density					
Al-Ce-Fe phases	183				
aluminides	57	75	76	138	203
	299				
silicides	217	300			
trialuminides	151	152	174		
Diamond-pyramid hardness					
high-temperature intermetallics	253				

Index termsLinksDiamond-pyramid hardness (*Continued*)*see also* Hardness

Diesel engine parts	43	44		
Dies and molds	43	50		
Diffusional creep	119	123		
Diffusion barriers				
applications	301			
in composites	301			
Diffusivity, transition metals in aluminum	180			
Direct chill casting, aluminum alloys	179	180		
Directionally solidified materials				
Ni ₃ Al alloys	37	40	41	41
superalloys	2			
Disilicides	215	223		
Schottky barrier heights	234			
<i>see also</i> Molybdenum disilicide				
Dislocation climb	138			
Dislocation-constriction energies	23			
Dislocation cores, computer simulations	17	21		
Dislocation creep	119	123		
Dislocation dynamics, superalloys	11			
Dislocation-particle interactions	264			
Dislocations				
dissociation of, in L1 ₂ alloys	20	143	166	
in iron aluminides	205			
line tension of	269	278		
mobility of	158			
pinning of	23			
in trialuminide compounds	153	166		
velocity-stress relationship	242			
Dislocation structure, Ni ₃ Al	25			

<u>Index terms</u>	<u>Links</u>				
Dispersion-strengthened aluminum alloys	179				
properties and applications	197				
Dispersoids	263				
Al-Cr-X compounds	190				
Al-Fe compounds	180				
Al-Ce-Fe system	182	198			
Al-Fe-Si-X system	184	198			
Al ₃ (Hf,Nb,Ti,V,Zr) compounds	191				
Al ₃ (Li _{1-x} Zr _x) compounds	192				
Al-Mn compounds	189				
aluminum-transition-metal compounds	180				
composite Al ₃ Li/Al ₃ Zr	194	195	198		
in composites	299				
Dorn [dislocation creep] equation	65				
Ductility					
effect of alloying	61	62	82	218	219
effect of grain size	31	80			
effect of microstructure	79	80			
effect of off-stoichiometry	30				
effect of test environment	220				
elevated-temperature					
Al-Fe-Si-V alloys	198				
aluminide alloys	115	116			
NiAl alloys compared with superalloys	64				
Ni ₃ Al alloys	37				
Ni ₃ Al, effect of alloying	36	37			
nickel aluminides	30	31	60	76	
nickel-based superalloys	4				
room-temperature					
aluminide alloys	71	79	82		
Ni ₃ Al alloys	36				
silicides	218	224			

Index termsLinksDuctility (*Continued*)

titanium aluminides	79	85	94	109	113
	115	116			
trialuminides	170	171			
Zr ₃ Al	144	146	148		
Ductility enhancement					
iron aluminide alloys	208				
nickel aluminides	27	61			
silicides	219				
titanium aluminides	82	93			
trialuminides	158				
Duplex microstructures					
nickel-based superalloys	9				
titanium aluminides	78	111			
Dynamic embrittling mechanism	31				
Dynamic recrystallization	143	146			

E

Easy-slip dislocations	76				
Elastic constants					
<i>Ab initio</i> /first-principles calculations	152	242			
of trialuminides	152	153			
Elastic moduli					
Al-Fe-Si-V alloys	188				
high-temperature intermetallics	242	245			
iron aluminides	211				
and melting temperatures	256				
nickel aluminides	58				
silicides	217				
Electrical resistivity					
aluminides	138				
silicides	215	235			
trialuminides	161				

Index termsLinksElectrical resistivity (*Continued*)

Zr ₃ Al	140			
Electrodischarge machining	67	70		
effect on fatigue behavior of NiAl alloys	67			
Electron energy-loss spectroscopy (EELS), Al-Li alloys studied by	195			
Electron hole calculations	7			
Electronic band structure, NiAl	56			
Electronics applications	217	233		
Electron microscopy, weak-beam (WB) technique	218	274	277	
Embedded-atom method (EAM), applicability	19	60		
Environmental embrittlement				
in aluminides	26	126	148	208
at elevated temperatures	28	37		
grain-boundary brittleness caused by	26			
in Ni ₃ Al alloys	26	47		
Environmental resistance				
NiAl alloys	59			
as selection criterion	247			
Epitaxial silicides	235			
Escaig effect	23	24		
Eutectic composites	294	301		
Eutectoid reaction	77			
Extrusion processes	41	69	157	165

F

Fabrication techniques	41	89		
Fast-neutron irradiation, properties of Zr ₃ Al affected by	142	147	148	
Fatigue behavior				
iron aluminides	211			
nickel aluminides	30	38	39	67
titanium aluminides	76	85		

Index termsLinks

Fatigue crack growth					
iron aluminides	211				
titanium aluminides	124	125			
Fault stabilities, methods of predicting	18				
Fe-Al system					
crystal structure	203	204			
phase diagram	204				
phase stability	203				
Ferritic alloys					
strengthening of	283	288			
with Fe ₂ SiTi precipitates	284	290			
with NiAl precipitates	283	290			
Fe-Si-Ti alloys	288				
strengthening of	284				
Fiber-reinforced composites	296				
First-principles calculations, elastic constants determined	152				
Floating-zone (FZ) method	70	157	225		
Flow stress					
effect of strain rate	143				
temperature dependence	11	21	34	36	143
Flow-stress anomaly	247				
in L ₁₂ alloys	22	34			
in Ni ₃ Al	34				
Foil rolling	130				
Forging	88	129	165		
Fractographs, Zr ₃ Al	145				
Fracture mechanisms	31				
Fracture properties					
aluminides	25	144	206		
B2 compounds	66				
effect of boron	25	66			
L ₁₂ compounds	25	144			

Index termsLinksFracture properties (*Continued*)

nickel aluminides	66				
trialuminides	170				
Fracture toughness	66				
Al-Fe-Si-V alloys	199				
aluminides	80	87	94	122	147
disilicides	225				
nickel-based superalloys	4				
Friedel-Fleischer statistics	265	266	269	270	272
	274				
Full-potential linearized plane-wave (FLAPW) method, applications	152				
Furnace fixtures	43	50			
Furnace heating elements	215				
FVS1212 [aluminum alloy]	182	198			

G

G phase	63				
γ phase, titanium aluminides	75				
γ phase	263				
elemental partitioning to	6				
morphology	7				
nickel aluminides	1	2	3	15	40
γ surface	18				
Gas atomization [processing technique]	89				
Gas-turbine applications	43	44	55	57	59
	67	70	75	90	293
	295	300	302		
Grain-boundary brittleness	25				
environmental embrittlement as cause	26				
Grain-boundary embrittlement, Ni ₃ Al alloys	27	50			
Grain-boundary pinning	193				
Grain-boundary structure, Al-Zr system	147				

<u>Index terms</u>	<u>Links</u>				
Grain-refining agents	87				
Grain shape, ductility of Ni ₃ Al alloys affected by	37				
Grain size					
coarsening rates for Al-Fe-Si-X alloys	189				
ductility affected by	31	80	81		
oxygen embrittlement affected by	31				
tensile properties affected by	81				
H					
Hall-Petch plots					
TiAl γ alloys	81				
Zr ₃ Al	143				
Hall-Petch relationship	63	81	141	142	208
Hardness					
high-temperature intermetallics	246				
of high-temperature intermetallics	252				
high-temperature intermetallics	253				
and melting temperature	256	257			
of trialuminide compounds	167				
Hastelloy-X [superalloy]	39				
Heavy-fermion compounds, superconducting materials	233				
High-resolution electron microscopy (HREM) observations					
Al-Li-Zr system	195				
dislocations	156				
High-temperature aluminum alloys	182	198			
High-temperature intermetallics	241				
cost considerations	254	256	258		
mechanical properties	244				
physical properties	247	253	257		
screening of compounds	245				
extensive/less-intensive survey	251				
limited-choice/data-intensive survey	249				
selection criteria for	245				

Index terms**Links**High-temperature intermetallics (*Continued*)

special tough alloys	254			
structure types	244	248	249	253
ternary alloys	255			
High-temperature strength	34	62	244	245
High-temperature superconductors	215	227		
Hot-corrosion resistance	59			
Hot isostatic pressing (HIP)	165	261		
Hybridized bonding orbitals	159			
Hydrogen embrittlement	26	37	44	49
Hydroturbine parts	43			

I

IC-145 alloy	29			
IC-192 alloy	38			
IC-194 alloy	38			
IC-218 alloy	38			
IC-221/221M alloys	39	40	50	
IC-438 alloy	50	51		
Image sensors	236			
Impact resistance, aluminides	68			
Impurities				
ductility affected by	61	84		
strength affected by	84			
IN-100 [superalloy]	4	5	6	
IN-713C [superalloy]	39			
IN-738 [superalloy]	5	6		
INCO-718, mechanical properties	94			
Inconel superalloys	5	6	40	288
Infrared detectors	236			
Ingot production	165	179		
Integrated-circuit applications	217	234		

<u>Index terms</u>	<u>Links</u>				
Interfacial energy, superalloy precipitate coarsening affected by	8				
Intergranular fracture					
aluminides	25	66	211		
L1 ₂ compounds	25				
trialuminides	170				
Internal combustion engine applications	44				
Interstitial-vacancy recombination	138				
Intrinsic stacking faults	17				
IrNb	254				
properties	249	253			
Iron, ductility of Ni ₃ Al alloys affected by	36	36			
Iron aluminides	203				
composites	212				
corrosion resistance	211				
effect of alloying	210				
effects of boron	208	210			
mechanical properties	206				
oxidation resistance	211				
polycrystalline behavior	206				
elevated-temperature properties	208				
room-temperature properties	206				
processing of	205				
single-crystal behavior	206				
two-phase	210				
Iron silicides	221				
J					
Joining techniques	42	130			
K					
Kear-Wilsdorf (KW) locks/mechanism	11	12	22	23	141

Index termsLinks**L**

L1 ₀ type compounds, crystal structure	76				
L1 ₂ type compounds					
AlNi ₃ and alloys	15				
Al ₃ Ti-based compounds	159	172			
antiphase boundaries in	17	18			
crystal structure	15	16	152	160	216
relation to D0 ₂₂ and D0 ₂₃ structures	152	160	160		
fault types	19				
flow of	21				
anomalous behavior	22				
normal behavior	21				
fracture of	25				
nickel aluminides	1	15			
L2 ₁ type compounds, crystal structure	64				
Lamellar microstructure	77				
anisotropic deformation properties	81	82			
Laminated composites	293	296	297		
Larson-Miller plots	64	248	299		
Lattice parameters					
Al-Fe/Al-Fe-Si systems	181	188			
Al ₃ Ti	152				
Ni and Ni ₃ Al solutions	8				
Zr ₃ Al	138				
Laves phases, velocity-stress relationships	242				
Line compounds	138	174	228		
Localized point obstacles, strengthening by	264				
Long-period superstructures	152				
Long-range order (LRO) alloys	16				
Lüders bands	141				

Index termsLinks**M**

MA6000 [superalloy]	244				
Machining techniques	70				
Macrostructures, titanium aluminides	86				
Magnetic applications	221				
Magnetron sputtering	296				
Manganese, ductility of Ni ₃ Al alloys affected by	36	36			
Mar-M superalloys	4	5	6		
Martensitic transformations					
in nickel aluminides	56				
and shape-memory effects	56				
in titanium aluminides	98				
Mechanical alloying, aluminum alloys prepared	179				
Mechanical properties					
disilicides	224				
high-temperature intermetallics	244	246			
iron aluminides	206				
nickel aluminides	33	60			
superalloys	5	6	11		
titanium aluminides	79	82	85	94	108
	122				
Zr ₃ Al	140				
Melting methods [for synthesis]	41				
Melting temperatures					
aluminides	70	138	203	299	
and brittle-to-ductile transition temperatures	250				
and hardness	257				
high-temperature intermetallics	247	248	249	250	253
	255	256	257		
intermetallic compounds	241	248	249		
nickel aluminides	58				
as selection criteria	245				
and shear moduli	256				

<u>Index terms</u>	<u>Links</u>				
Melting temperatures (<i>Continued</i>)					
silicides	217	224	300		
and specific gravity	247				
trialuminides	173	174			
Melt spinning [processing technique]	37	184			
Metal-base transistors	217	235			
Metallization [in integrated circuits]	235				
Metastable crystalline phases, synthesis, by rapid solidification	184	189			
Mg-Zn system	242				
Microalloying					
of AlNi	61				
of Al ₃ Ti	151	158			
Microhardness testing	206	252			
<i>see also</i> Hardness					
Microstructure-property relationships, titanium aluminides	79				
Microstructures					
Al ₃ Ti-based alloys	165				
creep affected by	117	118			
effect of processing	128	129			
Mo-Si system	294				
Nb-Si system	302				
titanium aluminides	77	86	99	100	128
	129				
Miscellaneous intermetallic compounds	241				
Models					
dislocation	21	242			
strengthening	266				
Molecular-beam epitaxy (MBE)	235				
Molybdenum disilicide	215	224	227	300	
composites	301				
crystal structure	216				
mechanical properties	224				

Index termsLinksMolybdenum disilicide (*Continued*)

physical properties	248	300
Mo-Ni-Si system	230	
Mo-Si system		
microstructure	294	
properties	248	
Mo-Si-Ti system, phase equilibria	223	
Mo-Si-Zr system	229	230
Multicomponent refractory silicides	229	

N

NASAIR 100 [superalloy]	65			
Nb-Si system, composites	301	307		
Near-net-shape processing	41	42	69	70
Necking [in tensile testing]	146			
Neumann's principle	18			
Neutron absorption capture cross section, Zr ₃ Al	138	148		
NiAl				
in composites	299			
creep behavior	65			
density	57			
ductility, room-temperature	60			
elastic modulus	58			
melting temperature	58			
physical properties	56			
as precipitate in ferritic alloys	283			
Young's modulus as function of temperature	58			
Ni-Al alloys, precipitation strengthening in	277			
NiAl-based alloys				
ductility	60			
elevated-temperature	64			
room-temperature	61			

Index terms**Links**

NiAl-based alloys (<i>Continued</i>)				
fabrication and processing of	69			
fatigue behavior	67			
fracture properties	66			
mechanical properties	60			
oxidation resistance	59			
strength	62			
in turbine airfoil design	67			
Ni-Al eutectic alloys	302			
Ni-Al system, phase diagram	3	57		
Ni ₃ Al				
crystal structure	1	15	16	16
environmental embrittlement of	26	47		
fault energies	20	21		
intergranular fracture of	25			
planar faults in	17			
solid-solution hardening of	242			
in superalloys	1			
Ni ₃ Al-based alloys	15			
alloy design	38			
polycrystalline alloys	38			
single crystals	39			
alloying effects	32			
dislocations in	20			
environmental embrittlement				
at elevated temperatures	28			
effect of aluminum concentration	28	29	30	
environmental embrittlement of	26			
fabrication techniques	39	41		
mechanical properties	33			
effect of boron	27			
processing of	41			
structural applications	43			

Index termsLinksNi₃Al-based alloys (*Continued*)

welding of 42

Nickel aluminides *see* NiAl; Ni₃Al

Nickel-based superalloys 1

alloying of 6

compared with intermetallics 39 40 41 58 59
59 64 65 67 76

composition 4

crack propagation rates 40

creep behavior 64

development advances 2

dislocations in 11

 γ/γ' misfit 8

historical perspective 1

microstructure 4 9 10

oxidation resistance 5

phase stability considerations 7

physical metallurgy 2

precipitate morphology 7

silicide coatings for 232

stress coarsening in 9

stress-rupture curves 5

stress-rupture life 12

tensile strength 5 11

yield strength 6 10 39

Nickel silicides 219

Ni-Cr-Al alloys

stress-rupture life affected by lattice mismatch 12

yield stress as function of temperature 11

Nimonic 80A 4 5 6 276 278
281 290

Nimonic 105 276 278 281 290

Nimonic 115 5

<u>Index terms</u>	<u>Links</u>				
Nimonic 901	40				
Nimonic PE16	276	278	279	290	
Nimonic superalloys	279				
chemical compositions listed	4	276			
crack growth curves	40				
precipitation strengthening of	278				
strengthening by bimodal dispersions of precipitates	286				
stress-rupture-temperature curves	5				
yield-strength-temperature curves	6				
Niobium					
oxidation behavior affected by	83				
plasticity of Ti ₃ Al alloys affected by	93				
Niobium-based alloys, coatings for	232				
Ni-Si-Ti system	219				
Notch sensitivity	147				
Notch strength ratio (NSR)	147				
For Zr ₃ Al	147	148			
Nuclear reactor structural materials	137				
requirements	137	138			
O					
O (orthorhombic) phase					
in Al-Fe-Si-V system	184	185			
in Al-Nb-Ti system	96	97	106	108	298
	299				
Off-stoichiometry effects					
in aluminides	28	30	33	34	62
iron aluminides	211				
in trialuminide compounds	167	168			
Ohmic contacts	217	235			
Ordered twinning	154				
Order strengthening mechanism	272				

<u>Index terms</u>	<u>Links</u>				
Orowan equation	266	274			
Orthorhombic symmetry, in Al-Nb-Ti system	96	97	106	108	247
Oxidation behavior					
aluminides	126	211			
coatings on Nb-based alloys	233				
silicides	231	232			
Oxidation resistance					
high-temperature intermetallics	248				
iron aluminides	211				
nickel aluminides	59				
as selection criterion	250				
silicides	217	231			
titanium aluminides	83	126			
trialuminides	171				
Zr ₃ Al	148				
Oxygen embrittlement	28	44	126		
dynamic effects	31				
effect of grain size	31				
Ni ₃ Al alloys	31	37			
P					
PA 107 [aluminum alloy]	182				
Paidar-Pope-Vitek (PPV) [dislocation-locking] model	22				
modifications	23				
Palladium, ductility of Ni ₃ Al alloys affected by	36	37			
Peak strength					
correlation with antiphase-boundary energies	289	290			
listed for various alloys	290				
model prediction	287				
Peak strengthening	274	289			
Peierls stress	17	21			
Peritectoid transformations	138				

<u>Index terms</u>	<u>Links</u>		
Permeable-base transistors (PBTs)	217	235	
Pest degradation effect/phenomenon	211	294	
PHACOMP [phase computation] analysis	7		
Phase diagrams			
Al-Ce-Fe system	183		
Al-Cr-Ti system	177		
Al-Fe-Si-V system	187	197	
Al-Fe-V system	188		
Al-M-Ni system	7	33	
Al-Nb-Ti system	95		
Fe-Al system	204		
Ni-Al system	3	57	
Ti-Al system	77		
Zr-Al system	139		
<i>see also</i> Pseudobinary...; Ternary phase diagrams			
Phase equilibria			
Al-Fe-Si system	221	222	
Al-Fe systems	187		
Fe-Al systems	203		
as selection criteria	247		
titanium aluminides	77	97	98
Phase equilibrium calculations, aluminum-transition metal systems	196		
Phase stability			
aluminides	56	203	
superalloys	7		
trialuminides	159		
Phase transformations, titanium aluminides	98		
Physical properties			
Al-Fe-Si-V alloys	188		
high-temperature intermetallics	247	253	257
nickel aluminide	56		
silicides	217		
titanium aluminides	75	76	

Index termsLinks

Physical properties (<i>Continued</i>)		
Zr ₃ Al	138	140
Physical vapor deposition (PVD)	304	
Planar faults		
in Al ₃ Ti	153	
in Ni ₃ Al	17	
in Zr ₃ Al	144	
Plastic deformation, of trialuminides	170	
Platinum silicide infrared detectors	238	
Point defects, in iron aluminides	203	
Poisson's ratio		
nickel aluminides	58	
silicides	217	
trialuminides	153	
Polycrystalline NiAl		
ductility	60	
tensile yield strength	62	63
Young's modulus	58	
Polycrystalline Ni ₃ Al	38	
environmental embrittlement of	26	48
Pore volume fraction, in trialuminide compounds	165	
Powder metallurgy		
for aluminide alloys	89	206
for Ni ₃ Al alloys	41	
techniques, reactive sintering	42	
Power-law creep	119	
Precipitation-hardened alloys	11	
Precipitation hardening	166	169
Precipitation strengthening	263	
in Al-Ni alloys	277	
mechanisms	272	
for overaged alloys	274	

<u>Index terms</u>	<u>Links</u>				
Precipitation strengthening (<i>Continued</i>)					
for underaged alloys	273				
Primary creep	121				
Process efficiency maps, Ti ₃ Al alloys	127				
Processing					
of Al-Ru alloys	261				
of composites	303				
forming techniques	41	69	140		
hot isostatic pressing	261				
ingot production	179	180			
of iron aluminides	205				
joining techniques	42	130			
melting methods, ingot production	165				
microstructures arising	128				
of Ni ₃ Al alloys	41				
of nickel aluminides	69				
of silicides	221				
thermomechanical operations					
casting	85	179	180		
extrusion	41	69	157	165	206
forging	88	129	165		
wrought processing	87				
of titanium aluminides	85	127	162		
of trialuminides	165				
Pseudobinary phase diagrams					
AlFe ₃ -Fe ₃ Si	222				
MoSi ₂ -Si ₂ Ti	223				
Pugh [brittleness] criterion	170				
PWA-1422 alloy	40	41			
PWA-1480 alloy	4				
PWA-1484 alloy	4				

Index termsLinks**Q**

Quasicrystals

decagonal phase	183	189
-----------------	-----	-----

icosahedral phase	184	189
-------------------	-----	-----

Quaternary alloying, silicides affected by	219
--	-----

Quenching transformations, in titanium aluminides	98
---	----

R

Radiation detectors	236
---------------------	-----

Radioisotope thermoelectric generators	254
--	-----

Rapid-solidification methods

Fe-Al-based alloys	182	183	206
--------------------	-----	-----	-----

TiAl-based alloys	89
-------------------	----

Reaction sintering	42
--------------------	----

Reduction in area

Ti ₃ Al-based alloys	115
---------------------------------	-----

Zr ₃ Al	144	146	148
--------------------	-----	-----	-----

Refractory-metal silicides	215	223
----------------------------	-----	-----

A15 silicides	227
---------------	-----

disilicides	223
-------------	-----

5:3 silicides	228
---------------	-----

multicomponent	229
----------------	-----

Reinforcements

continuous	293	296
------------	-----	-----

discontinuous	295
---------------	-----

René superalloys	40	62	63	64	67
------------------	----	----	----	----	----

Rice-Thomson [brittleness] criterion	171
--------------------------------------	-----

RuSc, properties	249	253	254
------------------	-----	-----	-----

RuTa	254
------	-----

properties	253
------------	-----

Ruthenium, price variations	258
-----------------------------	-----

Index termsLinks**S**

S phase, in Al-Li alloys	192		
Scalloped dislocation images	274		
Schottky-type devices	217	234	236
Schwarz-Labusch statistics	269	272	279
Screening approaches, high-temperature intermetallics	245		
Screw dislocations	21	107	
Selected area electron diffraction (SAED) observations	154	155	
Sendust [magnetic material]	221		
Shape-memory effects, and martensitic transformations	56		
Shear moduli			
high-temperature intermetallics	256		
nickel aluminides	58		
silicides	217		
trialuminides	153		
Shear stress, Al ₃ Ti	158	159	
Shockley partial dislocations	23	24	76
Silicides	215		
A15 silicides	227		
coatings based on	215	231	
crystal structure	216		
electrical resistivity	215	235	
epitaxial silicides	235		
5:3 silicides	228		
multicomponent silicides	229		
oxidation resistance	217	231	
physical properties	217		
refractory-metal	215	223	
superconductors	215	227	233
ternary silicides	229		
Ti-based alloys strengthened by	288		
transition-metal silicides	217		

Index termsLinks

Silicon carbide					
fibers	296	298			
whiskers	301				
Simulation methods, dislocation fine structure	21				
Single-crystal aluminides	69	206			
Ni ₃ Al	39				
NiAl, Young's modulus	58				
yield and flow behavior	35				
Single-crystal trialuminides	157				
Sintering, reactive sintering	42				
Si-Ti system, mechanical properties	244	247			
Slip systems					
NiAl	15				
Ti ₃ Al alloys	104	133			
trialuminide compounds	158	159	166		
Zr ₃ Al	147				
S-N curves, TiAl-based alloys	85				
Solid-solution hardening	40	44	167	204	210
	242				
Ni ₃ Al	33				
Solid-state transformation, TiAl alloys	77				
Solubility limits					
AlNi ₃ ternary phases	32				
transition metals in aluminum	180				
Space applications	233	293	295		
Specific gravity					
high-temperature intermetallics	247	248	249	253	
and melting temperature	247				
Specific strength	169				
as selection criterion	245				
Splat-cooled Al-Fe alloys	182				

<u>Index terms</u>	<u>Links</u>				
Stacking faults					
in Al_3Ti	153				
in Ni_3Al	17				
in Zr_3Al	143	144			
Stacking sequences	160				
Steady-state unzipping process	265				
Strain-rate sensitivity					
aluminides	67	68			
silicides	222				
Strength					
analyzing and modeling of experimental data	275				
and grain size	81				
of iron aluminides	207	209			
of nickel aluminides	34	35	36	40	62
of superalloys	6	10	39	76	
temperature dependence	34	36	39	62	88
	115	141	157	168	
of ternary trialuminides	168				
of titanium aluminides	76	85	88	94	109
	110	115	116		
of Zr_3Al	140				
Strengthening					
of Al-Ni alloys	277				
by bimodal dispersions of precipitates	285	287			
of Co-Cr-Ni alloys	282				
computer simulation of	266	268			
by extended obstacles	266				
of ferritic alloys	283				
by finite obstacles	268				
generalized addition rule for	267	288			
implications for alloy design	288				
mechanisms	272				
by mixtures of obstacles	267				

Index termsLinksStrengthening (*Continued*)

in overaged alloys	274
in peak-aged alloys	274
by point obstacles	264
precipitation strengthening	263
of superalloys	279
in underaged alloys	273

Stress-assisted grain-boundary oxidation	31
--	----

Stress exponents [in creep]	65	117
-----------------------------	----	-----

Stress-rupture behavior, titanium aluminide alloys	120
--	-----

Stress-rupture curves

NiAl alloys	64
superalloys	5 64

Stress-rupture life

superalloys	12
titanium aluminide alloys	94

Stress-strain diagrams

Al-Ru alloys	255
Al ₃ Ti	158
calculated/predicted curves	242 243
serrations in	158
Zr ₃ Al	142

Subtransus processing, Ti ₃ Al alloys	100	111
--	-----	-----

Subtransus structures	79
-----------------------	----

Superalloys

compared with intermetallics	39	40	41	58	59
	59	64	65	67	76
	244				
compositions listed	276				
nickel-based	1				
strengthening of	279	289			
<i>see also</i> Nickel-based superalloys					

Superconductors, silicides as	215	227	233
-------------------------------	-----	-----	-----

<u>Index terms</u>	<u>Links</u>			
Superdislocations, in aluminides	16	76		
Super Kanthal furnace elements	215			
Super-lattice dislocations	16	208		
Superlattice intrinsic stacking-fault (SISF) energies	18	157		
Superlattice intrinsic stacking faults (SISFs)	17	143	144	153
dissociation with	20			
Superpartial dislocations	16			
Superplasticity				
silicides	217			
titanium aluminide alloys	88	129		
Supersolvus structure	79			
SUPERTHERM alloy, compared with IC-438 alloy	51			
Surface energy, trialuminides	171			
T				
T phase, in Al-Li alloys	192			
Taylor orientation factor	35			
TD Nickel [superalloy]	5	6		
Tensile strength				
superalloys	11			
Zr ₃ Al	148			
Ternary compounds				
high-temperature intermetallics	255	258		
silicides	229			
trialuminides	162	168	169	
Ternary phase diagrams				
Al-Ce-Fe system	183			
Al-Fe-V system	188			
Al-M-Ni system	7	33		
Al-Nb-Ti system	95			
C-Mo-Si	230			
Cr-Fe-Si	230			

Index termsLinksTernary phase diagrams (*Continued*)

Mo-Ni-Si 230

Mo-Si-Zr 230

Tetragonal structures 75

Thermal conductivity

aluminides 76 299

nickel aluminides 58

silicides 300

Thermal expansion

Al-Fe-Si-V alloys 189

aluminides 59 138

silicides 228

Thermally activated dislocations, nickel-based superalloys 11

THERMO-CALC computer program 196

Thermocouples 215

TiAl₃ *see* Al₃Ti γ -TiAl

crystal structure 76

deformation mechanisms 75

physical properties 75

see also TiAl-based alloys

TiAl-based alloys 75

alloying modifications 82

applications 89

cast alloys 85

creep properties 80 84

ductility 31 79 82

at low temperatures 79 82 82

effect of interstitial impurities 84

fracture toughness 80

microstructures 77

oxidation resistance 83 126

powder metallurgy for 89

Index termsLinks

TiAl-based alloys (<i>Continued</i>)		
processing of	85	
tensile properties	81	82
wrought alloys	85	87
Ti-Al system, phase diagram	77	
Ti ₃ Al-based alloys	93	
in composites	297	300
creep behavior	116	134
crystal structures	96	
current status of development	93	95
deformation behavior	103	
fatigue crack growth	124	125
fracture toughness	122	
mechanical properties	94	
micromechanisms of fracture	110	
oxidation behavior	126	
phase equilibria	97	
phase transformations	98	
processing of	127	
tensile behavior	108	
effect of heat treatment	109	
effect of hydrogen	115	
effect of strain rate	115	
effect of temperature	114	
ternary O + B2 alloys	134	
Time-temperature-transformation (TTT) diagrams	139	140
Tinidur [superalloy]	1	4
Titanium aluminide alloys		
properties listed	76	
SiC-fiber-reinforced	296	
<i>see also</i> TiAl-based...; Ti ₃ Al-based alloys		
Titanium aluminides		
applications	89	173 178

Index termsLinksTitanium aluminides (*Continued*)

in composites 297 307
see also TiAl; Ti₃Al

Titanium disilicide 227

Titanium trialuminide

D0₂₂-structure compounds 152 171
 L1₂-structure compounds 159
 oxidation behavior 171
see also Al₃Ti

Toughness

Al-Fe-Si-V alloys 199
 high-temperature intermetallics 244 245 246
 nickel aluminides 66
 room-temperature 253
 titanium aluminides 80 85 87 94 122
 Zr₃Al 147
see also Chisel toughness

Transformations

martensitic 56 98
 peritectoid 138
 in titanium aluminides 98

Transistor applications 217 235

Transition metals

diffusivity in aluminum 180
 solubility in aluminum 180

Transition-metal silicides 217

Transmission electron microscopy (TEM) observations

Al-Cr-Ti compounds 167
 Al-Ni alloys 268
 Al-rich dispersoids in aluminum alloys 182 193 194 196
 Al-Ti-based alloys 103 104 170

Trialuminides 151

as dispersoids in aluminum alloys 191

Index termsLinks

Trialuminides (*Continued*)

see also Al₃Ti

Triple-defect model	56			
TRW-NASA IV A [superalloy]	5			
T-T-T diagrams <i>see</i> Time-temperature-transformation diagrams				
Tungsten disilicide	227			
Turbine applications	178			
<i>see also</i> Gas-turbine applications				
Turbocharger parts	43			
Tweed microstructure	99			
Twinning, in Al-Ti alloys	105	155		

U

Udimet superalloys	4	5	6	40
Ultimate tensile strength				
Al-Fe-Si-V alloys	198			
high-temperature intermetallics	248			
Ti ₃ Al-based alloys	115	116		
Unitemp superalloys	6			

V

Vacuum melting, superalloys	1			
Vegard's law	191			

W

Waspaloy [superalloy]	4			
Weight-reduction effects	57	75	295	
Weldability				
aluminide alloys	206			
Ni ₃ Al alloys	43			
Welding	42	130		

Index termsLinks

Wiedemann-Franz relation	140				
Workability, titanium aluminide alloys	88				
Work hardening, Zr_3Al	142	146			
Wrought alloys					
aluminides	79	85	87		
aluminum alloys	189				
banding in ingots	81	88			
nickel-based superalloys	5	6			
X					
X8019 [aluminum alloy]	182				
XD TM -processed alloys	88				
Y					
Yield anomaly					
Fe_3Al	209				
Ni_3Al	22	34			
Yield strength					
Al-Fe-Si-V alloys	198				
effect of grain size	81	141	142	208	
effect of irradiation	142				
effect of off-stoichiometry	33	34			
high-temperature intermetallics	244	245			
iron aluminides	207	209			
Ni_3Al alloys	40				
nickel aluminides	34	35	36	62	63
silicides	218	221	229	245	
superalloys	6	10	39	76	244
temperature dependence	34	36	39	62	88
	115	141	198	209	218
	221				
ternary Ni_3Al alloys					

Index termsLinksYield strength (*Continued*)

as function of solute concentration	34				
solid-solution hardening	34				
titanium aluminides	76	85	88	94	109
	110	115	116		
trialuminides	168				
Zr ₃ Al	140				
Yield stress, effect of orientation	35	82			
Young's modulus					
of Al-Fe-Si-V alloys	198				
of aluminides	58	58	138		
of high-temperature intermetallics	249	253			
of MoSi ₂	300				
temperature dependence	76				
of titanium aluminide alloys	76				
of trialuminides	153				

Z

Zener's ratio of elastic anisotropy	23				
Zircaloy alloys	137	148			
Zirconium, ductility of Ni ₃ Al alloys affected by	36	37			
Zirconium aluminide <i>see</i> Zr ₃ Al					
Zirconium-based alloys	137				
Zirconium trialuminide	191	249			
Zr ₃ Al	137				
compared with Zircaloy alloys	148				
ductility of	144	146			
fracture properties	145	146			
fracture toughness	147				
mechanical properties	138	140			
microstructure	138				
notch sensitivity	147				

<u>Index terms</u>	<u>Links</u>
<i>Zr₃Al (Continued)</i>	
physical properties	138 140
processing/forming to shape	140
work hardening of	142
Zr-Al system, phase diagram	139

Contents

Contributors ix

Preface to the 1995 Edition xi

Preface to Reprint Volumes xiii

Acronyms xv

Crystal Structure Nomenclature xxi

1. Ni₃Al in Nickel-Based Superalloys **1**

1.1 Introduction 1

1.2 Alloying 6

1.3 γ' Morphology 7

1.4 Deformation 11

1.5 Summary and Future Considerations 12

1.6 Acknowledgements 12

1.7 References 12

Addendum 13

2. Ni₃Al and Its Alloys **15**

2.1 Introduction 15

2.2 Planar Faults, Superlattice Dislocations and Flow Properties 16

2.3 Intergranular Fracture and Boron Effect in Polycrystalline NiAl 25

2.4 Environmental Embrittlement at Elevated Temperature 28

2.5 Alloying Effects and Alloy Design 32

2.6 Material Processing and Structural Applications 41

2.7	Summary and Future Research	44
2.8	Acknowledgements	45
2.9	References	45
	Addendum	49
3.	NiAl and Its Alloys	55
3.1	Introduction	55
3.2	Physical and Mechanical Properties of NiAl	56
3.3	Design of NiAl Airfoils	67
3.4	Processing, Fabrication, and Machining	69
3.5	Concluding Remarks	71
3.6	Acknowledgements	71
3.7	References	71
4.	Gamma TiAl and Its Alloys	75
4.1	Background	75
4.2	Basic Characteristics of γ -Based Materials	75
4.3	Microstructure Formation	77
4.4	Microstructural Dependence of Properties	79
4.5	Alloying Modifications	82
4.6	Processing to Useful Forms	85
4.7	Applications	89
4.8	Summary	90
4.9	References	90
5.	Ti₃Al and Its Alloys	93
5.1	Introduction	93
5.2	Crystal Structures, Phase Equilibria and Phase Transformations	96
5.3	Deformation Behavior of the α , O, and B2 Phases	103
5.4	Tensile Behavior of α Alloys	108
5.5	Creep	116
5.6	Fracture Toughness and Fatigue Crack Growth	122

5.7	Oxidation	126
5.8	Processing	127
5.9	Conclusion	130
5.10	Acknowledgments	130
5.11	References	130
	Addendum	133
6.	Zr₃Al: A Potential Nuclear Reactor Structural Material	137
6.1	Introduction	137
6.2	Background	137
6.3	Processing and microstructure of Zr ₃ Al	138
6.4	Physical Properties	140
6.5	Mechanical Properties	140
6.6	Comparison with Zircaloy-2 and Zr-2.5% Nb	148
6.7	Status	149
6.8	Acknowledgements	149
6.9	References	149
7.	Al₃Ti and Its L₁₂ Variations	151
7.1	Introduction	151
7.2	Al ₃ Ti with the D0 ₂₂ Structure	152
7.3	L ₁₂ Variations of Al ₃ Ti	159
7.4	Oxidation Behavior of AlTi and its L ₁₂ Variations	171
7.5	Application Potential and Summary	173
7.6	References	174
	Addendum	177
8.	Al-Rich Intermetallics in Aluminum Alloys	179
8.1	Introduction	179
8.2	Aluminum-Transition Metal Compounds	180
8.3	Al ₃ (Zr _x Li _{1-x}) Intermetallics	192
8.4	Intermetallic Phase Equilibrium Predictions	196

8.5	Properties and Applications	197
8.6	Summary	199
8.7	Acknowledgements	199
8.8	References	200
9.	FeAl and Fe₃Al	203
9.1	Introduction	203
9.2	Phase Stability and Defect Structures	203
9.3	Processing	205
9.4	Mechanical Properties	206
9.5	Oxidation and Corrosion Resistance	211
9.6	Composites	212
9.7	Summary	212
9.8	References	212
10.	Silicides: Science, Technology and Applications	215
10.1	Introduction	215
10.2	Structural Silicides	217
10.3	Silicides as High-Temperature Coatings	231
10.4	Silicides in the Electronics Industry	233
10.5	Summary	237
10.6	References	237
11.	Miscellaneous Novel Intermetallics	241
11.1	Introduction	241
11.2	Basic Studies	241
11.3	Screening High Melting-Temperature Compounds	245
11.4	Systematics, Trends, and Conclusions	256
11.5	Acknowledgements	259
11.6	References	259
	Addendum	260

12. Intermetallics as Precipitates and Dispersoids in High-Strength Alloys	263
12.1 Introduction	263
12.2 Dislocation-Particle Interactions: Statistics	264
12.3 Dislocation Line Tension	269
12.4 Mechanisms of Precipitation Strengthening	272
12.5 Procedures for Analyzing and Modeling Experimental Data	275
12.6 Examination of Experimental Data	276
12.7 Discussion	286
12.8 Summary	290
12.9 References	290
Addendum	292
13. Intermetallic Composites	293
13.1 Introduction	293
13.2 Intermetallic Composite Classes	295
13.3 Composite Systems	296
13.4 Composite Development	302
13.5 Processing	303
13.6 Concluding Remarks	304
13.7 Acknowledgements	304
13.8 References	305
Addendum	307
Index	309

Chapter 2

Ni₃Al and its Alloys

C. T. Liu

Metals and Ceramics Division, Oak Ridge National Laboratory, Oak Ridge, TN 37831-6115

David P. Pope

Department of Materials Science and Engineering, University of Pennsylvania, 3231 Walnut Street, Philadelphia, PA 19104-6272

1. Introduction

The L1₂ (cP4) nickel aluminide Ni₃Al has been studied extensively since the 1950s (Westbrook, 1959, 1967; Stoloff 1966; Stoloff, 1984; Stoloff *et al.*, 1987b; Liu and Stiegler, 1984; Liu *et al.*, 1984, 1989, 1992; Izumi, 1991; Johnson *et al.*, 1991; Kear *et al.*, 1970; Koch *et al.*, 1985; Whang *et al.*, 1990, 1992). This is because this aluminide is of both technological and scientific interest. Technologically, Ni₃Al is the most important strengthening constituent, generally referred to as the γ' phase, of commercial nickel-based superalloys used extensively as structural materials at elevated temperatures (see Chapter 1 by Anton). The γ' phase is responsible for the high-temperature strength and creep resistance of the superalloys. Ni₃Al alloys are generally resistant to air oxidation as a result of their ability to form adherent oxide surface scales that protect the base metal from excessive attack (Aitken, 1967; Meier and Pettit, 1992).

Scientifically, the aluminide shows a number of unusual mechanical properties, which are distinctly different from those of conventional solid-solution alloys (i.e. disordered alloys). It exhibits anomalous yield behavior, that is, its yield strength increases rather than decreases with increasing temperature (Copley and Kear, 1967; Thornton *et al.*, 1970; Takeuchi *et al.*, 1973; Takeuchi and Kuramoto, 1973; Pidar *et al.*, 1984). The strength reaches a maximum around 600 to 800 °C, above which Ni₃Al shows a change in slip systems from {111}<110> to {100}<110>. Single crystals of Ni₃Al

are ductile, but pure polycrystalline Ni₃Al is very brittle at room temperature because of grain-boundary fracture (Liu, 1991). Contrary to common experience with conventional materials, its grain boundaries are usually clean and free from impurities; as a result, they were considered to be intrinsically brittle. Boron additions dramatically improve the ductility of polycrystalline Ni₃Al, and the beneficial effect has been the subject of substantial studies in recent years (Liu, 1992b). The mechanical properties and alloying behavior of Ni₃Al are very sensitive to alloy off-stoichiometry, even though no major constitutional vacancies are detected above 25 at% Al. The solid-solution hardening behavior is not well understood at present (Dimiduk, 1989; Dimiduk *et al.*, 1992).

Ni₃Al is the first intermetallic compound formed as aluminum is added to nickel (Massalski, 1986). It has an L1₂ (cP4) ordered crystal structure (Figure 1a) below the peritectic temperature of 1395 °C (Guard and Westbrook, 1959). Its unit cell contains four atoms, with three nickel atoms occupying face-centred positions and with one aluminum atom at corner positions. The L1₂ crystal structure can be viewed as stacking of three close-packed planes in the stacking sequence of ABC (Figure 1b). Ni₃Al has a homogeneous phase field of about 3 at% around its stoichiometric composition. With off-stoichiometric compositions, antisite substitutions are formed on both nickel-rich and aluminum-rich sides of Ni₃Al (DasGupta *et al.*, 1985). This is quite different from

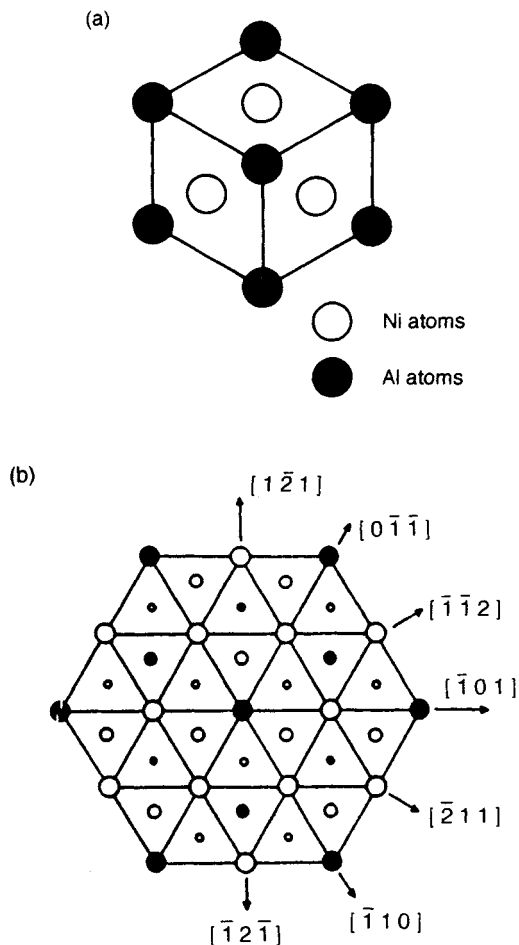


Figure 1. Ordered crystal structure of Ni₃Al: (a) the L1₂ crystal structure, and (b) three successive close-packed {111} planes, with large, medium and small circles representing atoms in upper, middle and lower planes, respectively

B2-NiAl, where antisite defects are stable in the nickel-rich side and vacancies are formed in the aluminum-rich side (Bradley and Taylor, 1932, 1937).

This chapter provides a comprehensive review of recent studies of Ni₃Al and its alloys. Some general articles on physical metallurgy and mechanical properties of Ni₃Al and other intermetallics were included in proceedings of intermetallic conferences and workshops and special journal issues on ordered intermetallics published recently (Westbrook, 1959, 1967; Stoloff and Davies, 1966; Stoloff, 1984; Stoloff *et al.*, 1987b; Liu and Stiegler, 1984; Liu *et al.*, 1989, 1992; Liu and Oliver, 1989; Izumi, 1991; Johnson *et al.*, 1991; Kear *et al.*, 1970; Koch *et al.*, 1985; Whang *et al.*, 1990,

1992; Yamaguchi and Umakoshi, 1990; Pope and Ezz, 1984; Schulson, 1984; Brooks *et al.*, 1984; Pope, 1984; Suzuki *et al.*, 1989; Dimiduk, 1991). Readers are urged to go over these volumes for detailed information. The role of Ni₃Al in deformation and fracture in nickel-based superalloys is described in Chapter 1 by Anton in this volume.

This chapter contains seven sections. Section 2 describes planar faults, superlattice dislocations, and flow properties of Ni₃Al alloys. Section 3 is devoted to the understanding of brittle intergranular fracture at ambient temperatures and the beneficial effect of boron additions. Section 4 concerns the reduction in ductility of Ni₃Al alloys when being tested at intermediate temperatures (300 to 900 °C) in oxidizing environments. Section 5 concerns alloying effects and alloy design of single and polycrystalline Ni₃Al alloys as elevated-temperature structural materials. Material processing and structural applications of Ni₃Al alloys are included in Section 6. The last section provides a brief summary and thoughts on future directions for research and development of Ni₃Al alloys.

2. Planar Faults, Superlattice Dislocations and Flow Properties

The L1₂ structure of Ni₃Al is an f.c.c.-derivative structure made up of close-packed planes having the correct stoichiometry, as shown in Figure 1, in which Ni–Al nearest neighbors are maximized and in which there are no Al–Al neighbors in the perfectly ordered state. The state of long-range order (LRO) in Ni₃Al is nearly perfect up to T_m (Pope and Garin, 1977), but it changes dramatically with temperature in other isostructural alloys such as Cu₃Au (Feder *et al.*, 1958) and in the so-called LRO alloys (Liu, 1984). In cases where the LRO changes with temperature, the mechanical properties can be dramatically affected (e.g. Cu₃Au; Pope, 1972), but in this discussion we will concentrate on Ni₃Al, in which the LRO does not change with temperature. Since most of the unusual properties of Ni₃Al are controlled by the state of LRO in the material, it is appropriate to mention some of them at the offset. Since the total dislocation Burgers vector must be a lattice translation vector, the $\frac{1}{2}\langle 110 \rangle$ Burgers vector observed in f.c.c. materials constitutes a partial dislocation in L1₂ materials. Dislocations having long Burgers vectors are commonly called superdislocations and the constituent partial dislocations, which are total dislocations in the f.c.c. lattice, are commonly called ‘superpartial dislocations’ or just

'superpartials'. If the fault energy is sufficiently low, unpaired or very widely separated superpartials are sometimes seen, for example, when the Bragg-Williams LRO parameter approaches zero. However, the more usual case is for some combination of superpartials to move together as a group, the first dislocation(s) creating local disorder along planar faults and the final dislocation(s) correcting the disorder, as first seen by Marcinkowski *et al.* (1961). The exact nature of the dissociation is controlled by a balance between the elastic energy decrease resulting from the dissociation and the energy increase due to the creation of the surface energy of planar faults between the partial dislocations. These aspects are discussed in more detail later in this chapter.

The flow properties of L1₂ alloys are quite different for different alloys and for different temperature ranges for a given alloy. In this section we take the point of view of Vitek (1985), that the nature of the dislocation core has a major effect on the plastic properties, particularly on the temperature dependence of the flow stress. The more traditional point of view is that the dislocation core as it is spread in the slip plane by a width w results in a Peierls stress τ_p given by (Nabarro, 1974; Foreman *et al.*, 1951; Christian and Vitek, 1970)

$$\tau_p = (2G/\alpha) \exp(-4\pi w/b) \quad (1)$$

where G is the shear modulus, $\alpha = 1$ for screw and $(1 - \nu)$ for edge dislocations, ν is Poisson's ratio, and b is the Burgers vector. Such a model results in an increasing τ_p with decreasing w . But even if the core width is reduced to b , τ_p is only about $10^{-5} G$ for $\nu = \frac{1}{3}$. Such a small stress can be overcome by thermal fluctuations (Friedel, 1982). Consequently, we conclude that the traditional point of view is not correct and a more detailed model of the Peierls stress is required. Such a model was developed initially for b.c.c. metals (Vitek, 1974; Takeuchi, 1981; Vitek and Yamaguchi, 1981; Takeuchi, 1982; Yamaguchi, 1982). The model depends on the prediction, based on computer modeling experiments, that the cores of $\frac{1}{2}\langle 111 \rangle$ screw dislocations in b.c.c. metals do not spread in a single $\{110\}$ plane, but rather they spread into three $\{110\}$ planes having the $\langle 111 \rangle$ zone. Such a nonplanar core configuration gives rise to the characteristic temperature dependence of the critical resolved shear stress (c.r.s.s.) at low temperatures seen in b.c.c. metals, the indeterminate nature of the slip plane, and the existence of mostly screw dislocations in b.c.c. metals after low-temperature deformation. Vitek (1985) has presented extensive evidence that similar core phenomena control the flow properties of many crystalline materials, both ordered

and disordered. One very important result of the existence of nonplanar cores is the fact that components of the stress tensor which have *no net resolved* shear stress on the total dislocation can have a large effect on the flow properties by changing the nature of the core dissociation. Vitek calls these the 'nonglide' components of the stress tensor. Such components are very important in the flow of Ni₃Al.

2.1 Planar Faults in Ni₃Al

A given dislocation can dissociate in a number of ways, depending on which faults are stable and how long the Burgers vectors of the superpartials are. Here we consider only faults on $\{111\}$ and $\{010\}$ planes because those are the important slip planes in Ni₃Al. On $\{111\}$ planes there are three different faults, as originally discussed by Kear *et al.* (1968, 1969a, b).

2.1.1 Antiphase Boundaries on $\{111\}$ Planes

Antiphase boundaries (APBs) can exist on any plane, as discussed by Flinn (1960), but for purposes of the present discussion, the most important planes are $\{111\}$ and $\{010\}$. An APB on the $\{111\}$ plane is shown separating the superpartials in Figure 2. Another way of visualizing this fault is to consider the close-packed (111) planes shown in Figure 3(a) and, as shown in Figure 3(b), consider shifting the top layer and all those above it by $\frac{1}{2}[\bar{1}01]$, shown as \bar{b}_A in Figure 3(b). A single-layer fault is created in which the stacking sequence is still locally f.c.c. (abcabc stacking), but there are now B-B nearest neighbors where none exist in the unfaulted material. APB energies on $\{111\}$ planes, γ , were measured by Taunt and Ralph (1974) using field ion microscopy (FIM) and were found to be 250 to 350 mJ m⁻² in Ni₃Al, while TEM measurements by Veyssi re (1989), Veyssi re *et al.* (1985) and Douin *et al.* (1986) were found to be 111 ± 15 mJ m⁻². More recent measurements by Dimiduk (1991) showed a range of 123 to 198 mJ m⁻² with a precision of ± 20 –30 mJ m⁻², depending on the ternary addition.

2.1.2 Superlattice Intrinsic Stacking Faults on $\{111\}$ Planes

The superlattice intrinsic stacking fault (SISF) is produced by shifting the top layer and all those above it by $\frac{1}{2}[\bar{2}11]$, as shown in Figure 3(c). The local stacking sequence becomes h.c.p. (abab stacking), but there are no nearest neighbor violations. This fault is analogous to ordinary stacking faults in f.c.c. materials,

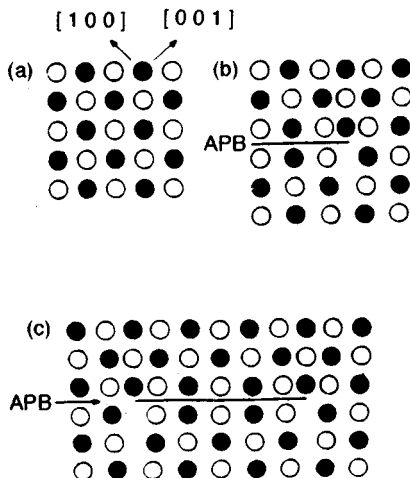


Figure 2. APBs on the (010) plane in L₁₂: (a) the (010) plane of the L₁₂ structure; (b) as in (a), but with a $\frac{1}{2}[\bar{1}01]$ dislocation on the {111} plane, producing an APB; (c) paired $\frac{1}{2}[\bar{1}01]$ dislocations, as in (b), with an APB between them

but note that a stacking fault in f.c.c. has a $\frac{1}{6}[\bar{1}\bar{1}2]$ fault vector while that of the SISF has a different direction and twice the magnitude. An SISF is expected to be of rather low energy; for example, Sastry and Ramaswami (1976) found the SISF energy in Cu₃Au to be 13 mJ m⁻² and Veyssi re *et al.* (1985) found the SISF energy in Ni₃Al to lie between 5 and 15 mJ m⁻².

2.1.3 Complex Stacking Faults on {111} Planes

A complex stacking fault (CSF) is produced when the top layer and all above it are shifted relative to those below it such that the B atoms in the top layer lie directly above the A atoms in the bottom layer, as shown in Figure 3(d). This shift results in a local h.c.p. stacking, as in the case of the SISF, but in this case there are also nearest neighbor violations, as shown by the dotted lines. This fault is expected to have a higher energy than either the SISF or the APB on {111} planes. Note also that the fault vector of a CSF is the same as that of an ordinary stacking fault in the f.c.c. structure.

2.1.4 Antiphase Boundaries on (010) Planes

The L₁₂ structure can be considered to be made up of alternate {010} planes, first one plane consisting only of A atoms and then one consisting of equal numbers of A and B atoms, as shown in Figure 4. If the top layer and those above it are shifted relative to those below it by $\frac{1}{2}[\bar{1}01]$, producing an APB on the (010) plane,

as shown in Figure 4(b), then there is no change in nearest neighbors. Again, as in the case of an SISF on {111} planes, we expect the energy γ_0 of this fault to be rather low; however, Horton and Liu (1985) and Douin *et al.* (1986) have recently shown that the ratio of APB energies γ_1/γ_0 on {111} planes (γ_1) and {100} planes (γ_0) is only about 1.2 in Ni₃Al, and γ_0 is 90 ± 5 mJ m⁻². Dimiduk (1991) found γ_0 to range from 92 to 170 mJ m⁻² and γ_1/γ_0 to range from 0.98 to 1.63, depending on the composition of the Ni₃Al-based ternary alloy.

2.1.5 Methods of Predicting Fault Stabilities

Some faults have never been observed, even though there is good reason to believe they exist, e.g. CSFs on {111} planes. Consequently, some other technique for determining fault stabilities is needed. A fault will be stable or metastable only if the energy of the faulted crystal is lower than that of the same crystal with a slightly smaller (or slightly larger) fault vector. A technique using this idea, based on the so-called γ surface, was developed for b.c.c. metals by Vitek (1974) and has also been subsequently applied to L₁₂ ordered alloys. A fault is produced on a given plane by making an imaginary planar cut in the crystal and then shifting one piece of the crystal relative to the other by a vector **f**. If the atomic interactions are known, then the fault energy can be calculated as a function of **f**, and stable faults occur at minima in the energy versus **f** plot (the γ surface).

Yamaguchi *et al.* (1981) calculated the γ surface for faults on {010} and {111} planes of L₁₂ materials using a series of different central force atomic potentials. Based on the results of these calculations and symmetry considerations based on Neumann's principle, they concluded the following.

- (i) APBs on (010) planes with fault vector $\frac{1}{2}[\bar{1}01]$ are always stable in L₁₂ materials.
- (ii) APBs are stable or unstable on {111} planes, depending on the interatomic potentials used, but their fault vectors are not necessarily $\frac{1}{2}[\bar{1}01]$. The fault vector can deviate from $\frac{1}{2}[\bar{1}01]$ by a component parallel to $\frac{1}{2}[\bar{1}\bar{1}2]$, i.e. a component perpendicular to $[\bar{1}01]$ in the {111} plane. This deviation of the fault vector from $\frac{1}{2}[\bar{1}01]$ has been also observed in the calculations of Beauchamp *et al.* (1987).
- (iii) SISFs are always stable on {111} planes, independent of the potentials used, as are stacking faults in f.c.c. materials.
- (iv) CSFs on {111} planes are stable or unstable, depending on the potentials used, and the stable fault vector deviates from $\frac{1}{6}[\bar{1}\bar{1}2]$ by a component which is parallel to $[\bar{1}\bar{1}2]$. As with the APB,

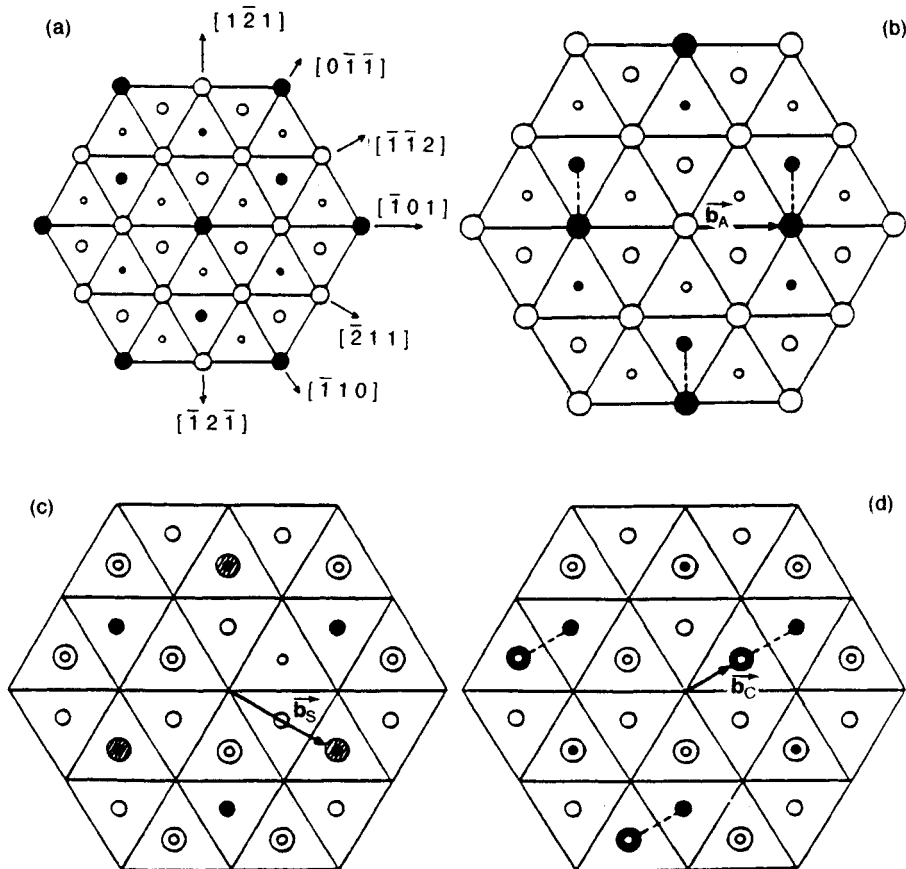


Figure 3. Four types of fault in an A_3B alloy with the $L1_2$ structure. Three successive (111) planes are shown. Large, medium, and small circles represent atoms in the upper, middle, and lower planes, respectively, and open and closed circles represent majority and minority atoms, respectively: (a) three (111) planes; (b) after sliding top layer in (a) by $b_A = \frac{1}{3} [1\bar{1}0]$ to produce an APB; dashed lines indicate 'incorrect B-B nearest neighbor bonds'; (c) after sliding top layer in (a) by $b_S = \frac{1}{3} [211]$ to produce a SISF; (d) after sliding top layer in (a) by $b_C = \frac{1}{6} [\bar{1}\bar{1}2]$ to produce a CSF

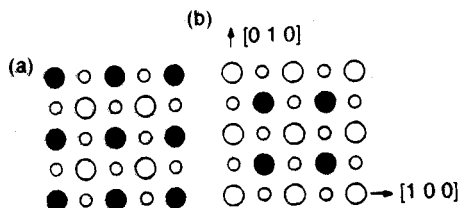


Figure 4. An APB with a $\frac{1}{3} [\bar{1}01]$ displacement vector is expected to have its minimum energy on (010) planes: (a) two successive (010) layers of an A_3B alloy, large circles representing the top layer and small circles the bottom layer; (b) top layer in (a) shifted by $\frac{1}{3} [110]$ relative to the bottom layer. Note that there are no nearest neighbor violations

the amount by which the fault vector deviates from that predicted based on the hard sphere model depends on the interatomic potentials.

Note that in reality what is called stable here is metastable, since a dislocation-free and fault-free crystal has the lowest energy.

More recent calculations of fault energies using more realistic potentials have given similar results; for example, Pasianot *et al.* (1991) used interatomic potentials based on the embedded atom method. (In general, the trends seen in calculations based on complex, many-body potentials agree remarkably well with those based on pair potentials.)

Table 1. APB energies in Ni₃Al^a

APB energy (mJ m ⁻²)			Reference
γ_1	γ_0	γ_1/γ_0	
250–350	—	—	Taunt and Ralph (1974)
—	—	1.2	Horton and Liu (1985)
111 ± 15	90 ± 5	1.2	Douin, Veyssi�re, and Beauchamp (1986)
169 ± 19	104 ± 8	1.63	Dimiduk (1991) (on Ni–22.9Al)

^a γ_1 is the APB energy on (111) and γ_0 is the APB energy on (010). Dimiduk (1991) has reported APB energies as a function of composition, but they are not given here.

2.3 Simulations of Dislocation Cores

As discussed in Section 2.2, there is ample evidence that dislocations dissociate in L1₂ materials according to schemes 1 (or 3) and 4. However, the direct observations cannot provide information about the shape of the dislocation cores themselves. To provide this information, computer modeling experiments have been carried out by Yamaguchi *et al.* (1982) and Paidar *et al.* (1982) using empirical central force potentials which represent a range of properties expected in L1₂ materials. Different potentials provide different combinations of fault energies while still keeping the L1₂ structure stable and holding the elastic moduli and lattice parameter constant. The results of these calculations are as follows (Yamaguchi, 1982).

- (i) If the APB energy on (111) planes is sufficiently low, a $\frac{1}{2}[\bar{1}01]$ screw dislocation dissociates into two $\frac{1}{2}[\bar{1}01]$ dislocations on the (111) planes, and the cores of these superpartial dislocations spread in the (111) plane into a configuration similar to two closely spaced Shockley partials (see Scheme 1, Section 2.2).
- (ii) When the APB energy on (111) planes is increased while the SISF energy remains relatively low, the screw dislocation then dissociates according to scheme 4 of Section 2.2. In this case the cores of the $\frac{1}{2}[\bar{2}11]$ and $\frac{1}{2}[\bar{1}\bar{1}2]$ dislocations are highly nonplanar.
- (iii) Dissociations of $\frac{1}{2}[\bar{1}01]$ screw dislocations on (010) planes always occur according to scheme 5, Section 2.2, and the cores of the $\frac{1}{2}[\bar{1}01]$ superpartials are always spread on the (111) or (1 $\bar{1}$ 1) planes, or on both simultaneously, i.e. the cores are also highly nonplanar.

The Peierls stress of these screw dislocations was modeled by Paidar *et al.* (1982) by applying a resolved shear stress (r.s.s.) to the leading superpartial and determining the stress at which it moved. These computer simulations revealed the following.

- (i) Screw dislocations that dissociated on (111) planes according to schemes 1 or 3 of Section 2.2 and which have planar cores are always glissile. Scheme 1 is the most important one at low temperatures in Ni₃Al.
- (ii) Screw dislocations dissociated on (111) planes according to scheme 4 have nonplanar cores and are always sessile, i.e. thermal activation is required before motion can occur. Given the deformational behavior of Ni₃Al, such slip is not believed to be important in Ni₃Al.
- (iii) Screw dislocations dissociated on (010) planes according to scheme 5 have nonplanar cores and are always sessile. This dissociation is important in Ni₃Al at temperatures above the peak in the c.r.s.s. versus temperature curve.

2.4 Flow of L1₂ Materials

The temperature dependence of the yield stress of L1₂ materials which do not disorder shows two quite distinct behaviors. One class of materials shows a rapid increase of c.r.s.s. with decreasing temperature below room temperature, similar to the behavior of b.c.c. materials, here called ‘normal yield behavior’ (Tichy, Vitek, and Pope, 1985), and another class shows an increasing c.r.s.s. with increasing temperature, here called ‘anomalous behavior’.

2.4.1 Normal Behavior

Normal behavior is observed in materials such as Pt₃Al (Wee and Suzuki, 1979; Wee *et al.*, 1980; Yadagawa *et al.*, 1980; Suzuki *et al.*, 1980; Wee and Suzuki, 1981; Wee *et al.*, 1984; Mishima *et al.*, 1985) and in the L1₂ form of Al₃Ti (Wu *et al.*, 1990). This behavior is not seen in Ni₃Al, and is included here only as a contrast with the anomalous behavior, which is always seen in Ni₃Al. The important characteristics of the deformation, for purposes of this discussion, are as follows.

- (i) the c.r.s.s. for dislocation glide increases rapidly with decreasing temperature.
- (ii) The operative slip system depends on the orientation of the compression axis. Samples oriented near (001) deform by (111)[$\bar{1}01$] slip and those oriented near ($\bar{1}$ 11) deform by (001)[$\bar{1}10$] slip.
- (iii) Single crystals are quite brittle, especially at low temperatures.

Unfortunately, no detailed examination of the dislocation configurations has been carried out on Pt₃Al. However, if it is hypothesized that the APB on {111} planes is unstable in Pt₃Al, then a dislocation according to scheme 4 of Section 2.2 with an SISF and a nonplanar

core is expected on $\{111\}$ planes. The cores of such dislocations have recently been investigated by Tichy *et al.* (1986a) who found that the cores are spread simultaneously in the (111) and $(\bar{1}\bar{1}1)$ planes. Dislocations can also dissociate on (010) planes according to scheme 5, since the APB on (010) planes is always stable. This configuration also results in dislocations with nonplanar cores. Consequently, there are two possible dislocation configurations, both with nonplanar cores: two $\frac{1}{2}\langle 112 \rangle$ dislocations separated by an SISF on $\{111\}$ planes or two $\frac{1}{2}\langle \bar{1}10 \rangle$ dislocations separated by an APB on $\{001\}$ planes. The c.r.s.s. for slip on either system is expected to increase dramatically with decreasing temperature, as is observed.

Recent calculations by Tichy *et al.* (1986b) have shown that a change from $(111)[\bar{1}01]$ to $(001)[\bar{1}10]$ slip should occur when the maximum resolved shear stress (m.r.s.s.) plane is inclined by 30° to the (001) plane. When the angle is less than 30° , $\{100\}$ slip is expected to occur and for angles greater than 30° , $\{111\}$ slip is expected. Experimental results are still fragmentary, but recent results of Heredia and Pope (1987) on Pt_3Al are consistent with this idea.

2.4.2 Anomalous Behavior

Most L_{12} ordered alloys exhibit the so-called anomalous yield behavior as first observed in hardness tests on Ni_3Al by Westbrook (1957), in flow stress measurements on polycrystalline Ni_3Al by Flinn (1960) and by Davies and Stoloff (1965), and in flow stress measurements on single crystalline Ni_3Al by Copley and Kear (1967). Since that time, this anomalous behavior has been observed in many materials (see Mishima *et al.* (1985) for a list of references), but Ni_3Al is the prototypical material. In the following discussion there will be no attempt to discuss all the work done on these different materials; rather, only the important trends will be discussed for Ni_3Al .

Materials exhibiting the anomalous yield behavior show the following characteristics.

- (i) The flow stress increases with increasing temperature (anomalous behavior) until a peak is reached, after which the flow stress decreases.
- (ii) In the temperature regime where the flow stress is increasing, slip occurs on the $\{111\}\langle 10\bar{1} \rangle$ systems (Staton-Bevan and Rawlings, 1975a, b).
- (iii) At temperatures above the peak, slip occurs on the $\{100\}\langle 011 \rangle$ systems (Staton-Bevan and Rawlings, 1975a, b) except for samples oriented near $\langle 001 \rangle$ which continue to slip on $\{110\}\langle \bar{1}01 \rangle$ above the peak (Umakoshi *et al.*, 1984).

- (iv) In the temperature regime where the anomalous behavior is observed, the dislocation structure consists primarily of long, straight $\langle \bar{1}01 \rangle$ screw dislocations on $\{111\}$ planes (Kear and Hornbecker, 1966).
- (v) The shape of the c.r.s.s. on $\{111\}\langle \bar{1}01 \rangle$ versus temperature curve below the peak depends on the orientation of the compression (or tensile) axis (Takeuchi and Kuramoto, 1973), i.e. nonglide components of the stress tensor are important.
- (vi) The c.r.s.s. on $\{111\}\langle \bar{1}01 \rangle$ depends on the sense of the applied uniaxial stress (Ezz *et al.* 1982; Umakoshi *et al.*, 1984).
- (vii) The c.r.s.s. for $\{111\}\langle \bar{1}01 \rangle$ slip below the peak temperature shows a small positive strain rate dependence, but that for $\{001\}\langle \bar{1}10 \rangle$ slip above the peak shows a strong positive strain rate dependence (Umakoshi *et al.*, 1984).

Most of the above characteristics are explained, and some were even predicted before being observed, by the so-called cross-slip model. If it is assumed that $\gamma_1 > \sqrt{3}\gamma_0$ (see Section 2.2), then a $(111)[\bar{1}01]$ screw dislocation dissociated according to schemes 1 or 3 (see also Section 2.2) can go to a lower energy state by cross slipping from the (111) to the (010) plane, shown in Figure 6, as first proposed by Kear and Wilsdorf (1962) and Kear (1964) to explain the high work-hardening rates observed in many L_{12} ordered materials. Thornton *et al.* (1970) first applied the model to explain the anomalous flow behavior of Ni_3Al , then Takeuchi and Kuramoto (1973) proposed a model involving cross slip which explained the orientation dependence of the c.r.s.s. for $\{111\}\langle \bar{1}01 \rangle$. Lall *et al.* (1979) modified the model to include the effect of the sense of the applied uniaxial stress; Paidar *et al.* (1984) further refined the model and made it more quantitative (now known as the 'PPV' model); and Yoo (1987) made further modifications which include not only the difference in the APB energy on $\{111\}$ and $\{010\}$ planes but also the effects of elastic anisotropy. More recent modifications are discussed at the end of this section.

The model and all of its modifications are based on the assumption that there is a driving force for $\{111\}$ to $\{010\}$ cross slip, that the cross slip is a localized process, and that the cross-slipped segments on $\{010\}$ planes are locally pinned (since their cores do not spread on the $\{010\}$ plane). Since the cross-slip process is thermally activated, the number of cross-slipped segments increases with increasing temperature, leading to an increasing c.r.s.s. for $\{111\}\langle \bar{1}01 \rangle$ slip until $\{001\}\langle \bar{1}10 \rangle$ slip begins and the flow stress decreases again. The

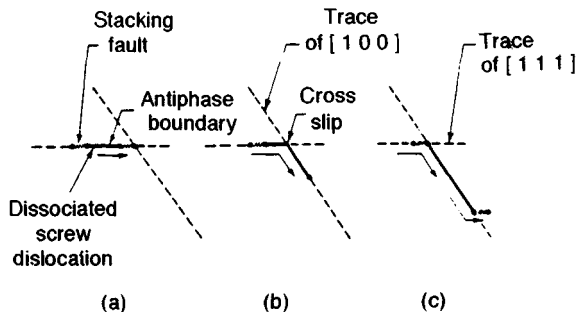


Figure 6. Mechanism of cross slip pinning as proposed by Kear and Wilsdorf (1962) and Kear (1964)

activation enthalpy for the process was derived as follows (Paidar *et al.*, 1984; Yoo, 1987), assuming the Takeuchi and Kuramoto (1973) form for the flow stress increase (equation 4)

$$H = W + b \left[\frac{\mu b^2}{8\pi} - \left(\frac{\mu b^3}{8\pi} F \right)^{1/2} \right] \quad (2)$$

$$F = \frac{\gamma_1}{\sqrt{3}} (1 + f_1 \sqrt{2}) - \gamma_0 + \tau_c b \quad (3)$$

$$\Delta\tau = B \exp(-H/3kT) \quad (4)$$

where μ is the appropriate shear modulus, b is $\frac{1}{2} [\bar{1}01]$, τ_c is the r.s.s. on the (010) plane in the $[\bar{1}01]$ direction, f_1 is $\sqrt{2}(A-1)/(A+2)$, where A is Zener's ratio of elastic anisotropy and is given by $2C_{44}/(C_{11}-C_{12})$. W is the sum of the energies of the constrictions formed on the $\frac{1}{2} [\bar{1}01]$ superpartials on the (111) and ($\bar{1}\bar{1}\bar{1}$) planes, respectively, as originally derived by Escaig (1968a, b) for f.c.c. metals. The constriction energies depend on the sense of the applied stress since the separation of the Shockley partials comprising the $\frac{1}{2} [\bar{1}01]$ superpartials on the (111) and ($\bar{1}\bar{1}\bar{1}$) planes depends on the edge components of those superpartials. The factor F is the driving force for (111) to (010) cross slip and includes the effect of APB anisotropy as well as the torque on the leading dislocation due to the trailing dislocation (an effect which arises due to elastic anisotropy through f_1). $\Delta\tau$ is the increase in c.r.s.s. for (111) $[\bar{1}01]$ slip over the low-temperature value, B is a proportionality constant, k is Boltzmann's constant and T is temperature. Yoo (1987) has shown that cross slip will occur only when $[3A/(A+2)](\gamma_1/\gamma_0) > \sqrt{3}$. Consequently, for Ni_3Al the APB anisotropy is expected to have a smaller effect on the temperature dependence of the c.r.s.s. than does the elastic anisotropy, whereas the reverse is true for Ni_3Ga (Yoo, 1987).

The temperature and orientation dependence of the c.r.s.s. for slip in binary Ni_3Al is shown in Figure 7 for both tensile and compressive tests. Note the substantial difference between the tensile and compressive results for most orientations at temperatures below the peak. The Paidar *et al.* (1984) theory predicts that the c.r.s.s. for (111) $[\bar{1}01]$ slip at elevated temperatures as measured in tension and compression should vary with orientation, as shown in Figure 8. Note the close correspondence between the predictions of Figure 8 and the results shown in Figure 7. There have been many subsequent observations of this same effect, e.g. Jablonski and Sargent (1981), Shah and Duhl (1984), Pope and Ezz (1985), Gabbet *et al.* (1986), Heredia and Pope (1986, 1987), Ezz *et al.* (1987), and Bonda *et al.* (1987).

2.4.3 Modifications to the PPV Model

The PPV model (Paidar *et al.*, 1984) with the additional term due to Yoo (1987) explains most, but not all, of the observed flow phenomena in Ni_3Al . Recent modifications to the model are based on the same thermally activated process for cross slip pinning, but additional assumptions are made regarding the post-pinning process. The most troubling aspect of the PPV model is that it contains no information about the strain rate sensitivity (which is small and positive over the temperature range of the anomaly, as discussed in Section 2.4.2), and therefore has no capability of predicting the large change in activation volume observed by Bonneville *et al.* (1991) well below the peak in the flow stress-temperature curve. In addition, there are apparent discrepancies between postdeformation dislocation structures (also *in situ* deformation structures) and those expected from the model.

Khantha *et al.* (1992a) modified the PPV model to include not only the thermally assisted formation of localized pinning points but also the thermally assisted breaking of those points. The process is relatively simple at low temperatures (and stresses) where the pinning points are relatively widely spaced and the release from one pinning point results in a complete release of the whole dislocation line. However, at higher stresses and temperatures where the repinning rate is substantially higher, release from several pinning points is required, thereby giving rise to the observed increase in activation volume at intermediate temperatures (Bonneville *et al.*, 1991). This model also provides the observed temperature dependence of the c.r.s.s. in the vicinity of the peak. An additional modification of the PPV model by Khantha *et al.* (1992b) involves the orientation

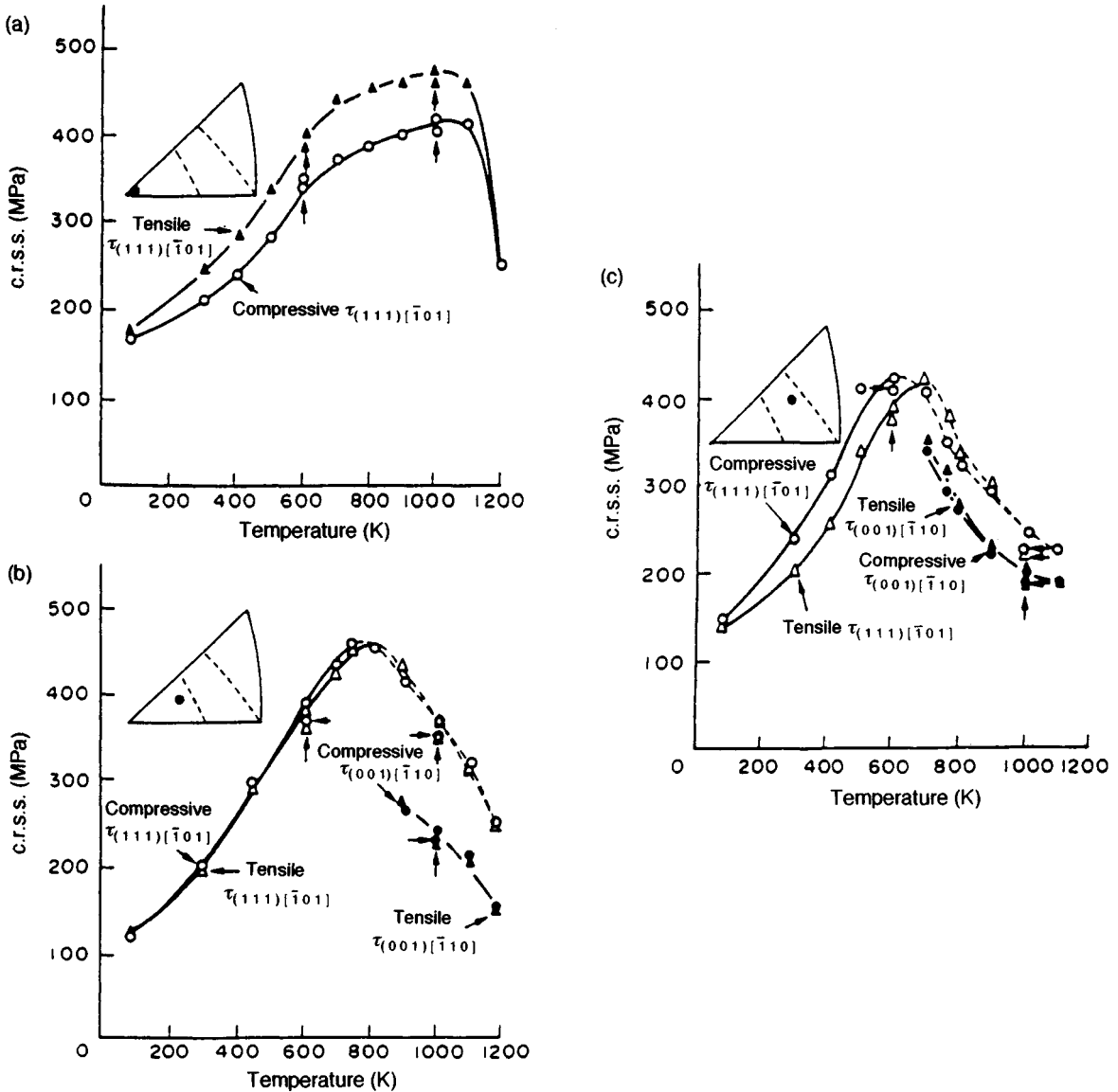


Figure 7. The temperature dependence of the c.r.s.s. for $\{111\}\langle 101 \rangle$ and $\{001\}\langle 110 \rangle$ slip in $\text{Ni}_3(\text{Al, Ta})$ under tension and compression (after Umakoshi, Pope, and Vitek, 1984)

dependence of the T/C asymmetry. The PPV model predicts that the asymmetry should disappear for the orientations shown in Figure 8; however, for binary Ni_3Al alloys the asymmetry disappears along the so-called ' $Q=0$ ' line, the $[012]-[\bar{1}13]$ great circle in the unit triangle (Heredia and Pope, 1991). As discussed in Section 2.4.2, the position of the $T=C$ line is assumed to be determined by the Escaig effect, i.e. by the width of the dislocation core on the (111) plane immediately

before cross slip and on the $(1\bar{1}1)$ plane immediately after. Khantha *et al.* (1992) propose that only the width prior to cross slip is important, since this is clearly the case for binary Ni_3Al . The change in position of the $T=C$ line towards $[001]$ for alloys containing ternary additions is then assumed to be the result of internal stresses due to the ternary atoms. These internal stresses alter the local spacing of the Shockley partial dislocations on the (111) primary slip plane and shift the $T=C$ line

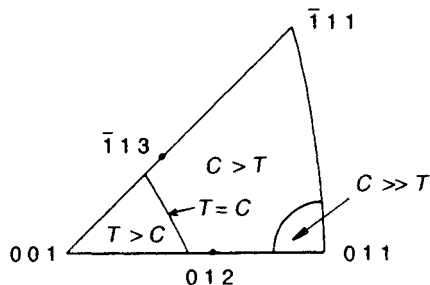


Figure 8. Summary of predictions from theory proposed by Paidar *et al.* (1984) for flow stress of L1₂ alloys. Near [001] the tensile (T) flow stress should exceed the compressive (C) flow stress; the opposite occurs on the other side of the triangle, where compressive flow stress should greatly exceed tensile flow stress for orientations near [011]. Tensile and compressive flow stresses are predicted to be equal on the [001] side of the [012]– $\bar{1}\bar{1}3$ great circle

towards [001] from the $Q=0$ line. The magnitude of the effect should be composition dependent, since the internal stress depends on the concentration of ternary atoms. This effect of ternary solute is observed.

The dislocation structure after deformation tends to consist of long, straight $\bar{1}01$ screw dislocations with large superjogs of mixed character between. There are two approaches to explaining this structure, the first due to Pope (1990) who explains it as the natural result of the bowing process between pinning points which then relax into the observed structure after the applied stress is removed. The second approach (Hirsch, 1992) involves the assumption that the segments that are pinned by cross slip are not localized, as in the PPV model, but spread rapidly along the length of the screw dislocation, thereby giving rise to the large superkinks observed on the dislocation line. In this model the unlocking process involves the motion of the superkinks of largely edge character separating the pinned screw dislocations. It gives the same results for the temperature and orientation dependence of the c.r.s.s. below the peak (since it contains the PPV model) but, in addition, it also gives the correct rate sensitivity. The temperature dependence of the c.r.s.s. near the peak temperature has not been determined for this model, however.

Finally, the *in situ* observations of Couret and Caillard (1989) on Ni₃Al show a jerky motion of straight screw dislocations with displacements approximately equal to the spacing of the superpartial dislocations, and instantaneous redissociation from (111) to ($\bar{1}\bar{1}1$) or (010). None of the cross-slip models is capable of explaining these observations and, in fact, Caillard *et al.* (1988) have proposed a different model which incorporates these dissociations based on the assumption

that $\bar{1}01$ dislocations are more stable on the ($\bar{1}\bar{1}1$) cross-slip plane than on the (111) plane. This model explains the jerky motion of the dislocations, but does not explain most of the macroscopic behavior described in Section 2.4.2, nor is it clear why there should be a difference in dislocation stability between the (111) and ($\bar{1}\bar{1}1$) planes. This is further discussed by Pope (1990).

3. Intergranular Fracture and Boron Effect in Polycrystalline Ni₃Al

3.1 Intrinsic Grain Boundary Brittleness?

Ni₃Al exhibits $\{111\}\langle 110\rangle$ slip and has sufficient slip systems for extensive plastic deformation. Single crystals of Ni₃Al are highly ductile, whereas polycrystals are brittle at ambient temperatures (Liu, 1991). The brittleness originates at grain boundaries. In most metals and alloys, brittle intergranular fracture is associated with strong segregation of harmful impurities, such as S, P, and O, to grain boundaries (Stein and Heldt, 1977), causing embrittlement. In earlier work, trace impurities were also suspected to be a possible cause for embrittlement of grain boundaries in Ni₃Al and other intermetallics. For example, sulfur was found on grain boundaries in polycrystalline Ni₃Al (White and Stein, 1978).

However, experimental studies of grain boundary compositions in sufficiently pure Ni₃Al and other intermetallics indicate that the grain boundaries are basically clean and free from detectable impurities (Liu and White, 1985; Liu *et al.*, 1985; Liu and George, 1990; Ogura *et al.*, 1985; Oliver and White, 1987; George and Liu, 1990) by Auger electron spectroscopy. As shown in Figure 9, all Auger peaks are associated with nickel and aluminum, and no impurities are detected at Ni₃Al grain boundaries. The aluminide, nevertheless, fractures intergranularly, implying that the grain boundaries may be intrinsically brittle. Similar observations were obtained in other intermetallics, including the L1₂ (cP4) compounds Ni₃Si, Ni₃Ga, and Ni₃Ge, and the B2 (cP2) compounds NiAl and FeAl.

Considerable efforts have been devoted to understanding the 'intrinsic' grain boundary brittleness in ordered intermetallics. A general finding is that the grain boundary brittleness is associated with the ordering energy, electronegativity difference, valency difference, and atomic size difference between the A and B atoms constituting the binary A_3B ordered intermetallic (Takasugi and Izumi, 1985; Takasugi *et al.*, 1985; Taub *et al.*, 1986; Taub and Briant, 1987a, b; Farkas and Rangarajan, 1987). This correlation appears to rank

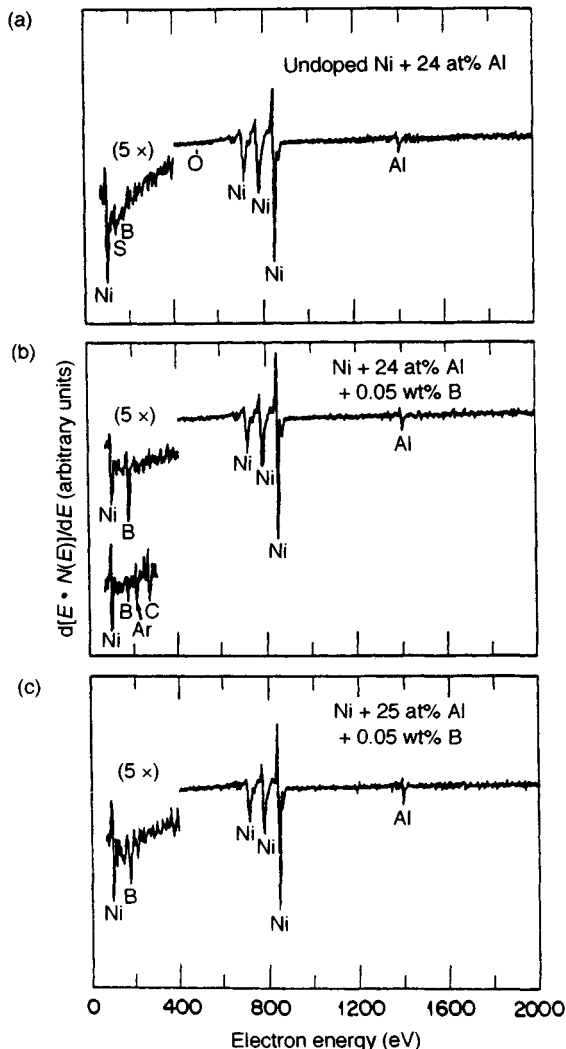
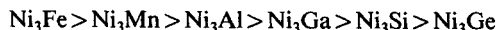


Figure 9. Auger spectra from the intergranularly fractured region in Ni_3Al specimens: (a) undoped Ni–24 at% Al; (b) Ni–24 at% Al doped with 500 w.p.p.m. B; (c) same as (b) after sputtering for 2 min; and (d) Ni–25 at% Al doped with 500 w.p.p.m. (Liu and White, 1985; Liu *et al.*, 1985a, b)

correctly the grain boundary cohesive strength of nickel-based L1_2 ordered intermetallics in the order



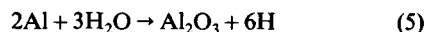
a sequence that is in good agreement with experimental observations. Atomistic simulation (Vitek *et al.*, 1988; Vitek *et al.*, 1989; Kruisman *et al.*, 1989; Vitek and Chen, 1991) calculations and dislocation/grain boundary interaction analyses (King and Yoo, 1985) are all

consistent with grain boundaries being intrinsically weak in strongly ordered intermetallics, such as Ni_3Al .

3.2 Environmental Embrittlement as a Major Cause of Grain-Boundary Brittleness

In the foregoing section, the grain boundary in binary Ni_3Al was considered to be intrinsically brittle because no impurities at the boundary were detected by Auger analyses. In 1991 (Liu and Oliver) and 1992 (Liu) made a first attempt to link brittle intergranular fracture with environmental embrittlement in binary Ni_3Si and Ni_3Al . Table 2 shows the tensile properties of recrystallized polycrystalline Ni_3Al alloys produced from repeated cold forging and 1000 °C annealing. The tensile elongation of the Ni_3Al alloys is sensitive to the test environment at room temperature. The aluminides showed only 2.5–2.6% elongation in air but 7.2–8.2% in dry oxygen, an increase in ductility by a factor of *ca* 3. These results clearly demonstrate that binary Ni_3Al alloys are prone to environmental embrittlement at room temperature. Thus, an extrinsic factor—environmental embrittlement—is a major cause of low ductility and brittle intergranular fracture in binary Ni_3Al (Liu, 1992b).

Environmental embrittlement in aluminides as well as other ordered intermetallics containing reactive elements (such as Al, Si, V and Ti) is explained by the following chemical reaction (Liu and Oliver, 1989; Liu, Lee, and McKamey, 1989; Liu *et al.*, 1989; Liu and George, 1990)

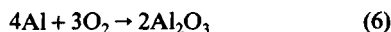


Aluminum atoms in the aluminides react with moisture in air, resulting in the generation of atomic hydrogen that penetrates into crack tips and causes brittle grain boundary crack propagation and premature failure. This embrittlement is similar to hydrogen embrittlement (Kuruvilla and Stoloff, 1985; Stoloff, 1988; Takasugi

Table 2. Effect of test environment on room-temperature tensile properties of Ni_3Al alloys tested at a strain rate of $3.3 \times 10^{-3} \text{ s}^{-1}$ (Liu, 1992)

Alloy composition (at%)	Test environment	Tensile ductility (%)	Yield strength (MPa)	Ultimate tensile strength (MPa)
Ni–24.0Al	Air	2.6	280	333
Ni–24.0Al	Oxygen	7.2	279	439
Ni–23.5Al	Air	2.5	193	230
Ni–23.5Al	Oxygen	8.2	194	351

and Izumi, 1986; Takasugi *et al.*, 1986), except that here hydrogen is generated by moisture in air, rather than hydrogen sources such as hydrogen gas or cathodically charged hydrogen. Consistent with equation (5), the best ductility is generally obtained in dry oxygen environments. This can be rationalized by considering that the reaction of aluminum atoms with oxygen



competes with the moisture reaction, thereby reducing the generation of atomic hydrogen from equation (5). Both specimens tested in air and oxygen showed mainly grain boundary fracture, with more propensity for transgranular fracture in the specimens tested in oxygen. Note that environmental embrittlement appears not to be the only cause of grain boundary brittleness in Ni₃Al, because the elimination of the environmental effect by testing in dry oxygen does not lead to extensive ductility and complete suppression of intergranular fracture in Ni₃Al (Liu, 1992b).

The environmental effect has also been observed in Ni₃Al alloys containing ternary alloying additions. Takasugi *et al.* (1986) first reported an environmental effect that lowered ductility in beryllium-doped Ni₃Al but not in binary Ni₃Al (24% Al). The Ni₃Al alloy doped with 1 at% Be showed a tensile ductility of 5% in vacuum, but 1% in air. On the other hand, no environmental effect was observed in cast binary Ni₃Al, which showed very limited plastic deformation at room temperature. Manganese at a level of 15 at% was added to enhance grain boundary cohesion in Ni₃Al (Masahashi *et al.* 1988a). Masahashi *et al.* (1988b) found that the tensile ductility of Ni₃(Al, Mn) is susceptible to environmental embrittlement at room temperature at different strain rates. For example, the alloy exhibited a ductility of 11% in air but 50% in vacuum at a strain rate of 10^{-3} s^{-1} . The reduction in ductility in air is accompanied by a change in fracture mode from ductile transgranular to brittle intergranular. The environmental effect was thought previously to be associated with the ternary alloying additions added to Ni₃Al (rather than in connection with binary Ni₃Al) until the report of a clear environmental effect in fabricated and recrystallized binary Ni₃Al and Ni₃Si.

Recently, George, Liu, and Pope (1992) studied the environmental effect in a carefully prepared Ni₃Al alloy with the composition Ni-22.65Al-0.26 Zr (all at%). In this case, the polycrystalline material was prepared by recrystallization of cold-worked single crystals. Table 3 shows the room-temperature tensile results obtained along the rolling direction and at 45°

Table 3. Effect of test environment and specimen orientation on the room-temperature tensile properties of Ni-22.65Al-0.26Zr^a tested at a strain rate of $5.3 \times 10^{-3} \text{ s}^{-1}$ (George, Liu, and Pope, 1992)

Specimen orientation	Test environment	Elongation to fracture (%)	Yield strength (MPa)	Ultimate tensile strength (MPa)
0°	Water	8.7	322	528
	Air	13.2	324	661
	Oxygen	50.6	326	1451
45°	Water	6.3	331	473
	Air	10.7	341	603
	Oxygen	47.8	327	1438

^aPolycrystalline material produced by recrystallizing a cold-worked single crystal.

to it. The polycrystalline specimens exhibited a room-temperature tensile ductility of 6–9% in water, 11–13% in air, and 48–51% in oxygen. All specimens showed mainly grain boundary fracture, including the ductile ones that exhibited in excess of 50% elongation to fracture. These results fit the model that the grain boundaries in this alloy are severely embrittled in the presence of moisture that reacts with the aluminide to release atomic hydrogen and causes hydrogen embrittlement.

All these results indicate that the grain boundaries in Ni₃Al and its alloys are actually not brittle. The low ductility and brittle grain boundary fracture in the polycrystalline materials are caused by an extrinsic factor: moisture in air. Moisture-induced hydrogen also embrittles grain boundaries in other intermetallic alloys, including Ni₃Si, Ni₃(Si, Ti), Co₃Ti and (Fe, Co)₃V alloys, all having the L1₂ crystal structure (Liu and Oliver, 1991; Liu and Izumi, 1992; Takasugi and Izumi, 1986; Takasugi *et al.*, 1986; Takasugi *et al.*, 1991; Masahashi *et al.*, 1988; Nishimura and Liu, 1991, 1992).

3.3 The Beneficial Effect of Boron

Boron has been found to be most effective in improving the tensile ductility of polycrystalline Ni₃Al containing less than 25 at% Al (Aoki and Izumi, 1979; Liu and Koch, 1983; Liu *et al.*, 1985; Liu *et al.*, 1985; Taub *et al.*, 1984) tested in air at room temperature. Figure 10 is a plot of room-temperature tensile ductility in air as a function of boron addition to Ni₃Al (24 at% Al). Microalloying with boron sharply increases the ductility and effectively suppresses intergranular fracture. A tensile ductility higher than 50% in air was achieved in Ni₃Al by microalloying with 0.1 wt% B. The striking

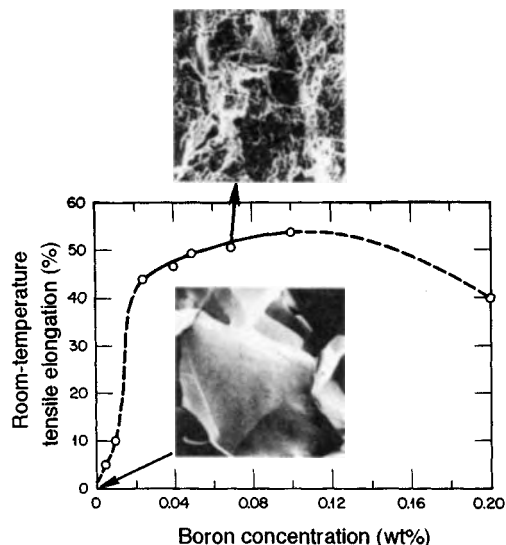


Figure 10. Effect of boron additions on tensile elongation and fracture behavior of Ni_3Al (24 at% Al) tested at room temperature

effect of boron on the ductility of Ni_3Al , first discovered by Aoki and Izumi (1979), occurs over a wide range of concentration of boron in solid solution (the solubility of boron ≈ 1.5 at%; Liu *et al.*, 1988). Both Auger microprobe (see Figure 9) and imaging atom probe (Miller and Horton, 1986; Horton and Miller, 1985; Sieloff *et al.*, 1985) studies revealed that boron segregates strongly to grain boundaries in Ni_3Al , although the extent of segregation varies from boundary to boundary within individual samples.

Considerable effort has been devoted to understanding the ductilizing effect of boron in Ni_3Al (Liu, 1991). As a result, two mechanisms were proposed to explain the beneficial effect of boron: (i) boron-enhanced grain boundary cohesive strength (Liu, White, and Horton, 1985; White *et al.*, 1984; Chen *et al.*, 1989; Bond *et al.*, 1987), and (ii) boron-facilitated slip transfer across the grain boundary (or slip nucleation at boundaries) (Schulson *et al.*, 1985; Khadkikar *et al.*, 1987; Baker *et al.*, 1987). In view of the recent finding of environmental embrittlement (Liu, 1992b), the ductilizing effect of boron also occurs by reduction in moisture-induced hydrogen embrittlement in Ni_3Al . Masahashi, Takasugi, and Izumi (1988a) first reported that the tensile ductility of boron-doped Ni_3Al is insensitive to test environment at room temperature, indicating that boron is effective in eliminating environmental embrittlement in Ni_3Al . Since boron and hydrogen both occupy similar sites, it is reasonable to assume that

the strong segregation of boron to Ni_3Al grain boundaries would block the diffusion of hydrogen along the boundaries and thus alleviate hydrogen embrittlement. Further studies are required to clarify this point.

An interesting finding in connection with the study of boron in Ni_3Al is the discovery of the effect of off-stoichiometry. Alloy off-stoichiometry strongly affects the hardness of grain boundaries in binary Ni_3Al (Westbrook and Wood, 1962/3) and the ductility and fracture behavior of boron-doped Ni_3Al (Liu and Koch, 1983; Liu, White, and Horton, 1985). Boron is most effective in improving the ductility and suppressing intergranular fracture in Ni_3Al alloys containing ≤ 24 at% Al. As the aluminum concentration is increased above 24%, the ductility decreases sharply (Figure 11), and the failure mode also changes from transgranular to mixed mode and then to mainly intergranular fracture. Auger (Liu, White, and Horton, 1985) and particle-tracking autoradiography (Lin, Chen, and Lin, 1991) studies reveal that alloy off-stoichiometry strongly influences boron segregation and grain boundary chemistry, and thus affects ductility and fracture in boron-doped Ni_3Al .

4. Environmental Embrittlement at Elevated Temperature

Test environments affect the ductility and fracture in polycrystalline Ni_3Al alloys, not only at ambient temperatures but also at elevated temperatures. As discussed in the previous section, ambient-temperature embrittlement is associated with hydrogen generated from the reaction of moisture in air with aluminum atoms in Ni_3Al . The embrittling agent at elevated temperatures is oxygen that penetrates along grain boundaries and causes brittle intergranular fracture (Liu and White, 1985, 1987; Liu, White, and Lee, 1985; Liu and Sikka, 1986; Taub, Chang, and Liu, 1986; Taub *et al.*, 1986). Single crystals of Ni_3Al also show a ductility minimum at intermediate temperatures (Thornton, Davies, and Johnston, 1970), which may be related to environmental embrittlement. However, the loss in ductility has not been studied in detail at the present time.

4.1 Effects of Test Temperature and Aluminum Concentration

Environmental embrittlement of Ni_3Al alloys is strongly affected by test temperature and aluminum concentration (Liu and White, 1987). Figure 12 shows

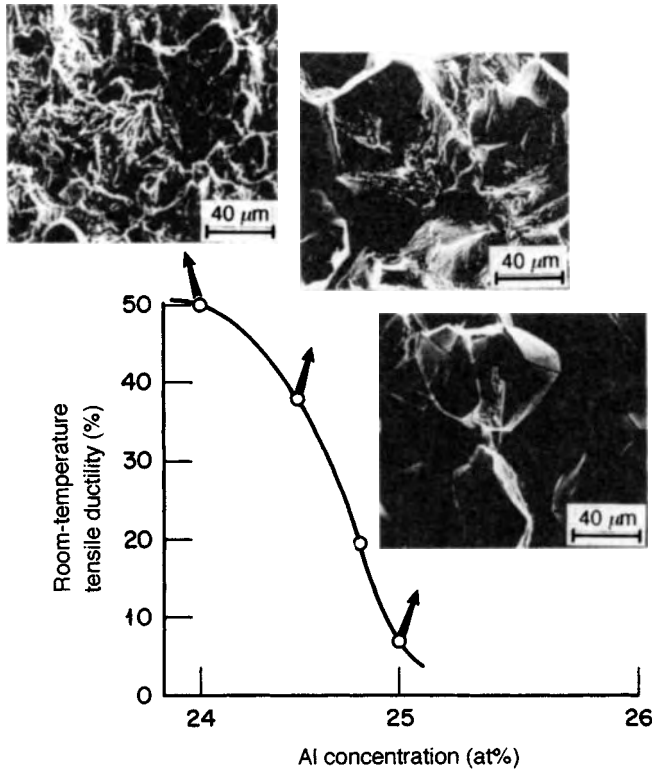


Figure 11. Effect of aluminum concentration of the room-temperature ductility and fracture behavior of Ni₃Al doped with 0.1 at% B

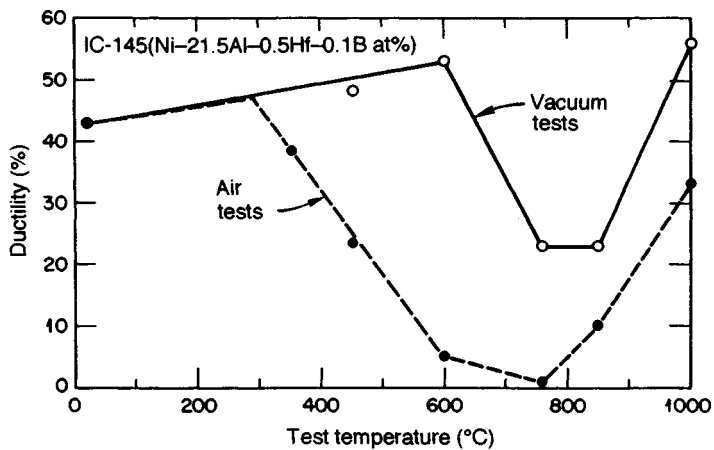


Figure 12. Comparison of tensile elongation of Ni-21.5Al-0.5Hf-0.1 B (at%) in vacuum and in air (Liu and White, 1987)

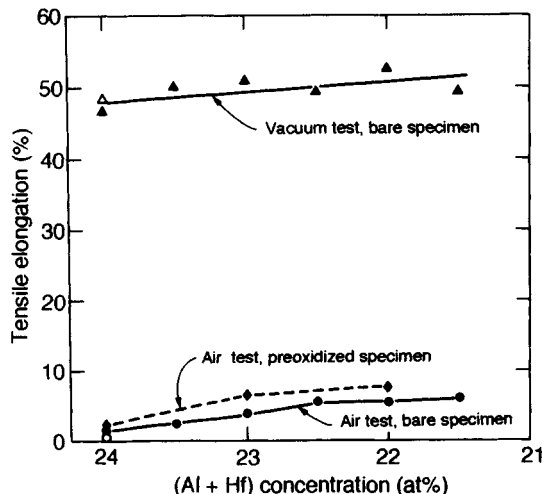


Figure 13. Plot of tensile elongation of Ni_3Al alloys as a function of (Al + Hf) concentration for bare specimens tested at 600 °C in vacuum and air and for specimens preoxidized at 1100 °C for 2 h and 850 °C for 5 h and tested in air. Solid symbols for alloys with 0.5% Hf and open symbols for the alloy without Hf (Liu and White, 1987)

the tensile ductility of an Ni_3Al alloy ($\text{Ni}-21.5\text{Al}-0.5\text{Hf}-0.1\text{B}$, all at%) as a function of test temperature and environment (air versus vacuum). The alloy shows distinctly lower ductility in air than in vacuum (10^{-3} Pa) above 300 °C, and the severe embrittlement occurs in the range 600 to 850 °C. The similarity in the profile of the two curves in Figure 12 suggests that a conventional vacuum in the range of 10^{-3} Pa is not good enough to suppress completely the environmental embrittlement. The environmental effect in oxygen-containing environments is vividly demonstrated in the study of the tensile ductility of a higher aluminum alloy ($\text{Ni}-23\text{Al}-0.5\text{Hf}-0.07\text{B}$) tested at 760 °C as a function of air pressure (Pope and Liu, 1989). The alloy exhibits only about 1% elongation when tested in air; however, the elongation increases steadily with decreasing air pressure in the vacuum system, and it reaches 25% at air pressures below 10^{-5} Pa.

The effect of aluminum concentration on the tensile ductility at 600 °C is shown in Figure 13 for Ni_3Al alloys containing 0 or 0.5 at% Hf (Liu and White, 1987). All the alloys exhibit excellent ductility when tested in vacuum, whereas the ductility is dramatically lowered in air. The corresponding fracture mode changes from ductile transgranular in vacuum to brittle intergranular in air. In both cases, the alloys show small but steady increases in ductility with decreasing aluminum concentration. The alloys are less embrittled in air if

they have lower levels of aluminum. Alloys that are preoxidized (1100 °C for 2 h and 850 °C for 5 h) prior to air testing exhibit better ductility than the unoxidized (bare) specimens. Again, the ductility of preoxidized specimens increases with decreasing aluminum concentration. Similar embrittlement was observed in a spray-formed $\text{Ni}_{66}\text{Co}_{10}\text{Al}_{24}$ alloy containing 0.25 at% B (Taub, Chang, and Liu, 1987).

The environment affects not only tensile properties but also fatigue behavior. Figure 14 is a plot of the fatigue life as a function of temperature for a boron-doped Ni_3Al (24 at% Al) prepared by powder metallurgy (Stoloff *et al.*, 1987a). The alloy showed a sharp drop in fatigue life above 500 °C. Note that the fatigue tests were conducted in vacuum (10^{-3} Pa), suggesting again that a conventional vacuum is not good enough to suppress the embrittlement in the alloy containing as high an aluminum level as 24 at%. The drop in the fatigue life is accompanied by a change in fracture mode from transgranular to intergranular.

In addition to Ni_3Al alloys, other intermetallic alloys exhibit severe environmental embrittlement in oxidizing environments at elevated temperatures. For Ni_3Si and $\text{Ni}_3(\text{Si}, \text{Ti})$ alloys with and without boron, tensile

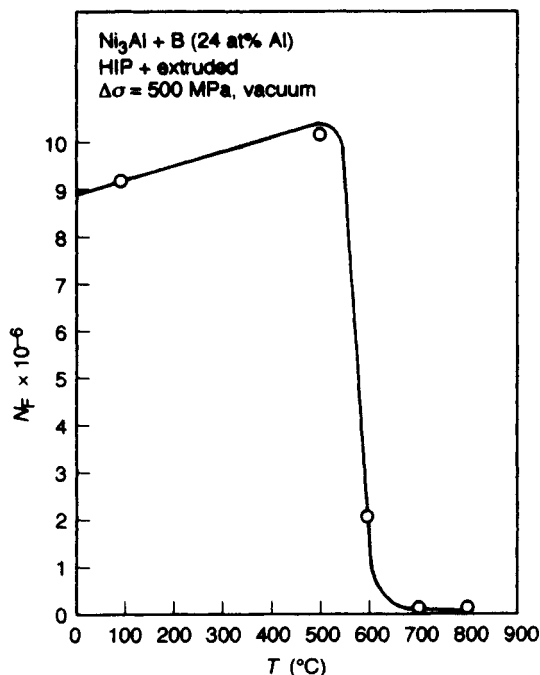


Figure 14. Change in high-cycle fatigue life with temperature for Ni_3Al doped with boron and tested in vacuum (Stoloff *et al.*, 1987a)

ductility decreases sharply above 300 °C in air and vacuum (Oliver, 1989; Takasugi, Suenaga, and Izumi, 1991), and it reaches a minimum around 600 °C for low silicon alloys (e.g. 19 at%). Titanium aluminides are also prone to oxygen-induced embrittlement at elevated temperatures. Recently, Chan and Kim (1992) reported a sharp decrease in tensile ductility of TiAl-based alloys when tested at low strain rates at elevated temperatures in oxidizing environments.

4.2 Dynamic Embrittling Mechanism

The embrittlement described in Section 4.1 is mainly caused by a dynamic effect of simultaneous high localized stress concentration, elevated temperature, and gaseous oxygen (Liu and White, 1987). Although the embrittlement takes place when samples are exposed in oxidizing environments, it is not necessarily associated with formation of oxide scales on specimen surfaces or with grain boundary oxidation. As shown in Figure 13, the preoxidation causes a slight increase rather than a decrease in ductility of Ni₃Al when tested in air at 600 °C. Also, the specimens that fractured in a brittle manner at elevated temperatures (600–800 °C) in air remain ductile in subsequent bend tests at room temperature. Such a dynamic effect basically involves repeatedly weakening and cracking of the grain boundary as a result of oxygen absorption and penetration at crack tips. The reduction in the ductility of Ni₃Al alloys is accompanied by a change in fracture mode from ductile transgranular to brittle intergranular.

Recently, Hipsley and DeVan (1989) proposed a model of stress-assisted grain boundary oxygen penetration to explain the dynamic embrittlement of Ni₃Al in oxidizing environments at elevated temperatures. This model is similar to the stress-assisted grain boundary oxidation (SAGBO) suggested for oxygen embrittlement (Carpenter, 1976) in superalloys. According to their model (Figure 15), the dynamic embrittlement involves the following four sequential steps: (i) occurrence of surface cracks at the initial stage of deformation; (ii) chemisorption of gaseous oxygen to the crack tips where a high localized stress field is involved; (iii) oxygen penetration in its atomistic form to the stress field ahead of tips; and (iv) inward development of surface cracks preferentially along the grain boundaries, leaving some secondary cracks. Steps (ii) to (iv) proceed continuously and repeatedly during deformation, leading to premature fracture and severe loss in ductility at elevated temperatures.

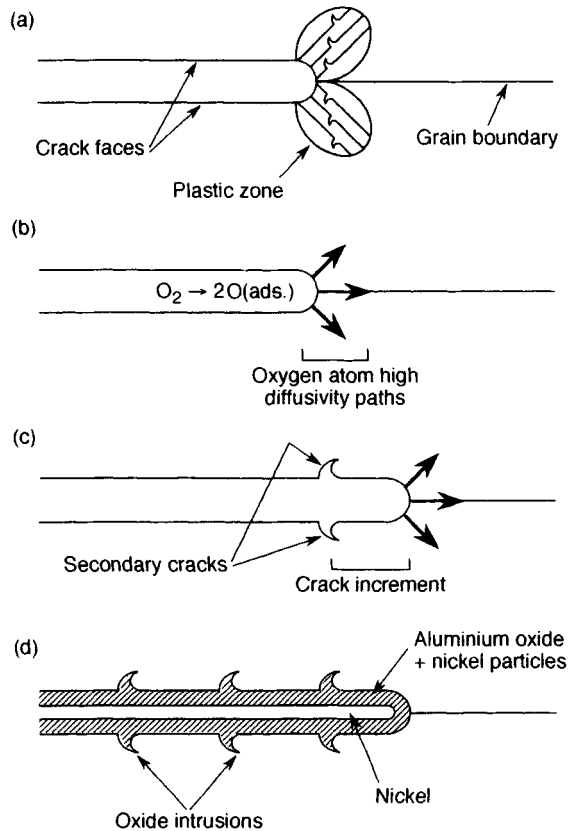


Figure 15. Schematic illustration of the steps in the proposed fracture mechanism of dynamic embrittlement at elevated temperatures (Hipsley and DeVan, 1989)

4.3 The Effect of Grain Size on Preoxidation and Embrittlement

Environmental embrittlement by oxygen is dependent on its penetration along grain boundaries at crack tips (i.e. step (iii) in Section 4.2). Takeyama and Liu (1989a, b) found that the grain size in Ni₃Al plays an important role in the formation of protective oxide films that affect oxygen penetration along grain boundaries. In their study, Ni₃Al specimens with various grain sizes (17–200 μm) were preoxidized at 1000 °C for 10 min and then tensile tested at 600 and 760 °C in vacuum. The results are compared with those from bare specimens tested in vacuum (Takeyama and Liu, 1988) in Figure 16. The preoxidation causes no embrittlement in the fine-grained, boron-doped Ni₃Al; however, the ductility of the preoxidized specimens decreases with increasing grain size, despite the fact that the ductility of bare specimens is nearly insensitive to the grain size. A severe

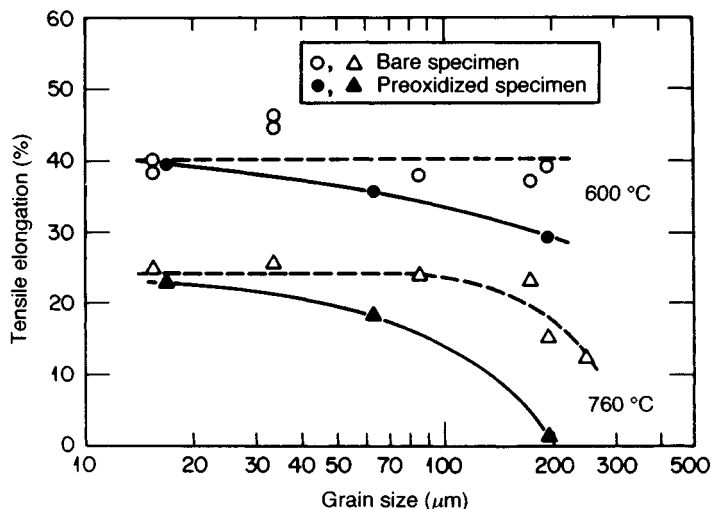


Figure 16. Change in ductility with grain size of bare and preoxidized Ni_3Al with boron ($\text{Ni-23Al-0.5Hf-0.5B}$, all at%) tested at 600 and 760 °C in vacuum (Takeyama and Liu, 1989b)

embrittlement occurs at 760 °C for the largest-grained material, with a change in fracture mode from ductile grain boundary fracture for the bare specimen to completely brittle grain boundary fracture for the preoxidized specimen. The loss of ductility is attributed to oxygen penetration along the grain boundary during the preoxidation treatment (Takeyama and Liu, 1989c). Auger analyses revealed a large amount of oxygen on the grain boundaries in the preoxidized, large-grained specimen but little oxygen in the bare specimen. The analyses also revealed an oxygen gradient from surface to specimen center, indicating a diffusion of oxygen along the grain boundaries in the preoxidized specimen. The presence of oxygen hardens the grain boundary region and causes embrittlement in other intermetallic alloys (Westbrook and Wood, 1962/3; Seybolt and Westbrook, 1964; Seybolt, Westbrook, and Turnbull, 1964).

The interesting result with the Ni_3Al preoxidation is the finding of no oxygen at grain boundaries by Auger analyses of preoxidized, fine-grained specimens. Such grain size dependence of oxygen penetration is related to the difference in formation of surface oxide films in the fine-grained and large-grained specimens: a continuous, thin, aluminum-rich oxide layer on the specimen surfaces of the fine-grained materials, and a predominantly nickel-rich oxide on the large-grained samples. The former layer effectively blocks oxygen penetration into the alloy and prevents any loss of ductility, whereas the latter allows oxygen to penetrate along the grain boundary and cause severe embrittlement. Formation of

aluminum-rich oxide in the fine-grained specimen is attributed to a short-circuit path for rapid diffusion of aluminum atoms from interior to surface along the grain boundaries. Preoxidation to produce a thin adherent oxide film is likely to be responsible for the reduction of the elevated-temperature embrittlement in the fine-grained specimens shown in Figure 13.

5. Alloying Effects and Alloy Design

The mechanical properties of Ni_3Al strongly depend on deviations from stoichiometry (i.e. Al/Ni ratio) and ternary alloying additions. The aluminide can dissolve substantial alloying additions without forming second phases; as a result, deformation and fracture behavior can be strongly altered by alloying. Recently, Suzuki, Mishima, and Miura (1989), Mishima, Ochiai, and Yodagawa (1986), Miura, Mishima, and Suzuki (1989a, b), and Ochiai, Mishima and Yodagawa (1986) compiled data for alloying effects on the yield and flow of single-crystal and polycrystalline Ni_3Al alloys with ternary additions. This section briefly describes alloy stoichiometry, solid-solution hardening and alloy design of engineering materials based on Ni_3Al .

5.1 Solubility Limit of Alloying Elements

The sublattice occupation is a key factor in determining the solubility limit of ternary alloying elements in Ni_3Al with an L1_2 (cP4) ordered structure. Ochiai, Oya,

Chapter 12

Intermetallics as Precipitates and Dispersoids in High-Strength Alloys

Alan J. Ardell

*Department of Materials Science and Engineering, University of California,
Los Angeles, CA 90024-1595, USA*

1. Introduction

Strengthening of alloys at room temperature by dispersed phases in the form of ordered intermetallic compounds is described in this chapter, starting with the general fundamentals of precipitation strengthening. The majority of the alloys considered are strengthened by $L1_2$ (cP4) coherent γ' precipitates, specifically Ni_3Al in aged binary Ni–Al alloys, but generally more complex chemically in commercial or experimental Ni-based and Co-based superalloys. The strengthening of ferritic alloys by coherent B2(cP2) NiAl precipitates or precipitates of a Heusler phase is also described and discussed. Quantitative evaluation of strengthening of the underaged alloys is attempted using a simple theory in conjunction with a minimum number of disposable parameters. This is accomplished with great success in the case of binary Ni–Al alloys using the best data available on the $\langle 111 \rangle$ antiphase boundary (APB) energy and dislocation line tension; there are no adjustable parameters for this alloy system in the analysis of the data. The other analyses of γ' strengthening are based on the Ni–Al analysis, and succeed to varying degrees, ranging from very good for the commercial alloy Nimonic PE16 to poor for an experimental Co–Cr–Ni–Ti alloy. The data on the ferritic alloys are quite consistent with the simple theory, but the APB energies are adjustable parameters, and large values are required to bring theory and experiment into agreement. Data on peak-aged and overaged alloys are also modeled with varying degrees of success. It is shown that a good,

though imperfect, correlation exists between the peak strengthening observed for the superalloys and the APB energy; the corresponding correlation with lattice mismatch is poor. The strengthening of alloys containing bimodal dispersions of γ' precipitates is also reviewed. A generalized addition rule for the contributions to the strength of each size class in the bimodal dispersion is capable of predicting the combined contribution of both size classes, but it is argued that the physical justification for such an addition rule is not well founded.

Intermetallic compounds are especially effective strengtheners when they are incorporated as minor phases in alloys. For example, small precipitates based on the ordered $L1_2$ (cP4) intermetallic compound Ni_3Al significantly contribute to the strength of many nickel-based and cobalt-based superalloys (Anton, Chapter 1 in this volume). These so-called γ' precipitates are introduced by aging the supersaturated alloys in the neighborhood of 600 to 800 °C; the dispersions can be controlled to produce particle diameters in the neighborhood of 10 nm or so and a volume fraction of less than 0.1. Even though the particles are finely dispersed and are a minor constituent in alloys such as Nimonic PE16, they can raise the room-temperature yield strength of the alloy by as much as a factor of five over that of the precipitate-free matrix solid solution. The impressive contribution of such a small quantity of nanometer-sized particles can only be appreciated by understanding the mechanisms of interaction between the dislocations responsible for plastic flow of the material and the particles themselves. A description of these mechanisms

and the extent to which models of precipitation strengthening are successful in predicting their contribution to the strength of alloys like Nimonic PE16 constitute the focus of this chapter.

The subject of the age hardening of metals and alloys, also known as precipitation strengthening, is a venerable one. It includes the topic that is often referred to separately as dispersion strengthening, which involves the most commonly encountered mechanism of over-aging, namely the Orowan mechanism (1948) of bypassing particles by bending between them rather than shearing them. The major reason for treating dispersion strengthening on its own is that dispersoid particles are not necessarily introduced by natural or artificial aging, but by some other method such as powder processing or mechanical alloying. Because of its status as a landmark phenomenon of physical metallurgy, there have been many reviews of precipitation strengthening; the interested reader is referred to those of Smith (1950), Kelly and Nicholson (1963), Brown and Ham (1971), Gerold (1979) and Ardell (1985) for an evolution of the history and knowledge in the field.

To lay the groundwork for what follows, the basic ingredients of the theory of precipitation and dispersion strengthening will be reviewed. These include the statistics of the interactions between dislocations and obstacles, and the mechanisms of interaction between dislocations and individual precipitates. We will then examine a representative body of data on strengthening of alloys by ordered intermetallic compounds. The emphasis will be on predicting the yield strength of such alloys at temperatures at which the precipitate dispersions are stable and present, for the most part, in minor amounts. This eliminates consideration of superalloys such as Nimonic MAR-M-200 or CSMX-2, which contain very large volume fractions of large γ' particles that are present at very high temperatures for the purpose of imparting high-temperature strength. Important issues involving the creep resistance and anomalous yielding behaviour at high temperatures of these kinds of alloys are dealt with elsewhere in these volumes.

2. Dislocation-Particle Interactions: Statistics

Real precipitates and dispersoids are always finite in size, are often nonspherical and sometimes nonequiaxed in shape, are often spatially correlated and can sometimes interact with dislocations at long range (i.e. beyond the physical limits of the particle itself). These factors can add sufficient complexity to frustrate any attempt at

comparing theory with experiment. However, when precipitates are small and relatively highly dispersed, a great deal of progress can be made by idealizing the array. At the simplest level of approximation a dispersion of precipitates can be regarded as an array of point obstacles distributed spatially at random throughout the matrix. We will start at this level and consider the consequences of the inevitable complexities later. The principles discussed in the following sections are also applicable to the topic of solid-solution strengthening, and in many cases were originally expounded to explain that phenomenon.

2.1 Localized Point Obstacles

A random array of localized point obstacles distributed in the glide plane of a dislocation is capable of being completely penetrated by the dislocation (or 'transparent' to it) when the applied stress τ reaches a critical value τ_c given by (Ardell, 1985)

$$\tau_c = \frac{2\Gamma}{bL_c} \beta_c \quad (1)$$

where b is the magnitude of the Burgers vector of the dislocation, Γ is its line tension, β_c is a dimensionless measure of the strength of the point obstacles and L_c is their spacing along the dislocation line at this critical shearing stress. The geometry of this process is shown schematically in Figure 1. The important parameter β_c is defined by the equation

$$\beta_c = \sin(\theta_c/2) = \frac{F_m}{2\Gamma} \quad (2)$$

where $\theta_c/2$ is the angle through which the dislocation bows out at the obstacle and F_m is the strength of the obstacle (Figure 1); we assume for now that the strength of each obstacle is identical.

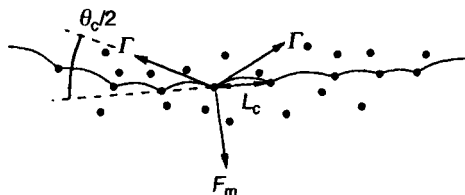


Figure 1. Schematic illustration of the penetration of a random array of point obstacles by a dislocation. Each segment shown is a circular arc of identical radius $R_c = \Gamma/\tau_c b$

Equation (1) is exact as it stands. However, what is missing is a criterion for evaluating L_c , because the spacing of the obstacles along the dislocation at the critical cutting configuration is as yet unknown. Physically, we expect this obstacle spacing to decrease as τ increases because as the dislocation bows out, more obstacles are encountered statistically (the spacing is infinite for a straight dislocation in a random array of points). By analogy, we expect that the stronger the obstacles, the more the dislocation will bow out and the shorter the obstacle spacing will be, i.e. L_c should decrease as F_m increases. An expression for L_c as a function of obstacle strength was obtained nearly simultaneously by Friedel (1962) and Fleischer and Hibbard (1963). They argued that the dislocation penetrates the array of obstacles in a steady-state unzipping process. The complicated statistics of the unzipping of segments of random lengths of curved dislocation segments were simplified by assuming, for the average configuration, that every time the dislocation is unpinned the new segment that bows out sweeps out a new area of the slip plane that contains one new obstacle that was not previously encountered.

The mathematics of this steady-state unzipping process are straightforward, involving only the approximation $\sin x \approx x - x^3/6$ (Brown and Ham, 1971; Ardell, 1985), and lead to the result

$$L_c \equiv L_F = \frac{L_s}{\beta_c^{1/2}} \quad (3)$$

where L_F is called the Friedel spacing (steady-state unzipping is often referred to as Friedel–Fleischer statistics) and L_s is referred to as the square-lattice spacing, which is formally related to the number of obstacles per unit area in the glide plane n_s by the equation

$$L_s = n_s^{-1/2} \quad (4)$$

The square-lattice spacing simply specifies the value of the lattice constant after removing all the obstacles from their random locations and placing them on the points of a square lattice.

We thus obtain the expected result that the obstacle spacing decreases as the strength of the obstacle increases. Equation (3) should be a reasonable approximation for obstacle strengths approaching $\beta_c \approx 0.7$ (Ardell, 1985), beyond which the dislocation bows into a semicircle after its release. An approximation implicit in the derivation of equation (3) is that the line tension of the dislocation is independent of its character, so that

any bowed-out segment takes the shape of a circular arc. The limitations of this assumption are discussed later.

Substitution of equation (3) into equation (1) leads to the result

$$\tau_c = \frac{2\Gamma}{bL_s} \beta_c^{3/2} \quad (5)$$

It is convenient to express equation (5) in dimensionless form involving the dimensionless stress τ_c^* , defined by the equation

$$\tau_c^* = \tau_c \frac{bL_s}{2\Gamma} \quad (6)$$

which through equation (1) implies the quite general result

$$\tau_c^* = \frac{\beta_c}{L_c/L_s} \quad (7)$$

In light of equation (6), equation (5) takes the simple form

$$\tau_c^* = \beta_c^{3/2} \quad (8)$$

The penetration of arrays of point obstacles of fixed strength by dislocations of constant line tension has been investigated in computer modeling experiments by Foreman and Makin (1966), Morris and Klahn (1974) and Hanson and Morris (1975a). The results of two of these experiments are shown in Figure 2, where it is evident that equation (8) provides a good fit to the data for β_c approaching 0.7 (the discrepancy here is of the order of 10%). At values of β_c approaching 1 the results of the computer simulations deviate increasingly from the predictions of equation (8). There is no analytical theory for this region of strong, penetrable obstacles. Brown and Ham (1971) have noted that the data in this region can be described quite well by the linear equation

$$\tau_c^* = 0.81\beta_c \quad (9)$$

where the coefficient 0.81 represents the limiting behavior at $\tau_c^* = 1$. Using equations (7) and (9) we see that the critical spacing of the obstacles along the dislocation, in the regime of strong obstacles, approaches the limiting value $L_c = 1.23L_s$. Again, there is no theory that predicts this result. In the limit $\beta_c = 1$ the obstacles

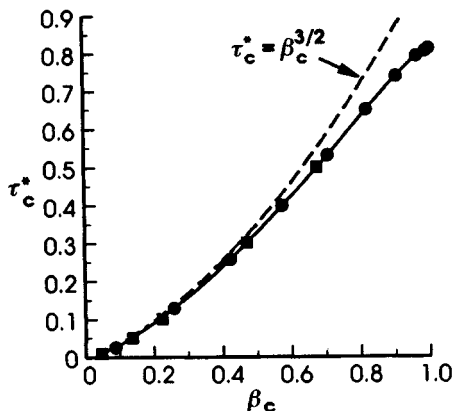


Figure 2. The results of the computer simulation experiments of (■) Foreman and Makin (1966) and (●) Hanson and Morris (1975a) illustrating the penetration of arrays of obstacles of identical strengths. The reduced critical stress for the array defined by equation (6) is plotted against the obstacle strength β_c . The predictions of Friedel-Fleischer statistics (equation 8) are indicated by the dashed curve

are impenetrable, and equation (9) becomes the dimensionless form of the Orowan (1948) equation, namely

$$\tau_c^* = 0.81 \quad (10)$$

Because of its simplicity it is perhaps surprising that the Friedel-Fleischer theory describes the results of the computer simulation experiments as well as it does. A more rigorous examination of the data in Figure 2 (Ardell, 1985) indicates that the equation

$$\tau_c^* = 0.956\beta_c^{3/2} \left(1 - \frac{\beta_c^2}{8} \right) \quad (11)$$

provides a very accurate fit (to within 5%) over the entire range of β_c . Like equation (9), it is empirical, but is not as convenient to use in the limit of strong obstacles. However, it demonstrates that in the weak-obstacle regime of Friedel-Fleischer statistics equation (8) slightly overestimates τ_c^* . Indeed, the most recent theoretical treatments of the penetration of an array of point obstacles of identical strength by a dislocation of constant line tension (Hanson and Morris, 1975a; Labusch, 1977) predict the result

$$\tau_c^* = C\beta_c^{3/2} \quad (12)$$

in the limit of weak obstacles, where C is a constant. In the theory of Hanson and Morris (1975a) $C = 0.887$,

while in that of Labusch (1977) $C = 0.949$, which is closer to the empirical value $C = 0.956$ in equation (11).

The Friedel-Fleischer theory and the results of the computer simulation experiments lead to the fundamental equations of the theory of precipitation strengthening. However, in order to see how well these equations are capable of predicting data on real alloys, many additional assumptions and approximations are required. Some of these are so simplified that the refinements of the basic theory leading to the distinction between equations (8) and (12) are completely overwhelmed by other factors. Therefore, while nuances of the issues concerning the fundamental behavior of obstacle-dislocation interactions remain unresolved, the practical application of the principles discussed above to the prediction of the yield strength of real alloys can proceed without regarding these subtleties. We shall proceed accordingly, using equations (8), (9) and (10) as the foundation for strengthening by weak obstacles, strong but penetrable obstacles and impenetrable obstacles, respectively.

2.2 Extended Obstacles

So long as the obstacles are localized, it is sufficient to consider only those in the glide plane itself, because obstacles in the neighboring glide planes above and below do not interact with a dislocation in the glide plane in question. Real obstacles are neither geometrical points nor necessarily localized in their effects. Instead, they are always finite in size and often possess a range of influence ω that extends beyond their geometrical limits. Diffuse obstacles can interact with dislocations in a fundamentally different manner from those dealt with in the previous section (Ardell, 1985), but we will not consider these further. Instead, we will limit the discussion to the results of the computer simulation experiments of Schwarz and Labusch (1978), who investigated the motion of dislocations through random arrays of diffuse obstacles.

Schwarz and Labusch considered obstacles with two different kinds of interaction profiles with dislocations (i.e. curves of interaction energy or force as a function of distance between the dislocation and the obstacle). Profiles containing attractive and repulsive contributions of equal magnitude are referred to as energy conserving, whereas profiles consisting only of repulsive interactions are called energy storing. Examples of these two types of profiles are illustrated schematically in Figure 3. The distinction between them is the presence of an attractive force of interaction (the region $F < 0$ in Figure 3a) during part of the encounter between the dislocation and the

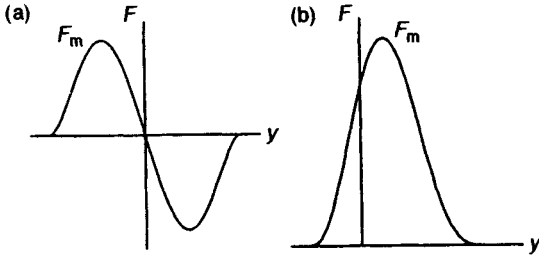


Figure 3. Schematic illustration of profiles of force F versus distance y for (a) energy-conserving and (b) energy-storing obstacles. The maximum force F_m associated with the repulsive portion of the interaction ($F > 0$) is also indicated

obstacle. The elastic interaction between the strain fields of the dislocation and the obstacle (e.g. a misfitting, spherical, coherent precipitate) is an example of an energy-conserving interaction (Figure 3a), whereas the cutting of a non-misfitting, coherent, ordered precipitate by a dislocation is an example of an energy-storing interaction (Figure 3b).

Examination of the results of their computer simulations led Schwarz and Labusch to propose two empirical equations for τ_c^* for the two types of interactions. For energy-storing interactions, which is the case of interest here

$$\tau_c^* = 0.94\beta_c^{3/2}(1 + 0.7\eta_0) \quad (13)$$

where the parameter η_0 is defined by the equation

$$\eta_0 = \frac{\omega}{\beta_c^{1/2}L_s} \quad (14)$$

Comparison of equation (13) with equation (1), utilizing equation (6), shows that the critical obstacle spacing for diffuse obstacles L_{SL} becomes

$$L_c = L_{SL} = \frac{1.064\beta_c^{-1/2}}{1 + 0.7\eta_0} \quad (15)$$

In the limit where η_0 approaches 0, L_{SL} approaches L_F (to within about 6%) and the behavior in the limit of Friedel–Fleischer statistics is recovered.

The computer simulations of Schwarz and Labusch provide considerable insight into the statistics of dislocation–obstacle interactions, and are particularly valuable for their contribution to understanding solid-solution strengthening. However, they must be applied to the interpretation of data on precipitation hardening with considerable caution because the simulation is only valid for very weak obstacles satisfying the approximate

criterion $\beta_c(\approx \theta_c/2) < 0.3$ (Ardell, 1985). Dislocations are bent through such small angles only by very small, weak precipitates.

2.3 Mixtures of Obstacles of Different Strengths

We have so far considered the strength imparted by random arrays of obstacles of identical strength. We will see shortly that the strength of an individual precipitate is related to its size, and since precipitates are never monodisperse, it is expected that a distribution of sizes implies a distribution of obstacle strengths (even in a monodisperse array the planar radius is distributed in the glide plane). It is therefore important to address several issues. (i) If there are two or more well-defined discrete classes of obstacle strengths, how does each class contribute to the combined strength of the entire array? (ii) If a continuous distribution of obstacle strengths exists, how accurately can the strength of the distribution be described by the strength of the average obstacle?

We consider first how the contributions of arrays of obstacles of two distinct strengths superimpose. Suppose there are n_s obstacles per unit area in the total array, n_{s1} having distinct strength β_{c1} and n_{s2} having distinct strength β_{c2} . The area fractions X_1 and X_2 of obstacles 1 and 2 are then $X_1 = n_{s1}/n_s$ and $X_2 = 1 - X_1 = n_{s2}/n_s$. The most generalized addition rule that we will consider has the form

$$\tau_c^q = \tau_{c1}^q + \tau_{c2}^q \quad (16)$$

where q is a constant. It is usually assumed that $q \geq 1$, although there is no physical reason why q cannot be smaller than unity. In terms of the dimensionless stresses τ_{c1}^* and τ_{c2}^* , equation (16) can be rewritten as

$$(\tau_c^*)^q = (\tau_{c1}^*)^q X_1^{q/2} + (\tau_{c2}^*)^q X_2^{q/2} \quad (17)$$

Equations (16) and (17) are versatile expressions for nearly all the addition rules in use to date. When $q = 1$ we obtain the familiar linear superposition law; when $q = 2$ we obtain the so-called Pythagorean superposition rule first proposed by Koppelaar and Kuhlmann-Wilsdorf (1964) and later verified theoretically by Hanson and Morris (1975b); when $q = 3/2$ the addition rule takes a form suggested by the theory of Labusch (1970). There is another addition rule, known as the rule of mixtures (Brown and Ham, 1971), which has been discussed in the context of precipitation strengthening; it does not appear to be important, however, and will not be considered further.

Strengthening by mixtures of obstacles of two distinct strengths has been investigated in other computer simulation experiments performed by Foreman and Makin (1967). They chose three different obstacle strengths, namely weak ($\tau_c^* = 0.260$), medium ($\tau_c^* = 0.530$) and strong ($\tau_c^* = 0.809$), and evaluated the strengths of the three possible pairs of arrays as a function of X_2 . The results are presented in Figure 4. It has been known for some time (Brown and Ham, 1971; Ardell, 1985) that linear and Pythagorean superposition, as well as the rule of mixtures, do not describe the data in Figure 4 particularly well. The best fits to the data are actually found using equation (17) with non-rational values of q . As seen in Figure 4, the appropriate values are $q = 1.70$ for the combination of strong and medium obstacles, $q = 1.45$ for the strong and weak combination and $q = 1.90$ for the combination of medium and weak obstacles. The last combination, i.e. obstacles of weak and medium strength, comes closest to fulfilling the Pythagorean superposition rule; this combination most closely approximates that treated theoretically by Hanson and Morris (1975b).

Real superalloys often contain two size classes of γ' precipitates (Anton, Chapter 1 in this volume). In some cases they are introduced deliberately by a two-step aging process. In other instances they are introduced inadvertently during cooling from the aging temperature because the matrix again becomes supersaturated as the alloy cools,

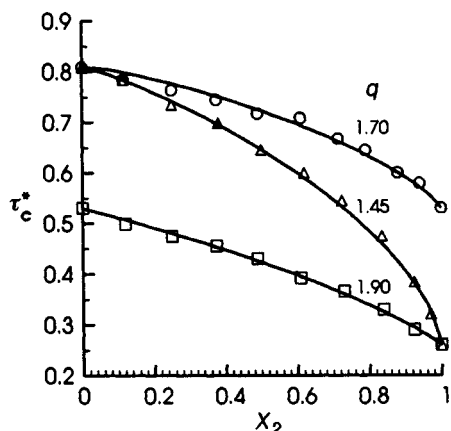


Figure 4. The results of the computer simulation experiments of Foreman and Makin (1967) for random mixtures of obstacles of two distinct strengths. The total reduced critical stress of the array is plotted against the areal concentration X_2 of the weaker obstacles. The symbols represent the following combinations of pairs of obstacle strengths: (\circ) $\tau_{c1}^* = 0.809$ and $\tau_{c2}^* = 0.530$; (Δ) $\tau_{c1}^* = 0.809$ and $\tau_{c2}^* = 0.260$; (\square) $\tau_{c1}^* = 0.530$ and $\tau_{c2}^* = 0.260$. The values of q providing the best fit to the data using equation (17) are indicated

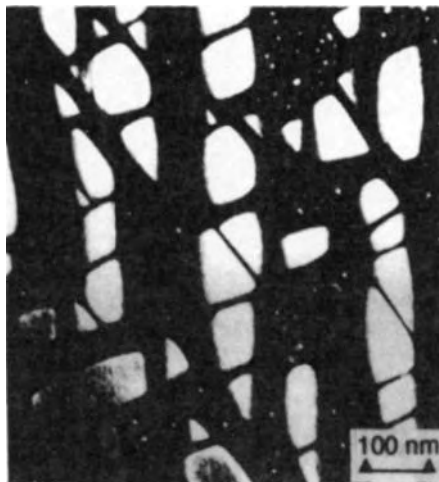


Figure 5. Dark-field transmission electron micrograph, taken using a (100) γ' superlattice reflection, of an Ni-7.53 wt% Al alloy aged for 32 h at 800 °C and 72 h at 600 °C (Chellman and Ardell, 1975). The populations of large and small precipitates were produced at the two aging temperatures. The thin foil was prepared parallel to a {111} slip plane and tilted into [013] orientation for observation; the open channels between the large precipitates are parallel to (100)

and the nucleation of γ' particles is so easy. An example of a bimodal γ' microstructure in a binary Ni-Al alloy is shown in Figure 5. The yield strength of such alloys can be predicted if the contribution of each size class is estimated and the addition rule is known.

Foreman and Makin (1967) also performed computer simulation experiments on arrays of obstacles having a particularly simple distribution of obstacle strengths. A detailed analysis (Ardell, 1985) has shown that the results of Foreman and Makin can be reproduced extremely well analytically assuming Pythagorean superposition. Furthermore, the strength of the array is accurately represented by the strength of the average obstacle in the array.

2.4 Finite Obstacles

Real precipitates, of course, are not point obstacles, so it is essential to adapt the equations derived in Sections 2.1 and 2.2 to obstacles of finite size, in which case their shapes must also be taken into account. Fortunately, most of the intermetallic compounds that exist as precipitates in Ni-based superalloys and steels are spherical, or at worst equiaxed in shape, which greatly simplifies the application of the equations derived herein to the particles actually encountered in real alloys. There is another potential complication owing to the fact that

precipitates are not monodisperse, as noted earlier. This serves to broaden the distribution of sizes, hence strengths, of the precipitates.

There is a purely geometrical relationship involving the volume fraction of precipitates f , the average radius of the dispersion $\langle r \rangle$ and the parameters we have already encountered, namely

$$L_s = \left(\frac{2\pi}{3f} \right)^{1/2} \langle r \rangle \quad (18)$$

the derivation of which utilizes the relationship between the average planar radius $\langle r_s \rangle$ and $\langle r \rangle$, i.e. $\langle r_s \rangle = \pi \langle r \rangle / 4$. These results are, strictly speaking, valid for a monodisperse assembly of particles of radius r , but are also good approximations for polydisperse arrays. For example, Nembach and Chow (1978) have calculated the numerical constant relating $\langle r_s \rangle$ and $\langle r \rangle$ for the particle size distribution of the theory of diffusion-controlled coarsening of Lifshitz and Slyozov (1961) and Wagner (1961) and found it to be 0.82, cf. $\pi/4 = 0.785$. The difference is less than 5%, which is far smaller than the uncertainties in the data we will ultimately analyze and the assumptions we will use in the analyses.

The quantitative consequences of finite particle size depend on the magnitude of τ_c^* , that is, whether we are dealing with weak, strong but penetrable, or impenetrable obstacles. When the particles are weak, which is the case for underaged alloys, there are two approaches, one involving the extension of the mathematical apparatus of Friedel–Fleischer statistics to obstacles of finite size and the other involving the application of the results of the computer simulation experiments of Schwarz and Labusch (1978). Ardell (1985) has discussed the consequences of the former approach, noting that the quantitative predictions of the Friedel–Fleischer theory depend to some extent on the mechanism of the dislocation–precipitate interaction. Quite generally, however, the critical shear stress for finite obstacles always exceeds that for point obstacles (the value of n_s being equal), and the magnitude of the increase becomes larger as f increases. When the results of Schwarz and Labusch are used, it is necessary to relate $\langle r_s \rangle$ and ω . The distinction between diffuse obstacles of finite range and localized discrete obstacles of finite size thus becomes clouded. For example, a coherent, spherical, ordered precipitate with no lattice mismatch is a localized discrete obstacle of finite size, and applying Schwarz–Labusch statistics to estimate the strength of an array of such particles is a possible misapplication of their results. On the other hand, the strain field of a misfitting solute atom and composition

fluctuations such as those arising in the early stages of spinodal decomposition are excellent examples of the kinds of obstacles to which Schwarz–Labusch statistics are, or should be, relevant.

When the precipitates are larger, hence stronger, but still shearable, the dispersion reaches its maximum capacity to strengthen the alloy, which then attains its peak strength; this is the peak-aged condition, and is the regime of obstacle strengths to which equation (9) applies. When the obstacles are so strong that they are impenetrable, the alloy is overaged and the critical shear stress is determined by equation (10). In both cases the critical spacing of point obstacles along the dislocation in this regime is $L_c = 1.235L_s$, but when the obstacles are finite and spherical it is appropriate to replace L_c by $L_c - 2\langle r_s \rangle$ because the actual spacing along the dislocation line has been reduced by the finite planar radius. The proper expression for L_c is thus

$$L_c = 1.571 \langle r \rangle (1.137 f^{-1/2} - 1) \quad (19)$$

Equation (19) differs from the more frequently encountered expression $L_c = L_s - 2\langle r_s \rangle$.

3. Dislocation Line Tension

The various equations presented to this point were derived assuming that the dislocation line bows into a circular arc, irrespective of the magnitude of the applied stress, i.e. the dislocation is assumed to remain circular even as $\theta_c/2$ approaches $\pi/2$ (β_c approaches 1). This assumption applies to the computer simulations as well as to the analytical theories. The implicit assumption here is that Γ is completely independent of the character of the dislocation, e.g. that the line tensions of pure edge and pure screw dislocations are identical. It has long been known that this is not the case, even for elastically isotropic crystals (De Wit and Koehler, 1959). Instead, Γ depends on the angle ξ between the dislocation line and its Burgers vector, as described by the equation

$$\Gamma = \frac{Gb^2}{4\pi} \left(\frac{1 + \nu - 3\nu \sin^2 \xi}{1 - \nu} \right) \ln \frac{\Lambda}{r_0} \quad (20)$$

where G is the shear modulus, ν is Poisson's ratio and Λ and r_0 are the outer and inner cutoff distances in the expression for the line energy of the dislocation. If the dislocation is initially pure edge ($\xi = \pi/2$), the value of ξ at the obstacle itself is $(\pi - \theta_c)/2$, whereas for a dislocation initially pure screw in character ($\xi = 0$) its value at the obstacle is $\theta_c/2$. The line tension of a pure edge

dislocation is smaller than that of a pure screw by the factor $(1 - 2\nu)/(1 + \nu)$; for $\nu = 1/3$ this is a factor of 4.

There are several important consequences of equation (20). One of them is that edge dislocations are more flexible than screws and will therefore bow out more than screws between two obstacles under a given applied shear stress. This further implies that an edge dislocation will encounter more obstacles than screws when the obstacles are weak. Another consequence is that the shape of the dislocation arc is strictly speaking not circular, although for weak obstacles the circular shape is a good approximation. The implication here is that the approximations of Friedel–Fleischer statistics and the results of the computer simulation experiments continue to be valid for weak obstacles. For stronger obstacles the dislocation arcs are elliptical, and the errors resulting from the assumption of a circular shape are not known. A third consequence of equation (20) is that Γ changes as the dislocation bows out, which means that if its initial character is edge type Γ increases as the dislocation acquires more screw character, and vice versa if its initial character is screw type. Since the difference in Γ between edge and screw dislocations can be quite significant, becoming very large in alloys for which ν is large, the assumption of constant Γ is particularly bad for quantitative comparisons between theory and experiment.

Actually, even equation (20) is a poor approximation to the line tension of real dislocations in anisotropic crystals. This is evident from the work of Barnett *et al.* (1972), who calculated the line tensions and energies of dislocations in several crystals. In their formulation Γ is given by an expression of the type

$$\Gamma = J(\xi) \ln \frac{\Lambda}{r_0} \quad (21)$$

where $J(\xi)$ is a complicated function of the single-crystal elastic constants as well as ξ . Comparisons of the variations of $J(\xi)$ and the coefficient of the logarithmic factor in equation (20) with ξ for Ni and α -Fe, the two base materials of principal interest in this chapter, are shown in Figure 6. The elastic constants of Ni and α -Fe used in equation (20) were taken from ASM (1979). It is evident that the calculation of Γ within the framework of elastic isotropy, through equation (20), is not a good approximation, although it is better overall for Ni than for α -Fe.

Obviously, any serious attempt to compare theory with experiment cannot rely on the simplifying assumptions of the past (e.g. $\Gamma \approx Gb^2/2$) to estimate the dislocation line tension. It is essential to employ the most accurate available representations of Γ , but even the anisotropic

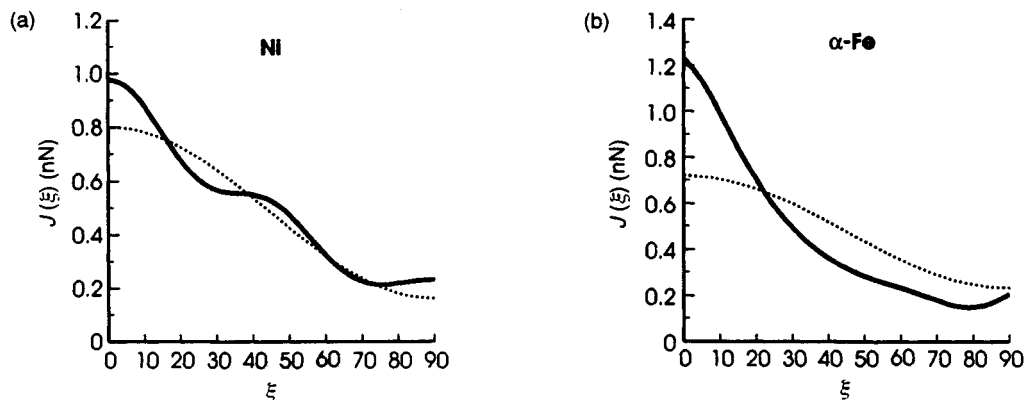


Figure 6. The variation of the line tension of dislocations in (a) Ni and (b) α -Fe with the angle ξ between the dislocation line and its Burgers vector. The solid curves represent the results of the calculations of Barnett *et al.* (1972) which include the effects of elastic anisotropy. The dashed curves are based on the assumption of isotropic elasticity theory (equation 20). The parameter $J(\xi)$ is the coefficient of the logarithmic factor in equations (20) and (21)

values of Γ tabulated by Barnett *et al.* (1972) and shown in Figure 6 are not necessarily in their most useful form because of the expected variation of Γ with ξ as the dislocation bows out. A more realistic line tension is the geometric mean value of Γ defined by

$$\langle \Gamma \rangle = [\Gamma(\xi)\Gamma(\pi/2)]^{1/2} \quad (22)$$

or

$$\langle \Gamma \rangle = [\Gamma(\xi)\Gamma(0)]^{1/2} \quad (23)$$

for dislocations that are initially edge or screw in character, respectively. These representations ensure that the average line tension of an initially edge dislocation will increase, and that of an initially screw dislocation will decrease, as the dislocation bows out.

The reason for employing the geometric mean, rather than some other average, is that as the regime of strong particles is approached, the values of Γ predicted by equations (22) and (23) approach those recommended by Hirsch and Humphreys (1969), although those authors actually prescribed the use of the geometric mean value of the edge and screw line energies. They justified this by arguing that a dislocation bowing between strong obstacles takes the shape of a semi-ellipse, and that the area swept out is the same irrespective of whether it is initially edge or screw. In anisotropic crystals the corresponding shape is not elliptical, but equations (22) and (23) retain the spirit of this argument, and they will be used here because there is no better alternative known.

The variations of $\langle J_e \rangle$ and $\langle J_s \rangle$ for Ni and α -Fe with β_c are shown in Figure 7. For dislocations initially edge in character $\beta_c = \sin(\pi/2 - \xi)$, whereas for screws $\beta_c = \sin \xi$. It can be appreciated that both $\langle J_e \rangle$ and $\langle J_s \rangle$ vary quite slowly with β_c compared to the variations of $J(\xi)$ with ξ (Figure 6). Specifically, $\langle J_e \rangle$ for Ni (Figure 7a) increases from about 0.23 to 0.35 nN (a little over 50%) as β_c approaches 0.8 (as the initially edge dislocation bows out to an angle of $\theta_c/2 \approx 53^\circ$ and ξ decreases from $\pi/2$ to about 37°), whereas $J(\xi)$ itself increases from 0.23 to 0.54 nN (Figure 6a). The variation is stronger for α -Fe (Figure 7b), $\langle J_s \rangle$ decreasing from about 1.22 to 0.6 nN while $J(\xi)$ itself decreases from 1.22 to 0.27 nN (Figure 6b) as the initially pure screw dislocation bows out to $\theta_c/2 \approx 53^\circ$.

Finally, we will employ the suggestion of Brown and Ham (1971) to estimate Λ and r_0 . They recommend that Λ be taken as L_F when the obstacles are weak, and as $2\langle r_s \rangle$ when they are strong. The former suggestion renders equation (21) transcendental, since L_F itself depends on Γ through equations (2) and (3), but a unique value of Γ is easily obtained. There is no hard and fast rule for choosing r_0 . Any value that is of the order of several Burgers vectors is reasonable; in this work we take $r_0 = pb$, where p is a constant expected to lie in the range 1 to 4. With these choices the equations for Γ for underaged alloys become

$$\Gamma = \langle J \rangle \ln \frac{L_F}{pb} \quad (24)$$

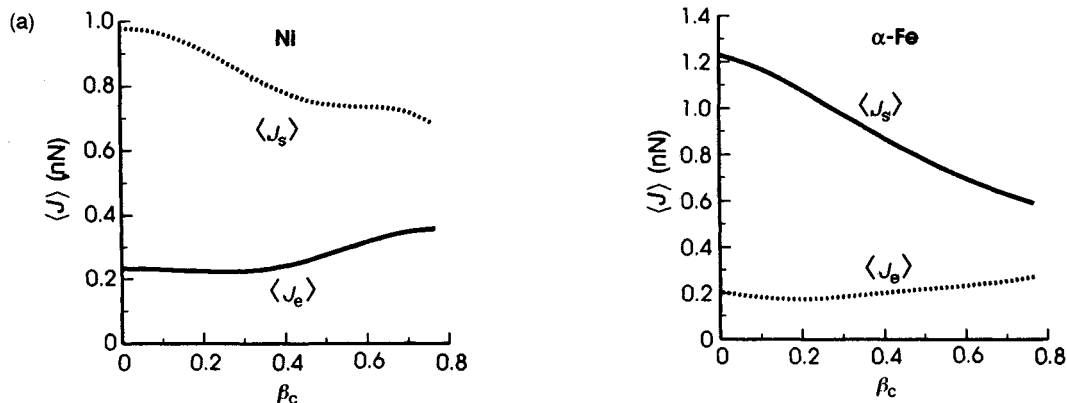


Figure 7. The variation of the geometric mean line tensions of initially pure edge and screw dislocations in (a) Ni and (b) α -Fe, plotted as a function of the obstacle strength β_c , which is related to ξ as discussed in the text. The solid curves in each figure ($\langle J_s \rangle$ for Ni and $\langle J_e \rangle$ for α -Fe) were used in subsequent calculations of Γ

or

$$\Gamma = \langle J_s \rangle \ln \frac{L_F}{pb} \quad (25)$$

Equation (24) obtains when edge dislocations control the critical resolved shear stress (CRSS) and (25) obtains when screw dislocations control. For alloys in the peak-aged or overaged conditions the expression for Γ is

$$\Gamma = (E_s E_e)^{1/2} \ln \frac{2\langle r_s \rangle}{pb} \quad (26)$$

where E_s and E_e are the line energies of pure screw and edge dislocations, respectively. These latter two quantities have also been calculated by Barnett *et al.* (1972), and it turns out that $(E_s E_e)^{1/2}$ for both Ni and α -Fe are only slightly smaller than the corresponding values of $(J_s J_e)^{1/2}$.

4. Mechanisms of Precipitation Strengthening

To this point we have concentrated on the phenomenology of strengthening by point or finite obstacles. Further progress is not possible without considering the detailed mechanisms by which dislocations interact with precipitates. These interactions govern the magnitude of β_c , and hence they ultimately enable us to predict how the strength of the alloy depends upon physical parameters characterizing the particles, e.g. their coherency strain fields if the precipitates are coherent and misfitting, the antiphase boundary energy if they are coherent and ordered, etc. For the majority of strengthening mechanisms the obstacle strength F_m is proportional to $\langle r \rangle$, i.e. the strength increases as the particles grow. This simple fact leads immediately to the familiar age-hardening response of alloys as a function of the average particle size $\langle r \rangle$, volume fraction f , and dislocation line tension Γ . For underaged alloys in which Friedel-Fleischer statistics govern the dislocation-precipitate interactions, the combination of equations (2), (5) and (18) leads to the proportionality $\tau_c \propto (\langle r \rangle f / \Gamma)^{1/2}$; this behavior is representative of strengthening by weak, penetrable obstacles. When the alloy is aged to peak strength, equations (2), (6), (9) and (18) predict $\tau_c \propto f^{1/2}$; this is the regime of strong, penetrable obstacles in which there is no dependence on either $\langle r \rangle$ or Γ . In the overaged condition the obstacles are impenetrable and the Orowan equation governs the strength; in this regime $\tau_c \propto \Gamma f^{1/2} / \langle r \rangle$ for small values of f via equations (2), (6), (10) and (18).

There are five mechanisms of precipitation strengthening that have received serious theoretical attention over the years: (i) chemical (or surface-energy) strengthening, caused by the new precipitate-matrix interface created when any precipitate is sheared; (ii) stacking-fault strengthening, arising when the stacking-fault energies of the precipitate and matrix phases differ; (iii) modulus strengthening, brought about when the elastic constants of the precipitate and matrix phases differ; (iv) coherency strengthening, arising through the elastic strains in the matrix that are generated when the lattice constants of the precipitate and matrix phases differ; and (v) order strengthening, coming into play when an ordered precipitate is sheared by a unit dislocation of a chemically disordered matrix.

Each of these mechanisms is characterized by a unique force-distance profile, some of which fulfill the Schwartz-Labusch definition of energy conserving (e.g. coherency and modulus strengthening), while others are energy storing (e.g. chemical, stacking-fault, and order strengthening). There is no reason why any specific mechanism must operate exclusively of the others, and the action of any combination can, in principle, be treated theoretically by adding the interaction forces impeding the dislocation as it approaches a precipitate. However, there has not been much progress in dealing with this aspect of the problem quantitatively because it is difficult to generalize; each combination of cases must be dealt with separately. What is sometimes assumed is that the values of τ_c predicted separately for each mechanism can be added to estimate the total strengthening. There is no justification for this procedure, and it can be rigorously proved erroneous.

The strengthening attributed to each of the mechanisms noted above has been predicted theoretically by numerous researchers whose efforts have been thoroughly reviewed (Brown and Ham, 1971; Ardell, 1985). Consequently, we will summarize here only the main predictions of the most important strengthening mechanism in alloys strengthened by ordered intermetallics, namely order strengthening. In the subsequent discussion it is understood that the order-strengthening mechanism refers strictly to systems in which the crystal structure of the precipitate phase is a derivative of that of the parent matrix phase. Ni_3Al precipitates with the L_{12} (cP4) crystal structure in a face-centered cubic (f.c.c.) matrix and NiAl precipitates with the B2 (cP2) crystal structure in a body-centered cubic (b.c.c.) matrix are straightforward examples. More complicated combinations can also satisfy this criterion, but Ni_3Al precipitates in a b.c.c. matrix, for example, is a combination that does not, because unit dislocations in

the b.c.c. structure cannot be superlattice partial dislocations in the Ni_3Al phase; strengthening in the latter case must obtain through another mechanism.

4.1 Underaged Alloys

The unique feature of order strengthening is that dislocations move in groups of two or more, depending on the number of dislocations necessary to restore perfect long-range order on the glide plane of the precipitate after it is sheared by the leading dislocation in the group. The most familiar example, which is the situation for which the theory was first developed, is that of ordered coherent γ' (Ni_3Al) precipitates in a disordered, Ni-rich, solid-solution matrix. Here a unit dislocation with $b = \frac{1}{2}a\langle 110 \rangle$ creates an antiphase boundary (APB) on the $\{111\}$ glide plane of the γ' phase, which is eliminated by the passage of another dislocation having the identical Burgers vector. The dislocations thus travel in pairs, and the theory of strengthening by this mechanism involves the details of how each of the two dislocations interacts with the γ' precipitates intersecting their slip plane, as well as how they interact with each other.

The first important step in the theory is a calculation of F_m , which several authors (Gleiter and Hornbogen, 1965; Castagné, 1966; Ham, 1968) have shown is given by the expression

$$F_m = 2\gamma_{\text{APB}}\langle r_s \rangle = \frac{\pi\gamma_{\text{APB}}\langle r \rangle}{2} \quad (27)$$

where γ_{APB} is the energy of the APB on $\{111\}$ and the precipitates are assumed to be spherical in shape. It is then necessary to take into account the interactions between the precipitates and the leading and trailing dislocations, and the two dislocations with each other, under the influence of an applied shear stress. A schematic representation of the geometry is depicted in Figure 8, which illustrates the complexity of the problem. The dislocations in Figure 8 are shown at the critical cutting configuration, wherein the spacing L_I of the precipitates along the leading dislocation (I) is assumed equal to L_F . The trailing dislocation (II) interacts with a different set of precipitates, which of course have already been sheared by dislocation I. The obstacle spacing L_{II} differs from L_I because the sheared, ordered precipitates are attractive obstacles to dislocation II. The distance D separating the two dislocations varies along the length of the pair.

The equilibrium dislocation configurations in this situation have not been solved exactly, but to a good

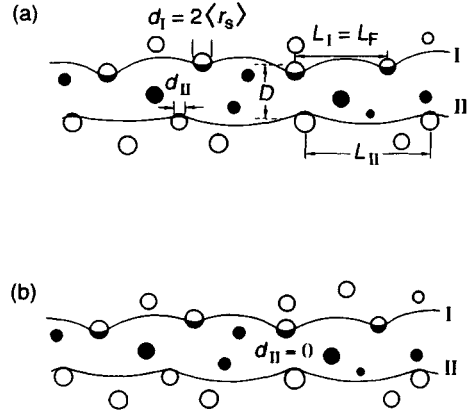


Figure 8. Schematic illustrations of the shearing of ordered, coherent precipitates by a pair of dislocations. In (a) d_{II} is finite and in (b) d_{II} is equal to zero

approximation it can be assumed that both dislocations are nearly straight and that the pair is weakly coupled, i.e. that both dislocations are unlikely to reside within the same particle. Under these conditions we can apply the force balance used by Brown and Ham (1971), which leads to the result

$$\tau_c = \frac{\gamma_{\text{APB}}}{2b} \left(\frac{d_I}{L_I} - \frac{d_{II}}{L_{II}} \right) \quad (28)$$

where d_I and d_{II} are defined in Figure 8. In the simplest case, that of a very dilute dispersion of γ' particles ($f \ll 1$), $d_I/L_I = 2\langle r_s \rangle/L_F$, while dislocation II is pulled through the previously sheared γ' precipitates as soon as it encounters them, resulting in $d_{II} = 0$. Under these conditions the predicted CRSS for underaged alloys becomes

$$\tau_c = \frac{\gamma_{\text{APB}}}{2b} \left(\frac{3\pi^2\gamma_{\text{APB}}f\langle r \rangle}{32\Gamma} \right)^{1/2} = \frac{\gamma_{\text{APB}}}{2b} B^{1/2} \quad (29)$$

where

$$B = \frac{3\pi^2\gamma_{\text{APB}}f\langle r \rangle}{32\Gamma} \quad (30)$$

It is frequently assumed, following Brown and Ham (1971), that the trailing dislocation is straight, in which case $d_{II}/L_{II} = f$. This is the simplest imaginable configuration the trailing dislocation can have if it cannot be pulled completely through the sheared precipitates because of the repulsive force it feels from the leading dislocation. Under these circumstances equation (29) becomes

$$\tau_c = \frac{\gamma_{APB}}{2b} (B^{1/2} - f) \quad (31)$$

Except for the factor of 2 in the denominators of equation (29) and (30), identical equations are obtained on substituting equation (27) into equation (8), utilizing equations (6) and (18).

There can be a considerable difference between the magnitudes of τ_c predicted by equations (29) and (31), so the configuration of the trailing dislocation becomes a matter of some significance. Nembach *et al.* (1985, 1987) have interpreted so-called 'scalloped' dislocation images in slip bands of deformed Nimonic PE16 and Nimonic 105 using *in situ* weak-beam transmission electron microscopy (TEM) as evidence that the trailing dislocation is nearly straight. However, their case is not convincing because the dislocations and γ' precipitates are never visible simultaneously under weak-beam diffracting conditions. Furthermore, the appearance of superlattice dislocations in slip bands, even in monolithic Ni_3Al containing no visible obstacles, is scalloped in weak-beam TEM images (Baker *et al.*, 1987), indicating that the interpretation of such images is far from certain.

Equation (29) requires modification when the volume fraction of γ' precipitates no longer satisfies the condition $f \ll 1$. This condition is rarely fulfilled because in most alloys $f \geq 0.1$. There have been two rather different ways of extending the theory of order strengthening to larger volume fractions. Ardell *et al.* (1976) modified the theory of Ham (1968), thereby proposing a theory utilizing Friedel-Fleischer statistics, but accounting for the effects of finite obstacle size and volume fraction. Haasen and Labusch (1979) adapted the results of the computer simulations of Schwarz and Labusch (1978) and associated the finite particle size with the range of an energy-storing obstacle. The theory of Ardell *et al.* (1976) predicts that the CRSS for a dislocation of any character is

$$\tau_c = \frac{\gamma_{APB} u}{2b} \quad (32)$$

where

$$u = \frac{(4B + B^2/3)^{1/2} - B}{2(1 - B/6)} \quad (33)$$

B being defined by equation (30).

Equation (32) assumes that the trailing dislocation is completely attracted through the already-sheared γ' particles. In the limit of small f or $\langle r \rangle$, equation (33) predicts that u approaches $B^{1/2}$, so that equation (29)

is recovered. All the analyses in this chapter will be based on these equations. The alternative theoretical approach of Haasen and Labusch (1979) has enjoyed an active following, and many of the data analyzed in this chapter have also been analyzed by other investigators using the ideas of Haasen and Labusch. The relative merits of the two approaches will therefore be compared later using an illustrative example.

4.2 Alloys Aged to Peak Strength

When the alloys are strong and the precipitates are highly dispersed the CRSS can be predicted using equation (28) with $d_1 = \pi \langle r \rangle / 2$, $L_1 = L_s / 0.81$ and $d_{11} = 0$, keeping in mind equation (18), yielding

$$\tau_c = 0.81 \frac{\gamma_{APB}}{2b} \left(\frac{3\pi f}{8} \right)^{1/2} \quad (34)$$

Note that τ_c is constant for fixed f . Equation (34) does not make complete allowance for particles of finite size. Possible modifications are relatively straightforward, but discussion of this point will be postponed until after the data analyzed in this chapter have been presented.

4.3 Overaged Alloys—The Orowan Equation

When coherent precipitates grow beyond a certain size they become so strong that they can no longer be sheared, i.e. at this point they become impenetrable obstacles. The dislocations then uncouple, the interactions considered in the previous sections become irrelevant in determining the strength of the alloy, and the dislocations bypass the obstacles by looping around them. The contribution of the precipitates is then determined by the Orowan equation, and the limiting size $\langle r \rangle_c$ at which the transition from shearing to looping occurs is determined approximately by the condition $\beta_c = 1$ or $F_m = \gamma_{APB} \langle r \rangle_c / 2 = 2\Gamma$, resulting in $\langle r \rangle_c = 4\Gamma / \gamma_{APB}$, where Γ is given by equation (26).

The Orowan equation in its simplest form is expressed by equation (10). In real alloys the effects of dislocation character and finite obstacle size must be taken into account. The various ways these factors affect the bypassing process have been discussed by Ashby (1969), Hirsch and Humphreys (1969) and Bacon *et al.* (1973). A suitable final result is

$$\tau_c = \frac{1.273\Gamma}{br} \frac{f^{1/2}}{(1.137 - f^{1/2})} \quad (35)$$

The major difference between equation (35) and previously published versions arises through the use of

equation (19) for L_c , which explicitly accounts for the effect of finite particle size and makes the obstacle spacing in the glide plane equal to $(L_s/0.81) - 2\langle r_s \rangle$, not $L_s - 2\langle r_s \rangle$ as is commonly assumed.

5. Procedures for Analyzing and Modeling Experimental Data

5.1 General Considerations

There have been numerous investigations of the strength of alloys containing ordered intermetallic compounds as dispersed phases. The vast majority of this work is not amenable to detailed analysis because the necessary data on the variation of particle size and volume fraction with aging time are not available. Fortunately, several alloys have been investigated thoroughly enough so that the theory of order strengthening can be tested, although several important assumptions are required before unequivocal evaluation is possible. Perhaps the most important of these involves the separation of the individual contributions of the matrix and precipitate phases. The combined strength of both is always measured in any individual test, but the theory predicts only the contribution of the precipitates to the total strength of the alloy.

It would seem that such a separation should be a simple matter, the contributions of the matrix τ_m and the precipitates $\Delta\tau_p$ (to be compared with τ_c) being linearly additive, i.e. $\Delta\tau_p$ can be obtained from the equation

$$\Delta\tau_p = \tau_T - \tau_m \quad (36)$$

where τ_T is the total CRSS of the alloy. Usage of this simplest of addition rules, however, has turned out to be surprisingly inconsistent. An alternative addition rule analogous to equation (16), namely

$$\Delta\tau_p^k = \tau_T^k - \tau_m^k \quad (37)$$

where k is a constant (> 1), has also received widespread application (Nembach and Neite, 1985; Reppich *et al.*, 1982). Whereas there is no theoretical basis for equation (37), equation (36) has a solid foundation both theoretically (Kocks, 1969) and experimentally (Ebeling and Ashby, 1966). It will be used exclusively herein to estimate the experimentally measured values of $\Delta\tau_p$.

Another factor that contributes significantly to uncertainties in the evaluation of experimental data on polycrystalline alloys is the Taylor factor M , which relates the yield stress σ_y to τ_T by the equation

$$\tau_T = \sigma_y / M \quad (38)$$

In a tensile or compression test on polycrystals σ_y is usually, but not always, taken as the flow stress at a plastic strain of 0.2% ($\sigma_{0.2}$). The only difficulty involved in using the disarmingly simple equation (38) is that accurate values of M are rarely available because preferred orientations in the polycrystalline alloys used in precipitation strengthening experiments are seldom, if ever, measured. We are then forced to guess what M is, and the value most commonly chosen in the literature, $M=3$, will be used herein. It should be kept in mind, however, that M can be different, which provides considerable latitude in assessing the value of τ_T , hence $\Delta\tau_p$, for comparison with theory. In most of the experiments on polycrystals the authors have reported $\sigma_{0.2}$ as the yield stress and $M=3$ as the Taylor factor. Unless specifically stated otherwise, these values are used in all subsequent analyses.

Finally, it is evident that theory cannot be compared with experiment in a meaningful way unless the APB energies of the precipitate phases are known. The theory described in Section 4.1 was developed for binary f.c.c. alloys strengthened by γ' precipitates, hence accurate values of γ_{APB} on {111} are required. Despite the vast amount of research on the important ordered intermetallic compound Ni_3Al , a precise measurement of the magnitude of γ_{APB} has proven to be quite elusive, and there is no consensus on its value. In commercial alloys the γ' precipitate phase contains additional elements, hence estimated values of γ_{APB} are generally unavailable. In alloys strengthened by other types of ordered intermetallic compounds the situation is even worse, and the only approach to quantitative description or modeling of data must rely on using γ_{APB} as a fitting parameter and appealing to some type of physical reasoning to decide whether the empirically estimated value of γ_{APB} is reasonable.

5.2 Modeling the CRSS of Underaged Alloys

The problem of predicting the strength of underaged alloys will be attacked using two different approaches. The first is applicable exclusively to the f.c.c. alloys strengthened by γ' precipitates, for which the binary Ni-Al system is regarded as the prototype. Here we argue that a reliable value of γ_{APB} exists and that the line tension Γ is the unknown quantity that must be obtained by fitting the data. Under these circumstances we will insist that the resulting line tension be consistent with the results in Figures 3 and 4, thereby also examining the suggestion $\Lambda = L_F$. The value of Γ that

emerges can then be used for other alloys because it is easily modified for minor differences in the elastic constants among the various γ' -containing alloys for which useful data are available. Using these values of Γ , data on these other alloys can then be fitted for the best value of γ_{APB} . The advantage of this procedure will become more evident in the section where it is applied to the data on strengthening of Ni–Al alloys by γ' precipitates. In anticipation of these results, we expect Γ for underaged alloys to obey an approximate relationship of the type

$$\Gamma = J'_e \ln \left[H \left(\frac{\langle r \rangle}{f} \right)^{1/2} \right] \quad (39)$$

where J'_e is close to the value of $\langle J_e \rangle$ and H is a constant.

In the absence of a reliable value of γ_{APB} , this method cannot generally be used to model the strength of underaged alloys, hence the only recourse is to calculate Γ and use γ_{APB} as a fitting parameter. This is the usual procedure, resulting in the expression for Γ given by

$$\Gamma = \langle J \rangle \ln \left[\frac{(8\Gamma/3\gamma_{APB})^{1/2}}{pb} \left(\frac{\langle r \rangle}{f} \right)^{1/2} \right] \quad (40)$$

which follows from equations (2), (3) and (27). In equation (40) $\langle J \rangle$ represents either $\langle J_e \rangle$ or $\langle J_s \rangle$, depending on whether the dislocations are initially pure edge or pure screw.

5.3 A General Method of Modeling the Strength for All Aging Conditions

Examination of equations (29), (34) and (35) suggests that $\Delta\tau_p/f^{1/2}$ is not quite, but almost, a universal function of the dimensionless parameter $(\gamma_{APB}\langle r \rangle/\Gamma)^{1/2}$ for all three aging conditions. Thus, plotting $\Delta\tau_p/f^{1/2}$ versus $(\gamma_{APB}\langle r \rangle/\Gamma)^{1/2}$ should provide a convenient method of representing all the data on a given alloy over a wide range of experimental conditions, provided that equation (39) or (40) is used to calculate Γ for underaged specimens and equation (26) is used (with

$\langle r_s \rangle = \pi\langle r \rangle/4$) for peak-aged and overaged specimens. This modeling procedure should be successful unless f varies dramatically among alloys in the same family.

The maximum value of $(\gamma_{APB}\langle r \rangle/\Gamma)^{1/2}$ for which underaged behavior should be observed can be estimated by equating equations (8) and (9), while the alloy should start to behave as if it is overaged when $\beta_c = 1$. These yield the following results:

underaged behavior	$0 < (\gamma_{APB}\langle r \rangle/\Gamma)^{1/2} < 0.91$
peak-aged behavior	$0.91 < (\gamma_{APB}\langle r \rangle/\Gamma)^{1/2} < 1.13$
overaged behavior	$(\gamma_{APB}\langle r \rangle/\Gamma)^{1/2} > 1.13$

The peak-aged condition obtains over a small, but finite, range of particle sizes, specifically $0.83\Gamma/\gamma_{APB} < \langle r \rangle < 1.27\Gamma/\gamma_{APB}$.

6. Examination of Experimental Data

6.1 Alloys Containing γ' Precipitates

In the following sections we consider most of the available data on the strengthening of alloys containing γ' -type precipitates. Data on binary Ni–Al alloys are considered first to establish the values of the constants J'_e and H in equation (39), after selecting a 'best' value of γ_{APB} . We then consider data on the strengthening of the Nimonic alloys PE16, 80A and 105, the iron-rich superalloy A-286 and a Co–Ni–Cr alloy. The chemical compositions of the four superalloys are given in Table 1.

6.1.1 Assessment of Data on γ_{APB} in Binary Ni–Al alloys

Direct measurements of the APB energy on $\{111\}$ in Ni_3Al have produced values ranging from a low of $111 \pm 15 \text{ mJ m}^{-2}$ (Douin *et al.*, 1986), evaluated using weak-beam transmission electron microscopy on deformed polycrystalline specimens, to a high of $300 \pm 25 \text{ mJ m}^{-2}$ (Taunt and Ralph, 1974), obtained from examination of field-ion micrographs of a deformed monocrystalline specimen. In between these are values of 169 ± 19 and $163 \pm 21 \text{ mJ m}^{-2}$ reported

Table 1. Nominal chemical compositions (wt%) of the superalloys discussed in this chapter (trace elements are excluded)

Alloy	Ni	Cr	Fe	Co	Mn	Mo	Ti	Al	Si	C
Nimonic PE16	43.2	16.5	34.2	0.2	—	3.3	1.3	1.1	0.2	0.06
Nimonic 105	53.2	15.1	0.7	19.7	—	5.1	1.3	4.8	—	0.12
Nimonic 80A	74.8	19.7	0.8	0.5	—	—	2.4	1.4	0.3	0.08
A-286	24.9	14.9	54.5	—	1.3	1.3	2.2	0.2	0.6	0.07

Chapter 8

Al-Rich Intermetallics in Aluminum Alloys

Santosh K. Das

AlliedSignal Inc., Morristown, NJ 07962, USA

1. Introduction

Aluminum-rich intermetallic compounds in aluminum alloys are the subject of extensive research because their crystal structure, chemical composition and morphology (e.g. size and shape) affect the mechanical properties, corrosion resistance, surface finish and electrical resistivity of aluminum alloy products. These intermetallic compounds can usually form, during solidification or during subsequent thermomechanical processing in commercially pure aluminum and aluminum-based alloys, either from unwanted impurities (e.g. Fe and Si) or by intentionally added elements, as reported earlier by Munson (1967), Miki *et al.* (1975), Kosuge and Mizukami (1975), Suzuki *et al.* (1978), and Dons (1984a,b). Owing to limited solid solubility of elements such as iron in aluminum the volume fractions of such intermetallic compounds are very limited; they are quite coarse (0.5 to 10 μm) in most metal produced by widely used methods, including the semicontinuous DC (direct chill) casting method for producing ingots for sheet and plate material as well as extrusions. However, these intermetallics have profound effects on such important properties as recovery, formability, recrystallized grain size and texture of cold-rolled sheets, as discussed by Skjerpe (1987), Mondolfo (1976), and Polmear (1981). Smaller, submicron dispersoids, 0.05 to 0.5 μm , which are intermetallic compounds containing the transition metals chromium, manganese or zirconium, have usually been intentionally added to serve primarily to retard recrystallization and grain growth. Examples are $\text{Al}_{20}\text{Cu}_2\text{Mn}_3$, $\text{Al}_{18}\text{Mg}_3\text{Cr}_2$ and Al_3Zr in copper-containing and manganese-containing alloys.

The discussion above clearly shows the importance of the formation and structure of aluminum-rich intermetallic compounds that are formed either by impurities or by intentionally added elements in ingot-cast aluminum alloys. The literature on this subject is quite extensive, as discussed in publications by Munson (1967), Miki *et al.* (1975), Kosuge and Mizukami (1975), Suzuki *et al.* (1978), Dons (1984), Skjerpe (1987), Grewen (1969), Kovac (1990), Rivlin and Raynor (1981), Hodgson and Parker (1981), Westengen (1982), and Stefaniay *et al.* (1987). The intermetallic compounds in ingot-cast aluminum alloys are reasonably understood. However, the limited solid solubility of transition metals (TMs) such as Fe, Mn, Cr, etc. and the nature of the Al-TM phase diagrams limit the volume fraction of intermetallic compound that can be achieved to provide appreciable dispersion strengthening. The progress on nonequilibrium processing of aluminum powder alloys using gas atomization (Griffith *et al.*, 1982; Adam, 1982; Palmer *et al.*, 1988), melt spinning/ribbon comminution (Das, 1988; Das and Davis, 1988; Das *et al.*, 1991), and mechanical alloying (Gilman *et al.*, 1986) has led to a new class of commercially significant aluminum alloys strengthened by dispersoids of aluminum-rich intermetallic compounds. These alloys derive their excellent mechanical and corrosion properties from a number of metastable intermetallic compounds that exhibit unique structures, thermal stability (up to 450 $^{\circ}\text{C}$) and desirable properties in an aluminum matrix. In the discussion to follow, the major focus will be on these classes of intermetallic compounds with some discussion on other conventionally processed materials of commercial significance.

Table 1. Diffusivity, and liquid and solid solubility of some transition metals in aluminum

Transition metal	Maximum equilibrium solid solubility at indicated temperature			D (cm ² s ⁻¹) at 618 K	Liquid solubility at 1400 K	
	(wt%)	(at%)			(wt%)	(at%)
Fe	0.04	0.025	at 928 K	5.4×10^{-14}	32	18.52
V	0.6	0.32	at 934 K	7.4×10^{-15}	1.6	0.85 ^a
Zr	0.28	0.085	at 934 K	3.4×10^{-18}	11.5	3.7
Cr	0.77	0.40	at 934 K	1.1×10^{-12}	15	8.4
Ce	0.05	0.01	at 910 K	8.4×10^{-16}	41.5	12
Mo	0.25	0.056	at 934 K	2.4×10^{-14}	3	0.86
Ti	1.3	0.57	at 938 K	3.0×10^{-16}	6.3	3.6

^aAt 1200 K.

2. Aluminum-Transition Metal Compounds

Transition metals typically have very low equilibrium solid solubilities in aluminum and very low diffusive fluxes. The former point means that iron, for example, is a likely contaminant in direct chill (DC) casting since, at very low concentrations, it precipitates in the melt to form very coarse intermetallic phases. However, low diffusive fluxes mean that, once retained in solid solution or in the form of dispersoid phases, the nucleation of new phases and/or the growth of existing dispersoids will be rather slow. The diffusivities of some transition metals in aluminum are compared in Table 1 (Adam, 1982).

In the following, because of their commercial significance we will first discuss the formation of Al-Fe intermetallic compounds with ternary or quaternary additions, their structure and thermal stability. This will be followed by a discussion of other aluminum-transition metal compounds.

2.1 Al-Fe Intermetallic Compounds

Intermetallic compounds containing aluminum, iron and other elements such as silicon are very common in commercial ingot aluminum alloys because iron and silicon, as mentioned earlier, are usually present as substantial impurity elements. The concentration of these elements may become quite considerable, often as high as 1 wt%. Since iron has a very low solid solubility in aluminum (Table 1), virtually all iron in aluminum alloys forms intermetallic phases of the Al-Fe or Al-Fe-Si type. A summary of reported intermetallic compounds is given in Table 2. Most of the phases have large unit cells with complex crystal structures. In addition to these complicated phases, incommensurable and quasiperiodic phases have also been reported by Skjerpe (1987) and Fung *et al.* (1986), respectively. The observation of so many compounds in a relatively

narrow compositional range has raised questions about structural interrelations among them, as discussed by Bendersky *et al.* (1988). The actual compound formed depends sensitively on the cooling rate. In the most commonly practiced direct chill casting (DC casting) the cooling rate is in the range 1–20 K s⁻¹, as estimated by Miki *et al.* (1975). Unfortunately, the Al-Fe-Si phase diagram is neither very useful for predicting the phases actually formed at such cooling rates (Miki *et al.*, 1975; Kosuge and Mizukami, 1975; Suzuki *et al.*, 1978; Westengen, 1982) nor even during subsequent homogenization of DC-cast ingots (Dons, 1984a,b). The main reason is that metastable Al-Fe-Si phases form easily instead of equilibrium phases. For example, in Al-Fe alloys Al₆Fe or Al_mFe may form instead of the equilibrium phase Al₃Fe. According to Kosuge and Mizukami (1975), Dons (1984a,b), and Polmear (1981), Al₆Fe forms at cooling rates of 1–10 K s⁻¹, whereas at cooling rates exceeding 10 K s⁻¹ Miki *et al.* (1975), Suzuki *et al.* (1978), and Young and Clyne (1981) suggest formation of Al_mFe.

An additional complication is the varying local cooling rate during DC casting, depending on the distance from the ingot surface and the shape of the casting. Accordingly, different Al-Fe-Si phases may form at different sites in the ingot; that is, gradients in the phase distribution may be introduced. In particular, Al_mFe may precipitate in a zone near the ingot surface and other phases (like Al₆Fe and Al₃Fe) in the interior zone of the ingot. Owing to the presence of different Al-Fe phases, the zones possess different etching properties (Munson, 1967; Miki *et al.*, 1975; Kosuge and Mizukami, 1975; Suzuki *et al.*, 1978; Westengen, 1982) and the interior zone is therefore called a 'fir-tree' structure. These fluctuations in surface properties introduce a quality problem for some material applications. Fast rates of solidification obtained in certain parts of the ingot are beneficial in refining the size of these brittle intermetallic compounds, which may

Table 2. Crystallographic data for Al-Fe and Al-Fe-Si phases in aluminum alloys

Name(s)	Bravais lattice	Lattice parameters (1 Å = 10 ⁻¹ nm)	Reference
Al ₃ Fe (mC102, D _{2h} ²³) Al ₁₃ Fe ₄	C-centered monoclinic (C2/m)	$a = 15.49 \text{ Å}$ $b = 8.08 \text{ Å}$ $c = 12.48 \text{ Å}$ $\beta = 107.75^\circ$	Black (1955a,b) Hudd and Taylor (1962)
Al _m Fe	Body-centered tetragonal	$a = 8.84 \text{ Å}$ $c = 21.60 \text{ Å}$	Kosuge and Mizukami (1972)
Al ₉ Fe ₂ (mP22, D8 _d)	Monoclinic	$a = 8.90 \text{ Å}$ $b = 6.35 \text{ Å}$ $c = 6.32 \text{ Å}$ $\beta = 93.4^\circ$	Simensen and Vellamy (1977) Douglas (1950)
Al ₆ Fe (oC28)	C-centered orthorhombic (Cmmm or Ccm2 ₁)	$a = 6.49 \text{ Å}$ $b = 7.44 \text{ Å}$ $c = 8.79 \text{ Å}$	Hollingsworth <i>et al.</i> (1962) Walford (1965) Nicol (1953) Black <i>et al.</i> (1961)
Al _x Fe	Unknown	Unknown	Westengen (1982) Young and Clyne (1981)
α -AlFeSi (cI138)	Body-centered cubic (Im3)	$a = 12.56 \text{ Å}$	Cooper (1967)
α -AlFeSi (cP138)	Primitive cubic (Pm3)	$a = 12.52 \text{ Å}$	Cooper and Robinson (1966)
α' -AlFeSi	Hexagonal (P6 ₃ /mmc)	$a = 12.30 \text{ Å}$ $c = 26.20 \text{ Å}$	Robinson and Black (1953) Rivlin and Raynor (1981)
α'' -AlFeSi q ₁ -AlFeSi	C-centered orthorhombic	$a = 12.70 \text{ Å}$ $b = 36.20 \text{ Å}$ $c = 12.70 \text{ Å}$	Westengen (1982) Liu <i>et al.</i> (1986)
a ₁ -AlFeSi	C-centered monoclinic	$a = 27.95 \text{ Å}$ $b = 30.62 \text{ Å}$ $c = 20.73 \text{ Å}$ $\beta = 97.74^\circ$	Holer (1985)
q ₂ -AlFeSi	Monoclinic	$a = 12.50 \text{ Å}$ $b = 12.30 \text{ Å}$ $c = 19.70 \text{ Å}$ $\beta = 111^\circ$	Liu <i>et al.</i> (1986)
β -AlFeSi	Monoclinic	$a = 6.12 \text{ Å}$ $b = 6.12 \text{ Å}$ $c = 41.50 \text{ Å}$ $\alpha = 91.0^\circ$	Phragmen (1950) Rivlin and Raynor (1981)
β' -AlFeSi	Monoclinic	$a = 8.90 \text{ Å}$ $b = 4.90 \text{ Å}$ $c = 41.60 \text{ Å}$ $\beta = 92.0^\circ$	Westengen (1982)
Al ₃ FeSi γ -AlFeSi	C-centered monoclinic	$a = 17.80 \text{ Å}$ $b = 10.25 \text{ Å}$ $c = 8.90 \text{ Å}$ $\beta = 132^\circ$	Munson (1967)
Al ₄ FeSi ₂ δ -AlFeSi	Tetragonal	$a = 6.14 \text{ Å}$ $c = 9.48 \text{ Å}$	Phragmen (1950) Rivlin and Raynor (1981)

otherwise crack during subsequent working of an ingot, and in some alloys alloying additions can change the morphology and structure of these intermetallic compounds. For example, to improve subsequent workability of DC-cast ingot, manganese in excess of 0.3%* is added to promote the formation of b.c.c. α -AlFeSi, which has a more desirable scriptic morphology.

In general, most of the commercial DC-cast ingots produce materials in which the major part of the intermetallic compound is present on the grain boundaries and between the dendrite arms. A review of the Al-Fe-Si system has been published by Rivlin and Raynor (1981). However, at present many crystallographic data about the numerous phases in the system are still missing, especially about the metastable phases. As shown in Table 2, only a few of the crystal structures are known; that is, atomic coordinates have been

*All compositions are in wt% unless otherwise stated.

determined only for Al_3Fe by Black (1955a,b), for Al_6Fe by Walford (1965) and for cubic $\alpha\text{-AlFeSi}$ by Cooper (1967) and Cooper and Robinson (1966). The reason for the scarcity of data is that the crystals are small, often metastable, and it is difficult to provide homogeneous material in sufficient quantities for successful X-ray diffraction analysis. At present, transmission electron microscopy (TEM) is the most useful technique for studying these particles because of the advances in X-ray microanalysis, convergent-beam electron diffraction and high-resolution electron microscopy.

All the aforementioned studies were limited to dilute Al-Fe-based alloys typical of DC-cast ingots. The advent of rapid solidification processing (Mehrabian *et al.*, 1977, 1980; Mehrabian and Parris, 1988; Das *et al.*, 1985; Das and Davis, 1988; Fine and Starke, 1986; Lee and Moll, 1988; Bye *et al.*, 1987) started a flurry of investigation into high solute containing Al-Fe alloys (up to 15%) in an effort to develop aluminum alloys containing high volume fractions of Al-Fe intermetallic compounds (dispersoids) (Das and Davis, 1988; Bye *et al.*, 1987; Griffith *et al.*, 1982; Adam and Bourdeau, 1980; Brown *et al.*, 1986; Skinner *et al.*, 1986) for elevated-temperature applications (Das *et al.*, 1989a,b). Beginning with the work of Jones (1969–1970) and Tonejc and Bonefacic (1969), it was demonstrated that rapid cooling of liquid to solid could result in the extension of the solid solubility of iron in aluminum by orders of magnitude (from 0.05 to about 10 wt%). It was further shown by Thursfield and Stowell (1974) that controlled nucleation and growth of metastable second phases (e.g. Al_6Fe) (Jacobs *et al.*, 1974) during extrusion of splat-cooled Al-Fe alloys lead to high stiffness and high strength because of the obstacles provided to dislocation motion by the dispersoids and to a retention of high strength to high temperatures because of the relative resistance of the Al-Fe dispersoids to Ostwald ripening. However, it was

discovered that metastable Al-Fe intermetallics such as Al_6Fe and Al_mFe have too limited a thermal stability to be of commercial significance. Attempts were made to increase the thermal stability of Al-Fe intermetallics by ternary and quaternary additions of Ce (Griffith *et al.*, 1982), Mo (Adam and Bourdeau, 1980), Mo and V (Adam *et al.*, 1982), V (Skinner and Okazaki, 1984) or V and Si (Brown *et al.*, 1986; Skinner *et al.*, 1986). Of these alloy systems only two, one based on Al-Fe-Ce and the other based on Al-Fe-V-Si, have reached commercial significance for elevated-temperature applications (Table 3). It should be mentioned that the high-temperature property benefits of these ternary and quaternary alloys were not discovered serendipitously, but the two alloys cited above were carefully selected from a number of potential Al-Fe-X intermetallics, some of the basis for selection being intermetallics of higher crystal symmetry, better lattice matching with the Al matrix, and high liquid solubility of ternary or quaternary elements at reasonable casting temperatures. It should be further noted that while alloy development of Al-Fe-X intermetallics has been successful, other potential systems such as Al-Zr-X (discussed in Section 2.4) have not been fully explored for elevated-temperature applications. In the following, we will discuss the dominant intermetallic compounds in the Al-Fe-Ce and Al-Fe-X-Si systems.

2.1.1 Al-Fe-Ce Intermetallics

The intermetallic phases in the Al-Fe-Ce system have been studied in some detail by Ayer *et al.* (1988), Zarechnyuk *et al.* (1968), Vivchar *et al.* (1970), and Zarechnyuk *et al.* (1969). The equilibrium phase in the aluminum-rich portion of the Al-Fe-Ce system has been suggested by Zarechnyuk *et al.* (1968), Vivchar *et al.* (1970) and Zarechnyuk *et al.* (1969) to be $\text{Al}_{10}\text{Fe}_2\text{Ce}$ with a body-centered tetragonal crystal structure. It was proposed that $\text{Al}_{10}\text{Fe}_2\text{Ce}$ was isostructural

Table 3. Al-Fe-based aluminum alloys for elevated-temperature applications; alloys are produced by rapid solidification/powder metallurgy

Designation	Developer	Composition (wt%)	Powder-processing method	Comments
X8019 (CU78)	Alcoa	Al-8.3Fe-4.0Ce	Atomization	Near commercial
CZ42	Alcoa	Al-7.0Fe-6.0Ce	Atomization	May be discontinued
8022 (FVS0611)	Allied Signal	Al-6.5Fe-0.6V-1.3Si	PFC/RC ^a	Commercial
8009 (FVS0812)	Allied Signal	Al-8.5Fe-1.3V-1.7Si	PFC/RC	Commercial
FVS1212	Allied Signal	Al-11.7Fe-1.3V-2.4Si	PFC/RC	Near commercial
PA 107	Sumitomo	Al-8Fe-2V-1Zr-2Cu-1Mg-3Si	Atomization	In development

^aPFC/RC: planar flow casting/ribbon comminution.

Table 4. Crystal structures of intermetallic phases in the Al-Fe-Ce system (Ayer *et al.*, 1988)

Phase	Crystal structure	Space group	Number of atoms in the unit cell	Calculated density (g cm ⁻³)
Al ₆ Fe ^a (oC28)	Orthorhombic <i>a</i> = 0.645 nm <i>b</i> = 0.744 nm <i>c</i> = 0.878 nm	Cmcm	28	—
Al ₁₃ Fe ₄	Monoclinic <i>a</i> = 1.549 nm <i>b</i> = 0.808 nm <i>c</i> = 1.248 nm <i>β</i> = 107° 43'	C2/m	—	—
Al ₄ Ce (ol30)	Orthorhombic <i>a</i> = 0.439 nm <i>b</i> = 1.30 nm <i>c</i> = 1.01 nm	Immm	30	—
Al ₂₀ Fe ₅ Ce ^a (Al ₄₀ Fe ₂₀ Ce ₄)	Quasicrystal	—	—	—
Al ₁₀ Fe ₂ Ce ^a (oC52)	Orthorhombic <i>a</i> = 1.02 nm <i>b</i> = 1.62 nm <i>c</i> = 0.42 nm	Cmm2/C222	52	4.99
Al ₁₃ Fe ₃ Ce (oC68) Al ₅₂ Fe ₁₂ Ce ₄	Orthorhombic <i>a</i> = 0.89 nm <i>b</i> = 1.02 nm <i>c</i> = 0.91 nm	Cmcm/Cmc2	68	5.32

^aMetastable.

with the tetragonal Al₈Mn₄Ce (tI26, D2_b) phase. Recently, Ayer *et al.* (1988) studied, using analytical electron microscopy, a rapidly solidified (RS) Al-8.8Fe-3.7Ce alloy and arc-melted buttons of aluminum-rich Al-Fe-Ce alloys and determined the characteristics of both the metastable and the equilibrium phases and

showed that Al₁₀Fe₂Ce is actually not the equilibrium phase. The rapidly solidified alloy contained binary and ternary metastable phases in the as-extruded condition (Table 4). The binary metastable phase was identified to be Al₆Fe, while the ternary metastable phases were identified to be Al₁₀Fe₂Ce and Al₂₀Fe₅Ce. The Al₂₀Fe₅Ce was a decagonal quasicrystal (see Kelton, Chapter 20 in Volume 1), while the Al₁₀Fe₂Ce phase was determined to have an orthorhombic crystal structure belonging to space group Cmmm, Cmm2 or C222. Microscopy studies of RS alloys and cast buttons annealed at 700 K established the equilibrium phases to be Al₁₃Fe₄, Al₄Ce, and an Al₁₃Fe₃Ce ternary phase (Figure 1). Figure 1 also shows the composition of the Zarechnyuk *et al.*'s (1969) equilibrium phase Al₁₀Fe₂Ce, which is most likely the same as the equilibrium Al₁₃Fe₃Ce phase in the study by Ayer *et al.* (1988). The location of the metastable phase Al₂₀Fe₅Ce with respect to the equilibrium phases is also indicated in Figure 1. The crystal structure of the equilibrium ternary phase was determined to be orthorhombic with a Cmcm or a Cmc2 space group. The metastable compounds decomposed to equilibrium phases upon annealing at elevated temperatures (700 K). After exposure at 700 K for 24 hours, the binary (Al₆Fe) and ternary (Al₁₀Fe₂Ce, Al₂₀Fe₅Ce) metastable phases had essentially transformed to their corresponding equilibrium phases (Ayer *et al.*, 1988). These transformations limit phase

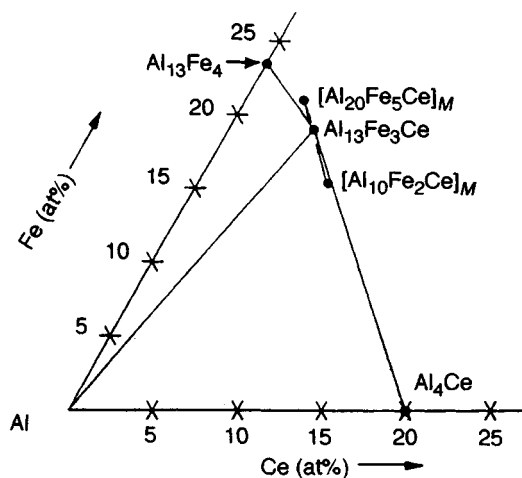


Figure 1. Isothermal section of the aluminum-rich portion of the Al-Fe-Ce diagram at 700 K, showing the locations of the equilibrium phases; metastable phases present in the system are also indicated (Ayer *et al.*, 1988)

changes in the extended-service application of Al-Fe-Ce alloys to 590 K (602 °F).

2.1.2 Al-Fe-X-Si ($X = V, Mn, Cr, Mo, Nb, Ta, W$) Intermetallics

In contrast to the metastable intermetallic compounds Al_6Fe , $Al_{10}Fe_2Ce$ and $Al_{20}Fe_5Ce$ discussed in the previous section, the metastable intermetallic compounds in Al-Fe-X-Si (particularly for $X = V, Mo, Nb, Ta, W$) exhibit exceptional thermal stability to temperatures in excess of 700 K (Das and Davis, 1988; Zedalis *et al.*, 1987; Skinner *et al.*, 1987). In addition, in the Al-Fe-V-Si system two metastable intermetallic compounds have been identified (Table 5): one is $Al_{13}(Fe,V)_3Si$, with a b.c.c. (Im3) structure (α -AlFeSi type), and the other is $Al_{12}(Fe,V)_3Si_2$, with a primitive cubic (Pm3) structure (α -AlMnSi type) (Rodriguez and Skinner, 1990). Both intermetallic compounds occur as metastable phases during rapid solidification at high cooling rates and remain with the aluminum matrix to temperatures in excess of 773 K (Zedalis *et al.*, 1987). In particular, owing to the exceptional stability of the intermetallic compound $Al_{13}(Fe,V)_3Si$, the Al-Fe-V-Si family of alloys shown in Table 3 has gained considerable attention in recent years, and the compound has been studied in some detail (Skinner, 1988; Rodriguez and Skinner, 1990).

The quaternary additions of V to Al-Fe-Si alloys stabilize the cubic $Al_{13}(Fe,V)_3Si$ phase over the hexagonal Al_8Fe_2Si and monoclinic Al_3Fe phases (Table 2) that would normally form in the absence of the V addition. This cubic phase can also be stabilized with Mn, Cr, and Mo (Munson, 1967; Skinner *et al.*, 1987), but in general it appears that stabilization can be achieved with most other b.c.c. elements such as Nb, Ta and W.

Alloys in the Al-Fe-V-Si system are usually made through the method of melt spinning (both jet casting

and planar flow casting) with an effective cooling rate of approximately 10^6 K s^{-1} (Das *et al.*, 1991). At slow cooling rates ($1\text{--}500 \text{ K s}^{-1}$) the first intermetallic to form is the equilibrium Al_3Fe . Thus it can qualitatively be said that the cooling rate necessary to produce an alloy with the silicide phase as its primary intermetallic has to be that which will successfully suppress the formation of the Al_3Fe phase (and the metastable Al_6Fe phase). The microstructures of the as-cast (rapid solidification) ribbons thus produced by the melt-spinning processes can be characterized as either microcellular or discrete silicide dispersoids. These structures are shown in Figures 2(a) and 2(b), respectively. Here the matrix is shown (by scanning transmission electron microscopy/energy dispersive X-ray (STEM/EDX) analysis) to be supersaturated with Fe, V and Si and the intercellular regions are of the quaternary silicide phase. The discrete silicide structure indicates that sufficient recalescence occurred during the cooling of the ribbon to decompose the intercellular regions into discrete silicide particles. In certain alloys and under unusual casting conditions the icosahedral symmetry 'quasicrystal' (also referred to as 'O' phase) can also be found (Figure 2c). The occurrence of this 'O' phase is indicative of the recent speculations that the icosahedral and silicide phases have similar structures whereby this icosahedral phase can be described as a disordered silicide phase (Elser and Henley, 1985; Guyot and Audier, 1985). The major advantage of this alloy system over others is that when the ribbon has been cast at its optimum cooling rate (and thus contains no 'O' phase), the as-cast microstructure contains no metastable precipitates that will decompose during the consolidation process. This is an advantage during consolidation because the dispersoid size can be controlled through a coarsening process rather than a transformation sequence. During this consolidation (via vacuum hot pressing and subsequent deformation processes) the as-cast microstructure coarsens (intercellular regions), and additional silicide dispersoids precipitate from the supersaturated matrix. Thus, the as-consolidated microstructure consists of nearly spherical dispersoids of composition approximately $Al_{13}(Fe,V)_3Si$ that decorate both grain and subgrain boundaries, and also lie within grain interiors (Figure 3). The size of the dispersoid obviously varies with the pressing/consolidation time and temperature but typically occurs in the 40–80 nm diameter range.

Table 5. Intermediate phases observed in Al-Fe-V-Si alloys (Rodriguez and Skinner, 1990)

Phase ^a	Control structure	Space group	Number of atoms in the unit cell
$Al_{13}(Fe,V)_3Si$ (cI138)	Body-centered cubic $a = 1.261\text{--}1.262 \text{ nm}$	Im3	138
$Al_{12}(Fe,V)_3Si_2$ (cP138)	Primitive cubic $a = 1.259\text{--}1.260 \text{ nm}$	Pm3	138

^aThe lattice parameter and actual composition of the intermetallic phase vary with alloy chemistry.

2.1.3 Structure of $Al_{13}(Fe,V)_3Si$

The intermetallic compound $Al_{13}(Fe,V)_3Si$ has a structure that is body-centered cubic (Im3) with 138

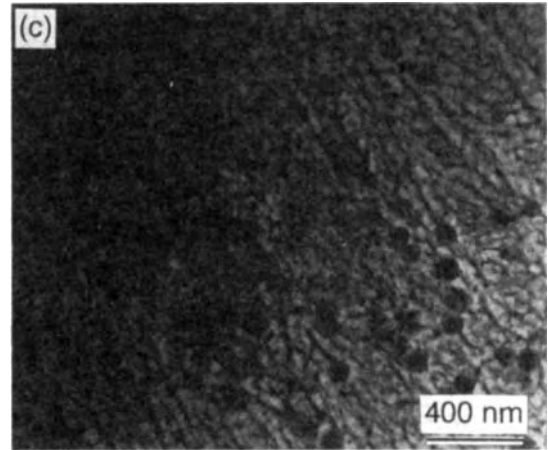
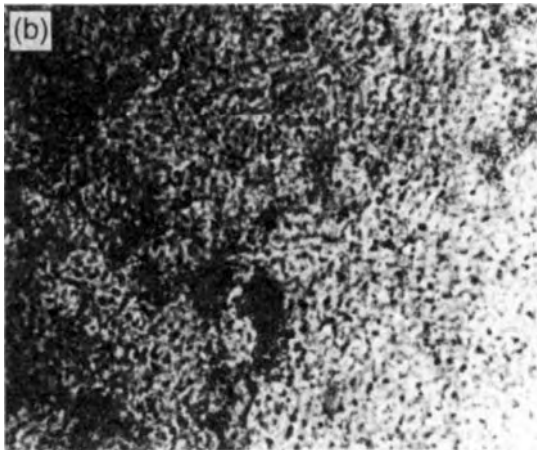
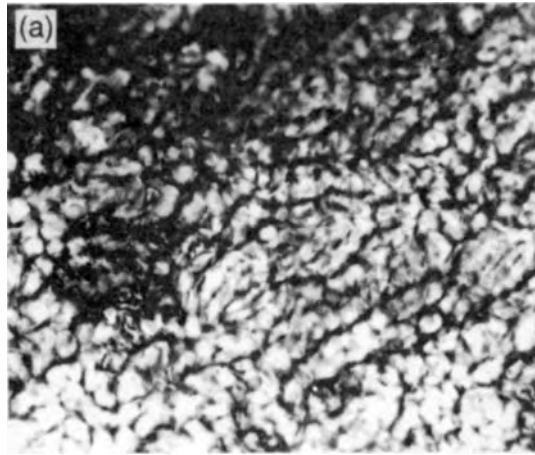


Figure 2. Micrographs of as-cast Al-Fe-V-Si alloys depicting (a) microcellular structures, (b) decomposed microcellular structures with discrete silicide dispersoids, and (c) microcellular structures plus 'O' phase (quasicrystalline) microstructures in Al-8.5Fe-1.3V-1.7Si (AA 8009) alloy

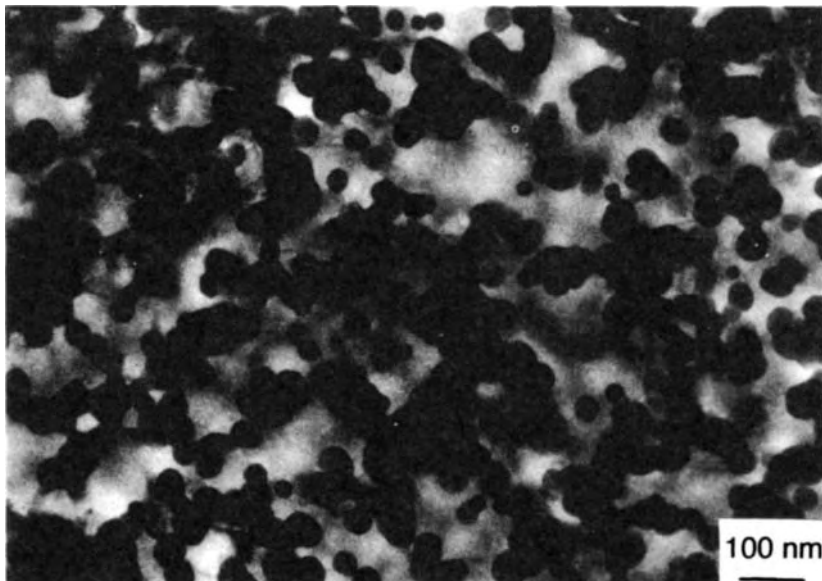


Figure 3. As-consolidated microstructure of Al-Fe-V-Si alloy 8009 showing the morphology of $\text{Al}_{13}(\text{Fe},\text{V})_3\text{Si}_2$ intermetallics

atoms per unit cell (cI138) (Cooper, 1967). The atomic structure of this intermetallic can be described as consisting of empty (Fe + V) icosahedra (i.e. with unoccupied centers) that are situated at the sites of a b.c.c. lattice; they are parallel, and each icosahedron is connected to its eight neighbors along the threefold axes parallel to the $\langle 111 \rangle$ direction. The connecting atoms form a slightly distorted octahedron. Each of these (Fe + V) icosahedra contains an empty (Al + Si) icosahedron of the same orientation, and these structures are connected through chains of three slightly distorted (Al + Si) octahedra that share their triangular faces (Figure 4). However, only five of the eight possible neighboring icosahedra are connected with these octahedra chains. The remaining (Al + Si) atoms primarily occupy positions on the cube faces while still maintaining the b.c.c. symmetry. The silicide phase has been regarded as isostructural with the $\text{Al}_{13}\text{Mn}_3\text{Si}_2$ intermetallic to be discussed later; although this has a primitive lattice (Pm3), the atomic structure is almost identical except that certain aluminum atoms have no b.c.c. counterpart (Cooper and Robinson, 1966).

The $\text{Al}_{13}(\text{Fe},\text{V})_3\text{Si}_2$ intermetallic is not a line compound: whilst the number of (Fe + V) atoms remains the same, there are definite limits as to the Fe:V ratio within this phase. Similarly the Al:Si ratio within the silicide phase can also be altered to some extent. Thus compositional variations do occur, but can be controlled because the nominal Fe:V and Al:Si ratios formulated

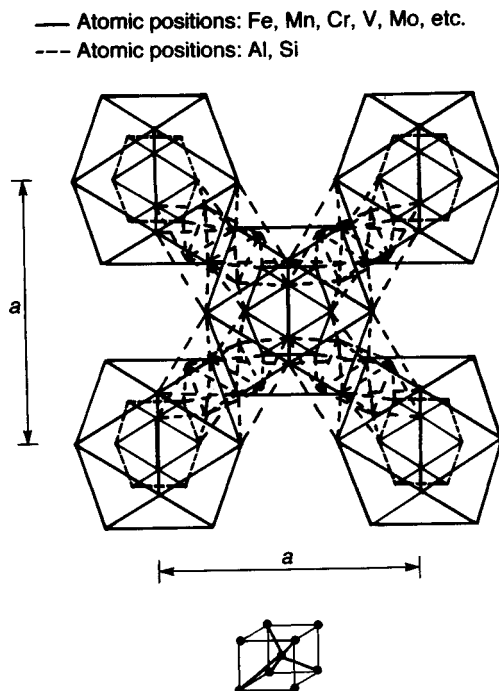


Figure 4. Partial schematic representation of the Im3 cubic silicide phase, showing the relationship between the (Fe + V) and (Al + Si) icosahedra

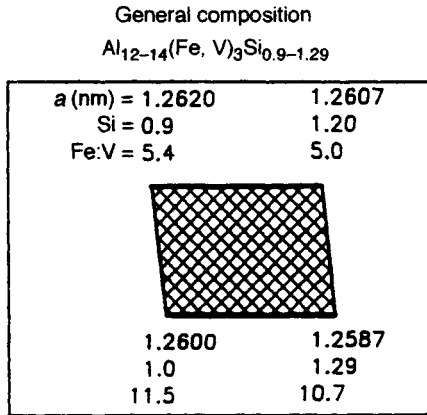


Figure 5. Schematic of the compositional variation within the aluminum plus silicide two-phase region in regard to the Fe:V and Al:Si ratios and their effect on the silicide lattice parameter

in the alloy compositions are carried through to the silicide phase in the consolidated material. A more specific composition for the silicide phase may be represented by $\text{Al}_{12.96-13.35}(\text{Fe}, \text{V})_3\text{Si}_{0.9-1.29}$, where the Fe:V ratio can also be altered to values between 5:1 and 11.5:1. Similar compositional variations are apparent in systems that replace V with other b.c.c. elements (Skinner *et al.*, 1987). These changes in composition will have effects on the physical properties of the silicide phase, which could result in changes in the bulk properties of the material. However, these effects so far have not proven to be significant relative to the other effects that alter mechanical properties in this alloy

system (i.e. volume fraction, grain size, particle size distribution, etc.). The lattice parameter of the silicide phase is significantly altered by changes in the Fe:V and Al:Si ratios, as can be seen from Figure 5.

The compositional variation discussed above is for those alloys that are formulated to exist in the two-phase region, aluminum plus silicide dispersoid. Figure 6 is a representation of the quaternary Al-Fe-V-Si alloy system for high Al at 748 K, and it reveals the phases in equilibrium with the silicide phase at this temperature. The diagram is a representation of the three-dimensional corner of the alloy system with the aluminum apex hidden; it is sliced at a constant aluminum content (95 at%) and is not a projection from three to two dimensions, as is more common. The diagram reveals two important observations. Firstly, there are two quaternary silicide phases: one is a b.c.c. $\alpha\text{-AlFeSi}$ type, the other a primitive $\alpha\text{-AlMnSi}$ type, and they can be distinguished from each other by composition and lattice parameter. Secondly, within the ternary Al-Fe-V alloy system significant amounts of Fe are dissolved in the Al_7V phase, as is V in Al_3Fe , such that the phase relationships are those described in Figure 7; Al_{10}V is in equilibrium only with aluminum and $\text{Al}_7(\text{V}, \text{Fe})$. The investigation into the quaternary system (Figure 6) also reveals that the Al_{10}V phase dissolves quite a considerable amount of Si and is also in equilibrium with the second silicide phase. This second silicide phase has a primitive cubic lattice and is thus equivalent to the α phase in the Al-Mn-Si system. The compositional range for this second silicide phase has been described as $\text{Al}_{12.0-12.8}(\text{Fe}, \text{V})_3\text{Si}_{1.8-2.17}$ (Rodriguez and Skinner, 1990).

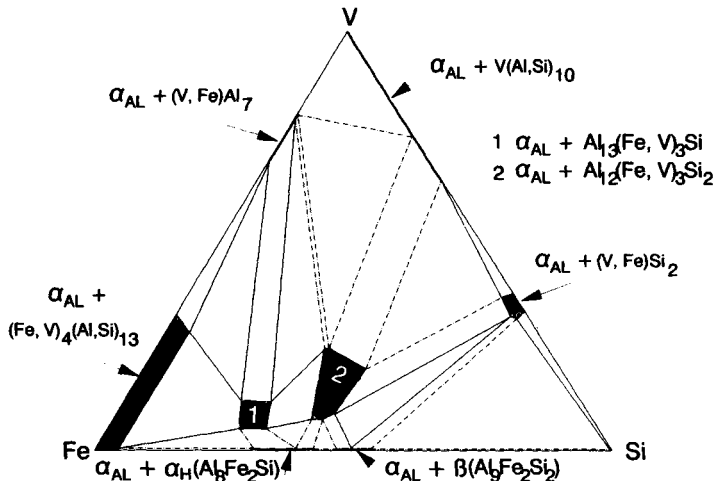


Figure 6. Equilibrium phase relationships within the Al-Fe-V-Si alloy system at 748 K

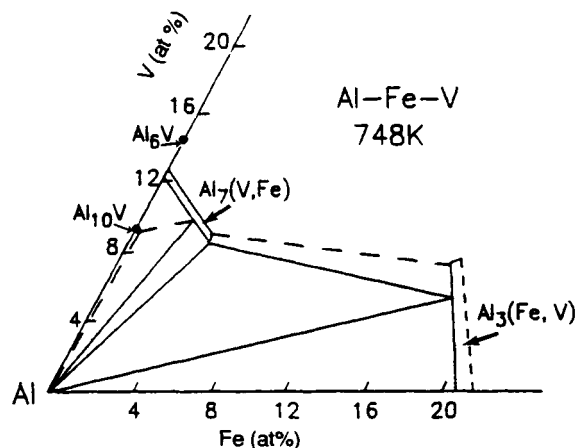


Figure 7. Equilibrium phase relationships within the Al-Fe-V alloy system at 748 K

This range is consistent with that found for the Al-Mn-Si intermetallic (Strid and Simensen, 1986; Hodgson and Parker, 1981). Although it may be conjectured that these two phases are the same and that the three-phase region (aluminum matrix plus both silicides) is an anomaly, the compositional variations found in alloys within this three-phase region were consistent with the premise that there are two different silicide phases. This interpretation has been confirmed in a series of alloys with constant aluminum content and Fe:V ratio but with increasing Si contents (so as to scan across both silicide-

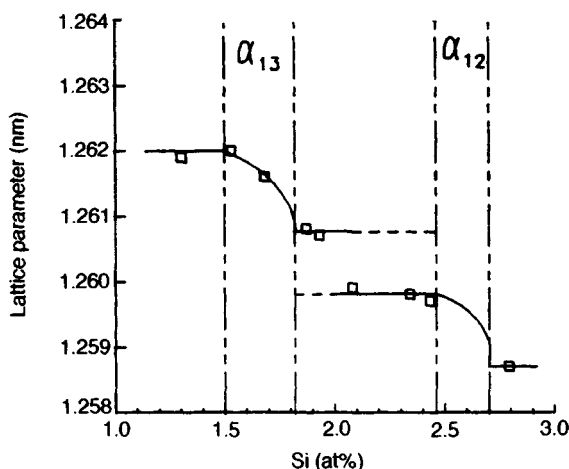


Figure 8. Lattice parameter versus Si content (at constant aluminum and Fe:V ratio) depicting the presence of two silicide phases α_{13} and α_{12} ($\text{Al}_{13}(\text{Fe},\text{V})_3\text{Si}$ and $\text{Al}_{12}(\text{Fe},\text{V})_3\text{Si}_2$) within the phase diagram

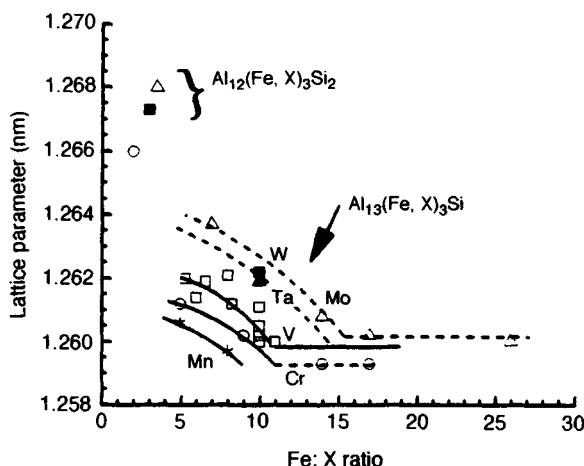


Figure 9. Comparison of the lattice parameters of the $\text{Al}_{13}(\text{Fe},\text{X})_3\text{Si}$ alloys stabilized with Mn, Cr, V, Mo, Ta or W

phase regions). The alloys analyzed for lattice parameter show (Figure 8) the occurrence of two silicide phases with a three-phase region between them. The silicide phases are the only quaternary intermetallics in the Al-Fe-V-Si system at the aluminum-rich end. The lattice parameter of the intermetallic silicide compound $\text{Al}_{13}(\text{Fe},\text{X})_3\text{Si}$ further depends on the Fe:X ratio (Figure 9) (Skinner *et al.*, 1987; Skinner, 1992). This plot also shows that the lattice parameter depends on the element (e.g. Mn, Cr, V, Mo, Ta, W) used for stabilizing the $\text{Al}_{13}(\text{Fe},\text{X})_3\text{Si}$ compound.

2.1.4 Physical Properties of $\text{Al}_{13}(\text{Fe},\text{V})_3\text{Si}$

The physical properties of the intermetallic phase $\text{Al}_{13}(\text{Fe},\text{V})_3\text{Si}$ can be fairly accurately extrapolated from the consolidated material containing different volume fractions. Two of the most important properties in the development of structural applications are modulus and thermal expansion coefficient. Of equal importance in consideration of the coarsening rates within the alloy system is the nature of the interface between the silicide phase and the aluminum matrix; these properties will be discussed below.

Elastic moduli, as measured by dynamic means, of various alloys can be plotted against volume fraction. By extrapolation the modulus of the silicide phase has been estimated to be 150 GPa (Skinner, 1988). This value appears, from the limited data available in the literature (Zogg *et al.*, 1979), to be high for an aluminum-based intermetallic, although not as high as that of the Al_3Zr phase (Zedalis, 1985).

Table 6. Aluminum-rich intermetallic compounds present in various aluminum–transition metal alloys together with their coarsening rates

Alloy system	Process	Intermediate compounds	Intermetallic coarsening rates at 425 °C ($\text{m}^3 \text{h}^{-1}$)	Reference
Al–Fe–Ce	Inert gas atomization	Al_3Fe (mC102, D_{23}^{23}), Al_6Fe (oC28), $\text{Al}_8\text{Fe}_4\text{Ce}$, $\text{Al}_{10}\text{Fe}_2\text{Ce}$	4.2×10^{-23}	Das and Davis (1988)
Al–Fe–Mo–V	Centrifugal helium atomization	Al_3Fe (mC102, D_{23}^{23}), Al_6Fe (oC28), $\text{Al}_{12}\text{Fe}(\text{Mo}, \text{V})$	1.7×10^{-23}	Das and Davis (1988)
Al–Cr–Zr	Helium atomization	Al_3Zr (L_{12} , cP4), $\text{Al}_{13}\text{Cr}_2$	—	
Al–Fe–V–Si	Melt-spun ribbon	$\text{Al}_{13}(\text{Fe}, \text{V})_3\text{Si}$ (cI138) Fe:V = 5:1 Fe:V = 10:1	2.9×10^{-26} 8.4×10^{-27}	Zedalis <i>et al.</i> (1987)
Al–Zr	Chill-cast ingot	Al_3Zr (D_{023} , tI16) Al_3Zr (L_{12} , cP4)	4.1×10^{-25} 2.5×10^{-26}	Zedalis (1985) Angers <i>et al.</i> (1988b) Zedalis (1985)
Al–Zr–V	Chill-cast ingot	$\text{Al}_3(\text{V}_{0.875}, \text{Zr}_{0.125})$ (L_{12} , cP4) $\text{Al}_3(\text{V}_{0.875}, \text{Zr}_{0.125})$ (D_{023} , tI16)	1.6×10^{-26} 1.30×10^{-25}	Angers <i>et al.</i> (1988b) Zedalis (1985) Angers <i>et al.</i> (1988b) Zedalis (1985) Angers <i>et al.</i> (1988b)

Thermal expansion coefficients for a number of Al–Fe–V–Si alloys have been measured between room temperature and 623 K (Skinner, 1988). Based on these data the extrapolated value for the $\text{Al}_{13}(\text{Fe}, \text{V})_3\text{Si}$ phase is reported to be $11.6 \times 10^{-6} \text{K}^{-1}$. Although this value is not as low as for conventional high-silicon alloys (e.g. 4000 series), the Al–Fe–V–Si alloys are competitive at temperatures in the 300–650 K range and could be used in low thermal expansion applications (i.e. automotive pistons, connecting rods, etc.).

2.1.5 Thermal Stability of $\text{Al}_{13}(\text{Fe}, \text{V})_3\text{Si}$

The $\text{Al}_{13}(\text{Fe}, \text{X})_3\text{Si}$ intermetallic phases have excellent thermal stability compared to many other aluminum-rich intermetallic compounds. Coarsening rates, as measured by increase in average size of the particle, from a number of Al–Fe–X–Si alloys are shown in Table 6 together with those of other alloy systems. The silicide dispersoids are shown to grow approximately four orders of magnitude more slowly than those in other alloy systems, with only the L_{12} phase $\text{Al}_3(\text{V}, \text{Zr})$ coming close to these values (Zedalis, 1985; Angers *et al.*, 1988a,b). The reason for such low coarsening rates of $\text{Al}_{13}(\text{Fe}, \text{X})_3\text{Si}$ intermetallics in an aluminum matrix is not well understood. The nature of the interface between the silicide and the aluminum matrix is of importance when coarsening rates of the silicide phase are considered. To a first approximation, from the lattice parameters of the silicide phase and the aluminum matrix (3.5% mismatch), the coarsening rates should be comparable with those in other Al–Fe alloy systems.

This anomaly has recently been addressed (Skinner, 1988). It has been suggested that a combination of an orientation relationship, ledge formation and a high coincidence-site interface (with localized five-fold symmetry) results in a low interfacial energy and thus in a low driving force for coarsening. The high thermal stability gives rise to the excellent high-temperature properties in aluminum alloys based on $\text{Al}_{13}(\text{Fe}, \text{X})_3\text{Si}$ intermetallic dispersoids.

2.2 Al–Mn Intermetallic Compounds

Recently, the Al–Mn system has received considerable interest since the identification of phases that possess noncrystallographic icosahedral (Shechtman *et al.*, 1984) and decagonal symmetry (Bendersky, 1985). These metastable phases exhibit sharp diffraction patterns. However, their respective fivefold and tenfold rotational symmetries are inconsistent with crystals that have lattice translation vectors, and as such these phases are termed quasicrystalline. The formation of the metastable icosahedral and decagonal phases in rapidly solidified Al–Mn alloys prepared by melt spinning and atomization is well documented (Shechtman and Blech, 1985; Bendersky *et al.*, 1985; Bendersky and Ridder, 1986; Schaefer *et al.*, 1986). However, the quasicrystalline phases still remain a scientific curiosity (see Chapter 20 by Kelton in Volume 1).

Many of the wrought commercial aluminum alloys classified as common (i.e. not heat treatable) contain manganese and magnesium together with the normal impurities of iron and silicon. The range of properties of the common alloys is obtained to a great extent

Table 7. Intermetallic compounds in Al-Mn-Si-Fe alloys

Phase	Crystal structure	Space group	Number of atoms in the unit cell	Alloy	Processing	Reference
α -AlMnSi (cP138) ($\text{Al}_9\text{Mn}_2\text{Si}_{1.8}$)	Primitive cubic $a = 1.268 \text{ nm}$	Pm3	138	Ingot Al	Ingot	Cooper and Robinson (1966)
$\text{Al}_{15}\text{Mn}_3\text{Si}_2$ (α -AlMnSi type)	Primitive cubic $a = 1.265\text{--}1.268 \text{ nm}$	Pm3	138	Al-12.6Mn-4.8Si	Powder atomization	Tibballs <i>et al.</i> (1989) Cooper and Robinson (1966)
$\text{Al}_{14}(\text{Mn},\text{Fe})_3\text{Si}$ (c138)	Body-centered cubic $a = 1.25 \text{ nm}$	Im3	138	Ingot Al	DC-cast ingot	Dons (1985)

by cold work followed by partial recovery and recrystallization. The Al-Mn-Fe-Si intermetallics play a large role in the properties of these alloys. For example, the ductility of the AA 3000 series of aluminum alloys, including the highly formable can-stock alloy (Tibballs *et al.*, 1989), is largely owing to the presence of a fine distribution of the cubic phase α -AlMnSi, or more generally α -AlMnFeSi. The precipitation of this phase rather than other, less advantageous phases is controlled by the level of silicon in solid solution after casting. This in turn depends on the melt composition and the silicon contents of intermetallic phases precipitated during casting. In the following, we will briefly discuss some of the common intermetallic phases that play a role in the commercially significant aluminum alloys.

The most common intermetallic phase observed in aluminum can stock is AlMnSi (Table 7). Despite an annual production of approximately 100 000 tons of this phase in can stock and the scientific interest in quasicrystalline phases, data on equilibria involving this α -AlMnSi phase are limited (Tibballs *et al.*, 1989).

The crystal structure of the α -AlMnSi phase has been described by Cooper and Robinson (1966) in terms of clusters of 54 atoms around vacant sites at the origin and body center positions. An icosahedron of aluminum atoms at a radius of 0.243 nm constitutes the inner shell of each cluster. The outer shell consists of an icosahedron of manganese atoms at 0.475 nm, along the same radii as the inner-shell atoms and on two crystallographic sublattices that form the 30 vertices of an almost regular icosidodecahedron. The dimensions of the clusters at the origin and the center differ by about 1%. Neighboring clusters are linked by octahedral packing between aluminum atoms in their outer shells and, in the interstices, by 12 tetrahedra of aluminum atoms containing a central atom. In the low-symmetry structure, the tetrahedra are ordered; in the body-centered structure they are disordered. This is quite similar to the structure of $\text{Al}_{13}(\text{Fe},\text{V})_3\text{Si}$ discussed earlier.

In a recent development, the α -AlMnSi phase has been suggested by Guyot and Audier (1985) to be the stable crystalline arrangement which forms the basic structural unit of the apparently quasicrystalline phases Al_mM , where M is a transition element (e.g. manganese, iron or chromium). The value of m has been determined as approximately 4 (Guyot, 1985). Furthermore, the icosahedral basis vector for the icosahedrally symmetric unit (which corresponds in radial dimension to the manganese atoms) has been estimated as 0.460 nm (Elser, 1985).

In commercial aluminum alloys containing iron impurities, iron and manganese are interchangeable within wide limits (Dons, 1984a,b, 1985), and the intermetallic phase may contain chromium instead of manganese (Westengen *et al.*, 1980).

Al-Mn-Si alloys have been studied by Paris *et al.* (1980), Hawk *et al.* (1989a,b), and Ahrens *et al.* (1985) by rapid solidification/powder metallurgy in order to improve elevated-temperature properties by intermetallic dispersoids. The intermetallic observed (Hawk *et al.*, 1988, 1989a,b) is primarily $\text{Al}_{15}\text{Mn}_3\text{Si}_2$ (Table 7). However, Ahrens *et al.* (1985) observed only Al_6Mn and Al_{12}Mn intermetallics; this they attributed to incomplete dissolution of silicon in the melt. The $\text{Al}_{15}\text{Mn}_3\text{Si}_2$ particles are spherical and about 0.1–0.5 μm in diameter in as-consolidated material (Hawk *et al.*, 1989a,b). The size is somewhat coarser than the $\text{Al}_{13}(\text{Fe},\text{V})_3\text{Si}$ intermetallic observed in Al-Fe-V-Si alloys discussed earlier. The elevated temperature properties of the $\text{Al}_{15}\text{Mn}_3\text{Si}_2$ -containing alloys are somewhat poorer than those of the Al-Fe-Ce or Al-Fe-V-Si alloys (Hawk *et al.*, 1989a,b; Ahrens *et al.*, 1985).

2.3 Al-Cr-X Intermetallics

The binary Al-Cr system has been studied by Swamy *et al.* (1989) by rapid quenching. The equilibrium η - $\text{Al}_{11}\text{Cr}_2$ phase is suppressed, and an icosahedral quasicrystalline phase is observed together with some Al_7Cr

Table 8. Intermetallics in rapidly solidified Al–Cr–X systems

Phase	Crystal Structure	Space groups	Alloy	Reference
$\Theta\text{-Al}_7\text{Cr}^a$	Monoclinic $a = 2.043 \text{ nm}$ $b = 0.762 \text{ nm}$ $c = 2.531 \text{ nm}$ $\beta = 155^\circ 10'$	C2/m	Al–20Cr	Cooper (1960)
$\text{Al}_{20}\text{Cr}_2\text{Y}$	Cubic $a = 1.437 \text{ nm}$	Fd3m		
Al_7Cr^a	Orthorhombic $a = 2.48 \text{ nm}$ $b = 2.47 \text{ nm}$ $c = 3.02 \text{ nm}$		Al–6Cr–5Y	Wilsdorf <i>et al.</i> (1989)
$\text{Al}_{13}\text{Cr}_2$	Monoclinic $a = 2.5196 \text{ nm}$ $b = 0.7574 \text{ nm}$ $c = 1.0949 \text{ nm}$ $\beta = 128.7^\circ$	C2/m	Al–5Cr–2Zr ^b	Palmer <i>et al.</i> (1988)

^aAl₇Cr is observed in both cubic and monoclinic structures.

^bBoth orthorhombic Al₇Cr and cubic Al₃Zr (L1₂) have been reported in rapidly solidified alloys.

and Al₇Cr₃ depending on chromium content. Upon annealing, the icosahedral phase decomposes to $\Theta\text{-Al}_7\text{Cr}$, whose structure has been determined by Cooper (1960). However, these binary intermetallics have primarily been of scientific curiosity, and ternary additions have been used to improve properties. For elevated-temperature applications intermetallic dispersion strengthened Al–Cr–Zr (Hughes *et al.*, 1984), Al–Cr–Zr–Mn (Wilsdorf *et al.*, 1989), and Al–Cr–Y (Hawk *et al.*, 1988) alloys have been investigated by rapid solidification processing. The intermetallics observed in these alloys have not been very well characterized. The available data are summarized in Table 8. The intermetallic Al₇Cr is reported to occur both in orthorhombic and monoclinic form in most of the alloys of commercial interest. It appears (from Table 8) that the intermetallic reported as Al₁₃Cr₂ has a structure very close to that of either orthorhombic Al₇Cr or orthorhombic Al₁₁Cr₂. Both phases have been reported to have the same lattice parameter, as given in Table 8, but with different numbers of atoms per unit cell; Al₇Cr has 145 and Al₁₁Cr₂ has 93 atoms per unit cell (Little *et al.*, 1951). No crystallographic data have been reported for Al₁₃Cr₂ in Al–5Cr–2Zr (Palmer *et al.*, 1988). Furthermore, in the same alloy Midson *et al.* (1985) did not find this Al₁₃Cr₂ phase. In Al–Cr–Zr alloys Al₃Zr (L1₂) is also observed (Palmer *et al.*, 1988; Midson *et al.*, 1985). These alloys appear to have overall mechanical properties that are inferior to those of the Al–Fe–Ce and Al–Fe–V–Si alloys despite the fact that they contain some cubic, coherent Al₃Zr (L1₂) dispersoids; this intermetallic is discussed further in the following section.

2.4 Al₃(V, Zr, Nb, Hf, Ti) Intermetallics

The Al₃X (X = V, Zr, Nb, Hf, Ti) intermetallic compounds have been of interest in the development of elevated-temperature aluminum alloys. These alloys derive their high-temperature properties from thermally stable dispersoids such as Al₃Zr (Palmer *et al.*, 1988; Angers *et al.*, 1988a,b), Al₃Ti (Hawk *et al.*, 1989a,b; Angers *et al.*, 1988), Al₃Nb (Hawk *et al.*, 1989a) and Al₃Hf (Furushiro and Hori, 1985). Since Al₃Ti is discussed in Chapter 7 of this volume by Yamaguchi and Inui, we will not elaborate. Among the transition metals Ti, V, Zr, etc. that are of interest as formers of thermally stable intermetallics, zirconium has the lowest diffusivity in aluminum, as discussed earlier in Table 1. Furthermore, the intermetallic Al₃Zr exhibits a very small lattice mismatch with the aluminum matrix, particularly when present as the metastable L1₂ (cP4) phase (Table 9). Table 9 also shows other intermetallics, Al₃Nb, Al₃V, Al₃Hf and Al₃Ti, as well as their metastable structures and the corresponding lattice mismatch. The L1₂ (cP4) cubic Al₃Zr can form at low temperatures from the supersaturated solid solution and transforms to the equilibrium tetragonal D0₂₃ (tI16) phase at elevated temperatures. Cubic L1₂ (cP4) phases have also been observed in rapidly solidified Al–Nb (Hawk *et al.*, 1989a) and Al–Hf (Furushiro and Hori, 1985) alloys. Even the tetragonal intermetallics Al₃Zr, Al₃Ti and Al₃Hf show low overall lattice discrepancy. Since tetragonal Al₃Ti, Al₃V, Al₃Zr and Al₃Hf are isostructural the mutual solubility between these phases is extensive. It has been observed that the lattice parameters of such dispersed phases vary with composition according to Vegard's law

Table 9. Al₃X-type (X = Zr, Nb, V, Ti, Hf) intermetallic compounds and their lattice mismatches and disregistries with the aluminum matrix

Phase	Structure	Space group	Lattice disregistry ^a (%)
Al ₃ Zr ^b	Cubic (L1 ₂) $a = 0.4073$ nm	14/mmm	0.58
	Tetragonal (D0 ₂₃) $a = 0.4013$ nm $c = 1.7321$ nm		2.91 (a , 0.9; c , 6.9)
Al ₃ Nb ^b	Cubic (L1 ₂) $a = 0.411$ nm	14/mmm	1.49
	Tetragonal (D0 ₂₂) $a = 0.3844$ nm $c = 0.8605$ nm		5.47 (a , 5.1; c , 6.3)
Al ₃ V	Tetragonal (D0 ₂₂) $a = 0.3780$ nm $c = 0.8321$ nm	14/mmm	3.57 (a , 7.1; c , 2.7)
Al ₃ Hf ^b	Tetragonal (D0 ₂₃) $a = 0.3919$ nm $c = 1.7653$ nm	14/mmm	2.94 (a , 3.2; c , 9.0)
Al ₃ Ti	Tetragonal (D0 ₂₂) $a = 0.3848$ nm $c = 0.8596$ nm	14/mmm	1.3 (a , 5.0; c , 6.1)

$$^a \text{Tetragonal disregistry } \delta = \frac{100}{3} \left[2 \left(1 - \frac{a}{a_0} \right) + \left(1 - \frac{c}{na_0} \right) \right]$$

$$n = 2 \text{ for } D0_{22}; n = 4 \text{ for } D0_{23}.$$

^bCubic (L1₂) phase is reported as a metastable phase in these alloys.

(i.e. linearly) (Angers *et al.*, 1988a,b). Interestingly, only a small amount of Al₃Hf or Al₃Zr added to Al₃Ti or Al₃V changes the structure of the ternary intermetallic phase from D0₂₂ (tI8) to D0₂₃ (tI16). Vanadium additions to Al₃Zr lower the lattice mismatch and have been observed to decrease the rate of Ostwald ripening for both metastable cubic L1₂ (cP4) and the equilibrium tetragonal D0₂₃ (tI16) phases (Table 6) (Angers *et al.*, 1988a,b). However, no commercially significant Al–Zr–V-based alloys have been developed for elevated-temperature applications. On the other hand, Al₃Zr intermetallics have played a significant role in the development of low-density, commercial aluminum–lithium alloys, as discussed in the next section.

3. Al₃(Zr_xLi_{1-x}) Intermetallics

Zirconium is a significant addition to the Al–Li-based alloys. Usually about 0.2% of Zr is added to DC-cast ingots (Sanders and Starke, 1984; Adam and Lewis, 1985), whereas 0.5–1.0% Zr can be added to rapidly solidified/powder metallurgy alloys (Das and Davis, 1988; Kim *et al.*, 1986, 1989; Kim and Das, 1987). Zirconium leads to either

Al₃Zr dispersoids in solution-treated and quenched alloys or to Al₃(Zr_xLi_{1-x}) in aged alloys. The exact nature of the latter dispersoid has been the subject of considerable investigation and will be considered here in some detail. The role of Al₃Zr in Al–Li alloys is to:

- (i) inhibit recrystallization and control grain size (Flower and Gregson, 1987; Palmer *et al.*, 1986; Welpman *et al.*, 1984; Ozbilen and Flower, 1989; Ryum, 1969; Makin and Stobbs, 1986) by the well-known grain boundary pinning effect of dispersoids; Figure 10 illustrates this for a rapidly solidified/powder metallurgy Al–Li alloy containing 1% Zr;
- (ii) improve toughness and stress-corrosion cracking resistance (Welpman *et al.*, 1984);
- (iii) control quench rate sensitivity (Ozbilen and Flower, 1989; Nes, 1972; Conserva *et al.*, 1971); and
- (iv) serve as preferential nucleation sites for Al₃Li (δ') and other strengthening precipitates in Al–Li-based alloys (Welpman *et al.*, 1984; Kanno and Ou, 1991; Gayle and Vandersande, 1986) (Figures 11 and 12).

In rapidly solidified/powder metallurgy Al–Li alloys (up to 1.0% Zr) high volume fractions of Al₃Zr can be obtained (Figures 10, 11 and 12). Hence, in addition to the above mentioned benefits, they aid in mechanical properties by causing slip to occur on a finer scale. The primary strengthening phase in ingot Al–Li alloys is δ' (Al₃Li), which is readily shearable, promoting planar slip. In order to insure that slip occurs on diverse slip systems (dispersed slip) rather than on one slip system (planar slip) in ingot alloys, several precipitates such as Al₂CuLi (T₁) and Al₂CuMg (S') are formed by appropriate alloying additions. However, these T-type and S-type phases form very sluggishly and nucleate heterogeneously at defects such as dislocations. For overaged samples, T₁ and S' can be seen to a small extent in powder metallurgy alloys (Figure 12). As a result, nucleation of these precipitates can occur at a useful rate only if the material is subjected to a controlled deformation step prior to aging. Thus, typical ingot aluminum–lithium alloys require a 4–10% cold stretch prior to aging. This stretch limits the useful shapes to which ingot aluminum–lithium alloys can be applied (e.g. sheet, plate and extrusions). Complex shapes typical of forgings that have adequate mechanical properties cannot be readily produced. The high volume fraction of Al₃Zr attainable in powder metallurgy alloys avoids the above mentioned deficiency. The similarities between δ' (Al₃Li) and Al₃Zr, both L1₂ (cP4) with little mismatch, permit the nucleation of δ' (Al₃Li) predominantly on the pre-existing Al₃Zr dispersoids forming 'composite' Al₃Li/Al₃Zr particles

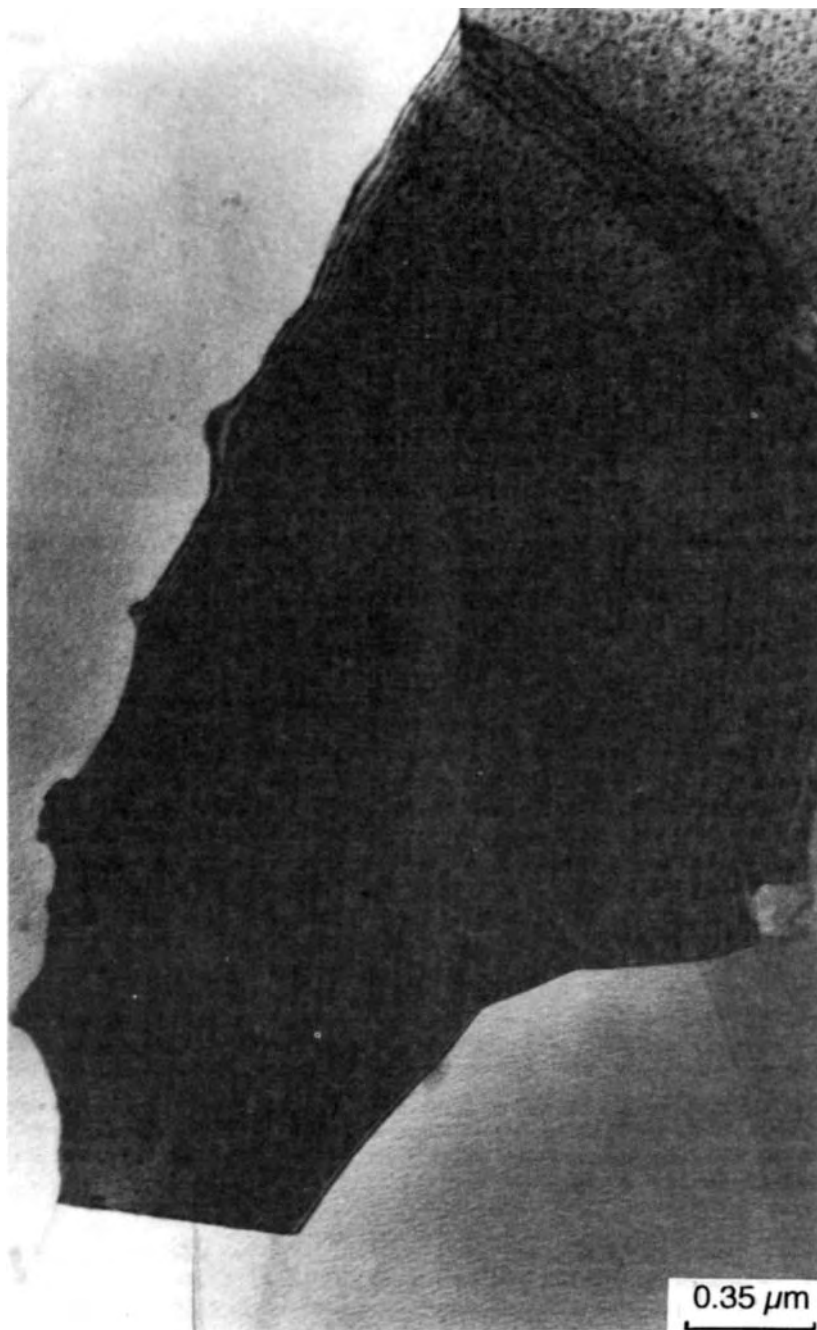


Figure 10. TEM micrograph showing grain boundary pinning by Al_3Zr particles in an $\text{Al-2.6Li-1Cu-0.5Mg-1Zr}$ alloy produced by powder metallurgy, solutionized at 540°C for one hour and ice-water quenched. The matrix contains a high volume fraction of $\text{L1}_2 \text{Al}_3\text{Zr}$ particles

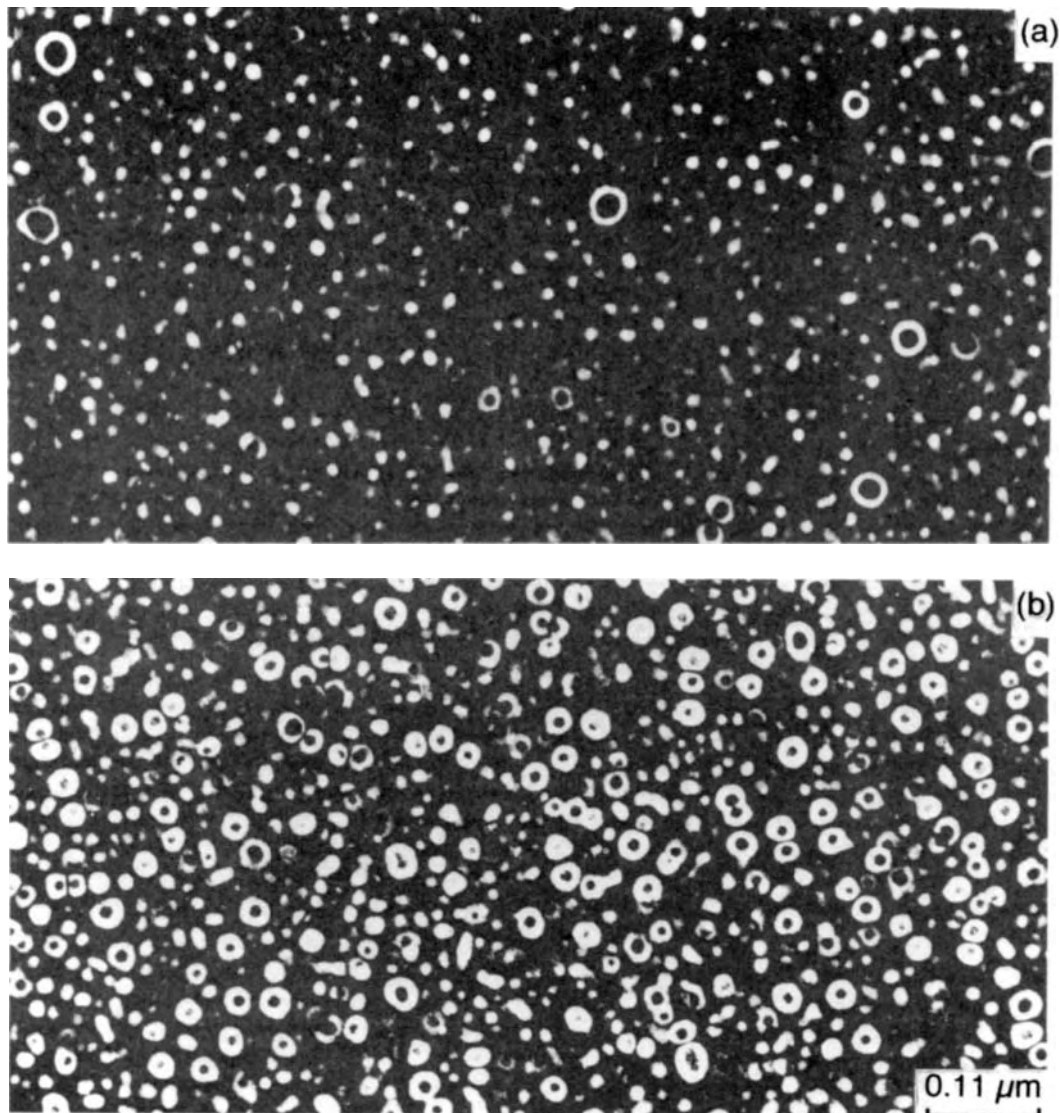


Figure 11. TEM centered dark-field images formed using the common superlattice reflection $g=001$ showing δ' (Al_3Li) and 'composite' (Al_3Zr core and Al_3Li shell) particles in $\text{Al-2.6Li-1.0Cu-0.5Mg-Zr}$ containing (a) 0.2% Zr and (b) 1% Zr after solution treatment at 540°C for two hours and aging at 135°C for 144 hours. Note that the volume fraction of 'composite' particles is much smaller in the 0.2% Zr alloy

(Gregson and Flower, 1984; Makin and Ralph, 1984; Kim and Das, 1986b; Gayle and Vandersande, 1986; Kim *et al.*, 1986; Makin and Stobbs, 1986; Flower and Gregson, 1987; Kim *et al.*, 1989) (Figures 11 and 12). The shear-resistant 'composite' particles do not promote pronounced planar slip; rather they induce Orowan bypassing of dislocations resulting in high strength and an improvement in ductility (Kim *et al.*, 1989; Kim and

Das, 1986a,b). Figure 13 is a comparison of the deformation modes between a binary Al-3Li alloy containing only δ' (Al_3Li) and a zirconium-containing alloy which contains 'composite' $\text{Al}_3\text{Li}/\text{Al}_3\text{Zr}$ particles.

The exact composition and structure of the core of the 'composite' $\text{Al}_3\text{Li}/\text{Al}_3\text{Zr}$ particle have been the subject of some controversy. It should be emphasized that the beneficial effect of Al_3Zr particles in Al-Li

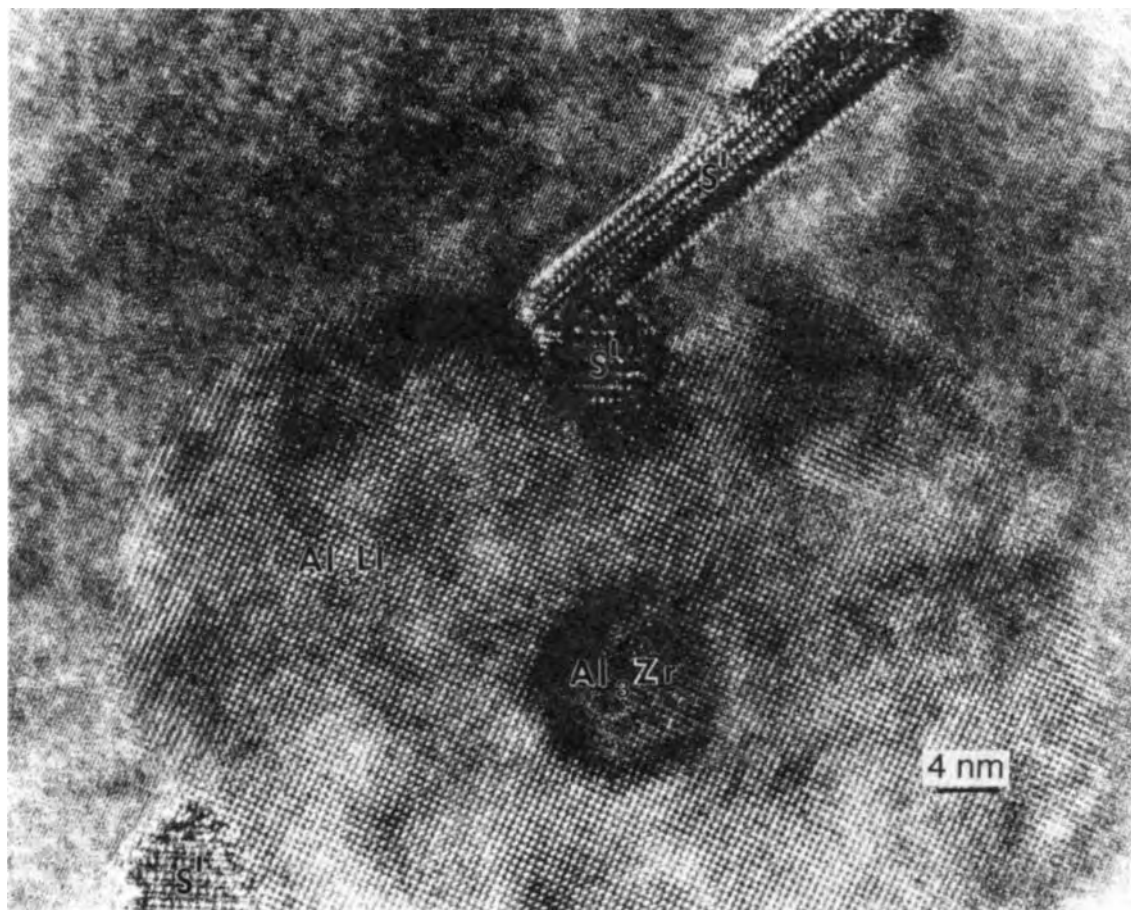


Figure 12. High resolution image on the $\mathbf{B} = [001]$ zone axis shows a composite δ' coarsened (Al_3Li) particle as a shell around $\text{Li}_2\text{Al}_3\text{Zr}$ and S' precipitates nucleated at the δ'/matrix boundary and a sub-boundary in the 1% Zr alloy solutionized at 540 °C for two hours, ice-water quenched, and aged at 225 °C for 36 hours

alloys mentioned above is owing to cubic $\text{Li}_2\text{Al}_3\text{Zr}$ (cP4) Al_3Zr particles with a cube-cube orientation relationship to the aluminum matrix and with a stoichiometric Al:Zr ratio of 3:1. Several techniques have been used to try to investigate the interaction of lithium with Al_3Zr particles and to determine whether Li partitions into the Al_3Zr core. Gayle and Vandersande (1989) proposed that the anomalous image contrast associated with the composite precipitates (Al_3Zr core and Al_3Li shell) observed by transmission electron microscopy is owing to lithium incorporation in the Al_3Zr , which gives rise to a small $[001]$ structure factor. They suggested that the dark contrast of the cores in 'composite' $\text{Al}_3\text{Li}/\text{Al}_3\text{Zr}$ particles is owing to the incorporation of Li into the Al_3Zr core. They proposed

that the composition of the 'composite' particle is very close to $\text{Al}_3(\text{Zr}, \text{Li})$ with the Li:Zr ratio between 2:1 and 1:4. Radmilovic *et al.* (1989) used high-resolution electron microscopy and image simulations to characterize the composition and structure of the 'composite' particles. Using different TEM techniques these authors concluded that there is partitioning of lithium between Al_3Zr and Al_3Li , and the exact composition of the ' Al_3Zr ' core is very close to $\text{Al}_3(\text{Li}_{0.6}\text{Zr}_{0.4})$. Sung *et al.* (1986) have examined the Al-Li alloys using electron energy loss spectroscopy (EELS) to quantify the Li concentration in ' Al_3Li ' precipitates. However, the presence of Li in Al_3Zr particles in multicomponent Al-Li-based alloys is difficult to quantify using EELS. The formation of such 'composite' phases has recently

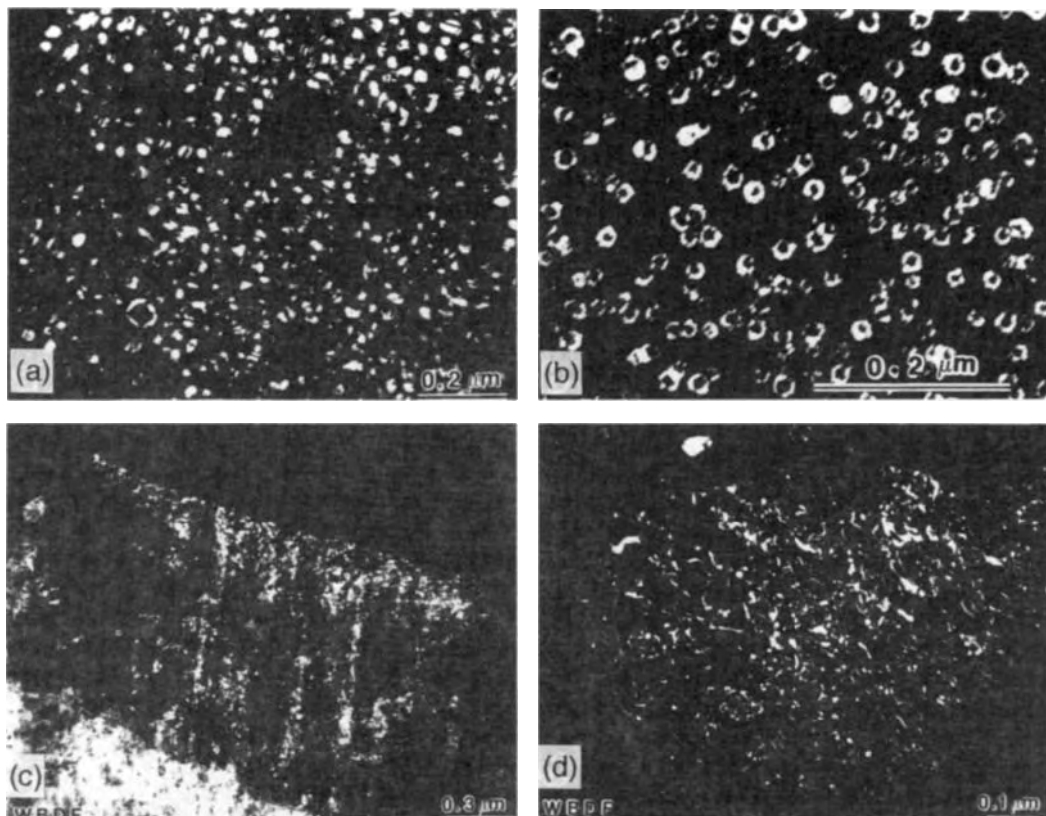


Figure 13. TEM centered dark-field images of: (a) an Al-3Li alloy showing shearing of δ' precipitates; (b) an Al-Li-Cu-Mg-Zr alloy showing Al_3Zr core surrounded by δ' ; (c) a deformed microstructure corresponding to (a) showing extensive planar slip; and (d) a deformed microstructure corresponding to (b) showing tangled dislocations

been predicted from phase equilibria calculations, as discussed below.

4. Intermetallic Phase Equilibrium Predictions

Multicomponent phase equilibrium calculations can in principle aid prediction of the structure of complex materials and assist in the design of alloys using such intermetallic phases (Miodownik, 1989). The calculation of a nucleation rate for each potential transformation product, including both stable and metastable phases, is a key concept in these calculations. Phase diagram calculations presuppose the thermodynamic characterization of each phase, both stable and metastable, so that the required driving force for nucleation can be directly extracted from the existing data bank. Although the liquid/solid interfacial energy can rarely be calculated directly, there is good evidence that a good working

value can be obtained from the heat of fusion, which is also available from the thermodynamic data bank. This means that the relative nucleation rates of all competing crystalline phases, stable or metastable, can be calculated unambiguously. The precise role played by heterogeneous nucleants is of course contentious. The main computer program used is THERMO-CALC, which has been developed by the Royal Institute of Technology, Stockholm, Sweden. Such computational techniques are particularly useful while designing alloys that are far from equilibrium and are to be made by processing techniques such as rapid solidification and mechanical alloying. In this section we will briefly discuss some of the pertinent results on the aluminum-rich intermetallic compounds discussed in this chapter.

Calculations for both stable and metastable phase equilibria in Al-Li-Zr alloys have been performed by Saunders (1989). Predictions have been made for the metastable equilibria between α -Al and the L_{12} (cP4)

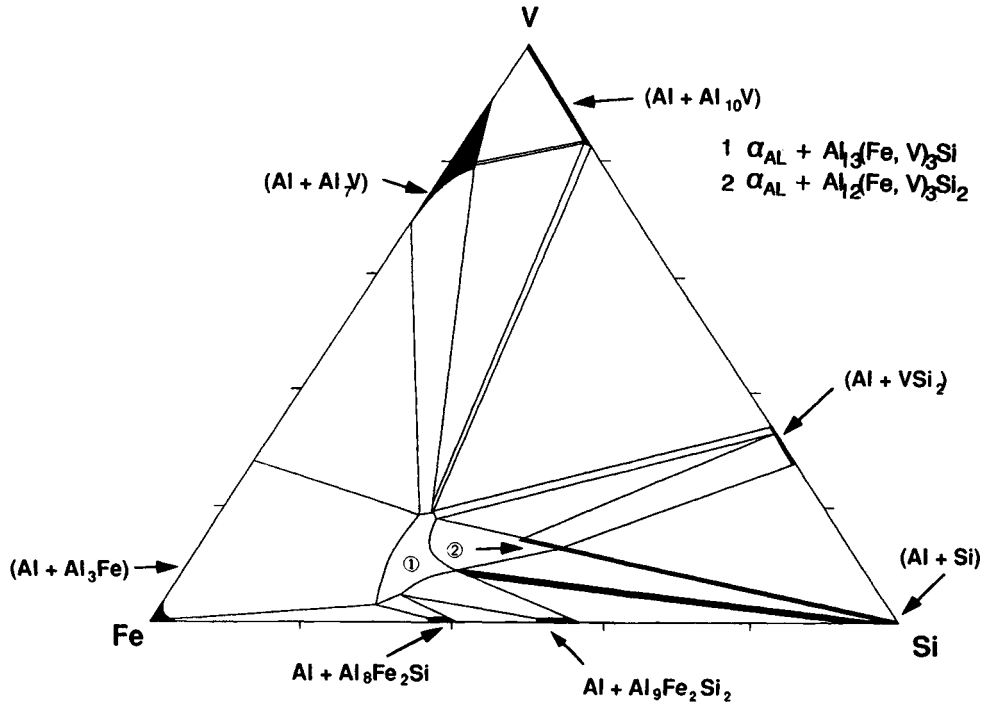


Figure 14. Calculated isothermal section at 823 K for equilibrium phases in Al-Fe-V-Si alloys

ordered phase in the Al-Li-Zr ternary. The tie lines show that during the high-temperature solution anneal at 500–550 °C for alloys in the composition range 7–12 at% Li and up to 1 at% Zr, the $L1_2$ (cP4) Al_3Zr particle, in addition to high levels of zirconium, contains substantial amounts of lithium. This agrees with the experimental results discussed in the previous section. The predicted tie lines between the Al solid solution and the intermetallic change sharply at low temperatures, and the direction of equilibrium then shifts to almost pure Al_3Li , as would be expected for this system which exhibits ‘composite’ particles.

The aluminum–transition metal systems Al-Fe (Saunders *et al.*, 1987–1989), Al-Mn (Saunders *et al.*, 1987–1989), Al-Zr (Saunders and Tsakiropoulos, 1988), Al-Cr (Saunders and Tsakiropoulos, 1988), Al-Mn-X-Si (Saunders *et al.*, 1987–1989), and Al-Fe-V-Si (Saunders *et al.*, 1987–1989) have been calculated with some degree of success. For example, the ranges of intermetallic structures obtained in rapidly solidified Al-Zr and Al-Cr powder alloys of a given powder particle size range have been related to critical cooling rate (Saunders and Tsakiropoulos, 1988). Al-Fe-V-Si phase equilibria have been calculated (Saunders *et al.*, 1987–1989) (Figure 14) in an effort to investigate the

metastable intermetallic $Al_{13}(Fe, V)_3Si$ phase fields. The calculated isothermal section at 823 K shows good qualitative agreement with the experimentally determined one at 748 K (Figure 6). These calculations also indicated that the composition range in which the aluminum matrix contains only the $Al_{13}(Fe, V)_3Si$ intermetallic phase is extremely limited at all temperatures. Furthermore, the prediction that this intermetallic phase is stable at 823 K agrees with the experimentally observed data of Zedalis *et al.* (1987). The narrow compositional range over which the intermetallic $Al_{13}(Fe, V)_3Si$ is stable has an important implication in controlling the mechanical properties of the alloy by avoiding third, possibly undesirable, intermetallics, as discussed in the next section.

5. Properties and Applications

The aluminum–transition metal intermetallics discussed have been successfully incorporated into aluminum alloys to improve elevated-temperature properties over conventional precipitation-strengthened aluminum alloys (Figure 15). Several commercial alloys

(8022, 8009 and X8019[†]) have been introduced into the marketplace (Table 3). Presently, the most prominent high-temperature aluminum alloys that are processed by rapid solidification/powder metallurgy technology are based on Al-Fe-Ce intermetallics and $\text{Al}_{13}(\text{Fe}, \text{V})_3\text{Si}$ (Table 6). Gas-atomized Al-Fe-Ce (Griffith *et al.*, 1982) alloys (e.g. alloy X8019) are capable of extended service up to ~ 590 K, beyond which the Al-Fe-Ce intermetallics coarsen appreciably as discussed earlier. The $\text{Al}_{13}(\text{Fe}, \text{V})_3\text{Si}$ -based Al-Fe-V-Si alloys (e.g. alloy 8009 and FVS1212), processed by melt spinning (planar flow casting) (Das, 1988; Das *et al.*, 1991), exhibit improved elevated-temperature strength to temperatures of 700 K, as shown in Figure 15 (Das and Davis, 1988; Brown *et al.*, 1986; Skinner, 1988). This is owing to the lower coarsening rate of the $\text{Al}_{13}(\text{Fe}, \text{V})_3\text{Si}$ intermetallics relative to Al-Fe-Ce intermetallics (Table 6). The volume fraction of the intermetallic phase has been varied to give a wide range of property combinations. For example, alloy 8022 was designed to contain nominally 16 vol% $\text{Al}_{13}(\text{Fe}, \text{V})_3\text{Si}$ silicide phase and is targeted for applications such as rivet wire, where high formability is required (Gilman and Das, 1988; Das *et al.*, 1989a). Alloy 8009 (27 vol% silicide) has been developed as a damage-tolerant alloy and has an excellent combination of strength (ambient and elevated temperature), fracture toughness and fatigue crack growth resistance. It should be emphasized that, if the alloy composition is not controlled properly, intermetallic phases (e.g. $\text{Al}_7(\text{V}, \text{Fe})$, $\text{Al}_{10}(\text{V}, \text{Si})$, Al_3Fe , Al_6Fe) other than $\text{Al}_{13}(\text{Fe}, \text{V})_3\text{Si}$ silicides can adversely affect fracture toughness at equivalent strength levels (Figure 16) (Skinner, 1988). Alloy 8009 is currently available in various aerospace and automotive product forms: sheet, plate, profiled extrusion and selected forgings (Das *et al.*, 1989; Gilman *et al.*, 1988). The nearly commercial alloy FVS1212 (37 vol% silicide) was designed for high-stiffness applications, primarily in the form of sheet and extrusions. FVS1212 offers increased strength and a room-temperature Young's modulus of ~ 95 GPa (14 Mp.s.i.) and is suitable for missile-fin applications. On the basis of specific strength this alloy is competitive with titanium at temperatures up to 700 K. The detailed mechanical properties and applications of these alloys have been discussed in a number of recent publications (Das and Davis, 1988; Skinner, 1988; Gilman and Das, 1988; Das *et al.*, 1989a,b; Gilman *et al.*, 1988; LaSalle *et al.*, 1989).

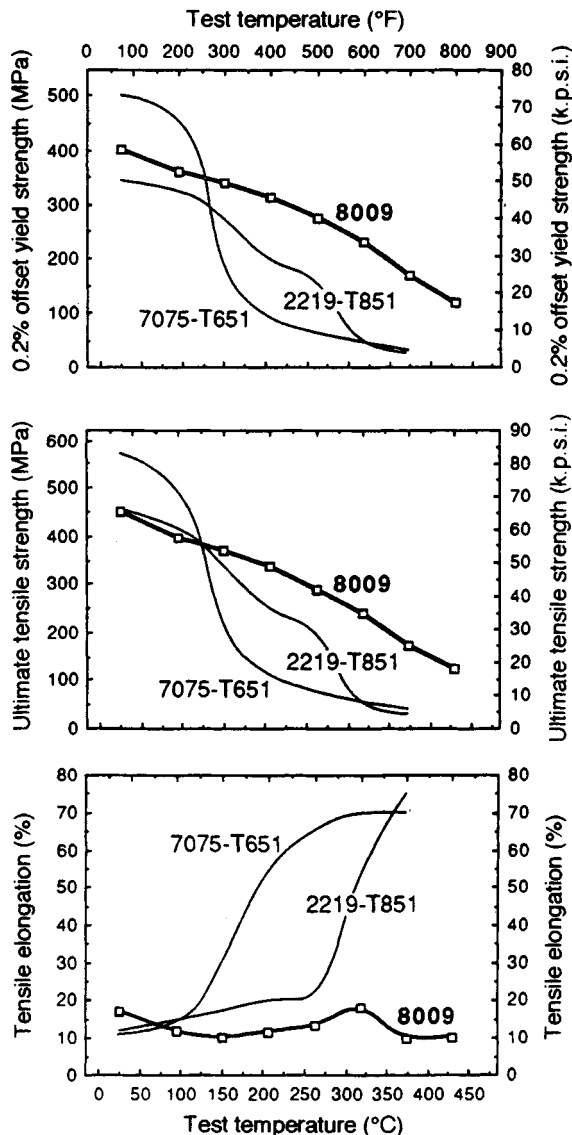


Figure 15. Comparison of elevated-temperature tensile properties of alloy 8009 containing $\text{Al}_{13}(\text{Fe}, \text{V})_3\text{Si}$ and conventional wrought aluminum alloys

The aluminum-lithium alloys based on $\text{Al}_3(\text{Zr}_x\text{Li}_{1-x})$ 'composite' dispersoids, particularly the ones containing high volume fractions, provide excellent combinations of strength, toughness and fracture properties in a wide variety of product forms (Kim *et al.*, 1986; Das *et al.*, 1989a; LaSalle *et al.*, 1989; LaSalle *et al.*, 1992). It was mentioned earlier that the presence of high volume fraction 'composite' particles in powder alloys allows almost net-shaped forgings to be fabricated without any need

[†]Alloys 8022, 8009 and X8019 are registered with the Aluminum Association.

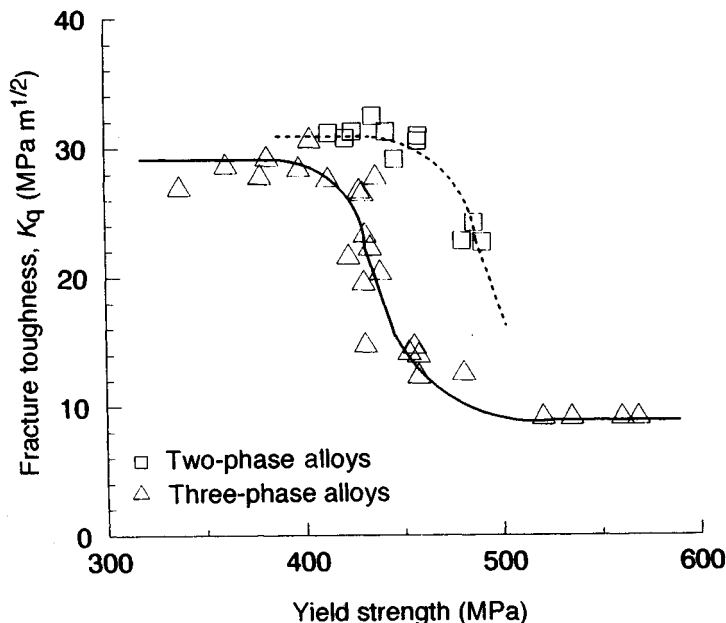


Figure 16. Effect of a third intermetallic phase on the fracture toughness of Al-Fe-V-Si alloys; the two-phase alloys contain $Al_{13}(Fe,V)_3Si$ as the only intermetallic

for subsequent cold stretching, as is required in low volume fraction 'composite' particle ingot alloys. The high 'composite' particle loading also reduces the anisotropy in tensile properties that is often a problem in ingot aluminum-lithium alloys. The ingot Al-Li alloys usually show a drop in strength and elongation at $\sim 45^\circ$ to the rolling direction, whereas no significant drop is seen for powder alloys. The 'composite' particles are not stable at very high temperatures, and hence the Al-Li alloys show good strength only to $\sim 150^\circ C$. In summary, the introduction of 'composite' Al_3Zr/Al_3Li particles into Al-Li alloys has made forging applications of these alloys possible. The components that are currently being developed are aircraft wheel forgings and net-shaped aircraft structural components (LaSalle *et al.*, 1989, 1992).

Both Al-Fe-based alloys and Al-Li-Zr alloys, processed by powder metallurgy, exhibit excellent corrosion resistance in saline environments (Das and Davis, 1988). The presence of intermetallics does not affect the corrosion properties, primarily because the dispersions are fine.

6. Summary

The aluminum-rich intermetallics have played a significant role in the development of aluminum alloys. An

understanding of the structures of intermetallics formed with common impurities such as Fe in conventional ingot aluminum alloys has been obtained. Utilizing the knowledge of aluminum-transition metal intermetallic compounds, diverse aluminum alloys have been investigated by nonequilibrium processing from the liquid state. Powder-processed Al-Fe-based and Al-Li-Zr-based alloys have been explored in depth. Novel Al-Fe-Ce and Al-Fe-V-Si alloys have been identified that have good-to-excellent combinations of high-temperature strength and stability; Al-Li-Zr alloys have been developed for forging applications with lower density and lower anisotropy than can be achieved in ingot alloys. The alloys based on the aluminum-rich intermetallics are finding applications predominantly in aerospace structural components.

7. Acknowledgements

The author is grateful to Dr D. J. Skinner for many helpful discussions and for providing some of the data used in this review.

8. References

- Adam, C. M. (1982). In *Rapidly Solidified Amorphous and Crystalline Alloys* (eds B. H. Kear, B. C. Giessen, and M. Cohen). Elsevier, Amsterdam, p. 411.
- Adam, C. M., and Bourdeau, R. G. (1980). In *Rapid Solidification Processing: Principles and Technologies II* (eds R. Mehrabian, B. H. Kear, and M. Cohen). Claitor's Publishing Division, Baton Rouge, LA, p. 256.
- Adam, C. M., and Lewis, R. E. (1985). In *Rapidly Solidified Crystalline Alloys* (eds S. K. Das, B. H. Kear, and C. M. Adam). TMS-AIME, Warrendale, PA, p. 157.
- Adam, C. M., Bourdeau, R. G., and Broch, J. W. (1982). In *Application of Rapidly Solidified Alloys*, Final Report. Contract AFWAL-TR-81-4188, February.
- Ahrens, T., Gysler, A., and Lutjering, G. (1985). *Z. Metallk.*, **76**, 391.
- Angers, L., Chen, Y., Fine, M. E., Weertman, J. R., and Zedalis, M. S. (1988a). In *Aluminum Alloys—Physical and Mechanical Properties* (eds E. A. Starke, Jr and T. H. Sanders, Jr). Engineering Materials Advisory Services, Warley, UK, p. 321.
- Angers, L. M., Konitzer, D. G., Murray, J. L., and Toruckner, W. G. (1988b). In *Dispersion Strengthened Aluminum Alloys* (eds Y. W. Kim and W. M. Griffith). TMS, Warrendale, PA, p. 355.
- Ayer, R., Angers, L. M., Mueller, R. R., Scanlon, J. C., and Klein, C. F. (1988). *Metall. Trans.*, **19A**, 1645.
- Bendersky, L. (1985). *Phys. Rev. Lett.*, **55**, 1461.
- Bendersky, L., and Ridder, S. D. (1986). *J. Mater. Res.*, **1**, 405.
- Bendersky, L., Schaefer, R. J., Biancianiello, F. S., Boettinger, W. J., Kaufmann, M. J., and Shechtman, D. (1985). *Scripta Metall.*, **19**, 909.
- Bendersky, L. A., McAlister, A. J., and Biancianiello, F. S. (1988). *Metall. Trans.*, **19A**, 2893.
- Black, P. J. (1955a). *Acta Crystallogr.*, **8**, 175.
- Black, P. J. (1955b). *Acta Crystallogr.*, **8**, 43.
- Black, P. J., Edwards, O. S., and Forsyth, J. B. (1961). *Acta Crystallogr.*, **14**, 993.
- Brown, A. M., Skinner, D. J., Raybould, D., Das, S. K., Bye, R. L., and Adam, C. M. (1986). In *Aluminum Alloys—Physical and Mechanical Properties* (eds E. A. Starke, Jr and T. H. Sanders, Jr). Engineering Materials Advisory Services, Warley, UK, p. 1029.
- Bye, R. L., Kim, N. J., Skinner, D. J., Raybould, D., and Brown, A. M. (1987). In *Processing of Structural Metals by Rapid Solidification* (eds F. H. Froes and S. J. Savage). ASM, Metals Park, OH, p. 283.
- Conserva, M., Di Russo, E., and Caloni, O. (1971). *Metall. Trans.*, **2**, 1227.
- Cooper, M. (1960). *Acta Crystallogr.*, **13**, 257.
- Cooper, M. (1967). *Acta Crystallogr.*, **23**, 1106.
- Cooper, M., and Robinson, K. (1966). *Acta Crystallogr.*, **20**, 614.
- Das, S. K. (1988). *Int. J. Powder Metall.*, **24**, 175.
- Das, S. K., and Davis, L. A. (1988). *Mater. Sci. Eng.*, **98**, 1.
- Das, S. K., Kear, B. H., and Adam, C. M. (eds) (1985). *Rapidly Solidified Crystalline Alloys*. TMS-AIME, Warrendale, PA.
- Das, S. K., Gilman, P. S., and Raybould, D. (1989a). *Key Eng. Mater.*, **38/39**, 367.
- Das, S. K., Gilman, P. S., LaSalle, J. C., Peltier, J., Raybould, D., and Zedalis, M. S. (1989b). In *P/M in Aerospace and Defense Technologies*, Vol. 1. Metal Powder Industries Federation, Princeton, NJ, p. 77.
- Das, S. K., Bye, R. L., and Gilman, P. S. (1991). *Mater. Sci. Eng.*, **A134**, 1103.
- Dons, A. L. (1984a). *Scand. J. Metall.*, **13**, 137.
- Dons, A. L. (1984b). *Z. Metallk.*, **15**, 170.
- Dons, A. L. (1985). *Z. Metallk.*, **76**, 151.
- Douglas, A. M. B. (1950). *Acta Crystallogr.*, **3**, 19.
- Elser, V. (1985). *Phys. Rev. B.*, **32**, 4892.
- Elser, V., and Henley, C. L. (1985). *Phys. Rev. Lett.*, **55**, 1883.
- Fine, M. E., and Starke, E. A. (eds) (1986). *Rapidly Solidified Powder Aluminum Alloys*, ASTM STP 890. ASTM, Philadelphia, PA.
- Flower, H. M., and Gregson, P. J. (1987). *Mater. Sci. Tech.*, **3**, 81.
- Fung, K. K., Yang, C. Y., Zhou, Y. Z., Zhou, J. G., Zhan, W. Z., and Shen, B. G. (1986). *Phys. Rev. Lett.*, **56**, 2060.
- Furushiro, N., and Hori, S. (1985). In *Rapidly Quenched Metals* (eds S. Steeb and H. Warlimont). Elsevier, Amsterdam, p. 907.
- Gayle, F. W., and Vandersande, J. B. (1986). In *Aluminum-Lithium Alloys III* (eds C. A. Baker, P. J. Gregson, S. J. Harris, and C. J. Peel). Institute of Metals, London, p. 376.
- Gayle, F. W., and Vandersande J. B. (1989). *Acta. Metall.*, **37**, 1033.
- Gilman, P. S., and Das, S. K. (1988). In *Proc. International Congress on PM Aerospace Materials*, Luzern. MPIF/APMI, Princeton, NJ, 27.1
- Gilman, P. S., Brooks, J. W., and Bridges, P. J. (1986). In *Aluminum-Lithium Alloys III* (eds C. A. Baker, P. J. Gregson, S. J. Harris, and C. J. Peel). Institute of Metals, London, p. 78.
- Gilman, P. S., Das, S. K., Raybould, D., Zedalis, M. S., and Peltier, J. M. (1988). In *Proc. 2nd International SAMPE Metals and Metals Processing Conference*, Vol. 2 (eds F. H. Froes and R. H. Cull). SAMPE, Corvina, CA, p. 91.
- Gregson, P. J., and Flower, H. M. (1984). *J. Mater. Sci. Lett.*, **3**, 829.
- Grewen, J. (1969). *Z. Metallk.*, **57**, 439.
- Griffith, W. M., Sanders, R. E., Jr, and Hildeman, G. J. (1982). In *High Strength Powder Metallurgy Aluminum Alloys* (eds M. J. Kocak and G. J. Hildeman). TMS-AIME, Warrendale, PA, p. 209.
- Guyot, P. (1985). *J. Microsc. Spectrosc. Electron*, **10**, 333.
- Guyot, P., and Audier, M. (1985). *Philos. Mag. B*, **52**, L15.
- Hawk, J. A., Angers, L. M., and Wilsdorf, H. G. F. (1988). In *Dispersion Strengthened Aluminum Alloys* (eds Y. W. Kim and W. M. Griffith). TMS, Warrendale, PA, p. 337.

- Hawk, J. A., Briggs, J. K., and Wilsdorf, H. G. F. (1989a). In *Advances in Powder Metallurgy*, Vol. 3. MPIF/APMI, Princeton, NJ, p. 285.
- Hawk, J. A., Briggs, J. K., and Wilsdorf, H. G. F. (1989b). In *Advances in Powder Metallurgy—1989*. MPIF, Princeton, NJ, p. 301.
- Hodgson, P., and Parker, B. A. (1981). *J. Mater. Sci.*, **16**, 1343.
- Holer, R., cited by Dons, A. L. (1985). *Z. Metallk.*, **76**, 151.
- Hollingsworth, E. H., Frank, G. R., Jr, and Willett, R. E. (1962). *Trans. TMS-AIME*, **224**, 188.
- Hudd, R. C., and Taylor, W. H. (1962). *Acta Crystallogr.*, **15**, 441.
- Hughes, I. R., Marshall, G. R., and Miller, W. S. (1984). In *Rapidly Quenched Metals*, Vol. II (eds S. Steeb and H. Warlimont). North-Holland, Amsterdam, p. 1743.
- Jacobs, M. H., Doggett, A. G., and Stowell, M. J. (1974). *Mater. Sci. Eng.*, **9**, 1631.
- Jones, H. J. (1969–1970). *Mater. Sci. Eng.*, **5**, 1.
- Kanno, M., and Ou, B. L. (1991). *Mater. Trans. KIM*, **32**, 445.
- Kim, N. J., and Das, S. K. (1986a). *Scripta Metall.*, **20**, 1107.
- Kim, N. J., and Das, S. K. (1986b). *Mater. Res. Soc. Symp. Proc.*, **58**, 281.
- Kim, N. J., and Das, S. K. (1987). *Mater. Res. Soc. Symp. Proc.*, **80**, 213.
- Kim, N. J., Bye, R. L., Brown, A. M., Das, S. K., and Adam, C. M. (1986). In *Aluminum Alloys—Physical and Mechanical Properties* (eds E. A. Starke, Jr and T. H. Sanders, Jr). Engineering Materials Advisory Services, Warley, UK, p. 975.
- Kim, N. J., Raybould, D., Bye, R. L., and Das, S. K. (1989a). In *Proc. 5th International Conference on Aluminum-Lithium Alloys* (eds T. H. Sanders, Jr and E. A. Starke, Jr). Materials and Components Engineering Publication, Birmingham, UK, p. 123.
- Kim, N. J., Skinner, D. J., Okazaki, K., and Adam, C. M. (1989b). In *Aluminum-Lithium Alloys III* (eds C. A. Baker, P. J. Gregson, S. J. Harris, and C. J. Peel). Institute of Metals, London, p. 78.
- Kosuge, H., and Mizukami, I. (1972). *J. Jpn Inst. Light Met.*, **22**, 437.
- Kosuge, H., and Mizukami, I. (1975). *J. Jpn Inst. Light Met.*, **25**, 48.
- Kovac, I. (ed.) (1990). *Effects of Iron and Silicon in Aluminum and its Alloys*. Trans Tech, Switzerland.
- LaSalle, J. C., Bye, R. L., Raybould, D., and Das, S. K. (1989). In *Advances in Powder Metallurgy*, Vol. 3. MPIF/APMI, Princeton, NJ, p. 225.
- LaSalle, J. C., Raybould, D., Limoncelli, E. V., and Das, S. K. (1992). In *Aluminum-Lithium Alloys VI* (eds M. Peters and P.-J. Winkler). DGM, Informationsgesellschaft, Oberursel, Germany, p. 513.
- Lee, P. W., and Moll, J. H. (eds) (1988). *Rapidly Solidified Materials: Properties and Processes*. ASM, Cleveland, OH.
- Little, L., Pratt, J. N., and Raynor, G. V. (1951). *J. Inst. Met.*, **80**, 456.
- Liu, D. R., and Williams, D. B. (1988). *Scripta Metall.*, **22**, 1361.
- Liu, P., Thorvaldsson, T., and Dunlop, G. L. (1986). *Mater. Sci. Tech.*, **2**, 1009.
- Makin, P. L., and Ralph, B. (1984). *J. Mater. Sci.*, **19**, 3835.
- Makin, P. L., and Stobbs, W. M. (1986). In *Aluminum-Lithium Alloys III* (eds C. A. Baker, P. J. Gregson, S. J. Harris, and C. J. Peel). Institute of Metals, London, p. 392.
- Mehrabian, R., and Parris, P. A. (eds) (1988). *Rapid Solidification Processing: Principles and Technologies IV*. Claitor's Publishing Division, Baton Rouge, LA.
- Mehrabian, R., Kear, B. H., and Cohen, M. (eds) (1977). *Rapid Solidification Processing: Principles and Technologies I*. Claitor's Publishing Division, Baton Rouge, LA.
- Mehrabian, R., Kear, B. H., and Cohen, M. (eds) (1980). *Rapid Solidification Processing: Principles and Technologies II*. Claitor's Publishing Division, Baton Rouge, LA.
- Midson, S. P., Buckley, R. A., and Jones, H. (1985). In *Rapidly Quenched Metals* (eds S. Steeb and H. Warlimont). Elsevier, Amsterdam, p. 923.
- Miki, I., Kosuge, H., and Nagahama, K. (1975). *J. Jpn Inst. Light Met.*, **25**, 1.
- Miodownik, A. P. (1989). *Powder Metall.*, **32**, 269.
- Mondolfo, L. F. (1976). *Aluminum Alloys: Structure and Properties*. Butterworths, London, pp. 282–291, 534–537.
- Munson, D. (1967). *J. Inst. Met.*, **95**, 217.
- Nes, E. (1972). *Acta Metall.*, **20**, 499.
- Nicol, A. D. I. (1953). *Acta Crystallogr.*, **6**, 285.
- Ozlbilen, S., and Flower, H. M. (1989). *Acta Metall.*, **37**, 1993.
- Palmer, I. G., Miller, W. S., Liloyd, D., and Bull, M. (1986). In *Aluminum-Lithium Alloys III* (eds C. A. Baker, P. J. Gregson, S. J. Harris, and C. J. Peel). Institute of Metals, London, p. 221.
- Palmer, I. G., Thomas, M. P., and Marshall, G. J. (1988). In *Dispersion Strengthened Aluminum Alloys* (eds Y. W. Kim and W. M. Griffiths). TMS, Warrendale, PA, p. 217.
- Paris, H. G., Billman, F. R., Cebulak, W. S., and Petit, J. I. (1980). In *Rapid Solidification Processing: Principles and Technologies II* (eds R. Mehrabian, B. H. Kear, and M. Cohen). Claitor's Publishing Division, Baton Rouge, LA, p. 331.
- Phragmen, G. (1950). *J. Inst. Met.*, **77**, 498.
- Polmear, I. J. (1981). *Light Alloys*. Edward Arnold, London, pp. 15–46.
- Radmilovic, V., Thomas, G., and Fox, A. J. (1989). *Acta Metall.*, **37**, 2385.
- Rivlin, V. G., and Raynor, G. V. (1981). *Int. Met. Rev.*, **3**, 133.
- Robinson, K., and Black, P. J. (1953). *Philos. Mag.*, **44**, 1392.
- Rodriguez, M., and Skinner, D. J. (1990). *J. Mater. Sci. Lett.*, **9**, 1292.
- Ryum, N. (1969). *Acta Metall.*, **17**, 269.
- Saunders, N. (1989). *Z. Metallk.*, **80**, 894.

- Saunders, N., and Tsakiropoulos, P. (1988). *Mater. Sci. Tech.*, **4**, 157.
- Saunders, N., Chandrasekaran, L., and Miodownik, A. P. (1987–1989). Unpublished research, University of Surrey.
- Schaefer, R. J., Bendersky, L., Shechtman, D., Boettinger, W. J., and Biacaniello, F. S. (1986). *Metall. Trans.*, **17A**, 2117.
- Shechtman, D., and Blech, I. (1985). *Metall. Trans.*, **16A**, 1005.
- Shechtman, D., Blech, I., Gratias, D., and Cahn, J. W. (1984). *Phys. Rev. Lett.*, **53**, 1951.
- Simensen, C. J., and Vellasamy, R. (1977). *Z. Metallk.*, **68**, 428.
- Skinner, D. J. (1988). In *Dispersion Strengthened Aluminum Alloys* (eds Y. W. Kin and W. M. Griffith). TMS, Warrendale, PA, p. 181.
- Skinner, D. J. (1992). Unpublished research.
- Skinner, D. J., Bye, R. L., Raybould, D., and Brown, A. M. (1986). *Scripta Metall.*, **20**, 867.
- Skinner, D. J., and Okazaki, K. (1984). *Scripta Metall.*, **18**, 905.
- Skinner, D. J., Bye, R. L., Raybould, D., Brown, A. M., and Zedalis, M. S. (1987). In *Processing of Structural Metals by Rapid Solidification* (eds F. H. Froes and S. J. Savage). ASM, Metals Park, OH, p. 291.
- Skjerpe, P. (1987). *Metall. Trans.*, **18A**, 189.
- Stefaniay, V., Gruger, A., and Turmezey, T. (1987). *J. Mater. Sci.*, **22**, 539.
- Strid, J., and Simensen, C. J. (1986). *Pract. Metall.*, **23**, 485.
- Sung, C. M., Chan, H. M., and Williams, D. B. (1986). In *Aluminum–Lithium Alloys III* (eds C. A. Baker, P. J. Gregson, S. J. Harris, and C. J. Peel), Institute of Metals, London, p. 337.
- Suzuki, H., Kanno, M., Tanabe, H., and Itoi, K. (1978). *J. Jpn Inst. Light Met.*, **28**, 284.
- Swamy, V. T., Ranganathan, S., and Chattopadhyay, K. (1989). *J. Mater. Res.*, **4**, 539.
- Thursfield, G., and Stowell, M. J. (1974). *J. Mater. Sci.*, **9**, 1644.
- Tibballs, J. E., Davis, R. L., and Parkey, B. A. (1989). *J. Mater. Sci.*, **24**, 2177.
- Tonejc, A., and Bonefacic, A. (1969). *J. Appl. Phys.*, **40**, 419.
- Vivchar, O. I., Zarechnyuk, O. S., and Ryabov, V. R. (1970). *Russ. Metall.*, No. 1, 140.
- Walford, L. K. (1965). *Acta Crystallogr.*, **18**, 287.
- Welpman, K., Peters, M., and Sanders, T. (1984). *Aluminum*, **60**, 2.
- Westengen, H. (1982). *Z. Metallk.*, **73**, 360.
- Westengen, H., Reiso, O., and Auran, L. (1980). *Aluminum*, **56**, 768.
- Wilsdorf, H. G. E., Angers, L. M., Briggs, J. K., and Hawk, J. A. (1989). In *Advances in Powder Metallurgy*, Vol. 3. MPIF/APMI, Princeton, NJ, p. 269.
- Young, R. M. K., and Clyne, T. W. (1981). *Scripta Metall.*, **15**, 1211.
- Zarechnyuk, O. S., Emes-Misenko, E. I., Ryabov, V. R., and Dikiy, I. I. (1968). *Russ. Metall.*, No. 3, 152.
- Zarechnyuk, O. S., Mys'kiv, M. G., and Ryabov, V. R. (1969). *Russ. Metall.*, No. 2, 133.
- Zedalis, M. S. (1985). *Development of Elevated Temperature Aluminum Alloys Containing Hafnium, Titanium, Vanadium and Zirconium*. PhD Thesis, Northwestern University, p 193.
- Zedalis, M. S., Raybould, D., Skinner, D. J., and Das, S. K. (1987). In *Processing of Structural Metals by Rapid Solidification* (eds F. H. Froes and S. J. Savage). ASM, Metals Park, OH, p. 347.
- Zogg, H., Torok, E., Hausch, G., and Warlimont, H. (1979). *Aluminum*, **55**, 332.

This chapter was originally published in 1995 as Chapter 8 in *Intermetallic Compounds*, Vol. 2: *Practice*, edited by J. H. Westbrook and R. L. Fleischer.

Chapter 1

Ni₃Al in Nickel-Based Superalloys

Donald L. Anton

United Technologies Research Center, East Hartford, CT 06108, USA

1. Introduction

The very successful utilization of nickel-based superalloys in both the land-based and aero-gas turbine industries is a testament to the possible commercialization of new materials that are predominantly intermetallic. Power generation and air travel would not be possible as we know them if it were not for the superalloys that have been developed over the past 60 years. The aim of this chapter is to introduce the reader to superalloy metallurgy starting with a brief historical review highlighting the major technological developments that led to the wide use of these alloys (Sims, 1984), with emphasis on cast alloys. Only cursory attention will be paid to such areas as casting, forging, oxidation and grain boundary phenomena, for a number of works are available which thoroughly cover these subjects (Sims *et al.*, 1987; Stoloff, 1990; Erickson, 1990; Harris *et al.*, 1990). A summary of properties for various superalloys with emphasis on end utilization requirements will be given. Since much of the current research interest in intermetallics is in high-temperature strength, this should be used as a basis for comparison. It is also important to understand how technical advancements led to stronger alloys so that similar thought processes can be brought to bear on the development of higher strength intermetallics.

The L1₂ (cP4) ordered Ni₃Al phase, referred to as γ' , will be dealt with specifically with respect to alloying and the prediction of phase instability with an introduction to PHACOMP (phase composition analysis). Precipitate size and coarsening rate directly affect strength, and thus both theoretical models and experimental evidence of γ' -coarsening mechanisms will be

discussed. Finally, the mechanisms by which the ordered Ni₃Al phase influences strength under tensile, creep and fatigue conditions will be reviewed.

1.1 Historical Perspective

Initially, with aircraft supercharger development and subsequently with the advent of the gas turbine engine as a replacement for the internal combustion engine as the primary power source in aviation in the late 1930s, the search for materials with ever higher temperature capabilities was inaugurated. The first high-temperature alloys used in these applications, namely Tinidor and A-286, were slightly modified austenitic stainless steels. These alloys slowly evolved through introduction of aluminum and chromium for enhanced corrosion and oxidation resistance. Aluminum and titanium additions also gave the unexpected benefit of enhanced high-temperature creep resistance. It is now known that the precipitation of the ordered Ni₃Al phase within the austenitic matrix was the predominant reason for the concurrent high-temperature strength in these alloys. Later, iron was replaced by nickel and cobalt additions to enhance creep strength and oxidation resistance further. By roughly 1950 superalloys were nickel based with approximately 30 to 40 vol% Ni₃Al.

Up to this time, all castings and master alloys were air melted, requiring all alloy components to be stable with their slag through the melting point. The invention and wide commercial acceptance of vacuum melting during the early 1950s led to the second phase of advancements in superalloy properties, as shown in Figure 1, by allowing the addition of refractory metal alloying as well as the reactive elements Al and Ti.

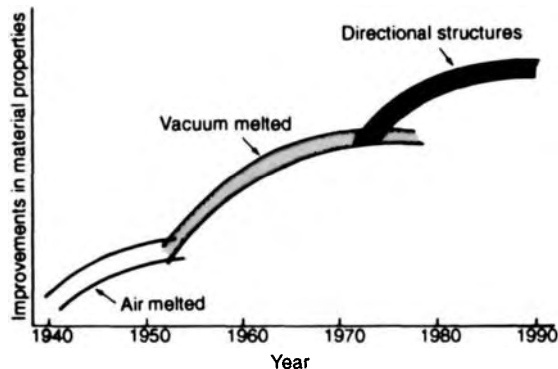


Figure 1. Major eras of superalloy development as defined by processing advancements (Hopkin, 1987)

In addition to producing grain boundary carbide control, the use of Mo, Nb, W and Ta resulted in enhanced solid-solution strengthening of both the disordered γ and the ordered Ni_3Al or γ' . The improved high-temperature properties of superalloys imparted by the additions of refractory metals came at the cost of long-term phase instabilities. Upon extended thermal exposures, platelike intermetallic phases such as μ , Laves and σ precipitated, leading to accelerated creep and premature failure. In the late 1950s and early 1960s, knowledge of highly complex multicomponent phase diagrams was, and to some extent still is, severely limited. While both empirical and theoretical models have been advanced that help in predicting long-term phase instabilities in these alloys, their implications were not fully appreciated until the early 1970s.

Figure 1 also identifies the next quantum improvement in superalloys, namely directional structures. Through both directionally aligned grains and later single crystals, superior performance was achieved. From an alloying standpoint, the elimination of grain boundaries, and the need for grain boundary stabilizing carbides, allowed higher matrix refractory element contents to be achieved, resulting in an overall superior performance that is utilized today.

The development of precision vacuum investment casting techniques has been pivotal to increasing the performance and efficiencies of gas turbine engines. This advance has allowed for the economical integration of complex cooling schemes, using compressed air, to cool efficiently the highest temperature components. This has allowed for significant increases in turbine gas inlet temperatures (allowing for a more nearly stoichiometric burn), while minimizing actual metal-temperature increases.

1.2 Physical Metallurgy Basis

Superalloys today are noted for their oxidation resistance and high-temperature strength, with the latter property being derived from incorporation of the coherent, ordered Ni_3Al γ' phase within the disordered, solid-solution γ . This interrelationship can be best shown by Figure 2, where the phase diagram, a typical microstructure and a schematic drawing of a coherent precipitate are given. While the Ni solid solution has the face-centered cubic (f.c.c.) A1 (cF4) structure, γ' is an ordered f.c.c. L1₂ (cP4) with aluminum atoms occupying alternating sites on every other (111) plane. The cubic nature of the γ' precipitates, as shown in Figure 2(b), is a consequence of the trade-off between the orientation dependences of interfacial energy and strain energy. Coherency strains result from the slight lattice mismatch between the disordered γ matrix and the ordered γ' precipitates. This lattice mismatch δ is paramount in determining the utility of superalloys, and will be discussed in depth in the following sections dealing specifically with γ' misfit, interfacial energies and elemental partitioning.

The two-phase material is highly alloyed to give enhanced strength and oxidation resistance to both phases of the binary system described above. Cobalt, and occasionally iron, is added to increase strength through solid-solution hardening of the Ni matrix. Cobalt additions are especially useful in altering the nickel lattice parameter and thus in affecting δ , as well as lowering the stacking fault energy. Molybdenum, tungsten and rhenium also are used as solid-solution strengtheners of the nickel matrix. Chromium and minor yttrium additions in conjunction with aluminum result in highly oxidation-resistant and corrosion-resistant alloys by forming a protective alumina film. Carbon, boron, hafnium and zirconium partition to the grain boundaries and form carbides and borides which are used to stabilize the grain size at elevated temperatures.

The ordered Ni_3Al has a wide solubility for Ti, and when used in conjunction with aluminum will precipitate large volume fractions of γ' . Niobium and tantalum are also added to strengthen both the ordered Ni_3Al precipitates and the γ matrix, as well as to stabilize carbides. Some typical superalloys, their approximate dates of inception and their nominal compositions are given in Table 1. Cobalt levels have generally decreased with time as higher refractory metal additions were made. Decreases have also occurred for chromium, which was found to strengthen these alloys only slightly. Chromium is used to enhance corrosion resistance, not a limiting

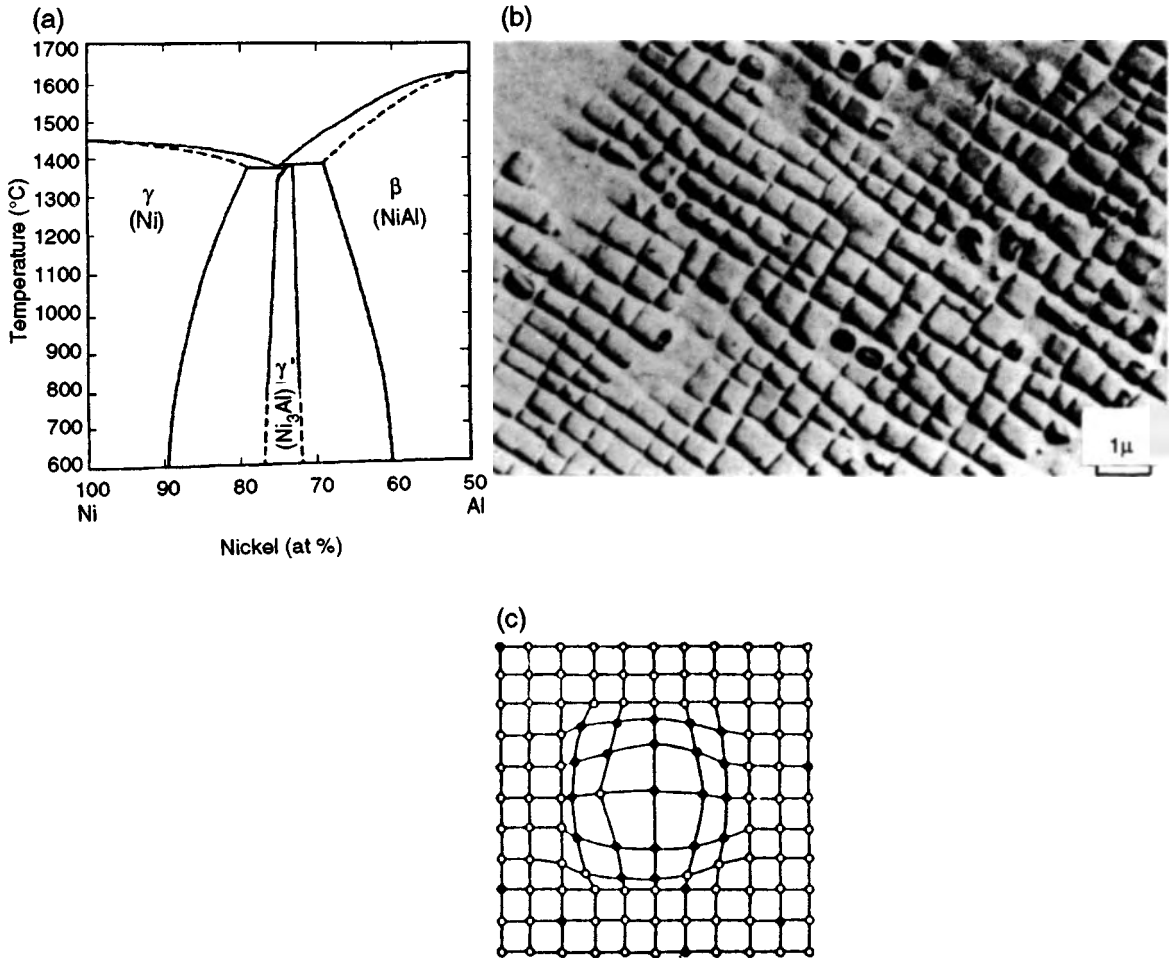


Figure 2. Superalloys can be characterized by (a) the Ni–Al binary phase diagram showing the two-phase field between the nickel solid solution and the ordered Ni₃Al of primary importance in superalloy metallurgy (Hanson, 1958), (b) a typical transmission electron micrograph and (c) a schematic diagram showing a coherent ordered γ' particle with positive misfit in a disordered matrix (Decker, 1969b)

failure mechanism in most applications. Notice that PWA-1480 (Gell *et al.*, 1980), a single-crystal alloy, alleviates the need for the grain boundary stabilizing elements carbon, boron and zirconium and allows for a high tantalum content.

A series of micrographs showing the microstructural evolution of superalloys is given in Figure 3*. The most important aspect of these micrographs, for the purposes of this chapter, is the change in volume fraction and morphology of the γ' precipitates. One clearly sees that in progressing from Waspaloy through U-700, IN-100, B-1900, Mar-M 200 and finally

PWA-1480, the γ' volume fraction increases to its optimum, approaching 70% by volume. At this limit the ordered precipitate spacings become too small, and the precipitates rapidly coalesce at elevated temperatures and lose their strengthening effect.

Given the microstructures and compositions of superalloys that have been described, we need to focus on the general properties of these alloys to elucidate their utility.

*The apparently large γ' -free regions are coincidental intersections of the polish plane and the γ matrix in between the precipitates.

Table 1. Compositions of superalloys showing changes with time

Alloy designation	Year of inception	Nominal composition (wt%)													
		Fe	Ni	Co	Cr	Al	Ti	Ta	Nb	Mo	W	Re	C	B	Zr
Tinidur	1935	53	30		15.0		1.8						0.15		
Nimonic 80A	1942		76		19.5	1.4	2.4							0.06	0.06
Waspaloy	1952		58	13	19.5	1.3	3.0			4.3			0.08	0.01	0.06
U-700/Astroloy	1958		53	18	15.0	4.0	3.5			5.0			0.08	0.03	
IN-100	1962		60	15	10.0	5.5	4.7			3.0			0.18	0.01	0.06
B-1900	1968		64	10	8.0	6.0	1.0	4.0		6.0			0.10	0.01	0.10
Mar-M 200	1973		59	10	9.0	5.0	2.0		1.0		12.5		0.15	0.01	0.05
PWA-1480	1983		63	5	10.0	5.0	1.5	12.0			4.0				
PWA-1484	1988		60	10	5.0	5.6		8.7		2.0	6.0	3.0			0.10

First, however, we must understand that there are many applications for these alloys, and the processing required to form a final article dictates the nature of the alloy. It has become customary to divide superalloys into two groups, namely wrought and cast. Wrought alloys are those which are hot deformable into bar, sheet or final articles such as turbine disks. These alloys are very strong in yielding at low and intermediate temperatures ($< 870^{\circ}\text{C}$) and have exceptional fracture toughness. Cast alloys are generally stronger in creep resistance

in all temperature ranges and in yielding at temperatures above 870°C . Their fracture toughness is, however, limited. They cannot be hot deformed and must be cast and machined. Many of the properties of these alloys will be separated into these subclassifications for clarity.

Present-day investment-cast superalloys maintain high tensile and creep strengths through 600°C while maintaining excellent oxidation resistance. In addition, room-temperature ductility is maintained at 2–3% and fracture toughness at $25\text{--}30\text{ MPa m}^{1/2}$. By far the

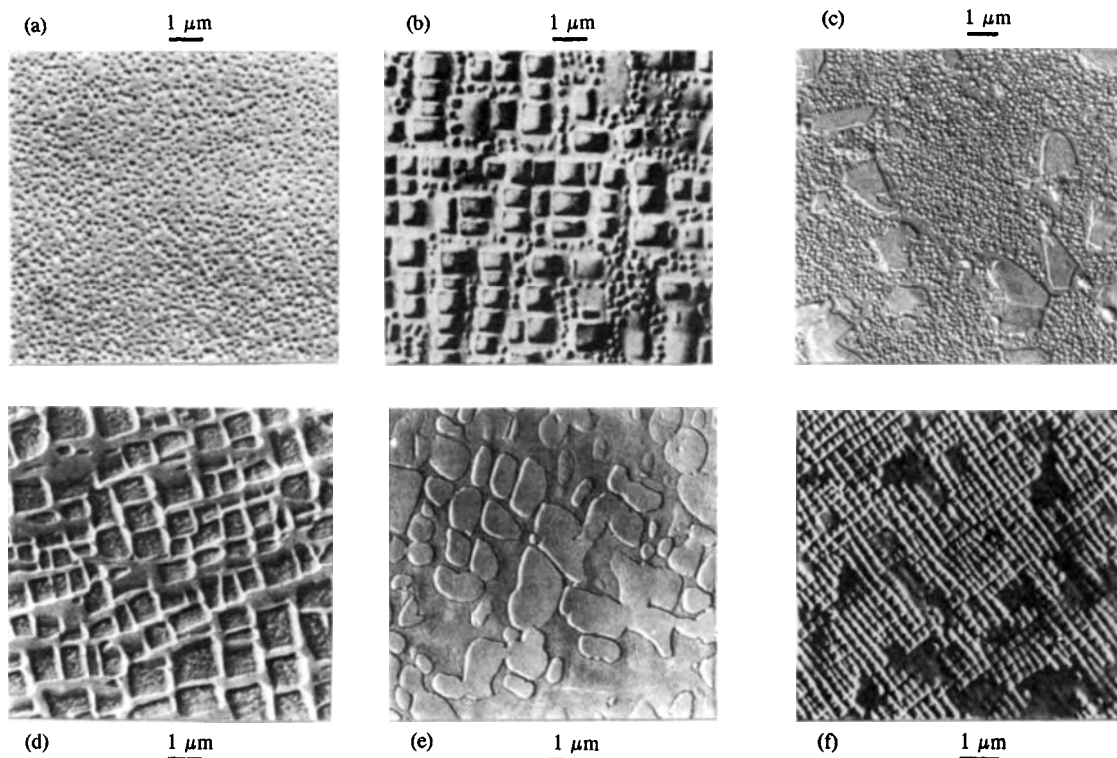


Figure 3. Microstructures of various superalloys showing the relative changes in γ' microstructure with time: (a) Waspaloy; (b) U-700; (c) IN-100; (d) B-1900; (e) Mar-M 200; (f) PWA-1480

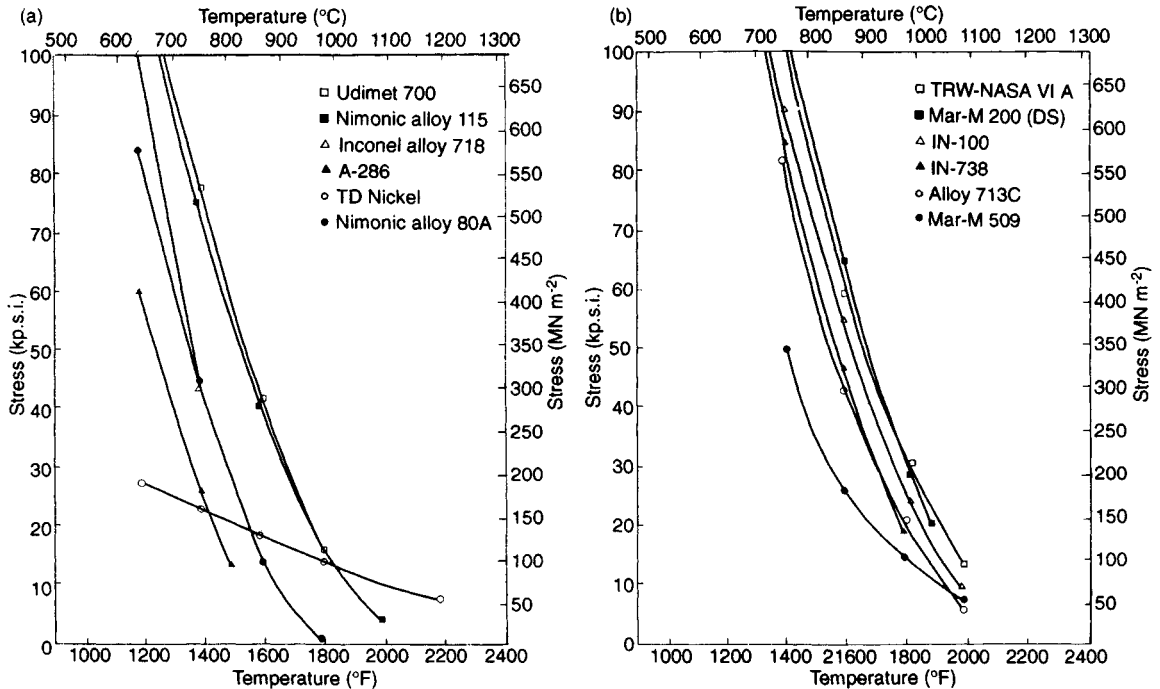


Figure 4. Stress-rupture curves for a number of superalloys showing stress required for rupture in 100 hours as a function of temperature for (a) wrought and (b) cast alloys (INCO, 1977)

most important aspect of superalloys is their ability to resist creep deformation at high loads to approximately 80% of the melting point. A summary of the stress-rupture strengths of a number of wrought and cast superalloys is given in Figure 4 (INCO, 1977). It should be noted that TD Nickel is an oxide dispersion strengthened solid solution and Mar-M 509 is a carbide dispersion strengthened, cobalt-based alloy, neither of which contains Ni₃Al precipitates but both are useful for comparative purposes. While the rupture strength of all these alloys decreases rapidly in the temperature range shown, they maintain sufficient strength to be useful through 1100 °C.

Not only do superalloys resist creep deformation upon exposure to high temperatures, but they retain strength even after exposure to elevated temperatures for prolonged periods of time. This is due to the very stable nature of the γ' precipitates. Dispersion strengthening is a function of precipitate size and spacing (Brown and Ham, 1971), and depends on the γ' particles maintaining their size after long-term, high-temperature exposure while in service. These coherent precipitates have a low particle/matrix surface energy and coarsen very slowly, in spite of high diffusion coefficients for both aluminum and nickel.

Tensile strength, another important property of superalloys, has been shown to display an anomalous increase with temperature. This behavior is shown in Figure 5 (INCO, 1977), where tensile strength is given as a function of temperature for both wrought and cast alloys. The anomalous rise in yield stress with temperature, first reported by Westbrook (1957), is most pronounced in Figure 5(b) for Mar-M 200, IN-100 and alloy 713C. These three alloys have the largest volume fractions of the ordered Ni₃Al, which is the source of this anomalous strengthening.

In addition to strength, superalloys maintain good oxidation resistance at their use temperatures. With an abundance of aluminum present in the form of Ni₃Al, many of these alloys are formers of very stable alumina. Under both static and cyclic thermal environments parabolic oxidation kinetics are initiated. However, to obtain maximum oxidation life, most superalloy hot parts are coated to enhance this property further.

Thus, these alloys possess a unique combination of properties which has been developed and honed for over 50 years. The combination of strength, ductility, fracture toughness and oxidation resistance has made superalloys unsurpassed by all other materials in high-temperature

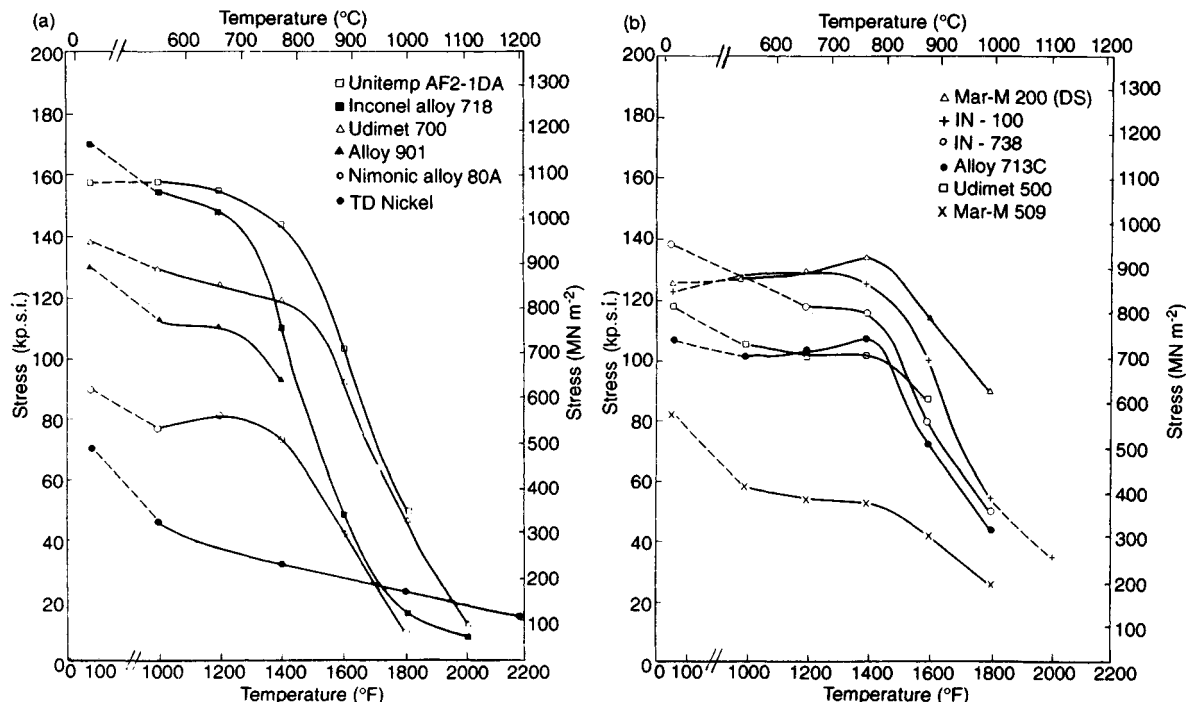


Figure 5. Yield strength curves for a number of superalloys showing stress required for yielding as a function of temperature for (a) wrought and (b) cast alloys (INCO, 1977)

structural applications. Not only is their performance outstanding at high absolute temperatures, but also in comparison to alloys of other classes with respect to their high homologous use temperature $T_{use}/T_m = 0.8$. We will now delve in a more systematic manner into the specific properties of these alloys with special attention to the role that the ordered Ni_3Al precipitates play.

2. Alloying

2.1 γ/γ' Partitioning of Alloying Additions

Table 1 shows some typical superalloy compositions, and we will briefly describe the elemental partitioning that takes place between the various microstructural components. A major work which defined the elemental partitioning to γ' was conducted by Kreige and Baris (1969), although many of the findings to be related below had been defined through other means. Through γ' phase and carbide extractions, subsequent wet chemical analysis of a number of superalloys showed broad outlines of elemental partitioning to the ordered phase.

Elements partitioning preferentially to the γ solid-solution matrix include the refractory metals V, Cr, Mo, W and Re. The Group VIIIA metals Fe and Co partition to both γ and γ' , but tend to have higher solubility within the γ' particles. Aluminum and Ti along with Nb and Ta strongly segregate to the ordered phase. The other alloy additions of B, C, Hf and Zr are used to stabilize grain boundary precipitates and have little solubility in γ' .

Titanium and Ni form the ordered Ni_3Ti phase which has the $L1_2$ -derivative $D0_{24}$ (hP16) structure. Thus Ti has a high degree of solubility in γ' , substituting for aluminum, and is the other primary γ' precipitate former. A number of superalloys rely primarily on Ti to form the ordered strengthening phase, an example being Waspaloy, as listed in Table 1.

Vanadium, Nb and Ta also substitute primarily for Al and act as solid-solution strengtheners within the ordered precipitates. Owing to atomic size relationships, Fe and Cr do not preferentially substitute within γ' but tend to occupy both Ni and Al sites. Cobalt, however, substitutes preferentially for Ni, being adjacent in the Periodic Table and chemically similar. The site occupancy of various alloying elements is very clearly displayed

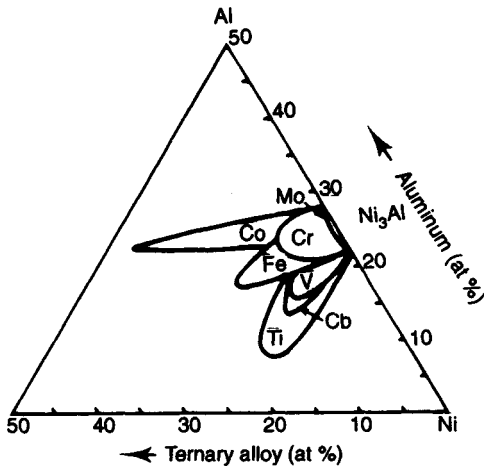


Figure 6. Ternary Ni–Al–M phase diagram at 1100 °C showing approximate solubility and site occupancy in Ni₃Al (Decker, 1969a)

in Figure 6, which shows a pseudoternary phase diagram for Ni–Al–M, where M is the ternary addition to the ordered γ' . Both the extent of solubility and the site occupancy can easily be found in this well-known diagram and have also been reviewed elsewhere (Ochaia *et al.*, 1984).

2.2 Phase Stability and Electron Hole Calculations

Early on in superalloy development it was determined that alloy modification would lead to enhanced properties. The limit to which various alloying additions could be made before unwanted phases such as σ , μ and Laves precipitated, needed to be predicted to accelerate alloy development (Sims *et al.*, 1987). These phases tend to precipitate in a platelike morphology and promote cracking during creep exposure. While electron hole calculations are not directly related to γ' in superalloys, they help predict the limits of alloying before precipitation of other intermetallics occurs. One must remember that in such complex multicomponent alloy systems, the phase rule allows a large number of phases to be present.

In studies of the magnetic properties of the first row of transition elements by Pauling (1938), calculations of electron hole numbers N_v were made. These electron holes can be thought of as hybridized spd electron orbitals which are used in bonding but are not filled. From these calculations and subsequent magnetic moment experiments, the following N_v element designations resulted: 4.66 for Cr, 3.66 for Mn, 2.22 for Fe, 1.71 for Co and 0.61 for Ni. It was further assumed

that all elements in a group maintained the same N_v number (i.e. the N_v for Group VIA elements Cr = Mo = W = 4.66).

The average electron hole number N_v for an alloy can be numerically summed such that

$$\bar{N}_v = \sum_{i=1}^n [m_i] (N_v)_i \quad (1)$$

where $[m_i]$ is the atomic concentration and $(N_v)_i$ is the electron hole number of metal i in a multicomponent alloy. This methodology was used by Greenfield and Beck (1954, 1956) to predict the occurrence of ternary σ (D8_b, tP30) phases in Cr–Ni–Mo, Cr–Co–Mo and Cr–Co–Fe alloys. This work resulted in the definition of σ phase stability in the N_v range of 3.16–3.66. Alloys with smaller N_v values would precipitate austenite while those with larger N_v values would precipitate the next ordered compound in that series. Ultimately, predictions of complex phase diagrams should be possible.

This analysis was first commercially used to predict long-term superalloy stability, and has come to be known as PHACOMP, an acronym for PHase COMPUtation. To perform these calculations in superalloys, it is assumed that the deleterious phase precipitates from the Ni solid solution, and thus the elemental concentrations in the γ phase are all that are of interest. An empirically derived set of relations has been determined for these alloys to take into account precipitation of carbides, borides and γ' . The remaining elemental composition in the austenitic matrix is input into equation (1) and an average electron hole number is generated for that matrix. In practice, the σ phase can be avoided if N_v is less than approximately 2.5. In complex alloys, N_v values vary downward and descend to about 2.15 for IN-713C.

3. γ' Morphology

3.1 γ' Coarsening

The major difference between superalloys and the ordered Ni₃Al alloys covered elsewhere in this volume by Liu and Pope is the vast interfacial area between the solid-solution γ and the ordered γ' precipitates. At 70 vol% γ' and a particle diameter of 0.1 μm the γ/γ' interface surface area is on the order of 4000 $\text{m}^2 \text{cm}^{-3}$. This expansive surface area greatly influences dislocations during deformation. To understand the significance of this interface, a discussion of the γ' precipitate-coarsening kinetics will be presented.

The long-term, high-temperature strength of superalloys is the direct result of the ability of γ' to resist coarsening. To understand this phenomenon, we can look at the mathematical model for precipitate coarsening first developed independently by Lifshitz and Sloyzov (1961) and Wagner (1961) and modified by Davies *et al.* (1980), as given below

$$r_t^3 - r_0^3 = \frac{64\zeta^*DC_0V_m^2\alpha^3}{9RT\beta} t \quad (2)$$

where r_t and r_0 are the particle radius at time t and initially, ζ^* is the matrix/particle interface energy, D is the solute diffusion coefficient, C_0 is the solute equilibrium concentration, V_m is the molar volume of precipitate, t is the time, R is the gas constant, T is the temperature and α and β are constants as described by Davies *et al.* (1980).

From equation (2) it can be seen that γ' coarsening is a function of interfacial energy. Since γ/γ' interfaces are coherent and of low strain, they are very low in energy. The solute concentration (the solubility of Al in Ni) is low and of the order of 2 wt% at 900 °C, as shown in Figure 2 and by Heslop (1964). The diffusivity of Al in Ni is quite high, however, with D_0 and Q having values of $1.87 \times 10^{-4} \text{ m s}^{-1}$ and 3.22 kJ mol^{-1} , respectively (Swalin and Martin, 1956). The overall result is a very stable high-temperature structure with precipitate sizes on the order of $0.1 \mu\text{m}$ at 1000 °C.

Alloying additions can modify the precipitate-coarsening kinetics significantly and hence provide further microstructural control. For example, Re additions to a complex alloy (Giamei and Anton, 1985; Giamei *et al.*, 1985a,b) were found to have negligible solubility in γ' . Since its diffusivity would be expected to be on the order of that for W in Ni, the growing γ' particles must push the Re from the γ/γ' interface. Thus Re diffusion becomes the rate-limiting step and coarsening kinetics are reduced by 30%.

3.2 γ/γ' Misfit

As previously shown, the cubic morphology of the γ' precipitates is a striking feature of superalloy metallography. This cubic shape is the result of the elastic strains generated by the small lattice misfit between the γ matrix and the γ' precipitates. As schematically depicted in Figure 2(c), the precipitates generally have a lattice parameter which is greater than that of the matrix.

This misfit δ is defined as

$$\delta = \frac{a_{\gamma'} - a_{\gamma}}{a_{\gamma}} = \frac{\Delta a}{a_{\gamma}} \quad (3)$$

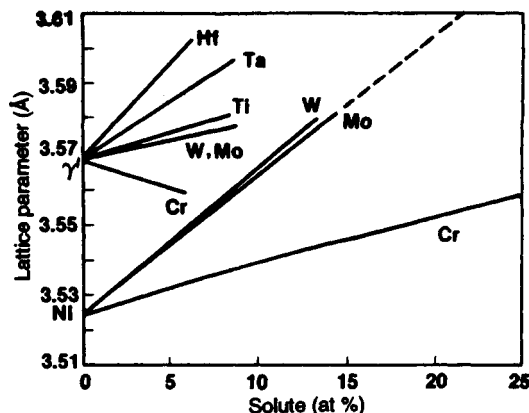


Figure 7. Lattice parameters of Ni and Ni_3Al solutions at room temperature versus alloy content (Giamei *et al.*, 1985)

where a_{γ} and $a_{\gamma'}$ are the lattice parameters for the γ and γ' phases, respectively. For superalloys, typical lattice misfits are +0.2 to +0.5% at room temperature. Alloy additions also have varying effects on the lattice parameter (Giamei *et al.*, 1985a,b). This strain energy is further complicated by a difference in thermal expansion between the two phases and differences in elastic compliances (Nathal *et al.*, 1985). These complications cause the differences in cuboid shape from one alloy to another, as can be seen in Figure 3. Where the misfit strain at temperature is minimal, the precipitates are spherical; high lattice misfits result in cuboids with straighter sides and sharper corners.

In some cases, the misfit strain becomes so high that interfacial dislocations are formed between the γ and γ' phases, the precipitates become semicoherent and the interfacial energy increases. These misfit dislocations will also influence glide dislocations as they shear through the ordered precipitates, but their full impact is not understood.

The lattice parameters of both γ and γ' phases are influenced by alloy additions. Figure 7 shows the ambient-temperature lattice parameters as a function of solute concentration. Increasing chromium concentrations, for instance, increase the lattice spacing in γ , while they decrease the lattice spacing in γ' . On the other hand, W and Mo additions increase both, but at different rates. Some of the newer single-crystal superalloys change their misfit sign from positive to negative as temperature is increased (Nathal *et al.*, 1985). This has profound implications for stress coarsening as will be described below.

3.3 Duplex Microstructure

Referring back to Figure 2(a), close examination of the Ni/Ni₃Al phase boundary shows that the solubility of Al within the Ni solid solution increases with increasing temperature. Heat treatments at progressively lower temperatures will thus precipitate successively finer γ' dispersions as the aluminum solubility decreases. The terms duplex and triplex microstructures refer respectively to two and three distinctively different γ' dispersion sizes. Representative duplex microstructures are given in Figure 3 in alloys U-700 and IN-100. These microstructural modifications can be exploited to widen further the operating conditions under which superalloys can be used. For instance, large precipitate size is beneficial in maximizing creep resistance, while a second smaller dispersion would better disperse planar slip and enhance yield and fatigue properties. These complex γ' structures are widely employed in turbine disk applications where a broad temperature range and diverse loading conditions are encountered in a single component, thus varying critical conditions.

3.4 Stress Coarsening

Stress coarsening of the ordered γ' precipitates has been studied extensively because of its occurrence in parts in

service. This phenomenon occurs when the alloy is subjected to high stresses and elevated temperatures simultaneously, as in creep testing or extended service. Remember that the elastic strains caused by the γ/γ' lattice mismatch result in cuboidal precipitate growth. If an external elastic strain is imposed on the crystal, the precipitate morphology will change to minimize the higher energy interfaces. This behavior is indeed observed, and the resultant γ' shape is a function of crystal orientation and the sign of the γ/γ' lattice mismatch (Tien and Copley, 1971). In a positive misfit, $\langle 001 \rangle$ -oriented single crystal, an imposed tensile strain will cause the precipitates to grow as rods parallel to the stress axis, while compressive strains will cause the precipitates to grow into plates perpendicular to the stress axis. In negative misfit alloys the reverse effects will occur. This behavior for the latter case is schematically depicted in Figure 8. After the alloys have been heat treated and the γ' precipitates reach approximately $0.5\ \mu\text{m}$, their morphology can only be changed through very long, high-temperature, stressed exposure. Long-term in-service exposures have been shown to induce such rafts (Nakada and Leslie, 1967; Mirkin and Kanchev, 1967). In the asolutioned and quenched condition, however, rafts of γ' can readily be formed.

A micrograph of a typical stress-coarsened γ' microstructure is given in Figure 9 along with a plot of yield

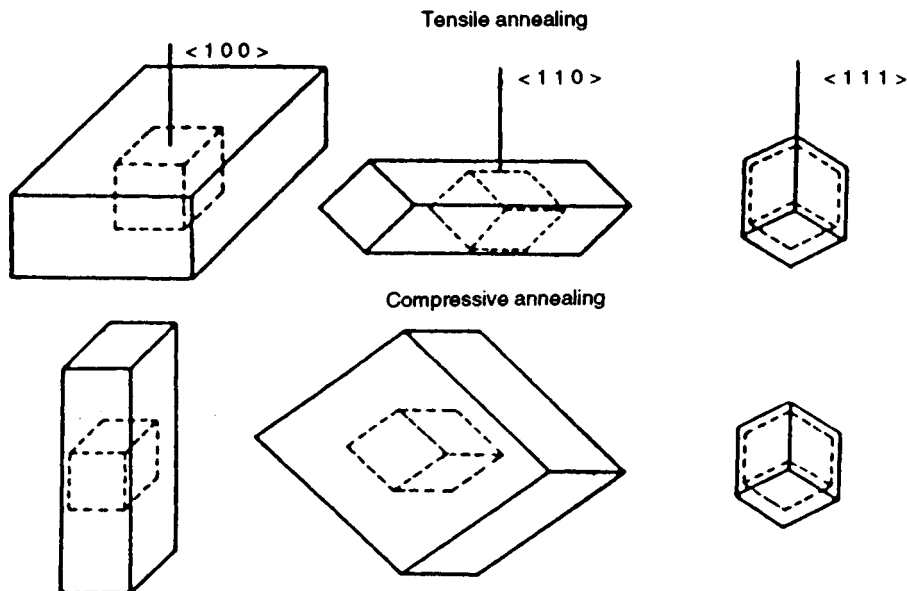


Figure 8. Schematic representation of γ' morphologies due to imposed elastic strains along the vertical axis during coarsening (Tien and Copley, 1971)

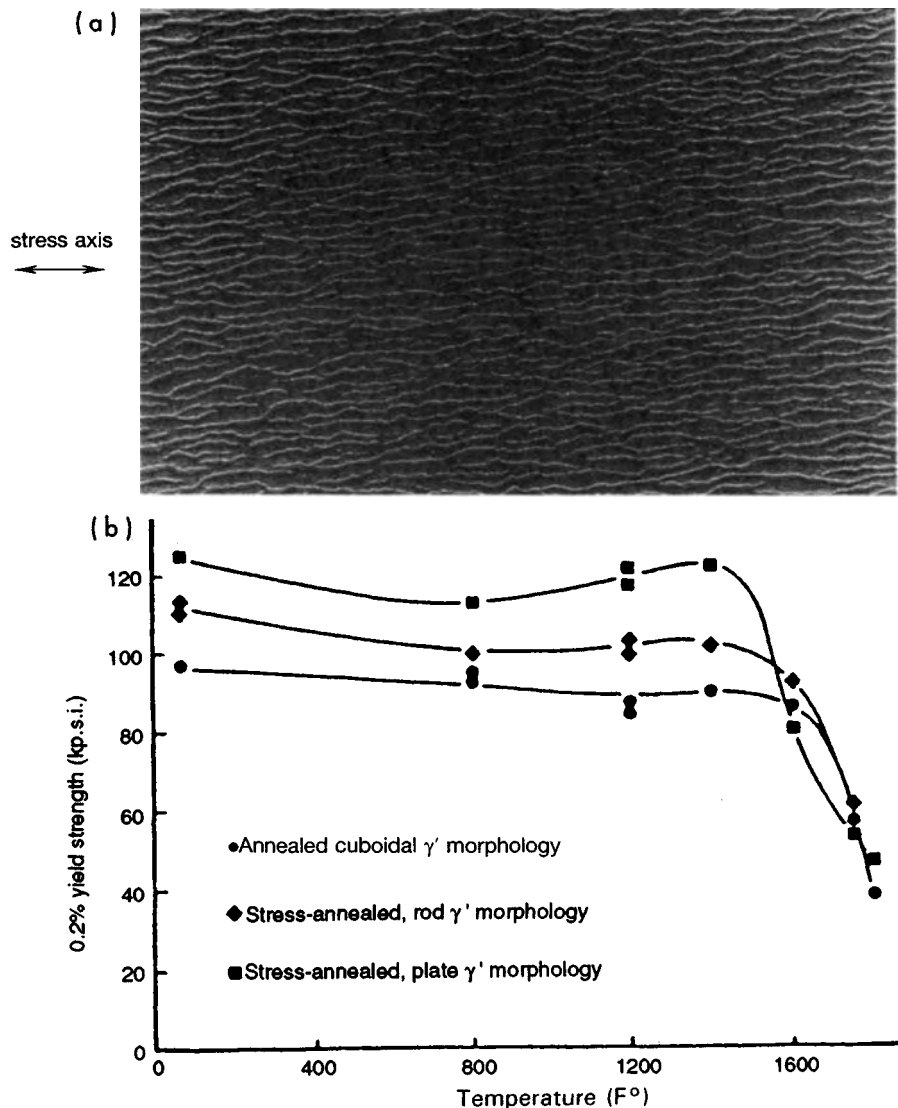


Figure 9. (a) Typical tensile stress coarsened γ' in a $\langle 001 \rangle$ -oriented, positive-misfit alloy and (b) plot of yield strength versus temperature showing strength increments of stress-coarsened superalloys (Tien and Gamble, 1972)

strength versus temperature for an alloy with varying γ' morphologies (Tien and Gamble, 1972). The micrograph was taken of a single crystal with the tensile load axis parallel to the $\langle 001 \rangle$ crystallographic axis and oriented in the horizontal direction. The resulting γ' laths or rafts are of a large aspect ratio and would pose a significant barrier to dislocation motion.

The yield stresses for cuboidal, rod and plate γ' in $\langle 001 \rangle$ -oriented U-700 single crystals are given in Figure 9(b). At low to intermediate temperatures, the platelike γ' is significantly stronger than the rodlike γ' , which

in turn is stronger than the cuboidal form. Additionally, the platelike γ' displays the anomalous hardening to a larger extent than the other two morphologies. The mechanism behind this strengthening involves the inability of glide dislocations to avoid or climb around elongated particles. In both the plate and rod forms, dislocations must intersect and cut the ordered phase, thus leading to greater strengths, whereas some of the dislocations can avoid shearing cuboidal precipitates through diffusional climb mechanisms or cross slip. While Figure 9(b) may imply that the strength differential

between these precipitate morphologies is negligible above 870 °C, platelike γ' has been shown to be an effective creep strengthener in $\langle 001 \rangle$ -oriented crystals at temperatures exceeding 1000 °C (Pearson *et al.*, 1981). Under these conditions, climb of dislocations around the precipitates cannot occur, effectively limiting dislocation motion.

4. Deformation

The high-temperature strength of superalloys cannot be explained solely from the properties of the disordered γ phase nor the ordered γ' phase, but through the intimate association between the two via their coherent nature. The strength in both tension and creep is thus a synergistic effect of the two phases, resulting in a very beneficial combination of properties. A brief discussion of the dislocation dynamics in superalloys will be given, followed by a summary of the mechanical properties in model alloys (see also the chapter in Volume 1 by Veyssi re and Douin).

4.1 Dislocation Dynamics

Motion of dislocations is essential to ductility and toughness. The primary glide dislocation type in the f.c.c. Ni solid solution is $\frac{1}{2}\langle 011 \rangle\{111\}$, and these dislocations are glissile throughout all temperatures. Since screw dislocations are considered rate limiting because their mobility is significantly lower than edge-type dislocations, they have attracted more theoretical attention. The $\frac{1}{2}\langle 011 \rangle\{111\}$ slip system is also operative in the L1₂ structure, but a number of other dislocation types formed at high temperatures have also been identified. These high-temperature dislocations are referred to as thermally activated dislocations since they are found only during high-temperature deformation. Reviews by many authors (Copley and Kear, 1967; Stoloff, 1989; Hirano, 1990; Memker *et al.*, 1991; Hirsch, 1992) go into the details of dislocation types, stacking faults, etc. found after elevated-temperature deformation of the ordered structure (see also the chapters by Ardell (this volume, Chapter 12), Liu and Pope (this volume, Chapter 2), Sun (Volume 1) and Veyssi re and Douin (Volume 1, Chapter 22)).

The most important competing slip system to $\langle 011 \rangle\{111\}$ is the $\langle 011 \rangle\{001\}$ type, referred to as cube slip since it occurs on the crystallographic cube planes. The occurrence of this thermally activated glide system is thought to be in large part responsible for the anomalous strengthening in Ni₃Al and superalloys. At temperatures above 400 °C, a $\langle 011 \rangle\{111\}$ glide dislocation

moving through the disordered matrix will eventually encounter one of the γ' particles. When it enters the ordered particle, it becomes susceptible to cross slip onto one of the $\{001\}$ planes. As sections of the dislocation cross slip first onto the $\{001\}$ plane and subsequently back onto the $\{111\}$ plane, kinks of sessile $\langle 011 \rangle\{001\}$ dislocations are left behind. These immobile dislocation segments, known as Kear–Wilsdorf locks (Kear and Wilsdorf, 1962), are only mobile through diffusional processes at this temperature. The formation of the locks within the γ' particles causes rapid work hardening of the structure.

At temperatures above 700 °C, the $\langle 011 \rangle\{001\}$ segments become glissile, and the locks are lost. General alloy softening results, with a rapid decrease in strength with temperature.

4.2 Mechanical Response

The tensile strengths of an Ni–Cr solid solution and various γ' volume fractions in Ni–Cr–Al alloys as a function of temperature are given in Figure 10 (Beardmore *et al.*, 1969), which illustrates the effect of γ' volume fraction on the flow stress. The critical point in this figure is that the single-phase compositions of either phase are weak at room and intermediate temperatures while the precipitation-hardened alloys show considerable strength from ambient through 800 °C. As the γ' volume fraction increases from 20 to 60%, the anomalous strength increase with temperature becomes more apparent

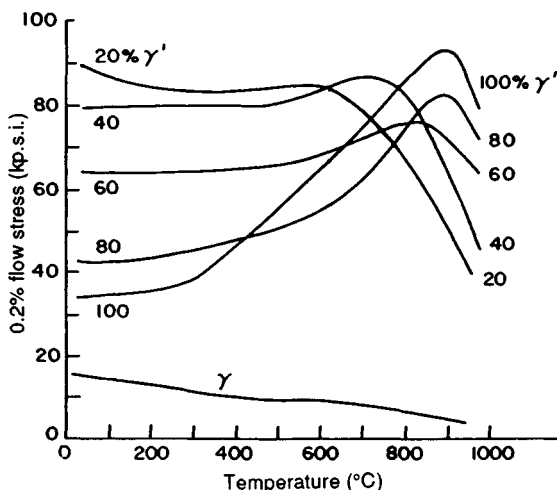


Figure 10. Yield stress as a function of temperature for Ni–Cr–Al alloys containing various amounts of the ordered γ' within the disordered, solid-solution γ . Note that the anomalous hardening with increasing temperature is evident in alloys with as little as 40% γ' (Beardmore *et al.*, 1969)

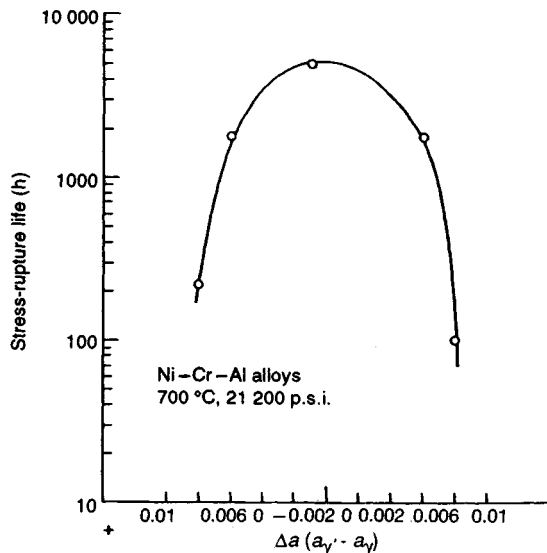


Figure 11. The influence of lattice mismatch on stress-rupture life in Ni-Cr-Al alloys showing maximum creep resistance with minimum lattice mismatch (Mirkin and Kanchev, 1967)

while the intermediate-temperature strength drops. The cube cross slip mechanism and the formation of Kear-Wilsdorf locks have been used to model this intermediate-temperature and high-temperature thermally activated strengthening, while the mechanisms behind the low and intermediate strength lie in classical dispersion-strengthening theory. In this special system, we can obtain the combined strengths of the two individual phases, a unique situation in nature.

Following from the description given above, the creep strength of these two-phase alloys is dominated by the properties of the ordered phase at high temperatures. This can only be achieved because a dislocation passes through both phases simultaneously. The weak link is thus avoided, and the stronger phase dominates. The γ/γ' interface is of critical importance, however, as pointedly illustrated by Mirkin and Kanchev (1967) in Figure 11. Rupture life at 700 °C and 150 MPa, plotted as a function of lattice parameter difference $a_{\gamma'} - a_{\gamma}$, is clearly maximized with minimum Δa . It has been recognized that enhanced creep life in these alloys is due to maintenance of a fine γ' dispersion. Referring back to equation (2), one can see that the precipitate-coarsening rate is proportional to the matrix/particle interface energy, which in turn is minimized with diminished lattice mismatch interfacial strains.

5. Summary and Future Considerations

After first being commercially utilized in the late 1930s, superalloys and their austenitic predecessors developed rapidly over the subsequent 50 years. Many of the advances in high-temperature capability evolved through innovative processing techniques such as vacuum melting and controlled solidification.

The high-temperature strength and stability of nickel-based superalloys are due to the presence of the coherent Ni_3Al precipitates (L1_2 crystal structure) with low interfacial surface energy, thereby minimizing the precipitate-coarsening rate. Creep and tensile strengths, as well as oxidation resistance, have been optimized through alloy additions both to enhance solid-solution hardening of γ and γ' , the two constituent phases, and to optimize the effect of the interface between them. The interface which can be either positive or negative in misfit, dictates much of the high-temperature behavior of these alloys.

Future research in the superalloy field is turning from strength enhancement towards processing improvements. These alloys are now being used to 80–90% of their homologous melting temperature, far in excess of any other alloy system. Industrial research is focused on new and more efficient methods of processing these alloys as well as on being able to manufacture more consistent products.

This model of an alloy systems concept, development and maturation should be used as a road map for those working in the area of intermetallics. With eight to ten years of advanced intermetallic development behind us, the 60 years of superalloy development that went into highly successful utilization should serve as an inspiration.

6. Acknowledgements

The author would like to acknowledge the helpful discussions with Dr D. M. Shah in preparing this manuscript. The help of Mr G. McCarthy and especially Mr M. Donachie in obtaining various superalloy micrographs is also gratefully recognized.

7. References

- Beardmore, P., Davies, R. G., and Johnston, T. L. (1969). *Trans. Metall. Soc. AIME*, **245**, 1537.
- Brown, L. M., and Ham, R. K. (1971). In *Strengthening Methods in Crystals* (eds A. Kelly and R. B. Nicholson). John Wiley & Sons Ltd, New York.

- Copley, S. M., and Kear, B. H. (1967). *Trans. Metall. Soc. AIME*, **239**, 984.
- Davies, C. K. L., Nash, P., and Steves, R. N. (1980). *Acta Metall.*, **28**, 179.
- Decker, R. F. (1969a). Climax Molybdenum Co. Symposium, Zurich, May.
- Decker, R. F. (1969b). *Trans. ASM*, **62**, 481.
- Erickson, G. L. (1990). In *Metals Handbook*, 10th edn, Vol. 1. ASM International, Metals Park, OH, p. 981.
- Gell, M., Duhl, D. N., Giamei, A. F. (1980). In *Superalloys 1980* (eds J. K. Tien, S. T. Wlodek, H. Morrow, III, M. Gell, and G. E. Maurer). ASM International, Metals Park, OH, p. 205.
- Greenfield, P., and Beck, P. A. (1954). *Trans. TMS-AIME*, **200**, 253.
- Greenfield, P., and Beck, P. A. (1956). *Trans. TMS-AIME*, **206**, 256.
- Giamei, A. F., and Anton, D. L. (1985). *Metall. Trans.*, **16A**, 1997.
- Giamei, A. F., Pearson, D. D., and Anton, D. L. (1985a). *Metall. Trans.*, **16A**, 1997.
- Giamei, A. F., Pearson, D. D., and Anton, D. L. (1985b). In *High Temperature Ordered Intermetallic Alloys* (eds C. C. Koch, C. T. Liu, and N. S. Stoloff). *MRS Proc.*, **39**, 293.
- Hansen, M. (1958). *Constitution of Binary Phase Diagrams*. McGraw-Hill, New York, p. 119.
- Harris, K., Erickson, G. L., and Schwer, R. E. (1990). In *Metals Handbook*, 10th edn, Vol. 1. ASM International, Metals Park, OH, p. 995.
- Heslop, J. (1964). *Cobalt*, **24**, 128.
- Hirano, T. (1990). *Acta Metall. Mater.*, **38**, 2667.
- Hirsch, P. J. (1992). *Prog. Mater. Sci.*, **36**, 63.
- Hoppin, III, G. S., and Danesi, W. P. (1987). In *Superalloys II* (eds C. T. Sims, N. S. Stoloff, and W. C. Hagel). John Wiley & Sons, Inc., New York, p. 549.
- INCO (1977). *Nickel Base Alloys*. International Nickel Co., New York, p. 28.
- Kear, B. H., and Wilsdorf, H. G. F. (1962). *Trans. AIME*, **224**, 382.
- Kreige, O. H., and Baris, J. M. (1969). *Trans. ASM*, **62**, 195.
- Lifshitz, I. M., and Sloyzov, V. V. (1961). *J. Phys. Chem. Solids*, **19**, 35.
- Memker, K. J., Mills, M. J., and Nix, W. D. (1991). *Acta Metall. Mater.*, **39**, 1901.
- Mirkin, I. L., and Kancheev, O. D. (1967). *Met. Sci. Heat Treat.*, **1/2**, 10.
- Nakada, Y., and Leslie, W. C. (1967). *Trans. ASM*, **60**, 223.
- Nathal, M. V., Mackay, R. A., and Garlick, R. G. (1985). *Mater. Sci. Eng.*, **75**, 195.
- Ochaia, S., Oya, Y., and Suzuki, T. (1984). *Acta Metall.*, **32**, 289.
- Pauling, L. (1938). *Phys. Rev.*, **54**, 899.
- Pearson, D. D., Kear, B. H., and Lemkey, F. D. (1981). In *Creep Fracture of Engineering Materials and Structures* (eds R. W. Evans and B. Wilshire), Pineridge Press, London, p. 213.
- Sims, C. T. (1984). In *Superalloys 1984* (eds M. Gell, C. S. Kortovich, R. H. Bricknell, W. B. Kent, and J. F. Radavich). TMS, Warrendale, PA, p. 399.
- Sims, C. T., Stoloff, N. S., and Hagel, W. C. (eds) (1987). *Superalloys II*. John Wiley & Sons Ltd, New York.
- Stoloff, N. S. (1989). *Intl. Met. Rev.*, **34**, 153.
- Stoloff, N. S. (1990). In *Metals Handbook*, 10th edn, Vol. 1. ASM International, Metals Park, OH, p. 950.
- Swalin, R. A., and Martin, A. (1956). *Trans. AIME*, **206**, 483.
- Tien, J. K., and Copley, S. M. (1971). *Metall. Trans.*, **2**, 543.
- Tien, J. K., and Gamble, R. P. (1972). *Metall. Trans.*, **3**, 2157.
- Wagner, R. (1961). *Z. Elektrochem.*, **65**, 581.
- Westbrook, J. H. (1957). *Trans. AIME*, **209**, 898.

This chapter was originally published in 1995 as Chapter 1 in *Intermetallic Compounds*, Vol. 2: *Practice*, edited by J. H. Westbrook and R. L. Fleischer.

Addendum

Westbrook (1996) has recently published a review of the history of superalloys, emphasizing the development of the concept of dislocations and their behavior in superalloys and in the intermetallics contained therein. In this article he

also projects likely future developments and challenges.

Westbrook, J. H. (1996). Chapter 48 in *Dislocations in Solids* F. R. N. Nabarro and M. S. Duesbery, eds., pp. 1-26, Elsevier Science BV.

Chapter 4

Gamma TiAl and its Alloys

S. C. Huang

General Electric Corporate Research and Development, PO Box 8, K1-MB275, Schenectady, NY 12301, USA

J. C. Chesnutt

General Electric Aircraft Engines, 1 Neumann Way, M-89, Cincinnati, OH 45215, USA

1. Background

TiAl-based materials are pursued mainly because of the desire to raise the thrust-to-weight ratio of high-performance aircraft engines. The aircraft industry has realized much of its success through steady increases in the temperature capability of critical parts. To increase further the specific thrust, one would have to develop lightweight materials such as those based on γ -TiAl. The interest in γ (L1₀, tP4) started about 40 years ago, but there were no practical breakthroughs in the alloy design and processing until the past five years. The recent progress has raised the interest to a high level. Several applications are being considered for aircraft and automobile engines.

The purpose of this chapter is to review the recent progress in the development of this new class of materials. Although most of the alloys of interest for applications are multiphased, it will be instructive to review the characteristics of the compound before discussing ways in which different microstructures can be produced by stoichiometric control and alloying additions. The effect of microstructure on properties will then be reviewed, followed by a discussion of the methods of processing to achieve desired properties and obtain useful product forms. Finally, the potential applications that provide the impetus for the development of γ -based materials will be discussed.

2. Basic Characteristics of γ -Based Materials

In this section, the physical attributes and the deformation barriers will be briefly described.

2.1 Physical Properties

γ -TiAl (L1₀, tP4) is an ordered, equiatomic compound of the lightweight elements Ti and Al. Its low density, which is less than half of that of superalloys, is an important attribute for gas turbine engine applications. Lightweight materials increase the engine performance as measured by thrust-to-weight ratio. The benefit can be more than pound for pound savings, since the use of a lightweight rotating part frequently reduces the dimensions of the stress-supporting structures. Additionally, the high aluminum content of this compound increases the resistance to oxidation and burning, two critical concerns in the use of titanium-based materials.

γ -TiAl remains ordered to melting at $\sim 1440^\circ\text{C}$. The strong Ti-Al bond leads to a high activation energy for diffusion. This high-energy barrier helps to retain strength and resist creep to high temperatures when diffusion becomes the rate-controlling process. It also results in high stiffness over a wide temperature range, as shown in Figure 1, making possible its use for static parts that need only to sustain elastic deflection (Lipsitt, 1985). However, the rigid bond structure restricts the ability to accommodate plastic deformation. As with most other intermetallic compounds, γ , without modification, lacks the ductility and toughness that are necessary for structural applications. Its high thermal conductivity allows easier cooling of hot parts. Some properties of titanium aluminide alloys and superalloys are shown in Table 1.

2.2 Deformation Mechanisms

The brittle behavior of γ -TiAl is inherently related to its crystal structure, which is a face-centered tetragonal

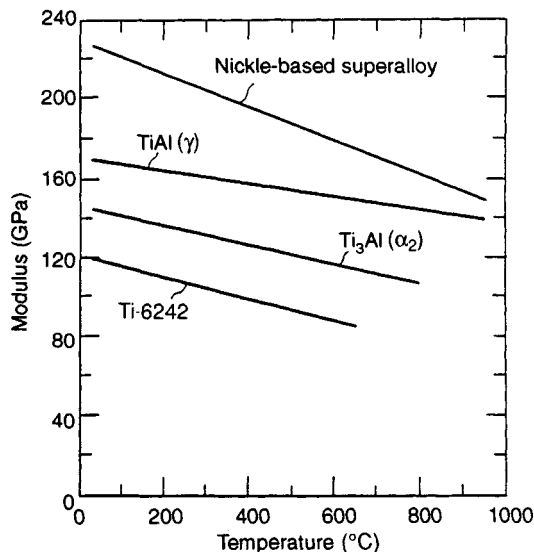


Figure 1. Modulus of TiAl as a function of temperature in comparison to other materials

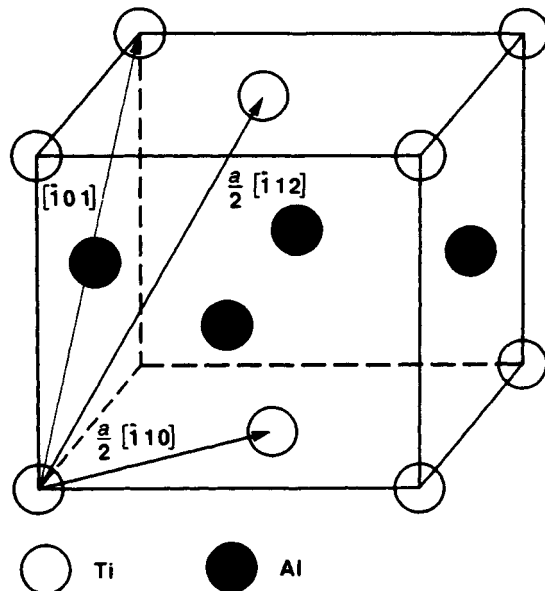


Figure 2. The unit cell of TiAl, with the three slip vectors of lowest energy in the $\{111\}$ planes

(f.c.t.) $L1_0$ with alternating (002) planes of Ti and Al atoms (Figure 2). The tetragonality is very small ($c/a=1.02$), but the $L1_0$ ordered structure creates a non-equivalency among the $\langle 110 \rangle$ slip vectors. As in cubic structures, slip generally occurs on $\{111\}$ planes in close-packed directions (Marcinkowski *et al.*, 1961). There are three low-energy Burgers vectors (Figure 2). The $\frac{1}{2} [110]$ dislocations are the lowest in energy and equivalent to the normal slip mode in face-centered cubic (f.c.c.) materials. They have been referred to as the 'easy slip' dislocations. The $[101]$ dislocations, which are equivalent to $[011]$ but not $[110]$, are higher-energy superdislocations. The $\frac{1}{2} [112]$ are also

superdislocations on the close-packed planes. Slip systems on planes that are not close packed, such as $\langle 100 \rangle [110]$, have even higher energies, and they are active only at elevated temperatures.

A number of dissociation reactions are possible for the superdislocations. Much as in the related $L1_2$ structure such as Ni_3Al , the reactions can occur on the $\{111\}$ planes and will create partial dislocations that are separated by either an antiphase boundary, a stacking fault or both. In TiAl, the antiphase boundary energy is two to four times higher than the stacking fault energy, and this difference affects the configuration of superdislocation core structures (Greenberg, 1970, 1973). Note that dissociation of superdislocations leads to the separation of a Shockley partial $\frac{1}{2} [112]$, creating a $\{111\}$ stacking fault. Note further that the Shockley is a twin dislocation in TiAl.

Dissociation of dislocations on intersecting $\{111\}$ or other crystallographic planes is possible (Greenberg, 1970, 1973). A cross slip of a partial dislocation frequently develops a sessile configuration which further reduces the mobility of superdislocations. The mobility of the 'easy slip' unit dislocations has also been called into question according to a Peierls stress calculation (Greenberg *et al.*, 1991). The dislocation mobility has a significant implication for the strength and fracture behavior of γ . Other fracture mechanisms involve the interaction of different dislocations, which leads to

Table 1. Properties of titanium aluminide alloys and superalloys

Property	α_2 alloys	γ alloys	Superalloys
Density (g cm^{-3})	4.1–4.7	3.8–4.0	8.3
Young's modulus (GPa)	120–145	160–175	206
Ductility (%)	2–5	1–3	3–5
Yield strength (MPa)	700–990	400–650	1100
Thermal conductivity ($\text{W m}^{-1} \text{K}^{-1}$)	7	22	11
Phase stability limit (°C)	1180	1440	1450
Creep limit (°C)	750	900	1090
Oxidation limit (°C)	650	900	1090

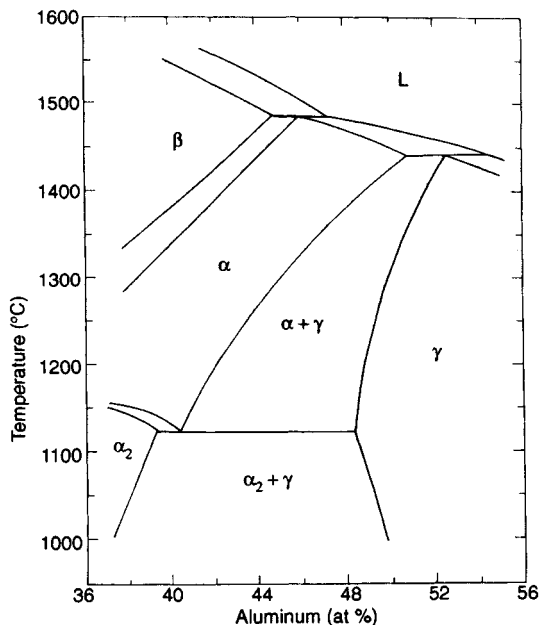


Figure 3. A partial Ti–Al phase diagram near the stoichiometric TiAl composition

locking, pileup and cleavage crack nucleation (Kawabata *et al.*, 1988b).

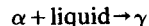
3. Microstructure Formation

One effective way to improve the deformability of γ is through microstructural control. As in conventional metallic materials, microstructural control forms the foundation for alloy design. In this section, the homogeneous microstructures obtainable by wrought processing of ingots or rapid solidification will be discussed.

3.1 High-Temperature Phase Relationships

The Ti–Al binary phase diagram of Murray (1986) was commonly used in the past. Recently, there have been significant modifications on the diagram near the γ -TiAl phase field (McCullough *et al.*, 1989; Huang and Siemers, 1989; Mishuda and Perepezko, 1991). For example, γ has been shown to be in equilibrium with α -Ti (A3, hP2) not just to 1240 °C but to the melting temperature of \sim 1460 °C. Figure 3 is a diagram reflecting these modifications. It appears very similar to what Ence and Margolin (1961) developed more than 30 years ago.

A key point illustrated in the diagram is that the solidification and solid-state equilibria of γ -based alloys are complex and sensitive to the Al concentration. For example, γ is quite stable in Al-rich compositions. In Al-lean compositions, α -Ti can form as a result of solidification or heat treatment. Most γ alloys of technical interest contain 45–50 at% Al, and they would solidify into α -Ti as the primary phase. The γ phase only forms as a secondary phase in Al-lean alloys via the reaction



This peritectic solidification tends to result in heavy segregation and nonuniform structures, as will be discussed in detail in Section 6.1. By heat treatment, α can be equilibrated, either as a second phase in the $\alpha + \gamma$ field or as a single phase above the α transus. The transus decreases with decreasing Al content. At 45 at% Al, a single-phase α structure can be readily obtained by heat treatment above 1300 °C.

3.2 Solid-State Transformation

The phase diagram shows a eutectoid reaction, which transforms α to $\alpha_2 + \gamma$ at about 1125 °C and 40 at% Al (α_2 is D0₁₉, hP8 Ti₃Al). This univariant reaction requires diffusion-controlled phase separation. In γ -based alloys, which typically contain hypereutectoid α , the transformed structures are lamellar with typical fine spacings of only 0.1–1 μm . The transformation appears to be a fast process since it can only be suppressed by extreme quenching. Although direct evidence is lacking, most of the results suggest that the lamellar structure forms by nucleation and growth of γ plates (Blackburn, 1970; Jones *et al.*, 1988; McQuay *et al.*, 1991; Kikuchi and Yamabe, 1991). This phase separation involves very little compositional adjustment. The two-phase lamellar structure has the orientation relationship

$$(0001)_{\alpha_2} \parallel (111)_{\gamma}$$

$$[2110]_{\alpha_2} \parallel [110]_{\gamma}$$

While all the α_2 plates have the same orientation in a grain, more than one variant of γ can be found (Shechtman *et al.*, 1974). The γ plates may contain twins and antiphase domains (Feng *et al.*, 1990; Inui *et al.*, 1991), while the lamellar interfaces contain dislocation networks (Zhao and Tangri, 1991; Mahon and Howe, 1990).

The fine lamellar structure, once formed, is quite resistant to heat. It tends to coarsen slowly by the

continuous-coarsening mechanism typically associated with lamellar structures (Yamabe *et al.*, 1991). While this stability is desirable for high-temperature applications, it presents difficulties for microstructural control by heat treatment. Once a fully lamellar structure forms by solidification, for example, it tends to pin the grain boundaries and prevent the breaking up of the solidification structure. However, discontinuous coarsening is possible if single-phase γ grains are also present (Shong and Kim, 1989). The faster discontinuous-coarsening mechanism removes plates by shortening them, instead of thinning as in the case of continuous coarsening. The γ grain can readily nucleate in wrought materials where strain energy allows recrystallization or in cast materials where a significant amount of Al has segregated to the boundary areas.

β -Ti can form in low-Al compositions. However, it is only stable at high temperatures, and can readily transform to α and then the $\alpha_2 + \gamma$ lamellar structure on cooling. Since the end product is the same, it may be difficult to determine whether a lamellar structure originates from α -Ti or β -Ti.

3.3 Microstructural Types

With the aid of the phase diagram in Figure 3, we can describe various microstructures obtainable in TiAl-based materials. The classification here is primarily based on phase equilibria as a function of heat treatment temperature and alloy composition. The microstructural size scale is also a function of heat treatment time and cooling schedule, and only typical values are given below for comparison. The structures here can be readily obtained by rapid solidification or wrought processing of ingots. These processing approaches break up the solidification structure and achieve homogeneity and grain refinement through rapid solidification or work-induced recrystallization. In conventionally cast materials, the solidification structure does not respond to heat treatment as readily. It generally remains coarse and inhomogeneous after annealing, but the same microstructural classification still applies.

3.3.1 The γ , Duplex and Lamellar Structures

As a result of the solid-state phase equilibria shown in Figure 3, three distinctly different types of microstructures can be obtained by annealing (Huang and Siemers, 1989). These are shown in Figure 4. Alloys above 52 at% Al generally lie in the single-phase γ field during heat treatment, and are single-phase γ after cooling to room temperature (Figure 4a). The grains are

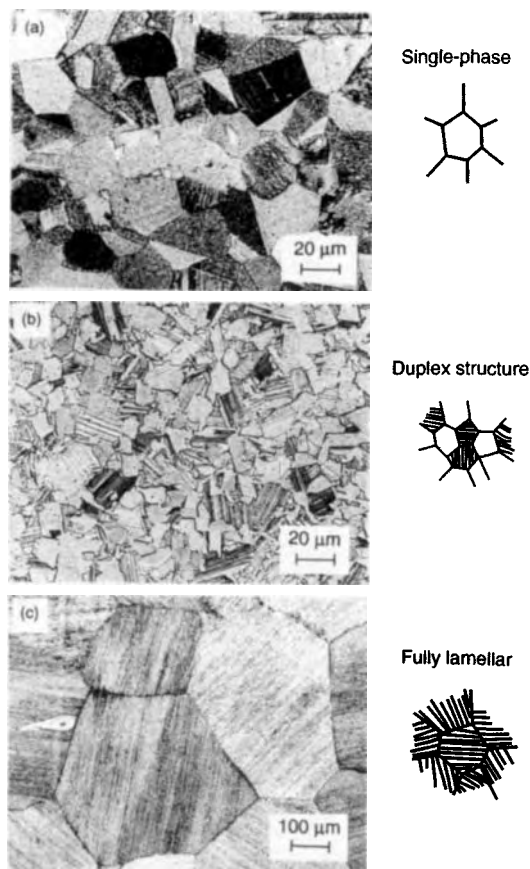


Figure 4. Typical wrought microstructures of (a) single-phase γ , (b) duplex of γ and lamellar, and (c) fully lamellar

equiaxed and about $50\text{ }\mu\text{m}$ in diameter. For alloys between 46 and 50 at% Al, heat treatment in the $\alpha + \gamma$ phase field results in a two-phase structure upon cooling (Figure 4b). This structure consists of γ grains and grains of a lamellar structure. The lamellar grains contain alternating α_2 and γ plates, which form as a result of transformation from the primary α during cooling to room temperature. The grains are typically $10\text{--}35\text{ }\mu\text{m}$ in diameter, and the lamellar plates are $0.1\text{--}1\text{ }\mu\text{m}$ thick. This structure is referred to as the duplex structure. Finally, alloys below 48 at% Al that are heat treated in the single-phase α field can form the fully lamellar structure, as shown in Figure 4(c). The grains are typically greater than $500\text{ }\mu\text{m}$ in diameter, which reflects the rapid coarsening rate of the disordered α .

3.3.2 Other Two-Phase Structures

Additional microstructures that are variations of the above can be obtained (Huang and Shih, 1991). For the duplex structure, the volume ratio between the transformed α and primary γ increases with heat treatment temperature. If a composition is heat treated at a temperature only slightly above the γ solvus, a small fraction of α will form at grain boundaries or triple points. These small α particles will still retard the growth of the γ grains, but they tend just to order into α_2 rather than transforming into the two-phase lamellar structure. This structure is referred to as the supersolvus structure. On the other hand, if the heat treatment is done at a temperature just below the α transus, a structure consisting of large transformed grains that are dispersed with small islands of undissolved γ may be obtained. This structure is referred to as the subtransus structure. Additionally, an equiaxed structure consisting of single-phase γ grains and single-phase α_2 grains may be obtained by a long-time aging in the $\alpha_2 + \gamma$ phase field below the eutectoid temperature. This structure is referred to as the dual-phase structure.

Finally, Takeyama (1992) has obtained an equiaxed γ structure containing Widmanstätten precipitation of α_2 by heat treating in the γ nose region (~ 49 at% Al at 1125°C). The α_2 plates, which have four variants of orientation, form when the annealing is followed with an up-quench to the $\alpha + \gamma$ phase region. It can also form by slow cooling through the $\alpha_2 + \gamma$ field.

4. Microstructural Dependence of Properties

The γ -TiAl compound was notorious for its low ductility, which prevented any actual uses. To resolve the low-temperature brittleness problem, early studies focused on understanding the deformation behavior of single-phase γ . Recently, Al-lean alloys containing a small fraction of Ti_3Al (α_2) were found to be significantly more ductile than single-phase alloys. The two-phase alloy concept forms the foundation for the development of current γ -based alloys.

The incorporation of α_2 as a second phase allows greater freedom for microstructural control. As we will see, microstructure strongly affects the mechanical properties of γ -based alloys. Further, there are property trade-offs among different microstructures. Each structure can be beneficial to certain properties, but detrimental to others. In the following, we discuss fundamental microstructure-property relationships which have been demonstrated in wrought binary alloys with well-defined microstructures.

4.1 Structure-Induced Property Trade-Offs

The trade-offs among ductility, toughness and creep resistance will be discussed here. Generally, the duplex structure is desirable for ductility, but poor for toughness and creep resistance. The reverse is true for the fully lamellar structure. Other trade-offs are possible, such as in the fatigue resistance, which will be discussed later. As a result, the selection of microstructure should be specific to application according to its property requirements.

4.1.1 Low-Temperature Ductility

Single-phase γ , like most other intermetallic compounds, is brittle at low temperatures (Figure 5). Even in fine-grained materials, less than 1% plastic elongation can be measured before fracture (McAndrew and Kessler, 1956; Shechtman *et al.*, 1974; Huang and Hall, 1991a). The brittle behavior appears to be intrinsic in nature, since single crystals of various orientations all have little ductility (Kawabata *et al.*, 1985).

The brittleness is likely a result of the limited dislocation mobility in this compound. A detailed deformation study (Shechtman *et al.*, 1974) shows that superdislocations do not dissociate over the entire length. Instead, the dissociation occurs locally to form faulted dipole loops, which are bounded by the $\frac{1}{2} [112]$ Shockley partials. It appears that the partials tend to be pinned, perhaps by a jog mechanism as proposed by Hug *et al.* (1986). Additionally, the density of the $\frac{1}{2} [110]$ 'easy-slip' dislocations is low in the fractured materials. This latter result, confirmed by Court *et al.* (1990), is evidence that the unit dislocations are not

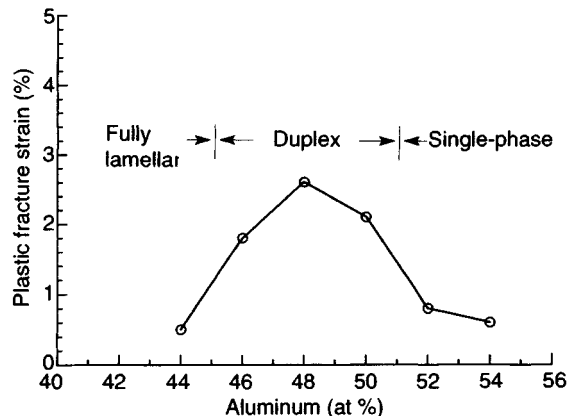


Figure 5. Room-temperature tensile ductility of wrought binary γ -based alloys as a function of Al concentration, showing the effects of microstructures

mobile either. They have been suggested to be trapped by deep Peierls stress valleys due to anisotropic chemical bonding (Greenberg *et al.*, 1991).

The brittle behavior was to be improved by alloying modification, but no practical breakthrough was made until binary alloys were systematically studied as a function of Al concentration (Huang and Hall, 1991a). Two results from the binary alloy study are critical to alloy design. First, the ductility is sensitive to microstructure. Among the three microstructures in Figure 5, the duplex structure is significantly more ductile at room temperature than the others. Second, the ductile duplex structure exists in a narrow range of Al concentration. Only the duplex alloys containing 45–50 at% Al show appreciable plasticity. The ductility peak occurs at 48 at% Al, particularly when the alloy is heat treated near the center of the $\alpha + \gamma$ phase field where the two phases have equal volume fractions. Alloys outside this composition range tend to have either the single-phase γ or the lamellar structure, and they are relatively brittle. Since the low-temperature ductility is a major concern for structural applications, the 45–50 at% Al range is usually the basis for further alloying.

The plasticity of the duplex binary alloys has been attributed to both structural and intrinsic changes (Huang and Hall, 1991a). Since the duplex structure is obtained by a two-phase ($\alpha + \gamma$) annealing, its grain size is the smallest among the three structures. Further, the primary γ grains can deform by slip of the $\frac{1}{2}$ [110] unit dislocations and twinning of the $\frac{1}{2}$ [112] Shockley partials, two deformation modes that are not active in single-phase γ alloys at room temperature. Their activation in the duplex structure may be attributed to the presence of α_2 , which absorbs interstitial oxygen from γ and modifies its dislocation core structure or stacking fault energy (Hall and Huang, 1989; Vasudevan *et al.*, 1989b). The oxygen-scavenging effect of α_2 has been confirmed by Uemori *et al.* (1992).

4.1.2 Fracture Toughness

The fracture toughness of γ -based materials is also sensitive to microstructure (Huang, 1992). For example, when Ti–48 at% Al is wrought and heat treated below the α transus to form a duplex structure, the toughness is $\sim 12 \text{ MPa m}^{1/2}$, which is about the same as a single-phase γ material. As soon as it is heat treated above the α transus to form a fully lamellar structure, the toughness increases to $\sim 22 \text{ MPa m}^{1/2}$ (Figure 6). Thus, the lamellar structure, while less ductile, is significantly tougher than the γ and duplex structures.

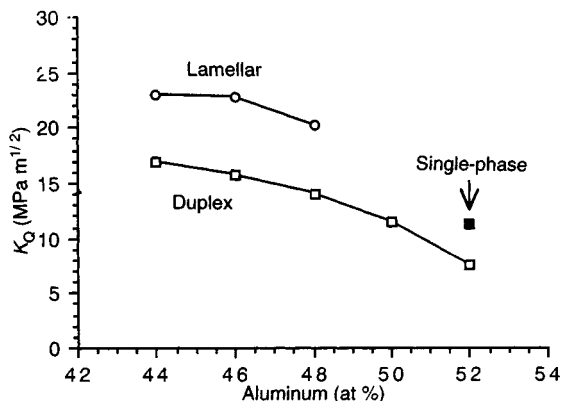


Figure 6. The fracture toughness as a function of the microstructure and Al concentration of wrought binary γ -based alloys

The lamellar toughening has been shown to arise from a composite reinforcement effect (Chan, 1992). The lamellar reinforcement is particularly effective when the crack front is perpendicular to the edges of the $\alpha_2 + \gamma$ plates (Mitao *et al.*, 1992). In this 'crack divider' orientation, the α_2 plates provide resistance to crack growth by deformation blunting and interface debonding. The local strain in front of the crack tip in the lamellar structure has been measured to reach $\sim 20\%$ (Chan, 1992), which is substantially higher than the nominal tensile ductility. The inverse relationship between toughness and ductility suggests that there is an inverse effect of grain size on the two properties. Independently, deformation by twinning in γ has also been shown to result in significant toughening (Deve *et al.*, 1992).

4.1.3 Creep Properties

The lamellar structure is not only tougher, but more resistant to creep than the γ and duplex structures (Huang, 1992; Mitao *et al.*, 1991). It significantly reduces the transient creep and the rate of the steady-state creep (Figure 7). As a result, the creep time to 0.2% strain can be increased by nearly two orders over that of the duplex structure.

The α_2 plates in the lamellar structure have been shown to resist deformation and fracture at low temperatures (Hall and Huang, 1989; Wunderlich *et al.*, 1990). However, they should become weaker than γ at the creep temperature, and provide no strengthening. Unless there is a peculiar lamellar interface-strengthening effect, we believe that the creep resistance of the lamellar structure is primarily a result of its large

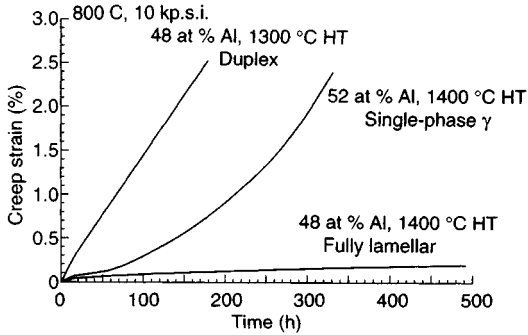


Figure 7. A comparison of the creep curves of the three typical microstructures in γ -based alloys (HT = heat treatment)

grain size. Without special control, the grain size of a lamellar structure is at least 10 times larger than the grain sizes of the other two structures. A large grain size effect has been found in a single-phase γ alloy (Takahashi *et al.*, 1990).

4.2 Further Microstructure-Property Relationships

The property trade-offs discussed above may be attributed to differences in either phase, phase distribution or grain size. The duplex structure typically has a grain size of $\sim 25 \mu\text{m}$, the single-phase γ structure $\sim 50 \mu\text{m}$, and the fully lamellar structure $\sim 1000 \mu\text{m}$. These grain size variations alone may be used to explain the observed variations in ductility. Accordingly, an interesting question is whether significantly higher ductility can be achieved in the fully lamellar structure if its grain size can be reduced. To answer this type of question, more careful measurements are needed to separate the effects of grain size and phase distribution. Some such measurements are becoming available, although significantly more work needs to be done in this area. In the following, we describe the results of two 'second-order' characterizations of the microstructure-property relationships in γ -based alloys.

4.2.1 The Grain Size Effect on γ Tensile Properties

The tensile behavior of single-phase alloys has been studied as a function of grain size controlled by varying heat treatment temperature (Huang and Shih, 1991). The yield strength σ_y systematically increases with decreasing grain sizes d (Figure 8). It shows a Hall-Petch relationship

$$\sigma_y = \sigma_0 + k_y d^{-1/2}$$

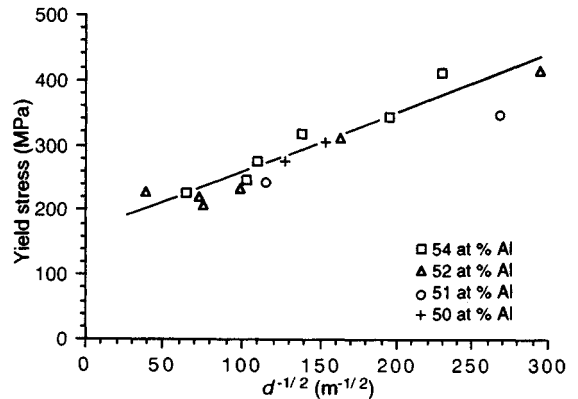


Figure 8. The Hall-Petch correlation in wrought, single-phase γ alloys

with constants $\sigma_0 \approx 150 \text{ MPa}$ and $k_y \approx 1.1 \text{ MPa m}^{1/2}$. These values are lower than those obtained by Vasudevan *et al.* (1989a), who deduced $\sigma_0 \approx 200 \text{ MPa}$ and $k_y \approx 1.4 \text{ MPa m}^{1/2}$. The measured ductility fluctuates with grain size, but all measurements remain $< 1\%$ elongation. This result confirms that the high ductility of the duplex structure cannot be solely attributed to grain refinement, and intrinsic factors such as deformation mechanism changes are also involved.

4.2.2 The Anisotropic Deformation of the Lamellar Structure

The deformation behavior of the lamellar structure has been studied in detail by Yamaguchi and coworkers (Inui *et al.*, 1992). Both the yield stress and ductility are a sensitive function of the lamellar orientation (Figure 9). When the lamellar structure is parallel or perpendicular to the loading axis, the yield stress is high. In those orientations, the γ deformation, in the form of $\frac{1}{2}[112]$ twinning and $\frac{1}{2}[110]$ slip, as discussed above for the duplex structure, needs to cross the interphase boundaries into the α_2 phase. For intermediate orientations, the yield stress is low, since the deformation occurs parallel to the interphase boundaries within γ . The low strength also corresponds to high ductility. Near the 45° shear orientation, the ductility can be as high as 20% elongation at room temperature. This result has several practical implications, and it can be used to explain the 'banding' structure in wrought ingots, for example.

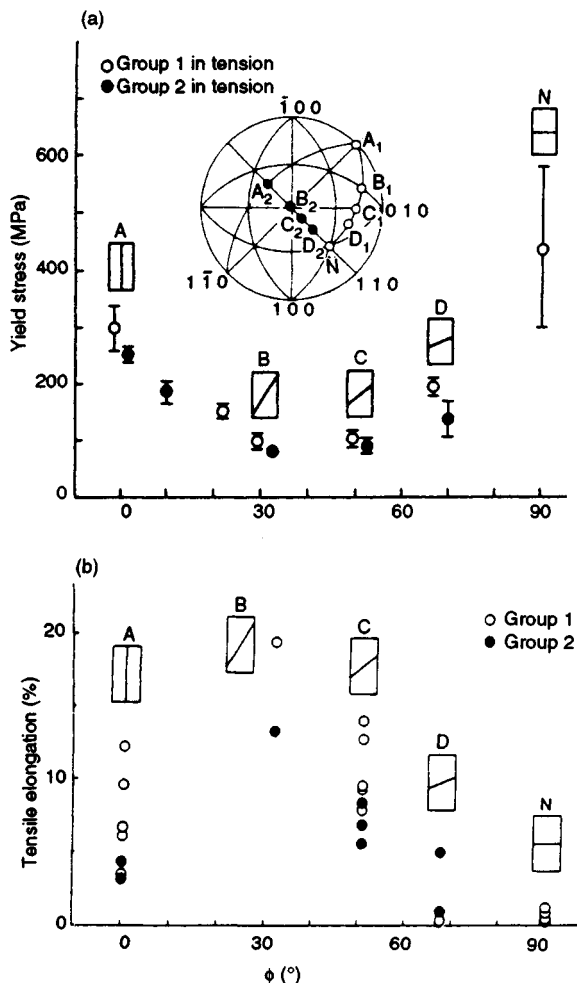


Figure 9. The room-temperature yield stress (a) and ductility (b) measured as a function of the lamellar orientation (Inui *et al.*, 1992)

5. Alloying Modifications

The discussion above indicates that microstructure strongly affects the mechanical properties, and the selection of the Al concentration is an important consideration in the design of γ -based alloys. The microstructure of binary alloys can be modified by ternary and multielement additions, some of which lead to further property improvements. As we will see, a specific alloying addition may only benefit a specific property. For this reason, we consider the alloying effects on a property by property basis as follows.

5.1 Ductilization

Several groups have studied the effect of ternary additions to binary alloys and found that V, Mn and Cr generally increase ductility (Blackburn and Smith, 1981; Tsujimoto and Hashimoto, 1989; Huang and Hall, 1991b). However, the properties of those ternary systems are still a sensitive function of the Al concentration and microstructure. To be effective in ductilization, the additions are limited to 1–3 at% to avoid the excessive formation of a B2 phase. As in binary alloys, the Al concentration has to be restricted to 45–50 at% (Figure 10). Also, the duplex structure has to be maintained. V, Mn and Cr impart no ductilization to the single-phase γ or the fully lamellar structure.

To explain the above alloying effect, one would have to preclude generalized arguments, such as those based on the reduction of the c/a ratio or lattice unit cell volume. Those reductions occur in single-phase γ materials without change in the deformation mechanism or ductilization (Huang and Hall, 1991c). The addition of Mn has been measured to lower the stacking fault energy (Hug and Veyssi re, 1989), but only with the presence of the α_2 second phase. On the other hand, it has been argued that the ductilizing elements substitute for Al and reduce the covalency of the Ti–Al bond (Morinaga *et al.*, 1990). Evidence indicates that they indeed tend to substitute for Al, and the tendency is greater in a duplex structure than in a single-phase structure (Huang and Hall, 1991b,c). The Al substitution measurements correlate well with the result that the effectiveness of the ductilizing elements depends on the type of microstructure.

In addition to the intrinsic modifications above, the ductilizing elements tend to modify the duplex structure

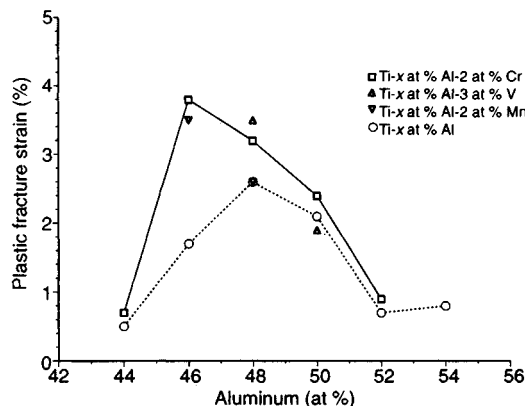


Figure 10. The effect of ternary additions V, Mn and Cr on the ductility of wrought, γ -based alloys

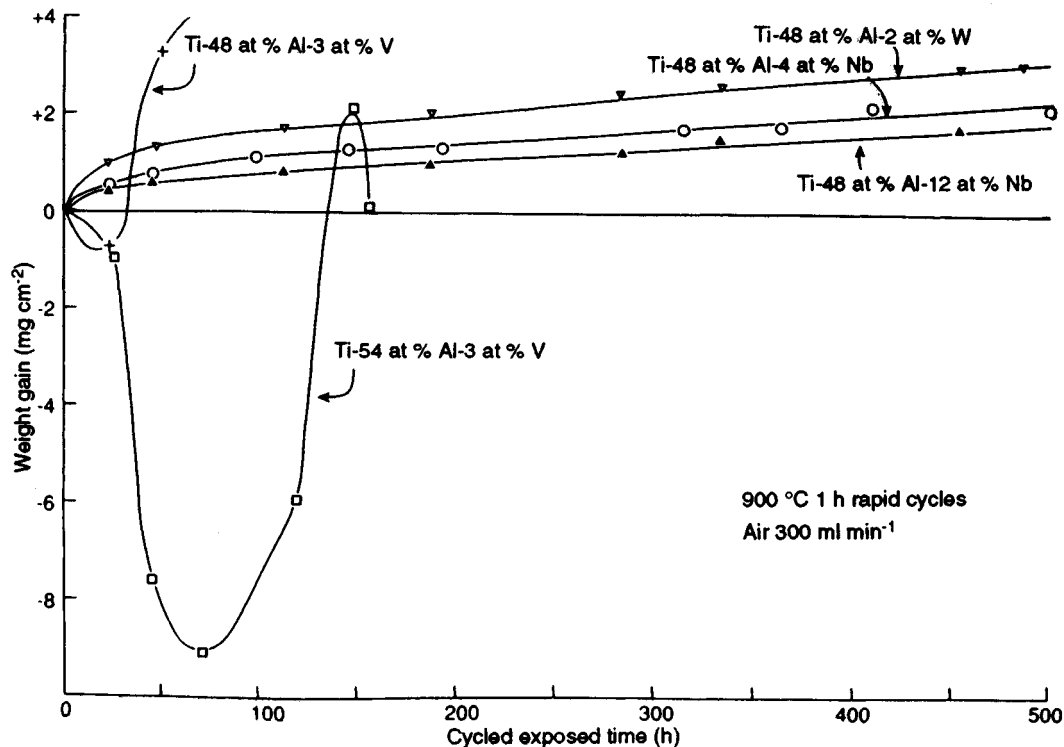


Figure 11. The effect of ternary additions on the oxidation resistance of γ -based alloys

by redistribution of the lamellar α_2 . The overall grain size is still small and the fraction of transformed grains containing $\alpha_2 + \gamma$ lamellae is still large. However, the lamellar structure does not distribute uniformly as it does in most binary duplex alloys. Some lamellae appear to have been removed by coarsening to form single-phase γ regions within the transformed grains (Hanamura *et al.*, 1988; Huang and Hall, 1991b; McQuay *et al.*, 1993). The coarsening should favor homogeneous deformation, since α_2 plates have been shown to resist deformation transfer (Hall and Huang, 1989; Wunderlich *et al.*, 1990; Inui *et al.*, 1992; Seeger and Mecking, 1993). The instability is likely a result of the α transus suppression imparted by the ternary elements (Huang and Hall, 1991b), which effectively reduces the equilibrium volume fraction of the lamellar α_2 .

5.2 Oxidation Resistance

There are a number of refractory elements that can pronouncedly improve the oxidation resistance of γ -based materials. One such element is Nb (McAndrew

and Kessler, 1956; McKee and Huang, 1992). The Nb effect can be quite dramatic even at the low concentrations used (1–2 at%), and the degree of improvement increases quite linearly with the level of addition (Figure 11). With the Nb addition, it becomes possible to use γ alloys at 800 °C without coating. Tungsten and molybdenum have a similar effect (McKee and Huang, 1992; Maeda *et al.*, 1991a). The addition of Cr is detrimental below 4 at%, but it becomes extremely protective at 8 at% and above (Perkins *et al.*, 1987; McKee and Huang, 1992). Tantalum is capable of reducing the oxidation rate (McAndrew and Kessler, 1956), but the oxide scale tends to spall under a rapid thermal cycling condition (McKee and Huang, 1992).

All the above elements, when effective, form a continuous layer of Al_2O_3 that is absent in oxidation-prone alloys (Perkins *et al.*, 1987; McKee and Huang, 1992). A continuous Al_2O_3 layer (instead of a mixed $\text{Al}_2\text{O}_3 + \text{TiO}_2$ layer without the additions) generally slows the influx of oxygen and the rate of internal oxidation, but how those ternary elements promote the alumina formation is not clear. Since Al_2O_3 tends to form at a high Al activity or a low Ti activity (Meier

et al., 1988; Kasahara *et al.*, 1989), it is likely that the observed alloying effect is thermodynamic in origin. The above elements all tend to substitute for Ti, thereby reducing the Ti activity and promoting the formation of the protective alumina scale. They might also simply increase the diffusivity and thus the supply of Al to the surface, or decrease the oxygen solubility in the alloy by increasing the electron/atom ratio (Meier *et al.*, 1988). These mechanisms explain the overall alloying effect observed, but cannot distinguish the specific influence of each element.

The ability of the above elements to increase oxidation resistance is affected by the type of quaternary elements (Perkins *et al.*, 1987; McKee and Huang, 1992). The alloy Ti-48 at% Al-2 at% Cr is ductile, but not resistant to oxidation. With the addition of 2 at% Nb, its oxidation resistance can be significantly improved (Huang *et al.*, 1991). On the other hand, the Nb addition is not effective in improving the oxidation resistance of the ductile alloy Ti-48 at% Al-2 at% V.

Besides the above refractory elements, P is reported to decrease significantly the oxidation rate at the 0.1 at% level (Ikematsu *et al.*, 1991). The effect is attributed to the reduction of the oxygen vacancy concentration and its diffusion in the outer TiO₂ layer. It is also reported that Si decreases the oxidation rate by forming an SiO₂ layer that is more protective than TiO₂, and Y improves the adhesion of surface oxide (Kasahara *et al.*, 1990). See also the chapter on oxidation by Doychak (Volume 1).

5.3 Creep Resistance

There are several alloying elements that were reported to improve the creep resistance of γ -based alloys. The additions of Nb and Ta appear to reduce creep rates by slowing down diffusion (McAndrew and Kessler, 1956). Interstitial nitrogen and perhaps carbon appear to provide dislocation drag (Loiseau and Lasalmonie, 1984). Tungsten and Si are beneficial to creep resistance through microstructural modification (Martin *et al.*, 1983; Tsuyama *et al.*, 1992). The addition of W tends to form β particles and promote the $\alpha_2 + \gamma$ lamellar structure at the same time. It is not clear which aspect of the microstructural modification is more responsible for the observed creep resistance improvement shown in Figure 12. The addition of Si forms Ti₅Si₃, which stabilizes the lamellar structure.

5.4 Effects of Interstitial Impurities

Interstitial oxygen generally increases the strength of γ -based alloys, but may or may not lower the ductility,

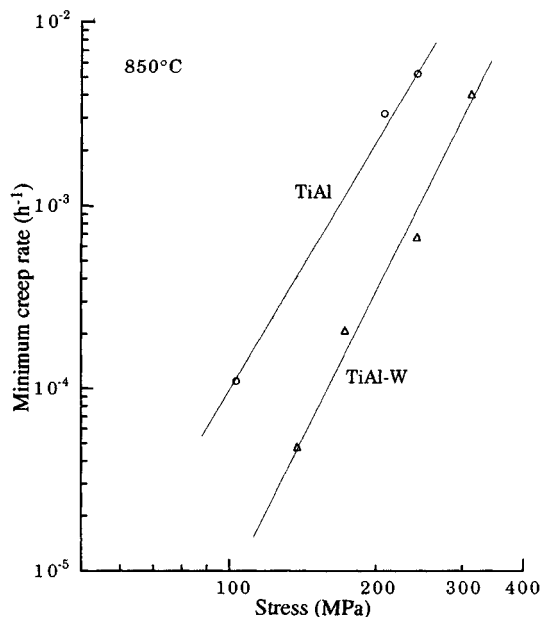


Figure 12. A comparison of the minimum creep rates measured in TiAl and TiAl-W alloys based on the data points of Martin *et al.* (1983)

depending on the oxygen concentration and whether α_2 is present (Austin *et al.*, 1993). The nominal oxygen contents in γ -based materials are typically 500–1000 p.p.m. However, the actual content can be lower in the γ phase of a duplex alloy, since the α_2 second phase tends to absorb oxygen preferentially (Uemori *et al.*, 1992). The oxygen depletion has been speculated to change the deformation mechanisms and increase the ductility (Kawabata *et al.*, 1988a; Huang and Hall, 1991a). In single-phase γ , interstitial oxygen can be lowered by additions of Er to form oxide (Vasudevan *et al.*, 1989a; Sriram *et al.*, 1991). The critical interstitial oxygen level necessary for the deformation change and the ductility increase is not known, but is likely to be <300 p.p.m.

Impurities of nitrogen and carbon are usually present in the amounts of 20–50 p.p.m. and 5–20 p.p.m. respectively. They rarely cause precipitation in duplex alloys, but may form nitrides and carbides in single-phase γ materials. It appears that the α_2 phase in the duplex structure can also absorb nitrogen and carbon. Like oxygen, they tend to increase strength (possibly by pinning dislocations) and reduce ductility. Additionally, they may have the beneficial effect of reducing the creep rate (Blackburn and Smith, 1981; Loiseau and Lasalmonie, 1984).

5.5 Current γ -based Alloys

The first γ -based alloy that has been studied for engineering purposes is Ti-48 at% Al-1 at% V-0.1 at% C (Blackburn and Smith, 1981; Dowling, Jr *et al.*, 1991). The addition of V improves ductility, while C improves the creep resistance. More current γ alloys contain at least one ductilization element and one element that improves the oxidation resistance, as reviewed by Kim and Dimiduk (1991). In at%, they generally fit the formula $\text{Ti}_{45-52}-\text{Al}_{45-48}-(\text{Cr}, \text{Mn}, \text{V})_{1-3}-(\text{Nb}, \text{Ta}, \text{Mo}, \text{W})_{2-4}$. The most notable of this class of alloys is Ti-48 at% Al-2 at% Cr-2 at% Nb (Huang *et al.*, 1991; Shih *et al.*, 1991; London and Kelly, 1991; Austin *et al.*, 1993; Fuchs, 1993).

Table 2 summarizes the wrought properties of this alloy. The α transus of this alloy is $\sim 1350^\circ\text{C}$, and it can be heat treated to a duplex or a fully lamellar structure below or above the transus. Consistent with the property trade-offs observed in binary alloys, the duplex structure is superior in strength and ductility, while the transformed structure is superior in toughness. Regarding the high-cycle fatigue, creep and rupture properties, the duplex structure is favored at lower temperatures, while the transformed structure is favored at higher temperatures. The crossover in properties occurs at $\sim 650^\circ\text{C}$. Figure 13 shows the crossover of the S-N curves for the two structures.

The high-cycle and low-cycle fatigue behavior of γ alloys is generally acceptable and does not need further improvement (Sastry and Lipsitt, 1977; Dowling, Jr *et al.*, 1991; Austin and Kelly, 1993). Fatigue crack growth curves of both wrought and cast γ alloys exhibit

Table 2. Microstructural effects on the mechanical properties of wrought Ti-48 at% Al-2 at% Cr-2 at% Nb

Mechanical properties	Test temperature	Duplex structure	Transformed structure
Plastic elongation (%)	RT ^a	3.1	0.4
	760 °C	50.0	2.8
Yield strength (MPa)	RT	480	455
	760 °C	406	403
Toughness (MPa m ^{1/2})	RT	14.3	28.3
	760 °C	19.2	—
Fatigue strength for 10 ⁷ stress cycles (MPa)	760 °C	172	207
Creep rate at 105 MPa (h ⁻¹)	760 °C	3.3×10^{-5}	4.0×10^{-7}
Creep time to 0.2% strain (h)	760 °C	25	800
100 h rupture (MPa)	538 °C	580	525
	650 °C	480	510
	760 °C	230	370

^aRoom temperature.

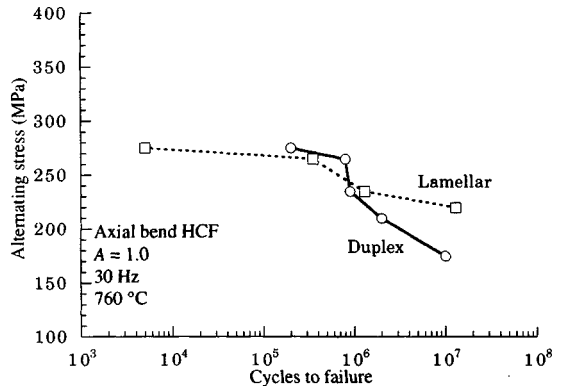


Figure 13. The S-N curves for the duplex and fully lamellar structures in Ti-48 at% Al-2 at% Cr-2 at% Nb

threshold levels that are in the range of conventional materials (about $5 \text{ MPa m}^{1/2}$), but have very steep slopes in the steady-state portion of the curves (Soboyejo *et al.*, 1991; James and Bowen, 1992).

6. Processing to Useful Forms

The alloying modifications discussed above improve the properties of γ -based alloys. For example, the previous pitfall of low ductility has been corrected, and plastic elongation of $> 3\%$ has been measured. Those property improvements were mostly developed through rapid solidification or wrought processing. As the potential use of this new class of materials becomes imminent, several other processing routes have also been investigated. In the following, we consider issues related to the processibility of γ -based alloys.

6.1 Casting

The phase diagram of Figure 3 shows three possible primary solidification phases and two peritectic reactions near the equiatomic composition. Dramatically different cast structures can be obtained at different Al levels, depending on the primary phase (Figure 14). Further, the peritectic reactions lead to severe segregation of Al and formation of phases that are not stable after solidification. For example, the stoichiometric composition would first solidify into α , instead of γ , which only forms secondarily at grain boundaries due to Al segregation (Huang and Siemers, 1989; McCullough *et al.*, 1989). The result is a highly segregated, non-equilibrium cast structure, which needs homogenization

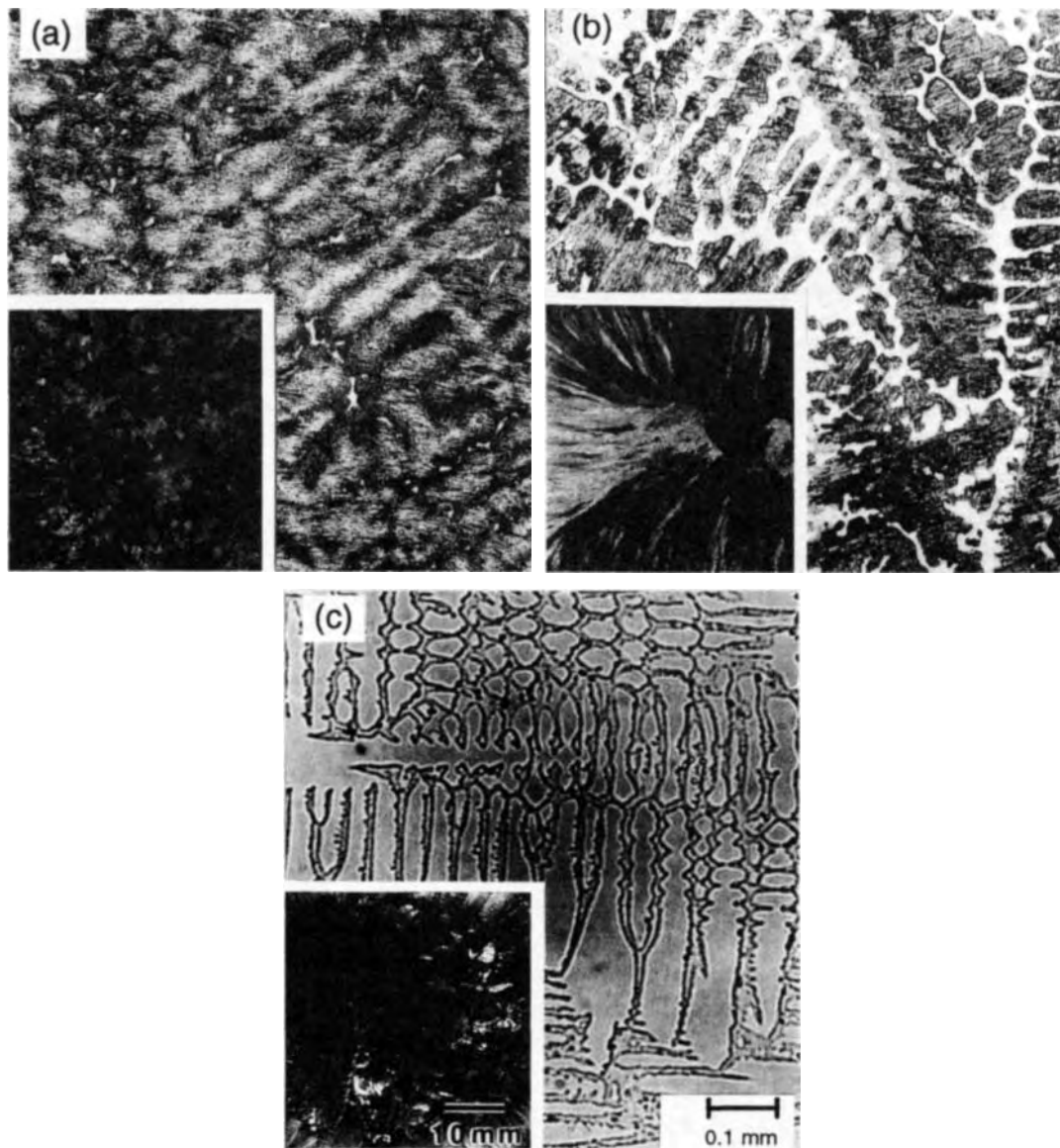


Figure 14. Macrostructures and microstructures of cast binary alloys showing (a) the equiaxed β solidification near 45 at% Al, (b) the columnar α solidification near 50 at% Al, and (c) the equiaxed/columnar γ solidification above 55 at% Al

and equilibration. Figure 15 shows the volume fraction of secondary γ as a function of Al concentration in binary alloy ingots.

γ -TiAl does not solidify as a primary phase until the alloy contains over 55 at% Al. On the other hand, alloys containing less than 46 at% Al first solidify into β , which is unstable at low temperatures. A recent study suggests that β solidification can occur in alloys containing as high as 49 at% Al (Anderson *et al.*, 1992).

Generally, β solidification tends to form equiaxed grains, while α solidification tends to form columnar grains.

The structure and properties of a cast γ -based alloy are strong functions of the Al concentration. Nishiyama *et al.* (1990) have reported that the tensile strength, ductility, creep rupture life and fatigue strength of binary alloys reach maximum values near 47 at% Al. Mitao *et al.* (1991) studied the fracture toughness and

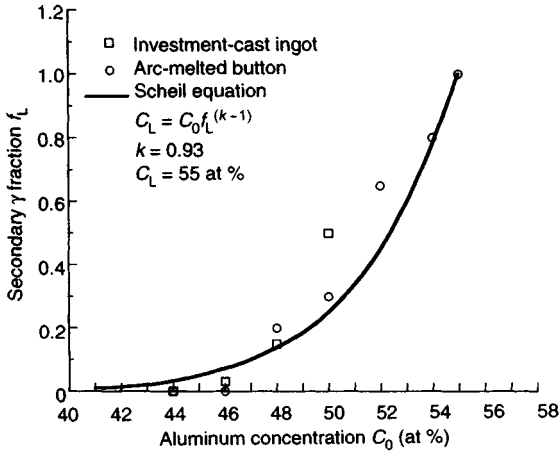


Figure 15. The volume fraction of secondary solidification γ phase as a function of Al concentration near the stoichiometric composition. The solid line corresponds to the Scheil (1942) equation

found a similar Al concentration dependence (Figure 16), a result that has been confirmed by one of the present authors (Huang) and by others (Reuss and Vehoff, 1990). The toughness values below 45 at% Al are quite high, likely a result of the equiaxed-grain lamellar structure due to β solidification (Figure 14a). Alloys containing 46–48 at% Al are particularly tough, which is likely a result of the large columnar lamellar grains with wavy boundaries due to α solidification (Figure 14b). Wrought materials of the same compositions tend to have the weak duplex structure. Above 48 at% Al, γ starts to form at grain boundaries, and the toughness decreases significantly.

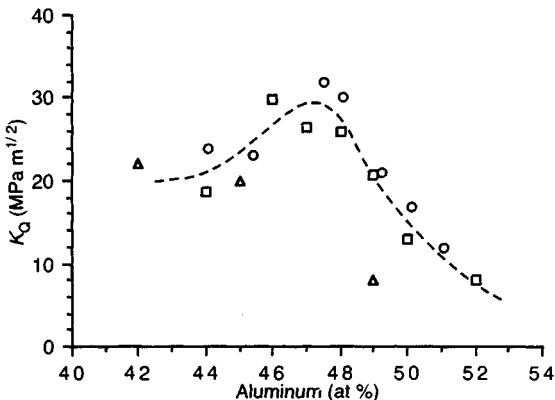


Figure 16. The fracture toughness of as-cast binary alloys as a function of Al concentration: (○) Mitao *et al.* (1991); (□) Huang (1992); (△) Reuss and Vehoff (1990)

Although the cast lamellar structure is tough, it is still quite brittle. Further, the structure cannot be easily modified by annealing to increase ductility, since only the slow continuous lamellar coarsening can occur without recrystallization. If γ grains form during solidification (Figure 15), they can facilitate discontinuous lamellar coarsening and form the more ductile duplex structure. For this reason, the composition of 47 at% Al offers a balance of mechanical properties after heat treatment. This optimal Al concentration has been confirmed in multicomponent cast alloys by Austin *et al.* (1993). Note that the selection of the 47 at% Al concentration is essentially the same as for wrought alloys.

Cast γ -based materials, even those having the duplex structure and containing the ductilizing elements Cr, Mn and V, are generally weaker and less ductile than wrought materials (Austin *et al.*, 1993). This is because the coarse cast structure is usually retained after heat treatment without recrystallization. There is thus a need to modify the alloy, so that a fine and uniform structure can be obtained in the as-cast condition. Heavy elements, like Ta and W, can refine the dendritic size scale. The equiaxed structure of Figure 14(a) is more uniform than the columnar structure of Figure 14(b), but it only occurs in an unsuitably low Al range with the fully lamellar structure. A dramatic method to modify the cast structure is the use of grain-refining agents, most notably TiB_2 . It can be added in the form of boride particles (Larsen *et al.*, 1990) or elemental boron (Huang and Hall, 1991d). The boride-induced grain refinement generally results in a large strengthening and a moderate reduction in ductility. The addition of nitrogen is also effective in grain refinement and strengthening, but it results in large ductility losses.

A fine-grained structure may not retain strength to high temperatures. To increase the high-temperature strength, a fully lamellar structure is more desirable than a duplex structure (Shih *et al.*, 1991). The addition of heavy refractory elements should also increase the temperature capability. An example of such high-strength, high-temperature alloys is Ti-44 at% Al-10 at% Nb (Figure 17). This alloy has a yield strength of 550 MPa at 871 °C (1600 °F).

For thin-walled castings, the additions of Ni, Fe and B have been reported to increase castability (Nakagawa *et al.*, 1992).

6.2 Wrought Processing

Wrought processing breaks up the ingot structure and can be used to form near-net shapes. The ability to work

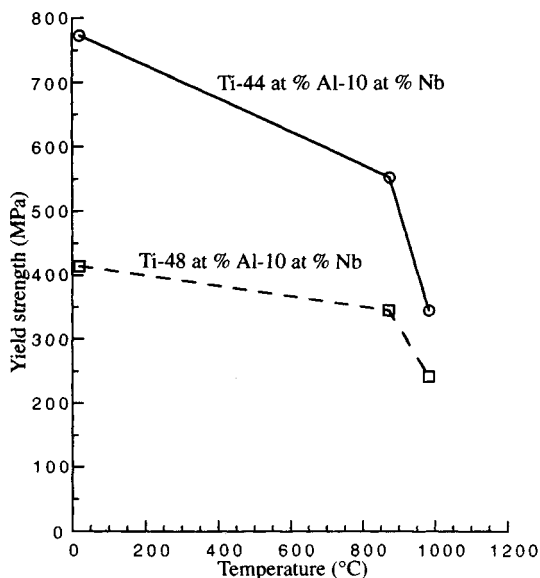


Figure 17. The temperature dependence of the tensile yield strength of high-Nb cast alloys

a γ -based alloy without cracking is a sensitive function of the alloy composition. Nobuki and Tsujimoto (1991) have shown in binary alloys that the workability increases with increasing Al concentration. This effect is related to the formation of lamellar α_2 , which tends to resist deformation. As the Al concentration increases, the volume fraction of α_2 decreases, and the alloy can be worked homogeneously without cracking.

The workability of a γ -based alloy is further affected by alloying additions. The addition of Cr has been shown to increase the workability by forming a B2 phase, which promotes grain sliding at the forging temperature (Masahashi *et al.*, 1991). Some of the Cr-modified alloys showed superplasticity. This is consistent with the result that Ti-48 at% Al-2 at% Cr-2 at% Nb is more workable than Ti-48 at% Al (Shih and Scarr, 1991), as shown in Figure 18. Large additions of V have a similar effect on workability. A refined cast structure, such as one resulting from TiB₂ modification, also improves the workability (Szaruga *et al.*, 1992).

A major need in the wrought processing is the ability to break up completely the coarse and segregated cast structure in large ingots. Frequently, after forging and heat treatment, bands of unrecrystallized grains can be seen that appear to be columnar grains perpendicular to the forging direction. Because the yield strength of the lamellar structure is very anisotropic, unfavorably oriented columnar grains could not be sufficiently worked

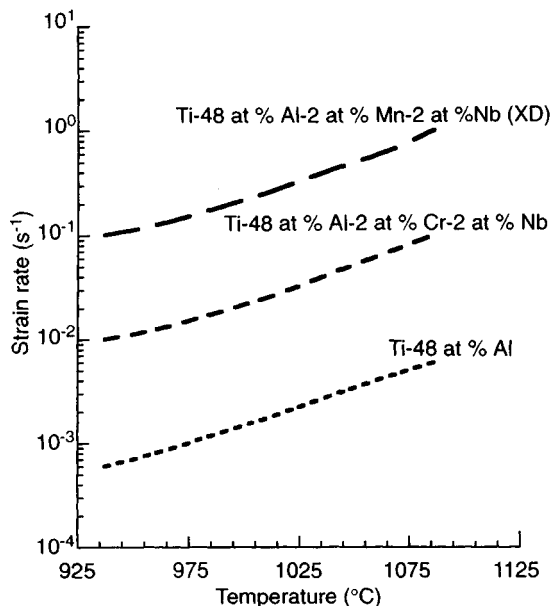


Figure 18. The deformability limits of three γ -based alloys. XD is a proprietary process of Martin Marietta Laboratories, Baltimore

to facilitate recrystallization. Solute segregation can also cause variations in local strength and result in nonuniform deformation. An equiaxed ingot structure, such as those obtained in the low-Al or B-modified alloys, is generally more homogeneous than the columnar structure, and it may be required to prevent banding.

Another solution to the banding problem is to work in multiple directions (Nobuki and Tsujimoto, 1991), and still another is to remove the cast structure by a super- α homogenization before working. For the latter approach, it is important to define the homogenization conditions so that the α grains do not grow too large to cause difficulties in forging. Semiatin and his coworkers (Semiatin and McQuay, 1992) have successfully demonstrated the feasibility of this approach.

An interesting challenge for wrought processing is for it to produce a fine-grained, fully lamellar structure, which would have an attractive combination of properties (Kim and Dimiduk, 1991; Huang, 1992). By working or annealing very close to the transus, Kim (1992) has forced the dynamic recrystallization and grain refinement of α to produce an essentially fully lamellar structure with $\sim 250 \mu\text{m}$ grain size. This unique structure shows a tensile behavior comparable to the duplex structure, and is likely to have superior toughness and creep resistance owing to its lamellar structure.

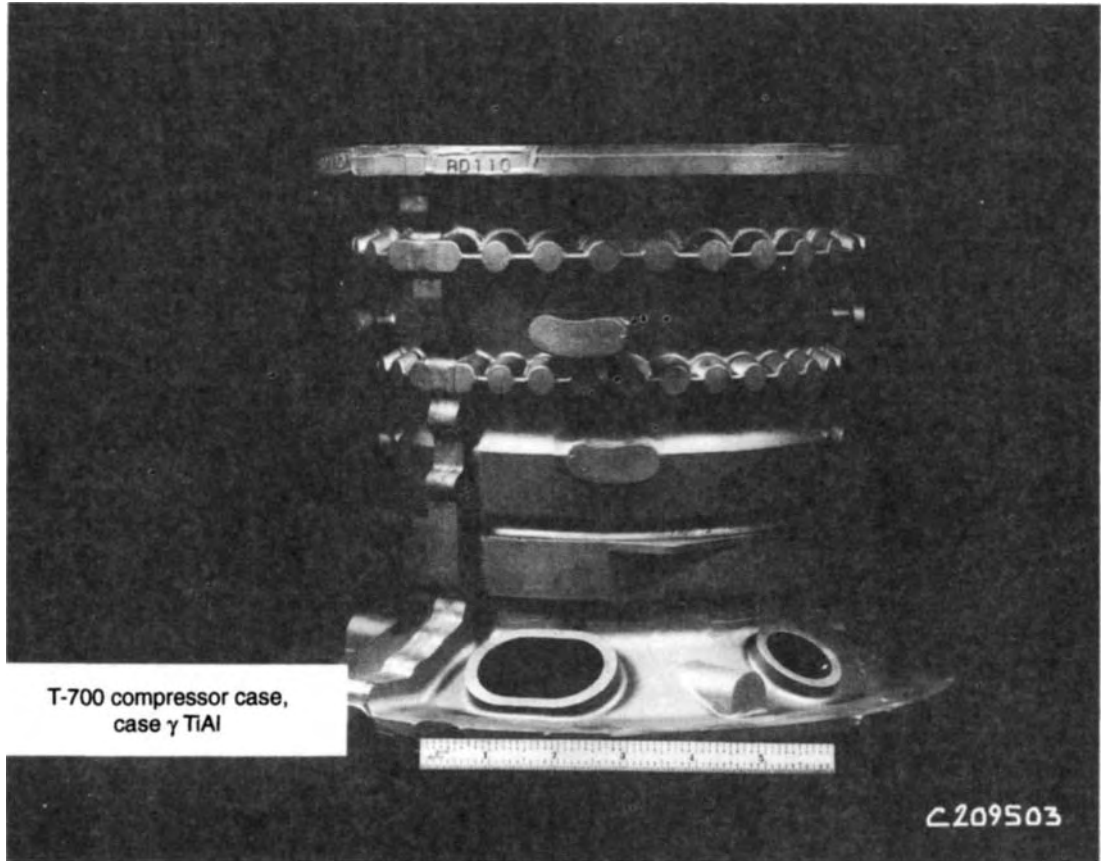


Figure 19. Cast Ti-48 at% Al-2 at% Cr-2 at% Nb, T-700 compressor case

6.3 Powder Metallurgy

Rapid solidification techniques have been used to avoid the heavily segregated peritectic solidification structure. They refine the solidification microstructural size scale and produce homogeneous materials after consolidation. They have helped to define fundamental microstructural and alloying effects (Shechtman *et al.*, 1974; Martin *et al.*, 1983; Huang and Hall, 1991a), but interstitial contamination is a concern for production. Plasma rotating electrode processed powder is generally cleaner than gas-atomized powder, but even in the latter the oxygen contamination has been reduced to below 1000 p.p.m., similar to cast materials. Microstructures and properties comparable to wrought materials have been generated in hot isostatically pressed materials (Fuchs, 1992, 1993; Yolton and Eylon, 1993), and powder metallurgy remains a viable technique for near-net-shapes to fabricate high-quality γ parts.

6.4 Other Processing Methods

γ -TiAl alloys are being studied by sheet casting (Matsuo, 1991), foil rolling, superplastic forming (Masahashi *et al.*, 1991; Maeda *et al.*, 1991b) and directional solidification (Oliver and Kad, 1991; Inui *et al.*, 1992; Takeyama *et al.*, 1991). These processes are expected to result in useful products, but are in an early stage of research.

7. Applications

Austin and Kelly (1993) pointed out that one of the major payoff areas for γ -based materials is stiffness. γ -TiAl has a specific stiffness 50% greater than commonly used alloys (Figure 1). Stiffness is of value in aircraft engines whenever clearances are concerned, such as frames, seal supports and cases. The sharply higher specific stiffness also shifts vibration frequencies

upwards, which is usually beneficial for structural components. These authors also pointed out that initial applications of γ may not all utilize the full high-temperature strength capabilities of γ . There are many current components that are sized to manufacturing tolerances, vibration, aerodynamics, ignition resistance or other factors. A notable case is superalloy low-pressure turbine blades, which are thicker than required from strength and modulus considerations. γ -TiAl appears to be capable of directly substituting for many of those cast parts with substantial weight saving and minimal redesign.

Fabrication techniques have been demonstrated for many components, including a cast γ compressor casing (Figure 19). These demonstrations have increased confidence that components can be commercially fabricated.

All major aircraft engine manufacturers are pursuing the qualification and introduction of γ components. Postans *et al.* (1993) indicate that Rolls-Royce considers high-pressure compressor stators and civil low-pressure turbine blades as the most important applications for γ titanium aluminides. Yamaguchi (1992) and Winkler *et al.* (1993) foresee similar applications in Japan and Germany. Austin and Kelly (1993) describe a planned factory engine test of low-pressure turbine blades in a CF6-80C2 engine, and a test of transition duct supports in a GE90 engine. Components of wrought-processed γ are also being pursued (Chesnutt, 1992; Bondarev *et al.*, 1991).

At the same time, automobile manufacturers are pursuing γ applications such as turbocharger wheels (Nishiyama *et al.*, 1990) and combustion valves. Because of their light weight, these γ parts provide excellent transient response at the engine start-up.

8. Summary

A great deal of progress has been made in the development of γ -based alloys over the last five years. The selection of Al concentration is a critical factor that affects processibility and mechanical properties through microstructural control. Duplex alloys containing 45–50 at% Al are generally most desirable. Alloying additions that improve the ductility, oxidation, creep resistance, and fabricability have been identified. The alloys based on γ -TiAl developed so far generally have excellent castability, and many cast applications are being evaluated for aircraft and automobile engines. The industry appears to be on the threshold of significant use of this new class of alloys. Much more work is needed to extend use to wrought or sheet parts.

9. References

- Anderson, C. D., Hofmeister, W. H., and Bayuzick, R. J. (1992). *Metall. Trans.*, **23A**, 2699.
- Austin, C. M., and Kelly, T. J. (1993). In *Proc. International Symposium on Structural Intermetallics* (eds R. Darolia, J. J. Lewandowski, C. T. Liu, P. L. Martin, D. B. Miracle, and M. V. Nachal), TMS, Warrendale, PA, p. 143.
- Austin, C. M., Kelly, T. J., and Huang, S. C. (1993). In *Titanium 92, Science and Technology* (eds F. H. Froes and I. L. Caplan). TMS, Warrendale, PA, Vol. II, p. 1065.
- Blackburn, M. J. (1970). In *The Science, Technology and Applications of Titanium* (eds R. I. Jaffee and N. E. Promisel). Pergamon Press, London, p. 633.
- Blackburn, M. J., and Smith, M. P. (1981). *U.S. Pat.*, 4294615.
- Bondarev, B., Anoshkin, N., Molotkov, A., Notkin, A., and Elagin, D. (1991). In *Intermetallic Compounds—Structure and Mechanical Properties* (ed. O. Izumi). The Japan Institute of Metals, Sendai, p. 1009.
- Chan, K. S. (1992). *J. Met.*, **44**, 30.
- Chesnutt, J. C. (1992). In *Superalloys 1992* (eds S. D. Antolovich, R. W. Stusrud, R. A. McKay, *et al.*). TMS, Warrendale, PA, p. 381.
- Court, S. A., Vasudevan, V. K., and Fraser, H. L. (1990). *Philos. Mag.*, **61**, 144.
- Deve, H. E., Evans, A. G., and Shih, D. S. (1992). *Acta Metall. Mater.*, **40**, 1259.
- Dowling, W. E., Jr, Donlon, W. T., and Allison, J. E. (1991). *Mater. Res. Soc. Symp. Proc.*, **213**, 561.
- Ence, E., and Margolin, H. (1961). *Trans. AIME*, **211**, 151.
- Feng, C. R., Michel, D. J., and Crowe, C. R. (1990). *Philos. Mag. Lett.*, **61**, 95.
- Fuchs, G. E. (1992). *Mater. Res. Soc. Symp. Proc.*, **288**, 847.
- Fuchs, G. E. (1993). In *Titanium 92, Science and Technology* (eds F. H. Froes and I. L. Caplan). TMS, Warrendale, PA, Vol. II, p. 1275.
- Greenberg, B. A. (1970). *Phys. Stat. Sol.*, **42**, 459.
- Greenberg, B. A. (1973). *Phys. Stat. Sol. (B)*, **55**, 59.
- Greenberg, B. A., Antonova, O. V., Indenbaum, V. N., Karkina, L. E., Notkin, A. B., Ponomarev, M. V., and Smirnov, L. V. (1991). *Acta Metall. Mater.*, **39**, 233.
- Hall, E. L., and Huang, S. C. (1989). *J. Mater. Res.*, **4**, 595.
- Hanamura, T., Uemori, R., and Tanino, M. (1988). *J. Mater. Res.*, **3**, 656.
- Huang, S. C. (1992). *Metall. Trans.*, **23A**, 375.
- Huang, S. C., and Hall, E. L. (1991a). *Metall. Trans.*, **22A**, 427.
- Huang, S. C. and Hall, E. L. (1991b). *Metall. Trans.*, **22A**, 2619.
- Huang, S. C., and Hall, E. L. (1991c). *Acta Metall. Mater.*, **6**, 1053.
- Huang, S. C., and Hall, E. L. (1991d). *Mater. Res. Soc. Symp. Proc.*, **213**, 827.
- Huang, S. C., and Siemers, P. A. (1989). *Metall. Trans.*, **20A**, 1899.
- Huang, S. C., and Shih, D. S. (1991). In *Microstructure/Property Relationships in Titanium Aluminides and Alloys* (eds Y.-W. Kim and R. R. Boyer). TMS, Warrendale, PA, p. 105.

- Huang, S. C., McKee, D. W., Shih, D. S., and Chestnutt, J. C. (1991). In *Intermetallic Compounds—Structure and Mechanical Properties* (ed. O. Izumi). The Japan Institute of Metals, Sendai, p. 363.
- Hug, G., and Veyssi re, P. (1989). In *Proc. International Symposium on Electron Microscopy in Plasticity and Fracture Research of Materials*, Dresden, October.
- Hug, G., Loiseau, A., and Lasalmonie, A. (1986). *Philos. Mag. A*, **54**, 47.
- Ikematsu, Y., Hanamura, T., Morikawa, H., Tanino, M., and Takamura, J. (1991). In *Intermetallic Compounds—Structure and Mechanical Properties* (ed. O. Izumi). The Japan Institute of Metals, Sendai, p. 191.
- Inui, H., Nakamura, A., Oh, M. H., and Yamaguchi, M. (1991). *Ultramicroscopy*, **39**, 268.
- Inui, H., Oh, A., Nakamura, A., and Yamaguchi, M. (1992). *Acta Metall. Mater.*, **40**, 3095.
- James, A. W., and Bowen, P. (1992). *Mater. Sci. Eng. A*, **153**, 486.
- Jones, S. A., Shull, R. D., McAlister, A. J., and Kaufman, M. J. (1988). *Scripta Metall.*, **22**, 1235.
- Kasahara, K., Hashimoto, K., Doi, H., and Tsujimoto, T. (1989). *J. Jpn Inst. Met.*, **53**, 58.
- Kasahara, K., Hashimoto, K., Doi, H., and Tsujimoto, T. (1990). *J. Jpn Inst. Met.*, **54**, 948.
- Kawabata, T., Kanai, T., and Izumi, O. (1985). *Acta Metall.*, **33**, 1355.
- Kawabata, T., Tadano, M., and Izumi, O. (1988a). *Scripta Metall.*, **22**, 1725.
- Kawabata, T., Takezono, Y., Kanai, T., and Izumi, O. (1988b). *Acta Metall.*, **36**, 963.
- Kikuchi, M., and Yamabe, Y. (1991). In *Intermetallic Compounds—Structure and Mechanical Properties* (ed. O. Izumi). The Japan Institute of Metals, Sendai, p. 815.
- Kim, Y.-W. (1992). *Acta Metall. Mater.*, **40**, 1121.
- Kim, Y.-W., and Dimiduk, D. M. (1991). *J. Met.*, **43**, 40.
- Larsen, D. E., Jr, Kampe, S., and Christodoulou, L. (1990). *Mater. Res. Soc. Symp. Proc.*, **194**, 285.
- Lipsitt, H. A. (1985). *Mater. Res. Soc. Symp. Proc.*, **39**, 351.
- Loiseau, A., and Lasalmonie, A. (1984). *Mater. Sci. Engl.*, **67**, 163.
- London, B., and Kelly, T. J. (1991). In *Microstructure/Property Relationships in Titanium Aluminides and Alloys* (eds Y.-W. Kim and R. R. Boyer). TMS, Warrendale, PA, p. 285.
- Maeda, T., Anada, H., Okada, M., and Shida, Y. (1991a). In *Intermetallic Compounds—Structure and Mechanical Properties* (ed. O. Izumi). The Japan Institute of Metals, Sendai, p. 463.
- Maeda, T., Okada, M., and Shida, Y. (1991b). In *Superplasticity in Advanced Materials* (eds S. Hori, M. Tokizane, and N. Furushiro). The Japan Society for Research on Superplasticity, p. 311.
- Mahon, G. J., and Howe, J. M. (1990). *Metall. Trans.*, **21A**, 1655.
- Marcinkowski, M. J., Brown, N., and Fisher, R. M. (1961). *Acta Metall.*, **9**, 129.
- Martin, P. L., Mendiratta, M. G., and Lipsitt, H. A. (1983). *Metall. Trans.*, **14A**, 2170.
- Masahashi, N., Mizuhara, Y., Matsuo, M., Kimura, M., Hanamura, T., and Fujii, H. (1991). *Mater. Res. Soc. Symp. Proc.*, **213**, 795.
- Matsuo, M. (1991). *ISIJ Int.*, **31**, 1212.
- McAndrew, J. B., and Kessler, H. D. (1956). *J. Met.*, **8**, 1348.
- McCullough, C., Valencia, J. J., Levi, C. G., and Mehrabian, R. (1989). *Acta Metall.*, **37**, 1321.
- McKee, D. W., and Huang, S. C. (1992). *Corrosion Sci.*, **33**, 1899.
- McQuay, P. A., Dimiduk, D. M., and Semiatin, S. L. (1991). *Scripta Metall. Mater.*, **25**, 1689.
- McQuay, P. A., Dimiduk, D. M., Lipsitt, H. A., and Semiatin, S. L. (1993). In *Titanium 92, Science and Technology* (eds F. H. Froes and I. L. Caplan). TMS, Warrendale, PA, Vol. II, p. 1041.
- Meier, G. H., Appalonia, D., Perkins, R. A., and Chang, K. T. (1988). In *Oxidation of High-Temperature Intermetallics* (eds T. Grobstein and J. Doychak). TMS, Warrendale, PA, p. 185.
- Mishuda, J. C., and Perepezko, J. H. (1991). In *Microstructure/Property Relationships in Titanium Aluminides and Alloys* (eds Y.-W. Kim and R. R. Boyer). TMS, Warrendale, PA, p. 3.
- Mitao, S., Tsuyama, S., and Minakawa, K. (1991). *Mater. Sci. Engl. A*, **143**, 51.
- Mitao, S., Isawa, T., and Tsuyama, S. (1992). *Scripta Metall. Mater.*, **26**, 1405.
- Morinaga, M., Saito, J., Yukawa, N., and Adachi, H. (1990). *Acta Metall.*, **38**, 25.
- Murray, J. L. (1986). In *Binary Alloy Phase Diagrams*, Vol. 1 (ed. T. B. Massalski). ASM, Metals Park, OH, p. 173.
- Nakagawa, Y. G., Yokoshima, S., and Mastuda, K. (1992). *Mater. Sci. Eng. A*, **153**, 722.
- Nishiyama, Y., Miyashita, T., Isobe, S., and Noda, T. (1990). In *High Temperature Aluminides and Intermetallics* (eds S. H. Whang, D. P. Pope, and C. T. Liu). TMS, Warrendale, PA, p. 557.
- Nobuki, M., and Tsujimoto, T. (1991). *ISIJ Intl*, **31**, 931.
- Oliver, B. F., and Kad, B. (1991). *J. Less-Common Met.*, **168**, 81.
- Perkins, R. A., Chiang, K. T., and Meier, G. H. (1987). *Scripta Metall.*, **21**, 1505.
- Postans, P. J., Cope, M. T., Moorhouse, S., and Thakker, A. B. (1993). In *Titanium 92, Science and Technology* (eds F. H. Froes and I. L. Caplan). TMS, Warrendale, PA, Vol. III, p. 2907.
- Reuss, S., and Vehoff, H. (1990). *Scripta Metall. Mater.*, **24**, 1021.
- Sastry, S. M., and Lipsitt, H. A. (1977). *Metall. Trans.*, **8A**, 299.
- Scheil, E. (1942). *Z. Metallk.*, **34**, 70.
- Seeger, J., and Mecking, H. (1993). *Scripta Metall. Mater.*, **29**, 13.
- Semiatin, S. L., and McQuay, P. A. (1992). *Metall. Trans.*, **23A**, 149.
- Shechtman, D., Blackburn, M. J., and Lipsitt, H. A. (1974). *Metall. Trans.*, **5**, 1373.
- Shih, D. S., and Scarr, G. K. (1991). *Mater. Res. Soc. Symp. Proc.*, **213**, 727.

- Shih, D. S., Huang, S. C., Scarr, G. K., Jang, H., (1991). In *Microstructure/Property Relationships in Titanium Aluminides and Alloys* (eds Y.-W. Kim and R. R. Boyer). TMS, Warrendale, PA, p. 135.
- Shong, D. S., and Kim, Y.-W. (1989). *Scripta Metall.*, **23**, 257.
- Soboyejo, W. O., Deffeyes, J. E., and Aswath, P. B. (1991). *Mater. Sci. Engl. A*, **138**, 95.
- Sriram, S., Vasudevan, V. K., and Dimiduk, D. M. (1991). *Mater. Res. Soc. Symp. Proc.*, **213**, 375.
- Szaruga, A., Rothenflue, L., Srinivasan, R., and Lipsitt, H. A. (1992). *Scripta Metall. Mater.*, **26**, 1565.
- Takahashi, T., Nagai, H., and Oikawa, H. (1990). *Mater. Sci. Eng. A*, **128**, 195.
- Takeyama, M. (1992). *Mater. Sci. Eng. A*, **152**, 269.
- Takeyama, M., Hirano, T., and Tsujimoto, T. (1991). In *Intermetallic Compounds—Structure and Mechanical Properties* (ed. O. Izumi). The Japan Institute of Metals, Sendai, p. 507.
- Tsujimoto, T., and Hashimoto, K. (1989). *Mater. Res. Soc. Symp. Proc.*, **133**, 391.
- Tsuyama, S., Mitao, S., and Minakawa, K. (1992). *Mater. Sci. Eng. A*, **153**, 451.
- Uemori, R., Hanamura, T., and Morkawa, H. (1992). *Scripta Metall. Mater.*, **26**, 969.
- Vasudevan, V. K., Court, S. A., Kurath, P., and Fraser, H. L. (1989a). *Scripta Metall.*, **23**, 467.
- Vasudevan, V. K., Court, S. A., Kurath, P., and Fraser, H. L. (1989b). *Phil. Mag.*, **59**, 299.
- Winkler, P.-J., Daubler, M. A., and Peters, M. (1993). In *Proc. 7th World Conference on Titanium*. TMS, Warrendale, PA.
- Wunderlich, W., Kremser, T., and Frommeyer, G. (1990). *Z. Metallk.*, **81**, 802.
- Yamabe, Y., Honjo, N., and Kikuchi, M. (1991). In *Intermetallic Compounds—Structure and Mechanical Properties* (ed. O. Izumi). The Japan Institute of Metals, Sendai, p. 821.
- Yamaguchi, M. (1992). *Mater. Sci. Tech.*, **8**, 299.
- Yolton, C. F., and Eylon, D. (1993). In *Titanium 92, Science and Technology* (eds F. H. Froes and I. L. Caplan). TMS, Warrendale, PA, Vol. II, p. 1083.
- Zhao, L., and Tangri, K. (1991). *Philos. Mag. A*, **64**, 361.

This chapter was originally published in 1995 as Chapter 4 in *Intermetallic Compounds*, Vol. 2: *Practice*, edited by J. H. Westbrook and R. L. Fleischer.

Chapter 5

Ti₃Al and its Alloys

Dipankar Banerjee

Defence Metallurgical Research Laboratory, P. O. Kanchanbagh, Hyderabad 500258, India

1. Introduction

The intermetallic Ti₃Al(α_2) has an h.c.p. structure (D019, hP8) and disorders at 1180 °C to the α phase (A3, hP2) (Murray, 1987). The development of alloys based on this intermetallic has been driven by the need to bridge the gap in temperature capability between current conventional near- α titanium alloys (550–600 °C) and nickel-based superalloys such as INCO 718 or INCO 713 (650–800 °C). Ti₃Al has a specific modulus and stress rupture resistance comparable to that of the superalloys (Lipsitt, 1985); but, as with many other intermetallics, the complete absence of room-temperature plasticity posed the primary challenge in engineering a structural alloy. Early efforts at alloy development include those of McAndrew and Simcoe (1961) and Winter (1968), and both these studies identified Nb as a primary ternary additive. However, the first Ti₃Al-based composition with demonstrated room-temperature ductility appears to be the Ti–24Al–11Nb alloy (Blackburn and Smith, 1978). Studies on higher aluminum compositions up to the limits of the single-phase region of Ti₃Al were also reported at this time (Rhodes *et al.*, 1978). Alloy development has significantly preceded any real understanding of the physical metallurgy of Ti₃Al-based alloys. While the first studies on mechanical behavior of Ti₃Al and alloy modifications appeared in the late 1970s and early 1980s as reviewed by Lipsitt (1985), a knowledge of the phase equilibria in the Ti–Al–Nb ternary system and of composition–microstructure–property relationships has only recently evolved.

1.1 The Current Status of Alloy Development

The work of Blackburn and Smith (1978) clearly demonstrated that plasticity at room temperature could be obtained by the addition of enough Nb (> 10 at%) to stabilize the high-temperature b.c.c. phase of titanium in the structure. Three distinct classes of alloys have subsequently emerged (Figure 1) based primarily on Ti–Al–Nb compositions with different quaternary additions. These can be categorized based on β stabilizer content (see Figure 1). Alloys in the first category are Ti–24Al–11Nb (Blackburn and Smith, 1978) and Ti–25Al–8Nb–2Mo–2Ta (Marquardt *et al.*, 1989), and typically contain β stabilizers in the range of 10–12 at%. Alloys with a medium β stabilizer content of 14–17% include Ti–24Al–(14–15)Nb (Blackburn and Smith, 1980), Ti–24Al–10Nb–3V–1Mo (Blackburn and Smith, 1982), and Ti–24Al–17Nb and its derivatives (Blackburn and Smith, 1989). The third class of alloys, containing 25–30 at% β stabilizers, has been developed far more recently (Rowe, 1991). The alloy designations are listed in Table 1.

A comparison with the ternary isotherm of the Ti–Al–Nb system at 900 °C (Figure 2) further suggests that the first class of alloys consists of two phase microstructures of α_2 (based on Ti₃Al) and β (B2) (disordered or ordered b.c.c.); the second class consists of, depending on heat treatment, the three phases α_2 , β (B2) and O (a distorted form of α_2 based on Ti₂AlNb); and the third class consist of two phase structures of O and β (B2). The crystal structures are given in Figure 3. The compositional regime between the first and second category of alloys has been explored very recently at a

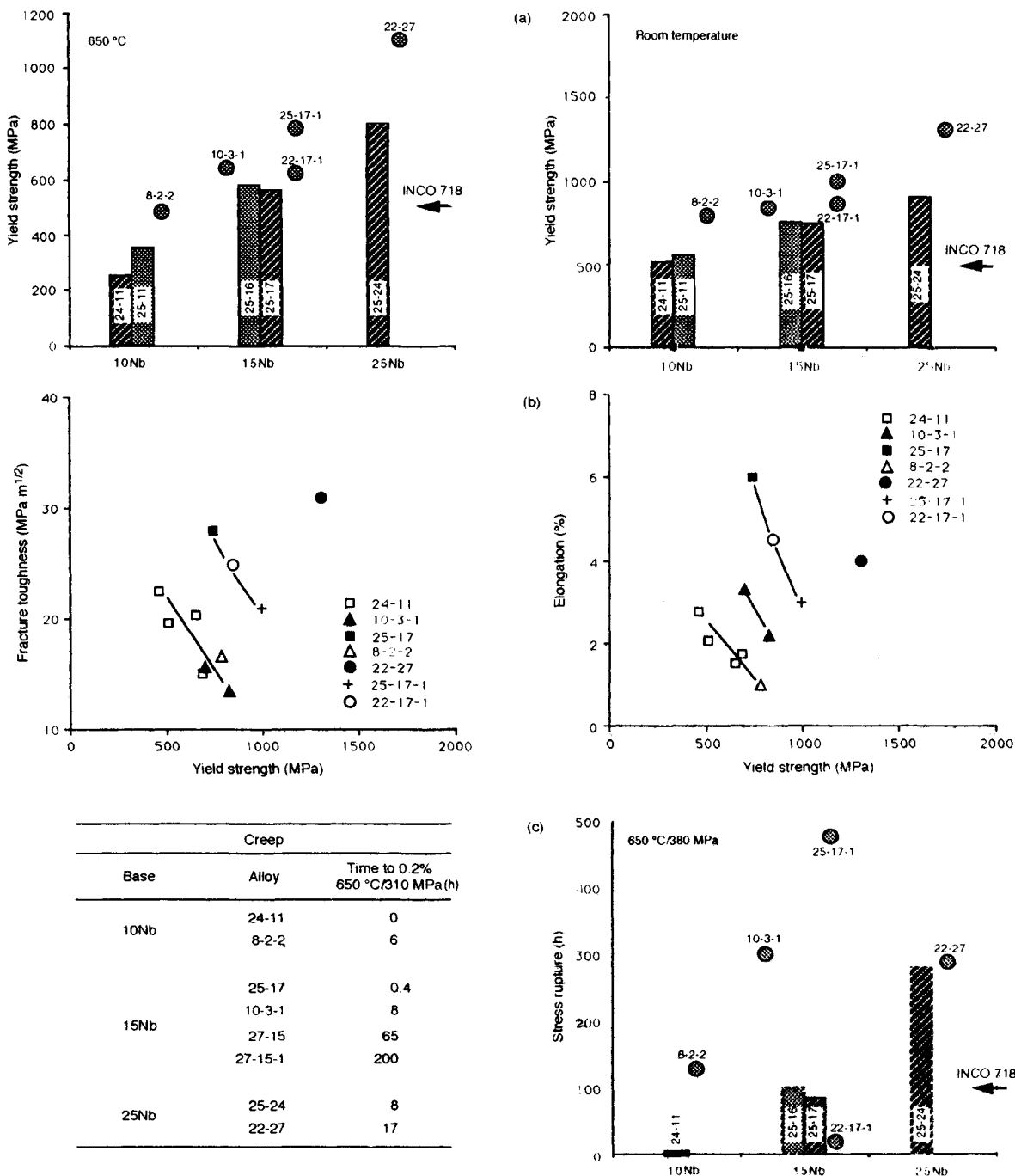


Figure 1. Properties of Ti₃Al-based alloys categorized into three classes based on β stabilizer content. All data are for lath α_2 /O structures: (a) yield strength; (b) fracture toughness and elongation; and (c) creep and stress rupture

Table 1 Alloy designations, compositions and source references for data

Designation	Composition	Reference
24-11	Ti-24Al-11Nb	DeLuca <i>et al.</i> (1989)
25-11	Ti-25Al-11Nb	Gogia <i>et al.</i> (1991)
25-16	Ti-25Al-16Nb	Gogia <i>et al.</i> (1991)
25-17	Ti-25Al-17Nb	Blackburn and Smith (1989)
27-15	Ti-27Al-15Nb	Gogia <i>et al.</i> (1991)
25-24	Ti-25Al-24Nb	Rowe (1991, 1993)
22-27	Ti-22Al-27Nb	Rowe <i>et al.</i> (1991)
27-15-1	Ti-27Al-15Nb-1 Mo	Gogia <i>et al.</i> (1991)
8-2-2	Ti-25Al-8Nb-2Mo-2Ta	Marquardt <i>et al.</i> (1989)
10-3-1	Ti-25Al-10Nb-3V-1Mo	Blackburn and Smith (1982), DeLuca <i>et al.</i> (1989)
22-17-1	Ti-22Al-17Nb-1Mo	Blackburn and Smith (1989)
25-17-1	Ti-25Al-17Nb-1Mo	Blackburn and Smith (1989)

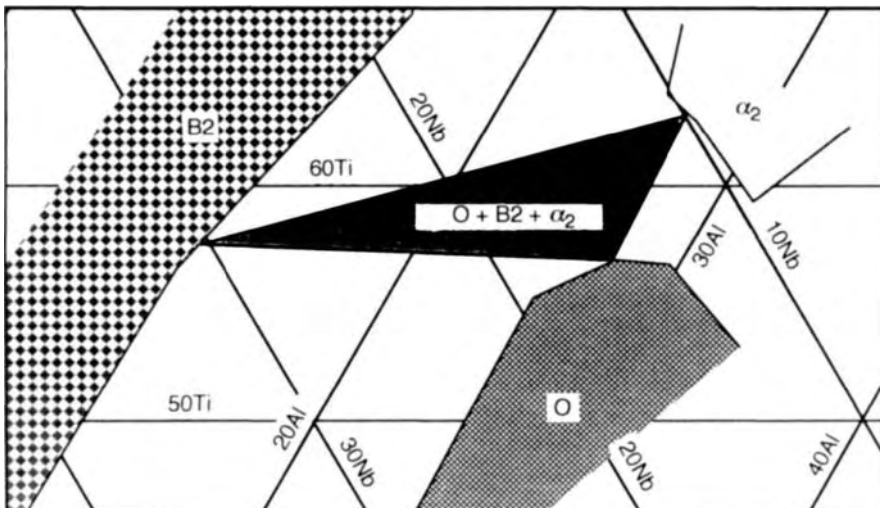
fixed Mo level (Marquardt, 1993), and the role of silicon as an alloying addition has been evaluated (Kerry, 1993).

Several overall trends in properties as a function of composition are readily apparent. Stress rupture and creep are enhanced with increasing Al and Mo, but beyond optimum levels these elements adversely affect toughness and ductility. Strength, toughness and ductility all increase with Nb. The data in Figure 1

indicate that a typical development goal of simultaneously meeting specific stress rupture, creep and yield stress values of INCO 718, together with 'acceptable' fracture toughness and impact resistance, remains elusive. In addition, there is a significant environmental resistance problem at temperatures above 550 °C and a stress-assisted microstructural instability exists within this temperature range.

1.2 Chapter Overview

While the extensive alloy development programs referred to in the previous section broadly define composition ranges within which certain combinations of properties can be achieved, several review articles provide greater insight into various aspects of the physical metallurgy of this class of alloys: the early understanding of the behavior of single-phase Ti₃Al and typical applications (Lipsitt, 1985); compositional effects on a wide variety of properties (Larsen *et al.*, 1990); deformation and fracture (Koss *et al.*, 1990); more recent trends in alloy development (Rowe, 1990, 1991, 1993); and finally microstructure and fracture (Ward, 1993). The subsequent sections of this chapter summarize and extend this understanding in a sequence which proceeds from a description of crystal structures, phase equilibria and transformations to the deformation behavior of individual phases, and then the effect of multiphase mixtures on mechanical properties. A description of environmental effects and processing studies concludes the article.

**Figure 2.** The 900 °C isothermal sections in the ternary Ti-Al-Nb system (from Rowe *et al.*, 1992b)

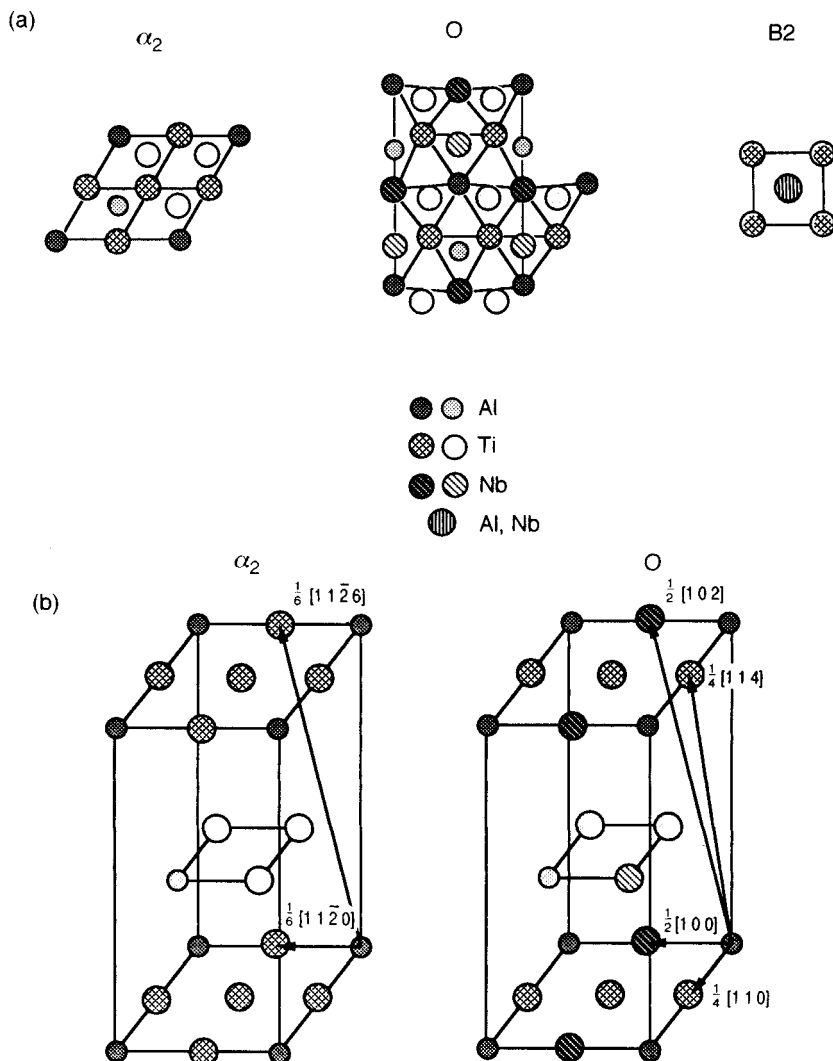


Figure 3. Crystal structures in the Ti–Al–Nb system. (a) Projected atom positions for the α_2 phase (0001), the O phase (001) and B2 (001). In-plane atoms are connected by lines while atoms lying in the plane below, at half the distance of the ‘c’ axis in each case, are shaded lightly. The hexagonal equivalent of the O phase unit cell is also shown to illustrate the similarity with α_2 . Note the distorted hexagon in the O phase. (b) Schematics of the α_2 and O phase unit cells showing the important vectors. The unit cell of the O phase has been chosen to be the same as that of the α_2 phase to illustrate similar vectors

2. Crystal Structures, Phase Equilibria and Phase Transformations

As described in Section 1, the development of engineering alloys based on Ti_3Al has centered on the addition of Nb at levels up to about 25% to replace titanium in compositions based on Ti–(21–25)Al. Therefore, this section will cover the known details of phase equilibria and phase transformations in this region of the ternary Ti–Al–Nb system.

2.1 Crystal Structures

Three phases play a key role in determining phase equilibria in compositions of interest. The first, of course, is the α_2 phase (Figure 3) based on the stoichiometry Ti_3Al which has a DO_{19} (hP8) structure and $\text{P6}_3/\text{mmc}$ symmetry. The structure is characterized by an atomic arrangement on the close-packed (0001) planes which ensures that Al atoms share bonds only with Ti atoms in the nearest-neighbor positions, and

which can be described in terms of four interpenetrating primitive sublattices of which three contain Ti atoms and one contains Al atoms. It has been shown that Nb (Konitzer *et al.*, 1986) and other alloying additions such as Mo, Hf, and Zr (Nandy *et al.*, 1988) all substitute in the Ti sites in the structure. Ga, Sn, and possibly Si (Arrell *et al.*, 1993) are thought to substitute in Al sites.

The existence of an ordered B2 (cP2) phase derived from the high-temperature b.c.c. allotrope (β) of titanium is well known (Bohm and Lohberg, 1958; Molchanova, 1965) to be centered around the Ti₂AlX composition, where X is a β stabilizer. This phase has been specifically identified in the Ti₃Al–Nb system (Strychor and Williams, 1982), and it has been shown that Ti and Al occupy the two separate primitive sublattices constituting the structure while Nb occupies, in the main, the Al sublattice (Banerjee *et al.*, 1987). Alloying additions such as Mo and V substitute in the Al sublattice while Hf and Zr substitute in the Ti sublattice (Nandy *et al.*, 1988).

The third important phase is the O phase, identified by Banerjee *et al.* (1988a) and shown to possess a Cmc_m (oC16) symmetry with an orthorhombic crystal structure which can be viewed as a slightly distorted form of α_2 . The O phase is a ternary ordered structure based on the Ti₂AlNb composition in which Nb atoms can be associated with a distinct sublattice—atoms in one of the three Ti sublattices of α_2 are replaced by Nb. The specific atomic positions and fractional site occupation have been obtained by neutron diffraction (Mozer *et al.*, 1990). An alternative site occupation in which Nb atoms occupy Ti sites randomly, as in α_2 , has also been observed (Muraleedharan *et al.*, 1990; Muraleedharan *et al.*, 1992b). The O phase has thus far been identified in only one other ternary Ti–Al–X system, that is Ti–Al–V (Banerjee *et al.*, 1990b).

2.2 Phase Equilibria

Early work on phase equilibria in the Ti–Al–Nb system (see Zakharova *et al.*, 1984 for an example) did not consider the ordering of the β phase or the presence of the O phase. Recent studies include the determination of the 1200 °C isothermal section (Perepezko *et al.*, 1990), and work is in progress in defining lower temperature isotherms both experimentally (Banerjee *et al.*, 1988b; Muraleedharan *et al.*, 1992a; Rowe *et al.*, 1992b) and through calculation (Kattner and Boettinger, 1992). Figure 2 reproduces the 900 °C section, as currently defined (though not necessarily

complete), of the composition range of interest. The significant features are the presence of the single-phase field O and the ternary-phase field O + B2 + α_2 which separates the α_2 + B2, α_2 + O and O + B2 phase fields. The O phase has extended solid solubility for Ti and Nb and appears to be stable to about 1000 °C around the Ti–27Al–20Nb composition (Rowe *et al.*, 1992a). The T2 phase reported earlier (Perepezko *et al.*, 1990) may not exist. The interaction between the σ (Nb₃Al), α_2 and O phases is of critical interest in alloy design—since the brittle σ phase must be avoided—but is not currently defined. A feature of phase equilibria not shown in Figure 2 is that at lower temperatures (<700 °C) the B2 phase is found to disorder such that there exists an equilibrium between Al-lean disordered β and α_2 phases (Kestner-Weykamp *et al.*, 1989) and the O phase (Rowe and Hall, 1991; Bendersky *et al.*, 1991a). Oxygen has been found to influence the α_2 /B2 transus far more strongly than the α_2 / β transus (Szaruga *et al.*, 1992). No work has been carried out thus far on the effect of oxygen on the O/B2 or O/ β transus. The solubility of hydrogen in both Ti₃Al and the Ti–24Al–11Nb alloy has been determined and the hydride identified as isomorphous with the fluorite γ -TiH structure in the Ti–H binary system (Chu *et al.*, 1992). There have been indications that hydrogen may stabilize the O phase in relation to α_2 (Muraleedharan *et al.*, 1990), apart from its conventional effect as a β stabilizer.

Figure 4 shows the vertical section of Ti₃Al–Nb up to 25 at% Nb. The data used to draw this diagram have been culled from a variety of sources (Rowe *et al.*, 1992a, b; Muraleedharan *et al.*, 1992a, b; Bendersky *et al.*, 1991a; Banerjee *et al.*, 1988b; Kestner-Weykamp *et al.*, 1989, 1990; Kattner and Boettinger, 1992). The figure represents the current knowledge of this important section, and again must not be treated as either completely accurate (with respect to temperature and composition) or complete. The thin line delineates the boundary between the ordered B2 and disordered β phases. The high-temperature section of this line indicates the critical temperature for the conventional transformation from disordered β to B2. The low-temperature section of the line indicates a transformation from B2 to β at temperatures below ~750 °C, and this transformation occurs because the b.c.c. phase in equilibrium with α_2 or O below this temperature is considerably leaner in Al and richer in Nb (Kestner-Weykamp *et al.*, 1989). The latter effect cannot, of course, be seen in the vertical section since tie lines do not run parallel to this section (Rowe *et al.*, 1992b; Kattner and Boettinger, 1992).

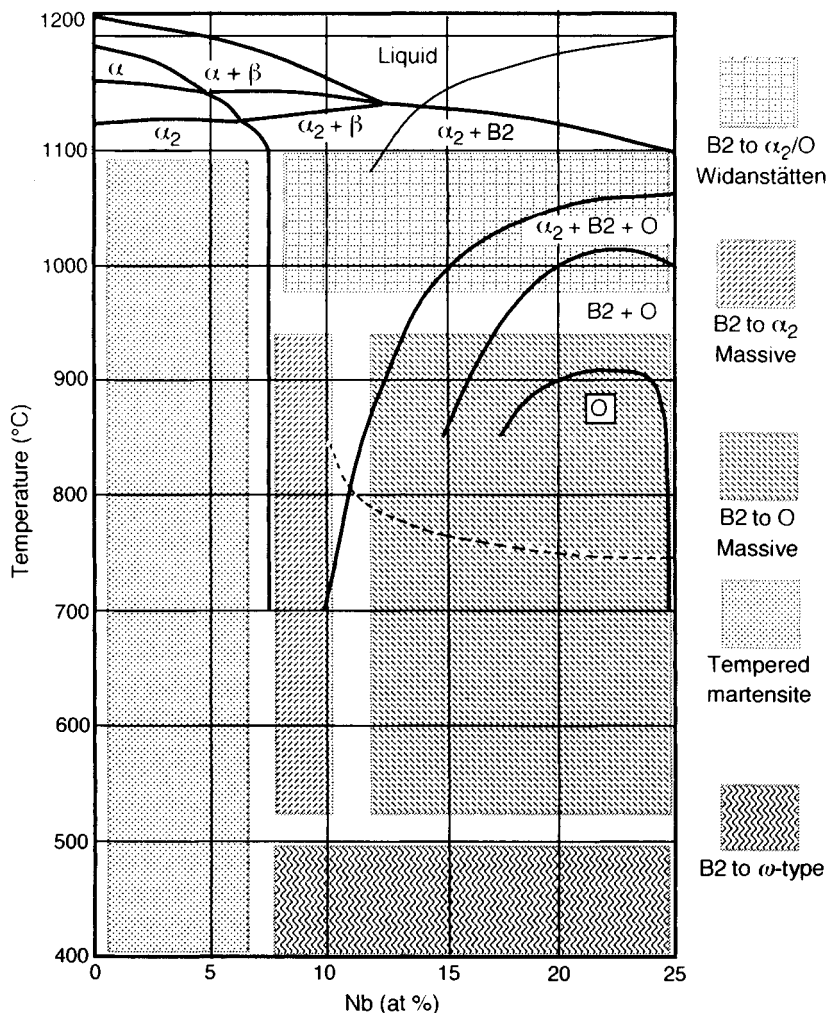


Figure 4. The vertical section of Ti₃Al-Nb. The phase boundaries indicated are not completely accurate with respect to temperature and composition. The dashed line indicates the boundary between the β and B2 phases. Quenching from above the dashed line results in β to B2 ordering. Typical decomposition modes of the β phase are superimposed on the vertical section

2.3 Phase Transformations

The systematics of phase transformations are discussed with reference to Figure 4 under (1) quenching transformations from the β phase, (2) continuous cooling transformations, (3) β quench and age transformations, and (4) thermomechanically processed structures.

2.3.1 Quenching Transformations

At low Nb contents (<7.5 at% Nb), quenching from the β phase results in a martensitic transformation of β to hexagonal martensite α'. However, the ordering

of α' to α₂ cannot be suppressed, resulting in the formation of α₂ laths with a fine APB structure (Figure 5a). The *M_s* (Martensite transformation) curve is rapidly depressed beyond 7.5 at% Nb (Strychor *et al.*, 1988). This decrease appears to be related to the relative stability of the α phase with respect to α₂, since a martensitic transformation from β to α₂/O or B2 to α₂/O is not possible as no atomic site correspondence exists between the parent and product phases. Therefore, at higher Nb contents, the b.c.c. phase can be retained by quenching (Strychor *et al.*, 1988), though it is unstable towards ordering to the B2 phase and a variety of elastic instabilities. The quenched-in β phase shows a fine APB

structure as a consequence of β to B2 ordering if the quenching is from a temperature above the β to B2 transition (Figure 5b). In addition to the presence of superlattice spots, diffraction patterns (Figures 5d and 5e) from the β phase show the presence of $\langle 1\ 1\ 0 \rangle$ streaking, $\langle 1\ 1\ 2 \rangle$ streaking and extra maxima which originate from elastic instabilities towards both $\{1\ 1\ 0\}\langle 1\ 1\ 0 \rangle$ and

$\{1\ 1\ 2\}\langle 1\ 1\ 1 \rangle$ transverse waves. The former is associated with a martensite precursor and the latter with ω phase formation, in this case ordered (Strychor *et al.*, 1988). The $\{1\ 1\ 0\}\langle 1\ 1\ 0 \rangle$ instability also gives rise to tweed contrast in the image (Figure 5c). The microstructure and diffraction patterns shown in Figures 5(b)–(e) are representative across the entire range of Nb compositions from ~ 7 at% Nb to ~ 25 at% Nb.

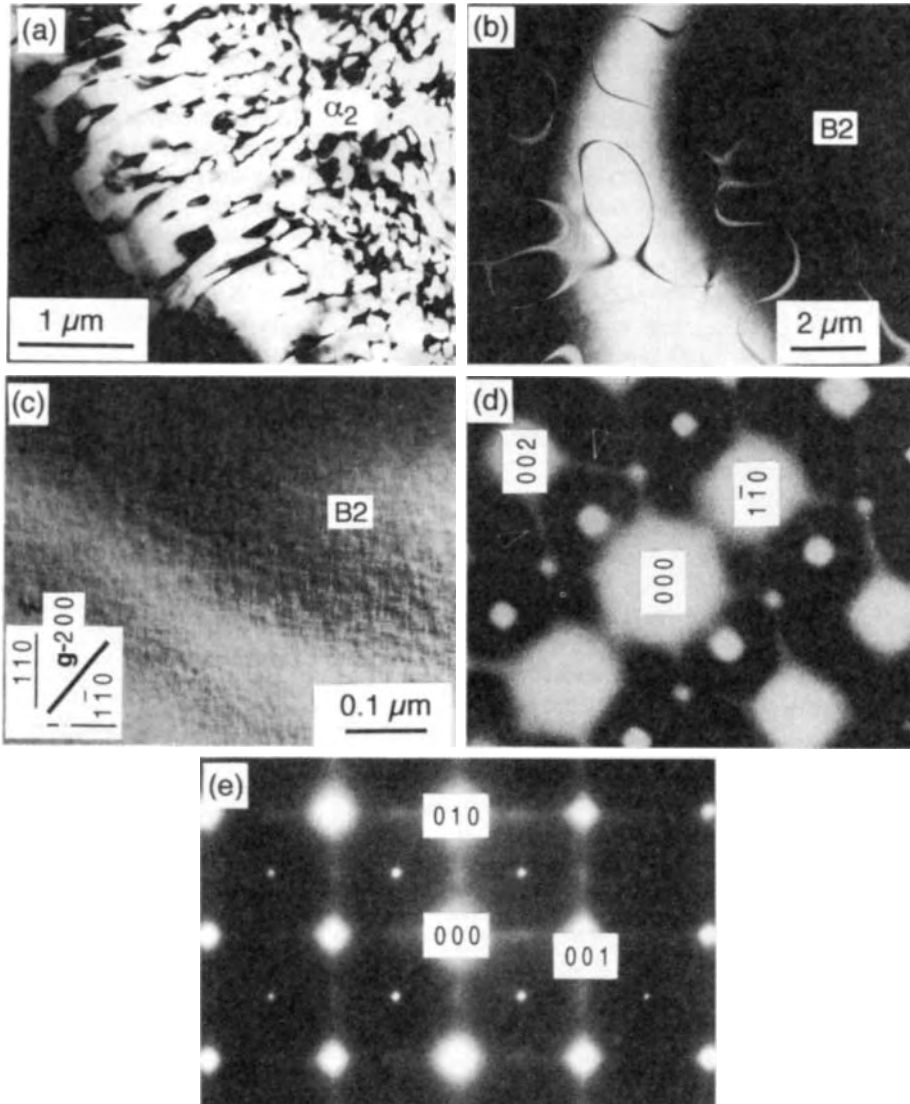


Figure 5. Microstructures in the Ti₃Al–Nb section formed by quenching from the β phase field; (a) lath α_2 with APB arising from the α' to α_2 transformation; (b) APB in the β phase; (c) tweed structure in the β phase; (d) the $[1\ 1\ 0]\beta$ zone axis; (e) the $[1\ 0\ 0]\beta$ zone axis

2.3.2 Continuous Cooling Transformations (CCTs)

Continuous cooling from the β phase region results in precipitation of lath α or α_2 in compositions of up to at least 11% Nb (Kestner-Weykamp *et al.*, 1990). It is on this basis that the $\alpha + \beta$ phase field and also the three-phase region $\alpha + \alpha_2 + \beta$ have been extended to just beyond 11% in Figure 4. In more enriched Nb compositions (as in Ti-25Al-16Nb) the sequence of transformations is more complicated, since alloys in this range pass through the $\alpha_2 + \text{B2}$, $\alpha_2 + \text{B2} + \text{O}$ and $\text{O} + \text{B2}$ phase fields on cooling. A typical CCT curve from this alloy is shown in Figure 6(a), and products from the main reactions B2 to $\alpha_2 + \text{B2}$, B2 to $\text{O} + \text{B2}$ and the subsidiary reactions α_2 to $\alpha_2 + \text{O}$ and $\alpha_2 + \text{B2}$ to O are shown in Figures 6(b)–(e). Invariably, α_2 or O laths precipitate in the Burgers orientation $(0001)\alpha_2 \parallel (110)\beta$; $[11\bar{2}0]\alpha_2 \parallel [1\bar{1}1]\beta$ and the equivalent relationship for the O phase, $(001)_\text{O} \parallel (110)_\beta$; $[110]_\text{O} \parallel [1\bar{1}1]_\beta$ (Bendersky *et al.*, 1991a). The transformation from α_2 to O results in typical lamellar or mosaic structures (depending on whether α_2 is absent or retained) of twin-related O plates arising from the orientation relationship $(001)_\text{O} \parallel (0001)\alpha_2$; $[110]_\text{O} \parallel [10\bar{1}0]\alpha_2$ (Banerjee *et al.*, 1988a). The initial α_2 phase (which subsequently transforms to O) decreases with increasing Nb content and is located only at grain boundaries in compositions approaching 25% Nb. The variation in lath morphology (of α_2 or O) with cooling rate is typical of that observed in conventional α/β alloys and is shown in Figure 7. The lath distribution changes from a colony structure to increasingly fine basket-weave structures with increasing cooling rate.

2.3.3 Decomposition of the Quenched-in β Phase

The wide variety of decomposition modes observed on isothermal aging of the quenched-in β (B2) phase is also given in Figure 4. Figure 8 displays the variety of structures resulting from these decomposition modes. At this time, the details of composition and temperature effects on each of these modes remain to be investigated systematically, although some trends are indicated in Figure 4. In compositions below 7.5% Nb, the β -quenched structure is martensitic α' , with an APB from the α to α_2 transition. Tempering of the martensite results in very rapid APB growth (Sastry and Lipsitt, 1977), β phase precipitation and some recrystallization to an equiaxed structure (Martin *et al.*, 1980). The

metastable, quenched-in β phase ($< 7.5\%$ Nb) decomposes to ω -related structures below 500 °C (Strychor *et al.*, 1988; Chang and Loretto, 1991). At higher temperatures a composition-invariant transformation to α_2 or O is observed. This decomposition mode results in two distinct microstructural products: a platelike O phase which shows many substructural features associated with a martensitic transformation (Figure 8a) and designated O_M ; and an equiaxed product (Figure 8b) very similar to a conventional massive structure designated either O_R or α_R . These two decomposition modes can proceed in parallel or sequentially with the O_R grains finally consuming the O_M product (Muraleedharan *et al.*, 1992a, b; Bendersky *et al.*, 1991a). Subsequent decomposition of O_R or O_M occurs to equilibrium phases α_2 and/or β (B2) (Figure 8c). At temperatures above 1000 °C, conventional precipitation to Widmanstätten α_2 or O occurs, and a cellular transformation has been observed (Rowe *et al.*, 1992a) at Nb levels greater than 25% (Figure 8d).

The observation of metastable $\beta/\text{B2}$ decomposition without long-range diffusion suggests that a hierarchy of structures can occur in proceeding from β to α_2 or O through a set of displacive or replacive transformations which can be analyzed using subgroup/supergroup symmetry relations (Bendersky *et al.*, 1991b). The tetragonal phase recently proposed by Hsiung and Wadley (1992a, b) to form during the first stages of B2 decomposition appears to be erroneously identified because of incorrect interpretation of diffraction data.

2.3.4 Microstructures from Thermomechanical Treatment

As in conventional α/β alloys, processing in temperature regimes where a two-phase O/α_2 and β (B2) equilibrium exists results in equiaxed α_2 or O (in contrast to Widmanstätten α_2/O), as seen in Figure 9. Sub-transus solution treatment determines the volume fraction of primary equiaxed α_2/O phase. The β (B2) present at the solution treatment temperatures decomposes on cooling or quenching/aging to structures similar to those shown in Figures 5–8. It must be noted that the composition of the B2 phase is established at the solution treatment temperature and decreases in Al and increases in Nb with decreasing solution treatment temperature. At lower solution treatment temperatures (in relation to Figure 4, which is essentially for the Ti₃Al–Nb section), the β phase is stabilized with respect to α_2/O , and the conventional Widmanstätten transformation mode is stabilized to lower temperatures in relation to the massive decomposition mechanism.

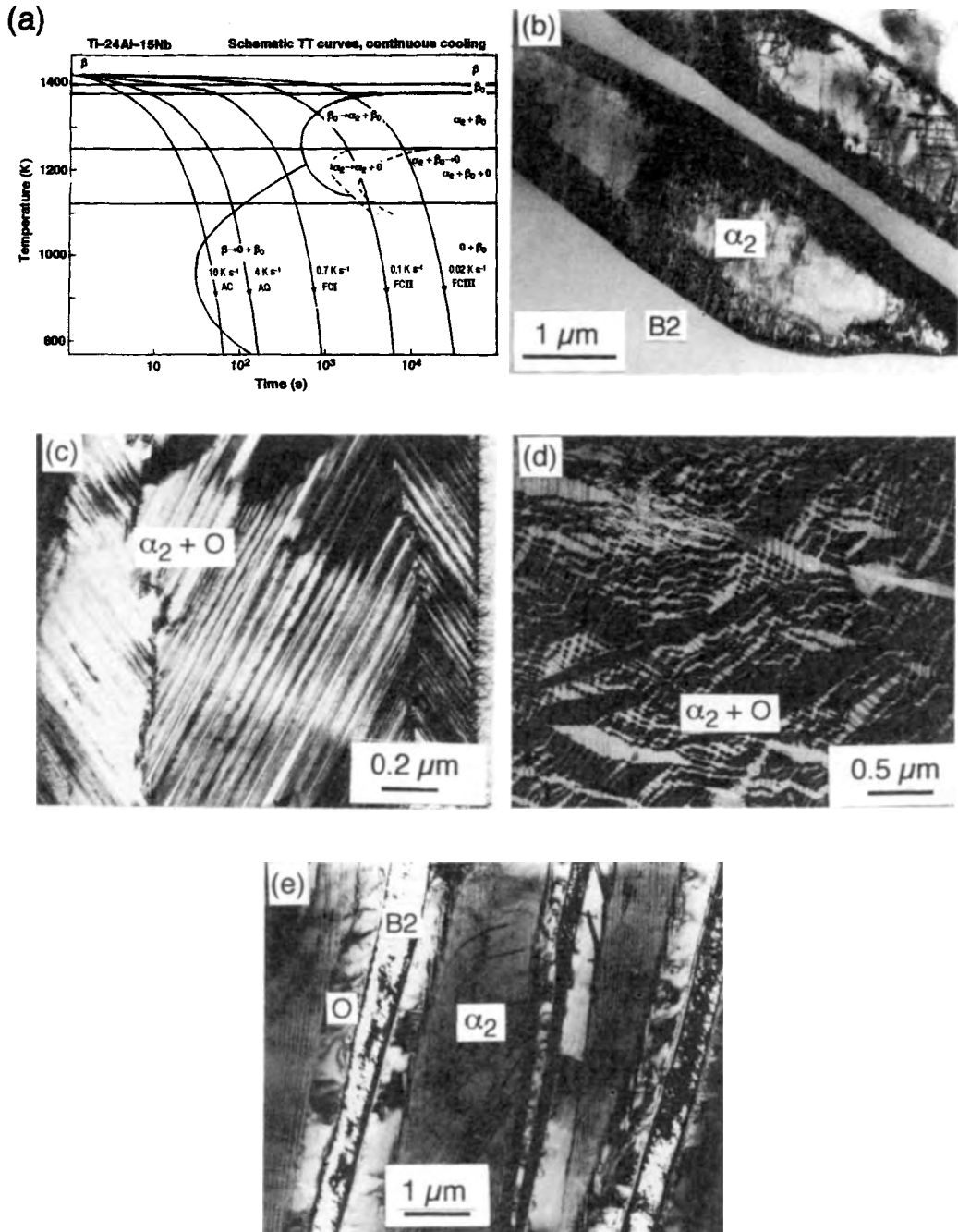


Figure 6. Continuous cooling transformations: (a) a CCT curve for the Ti-25Al-16Nb alloy; (b) lath α_2 phase formed directly from β (B2); (c) lamellar and (d) mosaic structures within lath α_2 from the α_2 to $\alpha_2 + O$ transformation; and (e) O rim around the α_2 from the B2 + α_2 to O transformation

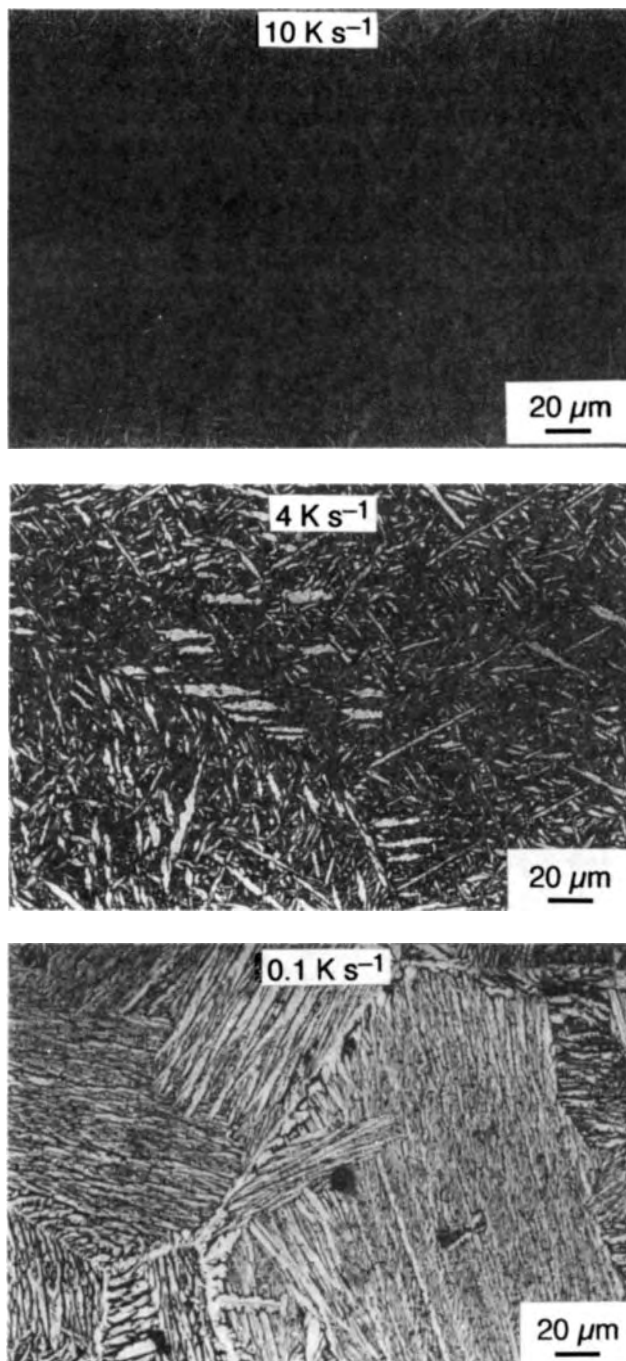


Figure 7. The effect of cooling rate from the β phase field on α_2 lath size and distribution in a Ti-25Al-11Nb alloy

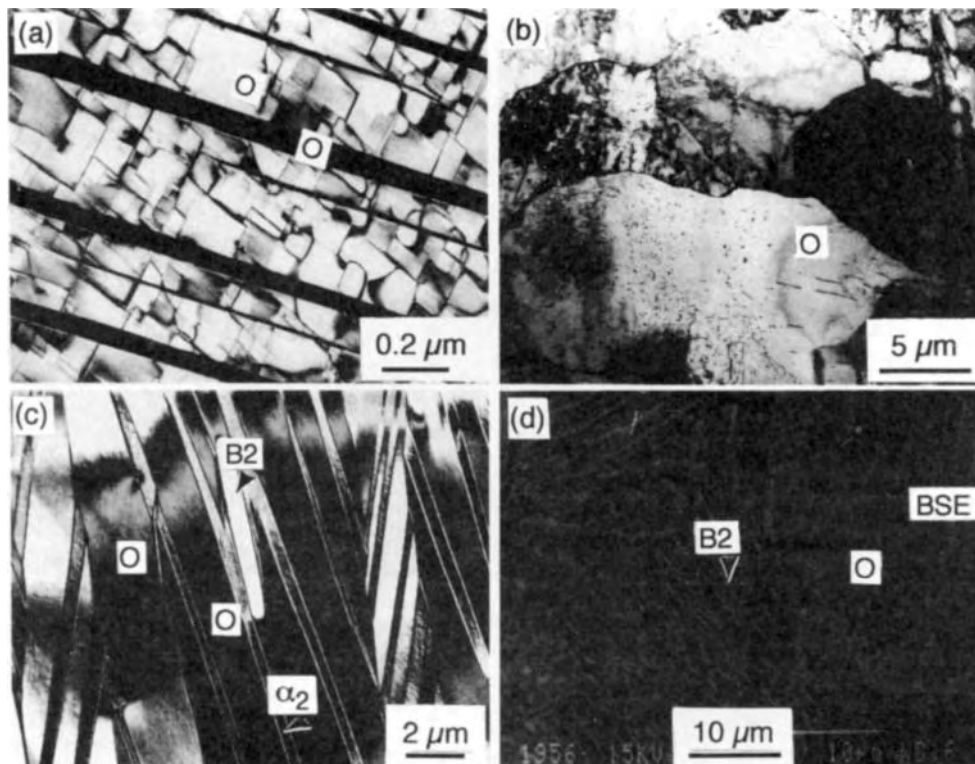


Figure 8. Microstructures arising from B2 decomposition on isothermal aging: (a) platelike O with substructure from the β to O_M reaction in Ti-25Al-16Nb; (b) equiaxed O with B2 precipitates from the β to O_R reaction in Ti-25Al-16Nb; (c) α_2 and B2 precipitates in O from the O_M to $\alpha_2 + B2 + O$ reaction in Ti-25Al-16Nb; and (d) cellular transformation B2 to O + B2 in Ti-25Al-30Nb back scattered electron (BSE) image

In addition, a cellular transformation mode initiated at primary α_2 boundaries is seen (Gogia *et al.*, 1992; Muraleedharan *et al.*, 1992a), which could also occur in a stress-assisted fashion (Rowe and Hall, 1991; Rowe *et al.*, 1990).

2.3.5 Summary

The brief description of equilibria and transformations given in this section indicates that past experience with conventional α/β alloys of titanium can be used for the most part as a guideline to the overall microstructural features which may be expected from processing and heat treatment of Ti₃Al-Nb-based alloys; the O phase behaves very similarly to the α_2 phase in terms of transformation characteristics. Important exceptions are the massive decomposition of the B2 phase in the temperature range 500–900 °C to O or α_2 which results in dramatically different phase distributions, and the tendency for cellular decomposition of β or stress-

assisted cellular coarsening modes of fine B2/O phase mixtures. Neither of these transformation modes are observed in conventional α/β titanium alloys. The effects of quaternary additions such as V, Ta, and Mo remain to be studied in detail. The presence of an equilibrium B8₂ phase at higher Al contents (Bendersky *et al.*, 1990) has not been discussed as it is not strictly relevant to the range of compositions of current engineering alloys.

3. Deformation Behavior of the α_2 , O, and B2 Phases

This section reviews the observations of dislocation arrangements in the α_2 , O, and B2 phases by transmission electron microscopy (TEM), and gives a description of the mechanical behavior of the individual phases; it is thus intended to serve as a link between the preceding section on microstructural evolution and the

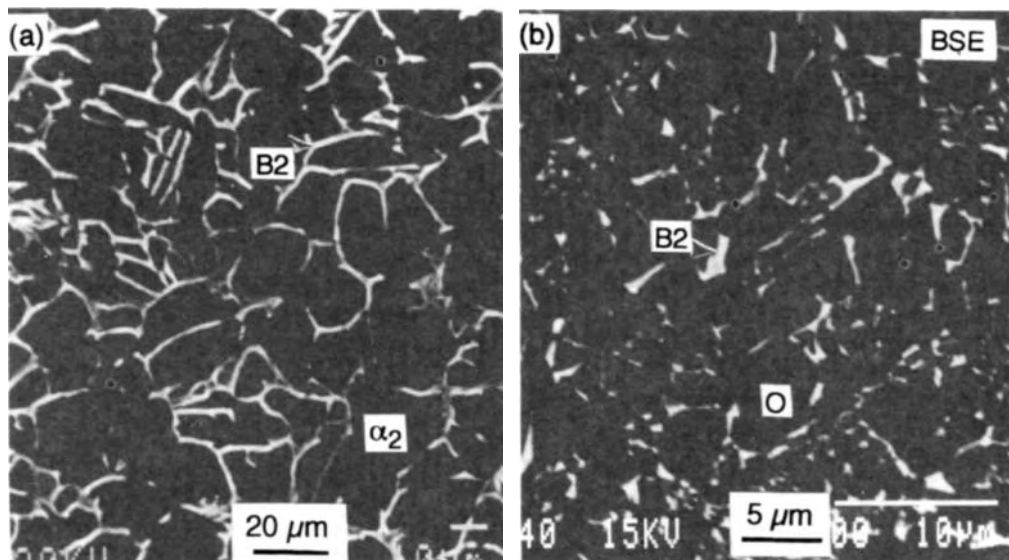


Figure 9. Equiaxed structures obtained by subtransus processing at temperatures at which high volume fractions of α_2 or O are present: (a) Ti-25Al-11Nb alloy with equiaxed α_2 ; and (b) Ti-25Al-27Nb alloy with equiaxed O; back scattered electron images

following sections on the mechanical properties of complex alloys.

3.1 The α_2 Phase

The nature of dislocation arrangements generated by tensile deformation in Ti_3Al (Lipsitt, 1985; Court *et al.*, 1990) and Ti_3Al alloyed with Nb (Lipsitt, 1985; Court *et al.*, 1990; Banerjee *et al.*, 1990a; 1991) has been extensively investigated since the 1980s, and has most recently been supplemented with single-crystal studies (Minonishi, 1990, 1991).

The α_2 phase deforms on three distinct slip systems: $\langle 11\bar{2}0 \rangle \{0001\}$, $\langle 11\bar{2}0 \rangle \{10\bar{1}0\}$ and $\langle 11\bar{2}6 \rangle \{11\bar{2}1\}$. The Burgers vectors are shown in Figure 3. Figure 10 gives the CRSS for these slip systems as a function of temperature. Anomalous flow stress behavior is observed only for $\langle 11\bar{2}6 \rangle \{11\bar{2}1\}$ slip. Since the CRSS for this system is higher than for the others, polycrystalline samples deformed in compression rarely show this slip mode unless individual grains are fortuitously oriented to the tensile axis such that the resolved shear stress for ' a ' slip is minimized (Marquardt *et al.*, 1988; Court *et al.*, 1990). $\langle 11\bar{2}6 \rangle$ dislocations are generally observed in paired configurations of $\frac{1}{6}\langle 11\bar{2}6 \rangle$ superpartials in distinct slip bands, and are in near-edge orientations; thus, Kear-Wilsdorf-type locks cannot explain the flow stress increase with temperature (Minonishi, 1991).

The ' a ' dislocations glide as paired $\frac{1}{6}\langle 11\bar{2}0 \rangle$ superpartials on both prismatic and basal planes. Deformation on basal planes occurs inhomogeneously as planar slip, and superdislocations are observed in

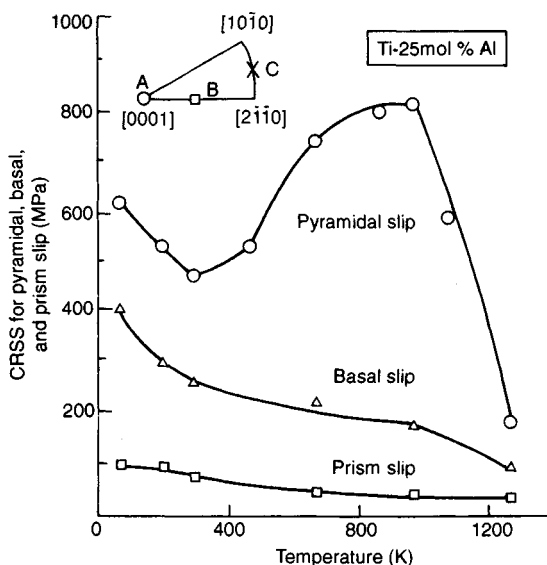


Figure 10. CRSSs for basal slip $\langle 11\bar{2}0 \rangle \{0001\}$, prismatic slip $\langle 11\bar{2}0 \rangle \{10\bar{1}0\}$ and pyramidal slip $\langle 11\bar{2}6 \rangle \{11\bar{2}1\}$ in Ti_3Al as a function of temperature (Minonishi, 1993)

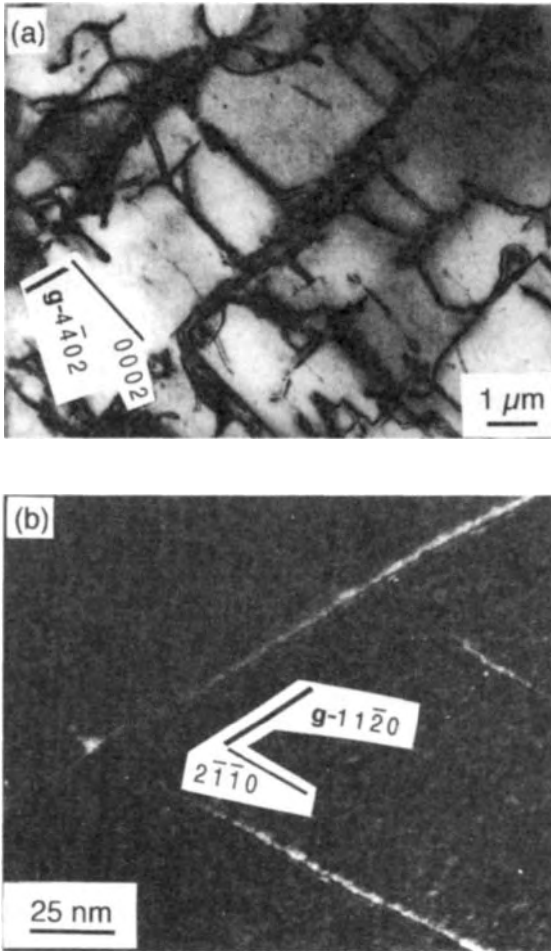


Figure 11. Basal slip in α_2 with a Ti-27Al-10Nb composition (Banerjee *et al.*, 1991): (a) basal slip bands seen nearly edge-on near a $\langle 1\ 1\ 2\ 0 \rangle$ zone axis; and (b) dissociation of $\langle 1\ 1\ 2\ 0 \rangle$ dislocations into $\frac{1}{6}\langle 1\ 1\ 2\ 0 \rangle$ superpartials in the basal plane

screw orientations on the basal plane (Figure 11). Other 'a' dislocations on prismatic planes are homogeneously distributed as dipoles, in junctions with other 'a' dislocations (Banerjee *et al.*, 1991), and as edge dipole segments parallel to $[0001]$ (Minonishi, 1990). These features and dissociated 'a' superdislocations on prismatic planes are shown in Figure 12.

While $[0001]$ dislocations have been observed and characterized (Thomas *et al.*, 1989; Lofvander *et al.*, 1989), these are not generated in tensile strain but arise from the β to α_2 transformation (Mishra and Banerjee, 1990a). Climb of 'a' dislocations has been inferred to occur at higher temperatures (650 °C), but no evidence

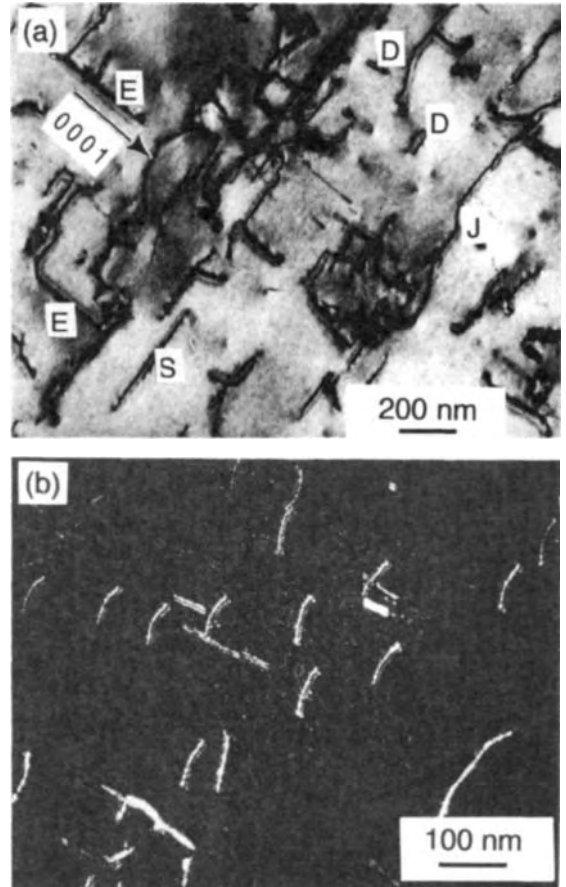


Figure 12. Prismatic slip in the α_2 phase with a Ti-27Al-10Nb composition (Banerjee *et al.*, 1991): (a) screw dislocations (S), dipoles (D and E) and junctions (J) of 'a' dislocations; and (b) dissociation into $a/6\langle 1\ 1\ 2\ 0 \rangle$ superpartials in the prismatic plane

exists of increased 'c' component activity with increasing temperature either in tension or creep (Thomas *et al.*, 1988; Court *et al.*, 1990; Mishra and Banerjee, 1990a).

In summary, Ti₃Al deforms primarily by 'a' slip on prismatic planes with Nb additions increasing the propensity for basal 'a' slip (Court *et al.*, 1990; Banerjee *et al.* 1990a). Twinning, a common deformation mode in hexagonal α -Ti, is excluded by the ordered structure. Thus, only four independent slip systems exist in polycrystalline material. Nb addition increases the tendency for basal slip and perhaps homogeneous prismatic slip, but does not increase the propensity for 'c' component slip. The separations of 'a' superpartials are typically 60 Å on the prismatic plane in Ti₃Al (Court *et al.*, 1990) and 36 Å on the prismatic plane and 42 Å on the

basal plane of α_2 of Ti-27Al-10Nb composition (Banerjee and Rowe, 1990; 1990b), but little can be concluded about the APB energies on these planes without a knowledge of the elastic compliances.

3.2 The O Phase

Since the O structure is only a slight distortion of α_2 (although with ternary ordering), it is useful to look at the Burgers vectors of O in relation to α_2 . Figure 3 shows that the three $\langle 11\bar{2}0 \rangle$ vectors in α_2 are not equivalent in the O phase and are changed slightly with respect to magnitude as well as the associated APB configurations. Thus, the $\frac{1}{2}[100]$ vector breaks Nb-Al nearest-neighbor bonds, while the $\frac{1}{4}[110]$ vector breaks both Ti-Al and Ti-Nb bonds. A similar situation pertains to the $\frac{1}{2}[102]$ and $\frac{1}{4}[114]$ vectors. Banerjee *et al.* (1991) have shown that the overall arrangement of 'a' dislocations is very similar to that in α_2 after room-temperature tensile deformation. Both $[100]$ and $\langle 110 \rangle$ vectors are operative and dissociated into

$\frac{1}{2}[100]$ and $\frac{1}{4}\langle 110 \rangle$ superpartials on the basal (001) and prismatic $\{110\}$ and $\{010\}$ planes with typical separations on the order of 50 Å and 60 Å, respectively (Figure 13). In contrast to α_2 behavior, however, profuse 'c' component slip of both $[102]$ and $\langle 114 \rangle$ is observed, albeit heterogeneously in slip bands parallel to (041) and (221) . These latter slip planes are equivalent to $\{2\bar{2}01\}$ in α_2 . These dislocations are in mixed orientations and are dissociated into their component superpartials, and the trailing superpartial is observed to be profusely pinned leaving behind loops (Figure 14a). The frequent observation of $c + a/2$ slip indicates that the CRSS for this system and 'a' slip may be closer in magnitude than in the α_2 phase.

At high temperatures (650 °C) (Banerjee and Rowe, 1993), climb of $[100]$ dislocations occurs (but apparently not of $\langle 110 \rangle$, while 'c' component dislocations are now seen as extended screw dipoles again on the (041) and $\{221\}$ planes. The separation between the superpartials is now barely resolvable (~ 15 Å) (Figure 14b). No single-crystal work is currently

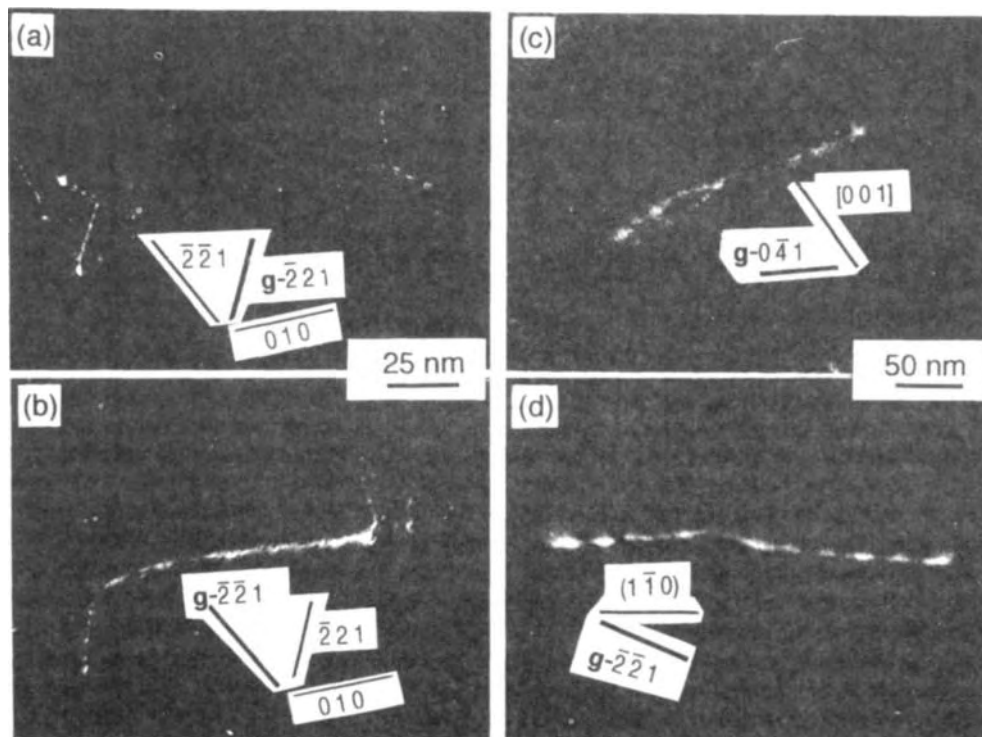


Figure 13. Dislocation structures in the O phase. Dislocation junctions of 'a' dislocations are shown in (a) and (b) (the same junction with different *g* vectors). An 'a' dislocation dissociated on the prismatic and basal planes of the O phase with cross slip is shown in (c) and (d). The dislocation is shown in (c) with the (001) plane nearly edge-on and in (d) with the (110) plane edge-on

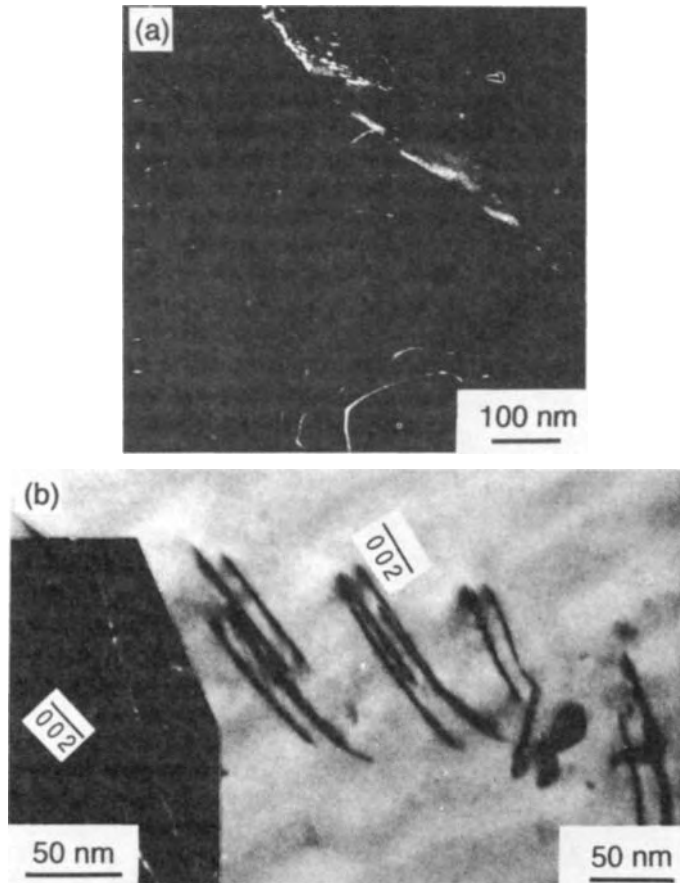


Figure 14. The 'c' component dislocations in the O phase (a) at room temperature (note the pinned trailing superpartials) and (b) at 650 °C. The screw superdislocation dipoles are on pyramidal planes. The separation of superpartials for each screw dislocation is shown as an inset (from Banerjee *et al.*, 1991; Banerjee and Rowe, 1992)

available for the O phase, but will be required to understand these polycrystalline observations.

3.3 The B2 Phase

Deformation in the B2 phase (Banerjee *et al.*, 1990a) is extremely inhomogeneous and localized into nonplanar slip bands (Figure 15). The structure in the slip band consists of heavily pinned edge dislocations with $\langle 111 \rangle$ Burgers vectors, which generate screw dislocations on secondary slip planes. The dislocations glide as loosely coupled $\frac{1}{2}\alpha\langle 111 \rangle$ superpartials in Ti-25Al-11Nb, but as closely spaced pairs in Ti-25Al-16Nb, consistent with the higher disordering temperature for the latter (Figure 4). $[100]$ dislocations have also been observed, but only in the vicinity of α_2 /B2 interfaces in a two-phase structure, where they are presumably generated by

incompatibility stresses. The choice of $\langle 111 \rangle$ as the glide vector is consistent with the significantly lower APB energy of this B2 composition relative to that of NiAl (Banerjee *et al.*, 1990a). While screw dislocations are generally less mobile in both disordered b.c.c. and B2 phases due to their nonplanar core structure (see for example Yamaguchi and Umakoshi, 1990), the pinned edge dislocation configurations seen in Figure 15 appear to arise from dislocation interactions with the defect structure from the $\{110\}\langle 110 \rangle$ elastic instability. Local segments of the slip bands have been identified to be parallel to $\{110\}$ and $\{112\}$ planes. The intense slip localization is believed to arise from slip plane softening owing to the shearing/dissolution of the ω phase present in the structure (a behavior also observed in disordered β with ω). As with all inhomogeneously deforming materials, grain size refinement results in

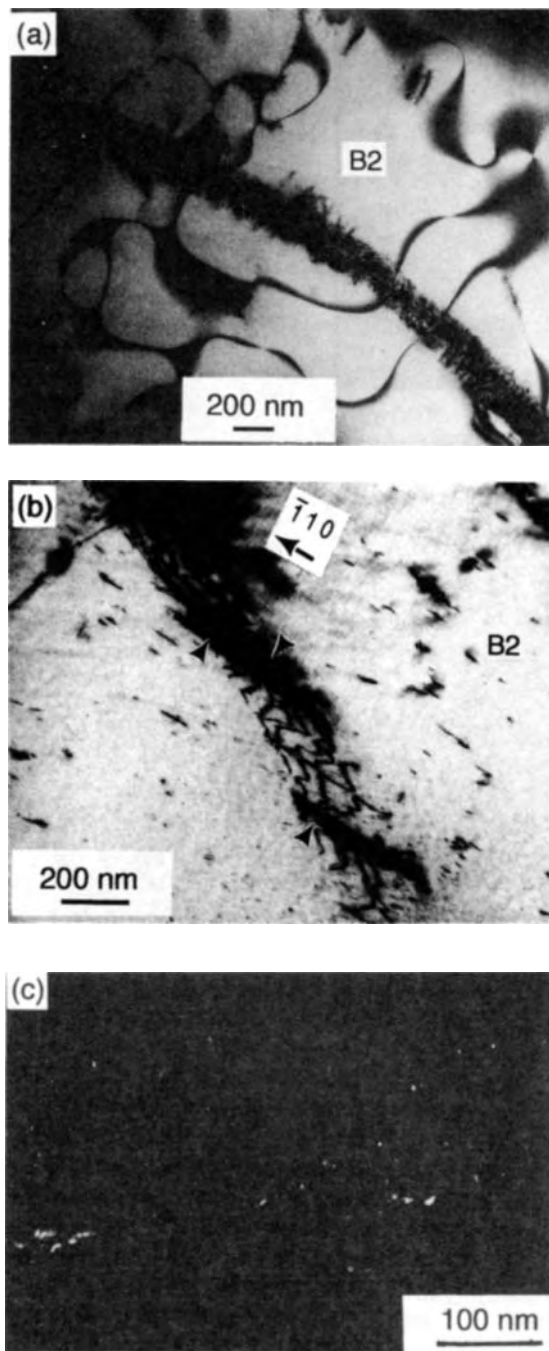


Figure 15. Dislocation structures in the B2 phase (Banerjee *et al.*, 1990): (a) slip bands in the B2 phase of Ti-25Al-11Nb; (b) pinned edge dislocations and generation of screw dislocations on secondary slip planes shown by arrows; and (c) dissociation into $\frac{1}{2}\langle 111 \rangle$ superpartials in Ti-25Al-16Nb

refinement and homogenization of slip (Gogia *et al.*, 1990). Since the β (B2) phase is metastable with respect to decomposition to α_2 or O, it has not been possible to generate information on its flow stress behavior as a function of temperature.

3.4 Summary

A reasonable description of dislocation structures generated by tensile deformation in the α_2 , O, and B2 phases exists at this time. Polycrystalline α_2 phase (alloyed with Nb) deforms by only four independent slip systems, since twinning does not occur and the CRSS for '*c*' component slip is higher than for '*a*' slip and increases with temperature. In contrast, the O phase, in spite of its lower symmetry, shows profuse '*c*' component slip in addition to all '*a*' slip modes. The B2 phase deforms by $\langle 111 \rangle$ slip. However, the advantage of the large number of independent slip systems associated with this slip mode is mitigated by extremely inhomogeneous deformation at larger grain sizes. The absence of single-crystal data on the O and B2 phases (and elastic compliances in the α_2 phase) precludes a quantitative assessment of deformation.

4. Tensile Behavior of α_2 Alloys

The experience with alloy development summarized in Section 1.1 made it clear that Ti₃Al must be alloyed sufficiently to stabilize the β (B2) phase in the microstructure to enhance both strength and ductility, and that Nb is the preferred β stabilizer. Even in such a microstructure, however, the α_2 or O phases fracture by cleavage under tensile loading. Factors which strongly influence the ductile-brittle behavior of metals, such as grain size and the extent of localized stress concentrations at grain boundaries (as influenced by slip modes and slip character), play a major role in determining tensile ductility (Koss *et al.*, 1990).

4.1 The Role of the B2 Phase

Figure 16 shows the variation of yield strength and ductility with α_2 volume fraction in a variety of ternary and quaternary alloys (Gogia, 1991; Gogia and Banerjee, 1991). The B2 phase is stronger and the rule of mixtures is essentially obeyed. The ductility at low B2 volume fractions is relatively high (3–8%) in comparison to single-phase α_2 , even though the critical event for fracture is still the onset of cleavage crack nucleation in α_2 . The B2 phase delays cleavage crack

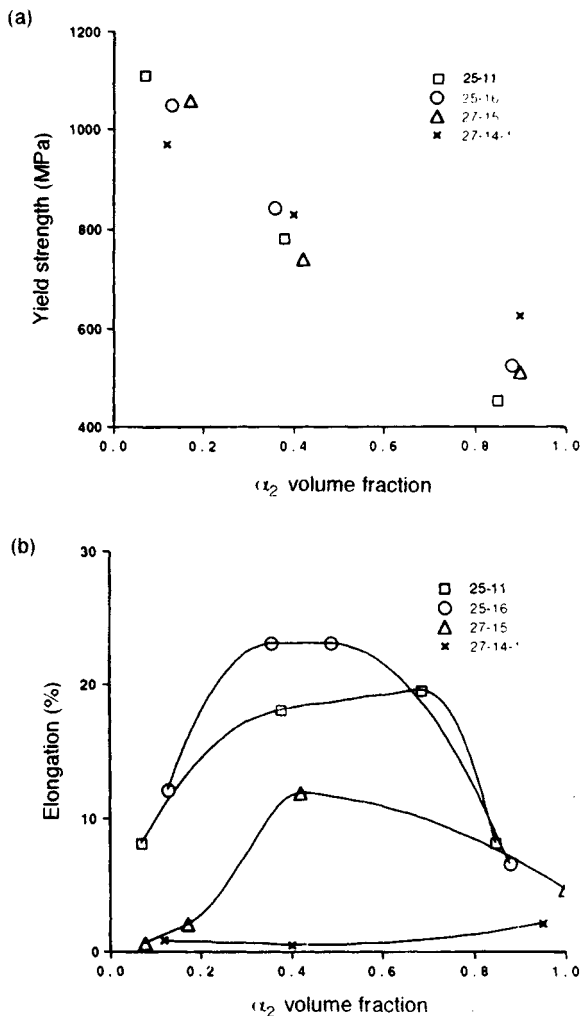


Figure 16. The variation of (a) yield strength and (b) elongation to failure as a function of α_2 volume fraction (Gogia and Banerjee, 1991)

nucleation in α_2 to higher strains (Figures 17a–d) by its ability to plastically accommodate incompatibility stresses at α_2 /B2 interfaces (with its large number of available slip modes; see Section 3.3). A corollary of this mechanism is that β (B2) distributions which avoid α_2 / α_2 grain boundary contact are more effective in imparting ductility. At higher volume fractions, the B2 phase acts as a barrier to crack extension from α_2 (Figure 17e and Figure 18a). The condition for fracture is then the local stress at which cleavage cracks in α_2 can propagate into the more ductile phase (rather than the nucleation event), and therefore the ductility rises steeply (Figure 16

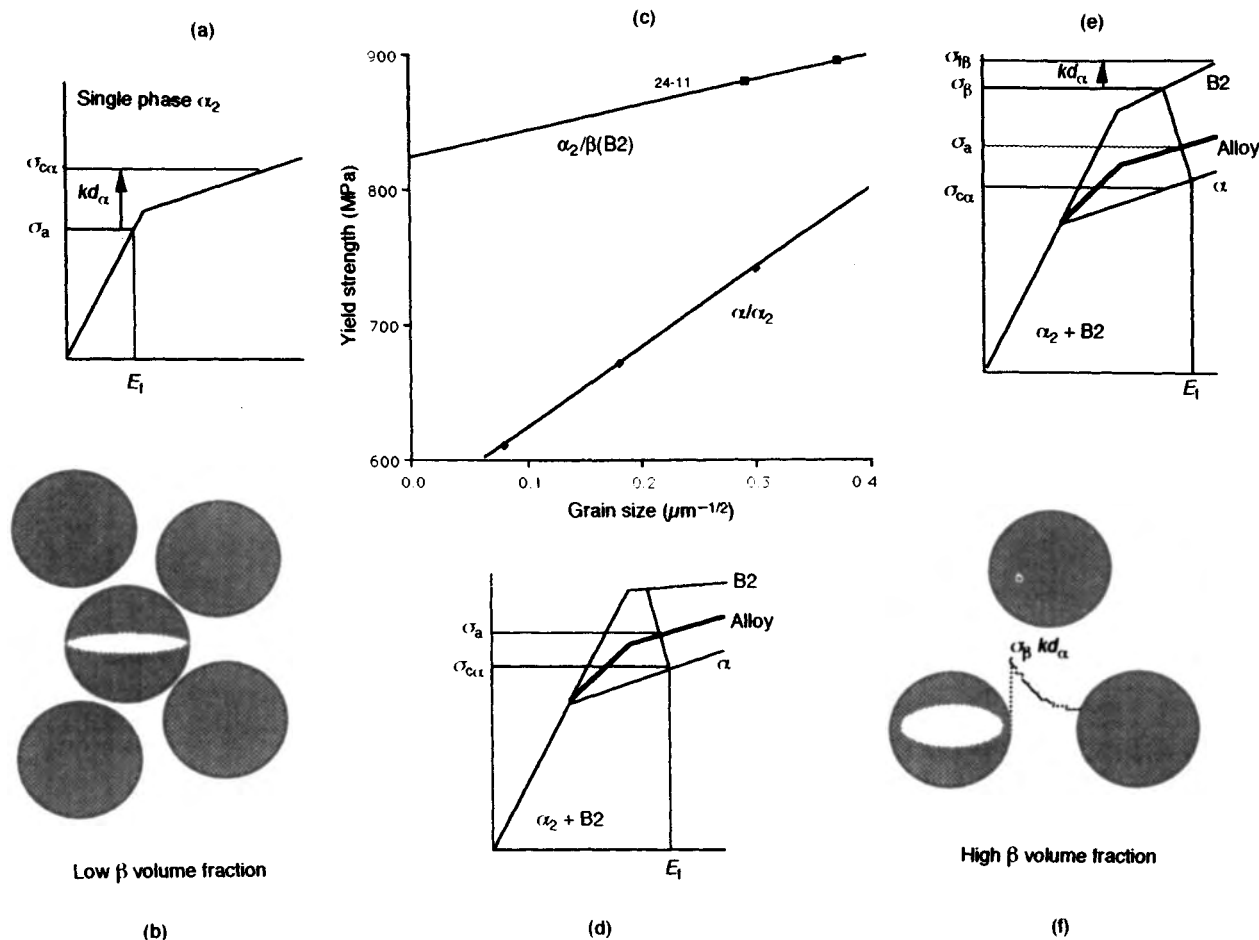
and Figures 17e, f). Nevertheless, single-phase B2 is by itself brittle at large grain size because of slip inhomogeneity, as described in Section 2.3, and it fractures by shear decohesion in intense slip bands (Figure 18b). Increasing Al beyond 25% and Mo additions embrittle the B2 phase, rendering it less effective as a ductilizer (Figures 16 and 19).

Fully heat-treated structures in α_2 alloys contain low overall volume fractions of the β (B2) phase to limit loss of creep strength, and the tensile ductility of such microstructural conditions is determined by crack nucleation in α_2 . The role of α_2 shape, size and distribution is therefore described next.

4.2 Lath α_2 /O Microstructures obtained by β Heat Treatment

The decomposition of the β (B2) phase following solution treatment above the $(\alpha_2 + \text{B2})/\beta$ (B2) transus results in microstructures composed entirely of Burgers-oriented α_2 /O laths, as shown in Figure 7. Figure 20 shows that the cooling rate after solution treatment strongly affects ductility and strength (Blackburn and Smith, 1978; Gogia *et al.*, 1990; Gogia *et al.*, 1992). While the yield strength increases as the lath size is refined, the ductility goes through a maximum. The colonies of similarly oriented α_2 /O variants which form at slow cooling rates are associated with large effective slip lengths since Widmanstätten α_2 /B2 interfaces are transparent to slip (Banerjee *et al.*, 1990a). Thus, in the context of cleavage, the increasing effective grain size at slower cooling rates results in loss of ductility and strength. At cooling rates that are higher than the optimum, failure is initiated at softer grain boundary nucleated α_2 , which is considerably coarser than the fine intragranular lath structure (Figure 7), and the critical cracks thus formed propagate instantaneously to fracture (Lukasak and Koss, 1990; Gogia *et al.*, 1992). The optimum lath structure is therefore a fine basket-weave of α_2 /O phase without any noticeable grain boundary film or grain boundary initiated colony structure. Thus the role of alloying additions must be considered in the context of their influence on the intrinsic properties of the α_2 /O and β (B2) phases, as well as the manner in which they affect microstructure parameters such as grain boundary α_2 /O and lath distribution (see for example Kerry, 1993).

Subsequent aging of the lath structure generated during cooling may result in spheroidization of β films (Gogia *et al.*, 1992), recrystallization into equiaxed morphologies (Muraleedharan *et al.*, 1992a) or coarsening by a cellular reaction (Rowe *et al.*, 1990).



Micromechanisms of fracture in α_2 alloys

Figure 17. (a) In single-phase α_2 , an inadequate number of slip systems results in local stress concentrations at grain boundaries and resultant cleavage fracture at $\sigma_{c\alpha}$ before macroscopic ductility can be attained. (b) The critical event for fracture in $\alpha_2 + \beta$ (B2) alloys with high α_2 volume fraction is still the onset of cleavage initiation in α_2 . However, (c) the Hall-Petch constant k for $\alpha_2 + \text{B2}$ structures is about three times lower than that for an $\alpha + \alpha_2$ alloy (data adapted from Terlinde and Lutjering, 1982). (d) Stress concentrations at $\alpha_2/\text{B2}$ interfaces are therefore plastically accommodated by the B2 phase through easy load transfer in the two-phase alloy, and deformation of the alloy proceeds to higher strains E_1 before the critical stress for cleavage in α_2 ($\sigma_{c\alpha}$) is reached. (e) At higher volume fractions of B2, microcracks in α_2 are blunted by the B2 phase, and therefore the critical event for fracture is reached when the fracture stress in B2 (σ_β) is attained within the β phase. (f) This occurs locally at the α_2/β interface owing to the intensification of the *in situ* stress in β (σ_β) by the cracks in α_2 .

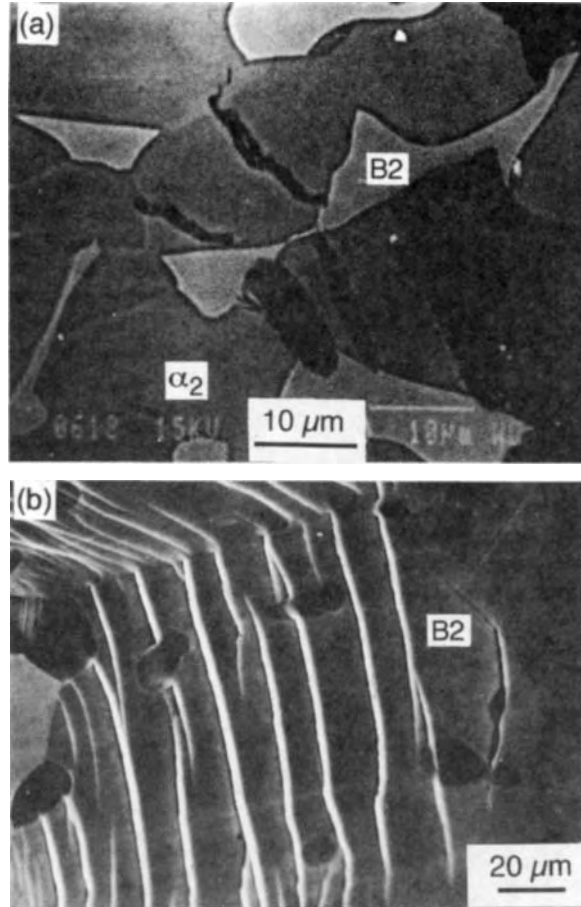


Figure 18. (a) Microcracks in α_2 are blunted by the B2 phase at high B2 volume fractions. (b) Slip band cracking in the B2 phase (from Gogia *et al.*, 1992)

Each of these reactions destroys the continuity of β (B2) and may result in reduced strength and ductility.

4.3 Duplex Structures through Sub-transus Processing and Heat Treatment

As described in Section 2.3.4, sub-transus processing and heat treatment generates duplex structures of equiaxed α_2 and transformed β with secondary lath α_2/O . The strength of such a microstructural condition may be understood in terms of the rule of mixtures

$$\sigma_a = \sigma_\alpha f_\alpha + \sigma_\beta f_\beta$$

where f and σ are the volume fractions and strengths of primary α_2 (subscript α) and transformed β (subscript β) and σ_a is the alloy strength. σ_β depends

inversely on the size of the secondary laths and directly on the amount of untransformed β (B2). While a generalized description of the effect of various combinations of solution treatment and aging temperature on tensile properties is schematically described in Figure 21, the specifics depend on the slopes of the various solvus lines $\alpha_2/\alpha_2 + \text{B2}$ and $\alpha_2 + \text{B2}/\text{B2}$ (Gogia *et al.*, 1992) and must be examined for each alloy composition within the framework of Figure 21.

In Figures 21(d) and 21(e), the strength of primary α (σ_α) is assumed to be independent of solution treatment temperature, while σ_β increases with decreasing solution treatment temperature since the amount of retained β increases. If the alloy composition and combination of solution treatment and aging temperature are such that the secondary α_2/O volume fraction is very high, then σ_β may almost be equal to

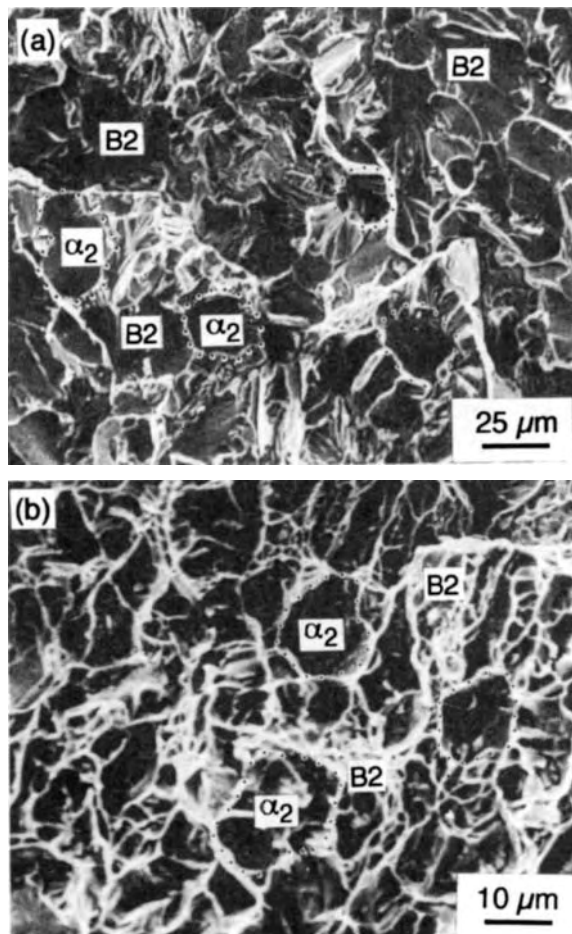


Figure 19. (a) Cleavage of B2 phase in a Ti-27Al-15Nb-1Mo alloy with 40 vol% α_2 in contrast to (b) dimple fracture of the B2 phase in Ti-25Al-16Nb with a similar α_2 volume fraction. Cleaved α_2 particles are outlined by dotted lines (from Gogia and Banerjee, 1991)

σ_α , especially if the microstructure of Figure 21(c) is promoted. In such a case (Figure 21d) the strength may not increase with solution treatment temperature, as shown by a simple application of the rule of mixtures, and may go through a maximum, as experimentally observed in some alloys (Figure 22a). If, however, σ_β is always much higher than σ_α , as in Figure 21(e), then the strength may increase with solution treatment temperature (Ward *et al.*, 1988; Kumpfert *et al.*, 1992) as seen experimentally for the Ti-10-3-1 alloy in Figure 22(b).

The influence of equiaxed microstructures on ductility is not understood very well. Crack initiation in both primary α and transformed β has been observed depending upon heat treatment (Ward, 1993). Clearly,

the partitioning of stress and strain between these microstructural constituents as well as geometrical parameters such as the size of the primary α_2 , the secondary laths and, importantly, the continuity of the β phase around both the primary α_2 and the secondary laths will all influence the macroscopic strain at which cracks initiate in either constituent. The data on the ternary alloys (Gogia *et al.*, 1992 and Figure 22) suggest that the volume fraction and continuity of retained β exert the most important influence, since lower solution treatment temperatures and high aging temperatures both increase ductility. Excellent combinations of strength and ductility in the aluminides can be obtained by thermomechanical processing to refine the overall microstructure and by a judicious combination of

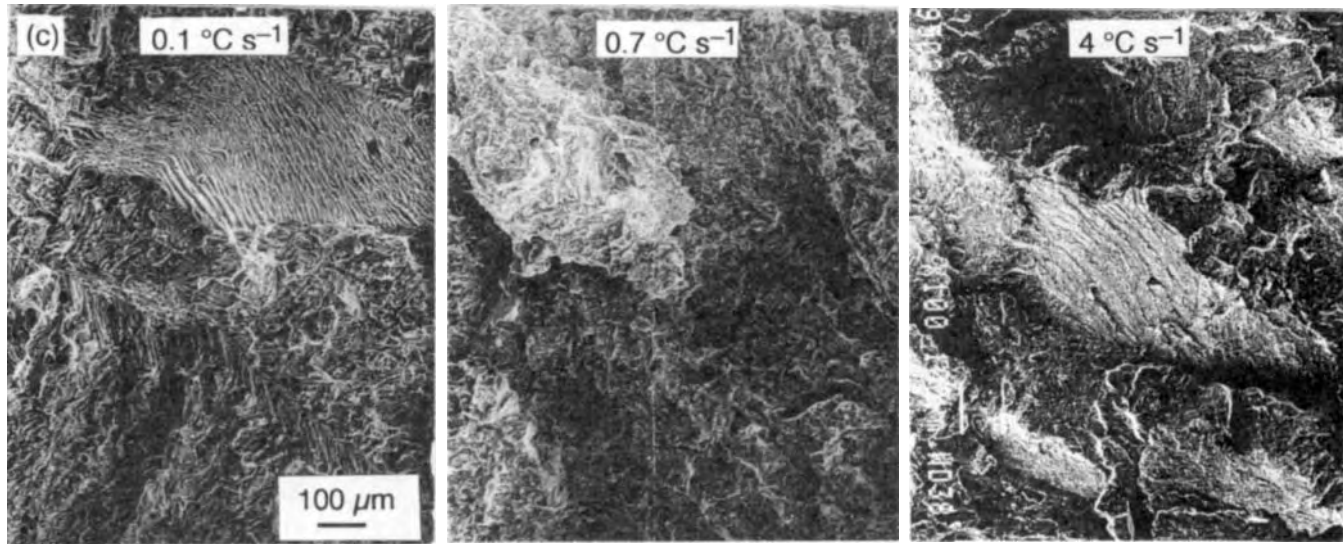
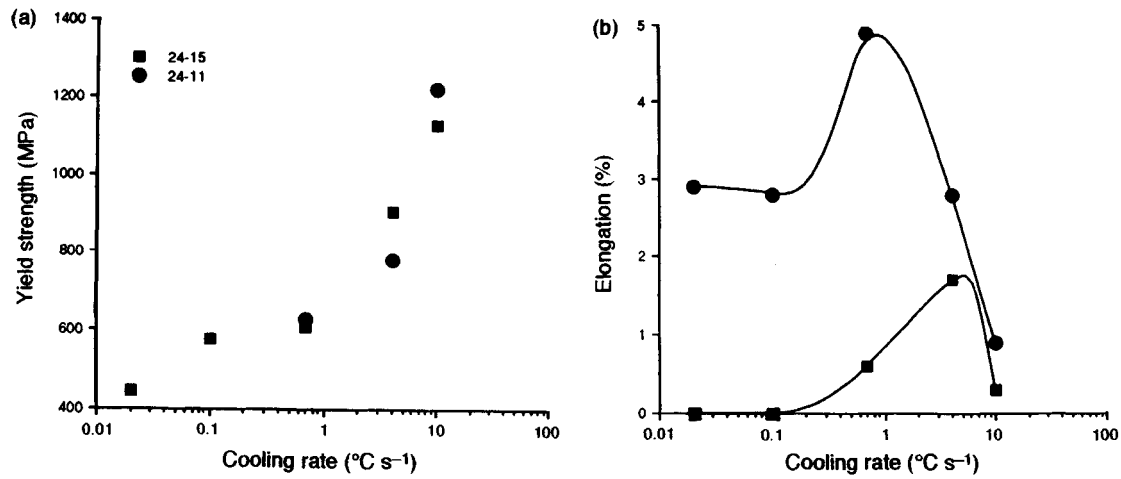


Figure 20. (a) Yield strength and (b) ductility of β heat treated Ti-25Al-11Nb and Ti-25Al-16Nb as a function of cooling rate. (c) Fractography of samples at different cooling rates in the Ti-25Al-16Nb alloy (from Gogia *et al.*, 1992)

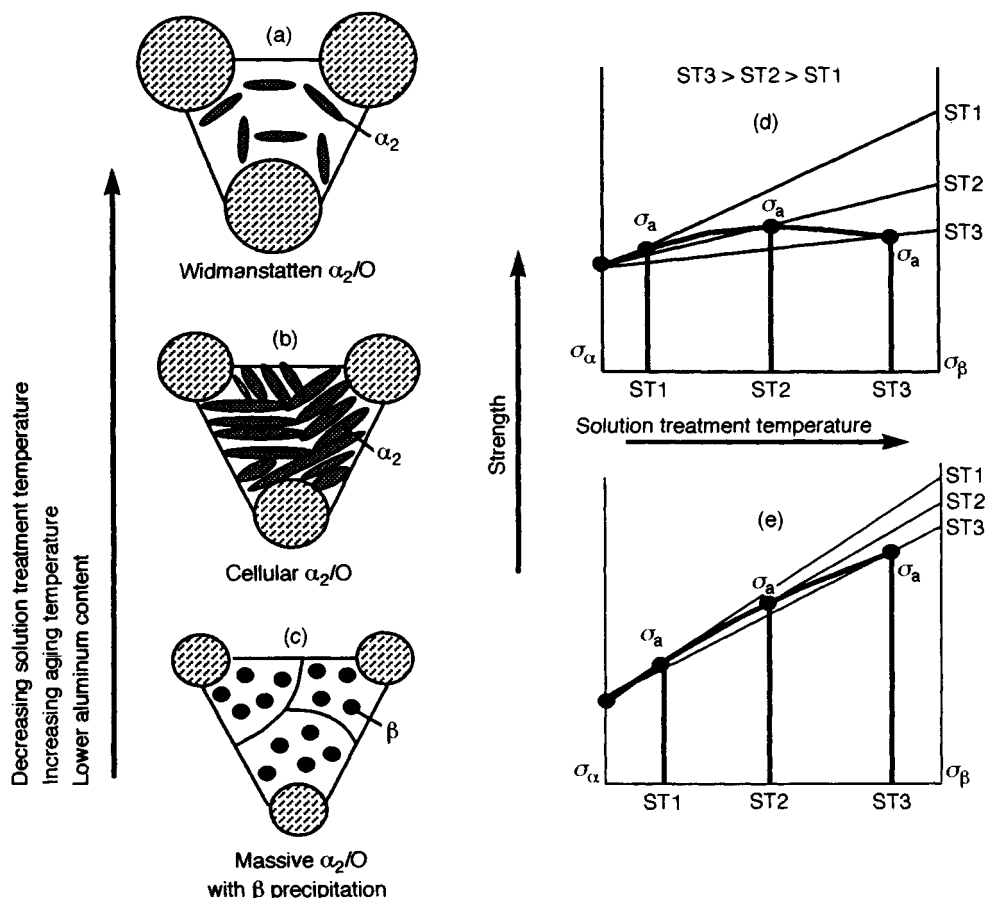


Figure 21. The effects of microstructure and heat treatment on the strength and ductility of duplex structures. (a–c) Transformation mechanisms which favor fine laths distributed in a continuous matrix of β promote high strength and ductility in the aged β constituent. Decreasing solution treatment temperatures promote β phase retention and the precipitation of lath structures through conventional precipitation mechanisms. (d,e) The application of the rule of mixtures $\sigma_a = \sigma_\alpha f_\alpha + \sigma_\beta f_\beta$ to understanding the effect of heat treatment on the strength of duplex structures. The alloy strength σ_a lies on the line joining σ_α and σ_β for any given solution treatment temperature. The thick line indicates the trend in σ_a as a function of solution treatment temperature

solution treatment and aging (Kumpfert *et al.*, 1991, 1992; Lutjering *et al.*, 1991).

4.4 Temperature, Strain Rate, Hydrogen Effects and Texture

Certain trends are common to the tensile behavior of all multiphase alloys. A broad plateau in yield stress exists to 650 °C. The ductility as measured by total elongation to failure rises significantly and then goes through a minimum beyond 500 °C (Figure 23). It has been demonstrated (Thompson 1991; Ward and Balsone, 1991) that the fracture stress for the multiphase alloys is independent of temperature to about 400 °C, in

agreement with ideas on stress-controlled cleavage, and therefore the initial rise in ductility is attributed to propagation resistance. The onset of decreasing ductility coincides with the incidence of environmentally induced surface cracking (Ward and Balsone, 1991; Balsone, 1988). The secondary rise in ductility beyond the minimum coincides with the yield stress drop and a change in fracture mode from cleavage to void nucleation at primary α_2 interfaces (Ward and Balsone, 1991). The ductility minimum is not reflected in a reduction of area, which rises uniformly with temperature; the secondary rise in ductility occurs only in total elongation and not in uniform elongation (Gogia *et al.*, 1991). The balance of the evidence therefore

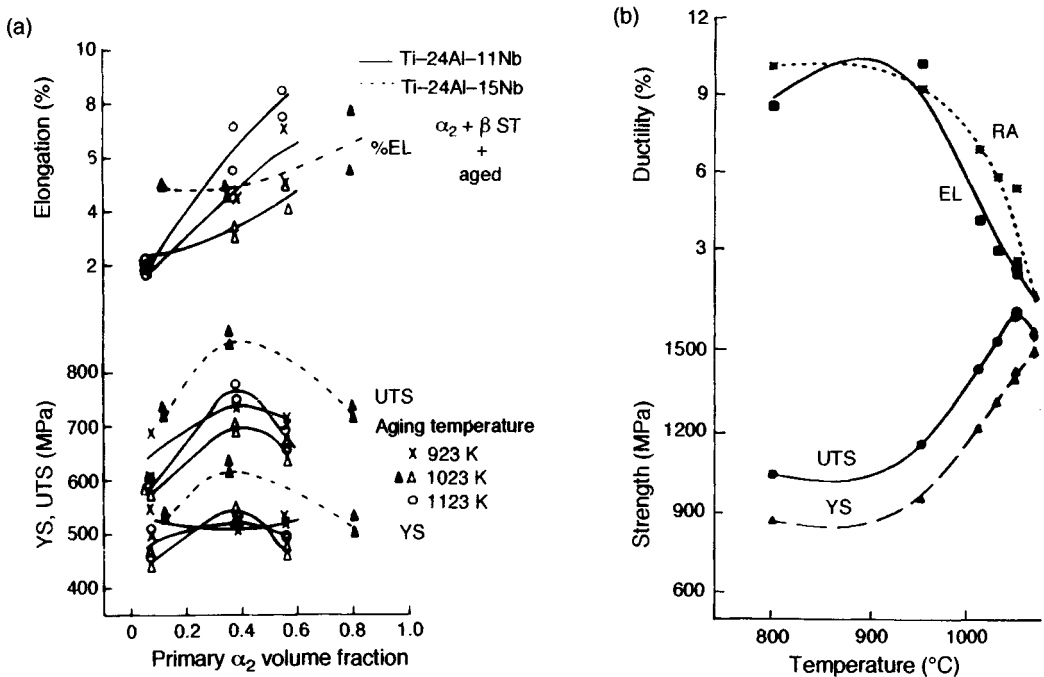


Figure 22. (a) Tensile properties as a function of equiaxed α_2 volume fraction and aging temperature in Ti-25Al-11Nb and Ti-25Al-16Nb (from Gogia *et al.*, 1992). (b) Yield strength as a function of solution treatment temperature in Ti-25Al-10Nb-3V-1Mo (after Kumpfert *et al.*, 1992). ST, solution treatment; El, elongation; RA, reduction in area; YS, yield strength; UTS, ultimate tensile strength

suggests that the ductility minimum is caused by an interaction between environmental effects and the variation of the intrinsic strain rate sensitivity of the material with temperature.

A transition to brittle behavior (the yield stress exceeding the fracture stress) has been observed with increasing strain rate at low temperatures, as shown in Figure 24. A similar transition is observed with increasing hydrogen content together with a smooth decrease in fracture toughness and a sustained-load cracking threshold (Thompson, 1991).

The issue of texture has received surprisingly less attention given that sheet applications of the α_2 alloys have been envisaged both in composite and monolithic form (Lipsitt, 1985; Larsen *et al.*, 1990). The most comprehensive studies on texture are those due to Hon *et al.* (1991a, b) who show that decreasing rolling temperatures and increasing reduction ratios both sharpen a (0001)(20 $\bar{2}$ 0) texture where the basal planes lie parallel to the rolling plane and (20 $\bar{2}$ 0) is along the rolling direction. Sharp basal textures are associated with low yield strengths and ductilities as high as 10% even in a Ti-25Al-10Nb alloy with very little

or no β phase (Hon *et al.*, 1991a), reflecting perhaps the greater ability of textured grains to accommodate grain boundary stress concentrations without the operation of five independent slip systems.

4.5 Summary

The overall picture that currently emerges of tensile behavior in α_2 -based alloys is that room-temperature behavior is consistent with effects related to the stress-controlled initiation of cleavage. The ability of the B2 phase at low volume fraction to impart ductility is directly related to its effect in increasing strain values at which the local critical stress for cleavage of α_2 is realized. Since the B2 phase also has a higher yield strength, it plays the dual role of ductilizing and strengthening α_2 , as shown in Figure 16. Increases in ductility with temperature or B2 content (beyond about 10%) arise from increasing resistance to microcrack propagation. A ductility minimum at around 550–650 $^{\circ}\text{C}$ is always observed. The systematics of this behavior require further definition. The behavior of two-phase O + B2 structures remains to be investigated in comparable detail.

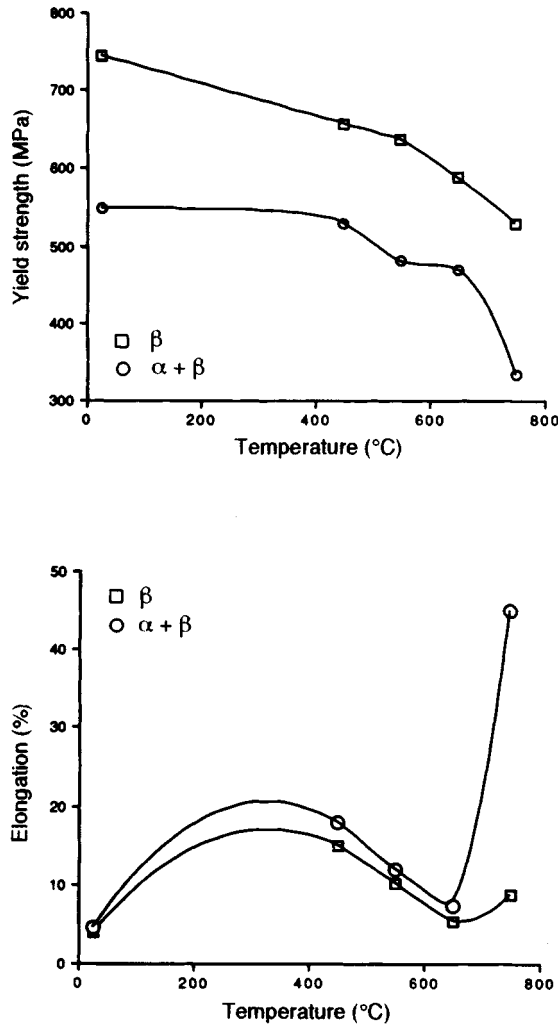


Figure 23. (a) Yield strength and (b) ductility of the Ti-25Al-16Nb alloy as a function of temperature for $\alpha + \beta$ duplex structures and β lath structures (from Gogia *et al.*, 1991)

5. Creep

While Figure 1 broadly indicates the level of stress rupture capability which can be attained by a range of Ti_3Al -based alloy compositions, a very large variability in steady-state creep rates and rupture lives with heat treatment and microstructure has been demonstrated in a variety of studies. This section is an overview of these results, separately for steady-state creep, stress rupture and primary creep.

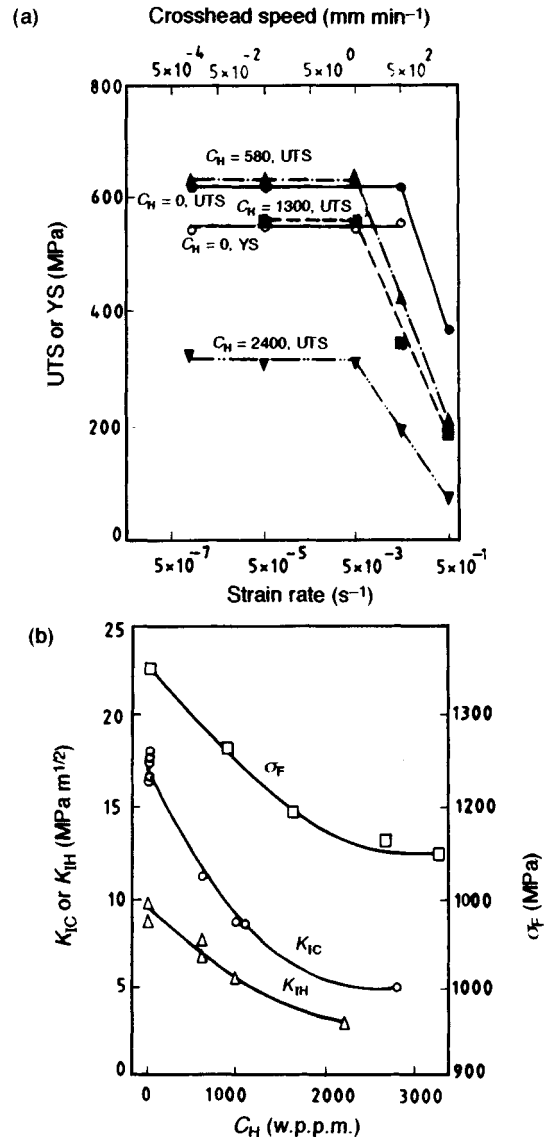


Figure 24. (a) Yield strength and fracture stress in Ti-24Al-11Nb at room temperature as a function of strain rate (after Thompson 1991). The hydrogen content is given in w.p.p.m. When fracture precedes yield, the stress is still designated as UTS. (b) Fracture strengths K_{IC} and K_{IH} as functions of hydrogen content in Ti-24Al-11Nb (after Thompson, 1991)

5.1 Steady-state Creep

The steady-state creep behavior in the temperature range 600–800 °C has been investigated in a variety of alloys following the original work on single-phase Ti_3Al by